East European Journal of Physics

East European Journal of Physics

East European Journal of Physics

ORIGINAL PAPERS

East European Journal of Physics

No 2.　　2021

POLYADIC HOPF ALGEBRAS AND QUANTUM GROUPS

Steven Duplij

WWU IT, Universität Münster, D-48149 Münster, Germany
E-mail: douplii@wwu.de, https://ivv5hpp.uni-muenster.de/u/douplii

This article continues the study of concrete algebra-like structures in our polyadic approach, where the arities of all operations are initially taken as arbitrary, but the relations between them, the arity shapes, are to be found from some natural conditions ("arity freedom principle"). In this way, generalized associative algebras, coassociative coalgebras, bialgebras and Hopf algebras are defined and investigated. They have many unusual features in comparison with the binary case. For instance, both the algebra and its underlying field can be zeroless and nonunital, the existence of the unit and counit is not obligatory, and the dimension of the algebra is not arbitrary, but "quantized". The polyadic convolution product and bialgebra can be defined, and when the algebra and coalgebra have unequal arities, the polyadic version of the antipode, the querantipode, has different properties. As a possible application to quantum group theory, we introduce the polyadic version of braidings, almost co-commutativity, quasitriangularity and the equations for the R-matrix (which can be treated as a polyadic analog of the Yang-Baxter equation). We propose another concept of deformation which is governed not by the twist map, but by the medial map, where only the latter is unique in the polyadic case. We present the corresponding braidings, almost co-mediality and M-matrix, for which the compatibility equations are found.

KEY WORDS: polyadic field, polyadic algebra, bialgebra, Hopf algebra, antipode, braid equation, braiding, R-matrix, Yang-Baxter equation, mediality, co-medaility, M-matrix, quasitriangularity

INTRODUCTION

Since Hopf algebras were introduced in connection with algebraic topology [1, 2], their role has increased significantly (see, e.g., [3]), with numerous applications in diverse areas, especially in relation to quantum groups [4–8]. There have been many generalizations of Hopf algebras (for a brief review, see, e.g., [9]).

From another perspective, the concepts of polyadic vector space, polyadic algebras and polyadic tensor product over general polyadic fields were introduced in [10]. They differ from the standard definitions of n-ary algebras [11–13] in considering an arbitrary arity shape for all operations, and not the algebra multiplication alone. This means that the arities of addition in the algebra, the multiplication and addition in the underlying field can all be different from binary and the number of places in the multiaction (polyadic module) can be more than one [14]. The connection between arities is determined by their arity shapes [10] ("arity freedom principle"). Note that our approach is somewhat different from the operad approach (see, e.g., [15, 16]).

Here we propose a similar and consequent polyadic generalization of Hopf algebras. First, we define polyadic coalgebras and study their homomorphisms and tensor products. In the construction of the polyadic convolution product and bialgebras we propose considering different arities for the algebra and coalgebra, which is a crucial difference from the binary case. Instead of the antipode, we introduce its polyadic version, the querantipode, by analogy with the querelement in n-ary groups [17]. We then consider polyadic analogs of braidings, almost co-commutativity and the R-matrix, together with the quasitriangularity equations. This description is not unique, as with the polyadic analog of the twist map, while the medial map is unique for all arities. Therefore, a new (unique) concept of deformation is proposed: almost co-mediality with the corresponding M-matrix. The medial analogs of braidings and quasitriangularity are introduced, and the equations for M-matrix are obtained.

POLYADIC FIELDS AND VECTOR SPACES

Let $\Bbbk = \Bbbk^{(m_k,n_k)} = \left\langle K \mid \nu_k^{(m_k)}, \mu_k^{(n_k)} \right\rangle$ be a polyadic or (m_k, n_k)-ary field with n_k-ary multiplication $\mu_k^{(n_k)}$: $K^{n_k} \to K$ and m_k-ary addition $\nu_k^{(m_k)}$: $K^{m_k} \to K$ which are (polyadically) associative and distributive, such that $\left\langle K \mid \mu^{(n_k)} \right\rangle$ and $\left\langle K \mid \nu^{(m_k)} \right\rangle$ are both commutative polyadic groups [18,19]. This means that $\mu_k^{(n_k)} = \mu_k^{(n_k)} \circ \tau_{n_k}$ and $\nu_k^{(m_k)} = \nu_k^{(m_k)} \circ \tau_{m_k}$, where $\tau_{n_k} \in S_{n_k}$, $\tau_{m_k} \in S_{m_k}$, and S_{n_k}, S_{m_k} are the symmetry permutation groups. A polyadic field $\Bbbk^{(m_k,n_k)}$ is *derived*, if $\mu_k^{(n_k)}$ and $\nu_k^{(m_k)}$ are iterations of the corresponding binary operations: ordinary multiplication and addition. The polyadic fields considered in [19] were derived. The simplest example of a nonderived $(2,3)$-ary field is $\Bbbk^{(2,3)} = \{i\mathbb{R}\}$, and of a nonderived $(3,3)$-ary field is $\Bbbk^{(3,3)} = \{ip/q\}$, where $p, q \in \mathbb{Z}^{odd}$ ($i^2 = -1$, and the operations are in $\mathbb{C}$). Polyadic analogs of prime Galois fields including nonderived ones were presented in [20].

Recall that a *polyadic zero* z in any $\langle X \mid \nu^{(m)} \rangle$ (with $\nu^{(m)}$ being an *addition-like* operation) is defined (if it exists) by

$$\nu^{(m)} [\hat{\boldsymbol{x}}, z] = z, \quad \forall \hat{\boldsymbol{x}} \in X^{m-1}, \tag{1}$$

where z can be on any place, and $\boldsymbol{x}$ is any *polyad* of length $m-1$ (as a sequence of elements) in X. A *polyadic unit* in any $\langle X \mid \mu^{(n)} \rangle$ (with μ being a *multiplication-like* operation) is an $e \in X$ (if it exists) such that

$$\mu^{(n)} \left[e^{n-1}, x \right] = x, \quad \forall x \in X, \tag{2}$$

where x can be on any place, and the repeated entries in a polyad are denoted by a power $\overbrace{x, \ldots, x}^{n} \equiv x^n$. It follows from (2), that for $n \geq 3$ the polyad $\boldsymbol{e}$ can play the role of a unit, and is called a neutral sequence [21]

$$\mu^{(n)} [\hat{\boldsymbol{e}}, x] = x, \quad \forall x \in X, \quad \hat{\boldsymbol{e}} \in X^{n-1}. \tag{3}$$

This is a crucial difference from the binary case, as the neutral sequence $\hat{\boldsymbol{e}}$ can (possibly) be nonunique.

The nonderived polyadic fields obey unusual properties: they can have several (polyadic) units or no units at all (*nonunital*, as in $\Bbbk^{(2,3)}$ and $\Bbbk^{(3,3)}$ above), no (polyadic) zeros (*zeroless*, as $\Bbbk^{(3,3)}$ above), or they can consist of units only (for some examples, see [20,22]). This may lead, in general, to new features of the algebraic structures using the polyadic fields as the underlying fields (e.g. scalars for vector spaces, etc.) [10].

Moreover, polyadic invertibility is not connected with units, but is governed by the special element, analogous to an inverse, the so called *querelement* $\bar{x}$, which for any $\langle X \mid \mu^{(n)} \rangle$ is defined by [17]

$$\mu^{(n)} \left[x^{n-1}, \bar{x} \right] = x, \quad \forall x \in X, \tag{4}$$

where $\bar{x}$ can be on any place (instead of the binary inverse "$xx^{-1} = e$"). An element $x \in X$ for which (4) has a solution under $\bar{x}$ is called *querable* or "polyadically invertible". If all elements in X are querable, and the operation $\mu^{(n)}$ is polyadically associative, then $\langle X \mid \mu^{(n)} \rangle$ is a *n*-ary group. *Polyadic associativity* in $\langle X \mid \mu^{(n)} \rangle$ can be defined as a kind of invariance relationship [14]

$$\mu^{(n)} \left[\hat{\boldsymbol{x}}, \mu^{(n)} [\hat{\boldsymbol{y}}], \hat{\boldsymbol{z}} \right] = invariant, \tag{5}$$

where $\hat{\boldsymbol{x}}, \hat{\boldsymbol{y}}, \hat{\boldsymbol{z}}$ are polyads of the needed size in X, and $\mu^{(n)} [\hat{\boldsymbol{y}}]$ can be on any place, and we therefore will not use additional brackets. Using polyadic associativity (5) we introduce *ℓ-iterated multiplication* by

$$\left(\mu^{(n)} \right)^{\circ \ell} [\hat{\boldsymbol{x}}] = \overbrace{\mu^{(n)}[\mu^{(n)}[\ldots \mu^{(n)}}^{\ell}[\hat{\boldsymbol{x}}]]], \quad \hat{\boldsymbol{x}} \in X^{\ell(n-1)+1}, \tag{6}$$

where ℓ is "number of multiplications". Therefore, the *admissible* length of any *n*-ary word is *not arbitrary*, as in the binary $n = 2$ case, but fixed ("quantized") to $\ell(n-1) + 1$.

Example 1. Consider the nonunital zeroless polyadic field $\Bbbk^{(3,3)} = \{ip/q\}$, $i^2 = -1$, $p, q \in \mathbb{Z}^{odd}$ (from the example above). Both the ternary addition $\nu^{(3)} [x, y, t] = x + y + t$ and the ternary multiplication $\mu^{(3)} [x, y, t] = xyt$ are nonderived, ternary associative and distributive. For each $x = ip/q$ $(p, q \in \mathbb{Z}^{odd})$ the *additive querelement* (denoted by a wave, a ternary analog of an inverse element with respect to addition) is $\tilde{x} = -ip/p'$, and the *multiplicative querelement* is $\bar{x} = -iq/p$ (see (4)). Therefore, both $\langle \{ip/q\} \mid \mu^{(3)} \rangle$ and $\langle \{ip/q\} \mid \nu^{(3)} \rangle$ are ternary groups (as it should be for a $(3, 3)$-field), but they contain *no neutral elements* (unit or zero).

The polyadic analogs of vector spaces and tensor products were introduced in [10]. Briefly, consider a set V of "polyadic vectors" with the addition-like m_v-ary operation $\nu_V^{(m_v)}$, such that $\langle V \mid \nu_v^{(m_v)} \rangle$ is a *commutative* m_v-ary group. The key differences from the binary case are: 1) The zero vector z_v does not necessarily exist (see the above example for $\Bbbk^{(3,3)}$ field); 2) The role of a negative vector is played by the additive querelement $\tilde{v}$ in $\langle V \mid \nu_V^{(m_v)} \rangle$ (which *does not* imply the existence of z_v). A polyadic analog of the binary multiplication by a scalar (λv) is the *multiaction* $\rho^{(r_\rho)}$ introduced in [14]

$$\rho_V^{(r_v)} : K^{r_v} \times V \to V. \tag{7}$$

If the unit e_k exists in $\Bbbk^{(m_k, n_k)}$, then the multiaction can be normalized (analog of "$1v = v$") by

$$\rho_V^{(r_v)} \left(e_k^{\times r_v} \mid v \right) = v, \quad v \in V. \tag{8}$$

Under the composition $\circ_{n_\rho}$ (given by the *arity changing formula* [14]), the set of multiactions form a n_ρ-ary semigroup $S_\rho^{(n_\rho)} = \left\langle \left\{ \rho_V^{(r_v)} \right\} \mid \circ_{n_\rho} \right\rangle$. Its arity is less or equal than n_k and depends on one integer parameter (the number of intact elements in the composition), which is less than $(r_v - 1)$ (for details see [10]).

A *polyadic vector space* over the polyadic field $\Bbbk^{(m_k, n_k)}$ is

$$V = V^{(m_v; m_k, n_k; r_\rho)} = \left\langle V, K \mid \nu_V^{(m_v)}; \nu_k^{(m_k)}, \mu_k^{(n_k)}; \rho_V^{(r_v)} \right\rangle, \tag{9}$$

where $\left\langle V \mid \nu_V^{(m_v)} \right\rangle$ is a commutative m_v-ary group, $\left\langle K \mid \mu_k^{(n_k)}, \nu_k^{(m_k)} \right\rangle$ is a polyadic field, $\left\langle \left\{ \rho_V^{(r_v)} \right\} \mid \circ_{n_\rho} \right\rangle$ is a n_ρ-ary semigroup, the multiaction $\rho^{(r_\rho)}$ is distributive with respect to the polyadic additions $\nu_V^{(m_v)}$, $\nu_k^{(m_k)}$ and compatible with $\mu_k^{(n_k)}$ (see (2.15), (2.16), and (2.9) in [10]). If instead of the underlying field, we consider a ring, then (9) define a *polyadic module* together with (7). The *dimension* d_v of a polyadic vector space is the number of elements in its polyadic basis, and we denote it $V_{d_v} = V_{d_v}^{(m_v; m_k, n_k; r_v)}$. The polyadic direct sum and polyadic tensor product of polyadic vector spaces were constructed in [10] (see (3.25) and (3.39) there). They have an unusual peculiarity (which is not possible in the binary case): the polyadic vector spaces of *different arities* can be added and multiplied. The polyadic tensor product is "$\Bbbk$-linear" in the usual sense, only instead of "multiplication by scalar" one uses the multiaction $\rho_V^{(r_v)}$ (see [10] for details). Because of associativity, we will use the *binary-like* notation for polyadic tensor products (implying $\otimes = \otimes_\Bbbk$) and powers of them (for instance, $\overbrace{x \otimes x \otimes \ldots \otimes x}^{n} = x^{\otimes n}$) to be clearer in computations and as customary in diagrams.

POLYADIC ASSOCIATIVE ALGEBRAS

Here we introduce operations on elements of a polyadic vector space, which leads to the notion of a polyadic algebra.

"Elementwise" description

Here we formulate the polyadic algebras in terms of sets and operations written in a manifest form. The arities will be initially taken as arbitrary, but then relations between them will follow from compatibility conditions (as in [10]).

Definition 2. A *polyadic (associative) algebra* (or $\Bbbk$-algebra) is a tuple consisting of 2 sets and 5 operations

$$A = A^{(m_a, n_a; m_k, n_k; r_a)} = \left\langle A, K \mid \nu_A^{(m_a)}, \mu_A^{(n_a)}; \nu_k^{(m_k)}, \mu_k^{(n_k)}; \rho_A^{(r_a)} \right\rangle, \tag{10}$$

where:

1. $\Bbbk^{(m_k, n_k)} = \left\langle K \mid \nu_k^{(m_k)}, \mu_k^{(n_k)} \right\rangle$ is a polyadic field with the m_k-ary *field (scalar) addition* $\nu_k^{(m_k)} : K^{m_k} \to K$ and n_k-ary *field (scalar) multiplication* $\mu_k^{(n_k)} : K^{m_k} \to K$;

2.
$$A_{vect} = A^{(m_a; m_k, n_k; r_a)} = \left\langle A, K \mid \nu_A^{(m_a)}; \nu_k^{(m_k)}, \mu_k^{(n_k)}; \rho_A^{(r_a)} \right\rangle \tag{11}$$

   is a polyadic vector space with the m_a-ary *vector addition* $\nu_A^{(m_a)} : A^{n_a} \to A$ and the r_a-*place multiaction* $\rho_A^{(r_a)} : K^{r_a} \times A \to A$;

3. The map $\mu_A^{(n_a)} : A^{n_a} \to A$ is a $\Bbbk$-linear map (*"vector multiplication"*) satisfying total associativity

$$\mu_A^{(n_a)} \left[\hat{\boldsymbol{a}}, \mu_A^{(n_a)} \left[\hat{\boldsymbol{b}} \right], \hat{\boldsymbol{c}} \right] = invariant, \tag{12}$$

   where the second product $\mu_A^{(n_a)}$ can be on any place in brackets and $\hat{\boldsymbol{a}}, \hat{\boldsymbol{b}}, \hat{\boldsymbol{c}}$ are polyads;

4. The multiacton $\rho_A^{(r_a)}$ is compatible with vector and field operations $\left(\nu_A^{(m_a)}, \mu_A^{(n_a)}; \nu_k^{(m_k)}, \mu_k^{(n_k)} \right)$.

Definition 3. We call the tuple $(m_a, n_a; m_k, n_k; r_a)$ an *arity shape* of the polyadic algebra A.

The compatibility of the multiaction $\rho_A^{(r_a)}$ (*"linearity"*) consists of [10, 14]:

1) Distributivity with respect to the m_a-ary vector addition $\nu_A^{(m_a)}$ ("$\lambda (a + b) = \lambda a + \lambda b$")

$$\rho_A^{(r_a)} \left\{ \lambda_1, \ldots \ldots, \lambda_{r_a} \mid \nu_A^{(m_a)} [a_1, \ldots, a_{m_a}] \right\}$$
$$= \nu_A^{(m_a)} \left[\rho_A^{(r_a)} \left\{ \lambda_1, \ldots \ldots, \lambda_{r_a} \mid a_1 \right\}, \ldots, \rho_A^{(r_a)} \left\{ \lambda_1, \ldots \ldots, \lambda_{r_a} \mid a_{m_a} \right\} \right]. \tag{13}$$

2) Compatibility with n_a-ary "vector multiplication" $\mu_A^{(n_a)}$ ("$(\lambda a) \cdot (\mu b) = (\lambda \mu)(a \cdot b)$")

$$\mu_A^{(n_a)} \left[\rho_A^{(r_a)} \left\{ \lambda_1, \ldots \ldots, \lambda_{r_a} \mid a_1 \right\}, \ldots, \rho_A^{(r_a)} \left\{ \lambda_{r_a(n_a-1)}, \ldots \ldots, \lambda_{r_a n_a} \mid a_{n_a} \right\} \right]$$

$$= \rho_A^{(r_a)} \left\{ \overbrace{\mu_k^{(n_k)} [\lambda_1, \ldots \ldots, \lambda_{m_k}], \ldots, \mu_k^{(n_k)} [\lambda_{m_k(\ell-1)}, \ldots \ldots, \lambda_{m_k \ell}]}^{\ell}, \right.$$

$$\left. \lambda_{m_k \ell+1}, \ldots \ldots, \lambda_{r_a n_a} \mid \mu_A^{(n_a)} [a_1, \ldots, a_{n_a}] \right\}, \tag{14}$$

$$\ell (n_k - 1) = r_a (n_a - 1), \tag{15}$$

where ℓ is an integer, and $\ell \leq r_a \leq \ell (n_k - 1)$, $2 \leq n_a \leq n_k$.

3) Distributivity with respect to the m_k-ary field addition $\nu_k^{(m_k)}$ ("$(\lambda + \mu) a = \lambda a + \mu a$")

$$\rho^{(r_a)} \left\{ \overbrace{\nu_k^{(m_k)} [\lambda_1, \ldots \ldots, \lambda_{m_k}], \ldots, \nu_k^{(m_k)} [\lambda_{m_k(\ell'-1)}, \ldots \ldots, \lambda_{m_k \ell'}]}^{\ell'}, \lambda_{m_k \ell'+1}, \ldots \ldots, \lambda_{r_a m_a} \mid a \right\}$$

$$= \nu_A^{(m_a)} \left[\rho^{(r_a)} \left\{ \lambda_1, \ldots \ldots, \lambda_{r_a} \mid a \right\}, \ldots, \rho^{(r_a)} \left\{ \lambda_{r_a(m_a-1)}, \ldots \ldots, \lambda_{r_a m_a} \mid a \right\} \right], \tag{16}$$

$$\ell' (m_k - 1) = r_a (m_a - 1), \tag{17}$$

where ℓ' is an integer, and $\ell' \leq r_a \leq \ell' (m_k - 1)$, $2 \leq m_a \leq m_k$.

4) Compatibility n_k-ary field multiplication $\mu_k^{(n_k)}$ ("$\lambda (\mu a) = (\lambda \mu) a$")

$$\rho_A^{(r_a)} \overbrace{\left\{ \lambda_1, \ldots \ldots, \lambda_{r_a} \mid \ldots \rho_A^{(r_a)} \left\{ \lambda_{r_a(n_\rho-1)}, \ldots \ldots, \lambda_{r_a n_\rho} \mid a \right\} \ldots \right\}}^{n_\rho}$$

$$= \rho_A^{(r_a)} \left\{ \overbrace{\mu_k^{(n_k)} [\lambda_1, \ldots \ldots, \lambda_{n_k}], \ldots, \mu_k^{(n_k)} [\lambda_{n_k(\ell''-1)}, \ldots \ldots, \lambda_{n_k \ell''}]}^{\ell''}, \lambda_{n_k \ell''+1}, \ldots \ldots, \lambda_{r_a n_\rho} \mid a \right\}, \tag{18}$$

$$\ell'' (n_k - 1) = r_a (n_\rho - 1), \tag{19}$$

where ℓ'' is an integer, and $\ell'' \leq r_a \leq \ell'' (n_k - 1)$, $2 \leq n_\rho \leq n_k$.

Remark 4. In the binary case, we have $m_a = n_a = m_k = n_k = n_\rho = 2$, $r_a = \ell = \ell' = \ell'' = 1$. The *n*-ary algebras [11, 12] have only one distinct arity $n_a = n$.

Definition 5. We call the triple (ℓ, ℓ', ℓ'') a ℓ-*arity shape* of the polyadic algebra A.

Proposition 6. *In the limiting ℓ-arity shapes the arity shape of A is determined by three integers(m, n, r), such that:*

1. *For the maximal $\ell = \ell' = \ell'' = r_a$, the arity shape of the algebra and underlying field coincide*

$$m_a = m_k = m, \tag{20}$$
$$n_a = n_k = n_\rho = n, \tag{21}$$
$$r_a = r. \tag{22}$$

2. *For the minimal ℓ-arities $\ell = \ell' = \ell'' = 1$ it should be $r_a | (m_k - 1)$ and $r_a | (n_k - 1)$, and*

$$m_a = 1 + \frac{m-1}{r}, \tag{23}$$

$$n_a = n_\rho = 1 + \frac{n-1}{r}, \tag{24}$$

$$m_k = m, \tag{25}$$

$$n_k = n, \tag{26}$$

$$r_a = r. \tag{27}$$

Proof. This follows directly from the compatibility conditions (14)–(18). ∎

Proposition 7. *If the multiaction $\rho_A^{(r_a)}$ is an ordinary action $K \times A \to A$, then all ℓ-arities are minimal $\ell = \ell' = \ell'' = 1$, and the arity shape of A is determined by two integers (m, n), such that the arities of the algebra and underlying field are equal, and the arity n_ρ of the action semigroup S_ρ is equal to the arity of multiplication in the underlying field*

$$m_a = m_k = m, \tag{28}$$

$$n_a = n_k = n_\rho = n. \tag{29}$$

As it was shown in [20], there exist zeroless and nonunital polyadic fields and rings. Therefore, the main difference with the binary algebras is the possible *absence* of a zero and/or unit in the polyadic field $\Bbbk^{(m_k, n_k)}$ and/or in the polyadic ring

$$A_{ring} = A^{(m_a, n_a)} = \left\langle A \mid \nu_A^{(m_a)}, \mu_A^{(n_a)} \right\rangle, \tag{30}$$

and so the additional axioms are needed iff such elements exist. This was the reason we have started from **Definition 2**, where no existence of zeroes and units in $\Bbbk^{(m_k, n_k)}$ and A_{ring} is implied.

If they exist, denote possible units and zeroes by $e_k \in \Bbbk^{(m_k, n_k)}$, $z_k \in \Bbbk^{(m_k, n_k)}$ and $e_A \in A^{(m_a, n_a)}$, $z_A \in A^{(m_a, n_a)}$. In this way we have 4 choices for each $\Bbbk^{(m_k, n_k)}$ and $A^{(m_a, n_a)}$, and these 16 possible kinds of polyadic algebras are presented in TABLE 1. The most exotic case is at the bottom right, where both $\Bbbk^{(m_k, n_k)}$ and $A^{(m_a, n_a)}$ are *zeroless nonunital*, which cannot exist in either binary algebras or n-ary algebras [11].

Table 1: Kinds of polyadic algebras depending on zeroes and units.

$\Bbbk^{(m_k,n_k)}$ \ $A^{(m_a,n_a)}$	z_A e_A	z_A no e_A	no z_A e_A	no z_A no e_A
z_k e_k	unital A unital $\Bbbk$	nonunital A unital $\Bbbk$	unital zeroless A unital $\Bbbk$	nonunital zeroless A unital $\Bbbk$
z_k no e_k	unital A nonunital $\Bbbk$	nonunital A nonunital $\Bbbk$	unital zeroless A nonunital $\Bbbk$	nonunital zeroless A nonunital $\Bbbk$
no z_k e_k	unital A unital zeroless $\Bbbk$	nonunital A unital zeroless $\Bbbk$	unital zeroless A unital zeroless $\Bbbk$	nonunital zeroless A unital zeroless $\Bbbk$
no z_k no e_k	unital A nonunital zeroless $\Bbbk$	nonunital A nonunital zeroless $\Bbbk$	unital zeroless A nonunital zeroless $\Bbbk$	nonunital zeroless A nonunital zeroless $\Bbbk$

The standard case is that in the upper left corner, when both $\Bbbk^{(m_k, n_k)}$ and $A^{(m_a, n_a)}$ have a zero and unit. *Example* 8. Consider the ("$\Bbbk$-linear") associative polyadic algebra $A^{(3,3;3,3;2)}$ over the zeroless nonunital $(3, 3)$-field $\Bbbk^{(3,3)}$ (from *Example* 1). The elements of A are pairs $a = (\lambda, \lambda') \in \Bbbk^{(3,3)} \times \Bbbk^{(3,3)}$, and for them the ternary addition and ternary multiplication are defined by

$$\mu_A^{(3)} [(\lambda_1, \lambda_1')(\lambda_2, \lambda_2')(\lambda_3, \lambda_3')] = (\lambda_1 \lambda_2' \lambda_3, \lambda_1' \lambda_2 \lambda_3'), \tag{31}$$

$$\nu_A^{(3)} [(\lambda_1, \lambda_1')(\lambda_2, \lambda_2')(\lambda_3, \lambda_3')] = (\lambda_1 + \lambda_2 + \lambda_3, \lambda_1' + \lambda_2' + \lambda_3'), \quad \lambda_i, \lambda_i' \in \Bbbk^{(3,3)} \tag{32}$$

where operations on the r.h.s. are in $\mathbb{C}$. If we introduce an element $0 \notin \Bbbk^{(3,3)}$ with the property $0 \cdot \lambda = \lambda \cdot 0 = 0$, then (31)–(32) can be presented as the ordinary multiplication and addition of three anti-diagonal 2×2 formal matrices $\begin{pmatrix} 0 & \lambda \\ \lambda' & 0 \end{pmatrix}$. There is no unit or zero in the ternary ring $\left\langle A \mid \nu_A^{(3)}, \mu_A^{(3)} \right\rangle$, but both $\left\langle A \mid \mu_A^{(3)} \right\rangle$ and $\left\langle A \mid \nu_A^{(3)} \right\rangle$ are ternary groups, because each $a = (ip/q, ip'/q') \in A$ has the *unique* additive querelement $\tilde{a} = (-ip/q, -ip'/q')$ and the unique multiplicative querelement $\bar{a} = (-iq'/p', -iq/p)$. The 2-place action ("2-scalar product") is defined by $\rho^{(2)}(\lambda_1, \lambda_2 \mid (\lambda, \lambda')) = (\lambda_1 \lambda_2 \lambda, \lambda_1 \lambda_2 \lambda')$. The arity shape (see *Definition* 5) of this *zeroless nonunital* polyadic algebra $A^{(3,3;3,3;2)}$ is $(2, 2, 2)$, and the compatibilities (13)–(19) hold.

Polyadic analog of the functions on group

In the search for a polyadic version of the algebra of $\Bbbk$-valued functions (which is isomorphic and dual to the corresponding group algebra) we can not only have more complicated arity shapes than in the binary case, but also the exotic possibility that the arities of the field and group are different as can be possible for multiplace functions.

Let us consider a n_g-ary group $G = G^{(n_g)} = \left\langle G \mid \mu_g^{(n_g)} \right\rangle$, which does not necessarily contain the identity e_g, and where each element is querable (see (4)). Now we introduce the set A_f of multiplace (s-place) functions $f_i(g_1, \ldots, g_s)$ (of finite support) which take value in the polyadic field $\Bbbk^{(m_k, n_k)}$ such that $f_i : G^s \to K$. To endow A_f with the structure of a polyadic associative algebra (10), we should consistently define the m_k-ary addition $\nu_f^{(m_k)} : A_f^{(m_k)} \to A_f$, n_k-ary multiplication ("convolution") $\mu_f^{(n_k)} : A_f^{(n_k)} \to A_f$ and the multiaction $\rho_f^{(r_f)} : K^{r_f} \times A_f \to A_f$ ("scalar multiplication"). Thus we write for the algebra of $\Bbbk$-valued functions

$$F_\Bbbk(G) = \left\langle A_f \mid \nu_f^{(m_k)}, \mu_f^{(n_k)}; \nu_k^{(m_k)}, \mu_k^{(n_k)}; \rho_f^{(r_f)} \right\rangle. \tag{33}$$

The simplest operation here is the addition of the $\Bbbk$-valued functions which, obviously, coincides with the field addition $\nu_f^{(m_k)} = \nu_k^{(m_k)}$.

Construction 9. Because all arguments of the multiaction $\rho_f^{(r_f)}$ are in the field, the only possibility for the r.h.s. is its multiplication (similar to the regular representation)

$$\rho_f^{(r_f)}\left(\lambda_1, \ldots, \lambda_{r_f} \mid f\right) = \mu_k^{(n_k)}\left[\lambda_1, \ldots, \lambda_{r_f}, f\right], \quad \lambda_i \in K, \quad f \in A_f, \tag{34}$$

and in addition we have the arity shape relation

$$n_k = r_f + 1, \tag{35}$$

which is satisfied "automatically" in the binary case.

The polyadic analog of $\Bbbk$-valued function convolution ("$(f_1 * f_2)(g) = \Sigma_{h_1 h_2 = g} f_1(h_1) f_2(h_2)$"), which is denoted by $\mu_f^{(n_k)}$ here, while the sum in the field is $\nu_k^{\ell_\nu(m_k-1)+1}$, where ℓ_ν is the "number of additions", can be constructed according to the arity rules from [10, 14].

Definition 10. The *polyadic convolution* of s-place $\Bbbk$-valued functions is defined as the admissible polyadic sum of $\ell_\nu(m_k - 1) + 1$ products

$$\mu_f^{(n_k)}\left[f_1(g_1, \ldots, g_s), \ldots, f_{n_k}(g_1, \ldots, g_s)\right] =$$
$$\left(\nu_k^{(m_k)}\right)^{\circ \ell_\nu} \left[\mu_k^{(n_k)}\left[f_1(h_1, \ldots, h_s), \ldots, f_{n_k}\left(h_{s(n_k-1)}, \ldots, h_{sn_k}\right)\right]\right], \tag{36}$$
$$\begin{cases} \mu_g^{(n_g)}[h_1, \ldots, h_{n_g}] = g_1, \\ \mu_g^{(n_g)}[h_{n_g+1}, \ldots, h_{2n_g}] = g_2, \\ \quad \vdots \\ \mu_g^{(n_g)}\left[h_{(s-\ell_{\mathrm{id}}-1)n_g}, \ldots, h_{(s-\ell_{\mathrm{id}})n_g}\right] = g_{s-\ell_{\mathrm{id}}}, \\ \quad h_{(s-\ell_{\mathrm{id}}+1)n_g} = g_{s-\ell_{\mathrm{id}}+1}, \\ \quad \vdots \\ \quad h_{sn_g} = g_s \end{cases}$$

where ℓ_{id} is the number of intact elements in the determining equations ("$h_1 h_2 = g$") under the field sum ν_k. The arity shape is determined by

$$sn_k = (s - \ell_{\mathrm{id}}) n_g + \ell_{\mathrm{id}}, \tag{37}$$

which gives the connection between the field and the group arities.

Example 11. If $n_g = 3$, $n_k = 2$, $m_k = 3$, $s = 2$, $\ell_{\mathrm{id}} = 1$, then we obtain the arity changing polyadic convolution

$$\mu_f^{(2)}\left[f_1(g_1, g_2), f_2(g_1, g_2)\right] =$$
$$\left(\nu_k^{(3)}\right)^{\circ \ell_\nu} \left[\mu_k^{(2)}\left[f_1(h_1, h_2), f_2(h_3, h_4)\right]\right], \tag{38}$$
$$\begin{cases} \mu_g^{(3)}[h_1, h_2, h_3] = g_1, \\ \mu_g^{(4)} = g_2 \end{cases}$$

where the ℓ_ν ternary additions are taken on the support. Now the multiaction (34) is one-place

$$\rho_f^{(1)}(\lambda \mid f) = \mu_k^{(2)}[\lambda, f], \quad \lambda \in K, \quad f \in A_f, \tag{39}$$

as it follows from (35).

Remark 12. The general polyadic convolution (36) is inspired by the main heteromorphism equation (5.14) and the arity changing formula (5.15) of [14]. The graphical dependence of the field arity n_k on the number of places s is similar to that on FIGURE 1, and the "quantization" rules (following from the solutions of (37) in integers) are in TABLE 1 there.

Proposition 13. *The multiplication* (36) *is associative.*

Proof. This follows from the associativity quiver technique of [14] applied to the polyadic convolution. ∎

Corollary 14. The $\Bbbk$-valued multiplace functions $\{f_i\}$ form a polyadic associative algebra $F_\Bbbk(G)$.

"Diagrammatic" description

Here we formulate the polyadic algebra axioms in the more customary "diagrammatic" form using the polyadic tensor products and mappings between them (denoted by bold corresponding letters). Informally, the $\Bbbk$-linearity is already "automatically encoded" by the polyadic tensor algebra over $\Bbbk$, and therefore the axioms already contain the algebra multiplication (but not the scalar multiplication).

Let us denote the $\Bbbk$-*linear algebra multiplication map* by $\boldsymbol{\mu}^{(n)}$ ($\boldsymbol{\mu}^{(n)} \equiv \mu_A^{(n_a)}$ from (10)) defined as

$$\boldsymbol{\mu}^{(n)} \circ (a_1 \otimes \ldots \otimes a_n) = \mu^{(n)}[a_1, \ldots, a_n], \quad a_1, \ldots, a_n \in A. \tag{40}$$

Definition 15 (*Algebra associativity axiom*). A *polyadic (associative n-ary) algebra* (or $\Bbbk$-algebra) is a vector space A_{vect} over the polyadic field $\Bbbk$ (11) with the $\Bbbk$-linear algebra multiplication map

$$A^{(n)} = \left\langle A_{vect} \mid \boldsymbol{\mu}^{(n)} \right\rangle, \qquad \boldsymbol{\mu}^{(n)} : A^{\otimes n} \to A, \tag{41}$$

which is totally associative

$$\boldsymbol{\mu}^{(n)} \circ \left(\mathrm{id}_A^{\otimes(n-1-i)} \otimes \boldsymbol{\mu}^{(n)} \otimes \mathrm{id}_A^{\otimes i}\right) = \boldsymbol{\mu}^{(n)} \circ \left(\mathrm{id}_A^{\otimes(n-1-j)} \otimes \boldsymbol{\mu}^{(n)} \otimes \mathrm{id}_A^{\otimes j}\right),$$
$$\forall i,j = 0, \ldots n-1, \ i \neq j, \ \mathrm{id}_A : A \to A, \tag{42}$$

such that the diagram

$$\begin{array}{ccc}
A^{\otimes(2n-1)} & \xrightarrow{\mathrm{id}_A^{\otimes(n-1-i)} \otimes \boldsymbol{\mu}^{(n)} \otimes \mathrm{id}_A^{\otimes i}} & A^{\otimes n} \\
{\scriptstyle \mathrm{id}_A^{\otimes(n-1-j)} \otimes \boldsymbol{\mu}^{(n)} \otimes \mathrm{id}_A^{\otimes j}} \downarrow & & \downarrow {\scriptstyle \boldsymbol{\mu}^{(n)}} \\
A^{\otimes n} & \xrightarrow{\boldsymbol{\mu}^{(n)}} & A
\end{array} \tag{43}$$

commutes.

Definition 16. A polyadic algebra $A^{(n)}$ is called *totally commutative*, if

$$\boldsymbol{\mu}^{(n)} = \boldsymbol{\mu}^{(n)} \circ \boldsymbol{\tau}_n, \tag{44}$$

where $\boldsymbol{\tau}_n \in S_n$, and S_n is the symmetry permutation group on n elements.

Remark 17. Initially, there are no other axioms in the definition of a polyadic algebra, because polyadic fields and vector spaces do not necessarily contain zeroes and units (see TABLE 1).

A special kind of polyadic algebra can appear, when the multiplication is "iterated" from lower arity ones, which is one of 3 kinds of arity changing for polyadic systems [14].

Definition 18. A polyadic multiplication is called *derived*, if the map $\boldsymbol{\mu}_{der}^{(n)}$ is ℓ_μ-iterated from the maps $\boldsymbol{\mu}_0^{(n_0)}$ of lower arity $n_0 < n$

$$\boldsymbol{\mu}_{der}^{(n)} = \overbrace{\boldsymbol{\mu}_0^{(n_0)} \circ \left(\boldsymbol{\mu}_0^{(n_0)} \circ \ldots \left(\boldsymbol{\mu}_0^{(n_0)} \otimes \mathrm{id}^{\otimes(n_0-1)}\right) \otimes \ldots \otimes \mathrm{id}^{\otimes(n_0-1)}\right)}^{\ell_\mu}, \tag{45}$$

where

$$n = \ell_\mu(n_0 - 1) + 1, \quad \ell_\mu \geq 2, \tag{46}$$

and ℓ_μ is the "number of iterations".

Example 19. In the ternary case $n = 3$ and $n_0 = 2$, we have $\boldsymbol{\mu}_{der}^{(3)} = \boldsymbol{\mu}_0^{(2)} \circ \left(\boldsymbol{\mu}_0^{(2)} \otimes \mathrm{id} \right)$, which in the "elementwise" description is $[a_1, a_2, a_3]_{der} = a_1 \cdot (a_2 \cdot a_3)$, where $\mu_{der}^{(3)} = [\,,\,,\,]_{der}$ and $\mu_0^{(2)} = (\cdot)$.

Introduce a $\Bbbk$-linear *multiaction map* $\boldsymbol{\rho}^{(r)}$ corresponding to the multiaction $\rho^{(r)} \equiv \rho_A^{(r_a)}$ (7) (by analogy with (40)) as

$$\boldsymbol{\rho}^{(r)} \circ (\lambda_1 \otimes \ldots \otimes \lambda_r \otimes a) = \rho^{(r)} (\lambda_1, \ldots, \lambda_r \mid a), \quad \lambda_1, \ldots, \lambda_r \in K, \; a \in A. \tag{47}$$

Let $\Bbbk$ and $A^{(n)}$ both be unital, then we can construct a $\Bbbk$-linear *polyadic unit map* $\boldsymbol{\eta}$ by "polyadizing" "$\mu \circ (\eta \otimes \mathrm{id}) = \mathrm{id}$" and the scalar product "$\lambda a = \rho (\lambda \mid a) = \eta (\lambda) a$" with "$\eta (e_k) = e_a$", using the normalization (8), and taking into account the standard identification $\Bbbk^{\otimes r} \otimes A \cong A$ [23].

Definition 20 (*Algebra unit axiom*). The *unital polyadic algebra* $A^{(n)}$ (41) contains in addition a $\Bbbk$-linear *polyadic (right) unit* map $\boldsymbol{\eta}^{(r,n)} : K^{\otimes r} \to A^{\otimes(n-1)}$ satisfying

$$\boldsymbol{\mu}^{(n)} \circ \left(\boldsymbol{\eta}^{(r,n)} \otimes \mathrm{id}_A \right) = \boldsymbol{\rho}^{(r)}, \tag{48}$$

such that the diagram

$$
\begin{array}{ccc}
K^{\otimes r} \otimes A & \xrightarrow{\boldsymbol{\eta}^{(r,n)} \otimes \mathrm{id}_A} & A^{\otimes n} \\
{\scriptstyle \boldsymbol{\rho}^{(r)}} \downarrow & \swarrow {\scriptstyle \boldsymbol{\mu}^{(n)}} & \\
A & &
\end{array}
\tag{49}
$$

commutes.

The normalization of the multiaction (8) gives the corresponding normalization of the map $\boldsymbol{\eta}^{(r,n)}$ (instead of "$\eta (e_k) = e_a$")

$$\boldsymbol{\eta}^{(r,n)} \circ \left(\overbrace{e_k \otimes \ldots \otimes e_k}^{r} \right) = \overbrace{e_a \otimes \ldots \otimes e_a}^{n-1}. \tag{50}$$

Assertion 21. *In the "elementwise" description the polyadic unit $\eta^{(r,n)}$ of $A^{(n)}$ is a $(n-1)$-valued function of r arguments.*

Proposition 22. *The polyadic unit map $\boldsymbol{\eta}^{(r,n)}$ is (polyadically) multiplicative in the following sense*

$$\overbrace{\boldsymbol{\mu}^{(n)} \circ \ldots \circ \boldsymbol{\mu}^{(n)}}^{r} \circ \left(\overbrace{\boldsymbol{\eta}^{(r,n)} \otimes \ldots \otimes \boldsymbol{\eta}^{(r,n)}}^{r(n-1)+1} \right) = \boldsymbol{\eta}^{(r,n)} \circ \left(\mu_k^{(n_k)} \right)^{\circ \ell}. \tag{51}$$

Proof. This follows from the compatibility of the multiaction with the "vector multiplication" (14) and the relation between corresponding arities (15), such that the number of arguments ("scalars" λ_i) in r.h.s. becomes $\ell (n_k - 1) + 1 = r (n - 1) + 1$, where ℓ is an integer. ∎

Introduce a "derived" version of the polyadic unit by analogy with the neutral sequence (3).

Definition 23. The $\Bbbk$-linear *derived polyadic unit* (*neutral unit sequence*) of n-ary algebra $A^{(n)}$ is the set $\hat{\boldsymbol{\eta}}^{(r)} = \left\{ \boldsymbol{\eta}_i^{(r)} \right\}$ of $n - 1$ maps $\boldsymbol{\eta}_i^{(r)} : K^{\otimes r} \to A$, $i = 1, \ldots, n-1$, satisfying

$$\boldsymbol{\mu}^{(n)} \circ \left(\boldsymbol{\eta}_1^{(r)} \otimes \ldots \otimes \boldsymbol{\eta}_{n-1}^{(r)} \otimes \mathrm{id}_A \right) = \boldsymbol{\rho}^{(r)}, \tag{52}$$

where id_A can be on any place. If $\boldsymbol{\eta}_1^{(r)} = \ldots = \boldsymbol{\eta}_{n-1}^{(r)} = \boldsymbol{\eta}_0^{(r)}$, we call $\boldsymbol{\eta}_0^{(r)}$ the *strong derived polyadic unit*. Formally (comparing (48) and (52)), we can write

$$\boldsymbol{\eta}_{der}^{(r,n)} = \boldsymbol{\eta}_1^{(r)} \otimes \ldots \otimes \boldsymbol{\eta}_{n-1}^{(r)}. \tag{53}$$

The normalization of the maps $\boldsymbol{\eta}_i^{(r)}$ is given by

$$\boldsymbol{\eta}_i^{(r)} \circ \left(\overbrace{e_k \otimes \ldots \otimes e_k}^{r} \right) = e_a, \quad i = 1, \ldots, n-1, \; e_a \in A, \; e_k \in K, \tag{54}$$

and in the "elementwise" description $\eta_i^{(r)}$ is a function of r arguments, satisfying

$$\eta_i^{(r)} (\lambda_1, \ldots, \lambda_r) = \rho^{(r)} \{\lambda_1, \ldots, \lambda_r \mid e_a\}, \quad \lambda_i \in K, \tag{55}$$

where $\rho^{(r)}$ is the multiaction (7).

Definition 24. A polyadic associative algebra $A_{der}^{(n)} = \left\langle A_{vect} \mid \boldsymbol{\mu}_{der}^{(n)}, \boldsymbol{\eta}_{der}^{(r,n)} \right\rangle$ is called *derived from* $A_0^{(n_0)} = \left\langle A_{vect} \mid \boldsymbol{\mu}_0^{(n_0)}, \boldsymbol{\eta}_0^{(r,n_0)} \right\rangle$, if (45) holds and further

$$\boldsymbol{\eta}_{der}^{(r,n)} = \overbrace{\boldsymbol{\eta}_0^{(r,n_0)} \otimes \ldots \otimes \boldsymbol{\eta}_0^{(r,n_0)}}^{\ell_\mu} \tag{56}$$

is true, where $\boldsymbol{\eta}_0^{(r,n_0)} = \overbrace{\boldsymbol{\eta}_0^{(r)} \otimes \ldots \otimes \boldsymbol{\eta}_0^{(r)}}^{n_0-1}$ (formally, because id_A in (52) can be on any place).

The particular case $n = 3$ and $r = 1$ was considered in [24, 25] (with examples).

Invertibility in a polyadic algebra is not connected with the unit or zero (as in n-ary groups [17]), but is determined by the querelement (4). Introduce the corresponding mappings for the subsets of the *additively querable elements* $A_{quer}^{(add)} \subseteq A$ and the *multiplicatively querable elements* $A_{quer}^{(mult)} \subseteq A$.

Definition 25. In the polyadic algebra $A^{(m,n)}$, the *additive quermap* $\boldsymbol{q}_{add} : A_{quer}^{(add)} \to A_{quer}^{(add)}$ is defined by

$$\boldsymbol{\nu}^{(m)} \circ \left(\mathrm{id}_A^{\otimes(m-1)} \otimes \boldsymbol{q}_{add} \right) \circ \boldsymbol{D}_a^{(m)} = \mathrm{id}_A, \tag{57}$$

and the *multiplicative quermap* $\boldsymbol{q}_{mult} : A_{quer}^{(mult)} \to A_{quer}^{(mult)}$ is defined by

$$\boldsymbol{\mu}^{(n)} \circ \left(\mathrm{id}_A^{\otimes(n-1)} \otimes \boldsymbol{q}_{mult} \right) \circ \boldsymbol{D}_a^{(n)} = \mathrm{id}_A, \tag{58}$$

where $\boldsymbol{D}_a^{(n)} : A \to A^{\otimes n}$ is the diagonal map given by $a \to \overbrace{a \otimes \ldots \otimes a}^{n}$, while $\boldsymbol{q}_{add}$ and $\boldsymbol{q}_{mult}$ can be on any place. They send an element to the additive querelement $a \overset{\boldsymbol{q}_{add}}{\mapsto} \tilde{a}$, $a \in A_{quer}^{(add)} \subseteq A$ and multiplicative querelement $a \overset{\boldsymbol{q}_{mult}}{\mapsto} \bar{a}$, $a \in A_{quer}^{(mult)} \subseteq A$ (see (4)), such that the diagrams

$$\begin{array}{ccc}
A & \xrightarrow{\boldsymbol{D}_a^{(m)}} & A^{\otimes m} \\
\boldsymbol{\nu}^{(m)} \uparrow & \swarrow{\scriptstyle \mathrm{id}_A^{\otimes(m-1)} \otimes \boldsymbol{q}_{add}} & \\
A^{\otimes m} & &
\end{array}
\qquad
\begin{array}{ccc}
A & \xrightarrow{\boldsymbol{D}_a^{(n)}} & A^{\otimes n} \\
\boldsymbol{\mu}^{(n)} \uparrow & \swarrow{\scriptstyle \mathrm{id}_A^{\otimes(n-1)} \otimes \boldsymbol{q}_{mult}} & \\
A^{\otimes n} & &
\end{array} \tag{59}$$

commute.

Example 26. For the polyadic algebra $A^{(3,3;3,3;2)}$ from *Example* 8 all elements are additively and multiplicatively querable, and so the sets of querable elements coincide $A_{quer}^{(add)} = A_{quer}^{(mult)} = A$. The additive quermap $\boldsymbol{q}_{add}$ and multiplicative quermap $\boldsymbol{q}_{mult}$ act as follows (the operations are in $\mathbb{C}$)

$$\left(i\frac{p}{q}, i\frac{p'}{q'} \right) \overset{\boldsymbol{q}_{add}}{\mapsto} \left(-i\frac{p}{q}, -i\frac{p'}{q'} \right), \tag{60}$$

$$\left(i\frac{p}{q}, i\frac{p'}{q'} \right) \overset{\boldsymbol{q}_{mult}}{\mapsto} \left(-i\frac{q'}{p'}, -i\frac{q}{p} \right), \quad i^2 = -1, \quad p, q \in \mathbb{Z}^{odd}. \tag{61}$$

Example 27. The polyadic field $\Bbbk^{(m_k,n_k)}$ is a polyadic algebra over itself. We identify $A = K$, $\mu_A^{(n)} = \mu_k^{(n_k)}$, and the multiplication is defined by the multiaction as

$$\boldsymbol{\mu}^{(n)} \circ (\lambda_1 \otimes \ldots \otimes \lambda_r \otimes \lambda) = \rho^{(r)} (\lambda_1, \ldots, \lambda_r \mid \lambda). \tag{62}$$

Therefore, we have the additional arity conditions

$$n = r + 1 = n_k, \tag{63}$$

which are trivially satisfied in the binary case. Now the polyadic unit map $\boldsymbol{\eta}^{(r,n)}$ (50) is the identity in each tensor component.

Medial map and polyadic permutations

Recall that the *binary medial map* for the tensor product of algebras (as vector spaces)

$$\boldsymbol{\tau}_{medial} : (A_1 \otimes A_2) \otimes (A_1 \otimes A_2) \to (A_1 \otimes A_1) \otimes (A_2 \otimes A_2) \tag{64}$$

is defined by (evaluation)

$$\left(a_1^{(1)} \otimes a_1^{(2)}\right) \otimes \left(a_2^{(1)} \otimes a_2^{(2)}\right) \overset{\tau_{medial}}{\mapsto} \left(a_1^{(1)} \otimes a_2^{(1)}\right) \otimes \left(a_1^{(2)} \otimes a_2^{(2)}\right). \tag{65}$$

It is obvious that

$$\boldsymbol{\tau}_{medial} = \mathrm{id}_A \otimes \boldsymbol{\tau}_{op} \otimes \mathrm{id}_A, \tag{66}$$

where $\boldsymbol{\tau}_{op} : A_1 \otimes A_2 \to A_1 \otimes A_2$ is the permutation of 2 elements (twist/flip) of the tensor product, such that $a^{(1)} \otimes a^{(2)} \overset{\tau_{op}}{\mapsto} a^{(2)} \otimes a^{(1)}$, $a^{(1)} \in A_1$, $a^{(2)} \in A_2$, $\tau_{op} \in S_2$. This may be presented (65) in the matrix form

$$\bigotimes (\boldsymbol{a})_{2\times2} \overset{\tau_{medial}}{\mapsto} \bigotimes (\boldsymbol{a}^T)_{2\times2}, \quad \bigotimes (\boldsymbol{a})_{2\times2} = \bigotimes \left(\begin{array}{cc} a_1^{(1)} & a_1^{(2)} \\ a_2^{(1)} & a_2^{(2)} \end{array} \right), \tag{67}$$

where T is the ordinary matrix transposition.

Let us apply (64) to arbitrary tensor products. By analogy, if we have a tensor product of mn elements (of *any* nature) grouped by n elements (e.g. m elements from n different vector spaces), as in (65), (67), we can write the tensor product in the $(m \times n)$-matrix form (cf. (3.18)–(3.19) in [14])

$$\bigotimes (\boldsymbol{a})_{m\times n} = \bigotimes \left(\begin{array}{cccc} a_1^{(1)} & a_1^{(2)} & \ldots & a_1^{(n)} \\ a_2^{(1)} & a_2^{(2)} & \ldots & a_2^{(n)} \\ \vdots & \vdots & \vdots & \vdots \\ a_m^{(1)} & a_m^{(2)} & \ldots & a_m^{(n)} \end{array} \right) \tag{68}$$

Definition 28. The *polyadic medial map* $\boldsymbol{\tau}_{medial}^{(n,m)} : (A^{\otimes n})^{\otimes m} \to (A^{\otimes m})^{\otimes n}$ is defined as the transposition of the tensor product matrix (68) by the evaluation (cf. the binary case (65))

$$\bigotimes (\boldsymbol{a})_{m\times n} \overset{\tau_{medial}^{(n,m)}}{\mapsto} \bigotimes (\boldsymbol{a}^T)_{n\times m}. \tag{69}$$

We can extend the mediality concept [26, 27] to polyadic algebras using the medial map. If we have an algebra with n-ary multiplication (40), then the mediality relation follows from (68) with $m = n$ and contains $(n + 1)$ multiplications acting on n^2 elements.

Definition 29. A $\Bbbk$-linear polyadic algebra $A^{(n)}$ (41) is called *medial*, if its n-ary multiplication map satisfies the relation

$$\boldsymbol{\mu}^{(n)} \circ \left(\left(\boldsymbol{\mu}^{(n)}\right)^{\otimes n} \right) = \boldsymbol{\mu}^{(n)} \circ \left(\left(\boldsymbol{\mu}^{(n)}\right)^{\otimes n} \right) \circ \boldsymbol{\tau}_{medial}^{(n,n)}, \tag{70}$$

where $\boldsymbol{\tau}_{medial}^{(n,n)}$ is given by (69), or in the manifest elementwise form (evaluation)

$$\mu^{(n)} \left[\mu^{(n)} \left[a_1^{(1)}, a_1^{(2)}, \ldots, a_1^{(n)} \right], \mu^{(n)} \left[a_2^{(1)}, a_2^{(2)}, \ldots, a_2^{(n)} \right], \ldots, \mu^{(n)} \left[a_n^{(1)}, a_n^{(2)}, \ldots, a_n^{(n)} \right] \right]$$

$$= \mu^{(n)} \left[\mu^{(n)} \left[a_1^{(1)}, a_2^{(1)}, \ldots, a_n^{(1)} \right], \mu^{(n)} \left[a_1^{(2)}, a_2^{(2)}, \ldots, a_n^{(2)} \right], \ldots, \mu^{(n)} \left[a_1^{(n)}, a_2^{(n)}, \ldots, a_n^{(n)} \right] \right]. \tag{71}$$

Let us "polyadize" the binary twist map $\boldsymbol{\tau}_{op}$ from (66), which can be suitable for operations with polyadic tensor products. Informally, we can interpret (66), as "omitting the fixed points" of the binary medial map $\boldsymbol{\tau}_{medial}$, and denote this procedure by "$\boldsymbol{\tau}_{op} = \boldsymbol{\tau}_{medial} \setminus \mathrm{id}$".

Definition 30. A (*medially allowed*) ℓ_τ-*place polyadic twist map* $\boldsymbol{\tau}_{op}^{(\ell_\tau)}$ is defined by

$$\text{"} \boldsymbol{\tau}_{op}^{(\ell_\tau)} = \boldsymbol{\tau}_{medial}^{(n,m)} \setminus \mathrm{id} \text{"}, \tag{72}$$

where $\ell_\tau = mn - k_{fixed}$, and k_{fixed} is the number of fixed points of the medial map $\boldsymbol{\tau}_{medial}^{(n,m)}$.

Assertion 31. *If $m \neq n$, then $\ell_\tau = mn - 2$. If $m = n$, then the polyadic twist map $\boldsymbol{\tau}_{op}^{(\ell_\tau)}$ is the reflection*

$$\boldsymbol{\tau}_{op}^{(\ell_\tau)} \circ \boldsymbol{\tau}_{op}^{(\ell_\tau)} = \mathrm{id}_A \tag{73}$$

and $\ell_\tau = n(n-1)$.

Table 2: Number of places ℓ_τ in the polyadic twist map $\boldsymbol{\tau}_{op}^{(\ell_\tau)}$.

m \ n	2	3	4	5	6	7
2	2	4	6	8	10	12
3	4	6	10	13	16	19
4	6	10	12	18	22	26
5	8	13	18	20	28	33
6	10	16	22	28	30	40
7	12	19	26	33	40	42

Proof. This follows from the matrix form (68) and (69). ■

Therefore the number of places ℓ_τ is "quantized" and for lowest m, n is presented in TABLE 2.

This generalizes the binary twist in a more unique way, which gives polyadic commutativity.

Remark 32. The polyadic twist map $\boldsymbol{\tau}_{op}^{(\ell_\tau)}$ is one element of the symmetry permutation group S_{ℓ_τ} which is fixed by the medial map $\boldsymbol{\tau}_{medial}^{(n,m)}$ and the special condition (72), and it therefore respects polyadic tensor product operations.

Example 33. In the matrix representation we have

$$\tau_{op}^{(4)}|_{n=3,m=2} = \begin{pmatrix} 0 & 0 & 1 & 0 \\ 1 & 0 & 0 & 0 \\ 0 & 0 & 0 & 1 \\ 0 & 1 & 0 & 0 \end{pmatrix}, \tau_{op}^{(6)}|_{n=3,m=3} = \begin{pmatrix} 0 & 0 & 1 & 0 & 0 & 0 \\ 0 & 0 & 0 & 0 & 1 & 0 \\ 1 & 0 & 0 & 0 & 0 & 0 \\ 0 & 0 & 0 & 0 & 0 & 1 \\ 0 & 1 & 0 & 0 & 0 & 0 \\ 0 & 0 & 0 & 1 & 0 & 0 \end{pmatrix}, \tag{74}$$

$$\tau_{op}^{(6)}|_{n=4,m=2} = \begin{pmatrix} 0 & 0 & 0 & 1 & 0 & 0 \\ 1 & 0 & 0 & 0 & 0 & 0 \\ 0 & 0 & 0 & 0 & 1 & 0 \\ 0 & 1 & 0 & 0 & 0 & 0 \\ 0 & 0 & 0 & 0 & 0 & 1 \\ 0 & 0 & 1 & 0 & 0 & 0 \end{pmatrix}. \tag{75}$$

The introduction of the polyadic twist gives us the possibility to generalize (in a way consistent with the medial map) the notion of the opposite algebra.

Definition 34. For a polyadic algebra $A^{(n)} = \left\langle A \mid \boldsymbol{\mu}^{(n)} \right\rangle$, an *opposite polyadic algebra*

$$A_{op}^{(n)} = \left\langle A \mid \boldsymbol{\mu}^{(n)} \circ \boldsymbol{\tau}_{op}^{(n)} \right\rangle \tag{76}$$

exists if the number of places for the polyadic twist map (which coincides in (76) with the arity of algebra multiplication $\ell_\tau = n$) is *allowed* (see TABLE 2).

Definition 35. A polyadic algebra $A^{(n)}$ is called *medially commutative*, if

$$\boldsymbol{\mu}_{op}^{(n)} \equiv \boldsymbol{\mu}^{(n)} \circ \boldsymbol{\tau}_{op}^{(n)} = \boldsymbol{\mu}^{(n)}, \tag{77}$$

where $\boldsymbol{\tau}_{op}^{(n)}$ is the medially allowed polyadic twist map.

Tensor product of polyadic algebras

Let us consider a polyadic tensor product $\bigotimes_{i=1}^n A_i^{(n)}$ of n polyadic associative n-ary algebras $A_i^{(n)} = \left\langle A_i \mid \boldsymbol{\mu}_i^{(n)} \right\rangle$, $i = 1, \ldots, n$, such that (see (40))

$$\boldsymbol{\mu}_i^{(n)} \circ \left(a_1^{(i)} \otimes \ldots \otimes a_n^{(i)} \right) = \mu_{A_i}^{(n)} \left[a_1^{(i)}, \ldots, a_n^{(i)} \right], \quad a_1^{(i)}, \ldots, a_n^{(i)} \in A_i, \quad \mu_{A_i}^{(n)} : A_i^{(n)} \to A_i. \tag{78}$$

To endow $\bigotimes_{i=1}^n A_i^{(n)}$ with the structure of an algebra, we will use the medial map $\boldsymbol{\tau}_{medial}^{(n,m)}$ (69).

Proposition 36. *The tensor product of n associative n-ary algebras $A_i^{(n)}$ has the structure of the polyadic algebra $A_\otimes^{(n)} = \left\langle \bigotimes_{i=1}^n A_i^{(n)} \mid \boldsymbol{\mu}_\otimes \right\rangle$, which is associative* (cf. (42))

$$\boldsymbol{\mu}_\otimes \circ \left(\mathrm{id}_{A_\otimes}^{\otimes(n-1-i)} \otimes \boldsymbol{\mu}_\otimes \otimes \mathrm{id}_{A_\otimes}^{\otimes i} \right) = \boldsymbol{\mu}_\otimes \circ \left(\mathrm{id}_{A_\otimes}^{\otimes(n-1-j)} \otimes \boldsymbol{\mu}_\otimes \otimes \mathrm{id}_{A_\otimes}^{\otimes j} \right),$$

$$\forall i,j = 0, \ldots n-1, \; i \neq j, \quad \mathrm{id}_{A_\otimes} : A_1^{\otimes n} \otimes \ldots \otimes A_n^{\otimes n} \to A, \tag{79}$$

if

$$\boldsymbol{\mu}_\otimes = \left(\boldsymbol{\mu}_1^{(n)} \otimes \ldots \otimes \boldsymbol{\mu}_n^{(n)} \right) \circ \boldsymbol{\tau}_{medial}^{(n,n)}. \tag{80}$$

Proof. We act by the multiplication map $\boldsymbol{\mu}_\otimes$ on the element's tensor product matrix (68) and obtain

$$\boldsymbol{\mu}_\otimes \circ \left(\left(a_1^{(1)} \otimes a_1^{(2)} \otimes \ldots \otimes a_1^{(n)} \right) \otimes \ldots \otimes \left(a_n^{(1)} \otimes a_n^{(2)} \otimes \ldots \otimes a_n^{(n)} \right) \right)$$

$$= \left(\boldsymbol{\mu}_1^{(n)} \otimes \ldots \otimes \boldsymbol{\mu}_n^{(n)} \right) \circ \boldsymbol{\tau}_{medial}^{(n,n)} \circ \left(\left(a_1^{(1)} \otimes a_1^{(2)} \otimes \ldots \otimes a_1^{(n)} \right) \otimes \ldots \otimes \left(a_n^{(1)} \otimes a_n^{(2)} \otimes \ldots \otimes a_n^{(n)} \right) \right)$$

$$= \left(\boldsymbol{\mu}_1^{(n)} \otimes \ldots \otimes \boldsymbol{\mu}_n^{(n)} \right) \circ \left(\left(a_1^{(1)} \otimes a_2^{(1)} \otimes \ldots \otimes a_n^{(1)} \right) \otimes \ldots \otimes \left(a_1^{(n)} \otimes a_2^{(n)} \otimes \ldots \otimes a_n^{(n)} \right) \right)$$

$$= \mu_1^{(n)} \left[a_1^{(1)}, a_2^{(1)}, \ldots, a_n^{(1)} \right] \otimes \ldots \otimes \mu_n^{(n)} \left[a_1^{(n)}, a_2^{(n)}, \ldots, a_n^{(n)} \right], \tag{81}$$

which proves that $\boldsymbol{\mu}_\otimes$ is indeed a polyadic algebra multiplication. To prove the associativity (79) we repeat the same derivation (81) twice and show that the result is independent of i, j. ∎

If *all* $A_i^{(n)}$ have their polyadic unit map $\boldsymbol{\eta}_i^{(r,n)}$ defined by (48) and acting as (50), then we have

Proposition 37. *The polyadic unit map of $A_\otimes^{(n)}$ is $\boldsymbol{\eta}_\otimes : K^{\otimes nr} \to A_1^{\otimes(n-1)} \otimes \ldots \otimes A_n^{\otimes(n-1)}$ acting as*

$$\boldsymbol{\eta}_\otimes \circ \left(\overbrace{e_k \otimes \ldots \otimes e_k}^{nr} \right) = \left(\overbrace{e_{a_1} \otimes \ldots \otimes e_{a_1}}^{n-1} \right) \otimes \ldots \otimes \left(\overbrace{e_{a_n} \otimes \ldots \otimes e_{a_n}}^{n-1} \right). \tag{82}$$

Assertion 38. *The polyadic unit of $A_\otimes^{(n)}$ is a $\left(n^2 - n \right)$-valued function of nr arguments.*

Note that concepts of tensor product and derived polyadic algebras are different.

Heteromorphisms of polyadic associative algebras

The standard homomorphism between binary associative algebras is defined as a linear map φ which "commutes" with the algebra multiplications ("$\varphi \circ \boldsymbol{\mu}_1 = \boldsymbol{\mu}_2 \circ (\varphi \otimes \varphi)$"). In the polyadic case there exists the possibility to change arity of the algebras, and for that, one needs to use the heteromorphisms (or multiplace maps) introduced in [14]. Let us consider two polyadic $\Bbbk$-algebras $A_1^{(n_1)} = \left\langle A_1 \mid \boldsymbol{\mu}_1^{(n_1)} \right\rangle$ and $A_2^{(n_2)} = \left\langle A_2 \mid \boldsymbol{\mu}_2^{(n_2)} \right\rangle$ (over the same polyadic field $\Bbbk$).

Definition 39. A *heteromorphism* between two polyadic $\Bbbk$-algebras $A_1^{(n_1)}$ and $A_2^{(n_2)}$ (of different arities n_1 and n_2) is a s-place $\Bbbk$-linear map $\boldsymbol{\Phi}_s^{(n_1,n_2)} : A_1^{\otimes s} \to A_2$, such that

$$\boldsymbol{\Phi}_s^{(n_1,n_2)} \circ \left(\overbrace{\boldsymbol{\mu}_1^{(n_1)} \otimes \ldots \otimes \boldsymbol{\mu}_1^{(n_1)}}^{s-\ell_{\mathrm{id}}} \otimes \overbrace{\mathrm{id}_{A_1} \otimes \ldots \otimes \mathrm{id}_{A_1}}^{\ell_{\mathrm{id}}} \right) = \boldsymbol{\mu}_2^{(n_2)} \circ \left(\overbrace{\boldsymbol{\Phi}_s^{(n_1,n_2)} \otimes \ldots \otimes \boldsymbol{\Phi}_s^{(n_1,n_2)}}^{n_2} \right), \tag{83}$$

and the diagram

$$\begin{array}{ccc}
A_1^{\otimes s n_2} & \xrightarrow{\left(\boldsymbol{\Phi}_s^{(n_1,n_2)} \right)^{\otimes n_2}} & A_2^{\otimes n_2} \\
{\scriptstyle \left(\boldsymbol{\mu}_1^{(n_1)} \right)^{\otimes(s-\ell_{\mathrm{id}})} \otimes \left(\mathrm{id}_{A_1} \right)^{\otimes \ell_{\mathrm{id}}}} \downarrow & & \downarrow {\scriptstyle \boldsymbol{\mu}_2^{(n_2)}} \\
A_1^{\otimes s} & \xrightarrow{\boldsymbol{\Phi}_s^{(n_1,n_2)}} & A_2
\end{array} \tag{84}$$

commutes. The arities satisfy

$$s n_2 = n_1 \left(s - \ell_{\mathrm{id}} \right) + \ell_{\mathrm{id}}, \tag{85}$$

where $0 \leq \ell_{\mathrm{id}} \leq s - 1$ is an integer (the number of "intact elements" of A_1), and therefore $2 \leq n_2 \leq n_1$.

Assertion 40. *If $\ell_{\mathrm{id}} = 0$ (there are no "intact elements"), then the (s-place) heteromorphism does not change the arity of the polyadic algebra.*

Definition 41. A *homomorphism* between two polyadic $\Bbbk$-algebras $A_1^{(n)}$ and $A_2^{(n)}$ (of the same arity or *equiary*) is a 1-place $\Bbbk$-linear map $\boldsymbol{\Phi}^{(n)} = \boldsymbol{\Phi}_{s=1}^{(n,n)} : A_1 \to A_2$, such that

$$
\boldsymbol{\Phi}^{(n)} \circ \boldsymbol{\mu}_1^{(n)} = \boldsymbol{\mu}_2^{(n)} \circ \left(\overbrace{\boldsymbol{\Phi}^{(n)} \otimes \ldots \otimes \boldsymbol{\Phi}^{(n)}}^{n} \right), \tag{86}
$$

and the diagram

$$
\begin{array}{ccc}
A_1^{\otimes n} & \xrightarrow{\left(\boldsymbol{\Phi}^{(n)}\right)^{\otimes n}} & A_2^{\otimes n} \\
\downarrow{\scriptstyle \boldsymbol{\mu}_1^{(n)}} & & \downarrow{\scriptstyle \boldsymbol{\mu}_2^{(n)}} \\
A_1 & \xrightarrow{\boldsymbol{\Phi}^{(n)}} & A_2
\end{array} \tag{87}
$$

commutes.

The above definitions do not include the behavior of the polyadic unit under heteromorphism, because a polyadic associative algebra need not contain a unit. However, if both units exist, this will lead to strong arity restrictions.

Proposition 42. *If in $\Bbbk$-algebras $A_1^{(n_1)}$ and $A_2^{(n_2)}$ (of arities n_1 and n_2) there exist both polyadic units (48) $\boldsymbol{\eta}_1^{(r,n_1)} : K^{\otimes r} \to A_1^{\otimes(n_1-1)}$ and $\boldsymbol{\eta}_2^{(r,n_2)} : K^{\otimes r} \to A_2^{\otimes(n_2-1)}$, then*

1. *The heteromorphism (83) connects them as*

$$
\overbrace{\boldsymbol{\eta}_2^{(r,n_2)} \otimes \ldots \otimes \boldsymbol{\eta}_2^{(r,n_2)}}^{s} = \left(\overbrace{\boldsymbol{\Phi}_s^{(n_1,n_2)} \otimes \ldots \otimes \boldsymbol{\Phi}_s^{(n_1,n_2)}}^{n_1-1} \right) \circ \left(\overbrace{\boldsymbol{\eta}_1^{(r,n_1)} \otimes \ldots \otimes \boldsymbol{\eta}_1^{(r,n_1)}}^{s} \right), \tag{88}
$$

   and the diagram

$$
\begin{array}{ccc}
K^{rs} & \xrightarrow{\left(\boldsymbol{\eta}_1^{(r,n_1)}\right)^{\otimes s}} & A_1^{\otimes s(n_1-1)} \\
\downarrow{\scriptstyle \left(\boldsymbol{\eta}_2^{(r,n_2)}\right)^{\otimes s}} & & \\
A_2^{\otimes s(n_2-1)} & \xleftarrow{\left(\boldsymbol{\Phi}_s^{(n_1,n_2)}\right)^{\otimes(n_1-1)}} &
\end{array} \tag{89}
$$

   commutes.

2. *The number of "intact elements" is fixed by its maximum value*

$$
\ell_{\mathrm{id}} = s - 1, \tag{90}
$$

   such that in the l.h.s. of (83) there is only one multiplication $\boldsymbol{\mu}_1^{(n_1)}$.

3. *The number of places s in the heteromorphism $\boldsymbol{\Phi}_s^{(n_1,n_2)}$ is fixed by the arities of the polyadic algebras*

$$
s\left(n_2 - 1\right) = n_1 - 1. \tag{91}
$$

Proof. Using (85) we obtain $s\left(n_2 - 1\right) = \left(s - \ell_{\mathrm{id}}\right)\left(n_1 - 1\right)$, then the $(n_1 - 1)$ power of the heteromorphism $\boldsymbol{\Phi}_s^{(n_1,n_2)}$ maps $A_1^{\otimes s(n_1-1)} \to A_2^{\otimes(n_1-1)}$, and we have $s - \ell_{\mathrm{id}} = 1$, which, together with (85), gives (90), and (91). ∎

Structure constants

Let $A^{(n)}$ be a finite-dimensional polyadic algebra (10) having the basis $e_i \in A, i = 1, \ldots, N$, where N is its dimension as a polyadic vector space

$$
A_{vect} = \left\langle A, K \mid \nu^{(m)}; \nu_k^{(m_k)}, \mu_k^{(n_k)}; \rho^{(r)} \right\rangle \tag{92}
$$

where we denote $\nu^{(m)} = \nu_A^{(m_a)}$ (see (9) and (11), here $N = d_v$). In the binary case "$a = \sum_i \lambda^{(i)} e_i$", any element $a \in A$ is determined by the number N_λ of scalars $\lambda \in K$, which coincides with the algebra dimension $N_\lambda = N$, because $r = 1$. In the polyadic case, it can be that $r > 1$, and moreover with $m \geq 2$ the admissible number of "words" (in the expansion of a by e_i) is "quantized", such that $1, m, 2m - 1, 3m - 2, \ldots \ell_N\left(m - 1\right) + 1$, where $\ell_N \in \mathbb{N}_0$ is the "number of additions". So we have

Definition 43. In N-dimensional n-ary algebra $A^{(n)}$ (with m-ary addition and r-place "scalar" multiplication) the expansion of any element $a \in A$ by the basis $\{e_i \mid i = 1, \ldots, N\}$ is

$$a = \left(\nu^{(m)}\right)^{\circ \ell_N} \left[\rho^{(r)} \left\{\lambda_1^{(1)}, \ldots, \lambda_r^{(1)} \mid e_1\right\}, \ldots, \rho^{(r)} \left\{\lambda_1^{(N)}, \ldots, \lambda_r^{(N)} \mid e_N\right\}\right], \tag{93}$$

and is determined by $N_\lambda \in \mathbb{N}$ "scalars", where

$$N_\lambda = rN, \tag{94}$$

$$N = \ell_N (m - 1) + 1, \quad \ell_N \in \mathbb{N}_0, \quad N \in \mathbb{N}, \quad m \geq 2. \tag{95}$$

In the binary case $m = 2$, the dimension N of an algebra is not restricted and is a natural number, because, $N = \ell_N + 1$.

Assertion 44. *The dimension of n-ary algebra $A^{(n)}$ having m-ary addition is not arbitrary, but "quantized" and can only have the following values for $m \geq 3$*

$$m = 3, \quad N = 1, 3, 5, \ldots, 2\ell_N + 1, \tag{96}$$

$$m = 4, \quad N = 1, 4, 7, \ldots, 3\ell_N + 1, \tag{97}$$

$$m = 5, \quad N = 1, 5, 9, \ldots, 4\ell_N + 1, \tag{98}$$

$$\ldots$$

Proof. It follows from (95) and demanding that the "number of additions" ℓ_N is natural or zero. ∎

In a similar way, by considering a product of the basis elements, which can also be expanded in the basis "$e_i e_j = \sum_k \chi_{(i,j)}^{(k)} e_k$", we can define a polyadic analog of the structure constants $\chi_{(i,j)}^{(k)} \in K$.

Definition 45. The *polyadic structure constants* $\chi_{r,(i_1,\ldots i_n)}^{(j)} \in K$, $i_1, \ldots i_n, j = 1, \ldots, n$ of the N-dimensional n-ary algebra $A^{(n)}$ (with m-ary addition $\nu^{(m)}$ and r-place multiaction $\rho^{(r)}$) are defined by the expansion of the n-ary product of the basis elements $\{e_i \mid i = 1, \ldots, N\}$ as

$$\mu^{(n)} [e_{i_1}, \ldots, e_{i_n}]$$
$$= \left(\nu^{(m)}\right)^{\circ \ell_N} \left[\rho^{(r)} \left\{\chi_{1,(i_1,\ldots i_n)}^{(1)}, \ldots, \chi_{r,(i_1,\ldots i_n)}^{(1)} \mid e_1\right\}, \ldots, \rho^{(r)} \left\{\chi_{1,(i_1,\ldots i_n)}^{(N)}, \ldots, \chi_{r,(i_1,\ldots i_n)}^{(N)} \mid e_N\right\}\right], \tag{99}$$

where

$$N_\chi = rN^{n+1}, \quad N, N_\chi \in \mathbb{N} \tag{100}$$

$$N = \ell_N (m - 1) + 1, \quad \ell_N \in \mathbb{N}_0, \quad m \geq 2. \tag{101}$$

As in the binary case, we have

Corollary 46. The algebra multiplication $\mu^{(n)}$ of $A^{(n)}$ is *fully* determined by the rN^{n+1} polyadic structure constants $\chi_{r,(i_1,\ldots i_n)}^{(j)} \in K$.

Contrary to the binary case $m = 2$, when N_χ can be any natural number, we now have

Assertion 47. *The number of the polyadic structure constants N_χ of the finite-dimensional n-ary algebra $A^{(n)}$ with m-ary addition and r-place multiaction is not arbitrary, but "quantized" according to*

$$N_\chi = r (\ell_N (m - 1) + 1)^{n+1}, \quad r \in \mathbb{N}, \quad \ell_N \in \mathbb{N}_0, \quad m, n \geq 2. \tag{102}$$

Proof. This follows from (100) and "quantization" of the algebra dimension N, see **Assertion 44**. ∎

POLYADIC COALGEBRAS

Motivation

The standard motivation for introducing the comultiplication is from representation theory [28, 29]. The first examples come from so-called addition formulas for special functions ("anciently" started from sin/cos), which actually arise from representations of groups [5, 30].

In brief (and informally), let $\boldsymbol{\pi}$ be a finite-dimensional representation of a group G in a vector space V over a field k, such that

$$\boldsymbol{\pi}(gh) = \boldsymbol{\pi}(g)\boldsymbol{\pi}(h), \quad \boldsymbol{\pi} : G \to \operatorname{End} V, \quad g, h \in G. \tag{103}$$

In some basis of V the matrix elements $\pi_{ij}(g)$ satisfy $\pi_{ij}(gh) = \sum_k \pi_{ik}(g)\pi_{kj}(h)$ (from (103)) and span a finite dimensional vector space C_π of functions with a basis e_{π_m} as $f_\pi = \sum_m \alpha_m e_{\pi_m}$, $f_\pi \in C_\pi$. Now (103) gives $f_\pi(gh) = \sum_{m,n} \beta_{mn} e_{\pi_m}(g) e_{\pi_n}(h)$, $f_\pi \in C_\pi$. If we omit the evaluation, it can be written in the vector space C_π using an additional linear map $\Delta_\pi : C_\pi \to C_\pi \otimes C_\pi$, in the following way

$$\Delta_\pi(f_\pi) = \sum_{m,n} \beta_{mn} e_{\pi_m} \otimes e_{\pi_n} \in C_\pi \otimes C_\pi. \tag{104}$$

Thus, to any finite-dimensional representation $\boldsymbol{\pi}$ one can define the map Δ_π of vector spaces C_π to functions on a group, called a *comultiplication*.

It is important that all the above operations are binary, and the defining formula for comultiplication (104) is fully determined by the definition of a representation (103).

The polyadic analog of a representation was introduced and studied in [14]. In the case of multiplace representations, arities of the initial group and its representation can be *different*. Indeed, let $G^{(n)} = \left\langle G \mid \mu_G^{(n)} \right\rangle$, $\mu_G^{(n)} : G^{\times n} \to G$, be a n-ary group and $G_{\mathrm{End}\,V}^{(n')} = \left\langle \{\mathrm{End}\,V\} \mid \mu_E^{(n')} \right\rangle$, $\mu_E^{(n')} : (\mathrm{End}\,V)^{\times n'} \to \mathrm{End}\,V$, is a n'-ary group of endomorphisms of a polyadic vector space V (9). In [14] $G_{\mathrm{End}\,V}^{(n')}$ was considered as a derived one, while here we *do not restrict* it in this way.

Definition 48. A *polyadic (multiplace) representation* of $G^{(n)}$ in V is a s-place mapping

$$\boldsymbol{\Pi}_s^{(n,n')} : G^{\times s} \to \mathrm{End}\,V, \tag{105}$$

satisfying the associativity preserving heteromorphism equation [14]

$$\boldsymbol{\Pi}_s^{(n,n')}\left(\overbrace{\mu_G^{(n)}[g_1,\ldots g_n],\ldots,\mu_G^{(n)}\left[g_{n(s-\ell'_{\mathrm{id}}-1)},\ldots,g_{n(s-\ell'_{\mathrm{id}})}\right]}^{s-\ell'_{\mathrm{id}}},\ldots,\overbrace{g_{n(s-\ell'_{\mathrm{id}})+1},\ldots,g_{n(s-\ell'_{\mathrm{id}})+\ell'_{\mathrm{id}}}}^{\ell'_{\mathrm{id}}}\right)$$
$$= \mu_E^{(n')}\left[\boldsymbol{\Pi}_s^{(n,n')}(g_1,\ldots g_s),\ldots,\boldsymbol{\Pi}_s^{(n,n')}\left(g_{s(n'-1)},\ldots g_{sn'}\right)\right], \tag{106}$$

such that the diagram

$$\tag{107}$$

commutes, and the arity changing formula

$$sn' = n(s - \ell'_{\mathrm{id}}) + \ell'_{\mathrm{id}}, \tag{108}$$

where ℓ'_{id} is the number of "intact elements" in l.h.s. of (106), $0 \le \ell'_{\mathrm{id}} \le s-1$, $2 \le n' \le n$.

Remark 49. Particular examples of 2-place representations of ternary groups ($s = 2$, which change arity from $n = 3$ to $n' = 2$), together with their matrix representations, were presented in [14, 31].

Polyadic comultiplication

Our motivations say that in constructing a polyadic analog of the comultiplication, one should not only "reverse arrows", but also pay thorough attention to arities.

Assertion 50. *The arity of polyadic comultiplication coincides with the arity of the representation and can differ from the arity of the polyadic algebra.*

Proof. It follows from (103), (104) and (105). ∎

Let us consider a polyadic vector space over the polyadic field $\Bbbk^{(m_k, n_k)}$ as (see (11))

$$C_{vect} = \left\langle C, K \mid \nu_C^{(m_c)}; \nu_k^{(m_k)}, \mu_k^{(n_k)}; \rho_C^{(r_c)} \right\rangle, \tag{109}$$

where $\nu_C^{(m_c)} : C^{\times m_c} \to C$ is m_c-ary addition and $\rho_C^{(r_c)} : K^{\times r_c} \times C \to C$ is r_c-place action (see (7)).

Definition 51. A *polyadic (n'-ary) comultiplication* is a $\Bbbk$-linear map $\boldsymbol{\Delta}^{(n')} : C \to C^{\otimes n'}$.

Definition 52. A *polyadic (coassociative) coalgebra (or $\Bbbk$-coalgebra)* is the polyadic vector space C_{vect} equipped with the polyadic comultiplication

$$C = C^{(n')} = \left\langle C_{vect} \mid \boldsymbol{\Delta}^{(n')} \right\rangle, \tag{110}$$

which is (totally) *coassociative*

$$\left(\mathrm{id}_C^{\otimes(n'-1-i)} \otimes \boldsymbol{\Delta}^{(n')} \otimes \mathrm{id}_C^{\otimes i} \right) \circ \boldsymbol{\Delta}^{(n')} = \left(\mathrm{id}_C^{\otimes(n-1-j)} \otimes \boldsymbol{\Delta}^{(n')} \otimes \mathrm{id}_C^{\otimes j} \right) \circ \boldsymbol{\Delta}^{(n')},$$

$$\forall i, j = 0, \dots n - 1, \ i \neq j, \ \mathrm{id}_C : C \to C, \tag{111}$$

and such that the diagram

$$
\begin{array}{ccc}
C^{\otimes(2n'-1)} & \xleftarrow{\ \mathrm{id}_C^{\otimes(n'-1-i)} \otimes \boldsymbol{\Delta}^{(n')} \otimes \mathrm{id}_C^{\otimes i}\ } & C^{\otimes n'} \\[4pt]
\mathrm{id}_C^{\otimes(n'-1-j)} \otimes \boldsymbol{\Delta}^{(n')} \otimes \mathrm{id}_C^{\otimes j} \Big\uparrow & & \Big\uparrow \boldsymbol{\Delta}^{(n')} \\[4pt]
C^{\otimes n'} & \xleftarrow{\qquad\qquad \boldsymbol{\Delta}^{(n')} \qquad\qquad} & C
\end{array}
\tag{112}
$$

commutes (cf.(43)).

Definition 53. A polyadic coalgebra $C^{(n')}$ is called *totally co-commutative*, if

$$\boldsymbol{\Delta}^{(n')} = \boldsymbol{\tau}_{n'} \circ \boldsymbol{\Delta}^{(n')}, \tag{113}$$

where $\boldsymbol{\tau}_{n'} \in S_{n'}$, and $S_{n'}$ is the permutation symmetry group on n' elements.

Definition 54. A polyadic coalgebra $C^{(n')}$ is called *medially co-commutative*, if

$$\boldsymbol{\Delta}_{cop}^{(n')} \equiv \boldsymbol{\tau}_{op}^{(n')} \circ \boldsymbol{\Delta}^{(n')} = \boldsymbol{\Delta}^{(n')}, \tag{114}$$

where $\boldsymbol{\tau}_{op}^{(n')}$ is the medially allowed polyadic twist map (72).

There are no other axioms in the definition of a polyadic coalgebra, following the same reasoning as for a polyadic algebra: the possible absence of zeroes and units (see TABLE 1). Obviously, in a polyadic coalgebra $C^{(n')}$, there is no "unit element", because there is no multiplication, and a polyadic analog of counit can be *only defined*, when the underlying field $\Bbbk^{(m_k, n_k)}$ is *unital* (which is not always the case [20]).

By analogy with (6), introduce the *ℓ'-coiterated n'-ary comultiplication* by

$$\left(\boldsymbol{\Delta}^{(n')} \right)^{\circ \ell'} = \overbrace{\left(\mathrm{id}_C^{\otimes(n'-1)} \otimes \dots \left(\mathrm{id}_C^{\otimes(n'-1)} \boldsymbol{\Delta}^{(n')} \right) \dots \circ \boldsymbol{\Delta}^{(n')} \right)}^{\ell'} \circ \boldsymbol{\Delta}^{(n')}, \quad \ell' \in \mathbb{N}. \tag{115}$$

Therefore, the *admissible* length of any co-word is fixed ("quantized") as $\ell'(n'-1)+1$, but not arbitrary, as in the binary case.

Let us introduce a co-analog of the derived n-ary multiplication (45) by

Definition 55. A polyadic comultiplication $\boldsymbol{\Delta}_{der}^{(n')}$ is called *derived*, if it is ℓ_d-coiterated from the comultiplication $\boldsymbol{\Delta}_0^{(n'_0)}$ of lower arity $n'_0 < n'$

$$\boldsymbol{\Delta}_{der}^{(n')} = \overbrace{\left(\mathrm{id}_C^{\otimes(n'_0-1)} \otimes \dots \left(\mathrm{id}_C^{\otimes(n'_0-1)} \boldsymbol{\Delta}_0^{(n'_0)} \right) \dots \circ \boldsymbol{\Delta}_0^{(n'_0)} \right)}^{\ell_d} \circ \boldsymbol{\Delta}_0^{(n'_0)}, \tag{116}$$

or

$$\boldsymbol{\Delta}_{der}^{(n')} = \left(\boldsymbol{\Delta}_0^{(n'_0)} \right)^{\circ \ell'}, \tag{117}$$

where

$$n' = \ell_d (n'_0 - 1) + 1, \tag{118}$$

and $\ell_d \geq 2$ is the "number of coiterations".

The standard coiterations of $\boldsymbol{\Delta}$ are binary and restricted by $n'_0 = 2$ ([1]).

Example 56. The matrix coalgebra generated by the basis e_{ij}, $i,j = 1,\ldots,N$ of $\mathrm{Mat}_N(\mathbb{C})$ with the binary coproduct $\Delta_0^{(2)}(e_{ij}) = \sum_k e_{ik} \otimes e_{kj}$ (see, e.g., [2]) can be extended to the *derived* ternary coalgebra by $\Delta_{der}^{(3)}(e_{ij}) = \sum_{k,l} e_{ik} \otimes e_{kl} \otimes e_{lj}$, such that (116) becomes $\boldsymbol{\Delta}_{der}^{(3)} = \left(\mathrm{id}_C \otimes \Delta_0^{(2)}\right) \boldsymbol{\Delta}_0^{(2)} = \left(\boldsymbol{\Delta}_0^{(2)} \otimes \mathrm{id}_C\right) \boldsymbol{\Delta}_0^{(2)}$.

Example 57. Let us consider the ternary coalgebra $\langle C \mid \boldsymbol{\Delta}^{(3)} \rangle$ generated by two elements $\{a,b\} \in C$ with the von Neumann regular looking comultiplication

$$\Delta^{(3)}(a) = a \otimes b \otimes a, \quad \Delta^{(3)}(b) = b \otimes a \otimes b. \tag{119}$$

It is easy to check that $\boldsymbol{\Delta}^{(3)}$ is coassociative and *nonderived*.

Definition 58. A polyadic coalgebra $C^{(n')}$ (110) is called *co-medial*, if its n'-ary multiplication map satisfies the relation

$$\left(\left(\boldsymbol{\Delta}^{(n')}\right)^{\otimes n'}\right) \circ \boldsymbol{\Delta}^{(n')} = \boldsymbol{\tau}_{medial}^{(n',n')} \circ \left(\left(\boldsymbol{\Delta}^{(n')}\right)^{\otimes n'}\right) \circ \boldsymbol{\Delta}^{(n')}, \tag{120}$$

where $\boldsymbol{\tau}_{medial}^{(n',n')}$ is the polyadic medial map given by (68)–(69).

Introduce a $\Bbbk$-linear r'-*place action map* $\bar{\boldsymbol{\rho}}^{(r')} : K^{\otimes r'} \otimes C \to C$ corresponding to $\rho_C^{(r_c)}$ by (see (47))

$$\bar{\boldsymbol{\rho}}^{(r')} \circ (\lambda_1 \otimes \ldots \otimes \lambda_{r'} \otimes c) = \rho_C^{(r')}(\lambda_1,\ldots,\lambda_{r'} \mid c), \quad \lambda_1,\ldots,\lambda_{r'} \in K, \ c \in C. \tag{121}$$

Let $\Bbbk^{(m_k,n_k)}$ be unital with unit e_k.

Definition 59. A $\Bbbk$-linear r'-*place coaction map* $\boldsymbol{\sigma}^{(r')} : C \to K^{\otimes r'} \otimes C$ is defined by

$$c \mapsto \overbrace{e_k \otimes \ldots \otimes e_k}^{r'} \otimes c. \tag{122}$$

Assertion 60. *The coaction map* $\boldsymbol{\sigma}^{(r')}$ *is a "right inverse" for the multiaction map* $\bar{\boldsymbol{\rho}}^{(r')}$

$$\bar{\boldsymbol{\rho}}^{(r')} \circ \boldsymbol{\sigma}^{(r')} = \mathrm{id}_C. \tag{123}$$

Proof. This follows from the normalization (8), (122). ∎

Remark 61. The maps (121) and (122) establish the isomorphism $\overbrace{\Bbbk \otimes \ldots \otimes \Bbbk}^{r'} \otimes C \cong C$, which is well-known in the binary case (see, e.g. [23]).

We can provide the definition of counit only in the case where the underlying field $\Bbbk$ has a unit.

Definition 62 (*Counit axiom*). The polyadic coalgebra $C^{(n)}$ (41) over the *unital* polyadic field $\Bbbk^{(m_k,n_k)}$ contains a $\Bbbk$-linear *polyadic (right) counit map* $\boldsymbol{\varepsilon}^{(n',r')} : C^{\otimes(n'-1)} \to K^{\otimes r'}$ satisfying

$$\left(\boldsymbol{\varepsilon}^{(n',r')} \otimes \mathrm{id}_C\right) \circ \boldsymbol{\Delta}^{(n')} = \boldsymbol{\sigma}^{(r')}, \tag{124}$$

such that the diagram

$$
\begin{array}{ccc}
K^{\otimes r'} \otimes C & \xleftarrow{\boldsymbol{\varepsilon}^{(n',r')} \otimes \mathrm{id}_C} & C^{\otimes n'} \\
\boldsymbol{\sigma}^{(r')} \uparrow & \nearrow \ \boldsymbol{\Delta}^{(n')} & \\
C & &
\end{array}
\tag{125}
$$

commutes (cf.(49)).

Remark 63. We cannot write the "elementwise" normalization action for the counit analogous to (50) (and state the **Assertion** 21), because a unit element in a (polyadic) coalgebra is not defined.

By analogy with the derived polyadic unit (see (52)), consider a "derived" version of the polyadic counit.

Definition 64. The $\Bbbk$-linear *derived polyadic counit* (*neutral counit sequence*) of the polyadic coalgebra $C^{(n')}$ is the set $\hat{\boldsymbol{\varepsilon}}^{(r)} = \left\{ \varepsilon_i^{(r')} \right\}$ of $n' - 1$ maps $\varepsilon_i^{(r')} : C \to K^{\otimes r'}$, $i = 1, \ldots, n' - 1$, satisfying

$$\left(\varepsilon_1^{(r')} \otimes \ldots \otimes \varepsilon_{n'-1}^{(r')} \otimes \mathrm{id}_C \right) \circ \boldsymbol{\Delta}^{(n')} = \boldsymbol{\sigma}^{(r')}, \tag{126}$$

where id_C can be on any place. If $\varepsilon_1^{(r')} = \ldots = \varepsilon_{n'-1}^{(r')} = \varepsilon_0^{(r')}$, we call it the *strong derived polyadic counit*. In general, we can define formally, cf. (53),

$$\varepsilon_{der}^{(n',r')} = \varepsilon_1^{(r')} \otimes \ldots \otimes \varepsilon_{n'-1}^{(r')}. \tag{127}$$

Definition 65. A polyadic coassociative coalgebra $C_{der}^{(n')} = \left\langle C_{vect} \mid \boldsymbol{\Delta}_{der}^{(n')}, \varepsilon_{der}^{(n',r')} \right\rangle$ is called *derived* from $C_0^{(n')} = \left\langle C_{vect} \mid \boldsymbol{\Delta}_0^{(n'_0)}, \varepsilon_0^{(n'_0,r')} \right\rangle$, if (116) and

$$\varepsilon_{der}^{(n',r')} = \overbrace{\varepsilon_0^{(n'_0,r')} \otimes \ldots \otimes \varepsilon_0^{(n'_0,r')}}^{\ell_d} \tag{128}$$

hold, where $\varepsilon_0^{(n'_0,r')} = \overbrace{\varepsilon_0^{(r')} \otimes \ldots \otimes \varepsilon_0^{(r')}}^{n'_0 - 1}$ (formally, because id_C in (126) can be on any place).

In [24, 25] the particular case for $n' = 3$ and $r' = 1$ was considered.

Homomorphisms of polyadic coalgebras

In the binary case, a morphism of coalgebras is a linear map $\psi : C_1 \to C_2$ which "commutes" with comultiplications ("$(\psi \otimes \psi) \circ \boldsymbol{\Delta}_1 = \boldsymbol{\Delta}_2 \circ \varphi$"). It seems that for the polyadic coalgebras, one could formally change the direction of all arrows in (84). However, we observed that arity changing is possible for multivalued morphisms only. Therefore, here we confine ourselves to homomorphisms (1-place heteromorphisms [14]).

Let us consider two polyadic (equiary) $\Bbbk$-coalgebras $C_1^{(n')} = \left\langle C_1 \mid \boldsymbol{\Delta}_1^{(n')} \right\rangle$ and $C_2^{(n')} = \left\langle C_2 \mid \boldsymbol{\Delta}_2^{(n')} \right\rangle$ over the same polyadic field $\Bbbk^{(m_k, n_k)}$.

Definition 66. A (*coalgebra*) *homomorphism* between polyadic (equiary) coalgebras $C_1^{(n')}$ and $C_2^{(n')}$ is a $\Bbbk$-linear map $\boldsymbol{\Psi}^{(n')} : C_1 \to C_2$, such that

$$\left(\overbrace{\boldsymbol{\Psi}^{(n')} \otimes \ldots \otimes \boldsymbol{\Psi}^{(n')}}^{n'} \right) \circ \boldsymbol{\Delta}_1^{(n')} = \boldsymbol{\Delta}_2^{(n')} \circ \boldsymbol{\Psi}^{(n')}, \tag{129}$$

and the diagram

$$\begin{array}{ccc} C_2^{\otimes n'} & \xleftarrow{\left(\boldsymbol{\Psi}^{(n')} \right)^{\otimes n'}} & C_1^{\otimes n'} \\ {\scriptstyle \boldsymbol{\Delta}_2^{(n')}} \Big\uparrow & & \Big\uparrow {\scriptstyle \boldsymbol{\Delta}_1^{(n')}} \\ C_2 & \xleftarrow{\boldsymbol{\Psi}^{(n')}} & C_1 \end{array} \tag{130}$$

commutes (cf. (84)).

Only when the underlying field $\Bbbk$ is unital, we can also define a morphism for counits.

Definition 67. The *counit homomorphism* for $\varepsilon_{1,2}^{(n',r')} : C_{1,2}^{\otimes(n'-1)} \to K^{\otimes r'}$ is given by

$$\varepsilon_2^{(n',r')} = \varepsilon_1^{(n',r')} \circ \left(\overbrace{\boldsymbol{\Psi}^{(n')} \otimes \ldots \otimes \boldsymbol{\Psi}^{(n')}}^{n'-1} \right), \tag{131}$$

and the diagram

$$
\begin{array}{ccc}
K^{r'} & \xleftarrow{\ \ \varepsilon_2^{(n',r')}\ \ } & C_2^{\otimes(n'-1)} \\
\varepsilon_1^{(n',r')}\Big\uparrow & & \\
C_1^{\otimes(n'-1)} & &
\end{array}
\tag{132}
$$

commutes (cf. (89)).

Tensor product of polyadic coalgebras

Let us consider n' polyadic equiary coalgebras $C_i^{(n')} = \left\langle C_i \mid \boldsymbol{\Delta}_i^{(n')} \right\rangle$, $i = 1, \ldots, n'$.

Proposition 68. *The tensor product of the coalgebras has a structure of the polyadic coassociative coalgebra* $C_{\otimes}^{(n')} = \left\langle C_{\otimes} \mid \boldsymbol{\Delta}_{\otimes}^{(n')} \right\rangle$, $C_{\otimes} = \bigotimes_{i=1}^{n'} C_i$, *if*

$$
\boldsymbol{\Delta}_{\otimes}^{(n')} = \boldsymbol{\tau}_{medial}^{(n',n')} \circ \left(\boldsymbol{\Delta}_i^{(n')} \otimes \ldots \otimes \boldsymbol{\Delta}_i^{(n')} \right),
\tag{133}
$$

where $\boldsymbol{\tau}_{medial}^{(n',n')}$ *is defined in (69) and* $\boldsymbol{\Delta}_{\otimes}^{(n')} : C_{\otimes} \to \overbrace{C_{\otimes} \otimes \ldots \otimes C_{\otimes}}^{n'}$.

The proof is in full analogy with that of **Proposition 36**. If all of the coalgebras $C_i^{(n')}$ have counits, we denote them $\varepsilon_i^{(n',r')} : C_i^{\otimes(n'-1)} \to K^{\otimes r'}$, $i = 1, \ldots, n'$, and the counit map of $C_{\otimes}^{(n')}$ will be denoted by $\varepsilon_{\otimes}^{(n',r')} : C_{\otimes}^{\otimes(n'-1)} \to K^{\otimes r'}$. We have (in analogy to "$\varepsilon_{C_1 \otimes C_2}(c_1 \otimes c_2) = \varepsilon_{C_1}(c_1)\varepsilon_{C_2}(c_2)$")

Proposition 69. *The tensor product coalgebra* $C_{\otimes}^{(n')}$ *has a counit which is defined by*

$$
\begin{aligned}
& \varepsilon_{\otimes}^{(n',r')} \circ \left(c_1 \otimes \ldots \otimes c_{n'(n'-1)} \right) \\
& = \boldsymbol{\mu}_k^{n_k} \circ \left(\varepsilon_1^{(n',r')} \circ \left(c_1 \otimes \ldots \otimes c_{(n'-1)} \right) \otimes \ldots \otimes \varepsilon_{n'}^{(n',r')} \circ \left(c_{(n'-1)(n'-1)} \otimes \ldots \otimes c_{n'(n'-1)} \right) \right),
\end{aligned}
\tag{134}
$$
$$
c_i \in C_i, \quad i = 1, \ldots, n'(n'-1),
$$

and the arity of the comultiplication coincides with the arity of the underlying field

$$
n' = n_k.
\tag{135}
$$

Polyadic coalgebras in the Sweedler notation

The $\Bbbk$-linear coalgebra comultiplication map $\boldsymbol{\Delta}^{(n')}$ defined in **Definition 51** is useful for a "diagrammatic" description of polyadic coalgebras, and it corresponds to the algebra multiplication map $\boldsymbol{\mu}^{(n)}$, which both manipulate with sets. However, for concrete computations (with elements) we need an analog of the polyadic algebra multiplication $\mu^{(n)} \equiv \mu_A^{(n_a)}$ from (12). The connection of $\boldsymbol{\mu}^{(n)}$ and $\mu^{(n)}$ is given by (40), which can be treated as a "bridge" between the "diagrammatic" and "elementwise" descriptions. The co-analog of (40) was not considered, because the comultiplication has only one argument. To be consistent, we introduce the "elementwise" comultiplication $\Delta^{(n')}$ as the coanalog of $\mu^{(n)}$ by the evaluation

$$
\boldsymbol{\Delta}^{(n')} \circ (c) = \Delta^{(n')}(c), \quad c \in C.
\tag{136}
$$

In general, one does not distinguish $\boldsymbol{\Delta}^{(n')}$ and $\Delta^{(n')}$ and may use one symbol in both descriptions.

In real "elementwise" coalgebra computations with many variables and comultiplications acting on them, the indices and various letters reproduce themselves in such a way that it is impossible to observe the structure of the expressions. Therefore, instead of different letters in the binary decomposition ("$\Delta(c) = \sum_i a_i \otimes b_i$" and (104)) it was proposed [32] to use the *same letter* ("$\Delta(c) = \sum_i c_{[1],i} \otimes c_{[2],i}$"), and then go from the *real* sum $\sum_i$ to the *formal* sum $\sum_{[c]}$ as ("$\Delta(c) = \sum_{[c]} c_{[1]} \otimes c_{[2]}$" remembering the place of the components $c_{[1]}, c_{[2]}$ only), because the real indices pullulate in complicated formulas enormously. In simple cases, the sum sign was also omitted ("$\Delta(c) = c_{[1]} \otimes c_{[2]}$"), which recalls the Einstein index summation rule in physics. This trick abbreviated

tedious coalgebra computations and was called the (*sumless*) *Sweedler* (*sigma*) *notation* (sometimes it is called the *Heyneman-Sweedler notation* [33]).

Now we can write $\Delta^{(n')}$ as a n'-ary decomposition in the manifest "elementwise" form

$$\Delta^{(n')}(c) = \left(\nu^{(m)}\right)^{\circ \ell_\Delta} \left[c_{[1],1} \otimes c_{[2],1} \otimes \ldots \otimes c_{[n'],1}, \ldots, c_{[1],N_\Delta} \otimes c_{[2],N_\Delta} \otimes \ldots \otimes c_{[n'],N_\Delta}\right], \quad c_{[j],i} \in C, \quad (137)$$

where $\ell_\Delta \in \mathbb{N}_0$ is a "number of additions", and $N_\Delta \in \mathbb{N}$ is the "number of summands". In the binary case, the number of summands in the decomposition is not "algebraically" restricted, because $N_\Delta = \ell_\Delta + 1$. In the polyadic case, we have

Assertion 70. *The admissible "number of summands" N_Δ in the polyadic comultiplication is*

$$N_\Delta = \ell_\Delta (m-1) + 1, \quad \ell_\Delta \in \mathbb{N}_0, \quad m \geq 2. \quad (138)$$

Therefore, the "quantization" of N_Δ coincides with that of the N-dimensional polyadic algebra (see **Assertion** 44).

Introduce the *polyadic Sweedler notation* by exchanging in (137) the *real m-ary addition* $\nu^{(m)}$ by the *formal addition* $\nu_{[c]}$ and writing

$$\Delta^{(n')}(c) = \nu_{[c]}\left[c_{[1]} \otimes c_{[2]} \otimes \ldots \otimes c_{[n']}\right] \Rightarrow c_{[1]} \otimes c_{[2]} \otimes \ldots \otimes c_{[n']}. \quad (139)$$

Remember here that we can formally add only N_Δ summands, because of the "quantization" (138) rule.

The polyadic Sweedler notation power can be seen in the following

Example 71. We apply (139) to the coassociativity (111) with $n' = 3$, to obtain

$$\left(\mathrm{id} \otimes \mathrm{id} \otimes \Delta^{(3)}\right) \circ \Delta^{(3)}(c) = \left(\mathrm{id} \otimes \Delta^{(3)} \otimes \mathrm{id}\right) \circ \Delta^{(3)}(c) = \left(\Delta^{(3)} \otimes \mathrm{id} \otimes \mathrm{id}\right) \circ \Delta^{(3)}(c) \Rightarrow \quad (140)$$

$$= \nu_{[c]}\left[c_{[1]} \otimes c_{[2]} \otimes \nu_{[c_2]}\left[\left(c_{[3]}\right)_{[1]} \otimes \left(c_{[3]}\right)_{[2]} \otimes \left(c_{[3]}\right)_{[3]}\right]\right]$$

$$= \nu_{[c]}\left[c_{[1]} \otimes \nu_{[c_2]}\left[\left(c_{[2]}\right)_{[1]} \otimes \left(c_{[2]}\right)_{[2]} \otimes \left(c_{[2]}\right)_{[3]}\right] \otimes c_{[3]}\right]$$

$$= \nu_{[c]}\left[\nu_{[c_2]}\left[\left(c_{[1]}\right)_{[1]} \otimes \left(c_{[1]}\right)_{[2]} \otimes \left(c_{[1]}\right)_{[3]}\right] \otimes c_{[2]} \otimes c_{[3]}\right]. \quad (141)$$

After dropping the brackets and applying the Sweedler trick for the second time, we get the same formal expression in all three cases

$$\left(\nu_{[c]}\right)^{\circ 2}\left[c_{[1]} \otimes c_{[2]} \otimes c_{[3]} \otimes c_{[4]} \otimes c_{[5]}\right]. \quad (142)$$

Unfortunately, in the polyadic case the Sweedler notation looses too much information to be useful.

Assertion 72. *The polyadic Sweedler notation can be applied to only the derived polyadic coalgebras.*

Nevertheless, if in an expression there are no coiterations, one can formally use it (e.g., in the polyadic analog (124) of the counting axiom "$\sum \varepsilon\left(c_{[1]}\right) c_{[2]} = c$").

Polyadic group-like and primitive elements

Let us consider some special kinds of elements in a polyadic coalgebra $C^{(n')}$. We should take into account that in the polyadic case, as in (137), there can only be the admissible "number of summands" N_Δ (138).

Definition 73. An element g of $C^{(n')}$ is called *polyadic semigroup-like*, if

$$\Delta^{(n')}(g) = \overbrace{g \otimes \ldots \otimes g}^{n'}, \quad g \in C. \quad (143)$$

When $C^{(n')}$ has the counit $\varepsilon^{(n',r')}$ (124), then g is called *polyadic group-like*, if ("$\varepsilon(g) = 1$")

$$\varepsilon^{(n',r')} \circ \left(\overbrace{g \otimes \ldots \otimes g}^{n'-1}\right) = \overbrace{e_k \otimes \ldots \otimes e_k}^{r'}, \quad (144)$$

where e_k is the unit of the underlying polyadic field $\Bbbk$.

Definition 74. An element x of $C^{(n')}$ is called *polyadic skew k_p-primitive*, if ("$\Delta(x) = g_1 \otimes x + x \otimes g_2$")

$$\Delta^{(n')}(x) = \left(\nu^{(m)}\right)^{\circ \ell_\Delta} \left[\left(\overbrace{g_1 \otimes \ldots \otimes g_{k_p}}^{k_p} \otimes \overbrace{x \otimes \ldots \otimes x}^{n'-k_p} \right), \ldots, \right.$$
$$\left. \left(\overbrace{x \otimes \ldots \otimes x}^{n'-k_p} \otimes \overbrace{g_{(N_\Delta-1)k_p+1} \otimes \ldots \otimes g_{N_\Delta k_p}}^{k_p} \right) \right], \tag{145}$$

where $1 \le k_p \le n'-1$, $N_\Delta = \ell_\Delta(m-1) + 1$ is the total "number of summands", here $\ell_\Delta \in \mathbb{N}$ is the "number of m-ary additions", and $g_i \in C$, $i = 1, \ldots, N_\Delta k_p$ are polyadic (semi-)group-like (143). In (145) the $n'-k_p$ elements x move from the right to the left by one.

Assertion 75. *If $k_p = n'-1$, then $\Delta^{(n')}(x)$ is "linear" in x, and $n' = \ell_\Delta(m-1) + 1$.*

In this case, we call x a *polyadic primitive element*.

Example 76. Let $n' = 3$ and $k_p = 2$, then $m = 3$, and we have only one ternary addition $\ell_\Delta = 1$

$$\Delta^{(3)}(x) = \nu^{(3)}[g_1 \otimes g_2 \otimes x, \ g_3 \otimes x \otimes g_4, \ x \otimes g_5 \otimes g_6], \tag{146}$$
$$\Delta^{(3)}(g_i) = g_i \otimes g_i \otimes g_i, \quad i = 1, \ldots, 6. \tag{147}$$

The ternary coassociativity gives $g_1 = g_2 = g_3$ and $g_4 = g_5 = g_6$. Therefore, the general form of the ternary primitive element is

$$\Delta^{(3)}(x) = \nu^{(3)}[g_1 \otimes g_1 \otimes x, \ g_1 \otimes x \otimes g_2, \ x \otimes g_2 \otimes g_2]. \tag{148}$$

Note that coassociativity leads to the *derived* comultiplication (116), because

$$\Delta^{(3)}(x) = \left(\mathrm{id} \otimes \Delta^{(2)}\right) \Delta^{(2)}(x) = \left(\Delta^{(2)} \otimes \mathrm{id}\right) \Delta^{(2)}(x), \tag{149}$$
$$\Delta^{(2)}(x) = g_1 \otimes x + x \otimes g_2. \tag{150}$$

The same situation occurs with the "linear" comultiplication of any arity n', i.e. when $k_p = n'-1$.

The most important difference with the binary case is the "intermediate" possibility $k_p < n'-1$, when the r.h.s. is "nonlinear" in x.

Example 77. In the case where $n' = 3$ and $k_p = 1$, we have $m = 3$, and $\ell_\Delta = 1$

$$\Delta^{(3)}(x) = \nu^{(3)}[g_1 \otimes x \otimes x, \ x \otimes g_2 \otimes x, \ x \otimes x \otimes g_3], \tag{151}$$
$$\Delta^{(3)}(g_i) = g_i \otimes g_i \otimes g_i, \quad i = 1, \ldots, 3. \tag{152}$$

Now ternary coassociativity cannot be achieved with any values of g_i. This is true for any arity n' and any "nonlinear" comultiplication.

Therefore, we arrive at the general structure

Assertion 78. *In a polyadic coassociative coalgebra $C^{(n')}$ polyadic primitive elements exist, if and only if the n'-ary comultiplication $\Delta^{(n')}$ is derived (116) from the binary comultiplication $\Delta^{(2)}$.*

Polyadic analog of duality

The connection between binary associative algebras and coassociative coalgebras (formally named as "reversing arrows") is given in terms of the dual vector space (dual module) concept. Informally, for a binary coalgebra $C^{(2)} = \langle C \mid \Delta, \varepsilon \rangle$ considered as a vector space over a binary field k (a k-vector space), its *dual* is $C_2^* = \mathrm{Hom}_k(C, k)$ with the natural *pairing* $C^* \times C \to k$ given by $f(c)$, $f \in C^*$, $c \in C$. The *canonical injection* $\theta : C^* \otimes C^* \to (C \otimes C)^*$ is defined by

$$\theta(f_1 \otimes f_2) \circ (c_1 \otimes c_2) = f_1(c_1) f_2(c_2), \quad c_{1,2} \in C, \quad f_{1,2} \in C^*, \tag{153}$$

which is an isomorphism in the finite-dimensional case. The transpose of $\Delta : C \to C \otimes C$ is a k-linear map $\Delta_* : (C \otimes C)^* \to C^*$ acting as $\Delta_*(\xi)(c) = \xi \circ (\Delta(c))$, where $\xi \in (C \otimes C)^*$, $c \in C$. The multiplication μ_* on the set C^* is the map $C^* \otimes C^* \to C^*$, and therefore we have to use the canonical injection θ as follows

$$\mu_* : C^* \otimes C^* \overset{\theta}{\to} (C \otimes C)^* \overset{\Delta_*}{\to} C^*, \tag{154}$$
$$\mu_* = \Delta_* \circ \theta. \tag{155}$$

The associativity of μ_* follows from the coassociativity of Δ. Since $k^* \simeq k$, the dual of the counit is the unit $\eta_* : k \xrightarrow{\varepsilon^*} C^*$. Therefore, $C^{(2)*} = \langle C^* \mid \mu_*, \eta_* \rangle$ is a binary associative algebra which is called the *dual algebra* of the binary coalgebra $C^{(2)} = \langle C \mid \Delta, \varepsilon \rangle$ (see, e.g. [3]).

In the polyadic case, arities of the comultiplication, its dual multiplication and the underlying field can be different, but connected by (153). Let us consider a polyadic coassociative coalgebra $C^{(n')}$ with n'-ary comultiplication $\Delta^{(n')}$ (136) over $\Bbbk^{(m_k, n_k)}$. In search of the most general polyadic analog of the injection (153), we arrive at the possibility of multiplace morphisms.

Definition 79. For the polyadic coalgebra $C^{(n')}$ considered as a polyadic vector space over $\Bbbk^{(m_k, n_k)}$, a *polyadic dual* is $C^* = \mathrm{Hom}_\Bbbk (C^{\otimes s}, K)$ with *s*-place pairing $C^* \times \overbrace{C \times \ldots \times C}^{s} \to K$ giving by $f^{(s)}(c_1, \ldots, c_s)$, $f \in C^*$, $c_i \in C$, $s \in \mathbb{N}$.

While constructing a polyadic analog of (153), recall that for any n'-ary operation the admissible length of a co-word is $\ell'(n'-1)+1$, where ℓ' is the number of the iterated operation (115).

Definition 80. A *polyadic canonical injection map* $\boldsymbol{\theta}^{(n^*, n', s)}$ of $C^{(n')}$ is defined by

$$\boldsymbol{\theta}^{(n^*, n', s)} \circ \left(f_1^{(s)} \otimes \ldots \otimes f_{n^*}^{(s)} \right) \circ \left(c_1 \otimes \ldots \otimes c_{\ell'(n'-1)+1} \right) =$$
$$\left(\mu_k^{(n_k)} \right)^{\circ \ell_k} \left[f_1^{(s)}(c_1, \ldots, c_s), \ldots, f_{\ell_k(n_k-1)+1}^{(s)} \left(c_{(n^*-1)s+1}, \ldots, c_{n^* s} \right) \right], \tag{156}$$

where

$$n^* s = \ell'(n'-1)+1, \quad \ell' \in \mathbb{N}, \quad n' \geq 2, \tag{157}$$
$$n^* = \ell_k(n_k-1)+1, \quad \ell_k \in \mathbb{N}, \quad n_k \geq 2. \tag{158}$$

It is obvious that $\theta^{(2,2,1)} = \theta$ from (153). Then, the *polyadic transpose map* of the n'-ary comultiplication $\Delta^{(n')} : C \to \overbrace{C \otimes \ldots \otimes C}^{n'}$ is a $\Bbbk$-linear map $\Delta_*^{(n'')} : \left(\overbrace{C \otimes \ldots \otimes C}^{n''} \right)^* \to C^*$ such that

$$\Delta_*^{(n'')} \circ \left(\xi^{(n'')} \right)(c) = \xi^{(n'')} \circ \left(\left(\Delta^{(n')} \right)^{\circ \ell'}(c) \right),$$
$$\xi^{(n'')} \in \left(\overbrace{C \otimes \ldots \otimes C}^{n''} \right)^*, \quad n'' = \ell'(n'-1)+1, \; c \in C \tag{159}$$

where ℓ' is the "number of comultiplications" (see (6) for multiplications and (115)).

Definition 81. A n^*-ary multiplication map $\boldsymbol{\mu}_*^{(n^*)}$ which is (*one way*) *dual* to the n'-ary comultiplication map $\boldsymbol{\Delta}^{(n')}$ is given by the composition of the polyadic canonical injection $\boldsymbol{\theta}^{(n^*, n', s)}$ (156) and the polyadic transpose $\boldsymbol{\Delta}_*^{(n'')}$ (159) by

$$\boldsymbol{\mu}_*^{(n^*)} = \boldsymbol{\Delta}_*^{(n'')} \circ \boldsymbol{\theta}^{(n^*, n', s)}. \tag{160}$$

Indeed, using (156) and (159) we obtain (in Sweedler notation)

$$\boldsymbol{\mu}_*^{(n^*)} \circ \left(f_1^{(s)} \otimes \ldots \otimes f_{n^*}^{(s)} \right) \circ (c) = \boldsymbol{\Delta}_*^{(n'')} \circ \boldsymbol{\theta}^{(n^*, n', s)} \circ \left(f_1^{(s)} \otimes \ldots \otimes f_{n^*}^{(s)} \right) \circ (c)$$
$$= \boldsymbol{\theta}^{(n^*, n', s)} \circ \left(f_1^{(s)} \otimes \ldots \otimes f_{n^*}^{(s)} \right) \circ \left(\left(\Delta^{(n')} \right)^{\circ \ell'}(c) \right)$$
$$= \left(\mu_k^{(n_k)} \right)^{\circ \ell_k} \left[f_1^{(s)} \left(c_{[1]}, \ldots, c_{[s]} \right), \ldots, f_{\ell_k(n_k-1)+1}^{(s)} \left(c_{[(n^*-1)s+1]}, \ldots, c_{[n^* s]} \right) \right], \tag{161}$$

and (157)–(158) are valid, from which we arrive at

Assertion 82. *In the polyadic case the arity n^* of the multiplication $\boldsymbol{\mu}_*^{(n^*)}$ can be different from the arity n' of the initial coalgebra $C^{(n')}$.*

Remark 83. If $n^* \neq n'$ and $s \geq 2$, the word "duality" can only be used conditionally.

Polyadic convolution product

If $A^{(2)} = \langle A \mid \mu, \eta \rangle$ is a binary algebra and $C^{(2)} = \langle C \mid \Delta, \varepsilon \rangle$ is a binary coalgebra over a binary field k, then a more general set of k-linear maps $\mathrm{Hom}_k(C, A)$ can be considered, while its particular case where $A^{(2)} = k$ corresponds to the above duality. The multiplication on $\mathrm{Hom}_k(C, A)$ is the *convolution product* ($\star$) which can be *uniquely* constructed in the natural way: by applying first comultiplication Δ and then multiplication $\mu \equiv (\cdot)$ to an element of C, as $C \xrightarrow{\Delta} C \otimes C \xrightarrow{f \otimes g} A \otimes A \xrightarrow{\mu} A$ or $f \star g = \mu \circ (f \otimes g) \circ \Delta$, where $f, g \in \mathrm{Hom}_k(C, A)$. The associativity of the convolution product follows from the associativity of μ and coassociativity of Δ, and the role of the identity (neutral element) in $\mathrm{Hom}_k(C, A)$ is played by the composition of the unit map $\eta : k \to A$ and the counit map $\varepsilon : C \to k$, such that $e_\star = \eta \circ \varepsilon \in \mathrm{Hom}_k(C, A)$, because $e_\star \star f = f \star e_\star = f$. Indeed, from the obvious relation $\mathrm{id}_A \circ f \circ \mathrm{id}_C = f$ and the unit and counit axioms it follows that

$$\mu \circ (\eta \otimes \mathrm{id}_A) \circ (\mathrm{id}_K \otimes f) \circ (\varepsilon \otimes \mathrm{id}_C) \circ \Delta = \mu \circ (\eta \circ \mathrm{id}_K \circ \varepsilon) \otimes (\mathrm{id}_A \circ f \circ \mathrm{id}_C) \circ \Delta = e_\star \star f = f, \qquad (162)$$

or in Sweedler notation $\varepsilon\left(c_{[1]}\right) \cdot f\left(c_{[2]}\right) = f\left(c_{[1]}\right) \cdot \varepsilon\left(c_{[2]}\right) = f(c)$.

The polyadic analog of duality and (161) offer an idea of how to generalize the binary convolution product to the most exotic case, when the algebra and coalgebra have *different arities* $n \neq n'$.

Let $A^{(n)}$ and $C^{(n')}$ be, respectively, a polyadic associative algebra and a coassociative coalgebra over the same polyadic field $\Bbbk^{(m_k, n_k)}$. If they are both unital and counital respectively, then we can consider a polyadic analog of the composition $\eta \circ \varepsilon$. The crucial difference from the binary case is that now $\boldsymbol{\eta}^{(r,n)}$ and $\boldsymbol{\varepsilon}^{(n',r')}$ are multiplace multivalued maps (48) and (124). Their composition is

$$\boldsymbol{e}_\star^{(n',n)} = \boldsymbol{\eta}^{(r,n)} \circ \boldsymbol{\gamma}^{(r',r)} \circ \boldsymbol{\varepsilon}^{(n',r')} \in \mathrm{Hom}_\Bbbk \left(C^{\otimes (n'-1)}, A^{\otimes (n-1)} \right), \qquad (163)$$

where the multiplace multivalued map $\boldsymbol{\gamma}^{(r',r)} \in \mathrm{Hom}_\Bbbk \left(K^{\otimes r'}, K^{\otimes r} \right)$ is, obviously, ($\simeq$), and the diagram

$$(164)$$

commutes.

The formula (163) leads us to propose

Conjecture 84. A polyadic analog of the convolution should be considered for *multiplace multivalued* $\Bbbk$-linear maps in $\mathrm{Hom}_\Bbbk \left(C^{\otimes (n'-1)}, A^{\otimes (n-1)} \right)$.

In this way, we arrive at the following

Construction 85. Introduce the $\Bbbk$-linear maps $\mathbf{f}^{(i)} : C^{\otimes (n'-1)} \to A^{\otimes (n-1)}$, $i = 1, \ldots, n_\star$, where $n_\star \geq 2$. To create a closed $n_\star$-ary operation for them, we use the ℓ-iterated multiplication map $\left(\boldsymbol{\mu}^{(n)}\right)^{\circ \ell} : A^{\otimes \ell (n-1)+1} \to A$ and ℓ'-iterated comultiplication map $\left(\boldsymbol{\Delta}^{(n')}\right)^{\circ \ell'} : C \to C^{\otimes \ell'(n'-1)+1}$. Then we compose the above $\Bbbk$-linear maps in the same way as is done above for the binary case

$$(165)$$

where $\boldsymbol{\tau}_{medial}^{(n_\star, n'-1)}$ and $\boldsymbol{\tau}_{medial}^{(n-1, n_\star)}$ are the medial maps (69) acting on the Sweedler components of c and $\mathbf{f}^{(i)}$, respectively. To make the sequence of maps (165) consistent, the arity $n_\star$ is connected with the iteration numbers ℓ, ℓ' by $n_\star = \ell(n-1) + 1 = \ell'(n'-1) + 1$, $\ell, \ell' \in \mathbb{N}$.

Definition 86. Let $A^{(n)}$ and $C^{(n')}$ be a n-ary associative algebra and n'-ary coassociative coalgebra over a polyadic field $\Bbbk$ (the existence of the unit and counit here is mandatory), then the set $\mathrm{Hom}_\Bbbk \left(C^{\otimes (n'-1)}, A^{\otimes (n-1)} \right)$

is closed under the $n_\star$-*ary convolution product* map $\boldsymbol{\mu}_\star^{(n_\star)}$ defined by

$$\boldsymbol{\mu}_\star^{(n_\star)} \circ \left(\mathbf{f}^{(1)} \otimes \ldots \otimes \mathbf{f}^{(n_\star)} \right) = \tag{166}$$

$$\left(\left(\boldsymbol{\mu}^{(n)} \right)^{\circ \ell} \right)^{\otimes (n-1)} \circ \boldsymbol{\tau}_{medial}^{(n-1,n_\star)} \circ \left(\mathbf{f}^{(1)} \otimes \ldots \otimes \mathbf{f}^{(n_\star)} \right) \circ \boldsymbol{\tau}_{medial}^{(n_\star,n'-1)} \circ \left(\left(\boldsymbol{\Delta}^{(n')} \right)^{\circ \ell'} \right)^{\otimes (n'-1)},$$

and its arity is given by the following $n_\star$-*consistency condition*

$$n_\star - 1 = \ell \, (n-1) = \ell' \, (n'-1). \tag{167}$$

Definition 87. The set of $\Bbbk$-linear maps $\mathbf{f}^{(i)} \in \mathrm{Hom}_\Bbbk \left(C^{\otimes (n'-1)}, A^{\otimes (n-1)} \right)$ endowed with the convolution product (166) is called a *polyadic convolution algebra*

$$C_\star^{(n',n)} = \left\langle \mathrm{Hom}_\Bbbk \left(C^{\otimes (n'-1)}, A^{\otimes (n-1)} \right) \mid \boldsymbol{\mu}_\star^{(n_\star)} \right\rangle. \tag{168}$$

Example 88. An important case is given by the binary algebra $A^{(2)}$ and coalgebra $C^{(2)}$ ($n = n' = 2$), when the number of iterations are equal $\ell = \ell'$, and the arity $n_\star$ becomes

$$n_\star = \ell + 1 = \ell' + 1, \quad \ell, \ell' \in \mathbb{N}, \tag{169}$$

while the $n_\star$-ary convolution product in $\mathrm{Hom}_\Bbbk (C, A)$ takes the form

$$\boldsymbol{\mu}_\star^{(n_\star)} \circ \left(\mathbf{f}^{(1)} \otimes \ldots \otimes \mathbf{f}^{(n_\star)} \right) = \boldsymbol{\mu}^{\circ (n_\star-1)} \circ \left(\mathbf{f}^{(1)} \otimes \ldots \otimes \mathbf{f}^{(n_\star)} \right) \circ \boldsymbol{\Delta}^{\circ (n_\star-1)}, \quad \mathbf{f}^{(i)} \in \mathrm{Hom}_\Bbbk (C, A), \tag{170}$$

where $\boldsymbol{\mu} = \boldsymbol{\mu}^{(2)}$ and $\boldsymbol{\Delta} = \boldsymbol{\Delta}^{(2)}$ are the binary multiplication and comultiplication maps respectively.

Definition 89. The polyadic convolution algebra $C_\star^{(2,2)}$ determined by the binary algebra and binary coalgebra (170) is called *derived*.

Corollary 90. The arity $n_\star$ of the derived polyadic convolution algebra is *unrestricted* and can take any integer value $n_\star \geq 2$.

Remark 91. If the polyadic tensor product and the underlying polyadic field $\Bbbk$ are derived (see discussion [10]), while all maps coincide $\mathbf{f}^{(i)} = \mathbf{f}$, the convolution product (170) is called the *Sweedler power* of $\mathbf{f}$ [34] or the *Adams operator* [35]. In the binary case they denoted it by $(\mathbf{f})^{n_\star}$, but for the $n_\star$-ary product this is the *first polyadic power* of $\mathbf{f}$ (see (6)).

Obviously, some interesting algebraic objects are nonderived, and here they are determined by $n + n' \geq 5$, and also the arities of the algebra and coalgebra can be different $n \neq n'$, which is a more exotic and exciting possibility. Generally, the arity $n_\star$ of the convolution product (166) is not arbitrary and is "quantized" by solving (167) in integers. The values $n_\star$ for minimal arities n, n' are presented in TABLE 3.

The most unusual possibility is the existence of nondiagonal entries, which correspond to unequal arities of multiplication and comultiplication $n \neq n'$. The table is symmetric, which means that the arity $n_\star$ is invariant under the exchange $(n, \ell) \longleftrightarrow (n', \ell')$ following from (167).

Example 92 ($\mathrm{Hom}_\Bbbk (C, A)$). In the simplest derived case (170), when both algebra $A^{(2)} = \langle A \mid \boldsymbol{\mu} \rangle$ and coalgebra $C^{(2)} = \langle C \mid \boldsymbol{\Delta} \rangle$ are binary with $n = 2, \ell = 2, n' = 2, \ell' = 2$, it is possible to obtain the ternary convolution product $\boldsymbol{\mu}_\star^{(3)}$ of the maps $\mathbf{f}^{(i)} : C \to A$, $i = 1, 2, 3$, using Sweedler notation for $\boldsymbol{\Delta}^{\circ 2} \equiv (\mathrm{id}_C \otimes \boldsymbol{\Delta}) \circ \boldsymbol{\Delta}$ as $\Delta^{\circ 2}(c) = c_{[1]} \otimes c_{[2]} \otimes c_{[3]}$, $\boldsymbol{\mu}^{\circ 2} \equiv \boldsymbol{\mu} \circ (\mathrm{id}_A \otimes \boldsymbol{\mu}) : A^{\otimes 3} \to A$, and the elementwise description using the evaluation

$$\boldsymbol{\mu}_{\star,der}^{(3)} \circ \left(\mathbf{f}^{(1)} \otimes \mathbf{f}^{(2)} \otimes \mathbf{f}^{(3)} \right) \circ (c) = \mu^{\circ 2} \left[f^{(1)} \left(c_{[1]} \right), f^{(2)} \left(c_{[2]} \right), f^{(3)} \left(c_{[3]} \right) \right]. \tag{171}$$

Example 93 ($\mathrm{Hom}_\Bbbk \left(C, A^{\otimes 2} \right)$, $\mathrm{Hom}_\Bbbk \left(C^{\otimes 2}, A \right)$). Nonbinary, nonderived and nonsymmetric cases:

1. The ternary algebra $A^{(3)} = \left\langle A \mid \boldsymbol{\mu}^{(3)} \right\rangle$ and the binary coalgebra $C^{(2)} = \langle C \mid \boldsymbol{\Delta} \rangle$, such that $n = 3, \ell = 1, n' = 2, \ell' = 2$ giving a ternary convolution product of the maps $\mathbf{f}^{(i)} : C \to A^{\otimes 2}$, $i = 1, 2, 3$. In the elementwise description $\mathbf{f}^{(i)} \circ (c) = f_{[1]}^{(i)}(c) \otimes f_{[2]}^{(i)}(c)$, $c \in C$. Using (166), we obtain the manifest form of the nonderived ternary convolution product by evaluation

$$\boldsymbol{\mu}_\star^{(3)} \circ \left(\mathbf{f}^{(1)} \otimes \mathbf{f}^{(2)} \otimes \mathbf{f}^{(3)} \right) \circ (c)$$

$$= \mu^{(3)} \left[f_{[1]}^{(1)} \left(c_{[1]} \right), f_{[1]}^{(2)} \left(c_{[2]} \right), f_{[1]}^{(3)} \left(c_{[3]} \right) \right] \otimes \mu^{(3)} \left[f_{[2]}^{(1)} \left(c_{[1]} \right), f_{[2]}^{(2)} \left(c_{[2]} \right), f_{[2]}^{(3)} \left(c_{[3]} \right) \right], \tag{172}$$

   where $\Delta^{\circ 2}(c) = c_{[1]} \otimes c_{[2]} \otimes c_{[3]}$.

Table 3: Arity values $n_\star$ of the polyadic convolution product (166), allowed by (167). The framed box corresponds to the binary convolution product.

n' \ n	$\boldsymbol{\mu}$ \ ℓ	$n=2$			$n=3$			$n=4$			$n=5$		
$\boldsymbol{\Delta}$ / ℓ'		$\ell=1$	$\ell=2$	$\ell=3$	$\ell=1$	$\ell=2$	$\ell=3$	$\ell=1$	$\ell=2$	$\ell=3$	$\ell=1$	$\ell=2$	$\ell=3$
$n'=2$	$\ell'=1$	$\boxed{2}$											
	$\ell'=2$		3		3								
	$\ell'=3$			4				4					
$n'=3$	$\ell'=1$		3		3								
	$\ell'=2$					5					5		
	$\ell'=3$						7		7				
$n'=4$	$\ell'=1$			4				4					
	$\ell'=2$						7		7				
	$\ell'=3$									10			
$n'=5$	$\ell'=1$					5					5		
	$\ell'=2$											9	
	$\ell'=3$												13

2. The algebra is binary $A^{(2)} = \langle A \mid \boldsymbol{\mu} \rangle$, and the coalgebra is ternary $C^{(3)} = \langle C \mid \boldsymbol{\Delta}^{(3)} \rangle$, which corresponds to $n = 2, \ell = 2, n' = 3, \ell' = 1$, the maps $\mathbf{f}^{(i)} : C^{\otimes 2} \to A$, $i = 1, 2, 3$ in the elementwise description are two place, $\mathbf{f}^{(i)} \circ (c_1 \otimes c_2) = f^{(i)}(c_1, c_2)$, $c_{1,2} \in C$, and $\left(\Delta^{(3)}\right)^{\otimes 2} \left(c^{(1)} \otimes c^{(2)}\right) = \left(c^{(1)}_{[1]} \otimes c^{(1)}_{[2]} \otimes c^{(1)}_{[3]}\right) \otimes \left(c^{(2)}_{[1]} \otimes c^{(2)}_{[2]} \otimes c^{(2)}_{[3]}\right)$. The ternary convolution product is

$$\boldsymbol{\mu}^{(3)}_\star \circ \left(\mathbf{f}^{(1)} \otimes \mathbf{f}^{(2)} \otimes \mathbf{f}^{(3)}\right) \circ \left(c^{(1)} \otimes c^{(2)}\right) = \mu^{\circ 2} \left[f^{(1)}\left(c^{(1)}_{[1]}, c^{(2)}_{[1]}\right), f^{(2)}\left(c^{(1)}_{[2]}, c^{(2)}_{[2]}\right), f^{(3)}\left(c^{(1)}_{[3]}, c^{(2)}_{[3]}\right)\right]. \quad (173)$$

Example 94 ($\mathrm{Hom}_{\Bbbk}\left(C^{\otimes 2}, A^{\otimes 2}\right)$). The last (fourth) possibility for the ternary convolution product (see TABLE 3) is nonderived and symmetric $n = 3, \ell = 1, n' = 3, \ell' = 1$, with both a ternary algebra $A^{(3)} = \langle A \mid \boldsymbol{\mu}^{(3)} \rangle$ and coalgebra $C^{(3)} = \langle C \mid \boldsymbol{\Delta}^{(3)} \rangle$. In the elementwise description the maps $\mathbf{f}^{(i)} : C^{\otimes 2} \to A^{\otimes 2}$, $i = 1, 2, 3$ are $\mathbf{f}^{(i)} \circ (c_1 \otimes c_2) = f^{(i)}_{[1]}(c_1, c_2) \otimes f^{(i)}_{[2]}(c_1, c_2)$, $c_{1,2} \in C$. Then

$$\boldsymbol{\mu}^{(3)}_\star \circ \left(\mathbf{f}^{(1)} \otimes \mathbf{f}^{(2)} \otimes \mathbf{f}^{(3)}\right) \circ \left(c^{(1)} \otimes c^{(2)}\right) = \mu^{(3)} \left[f^{(1)}_{[1]}\left(c^{(1)}_{[1]}, c^{(2)}_{[1]}\right), f^{(2)}_{[1]}\left(c^{(1)}_{[2]}, c^{(2)}_{[2]}\right), f^{(3)}_{[1]}\left(c^{(1)}_{[3]}, c^{(2)}_{[3]}\right)\right]$$
$$\otimes \mu^{(3)} \left[f^{(1)}_{[2]}\left(c^{(1)}_{[1]}, c^{(2)}_{[1]}\right), f^{(2)}_{[2]}\left(c^{(1)}_{[2]}, c^{(2)}_{[2]}\right), f^{(3)}_{[2]}\left(c^{(1)}_{[3]}, c^{(2)}_{[3]}\right)\right]. \quad (174)$$

The above examples present clearly the possible forms of the $n_\star$-ary convolution product, which can be convenient for lowest arity computations.

The *general polyadic convolution product* (166) in Sweedler notation can be presented as

$$\boldsymbol{\mu}^{(n_\star)}_\star \circ \left(\mathbf{f}^{(1)} \otimes \mathbf{f}^{(2)} \otimes \ldots \otimes \mathbf{f}^{(n_\star)}\right) = \mathbf{g}, \quad \mathbf{f}^{(i)}, \mathbf{g} \in \mathrm{Hom}_{\Bbbk}\left(C^{\otimes\left(n'-1\right)}, A^{\otimes(n-1)}\right),$$

$$\mathbf{g}_{[j]} \circ \left(c^{(1)} \otimes \ldots \otimes c^{\left(n'-1\right)}\right)$$

$$= \left(\mu^{(n)}\right)^{\circ\ell} \left[f^{(1)}_{[j]}\left(\overbrace{c^{(1)}_{[1]}, \ldots, c^{\left(n'-1\right)}_{[1]}}^{n'-1}\right), f^{(2)}_{[j]}\left(\overbrace{c^{(1)}_{[2]}, \ldots, c^{\left(n'-1\right)}_{[2]}}^{n'-1}\right), \ldots, f^{(n_\star)}_{[j]}\left(\overbrace{c^{(1)}_{[n_\star]}, \ldots, c^{\left(n'-1\right)}_{[n_\star]}}^{n'-1}\right)\right],$$

$$f^{(i)}_{[j]} \in \mathrm{Hom}_{\Bbbk}\left(C^{\otimes\left(n'-1\right)}, A\right), \quad i \in 1, \ldots, n_\star, \quad j \in 1, \ldots, n-1, \quad c \in C, \quad (175)$$

where $\mathbf{g}_{[j]}$ are the Sweedler components of $\mathbf{g}$.

Recall that the associativity of the binary convolution product ($\star$) is transparent in the Sweedler notation. Indeed, if $(f \star g) \circ (c) = f\left(c_{[1]}\right) \cdot g\left(c_{[2]}\right)$, $f, g, h \in \mathrm{Hom}_k(C, A)$, $c \in C$, $(\cdot) \equiv \mu^{(2)}_A$, then $((f \star g) \star h) \circ (c) = \left(f\left(c_{[1]}\right) \cdot g\left(c_{[2]}\right)\right) \cdot h\left(c_{[3]}\right) = f\left(c_{[1]}\right) \cdot \left(g\left(c_{[2]}\right) \cdot h\left(c_{[3]}\right)\right) = (f \star (g \star h)) \circ (c)$.

Lemma 95. *The polyadic convolution algebra $C_\star^{(n',n)}$ (168) is associative.*

Proof. To prove the claimed associativity of polyadic convolution $\boldsymbol{\mu}_\star^{(n_\star)}$ we express (5) in Sweedler notation. Starting from

$$\mathbf{h} = \boldsymbol{\mu}_\star^{(n_\star)} \circ \left(\mathbf{g} \otimes \mathbf{f}^{(n_\star+1)} \otimes \mathbf{f}^{(n_\star+2)} \otimes \ldots \otimes \mathbf{f}^{(2n_\star-1)}\right), \quad \mathbf{h} \in \mathrm{Hom}_\Bbbk\left(C^{\otimes(n'-1)}, A^{\otimes(n-1)}\right), \tag{176}$$

where $\mathbf{g}$ is given by (175), it follows that $\mathbf{h}$ should not depend of place of $\mathbf{g}$ in (176). Applying $\mathbf{h}$ to $c \in C$ twice, we obtain for its Sweedler components $\mathbf{h}_{[j]}, \quad j \in 1, \ldots, n-1$,

$$\mathbf{h}_{[j]} \circ \left(c^{(1)} \otimes \ldots \otimes c^{(n'-1)}\right) = \left(\mu^{(n)}\right)^{\circ\ell} \left[\left(\mu^{(n)}\right)^{\circ\ell} \left[f_{[j]}^{(1)}\left(\overbrace{c_{[1]}^{(1)}, \ldots, c_{[1]}^{(n'-1)}}^{n'-1}\right), f_{[j]}^{(2)}\left(\overbrace{c_{[2]}^{(1)}, \ldots, c_{[2]}^{(n'-1)}}^{n'-1}\right), \right.\right.$$

$$\left.\ldots, f_{[j]}^{(n_\star)}\left(\overbrace{c_{[2n_\star-1]}^{(1)}, \ldots, c_{[2n_\star-1]}^{(n'-1)}}^{n'-1}\right)\right], f_{[j]}^{(n_\star+1)}\left(\overbrace{c_{[1]}^{(1)}, \ldots, c_{[1]}^{(n'-1)}}^{n'-1}\right), f_{[j]}^{(n_\star+2)}\left(\overbrace{c_{[2]}^{(1)}, \ldots, c_{[2]}^{(n'-1)}}^{n'-1}\right),$$

$$\left.\ldots, f_{[j]}^{(2n_\star-1)}\left(\overbrace{c_{[2n_\star-1]}^{(1)}, \ldots, c_{[2n_\star-1]}^{(n'-1)}}^{n'-1}\right)\right], \tag{177}$$

and here coassociativity and (167) gives $\left(\Delta^{(n')}\right)^{\circ 2l'}(c) = c_{[1]} \otimes c_{[2]} \otimes \ldots \otimes c_{[2n_\star-1]}$. Since n-ary algebra multiplication $\mu^{(n)}$ is associative, the internal $\left(\mu^{(n)}\right)^{\circ\ell}$ in (177) can be on any place, and $\mathbf{g}$ in (176) can be on any place as well. This means that the polyadic convolution product $\boldsymbol{\mu}_\star^{(n_\star)}$ is associative. $\blacksquare$

Observe the polyadic version of the identity used in (162): for any $\mathbf{f} \in \mathrm{Hom}_\Bbbk\left(C^{\otimes(n'-1)}, A^{\otimes(n-1)}\right)$

$$\mathrm{id}_A^{\otimes(n-1)} \circ \mathbf{f} \circ \mathrm{id}_C^{\otimes(n'-1)} = \mathbf{f}. \tag{178}$$

Proposition 96. *If the polyadic associative algebra $A^{(n)}$ is unital with $\boldsymbol{\eta}^{(r,n)} : K^r \to A^{\otimes(n-1)}$, and the polyadic coassociative coalgebra $C^{(n')}$ is counital with $\boldsymbol{\varepsilon}^{(n',r')} : C^{\otimes(n'-1)} \to K^{r'}$, both over the same polyadic field $\Bbbk$, then the polyadic convolution algebra $C_\star^{(n',n)}$ (168) is unital, and its unit is given by $\boldsymbol{e}_\star^{(n',n)}$ (167).*

Proof. In analogy with (162) we compose

$$\mathbf{f} = \left(\left(\boldsymbol{\mu}^{(n)}\right)^{\circ\ell}\right)^{\otimes(n-1)} \circ \boldsymbol{\tau}_{medial}^{(n-1,n_\star)} \circ \left(\left(\boldsymbol{\eta}^{(r,n)}\right)^{\otimes(n_\star-1)} \otimes \mathrm{id}_A^{\otimes(n-1)}\right) \circ \left(\left(\boldsymbol{\gamma}^{(r',r)}\right)^{\otimes(n_\star-1)} \otimes \mathrm{id}_A^{\otimes(n-1)}\right)$$

$$\circ \left(\left(\mathrm{id}_K^{\otimes r'}\right)^{\otimes(n_\star-1)} \otimes \mathbf{f}\right) \circ \left(\left(\boldsymbol{\varepsilon}^{(n',r')}\right)^{\otimes(n_\star-1)} \otimes \mathrm{id}_C^{\otimes(n'-1)}\right) \circ \boldsymbol{\tau}_{medial}^{(n_\star,n'-1)} \circ \left(\left(\boldsymbol{\Delta}^{(n')}\right)^{\circ\ell'}\right)^{\otimes(n'-1)}$$

$$= \left(\left(\boldsymbol{\mu}^{(n)}\right)^{\circ\ell}\right)^{\otimes(n-1)} \circ \boldsymbol{\tau}_{medial}^{(n-1,n_\star)} \circ \left(\boldsymbol{\eta}^{(r,n)} \circ \boldsymbol{\gamma}^{(r',r)} \circ \boldsymbol{\varepsilon}^{(n',r')}\right)^{\otimes(n_\star-1)}$$

$$\circ \left(\mathrm{id}_A^{\otimes(n-1)} \circ \mathbf{f} \circ \mathrm{id}_C^{\otimes(n'-1)}\right) \circ \boldsymbol{\tau}_{medial}^{(n_\star,n'-1)} \circ \left(\left(\boldsymbol{\Delta}^{(n')}\right)^{\circ\ell'}\right)^{\otimes(n'-1)} = \boldsymbol{\mu}_\star^{(n_\star)} \circ \left(\left(\boldsymbol{e}_\star^{(n',n)}\right)^{\otimes(n_\star-1)} \otimes \mathbf{f}\right), \tag{179}$$

which coincides with the polyadic unit definition (2). We use the identity (178) and the axioms for a polyadic unit (48) and counit (124). The same derivation can be made for any place of $\boldsymbol{\mu}_\star^{(n_\star)}$. $\blacksquare$

As in the general theory of n-ary groups [17], the invertibility of maps in $C_\star^{(n',n)}$ should be defined not by using the unit, but by using the querelement (4).

Definition 97. For a fixed $\mathbf{f} \in C_\star^{(n',n)}$ its *coquerelement* $\boldsymbol{q}_\star(\mathbf{f}) \in C_\star^{(n',n)}$ is the querelement in the $n_\star$-ary convolution product

$$\boldsymbol{\mu}_\star^{(n_\star)} \circ \left(\mathbf{f}^{\otimes(n_\star-1)} \otimes \boldsymbol{q}_\star(\mathbf{f})\right) = \mathbf{f}, \tag{180}$$

where $\boldsymbol{q}_\star(\mathbf{f})$ can be on any place and $n_\star \geq 3$. The maps in a polyadic convolution algebra which have a coquerelement are called *coquerable*.

Define the *positive convolution power* $\ell_\star$ of an element $\mathbf{f} \in C_\star^{(n',n)}$ not recursively as in [36], but through the $\ell_\star$-iterated multiplication (6)

$$\mathbf{f}^{\langle \ell_\star \rangle} = \left(\boldsymbol{\mu}_\star^{(n_\star)} \right)^{\circ \ell_\star} \circ \left(\mathbf{f}^{\otimes (\ell_\star (n_\star - 1) + 1)} \right), \tag{181}$$

and an element in the *negative convolution power* $\mathbf{f}^{\langle -\ell_\star \rangle}$ satisfies the equation

$$\left(\boldsymbol{\mu}_\star^{(n_\star)} \right)^{\circ \ell_\star} \circ \left(\mathbf{f}^{\langle \ell_\star - 1 \rangle} \otimes \mathbf{f}^{\otimes (n_\star - 2)} \otimes \mathbf{f}^{\langle -\ell_\star \rangle} \right) = \left(\boldsymbol{\mu}_\star^{(n_\star)} \right)^{\circ \ell_\star} \circ \left(\mathbf{f}^{\otimes \ell_\star (n_\star - 1)} \otimes \mathbf{f}^{\langle -\ell_\star \rangle} \right) = \mathbf{f}. \tag{182}$$

It follows from (181) that the polyadic analogs of the exponent laws hold

$$\boldsymbol{\mu}_\star^{(n_\star)} \circ \left(\mathbf{f}^{\langle \ell_\star^{(1)} \rangle} \otimes \mathbf{f}^{\langle \ell_\star^{(2)} \rangle} \otimes \ldots \otimes \mathbf{f}^{\langle \ell_\star^{(n_\star)} \rangle} \right) = \mathbf{f}^{\langle \ell_\star^{(1)} + \ell_\star^{(2)} \ldots + \ell_\star^{(n_\star)} + 1 \rangle}, \tag{183}$$

$$\left(\mathbf{f}^{\langle \ell_\star^{(1)} \rangle} \right)^{\langle \ell_\star^{(2)} \rangle} = \mathbf{f}^{\langle \ell_\star^{(1)} \ell_\star^{(2)} (n_\star - 1) + \ell_\star^{(1)} + \ell_\star^{(2)} \rangle}. \tag{184}$$

Comparing (180) and (182), we have

$$\boldsymbol{q}_\star(\mathbf{f}) = \mathbf{f}^{\langle -1 \rangle}. \tag{185}$$

An arbitrary polyadic power ℓ_Q of the coquerelement $\boldsymbol{q}_\star^{\circ \ell_Q}(\mathbf{f})$ is defined by (180) recursively and can be expressed through the negative polyadic power of $\mathbf{f}$ (see, e.g. [37] for n-ary groups). In terms of the Heine numbers [38] (or q-deformed numbers [39])

$$[[l]]_q = \frac{q^l - 1}{q - 1}, \quad l \in \mathbb{N}_0, \quad q \in \mathbb{Z}, \tag{186}$$

we obtain [14]

$$\boldsymbol{q}_\star^{\circ \ell_Q}(\mathbf{f}) = \mathbf{f}^{\langle -[[\ell_Q]]_{2-n_\star} \rangle}. \tag{187}$$

POLYADIC BIALGEBRAS

The next step is to combine algebras and coalgebras into a common algebraic structure in some "natural" way. Informally, a bialgebra is defined as a vector space which is "simultaneously" an algebra and a coalgebra with some compatibility conditions (e.g., [1, 2]).

In search of a polyadic analog of bialgebras, we observe two structural differences with the binary case: **1**) since the unit and counit do not necessarily exist, we obtain *4 different kinds* of bialgebras (similar to the unit and zero in TABLE 1); **2**) where the most exotic is the possibility of *unequal arities* of multiplication and comultiplication $n \neq n'$. Initially, we take them as arbitrary and then try to find restrictions arising from some "natural" relations.

Let B_{vect} be a polyadic vector space over the polyadic field $\Bbbk^{(m_k, n_k)}$ as (see (11) and (109))

$$B_{vect} = \left\langle B, K \mid \nu^{(m)}; \nu_k^{(m_k)}, \mu_k^{(n_k)}; \rho^{(r)} \right\rangle, \tag{188}$$

where $\nu^{(m)} : B^{\times m} \to B$ is m-ary addition and $\rho^{(r)} : K^{\times r} \times B \to B$ is r-place action (see (7)).

Definition 98. A *polyadic bialgebra* $B^{(n',n)}$ is B_{vect} equipped with a $\Bbbk$-linear n-ary multiplication map $\boldsymbol{\mu}^{(n)} : B^{\otimes n} \to B$ and a $\Bbbk$-linear n'-ary comultiplication map $\boldsymbol{\Delta}^{(n')} : B \to B^{\otimes n'}$ such that:

1. (a) $B_A^{(n)} = \left\langle B_{vect} \mid \boldsymbol{\mu}^{(n)} \right\rangle$ is a n-ary algebra;

    (б) The map $\boldsymbol{\mu}^{(n)}$ is a coalgebra (homo)morphism (129).

2. (a) $B_C^{(n')} = \left\langle B_{vect} \mid \boldsymbol{\Delta}^{(n')} \right\rangle$ is a n'-ary coalgebra;

    (б) The map $\boldsymbol{\Delta}^{(n')}$ is an algebra (homo)morphism (86).

The equivalence of the compatibility conditions **1**b**)** and **2**b**)** can be expressed in the form (polyadic analog of "$\Delta \circ \mu = (\mu \otimes \mu)(\mathrm{id} \otimes \tau \otimes \mathrm{id})(\Delta \otimes \Delta)$")

$$\boldsymbol{\Delta}^{(n')} \circ \boldsymbol{\mu}^{(n)} = \left(\overbrace{\boldsymbol{\mu}^{(n)} \otimes \ldots \otimes \boldsymbol{\mu}^{(n)}}^{n'} \right) \circ \boldsymbol{\tau}_{medial}^{(n,n')} \circ \left(\overbrace{\boldsymbol{\Delta}^{(n')} \otimes \ldots \otimes \boldsymbol{\Delta}^{(n')}}^{n} \right), \tag{189}$$

where $\boldsymbol{\tau}_{medial}^{(n,n')}$ is the medial map (69) acting on B, while the diagram

$$\begin{array}{ccccc}
B^{\otimes n} & \xrightarrow{\left(\boldsymbol{\Delta}^{(n')}\right)^{\otimes n}} & \left(B^{\otimes n'}\right)^{\otimes n} & \xrightarrow{\boldsymbol{\tau}_{medial}^{(n,n')}} & \left(B^{\otimes n}\right)^{\otimes n'} \\
\boldsymbol{\mu}^{(n)} \downarrow & & & & \downarrow (\boldsymbol{\mu}^{(n)})^{\otimes n'} \\
B & \xrightarrow{\hspace{3.5cm} \boldsymbol{\Delta}^{(n')} \hspace{3.5cm}} & & & B^{\otimes n'}
\end{array} \tag{190}$$

commutes.

In an elementwise description it is the commutation of n-ary multiplication and n'-ary comultiplication

$$\Delta^{(n')}\left(\mu^{(n)}[b_1,\ldots,b_n]\right) = \mu^{(n)}\left[\Delta^{(n')}(b_1),\ldots,\Delta^{(n')}(b_n)\right], \tag{191}$$

which in the Sweedler notation becomes

$$\mu^{(n)}[b_1,\ldots,b_n]_{[1]} \otimes \mu^{(n)}[b_1,\ldots,b_n]_{[2]} \otimes \ldots \otimes \mu^{(n)}[b_1,\ldots,b_n]_{[n']}$$
$$= \mu^{(n)}\left[b_{[1]}^{(1)},\ldots,b_{[1]}^{(n)}\right] \otimes \mu^{(n)}\left[b_{[2]}^{(1)},\ldots,b_{[2]}^{(n)}\right] \otimes \ldots \otimes \mu^{(n)}\left[b_{[n']}^{(1)},\ldots,b_{[n']}^{(n)}\right]. \tag{192}$$

Consider the example of a nonderived bialgebra $B^{(n,n)}$ which follows from the von Neumann higher n-regularity relations [40–43].

Example 99 (*von Neumann n-regular bialgebra*). Let $B^{(n,n)} = \left\langle B \mid \boldsymbol{\mu}^{(n)}, \boldsymbol{\Delta}^{(n)} \right\rangle$ be a polyadic bialgebra generated by the elements $b_i \in B$, $i = 1,\ldots,n-1$ subject to the *nonderived n-ary multiplication*

$$\mu^{(n)}(b_1, b_2, b_3 \ldots, b_{n-2}, b_{n-1}, b_1) = b_1, \tag{193}$$

$$\mu^{(n)}(b_2, b_3, b_4 \ldots b_{n-1}, b_1, b_2) = b_2, \tag{194}$$

$$\vdots$$

$$\mu^{(n)}(b_{n-1}, b_1, b_2 \ldots b_{n-3}, b_{n-2}, b_{n-1}) = b_{n-1}, \tag{195}$$

and the *nonderived n-ary comultiplication* (cf. 119)

$$\Delta^{(n)}(b_1) = b_1 \otimes b_2 \otimes b_3 \ldots, b_{n-2} \otimes b_{n-1} \otimes b_1, \tag{196}$$

$$\Delta^{(n)}(b_2) = b_2 \otimes b_3 \otimes b_4 \ldots, b_{n-1} \otimes b_1 \otimes b_2, \tag{197}$$

$$\vdots$$

$$\Delta^{(n)}(b_{n-1}) = b_{n-1} \otimes b_1 \otimes b_2 \otimes \ldots \otimes b_{n-3} \otimes b_{n-2} \otimes b_{n-1}. \tag{198}$$

It is straightforward to check that the compatibility condition (191) holds. Many possibilities exist for choosing other operations—algebra addition, field addition and multiplication, action—so to demonstrate the compatibility we have confined ourselves to only the algebra multiplication and comultiplication.

If the n-ary algebra $B_A^{(n)}$ has unit *and/or* n'-ary coalgebra $B_C^{(n')}$ has counit $\boldsymbol{\varepsilon}^{(n',r')}$, we should add the following additional axioms.

Definition 100 (*Unit axiom*). If $B_A^{(n)} = \left\langle B_{vect} \mid \boldsymbol{\mu}^{(n)} \right\rangle$ is unital, then the unit $\boldsymbol{\eta}^{(r,n)}$ is a (homo)morphism of the coalgebra $B_C^{(n')} = \left\langle B_{vect} \mid \boldsymbol{\Delta}^{(n')} \right\rangle$ (see (129))

$$\left(\overbrace{\boldsymbol{\Delta}^{(n')} \otimes \ldots \otimes \boldsymbol{\Delta}^{(n')}}^{n-1} \right) \circ \boldsymbol{\eta}^{(r,n)} = \left(\overbrace{\boldsymbol{\eta}^{(r,n)} \otimes \ldots \otimes \boldsymbol{\eta}^{(r,n)}}^{n'} \right) \tag{199}$$

such that the diagram

$$
\begin{array}{ccc}
K^{\otimes r} & \xrightarrow{\;\boldsymbol{\eta}^{(r,n)}\;} & B^{\otimes(n-1)} \\
\simeq \Big\downarrow & & \Big\downarrow \left(\boldsymbol{\Delta}^{(n')}\right)^{\otimes(n-1)} \\
K^{\otimes rn'} & \xrightarrow{\;\left(\boldsymbol{\eta}^{(r,n)}\right)^{n'}\;} & B^{\otimes(n-1)n'}
\end{array}
\tag{200}
$$

commutes.

Definition 101 (*Counit axiom*). If $B_C^{(n')} = \left\langle B_{vect} \mid \boldsymbol{\Delta}^{(n')} \right\rangle$ is counital, then the counit $\boldsymbol{\varepsilon}^{(n',r')}$ is a (homo)morphism of the algebra $B_A^{(n)} = \left\langle B_{vect} \mid \boldsymbol{\mu}^{(n)} \right\rangle$ (see (86))

$$
\boldsymbol{\varepsilon}^{(n',r')} \circ \left(\overbrace{\boldsymbol{\mu}^{(n)} \otimes \ldots \otimes \boldsymbol{\mu}^{(n)}}^{n'-1} \right) = \left(\overbrace{\boldsymbol{\varepsilon}^{(n',r')} \otimes \ldots \otimes \boldsymbol{\varepsilon}^{(n',r')}}^{n} \right)
\tag{201}
$$

such that the diagram

$$
\begin{array}{ccc}
K^{\otimes r} & \xleftarrow{\;\boldsymbol{\varepsilon}^{(n',r')}\;} & B^{\otimes(n'-1)} \\
\simeq \Big\uparrow & & \Big\uparrow \left(\boldsymbol{\mu}^{(n)}\right)^{\otimes(n'-1)} \\
K^{\otimes rn} & \longleftarrow & B^{\otimes(n'-1)n}
\end{array}
\tag{202}
$$

commutes.

If *both* the polyadic unit and polyadic counit exist, then we include their compatibility condition

$$
\left(\boldsymbol{\varepsilon}^{(n',r')}\right)^{\otimes(n-1)} \circ \left(\boldsymbol{\eta}^{(r,n)}\right)^{\otimes(n'-1)} \simeq \mathrm{id}_K,
\tag{203}
$$

such that the diagram

$$
\begin{array}{ccc}
& B^{\otimes(n'-1)(n-1)} & \\
\left(\boldsymbol{\eta}^{(r,n)}\right)^{\otimes(n'-1)} \nearrow & & \searrow \left(\boldsymbol{\varepsilon}^{(n',r')}\right)^{\otimes(n-1)} \\
K^{\otimes r(n'-1)} & \xrightarrow{\quad\simeq\quad} & K^{\otimes r(n-1)}
\end{array}
\tag{204}
$$

commutes.

Assertion 102. *There are four kinds of polyadic bialgebras depending on whether the unit $\boldsymbol{\eta}^{(r,n)}$ and counit $\boldsymbol{\varepsilon}^{(n',r')}$ exist:*

    1) *nonunital-noncounital;* **2)** *unital-noncounital;* **3)** *nonunital-counital;* **4)** *unital-counital.*

Definition 103. A polyadic bialgebra $B^{(n',n)}$ is called *totally co-commutative*, if

$$
\boldsymbol{\mu}^{(n)} = \boldsymbol{\mu}^{(n)} \circ \boldsymbol{\tau}_n,
\tag{205}
$$

$$
\boldsymbol{\Delta}^{(n')} = \boldsymbol{\tau}_{n'} \circ \boldsymbol{\Delta}^{(n')},
\tag{206}
$$

where $\boldsymbol{\tau}_n \in S_n$, $\boldsymbol{\tau}_{n'} \in S_{n'}$, and $S_n, S_{n'}$ are the symmetry permutation groups on n and n' elements respectively.

Definition 104. A polyadic bialgebra $B^{(n',n)}$ is called *medially co-commutative*, if

$$
\boldsymbol{\mu}_{op}^{(n)} \equiv \boldsymbol{\mu}^{(n)} \circ \boldsymbol{\tau}_{op}^{(n)} = \boldsymbol{\mu}^{(n)},
\tag{207}
$$

$$
\boldsymbol{\Delta}_{cop}^{(n')} \equiv \boldsymbol{\tau}_{op}^{(n')} \circ \boldsymbol{\Delta}^{(n')} = \boldsymbol{\Delta}^{(n')},
\tag{208}
$$

where $\boldsymbol{\tau}_{op}^{(n)}$ and $\boldsymbol{\tau}_{op}^{(n')}$ are the medially allowed polyadic twist maps (72).

POLYADIC HOPF ALGEBRAS

Here we introduce the most general approach to "polyadization" of the Hopf algebra concept [1–3]. Informally, the transition from bialgebra to Hopf algebra is, in some sense, "dualizing" the passage from semigroup (containing noninvertible elements) to group (in which all elements are invertible). Schematically, if multiplication $\mu = (\cdot)$ in a semigroup G is binary, the invertibility of all elements demands *two* extra and *necessary* set-ups: **1**) *An additional element* (identity $e \in G$ or the corresponding map from a one point set to group ϵ); **2**) *An additional map* (inverse $\iota : G \to G$), such that $g \cdot \iota(g) = e$ in diagrammatic form is $\mu \circ (\mathrm{id}_G \times \iota) \circ D_2 = \epsilon$ ($D_2 : G \to G \times G$ is the diagonal map). When "dualizing", in a (binary) bialgebra B (with multiplication μ and comultiplication Δ) again *two* set-ups should be considered in order to get a (binary) Hopf algebra: **1**) *An analog of identity* $e_\star = \eta\varepsilon$ (where $\eta : k \to B$ is unit and $\varepsilon : B \to k$ is counit); **2**) *An analog of inverse* $S : B \to B$ called the *antipode*, such that $\mu \circ (\mathrm{id}_B \otimes S) \circ \Delta = e_\star$ or in terms of the (binary) convolution product $\mathrm{id}_B \star S = e_\star$. By multiplying both sides by S from the left and by id_B from the right, we obtain weaker (von Neumann regularity) conditions $S \star \mathrm{id}_B \star S = S$, $\mathrm{id}_B \star S \star \mathrm{id}_B = \mathrm{id}_B$, which do not contain an identity $e_\star$ and lead to the concept of weak Hopf algebras [44–46].

The crucial peculiarity of the polyadic generalization is the possible absence of an identity or **1**) in both cases. The role and necessity of the polyadic identity (2) is not so important: there polyadic groups without identity exist (see, e.g. [47], and the discussion after (3)). Invertibility is determined by the querelement (4) in n-ary group or the quermap (57) in polyadic algebra. So there are two ways forward: "dualize" the quermap (57) directly (as in the binary case) or use the most general version of the polyadic convolution product (166) and apply possible restrictions, if any. We will choose the second method, because the first one is a particular case of it. Thus, if the standard (binary) antipode is the convolution inverse (coinverse) to the identity in a bialgebra, then its polyadic counterpart should be a coquerelement (180) of some polyadic *analog* for the identity map in the polyadic bialgebra. We consider two possibilities to define a polyadic analog of identity: **1**) *Singular case.* The comultiplication is binary $n' = 2$; **2**) *Symmetric case.* The arities of multiplication and comultiplication need not be binary, but should coincide $n = n'$.

In the *singular case* a polyadic multivalued map in $\mathrm{End}_{\Bbbk}\left(B, B^{\otimes(n-1)}\right)$ is a reminder of how an identity can be defined: its components are to be functions of one variable. That is, with more than one argument it is not possible to determine its value when these are unequal.

Definition 105. We take for a *singular polyadic identity* $\mathbf{Id}_0$ the diagonal map $\mathbf{Id}_0 = \mathbf{D} \in \mathrm{End}_{\Bbbk}\left(B, B^{\otimes(n-1)}\right)$, such that $b \mapsto b^{\otimes(n-1)}$, for any $b \in B$.

We call the polyadic convolution product (166) with the binary comultiplication $n' = 2$ *reduced* and denote it by $\bar{\boldsymbol{\mu}}_\star^{(n_\star)}$ which in Sweedler notation can be obtained from (175)

$$\bar{\boldsymbol{\mu}}_\star^{(n_\star)} \circ \left(\mathbf{f}^{(1)} \otimes \mathbf{f}^{(2)} \otimes \ldots \otimes \mathbf{f}^{(n_\star)}\right) = \mathbf{g}, \quad \mathbf{f}^{(i)}, \mathbf{g} \in \mathrm{End}_{\Bbbk}\left(B, B^{\otimes(n-1)}\right),$$

$$\mathbf{g}_{[j]} \circ (b) = \left(\mu^{(n)}\right)^{\circ\ell}\left[f_{[j]}^{(1)}\left(b_{[1]}\right), f_{[j]}^{(2)}\left(b_{[2]}\right), \ldots, f_{[j]}^{(n_\star)}\left(b_{[n_\star]}\right)\right],$$

$$f_{[j]}^{(i)} \in \mathrm{End}_{\Bbbk}(B, B), \quad i \in 1, \ldots, n_\star, \quad j \in 1, \ldots, n-1, \quad b \in B, \tag{209}$$

The consistency condition (167) becomes *reduced*

$$n_\star = \ell(n-1) + 1 = \ell' + 1. \tag{210}$$

Definition 106. The set of the multivalued maps $\mathbf{f}^{(i)} \in \mathrm{End}_{\Bbbk}\left(B, B^{\otimes(n-1)}\right)$ (together with the polyadic identity $\mathbf{Id}_0$) endowed with the reduced convolution product $\bar{\boldsymbol{\mu}}_\star^{(n_\star)}$ is called a *reduced $n_\star$-ary convolution algebra*

$$C_\star^{(2,n)} = \left\langle \mathrm{End}_{\Bbbk}\left(B, B^{\otimes(n-1)}\right) \mid \bar{\boldsymbol{\mu}}_\star^{(n_\star)}\right\rangle. \tag{211}$$

Remark 107. The reduced convolution algebra $C_\star^{(2,n)}$ having $n \neq 2$ is not derived (**Definition** 89).

Having the distinguished element $\mathbf{Id}_0 \in C_\star^{(2,n)}$ as an analog of id_B and the querelement (180) for any $\mathbf{f} \in C_\star^{(2,n)}$ (the polyadic version of inverse in the convolution algebra), we are now in a position to "polyadize" the concept of the (binary) antipode.

Definition 108. A multivalued map $\boldsymbol{Q}_0 : B \to B^{\otimes(n-1)}$ in the polyadic bialgebra $B^{(2,n)}$ is called a *singular querantipode*, if it is the coquerelement of the polyadic identity $\boldsymbol{Q}_0 = \boldsymbol{q}_\star(\mathbf{Id}_0)$ in the reduced $n_\star$-ary convolution algebra

$$\bar{\boldsymbol{\mu}}_\star^{(n_\star)} \circ \left(\mathbf{Id}_0^{\otimes(n_\star-1)} \otimes \boldsymbol{Q}_0\right) = \mathbf{Id}_0, \tag{212}$$

where $\boldsymbol{Q}_0$ can be on any place, such that the diagram

$$
\begin{array}{ccc}
B & \xrightarrow{\quad \boldsymbol{\Delta}^{\circ(n_\star-1)} \quad} & B^{\otimes n_\star} \\
{\scriptstyle \mathbf{Id}_0}\downarrow & & \downarrow{\scriptstyle \mathbf{Id}_0^{\otimes(n_\star-1)}\otimes \boldsymbol{Q}_0} \\
B^{\otimes(n-1)} \xleftarrow{\left(\left(\boldsymbol{\mu}^{(n)}\right)^{\circ\ell}\right)^{\otimes(n-1)}} \left(B^{\otimes n_\star}\right)^{\otimes(n-1)} & \xleftarrow{\ \boldsymbol{\tau}_{medial}^{(n-1,n_\star)}\ } & \left(B^{\otimes(n-1)}\right)^{\otimes n_\star}
\end{array}
\tag{213}
$$

commutes.

In Sweedler notation

$$
\left(\mu^{(n)}\right)^{\circ\ell}\left[b_{[1]},b_{[2]},\ldots,b_{[n_\star-1]},Q_{0\,[j]}\left(b_{[n_\star]}\right)\right]=b,\qquad j\in 1,\ldots,n-1,\quad i\in 1,\ldots,n_\star,
\tag{214}
$$

where

$$
\boldsymbol{\Delta}^{\circ(n_\star-1)}\left(b\right)=b_{[1]}\otimes b_{[2]}\otimes\ldots\otimes b_{[n_\star]},\ \ \boldsymbol{Q}_0\circ\left(b\right)=Q_{0\,[1]}\left(b\right)\otimes\ldots\otimes Q_{0\,[n-1]}\left(b\right),\ b,b_{[i]}\in B
$$

.

Definition 109. A polyadic bialgebra $B^{(2,n)}$ equipped with the reduced $n_\star$-ary convolution product $\bar{\boldsymbol{\mu}}_\star^{(n_\star)}$ and the singular querantipode $\boldsymbol{Q}_0$ (212) is called a *singular polyadic Hopf algebra* and is denoted by $H_{sing}^{(n)}=\left\langle B^{(n,n)}\mid\bar{\boldsymbol{\mu}}_\star^{(n_\star)},\boldsymbol{Q}_0\right\rangle$.

Due to their exotic properties we will not consider singular polyadic Hopf algebras $H_{sing}^{(n)}$ in detail.

In the *symmetric case* a polyadic identity-like map in $\mathrm{End}_{\Bbbk}\left(B^{\otimes(n-1)},B^{\otimes(n-1)}\right)$ can be defined in a more natural way.

Definition 110. A *symmetric polyadic identity* $\mathbf{Id}:B^{\otimes(n-1)}\to B^{\otimes(n-1)}$ is a polyadic tensor product of ordinary identities in $B^{(n,n)}$

$$
\mathbf{Id}=\overbrace{\mathrm{id}_B\otimes\ldots\otimes\mathrm{id}_B}^{n-1},\quad \mathrm{id}_B:B\to B.
\tag{215}
$$

Indeed, for any map $\mathbf{f}\in\mathrm{End}_{\Bbbk}\left(B^{\otimes(n-1)},B^{\otimes(n-1)}\right)$, obviously $\mathbf{Id}\circ\mathbf{f}=\mathbf{f}\circ\mathbf{Id}=\mathbf{f}$.

The numbers of iterations are now equal $\ell=\ell'$, and the consistency condition (167) becomes

$$
n_\star-1=\ell\left(n-1\right).
\tag{216}
$$

Definition 111. The set of the multiplace multivalued maps $\mathbf{f}^{(i)}\in\mathrm{End}_{\Bbbk}\left(B^{\otimes(n-1)},B^{\otimes(n-1)}\right)$ (together with the polyadic identity $\mathbf{Id}$) endowed with the symmetric convolution product $\hat{\boldsymbol{\mu}}_\star^{(n_\star)}=\boldsymbol{\mu}_\star^{(n_\star)}|_{n=n'}$ (166) is called a *symmetric $n_\star$-ary convolution algebra*

$$
C_\star^{(n,n)}=\left\langle\mathrm{End}_{\Bbbk}\left(B^{\otimes(n-1)},B^{\otimes(n-1)}\right)\mid\hat{\boldsymbol{\mu}}_\star^{(n_\star)}\right\rangle.
\tag{217}
$$

For a polyadic analog of antipode in the symmetric case we have

Definition 112. A multiplace multivalued map $\boldsymbol{Q}_{\mathrm{id}}:B^{\otimes(n-1)}\to B^{\otimes(n-1)}$ in the polyadic bialgebra $B^{(n,n)}$ is called a *symmetric querantipode*, if it is the coquerelement (see (180)) of the polyadic identity $\boldsymbol{Q}_{\mathrm{id}}=\boldsymbol{q}_\star\left(\mathbf{Id}\right)$ in the symmetric $n_\star$-ary convolution algebra

$$
\hat{\boldsymbol{\mu}}_\star^{(n_\star)}\circ\left(\mathbf{Id}^{\otimes(n_\star-1)}\otimes\boldsymbol{Q}_{\mathrm{id}}\right)=\mathbf{Id},
\tag{218}
$$

where $\boldsymbol{Q}_{\mathrm{id}}$ can be on any place, such that the diagram

$$
\begin{array}{ccc}
B^{\otimes(n-1)} \xrightarrow{\left(\left(\boldsymbol{\Delta}^{(n)}\right)^{\circ\ell}\right)^{\otimes(n-1)}} \left(B^{\otimes n_\star}\right)^{\otimes(n-1)} & \xrightarrow{\ \boldsymbol{\tau}_{medial}^{(n_\star,n-1)}\ } & \left(B^{\otimes(n-1)}\right)^{\otimes n_\star} \\
{\scriptstyle \mathbf{Id}}\downarrow & & \downarrow{\scriptstyle \mathbf{Id}^{\otimes(n_\star-1)}\otimes \boldsymbol{Q}_{\mathrm{id}}} \\
B^{\otimes(n-1)} \xleftarrow{\left(\left(\boldsymbol{\mu}^{(n)}\right)^{\circ\ell}\right)^{\otimes(n-1)}} \left(B^{\otimes n_\star}\right)^{\otimes(n-1)} & \xleftarrow{\ \boldsymbol{\tau}_{medial}^{(n-1,n_\star)}\ } & \left(B^{\otimes(n-1)}\right)^{\otimes n_\star}
\end{array}
\tag{219}
$$

commutes.

In Sweedler notation we obtain (see (166) and (175))

$$\left(\mu^{(n)}\right)^{\circ\ell}\left[b_{[1]}^{(j)}, b_{[2]}^{(j)}, b_{[n_\star-1]}^{(j)}, Q_{[j]}\left(b_{[n_\star]}^{(1)}, b_{[n_\star]}^{(2)}, \dots, b_{[n_\star]}^{(n-1)}\right)\right] = b^{(j)}, \ j \in 1, \dots, n-1, \ i \in 1, \dots, n_\star, \qquad (220)$$

where $\left(\Delta^{(n)}\right)^{\circ\ell}\left(b^{(j)}\right) = b_{[1]}^{(j)} \otimes b_{[2]}^{(j)} \otimes \dots \otimes b_{[n_\star]}^{(j)}, \quad b_{[i]}^{(j)} \in B, \ell \in \mathbb{N}, Q_{[j]} \in \mathrm{End}_{\Bbbk}\left(B^{\otimes(n-1)}, B\right)$ are components of $\boldsymbol{Q}_{\mathrm{id}}$, and the convolution product arity is $n_\star = \ell(n-1) + 1$ (216).

Definition 113. A polyadic bialgebra $B^{(n,n)}$ equipped with the symmetric $n_\star$-ary convolution product $\hat{\boldsymbol{\mu}}_\star^{(n_\star)}$ and the symmetric querantipode $\boldsymbol{Q}_{\mathrm{id}}$ (218) is called a *symmetric polyadic Hopf algebra* and is denoted by $H_{sym}^{(n)} = \left\langle B^{(n,n)} \mid \hat{\boldsymbol{\mu}}_\star^{(n_\star)}, \boldsymbol{Q}_{\mathrm{id}} \right\rangle$.

Example 114. In the case where $n = n' = 3$ and $\ell = 1$ we have $\Delta^{(3)}\left(b^{(j)}\right) = b_{[1]}^{(j)} \otimes b_{[2]}^{(j)} \otimes b_{[3]}^{(j)}, j = 1, 2, 3,$

$$\mu^{(3)}\left[b_{[1]}^{(1)}, b_{[2]}^{(1)}, Q_{[1]}\left(b_{[3]}^{(1)}, b_{[3]}^{(2)}\right)\right] = b^{(1)}, \qquad \mu^{(3)}\left[b_{[1]}^{(2)}, b_{[2]}^{(2)}, Q_{[2]}\left(b_{[3]}^{(1)}, b_{[3]}^{(2)}\right)\right] = b^{(2)},$$

$$\mu^{(3)}\left[b_{[1]}^{(1)}, Q_{[1]}\left(b_{[2]}^{(1)}, b_{[2]}^{(2)}\right), b_{[3]}^{(1)}\right] = b^{(1)}, \qquad \mu^{(3)}\left[b_{[1]}^{(2)}, Q_{[2]}\left(b_{[2]}^{(1)}, b_{[2]}^{(2)}\right), b_{[3]}^{(2)}\right] = b^{(2)},$$

$$\mu^{(3)}\left[Q_{[1]}\left(b_{[1]}^{(1)}, b_{[1]}^{(2)}\right), b_{[2]}^{(1)}, b_{[3]}^{(1)}\right] = b^{(1)}, \qquad \mu^{(3)}\left[Q_{[2]}\left(b_{[1]}^{(1)}, b_{[1]}^{(2)}\right), b_{[2]}^{(2)}, b_{[3]}^{(2)}\right] = b^{(2)}, \qquad (221)$$

which can be compared with the binary case $(b_{[1]}S\left(b_{[2]}\right) = S\left(b_{[1]}\right)b_{[2]} = \eta\left(\varepsilon\left(b\right)\right))$ and (4), (180).

Recall that the main property of the antipode S of a binary bialgebra B is its "anticommutation" with the multiplication μ and comultiplication Δ (e.g., [1])

$$S \circ \mu = \mu \circ \tau_{op} \circ (S \otimes S), \quad S \circ \eta = \eta, \qquad (222)$$

$$\Delta \circ S = \tau_{op} \circ (S \otimes S) \circ \Delta, \quad \varepsilon \circ S = \varepsilon, \qquad (223)$$

where τ_{op} is the binary twist (see (66)). The first relation means that S is an algebra anti-endomorphism, because in the elementwise description $S\left(a \cdot b\right) = S\left(b\right) \cdot S\left(a\right), a, b \in B, (\cdot) \equiv \mu$.

We propose the polyadic analogs of (222)-(223) without proofs, which are too cumbersome, but their derivations almost coincide with those for the binary case.

Proposition 115. *The querantipode* $\boldsymbol{Q}_{\mathrm{id}} : B^{\otimes(n-1)} \to B^{\otimes(n-1)}$ *of the polyadic bialgebra* $B^{(n,n)} = \left\langle B \mid \boldsymbol{\mu}^{(n)}, \boldsymbol{\Delta}^{(n)} \right\rangle$ *satisfies the polyadic version of "antimultiplicativity" ("antialgebra map")*

$$\boldsymbol{Q}_{\mathrm{id}} \circ \left(\left(\boldsymbol{\mu}^{(n)}\right)^{\circ\ell}\right)^{\otimes(n-1)} = \left(\left(\boldsymbol{\mu}^{(n)}\right)^{\circ\ell}\right)^{\otimes(n-1)} \circ \boldsymbol{\tau}_{op}^{(\ell_\tau)} \circ \boldsymbol{Q}_{\mathrm{id}}^{\otimes n_\star} \circ \boldsymbol{\tau}_{medial}^{(n_\star, n-1)}, \qquad (224)$$

and "anticomultiplicativity" ("anticoalgebra map")

$$\left(\left(\boldsymbol{\Delta}^{(n)}\right)^{\circ\ell}\right)^{\otimes(n-1)} \circ \boldsymbol{Q}_{\mathrm{id}} = \boldsymbol{\tau}_{op}^{(\ell_\tau)} \circ \boldsymbol{Q}_{\mathrm{id}}^{\otimes n_\star} \circ \boldsymbol{\tau}_{medial}^{(n-1, n_\star)} \circ \left(\left(\boldsymbol{\Delta}^{(n)}\right)^{\circ\ell}\right)^{\otimes(n-1)}, \qquad (225)$$

where $\boldsymbol{\tau}_{medial}^{(n,m)}$ *is the medial map* (69), $\boldsymbol{\tau}_{op}^{(\ell_\tau)}$ *is the polyadic twist* (72) *and* $\ell_\tau = (n-1)n_\star$ *should be allowed (see* TABLE 2).

Proposition 116. *If the polyadic unit* $\boldsymbol{\eta}^{(r,n)}$ (48) *and counit* $\boldsymbol{\varepsilon}^{(n,r)}$ (124) *in* $B^{(n,n)}$ *exist, then*

$$\boldsymbol{Q}_{\mathrm{id}} \circ \boldsymbol{\eta}^{(r,n)} = \boldsymbol{\eta}^{(r,n)}, \qquad (226)$$

$$\boldsymbol{\varepsilon}^{(n,r)} \circ \boldsymbol{Q}_{\mathrm{id}} = \boldsymbol{\varepsilon}^{(n,r)}. \qquad (227)$$

Example 117. If $n = 3, \ell = 1, n_\star = 3, \ell_\tau = 6$ (and (75)), then using Sweedler notation, for (224) we have

$$Q_{[1]}\left(\mu^{(3)}[a_1, a_2, a_3], \mu^{(3)}[b_1, b_2, b_3]\right) = \mu^{(3)}\left[Q_{[2]}\left(a_2, b_2\right), Q_{[1]}\left(a_1, b_1\right), Q_{[1]}\left(a_3, b_3\right)\right], \qquad (228)$$

$$Q_{[2]}\left(\mu^{(3)}[a_1, a_2, a_3], \mu^{(3)}[b_1, b_2, b_3]\right) = \mu^{(3)}\left[Q_{[2]}\left(a_1, b_1\right), Q_{[2]}\left(a_3, b_3\right), Q_{[1]}\left(a_2, b_2\right)\right], \qquad (229)$$

where $\boldsymbol{Q}_{\mathrm{id}} \circ (a, b) = Q_{[1]}(a, b) \otimes Q_{[2]}(a, b) \in \mathrm{End}_{\Bbbk}\left(B \otimes B, B \otimes B\right), a, b, a_i, b_i \in B,$ (cf. (222)).

The key property of the binary antipode S is its involutivity $S^{\circ 2} = \mathrm{id}_B$ for either commutative ($\mu = \mu \circ \tau_{op}$) or co-commutative ($\Delta = \tau_{op} \circ \Delta$) Hopf algebras, which follows from (222) or (223) applied to $S \star S^{\circ 2}$ giving $\eta \varepsilon$ ($= S \star \mathrm{id}_B$).

Proposition 118. *If in a symmetric Hopf algebra $H_{sym}^{(n)}$ either multiplication or comultiplication is invariant under polyadic twist map $\boldsymbol{\tau}_{op}^{(\ell_\tau)}$ (72), then the querantipode $\boldsymbol{Q}_{\mathrm{id}}$ (218) satisfies*

$$\hat{\boldsymbol{\mu}}_\star^{(n_\star)} \left[\overbrace{\boldsymbol{Q}_{\mathrm{id}}, \ldots, \boldsymbol{Q}_{\mathrm{id}}}^{(n_\star - 1)}, \boldsymbol{Q}_{\mathrm{id}} \circ \boldsymbol{Q}_{\mathrm{id}} \right] = \boldsymbol{Q}_{\mathrm{id}}, \tag{230}$$

where $\boldsymbol{Q}_{\mathrm{id}}^{\circ 2}$ can be on any place, or the convolution querelement (180) of the querantipode $\boldsymbol{Q}_{\mathrm{id}}$ is

$$\boldsymbol{q}_\star \left(\boldsymbol{Q}_{\mathrm{id}} \right) = \boldsymbol{Q}_{\mathrm{id}}^{\circ 2}. \tag{231}$$

Proof. The proposition follows from applying either (224) or (225) to the l.h.s. of (230), to use (180). ∎

TOWARDS POLYADIC QUANTUM GROUPS

Bialgebras with a special relaxation of co-commutativity, almost co-commutativity, are the ground objects in the construction of quantum groups identified with the non-commutative and non-co-commutative quasitriangular Hopf algebras [4, 48].

Quantum Yang-Baxter equation

Here we recall the binary case (informally) in a notation that will allow us to provide the "polyadization" in a clearer way.

Let us consider a (binary) bialgebra $B^{(2,2)} = \langle B \mid \mu, \Delta \rangle$, where $\mu = \mu^{(2)}$ is the binary multiplication, $\Delta = \Delta^{(2)}$ (see **Definition** 98), and the opposite comultiplication is given by $\Delta_{cop} \equiv \tau_{op} \circ \Delta$, where τ_{op} is the binary twist (66). To relax the co-commutativity condition ($\Delta_{cop} = \Delta$), the following construction inspired by *conjugation* in groups was proposed [4, 48]. A bialgebra $B^{(2,2)}$ is *almost co-commutative*, if there exists $R \in B \otimes B$ such that (in the elementwise notation)

$$\mu \left[\Delta_{cop} \left(b \right), R \right] = \mu \left[R, \Delta \left(b \right) \right], \quad \forall b \in B. \tag{232}$$

A *fixed* element R of a bialgebra satisfying (232) is called a *universal R-matrix*. For a co-commutative bialgebra we have $R = e_B \otimes e_B$, where $e_B \in B$ is the unit (element) of the algebra $\langle B \mid \mu \rangle$.

If we demand that $\langle B \mid \Delta_{cop} \rangle$ is the opposite coalgebra of $\langle B \mid \Delta \rangle$, and therefore Δ_{cop} be coassociative, then R cannot be *arbitrary*, but has to satisfy some additional conditions, which we will call the *almost co-commutativity equations* for the R-matrix. Indeed, using (232) we can write

$$\mu \left[\left(\Delta_{cop} \otimes \mathrm{id}_B \right) \circ \Delta_{cop} \left(b \right), \mu \left[\left(R \otimes e_B \right), \left(\Delta \otimes \mathrm{id}_B \right) \left(R \right) \right] \right]$$
$$= \mu \left[\mu \left[\left(R \otimes e_B \right), \left(\Delta \otimes \mathrm{id}_B \right) \left(R \right) \right], \left(\Delta \otimes \mathrm{id}_B \right) \circ \Delta \left(b \right) \right], \tag{233}$$

$$\mu \left[\left(\mathrm{id}_B \otimes \Delta_{cop} \right) \circ \Delta_{cop} \left(b \right), \mu \left[\left(e_B \otimes R \right), \left(\mathrm{id}_B \otimes \Delta \right) \left(R \right) \right] \right]$$
$$= \mu \left[\mu \left[\left(e_B \otimes R \right), \left(\mathrm{id}_B \otimes \Delta \right) \left(R \right) \right], \left(\mathrm{id}_B \otimes \Delta \right) \circ \Delta \left(b \right) \right], \tag{234}$$

Therefore, the coassociativity of Δ_{cop} leads to the *first* almost co-commutativity equation

$$\mu \left[\left(R \otimes e_B \right), \left(\Delta \otimes \mathrm{id}_B \right) \left(R \right) \right] = \mu \left[\left(e_B \otimes R \right), \left(\mathrm{id}_B \otimes \Delta \right) \left(R \right) \right]. \tag{235}$$

On the other hand, directly from (232), we have relations which can be treated as the next *two* almost co-commutativity equations (*unconnected* to the coassociativity of Δ_{cop})

$$\mu \left[\left(R \otimes e_B \right), \left(\Delta \otimes \mathrm{id}_B \right) \left(R \right) \right] = \mu \left[\left(\Delta_{cop} \otimes \mathrm{id}_B \right) \left(R \right), \left(R \otimes e_B \right) \right]$$
$$= \mu \left[\left(\tau_{op} \otimes \mathrm{id}_B \right) \circ \left(\Delta \otimes \mathrm{id}_B \right) \left(R \right), \left(R \otimes e_B \right) \right], \tag{236}$$

$$\mu \left[\left(e_B \otimes R \right), \left(\mathrm{id}_B \otimes \Delta \right) \left(R \right) \right] = \mu \left[\left(\mathrm{id}_B \otimes \Delta_{cop} \right) \left(R \right), \left(e_B \otimes R \right) \right]$$
$$= \mu \left[\left(\mathrm{id}_B \otimes \tau_{op} \right) \circ \left(\mathrm{id}_B \otimes \Delta \right) \left(R \right), \left(e_B \otimes R \right) \right]. \tag{237}$$

The equations (235)–(237) for the components of

$$R = \sum_\alpha \mathsf{r}_\alpha^{(1)} \otimes \mathsf{r}_\alpha^{(2)} \in B \otimes B \tag{238}$$

are on $B \otimes B \otimes B$. In components the almost co-commutativity (232) can be expressed as follows

$$\sum_{[b]} \sum_\alpha \mu \left[b_{[2]}, \mathsf{r}_\alpha^{(1)} \right] \otimes \mu \left[b_{[1]}, \mathsf{r}_\alpha^{(2)} \right] = \sum_{[b]'} \sum_{\alpha'} \mu \left[\mathsf{r}_{\alpha'}^{(1)}, b_{[1]'} \right] \otimes \mu \left[\mathsf{r}_{\alpha'}^{(2)}, b_{[2]'} \right]. \tag{239}$$

Now introduce the "extended" form of the R-matrix $\mathscr{R}_{ij} \in B \otimes B \otimes B$, $i,j = 1,2,3$, by

$$\mathscr{R}_{12} = \sum_\alpha \mathsf{r}_\alpha^{(1)} \otimes \mathsf{r}_\alpha^{(2)} \otimes e_B \equiv R \otimes e_B, \tag{240}$$

$$\mathscr{R}_{13} = \sum_\alpha \mathsf{r}_\alpha^{(1)} \otimes e_B \otimes \mathsf{r}_\alpha^{(2)} = (\mathrm{id}_B \otimes \tau_{op}) \circ (R \otimes e_B), \tag{241}$$

$$\mathscr{R}_{23} = \sum_\alpha e_B \otimes \mathsf{r}_\alpha^{(1)} \otimes \mathsf{r}_\alpha^{(2)} \equiv e_B \otimes R. \tag{242}$$

Obviously, one can try to solve (235)–(237) with respect to the $\mathsf{r}_\alpha^{(1)}$, $\mathsf{r}_\alpha^{(2)}$ directly, but then we are confronted with a difficulty arising from the Sweedler components, because now (see (137)–(139))

$$(\Delta \otimes \mathrm{id}_B)(R) = \sum_{\left[\mathsf{r}_\alpha^{(1)} \right]} \sum_\alpha \mathsf{r}_{\alpha,[1]}^{(1)} \otimes \mathsf{r}_{\alpha,[2]}^{(1)} \otimes \mathsf{r}_\alpha^{(2)}, \tag{243}$$

$$(\mathrm{id}_B \otimes \Delta)(R) = \sum_{\left[\mathsf{r}_\alpha^{(2)} \right]} \sum_\alpha \mathsf{r}_\alpha^{(1)} \otimes \mathsf{r}_{\alpha,[1]}^{(2)} \otimes \mathsf{r}_{\alpha,[2]}^{(2)}. \tag{244}$$

To avoid computations in the Sweedler components, one can substitute them by the components of R directly as $\mathsf{r}_{[j]}^{(i)} \longrightarrow \mathsf{r}^{(i)}$ (schematically). This allows us to express (243)–(244) solely through elements of the "extended" R-matrix $\mathscr{R}_{ij}$ by

$$(\Delta \otimes \mathrm{id}_B)(R) = \mu [\mathscr{R}_{13}, \mathscr{R}_{23}] \equiv \sum_{\alpha,\beta} \mathsf{r}_\alpha^{(1)} \otimes \mathsf{r}_\beta^{(1)} \otimes \mu \left[\mathsf{r}_\alpha^{(2)}, \mathsf{r}_\beta^{(2)} \right], \tag{245}$$

$$(\mathrm{id}_B \otimes \Delta)(R) = \mu [\mathscr{R}_{13}, \mathscr{R}_{12}] \equiv \sum_{\alpha,\beta} \mu \left[\mathsf{r}_\alpha^{(1)}, \mathsf{r}_\beta^{(1)} \right] \otimes \mathsf{r}_\beta^{(2)} \otimes \mathsf{r}_\alpha^{(2)}, \tag{246}$$

which do not contain Sweedler components of R at all. The equations (245)–(246) *define* a *quasitriangular R-matrix* [4]. The corresponding almost co-commutative (binary) bialgebra $B_{braid}^{(2)} = \left\langle B^{(2,2)}, R \right\rangle$ is called a *quasitriangular almost co-commutative bialgebra* (or *braided bialgebra* [7]). Only for them can the almost co-commutativity equations (235)–(237) be expressed solely in terms of R-matrix components or through the "extended" R-matrix $\mathscr{R}_{ij}$, using (245)–(246).

Theorem 119. *In the binary case, three almost co-commutativity equations for the R-matrix coincide with*

$$\mu^{\circ 2} [\mathscr{R}_{12}, \mathscr{R}_{13}, \mathscr{R}_{23}] = \mu^{\circ 2} [\mathscr{R}_{23}, \mathscr{R}_{13}, \mathscr{R}_{12}]. \tag{247}$$

Conversely, any quasitriangular R-matrix is a solution of (247) by the above construction. The equation for the "extended" R-matrix $\mathscr{R}_{ij}$ (247) is called the *quantum Yang-Baxter equation* [8, 49] (or the *triangle relation* [48]). In terms of the R-matrix components (238) the quantum Yang-Baxter equation (247) takes the form

$$\sum_{\alpha,\beta,\gamma} \mu \left[\mathsf{r}_\alpha^{(1)}, \mathsf{r}_\beta^{(1)} \right] \otimes \mu \left[\mathsf{r}_\alpha^{(2)}, \mathsf{r}_\gamma^{(1)} \right] \otimes \mu \left[\mathsf{r}_\beta^{(2)}, \mathsf{r}_\gamma^{(2)} \right] = \sum_{\alpha',\beta',\gamma'} \mu \left[\mathsf{r}_{\beta'}^{(1)}, \mathsf{r}_{\alpha'}^{(1)} \right] \otimes \mu \left[\mathsf{r}_{\gamma'}^{(1)}, \mathsf{r}_{\alpha'}^{(2)} \right] \otimes \mu \left[\mathsf{r}_{\gamma'}^{(2)}, \mathsf{r}_{\beta'}^{(2)} \right]. \tag{248}$$

Let us consider modules over the braided bialgebra $B_{braid}^{(2,2)}$ and recall [50] how the universal R-matrix generalizes the standard flip $\boldsymbol{\tau}_{V_1 V_2} : V_1 \otimes V_2 \to V_2 \otimes V_1$. Define the isomorphism of modules (which in our notation correspond to a 1-place action ρ (7)) $\boldsymbol{c}_{V_1 V_2} : V_1 \otimes V_2 \to V_2 \otimes V_1$ by

$$\boldsymbol{c}_{V_1 V_2} \circ (v_1 \otimes v_2) = \boldsymbol{\tau}_{V_1 V_2} \circ R \circ (v_1 \otimes v_2) = \sum_\alpha \rho \left(\mathsf{r}_\alpha^{(2)} \mid v_2 \right) \otimes \rho \left(\mathsf{r}_\alpha^{(1)} \mid v_1 \right), \, v_i \in V_i, \, \mathsf{r}_\alpha^{(i)} \in B, i = 1, 2. \tag{249}$$

The quasitriangularity (245)–(246) and (249) on $V_1 \otimes V_2 \otimes V_3$ leads to (see, e.g., [7])

$$(\boldsymbol{c}_{V_1 V_3} \otimes \mathrm{id}_{V_2}) \circ (\mathrm{id}_{V_1} \otimes \boldsymbol{c}_{V_2 V_3}) = \boldsymbol{c}_{V_1 \otimes V_2, V_3}, \tag{250}$$

$$(\mathrm{id}_{V_2} \otimes \boldsymbol{c}_{V_1 V_3}) \circ (\boldsymbol{c}_{V_1 V_2} \otimes \mathrm{id}_{V_3}) = \boldsymbol{c}_{V_1, V_2 \otimes V_3}. \tag{251}$$

Similarly, the quantum Yang-Baxter equation (247) gives the *braid equation* [50] mapping $V_1 \otimes V_2 \otimes V_3 \to V_3 \otimes V_2 \otimes V_1$:

$$(\boldsymbol{c}_{V_2 V_3} \otimes \mathrm{id}_{V_1}) \circ (\mathrm{id}_{V_2} \otimes \boldsymbol{c}_{V_1 V_3}) \circ (\boldsymbol{c}_{V_1 V_2} \otimes \mathrm{id}_{V_3}) = (\mathrm{id}_{V_3} \otimes \boldsymbol{c}_{V_1 V_2}) \circ (\boldsymbol{c}_{V_1 V_3} \otimes \mathrm{id}_{V_2}) \circ (\mathrm{id}_{V_1} \otimes \boldsymbol{c}_{V_2 V_3}). \tag{252}$$

Putting $V_1 = V_2 = V_3 = V$ shows that $\boldsymbol{c}_{VV}$ is a solution of the braid equation (252) for any module V, if the R is a solution of the Yang-Baxter equation [7, 50].

n'-ary braid equation

Let us consider possible higher arity generalizations of the braid equation (252), informally. Introduce the modules V_i over the polyadic bialgebra $B^{(n',n)}$ (**Definition** 98) by the r-place actions $\rho_{V_i}^{(r)}(b_1, \ldots b_r \mid v_i)$, $b_j \in B$, $v_i \in V_i$, $i = 1, \ldots s$, $j = 1, \ldots, r$ (see (47)). Define the following morphisms of modules

$$\boldsymbol{c}_{V_1 \ldots V_{n'}} : V_1 \otimes \ldots \otimes V_{n'} \to V_{n'} \otimes \ldots \otimes V_1. \tag{253}$$

We use the shorthand notation $\boldsymbol{c}_{V^{n'}} \equiv \boldsymbol{c}_{V_1 \ldots V_{n'}}$, $\mathrm{id}_V \equiv \mathrm{id}_{V_i}$ and introduce indices manifestly only when it will be needed.

Proposition 120. *The n'-ary braid equation has the form*

$$\left(\boldsymbol{c}_{V^{n'}} \otimes \overbrace{\mathrm{id}_V \otimes \ldots \otimes \mathrm{id}_V}^{n'-1} \right) \circ \left(\mathrm{id}_V \otimes \boldsymbol{c}_{V^{n'}} \otimes \overbrace{\mathrm{id}_V \otimes \ldots \otimes \mathrm{id}_V}^{n'-2} \right) \circ \ldots$$

$$\circ \left(\overbrace{\mathrm{id}_V \otimes \ldots \otimes \mathrm{id}_V}^{n'-1} \otimes \boldsymbol{c}_{V^{n'}} \right) \circ \left(\boldsymbol{c}_{V^{n'}} \otimes \overbrace{\mathrm{id}_V \otimes \ldots \otimes \mathrm{id}_V}^{n'-1} \right)$$

$$= \left(\overbrace{\mathrm{id}_V \otimes \ldots \otimes \mathrm{id}_V}^{n'-1} \otimes \boldsymbol{c}_{V^{n'}} \right) \circ \left(\boldsymbol{c}_{V^{n'}} \otimes \overbrace{\mathrm{id}_V \otimes \ldots \otimes \mathrm{id}_V}^{n'-1} \right) \circ \ldots$$

$$\circ \left(\overbrace{\mathrm{id}_V \otimes \ldots \otimes \mathrm{id}_V}^{n'-2} \otimes \boldsymbol{c}_{V^{n'}} \otimes \mathrm{id}_V \right) \circ \left(\overbrace{\mathrm{id}_V \otimes \ldots \otimes \mathrm{id}_V}^{n'-1} \otimes \boldsymbol{c}_{V^{n'}} \right), \tag{254}$$

where each side consists of $(n' + 1)$ brackets with $(2n' - 1)$ multipliers.

Proof. Use the associative quiver technique from [14] (The Post-like quiver in **Section 6**). ∎

Remark 121. There can be additional equations depending on the concrete values of n' which can contain a different number of brackets determined by the corresponding diagram commutation.

Example 122. In case $n' = 3$ we have the *ternary braided equation* for $\boldsymbol{c}_{V_1 V_2 V_3} : V_1 \otimes V_2 \otimes V_3 \to V_3 \otimes V_2 \otimes V_1$ on the tensor product of modules $V_1 \otimes V_2 \otimes V_3 \otimes V_4 \otimes V_5$, as

$$(\boldsymbol{c}_{V_3 V_4 V_5} \otimes \mathrm{id}_{V_2} \otimes \mathrm{id}_{V_1}) \circ (\mathrm{id}_{V_3} \otimes \boldsymbol{c}_{V_2 V_5 V_4} \otimes \mathrm{id}_{V_1}) \circ (\mathrm{id}_{V_3} \otimes \mathrm{id}_{V_2} \otimes \boldsymbol{c}_{V_1 V_4 V_5}) \circ (\boldsymbol{c}_{V_1 V_2 V_3} \otimes \mathrm{id}_{V_4} \otimes \mathrm{id}_{V_5}) =$$
$$(\mathrm{id}_{V_5} \otimes \mathrm{id}_{V_4} \otimes \boldsymbol{c}_{V_1 V_2 V_3}) \circ (\boldsymbol{c}_{V_1 V_4 V_5} \otimes \mathrm{id}_{V_2} \otimes \mathrm{id}_{V_3}) \circ (\mathrm{id}_{V_1} \otimes \boldsymbol{c}_{V_2 V_5 V_4} \otimes \mathrm{id}_{V_3}) \circ (\mathrm{id}_{V_1} \otimes \mathrm{id}_{V_2} \otimes \boldsymbol{c}_{V_3 V_4 V_5}). \tag{255}$$

The ternary compatibility conditions for $\boldsymbol{c}_{V_1 V_2 V_3}$ (corresponding to (250)–(251)) are

$$(\boldsymbol{c}_{V_1 V_4 V_5} \otimes \mathrm{id}_{V_2} \otimes \mathrm{id}_{V_3}) \circ (\mathrm{id}_{V_1} \otimes \boldsymbol{c}_{V_2 V_5 V_4} \otimes \mathrm{id}_{V_3}) \circ (\mathrm{id}_{V_1} \otimes \mathrm{id}_{V_2} \otimes \boldsymbol{c}_{V_3 V_4 V_5}) = \boldsymbol{c}_{V_1 \otimes V_2 \otimes V_3, V_4, V_5}, \tag{256}$$

$$(\mathrm{id}_{V_3} \otimes \boldsymbol{c}_{V_2 V_5 V_4} \otimes \mathrm{id}_{V_1}) \circ (\mathrm{id}_{V_3} \otimes \mathrm{id}_{V_2} \otimes \boldsymbol{c}_{V_1 V_4 V_5}) \circ (\boldsymbol{c}_{V_1 V_2 V_3} \otimes \mathrm{id}_{V_4} \otimes \mathrm{id}_{V_5}) = \boldsymbol{c}_{V_1, V_2, V_3 \otimes V_4 \otimes V_5}. \tag{257}$$

Now we follow the opposite (to the standard [50]), but consistent way: using the equations (255)–(257) we find polyadic analogs of the corresponding equations for the R-matrix and the quasitriangularity conditions (245)–(246), which will fix the comultiplication structure of a polyadic bialgebra $B^{(n',n)}$.

Polyadic almost co-commutativity

We will see that the almost co-commutativity equations for the R-matrix are more complicated in the polyadic case, because the main condition (232) will have a different form coming from n-ary group theory [47]. Indeed, let $G^{(n)} = \langle G \mid \mu^{(n)} \rangle$ be an n-ary group and $H' = \langle H' \mid \mu^{(n)} \rangle$, $H'' = \langle H'' \mid \mu^{(n)} \rangle$ are its n-ary subgroups.

Recall [47] that H' and H'' are *semiconjugated* in $G^{(n)}$, if there exist $g \in G$, such that $\mu^{(n)}\left[g, h'_1, \ldots, h'_{n-1}\right] = \mu^{(n)}\left[h''_1, \ldots, h''_{n-1}, g\right]$, $h'_i \in H'$, $h''_i \in H''$, and if g can be on any place, then H' and H'' are *conjugated* in $G^{(n)}$. Based on this notion and on analogy with (3), we can "polyadize" the almost co-commutativity condition (232) in the following way.

Let $B^{(n',n)} = \left\langle B \mid \mu^{(n)}, \Delta^{(n')} \right\rangle$, be a polyadic bialgebra, and the opposite comultiplication $\Delta_{cop}^{(n')} = \tau_{op}^{(n')} \circ \Delta^{(n')}$, where $\tau_{op}^{(n')}$ is the polyadic twist (72).

Definition 123. A polyadic bialgebra $B^{(n',n)}$ is called *polyadic sequenced almost co-commutative*, if there exist fixed $(n-1)$ elements $R_i^{(n')} \in B^{\otimes n'}$, $i = 1, \ldots, n-1$, called a *polyadic R-matrix sequence*, such that

$$\mu^{(n)}\left[\Delta_{cop}^{(n')}(b), R_1^{(n')}, R_2^{(n')}, \ldots, R_{n-1}^{(n')}\right]$$

$$= \mu^{(n)}\left[R_1^{(n')}, \Delta^{(n')}(b), R_2^{(n')}, \ldots, R_{n-1}^{(n')}\right]$$

$$\vdots$$

$$= \mu^{(n)}\left[R_1^{(n')}, R_2^{(n')}, \ldots, R_{n-1}^{(n')}, \Delta^{(n')}(b)\right], \quad \forall b \in B. \tag{258}$$

Definition 124. A polyadic bialgebra $B^{(n',n)}$ is called *polyadic sequenced almost semico-commutative*, if only the first and the last relations in (258) hold

$$\mu^{(n)}\left[\Delta_{cop}^{(n')}(b), R_1^{(n')}, R_2^{(n')}, \ldots, R_{n-1}^{(n')}\right] = \mu^{(n)}\left[R_1^{(n')}, R_2^{(n')}, \ldots, R_{n-1}^{(n')}, \Delta^{(n')}(b)\right], \quad \forall b \in B. \tag{259}$$

Remark 125. Using $(n-1)$ polyadic R-matrices $R_i^{(n')}$ is the only way to build a polyadic analog for the almost commutativity concept, since now there is no binary multiplication.

The definition (258) is too general and needs to consider $(n-1)$ different polyadic analogs of the R-matrix which might not be unique. Therefore, in a similar way to the correspondence of the neutral sequence (3) and the polyadic unit (2), we arrive at

Definition 126. A polyadic bialgebra $B^{(n',n)} = \left\langle B \mid \mu^{(n)}, \Delta^{(n')} \right\rangle$ is called *polyadic almost (semi)co-commutative*, if there exists *one* fixed element $R^{(n')} \in B^{\otimes n'}$ called a *n'-ary R-matrix*, such that

$$\mu^{(n)}\left[\Delta_{cop}^{(n')}(b), \overbrace{R^{(n')}, \ldots, R^{(n')}}^{n-1}\right] = \mu^{(n)}\left[\overbrace{R^{(n')}, \ldots, R^{(n')}}^{n-1}, \Delta^{(n')}(b)\right], \quad \forall b \in B. \tag{260}$$

In components the n'-ary R-matrix $R^{(n')}$ is

$$R^{(n')} = \sum_\alpha \mathsf{r}_\alpha^{(1)} \otimes \ldots \otimes \mathsf{r}_\alpha^{(n')}, \quad \mathsf{r}_\alpha^{(i)} \in B. \tag{261}$$

Remark 127. Polyadic almost co-commutativity (260) can be expressed in component form, as in the binary case (239), only if we know concretely the polyadic twist $\tau_{op}^{(n')} \in S_{n'}$ (where $S_{n'}$ is the symmetry permutation group ON n' elements), which is not unique for arbitrary $n' > 2$.

Example 128. For $B^{(3,3)}$ the ternary almost (semi)co-commutativity (260) is given by

$$\mu^{(3)}\left[\Delta_{cop}^{(3)}(b), R^{(3)}, R^{(3)}\right] = \mu^{(3)}\left[R^{(3)}, R^{(3)}, \Delta^{(3)}(b)\right], \quad \forall b \in B, \tag{262}$$

which with $\tau_{op}^{(3)} = \binom{123}{321}$ becomes, in components,

$$\sum_{[b]} \sum_{\alpha,\beta} \mu^{(3)}\left[b_{[3]}, \mathsf{r}_\alpha^{(1)}, \mathsf{r}_\beta^{(1)}\right] \otimes \mu^{(3)}\left[b_{[2]}, \mathsf{r}_\alpha^{(2)}, \mathsf{r}_\beta^{(2)}\right] \otimes \mu^{(3)}\left[b_{[1]}, \mathsf{r}_\alpha^{(3)}, \mathsf{r}_\beta^{(3)}\right]$$

$$= \sum_{[b]'} \sum_{\alpha'\beta'} \mu^{(3)}\left[\mathsf{r}_{\alpha'}^{(1)}, \mathsf{r}_{\beta'}^{(1)}, b_{[1]'}\right] \otimes \mu^{(3)}\left[\mathsf{r}_{\alpha'}^{(2)}, \mathsf{r}_{\beta'}^{(2)}, b_{[2]'}\right] \otimes \mu^{(3)}\left[\mathsf{r}_{\alpha'}^{(3)}, \mathsf{r}_{\beta'}^{(3)}, b_{[3]'}\right]. \tag{263}$$

Example 129. In the exotic mixed case $B^{(4,3)}$ where the polyadic twist "without fixed points" (72) is $\tau_{op}^{(4)} = \left(\begin{smallmatrix} 1234 \\ 3142 \end{smallmatrix}\right)$, the polyadic almost co-commutativity (260) becomes

$$\sum_{[b]} \sum_{\alpha,\beta} \mu^{(3)} \left[b_{[3]}, r_\alpha^{(1)}, r_\beta^{(1)} \right] \otimes \mu^{(3)} \left[b_{[1]}, r_\alpha^{(2)}, r_\beta^{(2)} \right] \otimes \mu^{(3)} \left[b_{[4]}, r_\alpha^{(3)}, r_\beta^{(3)} \right] \otimes \mu^{(3)} \left[b_{[2]}, r_\alpha^{(4)}, r_\beta^{(4)} \right] =$$

$$\sum_{[b]'} \sum_{\alpha'\beta'} \mu^{(3)} \left[r_{\alpha'}^{(1)}, r_{\beta'}^{(1)}, b_{[1]'} \right] \otimes \mu^{(3)} \left[r_{\alpha'}^{(2)}, r_{\beta'}^{(2)}, b_{[2]'} \right] \otimes \mu^{(3)} \left[r_{\alpha'}^{(3)}, r_{\beta'}^{(3)}, b_{[3]'} \right] \otimes \mu^{(3)} \left[r_{\alpha'}^{(4)}, r_{\beta'}^{(4)}, b_{[4]'} \right]. \tag{264}$$

Equations for the n'-ary R-matrix

Here we consider the most consistent way (from a categorical viewpoint) to derive equations for the polyadic R-matrix, in other words, through using the braided equation (252) (and n'-ary braided equation (254)) with the concrete choice of the braiding $c_{V^{n'}}$.

Suppose that the n'-ary braiding $c_{V^{n'}}$ is defined still by a 1-place action $\rho^{(1)}$, as in the binary case (249). At first glance, we could define the braiding (similar to (249))

$$c_{V_1 \ldots V_{n'}} \circ (v_1 \otimes \ldots \otimes v_{n'}) = \tau_{V_1 \ldots V_{n'}} \circ R^{\left(n'\right)} \circ (v_1 \otimes \ldots \otimes v_{n'})$$

$$= \tau_{V_1 \ldots V_{n'}} \circ \left(\sum_\alpha \rho^{(1)} \left(r_\alpha^{(1)} \mid v_1 \right) \otimes \ldots \otimes \rho^{(1)} \left(r_\alpha^{(n')} \mid v_{n'} \right) \right), \quad v_i \in V_i, \quad r_\alpha^{(i)} \in B, \tag{265}$$

where $\rho^{(1)} : B \otimes V_i \to V_i$ is the 1-place action (see (7)). We recall that only the n-ary composition of 1-place actions (n is the arity of multiplication $\mu^{(n)}$) is defined here (see [10])

$$\overbrace{\rho^{(1)} \left(b_1 \mid \rho^{(1)} \left(b_2 \ldots \rho^{(1)} \left(b_n \mid v \right) \right) \right)}^{n} = \rho^{(1)} \left(\mu^{(n)} [b_1, \ldots b_n] \mid v \right), \quad b_i \in B, \quad v \in V. \tag{266}$$

As in the binary case (240)–(242), we need the "extended" polyadic R-matrix.

Remark 130. The standard definition of the "extended" n'-ary R-matrix can be possible, if the algebra $\langle B \mid \mu^{(n)} \rangle$ contains *one* polyadic unit (element) e_B, because in the polyadic case there are new intriguing possibilities (which did not exist in the binary case) of having several units, or even where all elements are units (see the discussion after (3) and [14]).

Definition 131. The "extended" form of the n'-ary R-matrix is defined by $\mathscr{R}_{i_1 \ldots i_{n'}}^{\left(2n'-1\right)} \in B^{\otimes \left(2n'-1\right)}$, such that

$$\mathscr{R}_{i_1 \ldots i_{n'}}^{\left(2n'-1\right)} = \sum_\alpha e_B \otimes \ldots \otimes r_\alpha^{(i_1)} \otimes \ldots \otimes r_\alpha^{(i_{n'})} \otimes \ldots \otimes e_B, \quad i_1, \ldots, i_{n'} \in \{1, \ldots 2n' - 1\} \tag{267}$$

where $r_\alpha^{(i_k)}$ are on the i_k-place.

In this way we can express in terms of the "extended" n'-ary R-matrix (267) the n'-ary braided equation (254), in full analogy with the binary case (247).

Example 132. For the ternary case

$$c_{V_1 V_2 V_3} \circ (v_1 \otimes v_2 \otimes v_3) = \tau_{V_1 V_2 V_3} \circ R^{(3)} \circ (v_1 \otimes v_2 \otimes v_3)$$

$$= \sum_\alpha \rho^{(1)} \left(r_\alpha^{(1)} \mid v_3 \right) \otimes \rho^{(1)} \left(r_\alpha^{(2)} \mid v_2 \right) \otimes \rho^{(1)} \left(r_\alpha^{(3)} \mid v_1 \right), \quad v_i \in V_i, \quad r_\alpha^{(i)} \in B, \tag{268}$$

and we define $\mathscr{R}_{i_1 i_2 i_3}^{(5)}$ by (267), $i_1, i_2, i_3 \in \{1, \ldots, 5\}$, $\tau_{V_1 V_2 V_3} = \left(\begin{smallmatrix} 123 \\ 321 \end{smallmatrix}\right)$, and consider the ternary braid equation (255). Using (266) we obtain (informally)

$$\mathscr{R}_{123}^{(5)} \mathscr{R}_{145}^{(5)} \mathscr{R}_{254}^{(5)} \mathscr{R}_{345}^{(5)} = \mathscr{R}_{345}^{(5)} \mathscr{R}_{254}^{(5)} \mathscr{R}_{145}^{(5)} \mathscr{R}_{123}^{(5)}. \tag{269}$$

Remark 133. Unfortunately, a "linear" $R^{\left(n'\right)}$ n'-ary braiding $c_{V_1 \ldots V_{n'}}$ (as in (265) and (268)) is not consistent with the polyadic analog of the quasitriangularity equations (250)–(251), because the polyadic almost co-commutativity (260) contains $(n-1)$ copies of n'-ary R-matrix $R^{\left(n'\right)}$.

Therefore, in order to agree with (260), instead of (265), we have

Definition 134. The polyadic braiding $\boldsymbol{c}_{V_1\ldots V_{n'}}$ is defined by

$$
\boldsymbol{c}_{V_1\ldots V_{n'}} \circ (v_1 \otimes \ldots \otimes v_{n'}) = \tau_{V_1\ldots V_{n'}} \circ \rho^{(n-1)} \left(\overbrace{R^{(n')},\ldots,R^{(n')}}^{n-1} \mid (v_1 \otimes \ldots \otimes v_{n'}) \right)
$$

$$
= \tau_{V_1\ldots V_{n'}} \circ \left(\sum_{\alpha_1,\ldots\alpha_{n-1}} \rho^{(n-1)} \left(\mathsf{r}^{(1)}_{\alpha_1},\ldots \mathsf{r}^{(1)}_{\alpha_{n-1}} \mid v_1 \right) \otimes \ldots \otimes \rho^{(n-1)} \left(\mathsf{r}^{(n')}_{\alpha_1},\ldots \mathsf{r}^{(n')}_{\alpha_{n-1}} \mid v_{n'} \right) \right),
$$

$$
v_i \in V_i, \quad \mathsf{r}^{(i)}_\alpha \in B, \tag{270}
$$

where $\rho^{(n-1)} : B^{n-1} \otimes V \to V$ the $(n-1)$-place action (see (7)).

Remark 135. The twist of the modules $\tau_{V_1\ldots V_{n'}}$ should be compatible with the polyadic twist $\tau^{(n')}_{op}$ in (258). In the binary case they are both the same flip $\binom{12}{21}$, but in the n'-ary case they can be different.

Example 136. Consider the ternary braided equation (255), but now for the braiding $\boldsymbol{c}_{V_1 V_2 V_3}$, instead of (268), where we have

$$
\boldsymbol{c}_{V_1 V_2 V_3} \circ (v_1 \otimes v_2 \otimes v_3) = \tau_{V_1 V_2 V_3} \circ \rho^{(2)} \left(R^{(3)}, R^{(3)} \mid (v_1 \otimes v_2 \otimes v_3) \right)
$$

$$
= \sum_{\alpha,\beta} \rho^{(2)} \left(\mathsf{r}^{(3)}_\alpha, \mathsf{r}^{(3)}_\beta \mid v_3 \right) \otimes \rho^{(2)} \left(\mathsf{r}^{(2)}_\alpha, \mathsf{r}^{(2)}_\beta \mid v_2 \right) \otimes \rho^{(2)} \left(\mathsf{r}^{(1)}_\alpha, \mathsf{r}^{(1)}_\beta \mid v_1 \right), \quad v_i \in V_i, \quad \mathsf{r}^{(i)}_{\alpha,\beta} \in B, \tag{271}
$$

where $\rho^{(2)} : B \otimes B \otimes V \to V$ is a 2-place action (7). In this way (271) is consistent with (262). In each place of the 2-place action $\rho^{(2)}$ we then obtain the relation (269).

Polyadic triangularity

A polyadic analog of triangularity [4] can be defined, if we rewrite (246) as

$$
(\mathrm{id}_B \otimes \Delta)(R) = \mu \left[\mathscr{R}_{13}, \mathscr{R}_{12} \right] \equiv \sum_{\alpha,\beta} \mu \circ \tau_{op} \left[\mathsf{r}^{(1)}_\alpha, \mathsf{r}^{(1)}_\beta \right] \otimes \mathsf{r}^{(2)}_\alpha \otimes \mathsf{r}^{(2)}_\beta, \tag{272}
$$

where τ_{op} is the binary twist. Instead of the R-matrix formulation (the left equality in (272)), we use the component approach by [3], and propose the following

Definition 137. A polyadic almost co-commutative bialgebra $B^{(n',n)} = \left\langle B \mid \mu^{(n)}, \Delta^{(n')} \right\rangle$ with the polyadic R-matrix $R^{(n')} = \sum_\alpha \mathsf{r}^{(1)}_\alpha \otimes \ldots \otimes \mathsf{r}^{(n')}_\alpha$, $\quad \mathsf{r}^{(i)}_\alpha \in B$ is called *quasipolyangular*, if the following n' relations hold

$$
\sum_\alpha \Delta^{(n')} \left(\mathsf{r}^{(1)}_\alpha \right) \otimes \mathsf{r}^{(2)}_\alpha \otimes \ldots \otimes \mathsf{r}^{(n')}_\alpha = \sum_{\alpha_1,\ldots\alpha_{n'}} \mathsf{r}^{(1)}_{\alpha_1} \otimes \mathsf{r}^{(1)}_{\alpha_2} \otimes \ldots \otimes \mathsf{r}^{(1)}_{\alpha_{n'}}
$$

$$
\otimes \left(\mu^{(n)} \right)^{\circ \ell} \left[\mathsf{r}^{(2)}_{\alpha_1} \otimes \mathsf{r}^{(2)}_{\alpha_2} \otimes \ldots \otimes \mathsf{r}^{(2)}_{\alpha_{n'}} \right] \otimes \ldots \otimes \left(\mu^{(n)} \right)^{\circ \ell} \left[\mathsf{r}^{(n')}_{\alpha_1} \otimes \mathsf{r}^{(n')}_{\alpha_2} \otimes \ldots \otimes \mathsf{r}^{(n')}_{\alpha_{n'}} \right], \tag{273}
$$

$$
\sum_\alpha \mathsf{r}^{(1)}_\alpha \otimes \Delta^{(n')} \left(\mathsf{r}^{(2)}_\alpha \right) \otimes \ldots \otimes \mathsf{r}^{(n')}_\alpha = \sum_{\alpha_1,\ldots\alpha_{n'}} \left(\mu^{(n)} \right)^{\circ \ell} \circ \tau^{(n')}_{op} \left[\mathsf{r}^{(1)}_{\alpha_1} \otimes \mathsf{r}^{(1)}_{\alpha_2} \otimes \ldots \otimes \mathsf{r}^{(1)}_{\alpha_{n'}} \right]
$$

$$
\otimes \mathsf{r}^{(2)}_{\alpha_1} \otimes \mathsf{r}^{(2)}_{\alpha_2} \otimes \ldots \otimes \mathsf{r}^{(2)}_{\alpha_{n'}} \otimes \ldots \otimes \left(\mu^{(n)} \right)^{\circ \ell} \left[\mathsf{r}^{(n')}_{\alpha_1} \otimes \mathsf{r}^{(n')}_{\alpha_2} \otimes \ldots \otimes \mathsf{r}^{(n')}_{\alpha_{n'}} \right], \tag{274}
$$

$$
\vdots
$$

$$
\sum_\alpha \mathsf{r}^{(1)}_\alpha \otimes \mathsf{r}^{(2)}_\alpha \otimes \ldots \otimes \Delta^{(n')} \left(\mathsf{r}^{(n')}_\alpha \right) = \sum_{\alpha_1,\ldots\alpha_{n'}} \left(\mu^{(n)} \right)^{\circ \ell} \circ \tau^{(n')}_{op} \left[\mathsf{r}^{(1)}_{\alpha_1} \otimes \mathsf{r}^{(1)}_{\alpha_2} \otimes \ldots \otimes \mathsf{r}^{(1)}_{\alpha_{n'}} \right]
$$

$$
\otimes \left(\mu^{(n)} \right)^{\circ \ell} \circ \tau^{(n')}_{op} \left[\mathsf{r}^{(2)}_{\alpha_1} \otimes \mathsf{r}^{(2)}_{\alpha_2} \otimes \ldots \otimes \mathsf{r}^{(2)}_{\alpha_{n'}} \right] \otimes \ldots \otimes \mathsf{r}^{(n')}_{\alpha_1} \otimes \mathsf{r}^{(n')}_{\alpha_2} \otimes \ldots \otimes \mathsf{r}^{(n')}_{\alpha_{n'}}, \tag{275}
$$

where $\tau^{(n')}_{op}$ is the polyadic twist map (72). The arity shape of a quasipolyangular $B^{(n',n)}$ is fixed by

$$
n' = \ell(n-1) + 1, \quad \ell \in \mathbb{N}. \tag{276}
$$

Remark 138. As opposed to the binary case (245)–(246), the right hand sides here can be expressed in terms of the extended R-matrix in the first equation (273) and the last one (275) only, because in the intermediate equations the sequences of R-matrix elements are permuted. For instance, it is clear that the binary product $\sum_{\alpha,\beta} \left(\mathsf{r}_\beta^{(1)} \otimes \mathsf{r}_\alpha^{(2)} \otimes e_B \right) \cdot \left(\mathsf{r}_\alpha^{(1)} \otimes \mathsf{r}_\beta^{(2)} \otimes e_B \right) = \sum_{\alpha,\beta} \left(\mathsf{r}_\beta^{(1)} \cdot \mathsf{r}_\alpha^{(1)} \otimes \mathsf{r}_\alpha^{(2)} \cdot \mathsf{r}_\beta^{(2)} \otimes e_B \right)$ cannot be expressed in terms of the extended binary R-matrix (240).

Almost co-medial polyadic bialgebras

The previous considerations showed that co-commutativity and almost co-commutativity in the polyadic case are not unique and do not describe the bialgebras to the fullest extent. This happens because mediality is a more general and consequent property of polyadic algebraic structures, while commutativity can be treated as a particular case of it (see (66)). Therefore, we propose here to deform *co-mediality* (rather than co-commutativity as in [4, 48, 50]).

Let $B^{(n',n)} = \left\langle B \mid \mu^{(n)}, \Delta^{(n')} \right\rangle$, be a polyadic bialgebra. Now we deform the co-mediality condition (120) in a similar way to the polyadic R-matrix (260).

Definition 139. A polyadic bialgebra $B^{(n',n)}$ is called *polyadic sequenced almost co-medial*, if there exist $(n'-1)$ fixed elements $M_i^{(n'^2)} \in B^{\otimes n'^2}$, $i = 1, \ldots, n-1$, called a *polyadic M-matrix sequence*, such that (see (120) and (260))

$$
\mu^{(n)} \left[\tau_{medial}^{(n',n')} \circ \left(\left(\Delta^{(n')} \right)^{\otimes n'} \right) \circ \Delta^{(n')}(b), M_1^{(n'^2)}, M_2^{(n'^2)}, \ldots, M_{n-1}^{(n'^2)} \right]
$$
$$
= \mu^{(n)} \left[M_1^{(n'^2)}, \left(\left(\Delta^{(n')} \right)^{\otimes n'} \right) \circ \Delta^{(n')}(b), M_2^{(n'^2)}, \ldots, M_{n-1}^{(n'^2)} \right]
$$
$$
= \mu^{(n)} \left[M_1^{(n'^2)}, M_2^{(n'^2)}, \ldots, M_{n-1}^{(n'^2)}, \left(\left(\Delta^{(n')} \right)^{\otimes n'} \right) \circ \Delta^{(n')}(b) \right], \quad \forall b \in B, \tag{277}
$$

where $\boldsymbol{\tau}_{medial}^{(n',n')}$ is the polyadic medial map (69).

Definition 140. A polyadic bialgebra $B^{(n',n)}$ is called *polyadic sequenced almost (semi)co-medial*, if only the first and the last relations in (277) hold

$$
\mu^{(n)} \left[\tau_{medial}^{(n',n')} \circ \left(\left(\Delta^{(n')} \right)^{\otimes n'} \right) \circ \Delta^{(n')}(b), M_1^{(n'^2)}, \ldots, M_{n-1}^{(n'^2)} \right]
$$
$$
= \mu^{(n)} \left[M_1^{(n'^2)}, \ldots, M_{n-1}^{(n'^2)}, \left(\left(\Delta^{(n')} \right)^{\otimes n'} \right) \circ \Delta^{(n')}(b) \right], \quad \forall b \in B, \tag{278}
$$

If all the elements in the sequence (similar to the neutral sequence for n-ary groups (3)) are the same $M_1^{(n'^2)} = M_2^{(n'^2)} = \ldots = M_{n-1}^{(n'^2)} \equiv M^{(n'^2)}$, we have

Definition 141. A polyadic bialgebra $B^{(n',n)}$ is called *polyadic almost (semi)co-medial*, if there exist *one* fixed element $M^{(n'^2)} \in B^{\otimes n'^2}$ called a *polyadic M-matrix*, such that (see (120) and (260))

$$
\mu^{(n)} \left[\tau_{medial}^{(n',n')} \circ \left(\left(\Delta^{(n')} \right)^{\otimes n'} \right) \circ \Delta^{(n')}(b), \overbrace{M^{(n'^2)}, \ldots, M^{(n'^2)}}^{n-1} \right]
$$
$$
= \mu^{(n)} \left[\overbrace{M^{(n'^2)}, \ldots, M^{(n'^2)}}^{n-1}, \left(\left(\Delta^{(n')} \right)^{\otimes n'} \right) \circ \Delta^{(n')}(b) \right], \quad \forall b \in B. \tag{279}
$$

Remark 142. The main advantage of the polyadic almost co-mediality property over polyadic almost co-commutativity is the *uniqueness* of the medial map $\boldsymbol{\tau}_{medial}^{(n,n)}$ and *nonuniqueness* of the polyadic twist map $\boldsymbol{\tau}_{op}^{(\ell_\tau)}$ (72).

The polyadic M-matrix $M^{(n')}$ in components is given by

$$
M^{(n'^2)} = \sum_\alpha \mathsf{m}_\alpha^{(1)} \otimes \ldots \otimes \mathsf{m}_\alpha^{(n'^2)}, \quad \mathsf{m}_\alpha^{(i)} \in B, \ i = 1, \ldots, n'^2. \tag{280}
$$

Example 143. In the binary case for $B^{(2,2)} = \langle B \mid \mu, \Delta \rangle$ we have an almost co-mediality (279) as

$$\mu \left[\tau_{medial} \circ (\Delta \otimes \Delta) \circ \Delta (b), M^{(4)} \right] = \mu \left[M^{(4)}, (\Delta \otimes \Delta) \circ \Delta (b) \right], \quad \forall b \in B. \tag{281}$$

which gives, in components (cf. for R-matrix (239))

$$\sum_{[b]_{[b]}} \sum_{\alpha} \mu \left[b_{[1]_{[1]}}, \mathsf{m}_\alpha^{(1)} \right] \otimes \mu \left[b_{[2]_{[1]}}, \mathsf{m}_\alpha^{(2)} \right] \otimes \mu \left[b_{[1]_{[2]}}, \mathsf{m}_\alpha^{(3)} \right] \otimes \mu \left[b_{[2]_{[2]}}, \mathsf{m}_\alpha^{(4)} \right]$$

$$= \sum_{[b]'_{[b]}} \sum_{\alpha'} \mu \left[\mathsf{m}_{\alpha'}^{(1)}, b_{[1]'_{[1]}} \right] \otimes \mu \left[\mathsf{m}_{\alpha'}^{(2)}, b_{[1]'_{[2]}} \right] \otimes \mu \left[\mathsf{m}_{\alpha'}^{(3)}, b_{[2]'_{[1]}} \right] \otimes \mu \left[\mathsf{m}_{\alpha'}^{(4)}, b_{[2]'_{[2]}} \right]. \tag{282}$$

Let us clarify the connection between the almost co-commutativity and almost co-mediality properties.

Theorem 144. *If* $B^{(n',n)}$ *is polyadic almost (semi)co-commutative with the polyadic twist map* $\tau_{op}^{(n')}$ *(72) and the n'-ary R-matrix $R^{(n')}$ (261), then (260) can be presented in the "medial-like" form*

$$\mu^{(n)} \left[\tau_R^{(n',n')} \circ \left(\left(\Delta^{(n')} \right)^{\otimes n'} \right) \circ \Delta^{(n')} (b), \overbrace{M_R^{(n'^2)}, \dots, M_R^{(n'^2)}}^{n-1} \right]$$

$$= \mu^{(n)} \left[\overbrace{M_R^{(n'^2)}, \dots, M_R^{(n'^2)}}^{n-1}, \left(\left(\Delta^{(n')} \right)^{\otimes n'} \right) \circ \Delta^{(n')} (b) \right], \quad \forall b \in B, \tag{283}$$

where

$$\tau_R^{(n',n')} = \overbrace{\tau_{op}^{(n')} \otimes \dots \otimes \tau_{op}^{(n')}}^{n'}, \tag{284}$$

$$M_R^{(n'^2)} = \overbrace{R^{(n')} \otimes \dots \otimes R^{(n')}}^{n'}. \tag{285}$$

Proof. Applying (260) to each Sweedler component $b_{[i]}$ of $\Delta^{(n')}(b)$, $i = 1, \dots, n'$, we obtain n' relations for the polyadic almost (semi)co-commutativity. Then multiplying them tensorially, we obtain

$$\left(\overbrace{\tau_{op}^{(n')} \otimes \dots \otimes \tau_{op}^{(n')}}^{n'} \right) \circ \left(\Delta^{(n')} (b_{[1]}) \otimes \dots \otimes \Delta^{(n')} (b_{[n']}) \right) \circ \left(\overbrace{R^{(n')} \otimes \dots \otimes R^{(n')}}^{n'} \right)$$

$$= \left(\overbrace{R^{(n')} \otimes \dots \otimes R^{(n')}}^{n'} \right) \circ \left(\Delta^{(n')} (b_{[1]}) \otimes \dots \otimes \Delta^{(n')} (b_{[n']}) \right),$$

which immediately gives (283). The converse statement is obvious. ∎

Corollary 145. Polyadic almost co-commutativity is a *particular case* of polyadic co-mediality with the special "medial-like" twist map $\boldsymbol{\tau}_R^{(n',n')}$ (284) and the composite M-matrix (285) consisting of n' copies of the R-matrix (261).

Example 146. In the binary case we compare the medial map (66) with the composed "medial-like" twist map (284) as

$$\boldsymbol{\tau}_{medial} = \mathrm{id}_B \otimes \boldsymbol{\tau}_{op} \otimes \mathrm{id}_B, \tag{286}$$

$$\boldsymbol{\tau}_R = \boldsymbol{\tau}_{op} \otimes \boldsymbol{\tau}_{op}, \tag{287}$$

or in components

$$b_1 \otimes b_2 \otimes b_3 \otimes b_4 \overset{\tau_{medial}}{\mapsto} b_1 \otimes b_3 \otimes b_2 \otimes b_4, \tag{288}$$

$$b_1 \otimes b_2 \otimes b_3 \otimes b_4 \overset{\tau_R}{\mapsto} b_2 \otimes b_1 \otimes b_4 \otimes b_3. \tag{289}$$

This shows manifestly the difference between (polyadic) almost co-commutativity and (polyadic) almost co-mediality.

Equations for the M-matrix

Let us find the equations for the M-matrix (279) using the medial analog of the n'-ary braid equation. Now the morphism of modules $\boldsymbol{c}_{V_1 \dots V_{n'2}}$ becomes (see for the R-matrix (265))

$$\boldsymbol{c}_{V_1 \dots V_{n'2}} \circ (v_1 \otimes \dots \otimes v_{n'2}) = \tau_{medial, V_1 \dots V_{n'2}}^{(n',n')} \circ \rho^{(n-1)} \left(\overbrace{M^{(n'^2)}, \dots, M^{(n'^2)}}^{n-1} \mid (v_1 \otimes \dots \otimes v_{n'2}) \right) =$$

$$\tau_{medial, V_1 \dots V_{n'2}}^{(n',n')} \circ \left(\sum_{\alpha_1, \dots \alpha_{n-1}} \rho^{(n-1)} \left(\mathsf{m}_{\alpha_1}^{(1)}, \dots \mathsf{m}_{\alpha_{n-1}}^{(1)} \mid v_1 \right) \otimes \dots \otimes \rho^{(n-1)} \left(\mathsf{m}_{\alpha_1}^{(n'^2)}, \dots \mathsf{m}_{\alpha_{n-1}}^{(n'^2)} \mid v_{n'2} \right) \right),$$

$$v_i \in V_i, \quad \mathsf{r}_\alpha^{(i)} \in B, \quad i = 1, \dots, n'^2, \tag{290}$$

where $\tau_{medial, V_1 \dots V_{n'2}}^{(n',n')}$ is the medial map (69) acting on n'^2 modules V_i, $M^{(n'^2)}$ is the polyadic M-matrix (280), and $\rho^{(n-1)}$ is the $(n-1)$-place action (7). Now instead of the n'-ary braid equation (254) we can have

Proposition 147. *The n'-ary medial braid equation is*

$$\left(\boldsymbol{c}_{V^{n'2}} \otimes \overbrace{\mathrm{id}_V \otimes \dots \otimes \mathrm{id}_V}^{n'^2-1} \right) \circ \left(\mathrm{id}_V \otimes \boldsymbol{c}_{V^{n'2}} \otimes \overbrace{\mathrm{id}_V \otimes \dots \otimes \mathrm{id}_V}^{n'^2-2} \right) \circ \dots$$

$$\circ \left(\overbrace{\mathrm{id}_V \otimes \dots \otimes \mathrm{id}_V}^{n'^2-1} \otimes \boldsymbol{c}_{V^{n'2}} \right) \circ \left(\boldsymbol{c}_{V^{n'2}} \otimes \overbrace{\mathrm{id}_V \otimes \dots \otimes \mathrm{id}_V}^{n'^2-1} \right)$$

$$= \left(\overbrace{\mathrm{id}_V \otimes \dots \otimes \mathrm{id}_V}^{n'^2-1} \otimes \boldsymbol{c}_{V^{n'2}} \right) \circ \left(\boldsymbol{c}_{V^{n'2}} \otimes \overbrace{\mathrm{id}_V \otimes \dots \otimes \mathrm{id}_V}^{n'^2-1} \right) \circ \dots$$

$$\circ \left(\overbrace{\mathrm{id}_V \otimes \dots \otimes \mathrm{id}_V}^{n'^2-2} \otimes \boldsymbol{c}_{V^{n'2}} \otimes \mathrm{id}_V \right) \circ \left(\overbrace{\mathrm{id}_V \otimes \dots \otimes \mathrm{id}_V}^{n'^2-1} \otimes \boldsymbol{c}_{V^{n'2}} \right), \tag{291}$$

where we use the notation $\boldsymbol{c}_{V^{n'2}} \equiv \boldsymbol{c}_{V_1 \dots V_{n'2}}$, $\mathrm{id}_V \equiv \mathrm{id}_{V_i}$, and each side consists of $\left(n'^2 + 1 \right)$ brackets with $\left(2n'^2 - 1 \right)$ multipliers.

Proof. This follows from the associative quiver technique [14]. ∎

We observe that even in the binary case the medial braid equations are cumbersome and nontrivial.

Example 148. In the binary case $n' = 2$ we have the map $\boldsymbol{c}_{V^{n'2}}$ (see (286), (288))

$$\boldsymbol{c}_{V_1 V_2 V_3 V_4} : V_1 \otimes V_2 \otimes V_3 \otimes V_4 \to V_1 \otimes V_3 \otimes V_2 \otimes V_4 \tag{292}$$

which acts on

$$V_1 \otimes V_2 \otimes V_3 \otimes V_4 \otimes V_5 \otimes V_6 \otimes V_7.$$

There are two medial braid equations which correspond to diagrams of different lengths (cf. the standard braid equation (252))

1) $V_1 \otimes V_2 \otimes V_3 \otimes V_4 \otimes V_5 \otimes V_6 \otimes V_7 \longrightarrow V_1 \otimes V_4 \otimes V_5 \otimes V_6 \otimes V_3 \otimes V_2 \otimes V_7$:

$$
\begin{aligned}
&(\boldsymbol{c}_{V_1 V_5 V_4 V_6} \otimes \mathrm{id}_{V_3} \otimes \mathrm{id}_{V_2} \otimes \mathrm{id}_{V_7}) \circ (\mathrm{id}_{V_1} \otimes \boldsymbol{c}_{V_5 V_6 V_4 V_3} \otimes \mathrm{id}_{V_2} \otimes \mathrm{id}_{V_7}) \\
&\circ (\mathrm{id}_{V_1} \otimes \mathrm{id}_{V_5} \otimes \boldsymbol{c}_{V_6 V_3 V_4 V_2} \otimes \mathrm{id}_{V_7}) \circ (\mathrm{id}_{V_1} \otimes \mathrm{id}_{V_5} \otimes \mathrm{id}_{V_6} \otimes \boldsymbol{c}_{V_3 V_2 V_4 V_7}) \\
&\circ (\boldsymbol{c}_{V_1 V_6 V_5 V_3} \otimes \mathrm{id}_{V_2} \otimes \mathrm{id}_{V_4} \otimes \mathrm{id}_{V_7}) \circ (\mathrm{id}_{V_1} \otimes \boldsymbol{c}_{V_6 V_3 V_5 V_2} \otimes \mathrm{id}_{V_4} \otimes \mathrm{id}_{V_7}) \\
&\circ (\mathrm{id}_{V_1} \otimes \mathrm{id}_{V_6} \otimes \boldsymbol{c}_{V_3 V_2 V_5 V_4} \otimes \mathrm{id}_{V_7}) \circ (\mathrm{id}_{V_1} \otimes \mathrm{id}_{V_6} \otimes \mathrm{id}_{V_6} \otimes \boldsymbol{c}_{V_2 V_4 V_5 V_7}) \\
&\circ (\boldsymbol{c}_{V_1 V_3 V_6 V_2} \otimes \mathrm{id}_{V_4} \otimes \mathrm{id}_{V_5} \otimes \mathrm{id}_{V_7}) \circ (\mathrm{id}_{V_1} \otimes \boldsymbol{c}_{V_3 V_2 V_6 V_4} \otimes \mathrm{id}_{V_5} \otimes \mathrm{id}_{V_7}) \\
&\circ (\mathrm{id}_{V_1} \otimes \mathrm{id}_{V_3} \otimes \boldsymbol{c}_{V_2 V_4 V_6 V_5} \otimes \mathrm{id}_{V_7}) \circ (\mathrm{id}_{V_1} \otimes \mathrm{id}_{V_3} \otimes \mathrm{id}_{V_2} \otimes \boldsymbol{c}_{V_4 V_5 V_6 V_7}) \\
&\circ (\boldsymbol{c}_{V_1 V_2 V_3 V_4} \otimes \mathrm{id}_{V_5} \otimes \mathrm{id}_{V_6} \otimes \mathrm{id}_{V_7}) = (\mathrm{id}_{V_1} \otimes \mathrm{id}_{V_4} \otimes \mathrm{id}_{V_5} \otimes \boldsymbol{c}_{V_6 V_2 V_3 V_7}) \\
&\circ (\boldsymbol{c}_{V_1 V_5 V_4 V_6} \otimes \mathrm{id}_{V_2} \otimes \mathrm{id}_{V_3} \otimes \mathrm{id}_{V_7}) \circ (\mathrm{id}_{V_1} \otimes \boldsymbol{c}_{V_5 V_6 V_4 V_2} \otimes \mathrm{id}_{V_3} \otimes \mathrm{id}_{V_7}) \\
&\circ (\mathrm{id}_{V_1} \otimes \mathrm{id}_{V_5} \otimes \boldsymbol{c}_{V_6 V_2 V_4 V_3} \otimes \mathrm{id}_{V_7}) \circ (\mathrm{id}_{V_1} \otimes \mathrm{id}_{V_5} \otimes \mathrm{id}_{V_6} \otimes \boldsymbol{c}_{V_2 V_3 V_4 V_7}) \\
&\circ (\boldsymbol{c}_{V_1 V_6 V_5 V_2} \otimes \mathrm{id}_{V_3} \otimes \mathrm{id}_{V_4} \otimes \mathrm{id}_{V_7}) \circ (\mathrm{id}_{V_1} \otimes \boldsymbol{c}_{V_6 V_2 V_5 V_3} \otimes \mathrm{id}_{V_4} \otimes \mathrm{id}_{V_7}) \\
&\circ (\mathrm{id}_{V_1} \otimes \mathrm{id}_{V_6} \otimes \boldsymbol{c}_{V_2 V_3 V_5 V_4} \otimes \mathrm{id}_{V_7}) \circ (\mathrm{id}_{V_1} \otimes \mathrm{id}_{V_6} \otimes \mathrm{id}_{V_2} \otimes \boldsymbol{c}_{V_3 V_4 V_5 V_7}) \\
&\circ (\boldsymbol{c}_{V_1 V_2 V_6 V_3} \otimes \mathrm{id}_{V_4} \otimes \mathrm{id}_{V_5} \otimes \mathrm{id}_{V_7}) \circ (\mathrm{id}_{V_1} \otimes \boldsymbol{c}_{V_6 V_3 V_5 V_2} \otimes \mathrm{id}_{V_4} \otimes \mathrm{id}_{V_7}) \\
&\circ (\mathrm{id}_{V_1} \otimes \mathrm{id}_{V_2} \otimes \boldsymbol{c}_{V_3 V_4 V_6 V_5} \otimes \mathrm{id}_{V_7}) \circ (\mathrm{id}_{V_1} \otimes \mathrm{id}_{V_2} \otimes \mathrm{id}_{V_3} \otimes \boldsymbol{c}_{V_4 V_5 V_6 V_7}) .
\end{aligned}
\tag{293}
$$

2) $V_1 \otimes V_2 \otimes V_3 \otimes V_4 \otimes V_5 \otimes V_6 \otimes V_7 \longrightarrow V_1 \otimes V_6 \otimes V_5 \otimes V_4 \otimes V_2 \otimes V_3 \otimes V_7$:

$$
\begin{aligned}
&(\mathrm{id}_{V_1} \otimes \mathrm{id}_{V_6} \otimes \boldsymbol{c}_{V_5 V_2 V_4 V_3} \otimes \mathrm{id}_{V_7}) \circ (\mathrm{id}_{V_1} \otimes \mathrm{id}_{V_6} \otimes \mathrm{id}_{V_5} \otimes \boldsymbol{c}_{V_2 V_3 V_4 V_7}) \\
&\circ (\boldsymbol{c}_{V_1 V_5 V_6 V_2} \otimes \mathrm{id}_{V_3} \otimes \mathrm{id}_{V_4} \otimes \mathrm{id}_{V_7}) \circ (\mathrm{id}_{V_1} \otimes \boldsymbol{c}_{V_5 V_2 V_6 V_3} \otimes \mathrm{id}_{V_4} \otimes \mathrm{id}_{V_7}) \\
&\circ (\mathrm{id}_{V_1} \otimes \mathrm{id}_{V_5} \otimes \boldsymbol{c}_{V_2 V_3 V_6 V_4} \otimes \mathrm{id}_{V_7}) \circ (\mathrm{id}_{V_1} \otimes \mathrm{id}_{V_5} \otimes \mathrm{id}_{V_2} \otimes \boldsymbol{c}_{V_3 V_4 V_6 V_7}) \\
&\circ (\boldsymbol{c}_{V_1 V_2 V_5 V_3} \otimes \mathrm{id}_{V_4} \otimes \mathrm{id}_{V_6} \otimes \mathrm{id}_{V_7}) \circ (\mathrm{id}_{V_1} \otimes \boldsymbol{c}_{V_2 V_3 V_5 V_4} \otimes \mathrm{id}_{V_6} \otimes \mathrm{id}_{V_7}) \\
&\circ (\mathrm{id}_{V_1} \otimes \mathrm{id}_{V_2} \otimes \boldsymbol{c}_{V_3 V_4 V_5 V_6} \otimes \mathrm{id}_{V_7}) = (\mathrm{id}_{V_1} \otimes \boldsymbol{c}_{V_6 V_4 V_5 V_2} \otimes \mathrm{id}_{V_3} \otimes \mathrm{id}_{V_7}) \\
&\circ (\mathrm{id}_{V_1} \otimes \mathrm{id}_{V_6} \otimes \boldsymbol{c}_{V_4 V_2 V_5 V_3} \otimes \mathrm{id}_{V_7}) \circ (\mathrm{id}_{V_1} \otimes \mathrm{id}_{V_6} \otimes \mathrm{id}_{V_4} \otimes \boldsymbol{c}_{V_2 V_3 V_5 V_7}) \\
&\circ (\boldsymbol{c}_{V_1 V_4 V_6 V_2} \otimes \mathrm{id}_{V_3} \otimes \mathrm{id}_{V_5} \otimes \mathrm{id}_{V_7}) \circ (\mathrm{id}_{V_1} \otimes \boldsymbol{c}_{V_4 V_2 V_6 V_3} \otimes \mathrm{id}_{V_5} \otimes \mathrm{id}_{V_7}) \\
&\circ (\mathrm{id}_{V_1} \otimes \mathrm{id}_{V_4} \otimes \boldsymbol{c}_{V_2 V_3 V_6 V_5} \otimes \mathrm{id}_{V_7}) \circ (\mathrm{id}_{V_1} \otimes \mathrm{id}_{V_4} \otimes \mathrm{id}_{V_2} \otimes \boldsymbol{c}_{V_3 V_5 V_6 V_7}) \\
&\circ (\boldsymbol{c}_{V_1 V_2 V_4 V_3} \otimes \mathrm{id}_{V_5} \otimes \mathrm{id}_{V_6} \otimes \mathrm{id}_{V_7}) \circ (\mathrm{id}_{V_1} \otimes \boldsymbol{c}_{V_2 V_3 V_4 V_5} \otimes \mathrm{id}_{V_6} \otimes \mathrm{id}_{V_7}) .
\end{aligned}
\tag{294}
$$

The equations for the M-matrix can be obtained by introducing the "extended" M-matrix, as in the case of the R-matrix, and this can also be possible if the n-ary algebra $\langle B \mid \mu^{(n)} \rangle$ has the unit (element) $e_B \in B$.

Definition 149. The "extended" M-matrix is defined by $\mathscr{M}_{i_1 \dots i_{n'2}}^{(2n'^2 - 1)} \in B^{\otimes (2n'^2 - 1)}$, such that

$$
\mathscr{M}_{i_1 \dots i_{n'2}}^{(2n'^2 - 1)} = \sum_\alpha e_B \otimes \dots \otimes \mathsf{m}_\alpha^{(i_1)} \otimes \dots \otimes \mathsf{m}_\alpha^{(i_{n'2})} \otimes \dots \otimes e_B, \quad i_1, \dots, i_{n'2} \in \left\{ 1, \dots, 2n'^2 - 1 \right\}
\tag{295}
$$

where $\mathsf{m}_\alpha^{(i_k)}$ are on the i_k-place.

It is difficult to write the general compatibility equations for the "extended" M-matrix (295).

Example 150. In the binary case $n = n' = 2$ we have for the polyadic M-matrix $M^{(4)}$ in components

$$
M^{(4)} = \sum_\alpha \mathsf{m}_\alpha^{(1)} \otimes \mathsf{m}_\alpha^{(2)} \otimes \mathsf{m}_\alpha^{(3)} \otimes \mathsf{m}_\alpha^{(4)}, \quad \mathsf{m}_\alpha^{(i)} \in B,
\tag{296}
$$

and $\mathscr{M}_{i_1 \dots i_4}^{(7)} \in B^{\otimes 7}$ with

$$
\mathscr{M}_{i_1 \dots i_4}^{(7)} = \sum_\alpha e_B \otimes \dots \otimes \mathsf{m}_\alpha^{(i_1)} \otimes \dots \otimes \mathsf{m}_\alpha^{(i_4)} \otimes \dots \otimes e_B, \quad i_1, \dots, i_4 \in \{ 1, \dots, 7 \} .
\tag{297}
$$

The map of modules $\boldsymbol{c}_{V_1 \dots V_4}$ (292) in the manifest form is

$$
\begin{aligned}
\boldsymbol{c}_{V_1 V_2 V_3 V_4} \circ (v_1 \otimes v_2 \otimes v_3 \otimes \otimes v_4) &= \tau_{medial} \circ \rho \left(M^{(4)} \mid (v_1 \otimes v_2 \otimes v_3 \otimes v_4) \right) \\
&= \tau_{medial} \circ \left(\sum_\alpha \rho \left(\mathsf{m}_\alpha^{(1)} \mid v_1 \right) \otimes \rho \left(\mathsf{m}_\alpha^{(2)} \mid v_2 \right) \otimes \rho \left(\mathsf{m}_\alpha^{(3)} \mid v_3 \right) \otimes \rho \left(\mathsf{m}_\alpha^{(4)} \mid v_4 \right) \right), \\
v_i &\in V_i, \quad \mathsf{m}_\alpha^{(i)} \in B, \quad i = 1, 2, 3, 4,
\end{aligned}
\tag{298}
$$

where τ_{medial} is the medial map (286), and $\rho : B \times V \to V$ is the ordinary 1-place action (7).

After inserting (298) into (293) and (294), using (297) we obtain the equations for M-matrix

$$\mathcal{M}^{(7)}_{1546}\mathcal{M}^{(7)}_{5643}\mathcal{M}^{(7)}_{6342}\mathcal{M}^{(7)}_{3247}\mathcal{M}^{(7)}_{1653}\mathcal{M}^{(7)}_{6352}\mathcal{M}^{(7)}_{3254}\mathcal{M}^{(7)}_{2457}\mathcal{M}^{(7)}_{1362}\mathcal{M}^{(7)}_{3264}\mathcal{M}^{(7)}_{2465}\mathcal{M}^{(7)}_{4567}\mathcal{M}^{(7)}_{1234}$$

$$= \mathcal{M}^{(7)}_{6237}\mathcal{M}^{(7)}_{1546}\mathcal{M}^{(7)}_{5642}\mathcal{M}^{(7)}_{6243}\mathcal{M}^{(7)}_{2347}\mathcal{M}^{(7)}_{1652}\mathcal{M}^{(7)}_{6253}\mathcal{M}^{(7)}_{2354}\mathcal{M}^{(7)}_{3457}\mathcal{M}^{(7)}_{1263}\mathcal{M}^{(7)}_{2364}\mathcal{M}^{(7)}_{3465}\mathcal{M}^{(7)}_{4567} \tag{299}$$

and

$$\mathcal{M}^{(7)}_{5243}\mathcal{M}^{(7)}_{2347}\mathcal{M}^{(7)}_{1562}\mathcal{M}^{(7)}_{5263}\mathcal{M}^{(7)}_{2364}\mathcal{M}^{(7)}_{3467}\mathcal{M}^{(7)}_{1253}\mathcal{M}^{(7)}_{2354}\mathcal{M}^{(7)}_{3456}$$

$$= \mathcal{M}^{(7)}_{6452}\mathcal{M}^{(7)}_{4253}\mathcal{M}^{(7)}_{2357}\mathcal{M}^{(7)}_{1462}\mathcal{M}^{(7)}_{4263}\mathcal{M}^{(7)}_{2365}\mathcal{M}^{(7)}_{3567}\mathcal{M}^{(7)}_{1243}\mathcal{M}^{(7)}_{2345}, \tag{300}$$

which respect the braid equations (293) and (294).

Remark 151. The unequal number of terms in (299) and (300) is governed by different commutative diagrams of modules (293) and (294), respectively (cf. (247) and (250)–(252)).

Medial analog of triangularity

Now we consider the possible analogs of the quasitriangularity conditions (similar to (245)–(246) and quasipolyangularity (273–275)) for a polyadic almost co-medial bialgebra $B^{(n',n)}$.

Definition 152. A polyadic almost co-medial bialgebra $B^{(n',n)} = \left\langle B \mid \mu^{(n)}, \Delta^{(n')} \right\rangle$ with the polyadic M-matrix $M^{(n'^2)} = \sum_\alpha \mathsf{m}^{(1)}_\alpha \otimes \ldots \otimes \mathsf{m}^{(n'^2)}_\alpha$, $\mathsf{m}^{(i)}_\alpha \in B$ is called *medial quasipolyangular*, if the following n'^2 relations hold

$$\sum_\alpha \left(\Delta^{(n')}\right)^{\otimes n'} \circ \Delta^{(n')} \left(\mathsf{m}^{(1)}_\alpha\right) \otimes \mathsf{m}^{(2)}_\alpha \otimes \ldots \otimes \mathsf{m}^{(n'^2)}_\alpha = \sum_{\alpha_1,\ldots\alpha_{n'^2}} \mathsf{m}^{(1)}_{\alpha_1} \otimes \mathsf{m}^{(1)}_{\alpha_2} \otimes \ldots \otimes \mathsf{m}^{(1)}_{\alpha_{n'^2}}$$

$$\otimes \left(\mu^{(n)}\right)^{\circ\ell} \left[\mathsf{m}^{(2)}_{\alpha_1} \otimes \mathsf{m}^{(2)}_{\alpha_2} \otimes \ldots \otimes \mathsf{m}^{(2)}_{\alpha_{n'^2}}\right] \otimes \ldots \otimes \left(\mu^{(n)}\right)^{\circ\ell} \left[\mathsf{m}^{(n'^2)}_{\alpha_1} \otimes \mathsf{m}^{(n'^2)}_{\alpha_2} \otimes \ldots \otimes \mathsf{m}^{(n'^2)}_{\alpha_{n'^2}}\right], \tag{301}$$

$$\sum_\alpha \mathsf{m}^{(1)}_\alpha \otimes \left(\Delta^{(n')}\right)^{\otimes n'} \circ \Delta^{(n')} \left(\mathsf{m}^{(2)}_\alpha\right) \otimes \ldots \otimes \mathsf{m}^{(n'^2)}_\alpha$$

$$= \sum_{\alpha_1,\ldots\alpha_{n'^2}} \left(\mu^{(n)}\right)^{\circ\ell} \circ \tau^{(n'^2,n'^2)}_{medial} \left[\mathsf{m}^{(1)}_{\alpha_1} \otimes \mathsf{m}^{(1)}_{\alpha_2} \otimes \ldots \otimes \mathsf{m}^{(1)}_{\alpha_{n'^2}}\right] \otimes \mathsf{m}^{(2)}_{\alpha_1} \otimes \mathsf{m}^{(2)}_{\alpha_2} \otimes \ldots \otimes \mathsf{m}^{(2)}_{\alpha_{n'^2}} \otimes \ldots$$

$$\otimes \left(\mu^{(n)}\right)^{\circ\ell} \left[\mathsf{m}^{(n'^2)}_{\alpha_1} \otimes \mathsf{m}^{(n'^2)}_{\alpha_2} \otimes \ldots \otimes \mathsf{m}^{(n'^2)}_{\alpha_{n'^2}}\right], \tag{302}$$

$$\vdots$$

$$\sum_\alpha \mathsf{m}^{(1)}_\alpha \otimes \ldots \otimes \mathsf{m}^{(n'^2-1)}_\alpha \otimes \left(\Delta^{(n')} \left(\mathsf{m}^{(n'^2)}_\alpha\right)\right)^{\otimes n'} \circ \Delta^{(n')} \left(\mathsf{m}^{(n'^2)}_\alpha\right)$$

$$= \sum_{\alpha_1,\ldots\alpha_{n'^2}} \left(\mu^{(n)}\right)^{\circ\ell} \circ \tau^{(n'^2,n'^2)}_{medial} \left[\mathsf{m}^{(1)}_{\alpha_1} \otimes \mathsf{m}^{(1)}_{\alpha_2} \otimes \ldots \otimes \mathsf{m}^{(1)}_{\alpha_{n'^2}}\right] \otimes \ldots$$

$$\otimes \left(\mu^{(n)}\right)^{\circ\ell} \circ \tau^{(n'^2,n'^2)}_{medial} \left[\mathsf{m}^{(n'^2-1)}_{\alpha_1} \otimes \mathsf{m}^{(n'^2-1)}_{\alpha_2} \otimes \ldots \otimes \mathsf{m}^{(n'^2-1)}_{\alpha_{n'^2}}\right] \otimes \mathsf{m}^{(n'^2)}_{\alpha_1} \otimes \mathsf{m}^{(n'^2)}_{\alpha_2} \otimes \ldots \otimes \mathsf{m}^{(n'^2)}_{\alpha_{n'^2}}, \tag{303}$$

where $\tau^{(n'^2,n'^2)}_{medial}$ is the *unique* medial twist map (69). The arity shape of a medial quasipolyangular bialgebra $B^{(n',n)}$ is given by (cf. (276))

$$n'^2 = \ell(n-1) + 1, \quad \ell \in \mathbb{N}. \tag{304}$$

Remark 153. Similar to *Remark* 138, the medial quasipolyangularity equations (301)–(303) can be expressed in terms of the extended M-matrix for the first equation (301) and the last one (303) only, because in the intermediate equations the sequences of M-matrix elements are permuted.

Example 154. In the case where $n' = n = 2$, $\ell = 3$, for the bialgebra $B^{(2,2)} = \langle B \mid \mu = (\cdot)\,, \Delta \rangle$ with the polyadic M-matrix

$$M^{(4)} = \sum_\alpha \mathsf{m}_\alpha^{(1)} \otimes \mathsf{m}_\alpha^{(2)} \otimes \mathsf{m}_\alpha^{(3)} \otimes \mathsf{m}_\alpha^{(4)}, \quad \mathsf{m}_\alpha^{(i)} \in B \tag{305}$$

we have the binary medial quasipolyangularity equations

$$\sum_\alpha (\Delta \otimes \Delta) \circ \Delta \left(\mathsf{m}_\alpha^{(1)} \right) \otimes \mathsf{m}_\alpha^{(2)} \otimes \mathsf{m}_\alpha^{(3)} \otimes \mathsf{m}_\alpha^{(4)} = \sum_{\alpha_1,\alpha_2,\alpha_3,\alpha_4} \mathsf{m}_{\alpha_1}^{(1)} \otimes \mathsf{m}_{\alpha_2}^{(1)} \otimes \mathsf{m}_{\alpha_3}^{(1)} \otimes \mathsf{m}_{\alpha_4}^{(1)}$$
$$\otimes \, \mathsf{m}_{\alpha_1}^{(2)} \cdot \mathsf{m}_{\alpha_2}^{(2)} \cdot \mathsf{m}_{\alpha_3}^{(2)} \cdot \mathsf{m}_{\alpha_4}^{(2)} \otimes \mathsf{m}_{\alpha_1}^{(3)} \cdot \mathsf{m}_{\alpha_2}^{(3)} \cdot \mathsf{m}_{\alpha_3}^{(3)} \cdot \mathsf{m}_{\alpha_4}^{(3)} \otimes \mathsf{m}_{\alpha_1}^{(4)} \cdot \mathsf{m}_{\alpha_2}^{(4)} \cdot \mathsf{m}_{\alpha_3}^{(4)} \cdot \mathsf{m}_{\alpha_4}^{(4)}, \tag{306}$$

$$\sum_\alpha \mathsf{m}_\alpha^{(1)} \otimes (\Delta \otimes \Delta) \circ \Delta \left(\mathsf{m}_\alpha^{(2)} \right) \otimes \mathsf{m}_\alpha^{(3)} \otimes \mathsf{m}_\alpha^{(4)} = \sum_{\alpha_1,\alpha_2,\alpha_3,\alpha_4} \mathsf{m}_{\alpha_1}^{(1)} \cdot \mathsf{m}_{\alpha_3}^{(1)} \cdot \mathsf{m}_{\alpha_2}^{(1)} \cdot \mathsf{m}_{\alpha_4}^{(1)}$$
$$\otimes \, \mathsf{m}_{\alpha_1}^{(2)} \otimes \mathsf{m}_{\alpha_2}^{(2)} \otimes \mathsf{m}_{\alpha_3}^{(2)} \otimes \mathsf{m}_{\alpha_4}^{(2)} \otimes \mathsf{m}_{\alpha_1}^{(3)} \cdot \mathsf{m}_{\alpha_2}^{(3)} \cdot \mathsf{m}_{\alpha_3}^{(3)} \cdot \mathsf{m}_{\alpha_4}^{(3)} \otimes \mathsf{m}_{\alpha_1}^{(4)} \cdot \mathsf{m}_{\alpha_2}^{(4)} \cdot \mathsf{m}_{\alpha_3}^{(4)} \cdot \mathsf{m}_{\alpha_4}^{(4)}, \tag{307}$$

$$\sum_\alpha \mathsf{m}_\alpha^{(1)} \otimes \mathsf{m}_\alpha^{(2)} \otimes (\Delta \otimes \Delta) \circ \Delta \left(\mathsf{m}_\alpha^{(3)} \right) \otimes \mathsf{m}_\alpha^{(4)} = \sum_{\alpha_1,\alpha_2,\alpha_3,\alpha_4} \mathsf{m}_{\alpha_1}^{(1)} \cdot \mathsf{m}_{\alpha_3}^{(1)} \cdot \mathsf{m}_{\alpha_2}^{(1)} \cdot \mathsf{m}_{\alpha_4}^{(1)}$$
$$\otimes \, \mathsf{m}_{\alpha_1}^{(2)} \cdot \mathsf{m}_{\alpha_3}^{(2)} \cdot \mathsf{m}_{\alpha_2}^{(2)} \cdot \mathsf{m}_{\alpha_4}^{(2)} \otimes \mathsf{m}_{\alpha_1}^{(3)} \otimes \mathsf{m}_{\alpha_2}^{(3)} \otimes \mathsf{m}_{\alpha_3}^{(3)} \otimes \mathsf{m}_{\alpha_4}^{(3)} \otimes \mathsf{m}_{\alpha_1}^{(4)} \cdot \mathsf{m}_{\alpha_2}^{(4)} \cdot \mathsf{m}_{\alpha_3}^{(4)} \cdot \mathsf{m}_{\alpha_4}^{(4)}, \tag{308}$$

$$\sum_\alpha \mathsf{m}_\alpha^{(1)} \otimes \mathsf{m}_\alpha^{(2)} \otimes \mathsf{m}_\alpha^{(3)} \otimes (\Delta \otimes \Delta) \circ \Delta \left(\mathsf{m}_\alpha^{(4)} \right) = \sum_{\alpha_1,\alpha_2,\alpha_3,\alpha_4} \mathsf{m}_{\alpha_1}^{(1)} \cdot \mathsf{m}_{\alpha_3}^{(1)} \cdot \mathsf{m}_{\alpha_2}^{(1)} \cdot \mathsf{m}_{\alpha_4}^{(1)}$$
$$\otimes \, \mathsf{m}_{\alpha_1}^{(2)} \cdot \mathsf{m}_{\alpha_3}^{(2)} \cdot \mathsf{m}_{\alpha_2}^{(2)} \cdot \mathsf{m}_{\alpha_4}^{(2)} \otimes \mathsf{m}_{\alpha_1}^{(3)} \cdot \mathsf{m}_{\alpha_3}^{(3)} \cdot \mathsf{m}_{\alpha_2}^{(3)} \cdot \mathsf{m}_{\alpha_4}^{(3)} \otimes \mathsf{m}_{\alpha_1}^{(4)} \otimes \mathsf{m}_{\alpha_2}^{(4)} \otimes \mathsf{m}_{\alpha_3}^{(4)} \otimes \mathsf{m}_{\alpha_4}^{(4)}. \tag{309}$$

According to *Remark* 153, we can express through the extended M-matrix (297) the first medial quasipolyangularity equation (306) and the last one (309) only, as follows

$$((\Delta \otimes \Delta) \circ \Delta \otimes \mathrm{id}_B \otimes \mathrm{id}_B \otimes \mathrm{id}_B) \left(M^{(4)} \right) = \mathscr{M}_{1567}^{(7)} \cdot \mathscr{M}_{2567}^{(7)} \cdot \mathscr{M}_{3567}^{(7)} \cdot \mathscr{M}_{4567}^{(7)}, \tag{310}$$

$$(\mathrm{id}_B \otimes \mathrm{id}_B \otimes \mathrm{id}_B \otimes (\Delta \otimes \Delta) \circ \Delta) \left(M^{(4)} \right) = \mathscr{M}_{1234}^{(7)} \cdot \mathscr{M}_{1236}^{(7)} \cdot \mathscr{M}_{1235}^{(7)} \cdot \mathscr{M}_{1237}^{(7)}. \tag{311}$$

The compatibility of (310)–(311) with the (binary) almost co-mediality (281) leads to

Proposition 155. *An extended binary M-matrix* (297) *of the binary almost co-medial bialgebra* $B^{(2,2)} = \langle B \mid \mu = (\cdot)\,, \Delta \rangle$ *satisfies the compatibility equations* (*cf.* (247))

$$\mathscr{M}_{1234}^{(7)} \cdot \mathscr{M}_{1567}^{(7)} \cdot \mathscr{M}_{2567}^{(7)} \cdot \mathscr{M}_{3567}^{(7)} \cdot \mathscr{M}_{4567}^{(7)} = \mathscr{M}_{1567}^{(7)} \cdot \mathscr{M}_{3567}^{(7)} \cdot \mathscr{M}_{2567}^{(7)} \cdot \mathscr{M}_{4567}^{(7)} \cdot \mathscr{M}_{1234}^{(7)}, \tag{312}$$

$$\mathscr{M}_{4567}^{(7)} \cdot \mathscr{M}_{1234}^{(7)} \cdot \mathscr{M}_{1236}^{(7)} \cdot \mathscr{M}_{1235}^{(7)} \cdot \mathscr{M}_{1237}^{(7)} = \mathscr{M}_{1234}^{(7)} \cdot \mathscr{M}_{1235}^{(7)} \cdot \mathscr{M}_{1236}^{(7)} \cdot \mathscr{M}_{1237}^{(7)} \cdot \mathscr{M}_{4567}^{(7)}. \tag{313}$$

Proof. The identities for the M-matrix

$$\left(M^{(4)} \otimes \mathrm{id}_B \otimes \mathrm{id}_B \otimes \mathrm{id}_B \right) \circ ((\Delta \otimes \Delta) \circ \Delta \otimes \mathrm{id}_B \otimes \mathrm{id}_B \otimes \mathrm{id}_B) \left(M^{(4)} \right)$$
$$= (\tau_{medial} \circ (\Delta \otimes \Delta) \circ \Delta \otimes \mathrm{id}_B \otimes \mathrm{id}_B \otimes \mathrm{id}_B) \left(M^{(4)} \right) \circ \left(M^{(4)} \otimes \mathrm{id}_B \otimes \mathrm{id}_B \otimes \mathrm{id}_B \right), \tag{314}$$

$$\left(\mathrm{id}_B \otimes \mathrm{id}_B \otimes \mathrm{id}_B \otimes M^{(4)} \right) \circ (\mathrm{id}_B \otimes \mathrm{id}_B \otimes \mathrm{id}_B \otimes (\Delta \otimes \Delta) \circ \Delta) \left(M^{(4)} \right)$$
$$= (\mathrm{id}_B \otimes \mathrm{id}_B \otimes \mathrm{id}_B \otimes \tau_{medial} \circ (\Delta \otimes \Delta) \circ \Delta) \left(M^{(4)} \right) \circ \left(\mathrm{id}_B \otimes \mathrm{id}_B \otimes \mathrm{id}_B \otimes M^{(4)} \right), \tag{315}$$

follow from the almost co-mediality condition (281), and then we apply quasipolyangularity (310)–(311). ■

Remark 156. Two other compatibility equations corresponding to the intermediate quasipolyangularity equations (307)–(308) can be written in component form only.

The solutions to (312)–(313) can be found in matrix form by choosing an appropriate basis and using the standard methods (see, e.g., [7, 49]).

CONCLUSIONS

We have presented the "polyadization" procedure of the following algebra-like structures: algebras, coalgebras, bialgebras and Hopf algebras (see [10,20] for ring-like structures). In our concrete constructions the initial arities of operations are taken as arbitrary, and we then try to restrict them only by means of natural relations which bring to mind the binary case. This leads to many exotic properties and unexpected connections between arities and a fixing of their values called "quantization". For instance, the unit and counit (which do not always exist) can be multivalued many place maps, polyadic algebras can be zeroless, the qeurelements should be considered instead of inverse elements under addition and multiplication, a polyadic bialgebra can consist of an algebra and coalgebra of different arities, and a polyadic analog of Hopf algebras contains (instead of the ordinary antipode) the querantipode, which has different properties.

The formulas and constructions introduced for concrete algebra-like structures can have many applications, e.g., in combinatorics, quantum logic, or representation theory. As an example, we have introduced possible polyadic analogs of braidings, almost co-commutativity and a version of the R-matrix. A new concept of deformation (using the medial map) is proposed: this is unique and therefore can be more consequential and suitable in the polyadic case.

ORCID IDs

Steven Duplij, https://orcid.org/0000-0003-1184-6952

REFERENCES

[1]   M.E. Sweedler, *Hopf Algebras*. (W.A. Benjamin, New York, 1969).
[2]   E. Abe, *Hopf Algebras*, (Cambridge Univ. Press, Cambridge, 1980).
[3]   D.E. Radford, *Hopf Algebras*, (World Scientific, Hackensack, 2012).
[4]   V.G. Drinfeld, in *Proceedings of the ICM, Berkeley*, edited by A. Gleason (AMS, Phode Island, 1987), pp. 798.
[5]   S. Shnider, and S. Sternberg, *Quantum Groups*, (International Press, Boston, 1993).
[6]   V. Chari, and A. Pressley, *A Guide to Quantum Groups*, (Cambridge University Press, Cambridge, 1996).
[7]   C. Kassel, *Quantum Groups*, (Springer-Verlag, New York, 1995).
[8]   S. Majid, *Foundations of Quantum Group Theory*, (Cambridge University Press, Cambridge, 1995).
[9]   G. Karaali, Commun. Algebra, **36**, 4341 (2008), https://doi.org/10.1080/00927870802182424.
[10] S. Duplij, J. Math. Physics, Analysis, Geometry, **15**(1), 3-56 (2019), (to appear), https://arxiv.org/abs/1703.10132.
[11] J.A. de Azcarraga, and J. M. Izquierdo, J. Phys. A, **43**, 293001 (2010), https://doi.org/10.1088/1751-8113/43/29/293001.
[12] P.W. Michor, and A.M. Vinogradov, Rend. Sem. Mat. Univ. Pol. Torino, **54**, 373 (1996), http://www.seminariomatematico.polito.it/rendiconti/cartaceo/54-4/373.pdf.
[13] M. Goze, and M. Rausch de Traubenberg, J. Math. Phys. **50**, 063508 (2009), https://doi.org/10.1063/1.3152631.
[14] S. Duplij, in: *Exotic Algebraic and Geometric Structures in Theoretical Physics*, edited by S. Duplij (Nova Publishers, New York, 2018), pp. 251, arXiv: math.RT/1308.4060, https://arxiv.org/abs/1308.4060.
[15] M. Markl, S. Shnider, and J. Stasheff, *Operads in Algebra, Topology and Physics*, (AMS, Providence, 2002).
[16] J.-L. Loday, and B. Vallette, *Algebraic operads*, (Springer, Heidelberg, 2012).
[17] W. Dörnte, Mathematische Zeitschrift, **29**, 1–19 (1929), https://doi.org/10.1007/BF01180515.
[18] G. Crombez, Abh. Math. Semin. Univ. Hamb. **37**, 180 (1972), https://doi.org/10.1007/BF02999695.
[19] J.J. Leeson, and A.T. Butson, Algebra Univers. **11**, 42 (1980), https://doi.org/10.1007/BF02483082.
[20] S. Duplij, p-Adic Numbers, Ultrametric Analysis and Appl. **9**, 267-291 (2017), https://arxiv.org/abs/1707.00719.
[21] J. Ušan, Mathematica Moravica, Special vol., 203 (2003), http://www.moravica.ftn.kg.ac.rs/Special/n-Groups_in_the_Light_of_Natural_Operations-v2006.pdf.
[22] S. Duplij, and W. Werner, Structure of unital 3-fields, (2015), https://arxiv.org/abs/1505.04393v1.
[23] Takeo Yokonuma, *Tensor Spaces and Exterior Algebra*, (AMS, Providence, 1992).
[24] S. Duplij, in: *Symmetry in Nonlinear Mathematical Physics*, edited by A.G. Nikitin, and V.M. Boyko (Institute of Mathematics, Kiev, 2001), pp. 25.
[25] S. Duplij, in: *Exotic Algebraic and Geometric Structures in Theoretical Physics*, edited by S. Duplij (Nova Publishers, New York, 2018), pp. 309.
[26] T. Evans, Duke Math J. **30**, 331 (1963), https://doi.org/10.1215/S0012-7094-63-03035-7.
[27] V.D. Belousov, *n-Ary Quasigroups*, (Shtintsa, Kishinev, 1972).
[28] C.W. Curtis, and I. Reiner, *Representation theory of finite groups and associative algebras*, (AMS, Providence, 1962).
[29] A.A. Kirillov, *Elements of the Theory of Representations*, (Springer-Verlag, Berlin, 1976).
[30] M. Hazewinkel, N. Gubareni, and V.V. Kirichenko, *Algebras, Rings and Modules: Lie Algebras and Hopf Algebras*, (AMS, Providence, 2010).
[31] A. Borowiec, W. Dudek, and S. Duplij, Commun. Algebra, **34**, 1651 (2006), https://doi.org/10.1080/00927870500542564.
[32] M.E. Sweedler, J. Algebra, **8**, 262 (1968), https://doi.org/10.1016/0021-8693(68)90059-8.
[33] R.G. Heyneman, and M.E. Sweedler, J. Algebra, **13**, 192 (1969), https://doi.org/10.1016/0021-8693(69)90071-4.
[34] Y. Kashina, S. Montgomery, and S.-H. Ng, Israel J. Math. **188**, 57 (2012), https://doi.org/10.1007/s11856-011-0092-7.
[35] M. Aguiar, and A. Lauve, Algebra Number Theory, **9**, 547 (2015), https://doi.org/10.2140/ant.2015.9.547.
[36] E.L. Post, Trans. Amer. Math. Soc. **48**, 208 (1940), https://doi.org/10.2307/1990085.

[37] W.A. Dudek, Discuss. Math., Gen. Algebra Appl. **27**, 199 (2007), http://dx.doi.org/10.7151/dmgaa.

[38] E. Heine, *Handbuch der Kugelfunktionan*, (Reimer, Berlin, 1878).

[39] V. Kac, and P. Cheung, *Quantum calculus*, (Springer, New York, 2002).

[40] S. Duplij, Pure Math. Appl. **9**, 283 (1998), http://duplij.univer.kharkov.ua/puma.pdf.gz.

[41] S. Duplij and W. Marcinek, Nucl. Phys. Proc. Suppl. **102**, 293 (2001), *Int. Conference on Supersymmetry and Quantum Field Theory: D.V. Volkov Memorial Conference*, (Kharkov, Ukraine, 2000).

[42] S. Duplij, and W. Marcinek, J. Math. Phys. **43**, 3329 (2002), https://doi.org/10.1063/1.1473681.

[43] S. Duplij, and W. Marcinek, in: *Exotic Algebraic and Geometric Structures in Theoretical Physics*, edited by S. Duplij, (Nova Publishers, New York, 2018), pp. 15.

[44] S. Duplij, and F. Li, Czech. J. Phys. **51**, 1306 (2001), https://doi.org/10.1023/A:1013313802053.

[45] F. Li, and S. Duplij, Commun. Math. Phys. **225**, 191 (2002), https://doi.org/10.1007/s002201000576.

[46] K. Szlach´anyi, in: *Operator Algebras and Quantum Field Theory*, edited by S. Doplicher, R. Longo, J.E. Roberts, and L. Zsid´o (International Press, New York, 1996), p. 221.

[47] A.M. Gal'mak, *n-Ary Groups, Part 1*, (Gomel University, Gomel, 2003).

[48] V.G. Drinfeld, Leningrad Math. J. **1**, 321 (1989), http://www.mathnet.ru/php/getFT.phtml?jrnid=aa&paperid=10&what=fullt&option_lang=rus. (in Russian)

[49] L.A. Lambe, and D.E. Radford, *Introduction to the Quantum Yang-Baxter Equation and Quantum Groups: An Algebraic Approach*, (Kluwer, Dordrecht, 1997).

[50] V.G. Drinfeld, in: *Problems of Modern Quantum Field Theory*, edited by A.A. Belavin, A.V. Klimyk, and A.B. Zamolodchikov (Springer-Verlag, Heidelberg, 1989), pp. 1.

ПОЛІАДИЧНІ АЛГЕБРИ ХОПФА І КВАНТОВІ ГРУПИ

С.А. Дуплій

Центр інформатики, Університет Монстеру, Німеччина

Ця стаття продовжує вивчення конкретних алгеброподібних структур у нашому поліадичному підході, де арності всіх операцій спочатку приймаються як довільні, але відносини між ними, форми арності, повинні бути знайдені з деяких природних умов («принцип свободи арності»). Таким чином, визначаються і досліджуються узагальнені асоціативні алгебри, коасоціативні коалгебри, біалгебри і алгебри Хопфа. Вони мають багато незвичайних особливостей у порівнянні з бінарним випадком. Наприклад, і алгебра, і поле, що лежить в її основі можуть бути нульовими і непоодинокими, існування одиниці і лічильника не обов'язково, а розмірність алгебри не довільна, а «квантована». Можуть бути визначені поліадичний твір згортки і біалгебра, і коли алгебра і коалгебра мають нерівні аріти, поліадична версія антипода, querantipode, має різні властивості. Як можливе застосування до квантової теорії груп ми вводимо поліадичну версію плетінь, майже кокоммутативність, квазітриангулярність і рівняння для R-матриці (які можна розглядати як поліадичний аналог рівняння Янга-Бакстера). Ми пропонуємо іншу концепцію деформації, яка керується не картою твіст, а медіальною картою, де тільки остання унікальна в поліадичному випадку.

КЛЮЧОВІ СЛОВА: поліадичне поле, поліадична алгебра, біалгебра, алгебра Хопфа, антипод, рівняння коси, плетіння, R-матриця, рівняння Янга-Бакстера, медіальність, ко-медіальність, M-матриця, квазітриангулярність

VORTEX DYNAMO IN AN OBLIQUELY ROTATING STRATIFIED NANOFLUID BY SMALL-SCALE NON-HELICAL FORCES

Michael I. Kopp[a]*, Anatoly V. Tur[c], Volodymyr V. Yanovsky[a,b]

aInstitute for Single Cristals, Nat. Academy of Science Ukraine
Nauky Ave. 60, Kharkov 31001, Ukraine
bV.N. Karazin Kharkiv National University
4, Svoboda Sq., Kharkiv, 61022, Ukraine
cUniversite Toulouse [UPS], CNRS, Institute of Research for Astrophysics and Planetology
9 avenue du Colonel Roche, BP 44346, 31028 Toulouse Cedex 4, France
*Corresponding Author: michaelkopp0165@gmail.com
Received February 9, 2021; revised March 11, 2021; accepted April 9, 2021

In this work, a large-scale instability of the hydrodynamic α-effect in an obliquely rotating stratified nanofluid taking into account the effects of Brownian diffusion and particle flux under the influence of a temperature gradient (thermophoresis) is obtained. The instability is caused by the action of an external small-scale non-spiral force, which excites small-scale velocity oscillations with zero helicity and a low Reynolds number. Nonlinear equations for large-scale motions are obtained using the method of multiscale asymptotic expansions by a small parameter (Reynolds number). A linear large-scale instability of hydrodynamic α-effect is investigated depending on the parameters of rotation D, temperature stratification $\widetilde{Ra}$, and concentration of nanoparticles $\widetilde{R}_n$. A new effect of the generation of large-scale vortex structures in nanofluid at $\widetilde{Ra} = 0$ is associated with an increase in the concentration of nanoparticles is obtained. The maximum instability increment is reached at inclination angles $\theta \approx \pi/5$ for the Prandtl numbers $\mathrm{Pr} = 5$, and for the Prandtl numbers $\mathrm{Pr} = 1$ at inclination angles $\theta \approx \pi/2$. It has been found that the frequency changing of the parametric impact will make it possible to control and track the generation of large-scale vortex structures. It is shown that circularly polarized Beltrami vortices appear in nanofluid as the result of new large-scale instability development. In this paper, the saturation regime of large-scale instability in an obliquely rotating stratified nanofluid with an external small-scale non-spiral force is investigated. In the stationary regime was obtained a dynamic system of equations for large-scale perturbations of the velocity field. Numerical solutions of this system of equations are obtained, which show the existence of localized vortex structures in the form of nonlinear Beltrami waves and kinks. The velocity profile of kink tends to be constant at large Z values.

KEY WORDS: stratified nanofluid, large-scale instability, Coriolis force, multiscale asymptotic expansions, α-effect, localized vortex structures

In recent years there has been considerable attention to the problem of transfer processes in nanofluids, which describe a two-phase system consisting of a carrier medium (base fluid or gas) and nanoparticles with characteristic sizes from 1 to 100 nm [1]. Typical base fluids are water or some organic fluids, polymer solutions etc., and nanoparticles are usually particles of metals (Al, Cu), metal oxides (Al_2O_3, CuO). It is obvious that the effective use of nanofluids will become possible only when carrying out the theoretical studies of transfer processes. Special attention should be paid to the processes of formation and evolution of large-scale structures that affect heat transfer in nanofluids.

In works [2-4] were investigated conditions for convective structures (convective cells) formation in rotating layers of nanofluids taking into account the effects of thermophoresis and Brownian motion of particles. In [2] it was shown that the temperature gradient and rotation have a stabilizing effect, while the volume fraction of nanoparticles and the ratio of nanoparticles density to the base fluid have a destabilizing effect on the system. In [3] was carried out a weakly nonlinear analysis of stability in a horizontal rotating nanofluid layer using the minimum order of the Fourier series expansion. The values of heat transfer Nu and transfer of nanoparticle concentration Nu_φ oscillate with time initially strongly but with time reach a stationary value. The parameters of the Rayleigh number concentration R_n and the Lewis number L_e increase the heat and mass transfer rates. An increase of the rotation parameter (Taylor number) leads to a decrease of the heat and mass transfer rates. In paper [4] was investigated the effect of variable gravity on the occurrence of thermal convection in a horizontal layer of rotating nanofluid for a porous medium. It was also shown there that a decrease in the gravity parameter has a stabilizing effect, while an increase in the gravity parameter has a destabilizing effect on the stationary convection. In this case, the critical Rayleigh number increases with an increase of the Taylor number, which indicates the suppression of the onset of convection. The influence of a periodic external action leads to the formation of oscillate convective structures. Therefore, it becomes possible to control the process of heat transfer through the cells, i.e., in the heat valve mode. Here it becomes possible to control the switching between high and low thermal conductivity modes of the cell [5].

Unlike preceding articles [2-5] in this paper we investigated the large-scale vortex structures (LSVS) formation mechanism in a rotating layer of stratified nanofluid under the influence of an external small-scale force. The generation

of LSVS in a Newtonian rotating and temperature stratified fluid under the action of a small-scale force with zero helicity $\vec{F}_0 rot \vec{F}_0 = 0$ was considered in [6]. A necessary condition for the occurrence of large-scale instability considered in [6] is the oblique rotation of the fluid.

The aim of this work is to study generation and nonlinear evolution of vortices fields in a rotating stratified nanofluid under the action of the nonhelical force $\vec{F}_0$. Similarly to study [6], we also will use a mathematical formalism based on the asymptotic method of multiscale expansions in the small parameter of the Reynolds number $R = \dfrac{v_0 t_0}{\lambda_0} \ll 1$ [7].

PROBLEM STATEMENT AND BASIC EVOLUTION EQUATIONS

We consider an infinite horizontal layer of incompressible nanofluid, which rotates with constant angular velocity $\vec{\Omega} = (\Omega_1, \Omega_2, \Omega_3)$. The vector of angular velocity of rotation $\vec{\Omega}$ is inclined concerning to the plane (X, Y) as shown in Fig. 1.
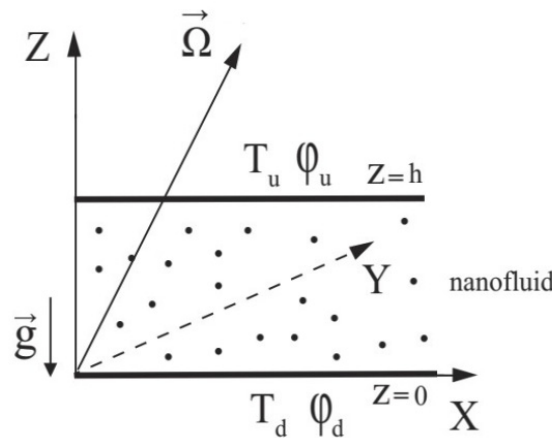
Figure 1. The angular velocity $\vec{\Omega}$ is inclined to the plane (X, Y) where the external force $\vec{F}_0$ is located.

The nanofluid is enclosed between two parallel planes $z = 0$ and $z = h$, where the temperature and volume fraction of nanoparticles are kept constant:

$$T = T_d, \varphi = \varphi_d \quad at \quad z = 0, \tag{1}$$

$$T = T_u, \varphi = \varphi_u \quad at \quad z = h,$$

here $T_d > T_u, \varphi_u > \varphi_d$. We assume that the both boundaries surfaces are free. The hydrodynamic equations of a viscous incompressible rotating nanofluid in the Boussinesq approximation has the following form (see for example [2-4]):

$$\rho_{00}\left(\frac{\partial \vec{V}}{\partial t} + \vec{V} \cdot \nabla \vec{V}\right) = -\nabla P + \mu \nabla^2 \vec{V} + [\varphi \rho_p + (1 - \varphi)\rho_{00}(1 - \beta(T - T_u))]\vec{g} + 2\rho_{00}\vec{V} \times \vec{\Omega} + \vec{F}_0 \tag{2}$$

$$(\rho c)_f\left(\frac{\partial T}{\partial t} + \vec{V} \cdot \nabla T\right) = k_f \nabla^2 T + (\rho c)_p\left(D_B \nabla \varphi \cdot \nabla T + D_T \frac{\nabla T \cdot \nabla T}{T_u}\right) \tag{3}$$

$$\frac{\partial \varphi}{\partial t} + \vec{V} \cdot \nabla \varphi = D_B \nabla^2 \varphi + \frac{D_T}{T_u}\nabla^2 T \tag{4}$$

$$\nabla \vec{V} = 0 \tag{5}$$

Equations (2)-(5) are supplemented with boundary conditions for the velocity of nanofluid motion. The condition of impermeability of layer boundaries in the vertical direction and the absence of shear stresses at the boundaries of the layer give the following boundary conditions for the velocity

$$V_z = 0, \quad \frac{\partial^2 V_z}{\partial z^2} = 0, \quad at \quad z = 0, h \tag{6}$$

Here μ is the viscosity of nanofluid, $\rho_{00} = \varphi\rho_p + (1-\varphi)\rho_f$ is the nanofluid density at the reference temperature T_u, ρ_p is the density of the nanoparticles, ρ_f is the base fluid density at the reference temperature T_u, φ is the volumetric fraction of nanoparticles, β is the thermal expansion coefficient, $\vec{e} = (0,0,1)$ is a unit vector in the direction of the axis OZ, $\vec{g}$ is the gravitational acceleration vector directed along the Z axis: $\vec{g} = (0,0,-g)$. $(\rho c)_f, (\rho c)_p$ are the effective heat capacities of the base fluid and nanoparticles. D_B and D_T denote the Brownian diffusion coefficient and thermophoretic diffusion, respectively. The signs of the coefficients D_B and D_T are positive and they are respectively equal:

$$D_B = \frac{k_B T}{3\pi\mu d_p}, \quad D_T = \left(\frac{\mu_f}{\rho_f}\right)\left(\frac{0.26 k_f}{2k_f + k_p}\right)\phi,$$

where d_p is the diameter of nanoparticles, k_B is the Boltzmann's constant, k_f, k_p are the thermal conductivity of base nanofluid and nanoparticle, μ_f is the viscosity of base nanofluid.

The external small-scale force $\vec{F}_0$ is included in the Navier-Stokes equation (2). This force simulates the excitation source of small-scale and high-frequency pulsations of the velocity field $\vec{v}_0$ in the medium with a small Reynolds number $R = \frac{v_0 t_0}{\lambda_0} \ll 1$. The main role of the force $\vec{F}_0$ is to maintain a moderate level of small-scale movements in the presence of dissipation. An explicit form of the external force $\vec{F}_0$ is given below. Let us pass in equations (2)-(5) and boundary conditions (1), (6) to dimensionless variables, which we denoted by the asterisk $(*)$:

$$(x^*, y^*, z^*) = \frac{(x,y,z)}{h}, \vec{V} = (V_x^*, V_y^*, V_z^*) = \frac{(V_x, V_y, V_z)h}{\chi_f}, t^* = \frac{t \cdot \chi_f}{h^2}, P^* = \frac{P \cdot h^2}{\chi_f \mu},$$

$$\vec{\Omega}^* = \frac{\vec{\Omega}}{\Omega_0}, \varphi^* = \frac{\varphi - \varphi_d}{\varphi_u - \varphi_d}, T^* = \frac{T - T_u}{T_d - T_u}, \vec{F}_0^* = \vec{F}_0 \frac{h^3}{\chi_f \mu}, \chi_f = \frac{k_f}{(\rho c)_f}.$$

Omitting the asterisk $(*)$ in the system of dimensionless equations (2)-(5) and boundary conditions (1), (6) we get

$$\frac{1}{\Pr}\left(\frac{\partial \vec{V}}{\partial t} + \vec{V}\cdot\nabla\vec{V}\right) = -\nabla P + \nabla^2\vec{V} - \vec{e}R_n\varphi - \vec{e}R_m + \vec{e}RaT + \sqrt{Ta}(\vec{V}\times\vec{\Omega}) + \vec{F}_0 \tag{7}$$

$$\frac{\partial T}{\partial t} + \vec{V}\cdot\nabla T = \nabla^2 T + \frac{N_B}{L_e}(\nabla\varphi\cdot\nabla T) + \frac{N_A N_B}{L_e}(\nabla T\cdot\nabla T) \tag{8}$$

$$\frac{\partial \varphi}{\partial t} + \vec{V}\cdot\nabla\varphi = \frac{1}{L_e}\nabla^2\varphi + \frac{N_A}{L_e}\nabla^2 T \tag{9}$$

$$\nabla\cdot\vec{V} = 0 \tag{10}$$

$$T_d = 1, \varphi_d = 0, V_z = \frac{\partial^2 V_z}{\partial z^2} = 0 \quad at \quad z = 0, \tag{11}$$

$$T_u = 0, \varphi_u = 1, V_z = \frac{\partial^2 V_z}{\partial z^2} = 0 \quad at \quad z = 1,$$

where $\Pr = \dfrac{\mu}{\rho_{00}\chi_f}$ is the Prandtl number, $R_n = \dfrac{(\rho_p - \rho_f)(\varphi_u - \varphi_d)gh^3}{\mu\chi_f}$ is the concentration Rayleigh number, $R_m = \dfrac{(\rho_p\varphi_d + \rho_f(1-\varphi_d))gh^3}{\mu\chi_f}$ is the basic density Rayleigh number, $Ra = \dfrac{(T_d - T_u)\rho_{00}g\beta h^3}{\mu\chi_f}$ is the thermal Rayleigh

number, $Ta = \dfrac{4\Omega_0^2 h^4 \rho_{00}^2}{\mu^2}$ is the Taylor number, $L_e = \chi_f / D_B$ is the Lewis number, $N_B = (\varphi_u - \varphi_d) \cdot \dfrac{(\rho c)_p}{(\rho c)_f}$ is the

modified particle density increment, $N_A = \dfrac{D_T (T_d - T_u)}{D_B T_u (\varphi_u - \varphi_d)}$ is the modified diffusivity ratio.

We represented all quantities in equations (7)-(10) as the sum of the ground (stationary) and perturbed states:

$$\vec{V} = \vec{V'}, T = T_b(z) + T', \varphi = \varphi_b(z) + \varphi', P = P_b(z) + P'. \tag{12}$$

After substituting (12) into equations (7)-(10), we find the evolution equations for perturbed quantities $\vec{V'}, T', \varphi'$

$$\frac{1}{\mathrm{Pr}}\left(\frac{\partial \vec{V'}}{\partial t} + \vec{V'} \cdot \nabla \vec{V'} \right) = -\nabla P' + \nabla^2 \vec{V'} - \vec{e} R_n \varphi' + \vec{e} Ra T' + \sqrt{Ta}(\vec{V'} \times \vec{\Omega}) + \vec{F}_0$$

$$\frac{\partial T'}{\partial t} + \vec{V'} \cdot \nabla T' + V_z' \frac{dT_b}{dz} = \nabla^2 T' + \frac{N_B}{L_e}(\nabla \varphi' \cdot \nabla T') + \frac{N_B}{L_e}\left(\frac{d\varphi_b}{dz}\frac{dT'}{dz} + \frac{d\varphi'}{dz}\frac{dT_b}{dz} \right) + \tag{13}$$

$$+\frac{N_A N_B}{L_e}(\nabla T' \cdot \nabla T') + \frac{2 N_A N_B}{L_e}\frac{dT'}{dz}\frac{dT_b}{dz}$$

$$\frac{\partial \varphi'}{\partial t} + \vec{V'} \cdot \nabla \varphi' + V_z' \frac{d\varphi_b}{dz} = \frac{1}{L_e}\nabla^2 \varphi' + \frac{N_A}{L_e}\nabla^2 T'$$

against the background of the ground equilibrium state given by constant gradients of temperature and volume fraction of nanoparticles:

$$0 = -\frac{dP_b}{dz} - R_m - R_n \varphi_b + Ra T_b$$

$$0 = \frac{d^2 T_b}{dz^2} + \frac{N_B}{L_e}\left(\frac{d\varphi_b}{dz}\frac{dT_b}{dz} \right) + \frac{N_A N_B}{L_e}\left(\frac{dT_b}{dz} \right)^2 \tag{14}$$

$$0 = \frac{d^2 \varphi_b}{dz^2} + N_A \frac{d^2 T_b}{dz^2}.$$

Using the boundary conditions (11), from the equations (14) we find solutions for $T_b = 1 - z$ and $\varphi_b = z$, which have a linear dependence on z.

Let the external force $\vec{F}_0$ have the following properties:

$$div\vec{F}_0 = 0, \vec{F}_0 rot\vec{F}_0 = 0, rot\vec{F}_0 \neq 0, \vec{F}_0 = f_0 \vec{F}_0\left(\frac{\vec{x}}{\lambda_0}; \frac{t}{t_0} \right) \tag{15}$$

where λ_0 is the characteristic scale, t_0 is the characteristic time, and f_0 is the characteristic amplitude. The external force $\vec{F}_0$ is specified in the (X, Y) plane orthogonal to the rotation axis and satisfy all properties (15), i.e.

$$F_{0z} = 0, \vec{F}_{0\perp} = f_0\left(\vec{i}cos\phi_2 + \vec{j}cos\phi_1 \right), \phi_1 = k_0 x - \omega_0 t, \phi_2 = k_0 y - \omega_0 t \tag{16}$$

Here ω_0, k_0 are the frequency and wavenumber of the external parametric action, respectively. A simple physical form of an external force (16) can be easily implemented in laboratory experiments. Let us rescale the variables in the equations for perturbations (13):

$$\vec{x} \to \frac{\vec{x}}{\lambda_0}, t \to \frac{t}{t_0}, \vec{V} \to \frac{\vec{V'}}{v_0}, P \to \frac{P'}{P_0}, \vec{F}_0 \to \frac{\vec{F}_0}{f_0},$$

$$T \to \frac{T'}{R}, \varphi \to \frac{\varphi'}{R}, \frac{P_0 t_0}{\lambda_0 v_0} = \frac{f_0 t_0}{v_0} = \frac{t_0}{\lambda_0^2} = 1.$$

As a result, we obtained the following system of equations for perturbations

$$\frac{1}{\text{Pr}}\left(\frac{\partial \vec{V}}{\partial t} + R\vec{V}\cdot\nabla\vec{V}\right) = -\nabla P + \nabla^2\vec{V} - \vec{e}\,\widetilde{R}_n\varphi + \vec{e}\,\widetilde{Ra}\,T + \vec{V}\times\vec{D} + \vec{F}_0 \tag{17}$$

$$\frac{\partial T}{\partial t} + R\vec{V}\cdot\nabla T - V_z = \nabla^2 T + R\frac{N_B}{L_e}(\nabla\varphi\cdot\nabla T) + \frac{N_B}{L_e}\left(\frac{dT}{dz} - \frac{d\varphi}{dz}\right) + \tag{18}$$

$$+R\frac{N_A N_B}{L_e}(\nabla T\cdot\nabla T) - \frac{2N_A N_B}{L_e}\frac{dT}{dz}$$

$$\frac{\partial \varphi}{\partial t} + R\vec{V}\cdot\nabla\varphi + V_z = \frac{1}{L_e}\nabla^2\varphi + \frac{N_A}{L_e}\nabla^2 T \tag{19}$$

where the new notation is introduced

$$\vec{D} = \frac{2h^2}{\mu}\rho_{00}\lambda_0^2\vec{\Omega}, \quad \widetilde{R}_n = R_n\cdot\lambda_0^3, \quad \widetilde{Ra} = Ra\cdot\lambda_0^3.$$

Let us consider the Reynolds number R for small-scale motions to be a small parameter of the asymptotic expansion and assume $\vec{D}, \widetilde{R}_n, \widetilde{Ra}$ to be arbitrary parameters that do not affect the expansion scheme. We consider the external force as being of small scale and high frequency. This force leads to small scale fluctuations in velocity. After averaging, these rapidly oscillating fluctuations vanish. Nevertheless, due to small nonlinear interactions in some orders of perturbation theory, nonzero terms can occur after averaging. In the next section, we consider in detail how to find the solvability conditions for the multi-scale asymptotic expansion, which define the evolution equations for large-scale perturbations.

EQUATIONS FOR LARGE-SCALE FIELDS

In this section, we consider in more detail the application of the method of multiscale asymptotic expansions to the problem of nonlinear evolution of large-scale vortex disturbances in an obliquely rotating nanofluid. The method of asymptotic equations is well presented in works [6-7]. Following these papers we introduce spatial and temporal derivatives in equations (17)-(19) in the form of asymptotic expansions:

$$\frac{\partial}{\partial t} \to \partial_t + R^4\partial_T, \quad \frac{\partial}{\partial x_i} \to \partial_i + R^2\nabla_i \tag{20}$$

where ∂_i and ∂_t denote derivatives concerning fast variables $x_0 = (\vec{x}_0, t_0)$ and ∇_i, ∂_T derivatives concerning slow variable $X = (\vec{X}, T)$. Variables x_0 and X can be called small-scale and large-scale variables. To construct the nonlinear theory, the variables $\vec{V}$, T, φ, P are presented in the form of asymptotic series:

$$\vec{V}(\vec{x},t) = \frac{1}{R}\vec{W}_{-1}(X) + \vec{v}_0 + R\vec{v}_1 + R^2\vec{v}_2 + R^3\vec{v}_3 + \cdots$$

$$T(\vec{x},t) = \frac{1}{R}T_{-1}(X) + T_0 + RT_1 + R^2 T_2 + R^3 T_3 + \cdots \tag{21}$$

$$\varphi(\vec{x},t) = \frac{1}{R}\varphi_{-1}(X) + \varphi_0 + R\varphi_1 + R^2\varphi_2 + R^3\varphi_3 + \cdots$$

$$P(x) = \frac{1}{R^3}P_{-3} + \frac{1}{R^2}P_{-2} + \frac{1}{R}P_{-1} + P_0 + R(P_1 + \overline{P}_1(X)) + R^2 P_2 + R^3 P_3 + \cdots$$

By substituting developments (20)-(21) into the initial equations (17)-(19) and then gathering together the terms of the same order, we obtained the equations of the multi-scale asymptotic development and wrote down the obtained equations up to order R^3 including. The algebraic structure of the asymptotic development of equations (17)-(19) in various orders of R is given in **Appendix A**. It is also shown that in the order R^3 we got the main secular equation or equation for the large-scale fields in a stratified nanofluid:

$$\frac{1}{\Pr}\left(\partial_T W_{-1}^i + \nabla_k \left(\overline{v_0^k v_0^i}\right)\right) = -\nabla_i \overline{P}_1 + \Delta W_{-1}^i \tag{22}$$

$$\partial_T T_{-1} + \nabla_k \left(\overline{v_0^k T_0}\right) = \Delta T_{-1} + \frac{N_B}{L_e}\left(\nabla_k \varphi_{-1} \nabla_k T_{-1}\right) + \frac{N_A N_B}{L_e}\left(\nabla_k T_{-1} \nabla_k T_{-1}\right) \tag{23}$$

$$\partial_T \varphi_{-1} + \nabla_k \left(\overline{v_0^k \varphi_0}\right) = \frac{1}{L_e}\Delta \varphi_{-1} + \frac{N_A}{L_e}\Delta T_{-1} \tag{24}$$

Equations (22)-(24) are supplemented by the secular equations obtained in **Appendix A**:

$$-\nabla_i P_{-3} - e_i \widetilde{R}_n \varphi_{-1} + e_i \widetilde{Ra} T_{-1} + \varepsilon_{ijk} W_j D_k = 0, \tag{25}$$

$$W_{-1}^z = 0, \quad \nabla_i W_{-1}^i = 0, \tag{26}$$

$$\frac{1}{\Pr}W_{-1}^k \nabla_k W_{-1}^i = -\nabla_i P_{-1}, \tag{27}$$

$$W_{-1}^k \nabla_k T_{-1} = \frac{N_B}{L_e}\left(\partial_Z T_{-1} - \partial_Z \varphi_{-1}\right) - \frac{2N_A N_B}{L_e}\partial_Z T_{-1}, \tag{28}$$

$$W_{-1}^k \nabla_k \varphi_{-1} = 0. \tag{29}$$

The influence of small-scale oscillations excited by the external force $\vec{F}_0$ on the evolution of large-scale motion $\vec{W}_{-1}$ is described by the equation (22). It can be seen from this equation that the large-scale temperature T_{-1} and the volume fraction of nanoparticles φ_{-1} do not influence on the dynamics of the large-scale velocity field $\vec{W}_{-1}$. Therefore, we restrict ourselves to studying the equation (22). This equation takes on a closed-form after calculating the correlation function - Reynolds stress $\nabla_k \left(\overline{v_0^k v_0^i}\right)$. The calculation of the Reynolds stress will be greatly simplified if we use the «quasi-two-dimensional» approximation, where the horizontal scales significantly exceed the vertical ones. As a part of this approach, the large-scale derivatives according to are more preferable, i.e

$$\nabla_Z \equiv \frac{\partial}{\partial Z} \gg \frac{\partial}{\partial X}, \frac{\partial}{\partial Y}$$

and the geometry of large-scale fields is following:

$$\vec{W}_{-1} = \left(W_{-1}^x(Z), W_{-1}^y(Z), 0\right), T_{-1} = T_{-1}(Z), \varphi_{-1} = \varphi_{-1}(Z), P_{-1} = const \tag{30}$$

Then the equation (22) is simplified and takes the following form:

$$\partial_T W_1 - \nabla_Z^2 W_1 + \nabla_Z \left(\overline{v_0^z v_0^x}\right) = 0, \quad W_{-1}^x = W_1 \tag{31}$$

$$\partial_T W_2 - \nabla_Z^2 W_2 + \nabla_Z \left(\overline{v_0^z v_0^y}\right) = 0, \quad W_{-1}^y = W_2 \tag{32}$$

Equations (31)-(32) describe the evolution of large-scale eddy fields $\vec{W}$. In order to obtain the final closed form of equations (31)-(32) we have to calculate the Reynolds stresses $\nabla_k \left(\overline{v_0^k v_0^i}\right)$. This shows that we need to find solutions for the small-scale velocity field $\vec{v}_0$. **Appendix B** contains a detailed technique to calculate the velocity field in a rotating stratified nanofluid. Further, in **Appendix C** solutions for small-scale velocity field $\vec{v}_0$ are used to find the Reynolds stresses. Then equations (31)-(32) take a closed form:

$$(\partial_T - \nabla_Z^2)W_1 = -\nabla_Z \left(\frac{f_0^2 D_2 k_0^2 (k_0^4 + \widetilde{\omega}_2^2 - \widetilde{Ra} - l_{n_2})}{2(k_0^4 + \widetilde{\omega}_2^2)\Lambda_2}\right) \tag{33}$$

$$(\partial_T - \nabla_Z^2)W_2 = \nabla_Z \left(\frac{f_0^2 D_1 k_0^2 (k_0^4 + \widetilde{\omega}_1^2 - \widetilde{Ra} - l_{n_1})}{2(k_0^4 + \widetilde{\omega}_1^2)\Lambda_1} \right) \tag{34}$$

We used here the following notations:

$$\widetilde{\omega}_{1,2}^2 = (\omega_0 - k_0 W_{1,2})^2, \quad \Lambda_{1,2} =$$

$$\left(k_0^4 + \mathrm{Pr}^{-2}\widetilde{\omega}_{1,2}^2 \right)\left(k_0^4 + \mathrm{Pr}^{-2}\widetilde{\omega}_{1,2}^2 + \frac{\widetilde{Ra}^2}{k_0^4 + \widetilde{\omega}_{1,2}^2} - 2\widetilde{Ra} \cdot \frac{k_0^4 - \mathrm{Pr}^{-1}\widetilde{\omega}_{1,2}^2}{k_0^4 + \widetilde{\omega}_{1,2}^2} + r_{n_{1,2}} \right) +$$

$$+ 2D_{1,2}^2 \left(k_0^4 - \mathrm{Pr}^{-2}\widetilde{\omega}_{1,2}^2 - \widetilde{Ra} \cdot \frac{k_0^4 + \mathrm{Pr}^{-1}\widetilde{\omega}_{1,2}^2}{k_0^4 + \widetilde{\omega}_{1,2}^2} + p_{n_{1,2}} \right) + D_{1,2}^4,$$

$$r_{n_{1,2}} = -2\widetilde{R}_n \cdot \frac{(k_0^4 + \widetilde{\omega}_{1,2}^2)(L_e^{-1}k_0^4 - \mathrm{Pr}^{-1}\widetilde{\omega}_{1,2}^2) + \frac{N_A}{L_e}k_0^2(L_e^{-1}k_0^2 - \mathrm{Pr}^{-1}\widetilde{\omega}_{1,2}^2 k_0^2 - \widetilde{\omega}_{1,2}^2 k_0^2(1 + \mathrm{Pr}^{-1} L_e^{-1}))}{(k_0^4 + \widetilde{\omega}_{1,2}^2)(L_e^{-2}k_0^4 + \widetilde{\omega}_{1,2}^2)} +$$

$$+ \widetilde{R}_n^2 \cdot \frac{k_0^4\left(1 + \frac{2N_A}{L_e} + \frac{N_A^2}{L_e^2}\right) + \widetilde{\omega}_{1,2}^2}{(k_0^4 + \widetilde{\omega}_{1,2}^2)(L_e^{-2}k_0^4 + \widetilde{\omega}_{1,2}^2)} + 2\widetilde{R}_n\widetilde{Ra} \cdot \frac{\widetilde{\omega}_{1,2}^2 + k_0^2 L_e^{-1}\left(1 + \frac{N_A}{L_e}\right)}{(k_0^4 + \widetilde{\omega}_{1,2}^2)(L_e^{-2}k_0^4 + \widetilde{\omega}_{1,2}^2)},$$

$$p_{n_{1,2}} = -\widetilde{R}_n \cdot \frac{(k_0^4 + \widetilde{\omega}_{1,2}^2)(L_e^{-1}k_0^4 + \mathrm{Pr}^{-1}\widetilde{\omega}_{1,2}^2) + \frac{N_A}{L_e}k_0^4(L_e^{-1}k_0^4 + \mathrm{Pr}^{-1}\widetilde{\omega}_{1,2}^2 + \widetilde{\omega}_{1,2}^2(\mathrm{Pr}^{-1} L_e^{-1} - 1))}{(k_0^4 + \widetilde{\omega}_{1,2}^2)(L_e^{-2}k_0^4 + \widetilde{\omega}_{1,2}^2)},$$

$$l_{n_{1,2}} = \widetilde{R}_n \cdot \frac{L_e^{-1} + \frac{N_A}{L_e}\left(k_0^2 L_e^{-1} - \frac{\widetilde{\omega}_{1,2}^2}{k_0^2}\right)}{L_e^{-2}k_0^4 + \widetilde{\omega}_{1,2}^2} \cdot (k_0^4 + \widetilde{\omega}_{1,2}^2).$$

Thus, in this section, we obtained the closed equations (33)-(34), which are called the equations of nonlinear vortex dynamo in obliquely rotating stratified nanofluid under the parametric action of a small-scale non-spiral force. The large-scale fields decay due to viscous dissipation if rotation ($\Omega = 0$) or external force ($f_0 = 0$) disappears. For the limit of a homogeneous fluid $\widetilde{Ra} = \widetilde{R}_n = 0$ and the absence of nanoparticles, the equation (33)-(34) coincide with the results of [8]. At first, we will consider the stability of small perturbations of fields (linear theory).

LARGE-SCALE INSTABILITY

Equations (33)-(34) describe the nonlinear dynamics of large scale disturbances of the vortex field $\vec{W} = (W_1, W_2)$.
Therefore it is interesting to clarify the question of the stability of small perturbations of the field $\vec{W}$. Then for small values (W_1, W_2) the equations (33)-(34) are linearized and can be reduced to the following system of linear equations:

$$\begin{cases} \partial_T W_1 - \nabla_Z^2 W_1 - \alpha_2 \nabla_Z W_2 = 0 \\ \partial_T W_2 - \nabla_Z^2 W_2 + \alpha_1 \nabla_Z W_1 = 0 \end{cases} \tag{35}$$

here $\alpha_{1,2}$ are the coefficients of the linear vortex dynamo:

$$\alpha_{1,2} = \frac{f_0^2}{2} \frac{D_{1,2} k_0^2}{\Lambda_{0(1,2)}} \left(R + \frac{\Lambda_{(1,2)}}{\Lambda_{0(1,2)}}(R_0 - 1) \right), \quad R_0 = \frac{\widetilde{Ra}}{k_0^4 + \omega_0^2} + \frac{a_6 \widetilde{R}_n}{a_0(k_0^4 + \omega_0^2)},$$

$$R = \frac{2k_0\omega_0\widetilde{Ra}}{(k_0^4+\omega_0^2)^2} + \frac{\widetilde{R}_n}{\tilde{a}_0(k_0^4+\omega_0^2)} \cdot \left(b_6 + \frac{a_6\tilde{b}_0}{\tilde{a}_0} + \frac{2k_0\omega_0 a_6}{k_0^4+\omega_0^2}\right), \tag{36}$$

$$\Lambda_{0(1,2)} = (k_0^4 + \mathrm{Pr}^{-2}\,\omega_0^2)^2 + 2(D_{1,2}^2 - \xi_0\widetilde{Ra})(k_0^4 - \mathrm{Pr}^{-2}\,\omega_0^2) + \xi_0(D_{1,2}^2 - \widetilde{Ra})^2 + \xi_0'D_{1,2}^4 +$$

$$+ \frac{a_4}{a_0}(k_0^4 + \mathrm{Pr}^{-2}\,\omega_0^2) - 2D_{1,2}^2\widetilde{R}_n\frac{a_5}{a_0},$$

$$\Lambda_{1,2} = 4k_0\omega_0\,\mathrm{Pr}^{-2}\,(k_0^4 + \mathrm{Pr}^{-2}\,\omega_0^2) - 2[2k_0\omega_0\,\mathrm{Pr}^{-2}\,(D_{1,2}^2 - \xi_0\widetilde{Ra}) - \xi_1\widetilde{Ra}(k_0^4 - \mathrm{Pr}^{-2}\,\omega_0^2)] -$$

$$-\xi_1(D_{1,2}^2 - \widetilde{Ra})^2 - \xi_1'D_{1,2}^4 - \frac{a_4b_0 - b_4a_0}{a_0^2}(k_0^4 + \mathrm{Pr}^{-2}\,\omega_0^2) + 2k_0\omega_0\,\mathrm{Pr}^{-2}\,\frac{a_4}{a_0} + 2D_{1,2}^2\widetilde{R}_n\cdot\frac{a_5b_0 - b_5a_0}{a_0^2}.$$

Here the coefficients $a_6, b_6, \tilde{a}_0, \tilde{b}_0, \xi_0, \xi_1, \xi_0', \xi_1', a_5, b_5, a_4, b_4, a_3, b_3, a_2, b_2. a_1, b_1, a_0, b_0$ included in (36) have the form:

$$a_6 = (k_0^4 + \omega_0^2)\left(L_e^{-1} + \frac{N_A}{L_e}\left(k_0^2 L_e^{-1} - \frac{\omega_0^2}{k_0^2}\right)\right),$$

$$b_6 = \frac{2N_A\omega_0}{L_e k_0}(k_0^4 + \omega_0^2) - 2k_0\omega_0\left(L_e^{-1} + \frac{N_A}{L_e}\left(\frac{k_0^2}{L_e} - \frac{\omega_0^2}{k_0^2}\right)\right),$$

$$\tilde{a}_0 = L_e^{-2}k_0^4 + \omega_0^2,\ \tilde{b}_0 = 2k_0\omega_0,\ \xi_0 = \frac{k_0^4 + \mathrm{Pr}^{-2}\,\omega_0^2}{k_0^4 + \omega_0^2},\ \xi_1 = \frac{2k_0^5\omega_0(1-\mathrm{Pr}^{-2})}{(k_0^4+\omega_0^2)^2},$$

$$\xi_0' = \frac{\omega_0^2(1-\mathrm{Pr}^{-2})}{k_0^4+\omega_0^2},\ \xi_1' = \frac{2k_0^5\omega_0(1-\mathrm{Pr}^{-2})}{(k_0^4+\omega_0^2)^2},\ a_4 = -2\widetilde{R}_n a_1 + \widetilde{R}_n^2 a_2 + 2a_3\widetilde{R}_n\widetilde{Ra},$$

$$b_4 = 2\widetilde{R}_n b_1 + \widetilde{R}_n^2 b_2 + 2b_3\widetilde{R}_n\widetilde{Ra},\ a_1 = (k_0^4 + \omega_0^2)(L_e^{-1}k_0^4 - \mathrm{Pr}^{-1}\,\omega_0^2) +$$

$$+ \frac{N_A}{L_e}k_0^2(L_e k_0^2 - \omega_0^2 k_0^2(1 + \mathrm{Pr}^{-1} + \mathrm{Pr}^{-1}\,L_e^{-1})),\ b_1 = 2k_0\omega_0(\mathrm{Pr}^{-1}\,(k_0^4 + \omega_0^2) - L_e^{-1}k_0^4 + \omega_0^2\,\mathrm{Pr}^{-1}) +$$

$$+ 2k_0^5\omega_0(1 + \mathrm{Pr}^{-1} + \mathrm{Pr}^{-1}\,L_e^{-1})\frac{N_A}{L_e},\ a_2 = k_0^4\left(1 + \frac{2N_A}{L_e} + \frac{N_A^2}{L_e^2}\right) + \omega_0^2,\ b_2 = 2k_0\omega_0,$$

$$a_3 = \omega_0^2 + L_e^{-1}k_0^2\left(1 + \frac{N_A}{L_e}\right),\ b_3 = b_2,\ a_0 = (k_0^4 + \omega_0^2)(L_e^{-2}k_0^4 + \omega_0^2),$$

$$b_0 = 2k_0\omega_0(k_0^4(1 + L_e^{-2}) + 2\omega_0^2),\ a_5 = (k_0^4 + \omega_0^2)(k_0^4 L_e^{-1} + \omega_0^2\,\mathrm{Pr}^{-1}) +$$

$$+ \frac{N_A}{L_e}k_0^4(k_0^4 L_e^{-1} + \omega_0^2(\mathrm{Pr}^{-1}(1 + L_e^{-1}) - 1)),$$

$$b_5 = 2k_0\omega_0\left[k_0^4(L_e^{-1} + \mathrm{Pr}^{-1}) + 2\omega_0^2\,\mathrm{Pr}^{-1} + \frac{N_A}{L_e}k_0^4(\mathrm{Pr}^{-1}(1 + L_e^{-1}) - 1)\right].$$

We choose perturbations (W_1, W_2) in (35) in the form of plane waves with the wave vector $\vec{K} \parallel OZ$, i. e.

$$W_1 = A_{W_1}\exp(\Gamma t)\sin KZ,\quad W_2 = A_{W_2}\exp(\Gamma t)\cos KZ \tag{37}$$

The solutions (37) describe a circularly polarized plane wave whose amplitude increases exponentially with time. Such

waves are called Beltrami waves because the large-scale velocity field (37) satisfies the Beltrami flow under which the following condition is fulfilled:

$$\vec{W} \times rot\vec{W} = 0$$

Substituting (37) into the system of equations (35) we obtained the dispersion equation:

$$\left(\Gamma + K^2\right)^2 - \alpha_1\alpha_2 K^2 = 0 \qquad (38)$$

From here we found:

$$\Gamma = \pm\sqrt{\alpha_1\alpha_2} K - K^2 \qquad (39)$$

Solutions (39) show the existence of instabilities for large-scale vortical perturbations when $\alpha_1\alpha_2 > 0$. When $\alpha_1\alpha_2 < 0$, damped oscillations arise with frequency $\omega_0 = \sqrt{\alpha_1\alpha_2} K$ instead of the instabilities. The maximum increment of instability $\Gamma_{max} = \dfrac{\alpha_1\alpha_2}{4}$ is reached on the wavenumber $K_{max} = \dfrac{\sqrt{\alpha_1\alpha_2}}{2}$. Coefficients α_1, α_2 give a positive feedback loop between velocity components. It should be noted that in the linear theory, the coefficients α_1, α_2 do not depend on field amplitudes but depend only on dimensionless parameters $D_{1,2}$, $\widetilde{Ra}$, $\Pr$, $\widetilde{R}_n, N_A, L_e$ and the external force amplitude f_0. Let us analyze the dependence of these coefficients on the dimensionless parameters assuming, for simplicity, that the dimensionless amplitude of the external force f_0 is equal to $f_0 = 10$. Fixing the level of dimensionless force means the selection of a certain level of the stationary background of small-scale and fast oscillations. As for the coefficients α_1, α_2, instead of the Cartesian projections D_1 and D_2 it is convenient to use their projections in the spherical coordinate system (D, φ, θ) (see Fig. 2). The coordinate surface $D = const$ is the sphere, θ is the latitude $\theta \in [0, \pi]$, φ is the longitude $\varphi \in [0, 2\pi]$. Let us analyze the dependence of the coefficients α_1, α_2 on the effects of rotation, stratification and concentration of nanoparticles. Then we assumed $D_1 = D_2$ for simplicity that corresponds to a fixed value of longitude $\varphi = \pi/4 + \pi n$, where $n = 0,1,2...k$, k is an integer. In this case, the amplification coefficients of the vortex perturbations are, respectively, equal to:

$$\alpha_{nf} = \alpha_1 = \alpha_2 = \frac{f_0^2}{4}\sqrt{2}D\sin\theta\frac{k_0^2}{\Lambda_0(\theta)}\left(R + \frac{\Lambda(\theta)}{\Lambda_0(\theta)}(R_0 - 1)\right)$$

It should be noted that at inclination angles $(\theta = 0, \theta = \pi)$ vortex disturbances are not generated since $\alpha_{nf} = 0$. It is also interesting to find out how the coefficient α_{nf} depends on the inclination angle θ of the nanofluid rotation axis.
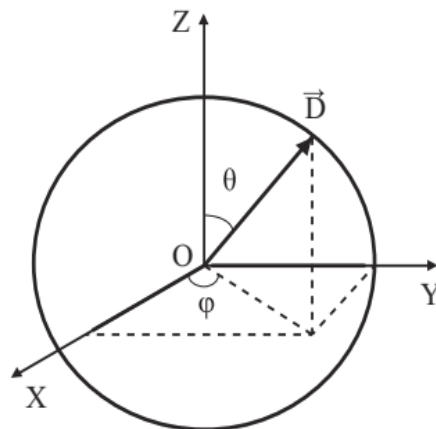
Figure 2. Relation of Cartesian projections of rotation parameter $\vec{D}$ (or angular rotation velocity $\vec{\Omega}$) with their projections in a spherical coordinate system.

This dependence $\alpha_{nf}(\theta)$ is shown in Fig. 3 by a solid line obtained for fixed values $D = 2, \widetilde{Ra} = 2, k_0 = \omega_0 = 1, \Pr = 5, \widetilde{R}_n = 0.122, N_A = 5, L_e = 5000$. The values of the nanofluid parameters $\Pr, \widetilde{R}_n, N_A, L_e$ (Al_2O_3-water) are taken from [2]. As seen from Fig. 3 a maximum value of α_{nf} for nanofluid is inclination angle $\theta_{max} \approx \pi/5 + \pi n$, and a minimum value for $\theta_{min} \approx \pi/2 + \pi n$. The dashed line in Fig. 3 a corresponds to the dependence

$\alpha_b(\theta)$ on the case of a pure fluid with the Prandtl number $Pr = 5$. Graphs Fig. 3a shows that the maximum coefficient $\alpha_b = (\alpha_{nf})_{\widetilde{R}_n=0}$ for a pure fluid is greater than for a nanofluid. This conclusion remains valid for the Prandtl numbers $Pr = 1$. In this case, the maximum coefficients $\alpha_{nf}^{(b)}$ in nano- and pure fluid are at inclination angles $\theta \approx \pi/2 + \pi n$ (see Fig. 3b).
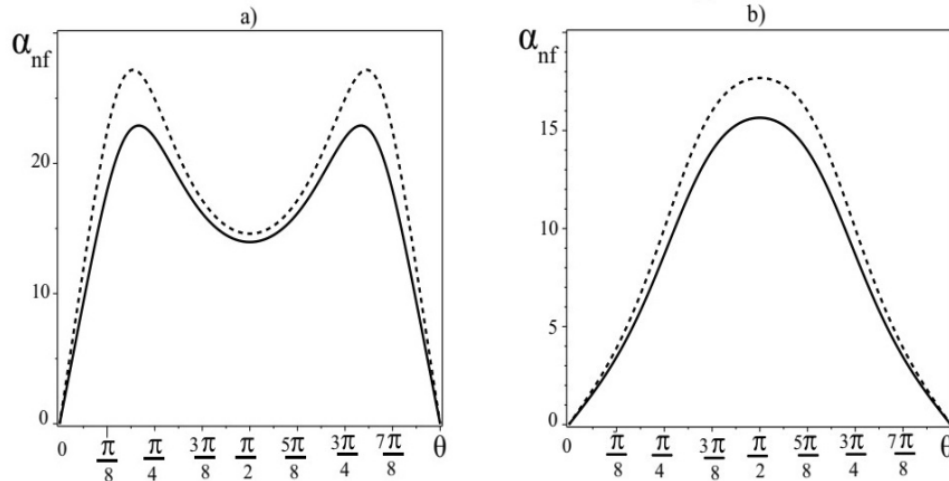
Figure 3. The solid line shows the dependence of the coefficient α_{nf} for nanofluid on the inclination angle θ and the dashed line shows the dependence of the coefficient α_b for the pure liquid on the inclination angle θ. Graphs a) and b) are plotted for the Prandtl numbers $Pr = 5$ and $Pr = 1$ respectively.

Consequently, the characteristic time T_{nf} and the characteristic scale L_{nf} of generated large-scale vortices in nanofluid exceed the corresponding scales T_b, L_b in a pure fluid

$$T_{nf} \gg T_b, \quad L_{nf} \gg L_b, T_{nf} \approx (\alpha_{nf}^2/4)^{-1}, L_{nf} \approx (\alpha_{nf}/2)^{-1}, T_b \approx (\alpha_b^2/4)^{-1}, L_b \approx (\alpha_b/2)^{-1}$$

Let us consider the influence of the nanofluid rotation effect on the coefficient α_{nf} or the process of generation of large-scale vortices. For this, we fixed the parameters of the nanofluid $Pr, \widetilde{R}_n, N_A, L_e$ and the Rayleigh number $\widetilde{Ra} = 2$. We chose the inclination angle equal to $\theta_{max} \simeq \pi/5$, which corresponds to maximum values of the coefficient α_{nf} (see Fig. 3a). As see from Fig. 4a for a certain value of the rotation parameter D the coefficient $\alpha_{nf}(\alpha_b)$ reaches its maximum value $\alpha_{max}^{(nf,b)}$. Then with the increasing of D the coefficient α tends gradually to zero i. e. the suppression of α - effect occurs. A similar phenomenon was described in [9].
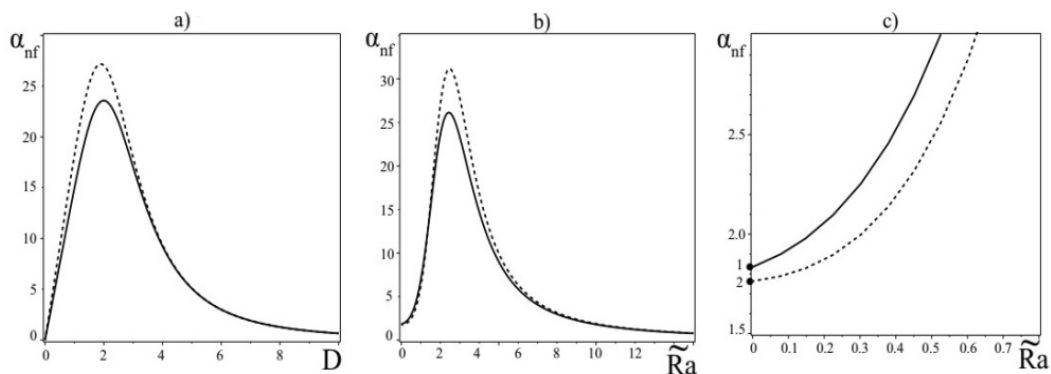
Figure 4. a) The solid line shows the dependence of the coefficient α_{nf} for the nanofluid on the rotation parameter D, and the dashed line shows the dependence of the coefficient α_b for the pure liquid on the rotation parameter D; b) The solid line shows the dependence of the coefficient α_{nf} for the nanofluid on the Rayleigh number $\widetilde{Ra}$, and the dashed line shows the dependence of the coefficient α_b for the pure fluid on the Rayleigh number $\widetilde{Ra}$; c) point 1 corresponds to the value of α_{nf} (nanofluid) at $\widetilde{Ra} = 0$, point 2 corresponds to the value of α_b (pure fluid) at $\widetilde{Ra} = 0$.

Next, fixing the parameters of nanofluid $\Pr, \widetilde{R}_n, N_A, L_e$, rotation $D = 2$ and inclination angle $\theta_{max} \simeq \pi/5$, we determine the dependence of the coefficient α_{nf} of Rayleigh number $\widetilde{Ra}$. From the graphs Fig. 4b it can be seen that the maximum value of the coefficient $\alpha_{nf}(\alpha_b)$ corresponds to small Rayleigh numbers $\widetilde{Ra}$. Large-scale vortices are efficiently generated in the range of Rayleigh numbers $\widetilde{Ra} \in [0,3]$, then we observed the decay $\alpha_{nf}(\alpha_b)$ (Fig. 4b) with an increase in $\widetilde{Ra}$ and the generation of the LSVS becomes ineffective. It means that for large Rayleigh numbers $\widetilde{Ra}$, large-scale instability in nano- and ordinary fluids is not realized and the ordinary convective instability is arisen. Under the condition that there is no heating $\widetilde{Ra} = 0$, the gain coefficient in pure fluid α_b (point 2 in Fig. 4c) is less than in nanofluid α_{nf} (point 1 in Fig. 4c): $\alpha_{nf} > \alpha_b$. In Fig. 4a-4b it is also seen that the maximum coefficient $\alpha_b = (\alpha_{nf})_{\widetilde{R}_n = 0}$ is larger for pure fluid than for nanofluid.

In Fig. 5a is a graph showing the combined effects of rotation and temperature stratification in the plane $(D, \widetilde{Ra})$. Here the instability region $\alpha_{nf} > 0$ is highlighted in gray. Curve 1 corresponds to the instability boundary for nanofluid ($\widetilde{R}_n = 0.122$) and curve 2 corresponds to the instability boundary for pure fluid ($\widetilde{R}_n = 0$).

Let us analyze the influence of the Rayleigh concentration number $\widetilde{R}_n$ on the coefficient α_{nf} or the generation of LSVS for the following fixed parameters $D = 2, \widetilde{Ra} = 3, k_0 = \omega_0 = 1, \Pr = 5, N_A = 5, L_e = 5000, \theta \simeq \pi/5$. In Fig. 5b shows the intersection of graphs (curve 1 and curve 2) at the point $C\left(\widetilde{R}_n^{(0)}, \alpha_{nf}^{(0)}\right)$. Curve 1 is plotted for the case when there is a temperature gradient $\widetilde{Ra} = 3$. For $\widetilde{R}_n = 0$, curve 1 shows the maximum value of α_b^{st} (point A) corresponding to a pure stratified fluid.
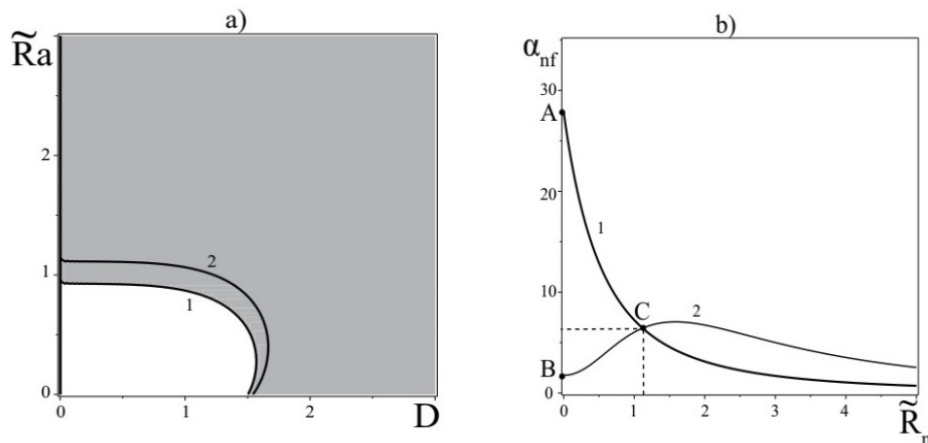
Figure 5. a) The plot for α_{nf} in the plane $(D, \widetilde{Ra})$, where the gray color shows the region corresponding to positive values α (unstable solutions), and the white color region shows negative values α. Curve 1 corresponds to the instability boundary for nanofluid ($\widetilde{R}_n = 0.122$), and curve 2 corresponds to the instability boundary for pure fluid ($\widetilde{R}_n = 0$). b) The plot of the dependence on the $\alpha_{nf} 9$ - effect on the Rayleigh concentration number $\widetilde{R}_n$.

A further increase in the concentration of nanoparticles leads to a decrease in α_{nf}. Curve 2 is plotted for the case when there is no temperature gradient $\widetilde{Ra} = 0$. It can be seen from the behavior of curve 2 that an increase in the concentration of nanoparticles at first leads to an increase in α_{nf}, and then to a decrease. For $\widetilde{R}_n = 0$, curve 2 shows the maximum value of α_b^h (point B), corresponding to the coefficient α for a homogeneous fluid [8]. Here we see that in a pure stratified fluid the generation of LSVS is more efficient than in a homogeneous fluid, which is consistent with the conclusions of the work [6]. Thus, for a certain value of the number $\widetilde{R}_n^{(0)}$ (concentration of nanoparticles), we obtained equal rates generation of LSVS (point C in Fig. 5b) in nanofluid as in the presence of a temperature gradient $\widetilde{Ra} \neq 0$, and without it $\widetilde{Ra} = 0$. Physically, this process can be explained as follows. An increase in the concentration of nanoparticles on the upper surface layer leads to the appearance of a flow due to the gravitational segregation of nanoparticles to the lower surface. In turn, the presence of a temperature gradient arises a heat flux $\vec{q} \sim \vec{e}(T_d - T_u)/h$, which prevents the deposition of nanoparticles on the lower surface layer. An increase in the concentration of nanoparticles $\widetilde{R}_n$ decreases the part of the heat flux and as a consequence, the coefficient α_{nf} is decreased.
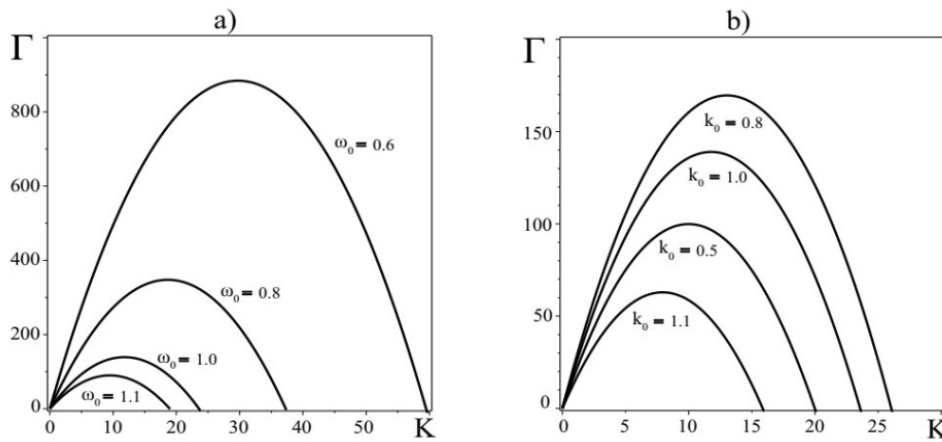
Figure 6. a) The graph of the dependence on the instability growth rate Γ on wavenumbers K for different frequencies ω_0 of the external force $\vec{F}_0$ at $k_0 = 1$. b) The graph of the dependence on the instability growth rate Γ on wavenumbers K for different wavenumbers k_0 of the external force $\vec{F}_0$ at $\omega_0 = 1$.

Fig. 6 shows the dependence on the instability increment Γ on the wavenumbers K for the hydrodynamic α_{nf}-effect in nanofluid at constant parameters $D = 2, \widetilde{Ra} = 2, \Pr = 5, \widetilde{R}_n = 0.122, N_A = 5, L_e = 5000, \theta \simeq \pi/5$. As it is shown in Fig. 6a with an increase in the frequency ω_0 of the external force $\vec{F}_0$ at $k_0 = 1$ the maximum growth rate Γ_{max} of large-scale vortex disturbances is decreased. Fixing the frequency of the external force $\vec{F}_0$ at $\omega_0 = 1$ we constructed a graph of the increment $\Gamma(K)$ (see Fig. 6b) when the small-scale wavenumber k_0 changes. For numbers $k_0 < 1$ we observed an increase in the maximum growth rate Γ_{max} of large-scale vortex disturbances ($k_0 = 0.8$) relative to the level Γ_{max} at $k_0 = 1$, and a decrease the maximum growth rate of large-scale vortex disturbances at $k_0 = 0.5$. This behavior is due to the structural dependence of the coefficient α_{nf} on the small-scale parameters of the external force (ω_0, k_0).

Thus, as a result of the large-scale instability development in an obliquely rotating stratified nanofluid, the large-scale spiral circularly polarized Beltrami-type vortices are generated.

INSTABILITY SATURATION AND NON LINEAR STRUCTURES

The increase of W_1 and W_2 leads to the saturation of the instability. As a result of the development and stabilization of the instability, non-linear structures appear. The study of these structures is of interest. In order to find these structures let us examine the stationary case of equations (33)-(34) and integrate once by Z. For the sake of simplicity, we assume that $D_1 = D_2$, $\theta = \pi/2$ (latitude), $\phi = \pi/4$ (longitude), and Prandtl number $\Pr = 1$. As a result, we get a system of nonlinear equations of the following form:

$$\frac{dW_1}{dZ} = \frac{f_0^2 \sqrt{2}}{4} \frac{Dk_0^2(k_0^4 + \widetilde{\omega}_2^2 - \widetilde{Ra} - l_{n_2})}{2(k_0^4 + \widetilde{\omega}_2^2)\Lambda_2} + C_1, \tag{40}$$

$$\frac{dW_2}{dZ} = -\frac{f_0^2 \sqrt{2}}{4} \frac{Dk_0^2(k_0^4 + \widetilde{\omega}_1^2 - \widetilde{Ra} - l_{n_1})}{2(k_0^4 + \widetilde{\omega}_2^2)\Lambda_1} + C_2. \tag{41}$$

Here C_1, C_2 are arbitrary constants of integration. It should be noted that the dynamic system of equations (40)-(41) is conservative, and hence is Hamiltonian. It's easy to find it we write down the equations (40)-(41) in the Hamiltonian form:

$$\frac{\mathrm{d}W_1}{\mathrm{d}Z} = \frac{\mathrm{d}H}{\mathrm{d}W_2}, \quad \frac{\mathrm{d}W_2}{\mathrm{d}Z} = -\frac{\mathrm{d}H}{\mathrm{d}W_1},$$

where the Hamiltonian has the form:

$$H = H_1(W_1) + H_2(W_2) + C_1 W_2 - C_2 W_1 \tag{42}$$

The functions $H_{1,2}$ are respectively equal to:

$$H_{1,2} = \frac{f_0^2 \sqrt{2}}{4} D \sin\theta \int \frac{k_0^2 (k_0^4 + \tilde{\omega}_{1,2}^2 - \widetilde{Ra} - l_{n_{1,2}}) dW_{1,2}}{2\Pr(k_0^4 + \tilde{\omega}_2^2)\Lambda_{1,2}} \tag{43}$$

The integral in the Hamiltonian $H_{1,2}$ cannot be calculated exactly in quadratures. We used the values of the nanofluid parameters $\Pr = 1, \widetilde{R}_n = 0.122, N_A = 5, L_e = 5000$ (for Al_2O_3 -water) from the paper [2]. The equations (40)-(41) are Hamiltonian thus only fixed points of two types: elliptic and hyperbolic can be observed in phase space. This can be checked if we carry out a qualitative analysis of the system of equations (40)-(41). Linearizing the right-hand sides of equations (40)-(41) in the neighborhood of fixed points, we establish their type and construct a phase portrait. As a result of the analysis, we find the appearance of four fixed points, two of hyperbolic and two of elliptic type. Phase portrait of a dynamical system of equations (40)-(41) for the constants $C_1 = -0.005$, $C_2 = 0.005$ and parameters $D = \widetilde{Ra} = 2$, $k_0 = \omega_0 = 1$, $f_0 = 10$ is shown in Fig. 7.
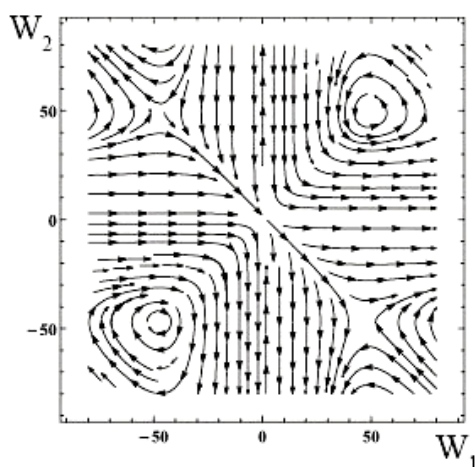
Figure 7. The phase plane of the dynamical system equations (40)-(41) with $C_1 = -0.05$ and $C_2 = 0.05$. One can see the presence of closed trajectories around the elliptic points and separatrices that connect the hyperbolic points.

The phase portrait allows us to describe qualitatively the possible stationary solutions. The most interesting localized solutions correspond to the phase portrait trajectories, which connect the stationary (singular) points on the phase plane. Fig. 7 presents closed trajectories on the phase plane around the elliptic points and separatrices which connect the hyperbolic points. Closed trajectories correspond to nonlinear periodic solutions or nonlinear waves. The separatrices correspond to localized vortex structures of the kinks type (see Fig. 8).
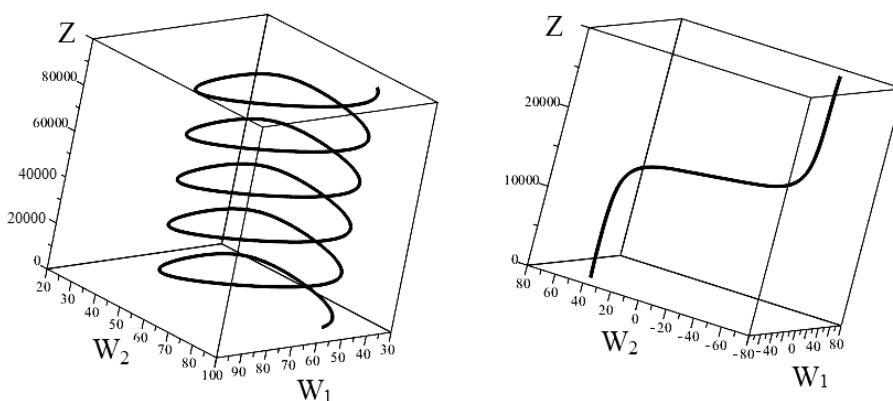
Figure 8. On the left a nonlinear helical wave, which corresponds to a closed trajectory on the phase plane; on the right a localized nonlinear vortex structure (kink), which corresponds to the separatrix on the phase plane.

CONCLUSION

In this work, we have obtained a new type of large-scale instability caused by the temperature gradient and the specific concentration of nanoparticles gradient under the action of a small-scale force with zero helicity $\vec{F}_0 rot\vec{F}_0 = 0$ in

an obliquely rotating nanofluid. This force maintains small-scale fluctuations in the nanofluid and simulates the action of small-scale turbulence with Reynolds number $R \ll 1$. We assumed that the external force is in the plane (X, Y) and the gravity field is directed $\vec{g}$ vertically downward along an axis OZ. Applying the method of multiscale asymptotic expansions we obtained a closed system of equations for large-scale perturbations of the nanofluid velocity $\vec{W}$. For small amplitudes $\vec{W}$ this system of equations describes the instability of the hydrodynamic α-effect, since positive feedback appears between the velocity components. We have shown that the instability occurs only when the vector of the angular velocity of rotation is inclined from the axis OZ. Moreover, for the Prandtl numbers $\text{Pr} = 5$, the maximum instability increment reaches inclination angles $\theta \approx \pi / 5$, and for the Prandtl numbers $\text{Pr} = 1$ inclination angles $\theta \approx \pi / 2$. Taking into account the effects of rotation and temperature stratification of the nanofluid together leads to a significant increase in large-scale vortex disturbances in contrast to the case of a homogeneous medium [8]. In addition, we have obtained a new effect of generation of LSVS in nanofluids at $\widetilde{Ra} = 0$ associated with an increase in the concentration of nanoparticles (see Fig. 5b, curve 2). With an increase in the frequency of the parametric action of an external force, the generation of LSVS becomes less efficient. This effect allows you to control and monitor the process of generating LSVS. The instability becomes nonlinear with increasing amplitude $\vec{W}$. In this case, the emergence of stationary nonlinear vortex structures is assumed. The numerical solutions show that in the non-linear stage, the instability saturation leads to specific velocity profiles (kinks) for which the velocity tends to be constant for large values of Z. The phase portrait contains elliptic stationary points therefore, there are nonlinear periodic solutions in the form of nonlinear Beltrami waves that correspond to closed trajectories. These structures are the result of saturation of large-scale instability (see section **LARGE-SCALE INSTABILITY**). Obtained results can find their applications in many problems of laboratory experiments on rotating stratified nanofluids.

APPENDIX

A. MULTISCALE ASYMPTOTIC DEVELOPMENTS

Let us find the algebraic structure of the asymptotic development in various orders of R, starting from the lowest one. In order of R^{-3} there is only one equation:

$$\partial_i P_{-3} = 0 \Rightarrow P_{-3} = P_{-3}(X) \tag{44}$$

In order R^{-2} appears the equations:

$$\partial_i P_{-2} = 0 \Rightarrow P_{-2} = P_{-2}(X) \tag{45}$$

In order R^{-1}, we obtain the more complicated system of equations:

$$\frac{1}{\text{Pr}}\left(\partial_t W_{-1}^i + W_{-1}^k \partial_k W_{-1}^i\right) = -\partial_i P_{-1} - \nabla_i P_{-3} + \partial_k^2 W_{-1}^i - e_i \widetilde{R}_n \varphi_{-1} + e_i \widetilde{Ra} T_{-1} + \varepsilon_{ijk} W_j D_k \tag{46}$$

$$\partial_t T_{-1} + W_{-1}^k \partial_k T_{-1} - W_{-1}^z = \partial_k^2 T_{-1} + \frac{N_B}{L_e} \partial_k \varphi_{-1} \partial_k T_{-1} + \frac{N_B}{L_e}\left(\partial_z T_{-1} - \partial_z \varphi_{-1}\right) + \tag{47}$$

$$+ \frac{N_A N_B}{L_e}\left(\partial_k T_{-1} \partial_k T_{-1}\right) - \frac{2 N_A N_B}{L_e} \partial_z T_{-1}$$

$$\partial_t \varphi_{-1} + W_{-1}^k \partial_k \varphi_{-1} + W_{-1}^z = \frac{1}{L_e} \partial_k^2 \varphi_{-1} + \frac{N_A}{L_e} \partial_k^2 T_{-1} \tag{48}$$

$$\partial_i W_{-1}^i = 0 \tag{49}$$

The averaging of equations (46)-(49) over the fast variables gives the following secular equations:

$$-\nabla_i P_{-3} - e_i \widetilde{R}_n \varphi_{-1} + e_i \widetilde{Ra} T_{-1} + \varepsilon_{ijk} W_j D_k = 0 \tag{50}$$

$$W_{-1}^z = 0 \tag{51}$$

In zero order in R^0 we have the equations:

$$\frac{1}{\text{Pr}}\left(\partial_t v_0^i + W_{-1}^k \partial_k v_0^i + v_0^k \partial_k W_{-1}^i\right) = -\partial_i P_0 - \nabla_i P_{-2} + \partial_k^2 v_0^i - e_i \widetilde{R}_n \varphi_0 + e_i \widetilde{Ra} T_0 + \varepsilon_{ijk} v_0^j D_k + F_0^i \tag{52}$$

$$\partial_t T_0 + W_{-1}^k \partial_k T_0 + v_0^k \partial_k T_{-1} - v_0^z = \partial_k^2 T_0 + \frac{N_B}{L_e} \left(\partial_k \varphi_{-1} \partial_k T_0 + \partial_k \varphi_0 \partial_k T_{-1} \right) + \tag{53}$$

$$+ \frac{N_B}{L_e} \left(\partial_z T_0 - \partial_z \varphi_0 \right) + \frac{N_A N_B}{L_e} \left(\partial_k T_{-1} \partial_k T_0 + \partial_k T_0 \partial_k T_{-1} \right) - \frac{2 N_A N_B}{L_e} \partial_z T_0$$

$$\partial_t \varphi_0 + W_{-1}^k \partial_k \varphi_0 + v_0^k \partial_k \varphi_{-1} + v_0^z = \frac{1}{L_e} \partial_k^2 \varphi_0 + \frac{N_A}{L_e} \partial_k^2 T_0 \tag{54}$$

$$\partial_i v_0^i = 0 \tag{55}$$

These equations give one secular equation:

$$\nabla P_{-2} = 0 \Rightarrow P_{-2} = const \tag{56}$$

Let us consider the equations of the first approximation R^1:

$$\frac{1}{\text{Pr}} \left(\partial_t v_1^i + W_{-1}^k \partial_k v_1^i + v_0^k \partial_k v_0^i + v_1^k \partial_k W_{-1}^i + W_{-1}^k \nabla_k W_{-1}^i \right) = -\nabla_i P_{-1} - \partial_i \left(P_1 + \overline{P_1} \right) + \partial_k^2 v_1^i +$$

$$+ 2 \partial_k \nabla_k W_{-1}^i - e_i \widetilde{R}_n \varphi_1 + e_i \widetilde{Ra} T_1 + \varepsilon_{ijk} v_1^j D_k \tag{57}$$

$$\partial_t T_1 + W_{-1}^k \partial_k T_1 + W_{-1}^k \nabla_k T_{-1} + v_0^k \partial_k T_0 + v_1^k \partial_k T_{-1} - v_1^z = \partial_k^2 T_1 + 2 \partial_k \nabla_k T_{-1} +$$

$$+ \frac{N_B}{L_e} \left(\partial_k \varphi_{-1} \partial_k T_1 + \partial_k \varphi_{-1} \nabla_k T_{-1} + \partial_k \varphi_0 \partial_k T_0 + \partial_k \varphi_1 \partial_k T_{-1} + \nabla_k \varphi_{-1} \partial_k T_{-1} \right) +$$

$$+ \frac{N_A N_B}{L_e} \left(\partial_k T_{-1} \partial_k T_1 + \partial_k T_{-1} \nabla_k T_{-1} + \partial_k T_0 \partial_k T_0 + \partial_k T_1 \partial_k T_{-1} + \nabla_k T_{-1} \partial_k T_{-1} \right) + \tag{58}$$

$$+ \frac{N_B}{L_e} \left(\partial_z T_1 + \partial_Z T_{-1} - \partial_z \varphi_1 - \partial_Z \varphi_{-1} \right) - \frac{2 N_A N_B}{L_e} \left(\partial_z T_1 + \partial_Z T_{-1} \right)$$

$$\partial_t \varphi_1 + W_{-1}^k \partial_k \varphi_1 + W_{-1}^k \nabla_k \varphi_{-1} + v_0^k \partial_k \varphi_0 + v_1^k \partial_k \varphi_{-1} + v_1^z = \tag{59}$$

$$= \frac{1}{L_e} \left(\partial_k^2 \varphi_1 + 2 \partial_k \nabla_k \varphi_{-1} \right) + \frac{N_A}{L_e} \left(\partial_k^2 T_1 + 2 \partial_k \nabla_k T_{-1} \right)$$

$$\partial_i v_1^i + \nabla_i W_{-1}^i = 0 \tag{60}$$

The secular equations follow from this system of equations:

$$\frac{1}{\text{Pr}} W_{-1}^k \nabla_k W_{-1}^i = -\nabla_i P_{-1}, \quad W_{-1}^k \nabla_k T_{-1} = \frac{N_B}{L_e} \left(\partial_Z T_{-1} - \partial_Z \varphi_{-1} \right) - \frac{2 N_A N_B}{L_e} \partial_Z T_{-1},$$

$$W_{-1}^k \nabla_k \varphi_{-1} = 0, \quad \nabla_i W_{-1}^i = 0 \tag{61}$$

Secular equations (61) satisfy the following field geometry:

$$\vec{W}_{-1} = \left(W_{-1}^x(Z), W_{-1}^y(Z), 0 \right), \ T_{-1} = T_{-1}(Z), \ \varphi_{-1} = \varphi_{-1}(Z), \ P_{-1} = const \tag{62}$$

In the second order R^2, we obtain the equations:

$$\frac{1}{\text{Pr}} \left(\partial_t v_2^i + W_{-1}^k \partial_k v_2^i + v_0^k \partial_k v_1^i + W_{-1}^k \nabla_k v_0^i + v_0^k \nabla_k W_{-1}^i + v_1^k \partial_k v_0^i + v_2^k \partial_k W_{-1}^i \right) =$$

$$= -\partial_i P_2 - \nabla_i P_0 + \partial_k^2 v_2^i + 2\partial_k \nabla_k v_0^i - e_i \widetilde{R}_n \varphi_2 + e_i \widetilde{Ra} T_2 + \varepsilon_{ijk} v_2^j D_k \tag{63}$$

$$\partial_t T_2 + W_{-1}^k \partial_k T_2 + W_{-1}^k \nabla_k T_0 + v_0^k \partial_k T_1 + v_0^k \nabla_k T_{-1} + v_1^k \partial_k T_0 + v_2^k \partial_k T_{-1} - v_2^z =$$

$$= \partial_k^2 T_2 + 2\partial_k \nabla_k T_0 + \tag{64}$$

$$+ \frac{N_B}{L_e}(\partial_k \varphi_{-1} \partial_k T_2 + \partial_k \varphi_{-1} \nabla_k T_0 + \partial_k \varphi_0 \partial_k T_1 + \partial_k \varphi_0 \nabla_k T_{-1} + \partial_k \varphi_1 \partial_k T_0 +$$

$$+ \partial_k \varphi_2 \partial_k T_{-1} + \nabla_k \varphi_{-1} \partial_k T_0 + \nabla_k \varphi_0 \partial_k T_{-1}) +$$

$$+ \frac{N_A N_B}{L_e}(\partial_k T_{-1} \partial_k T_2 + \partial_k T_{-1} \nabla_k T_0 + \partial_k T_0 \partial_k T_1 + \partial_k T_0 \nabla_k T_{-1} + \partial_k T_1 \partial_k T_0 +$$

$$+ \partial_k T_2 \partial_k T_{-1} + \nabla_k T_{-1} \partial_k T_0 + \nabla_k T_0 \partial_k T_{-1}) +$$

$$+ \frac{N_B}{L_e}(\partial_z T_2 + \partial_Z T_0 - \partial_z \varphi_2 - \partial_Z \varphi_0) - \frac{2N_A N_B}{L_e}(\partial_z T_2 + \partial_Z T_0)$$

$$\partial_t \varphi_2 + W_{-1}^k \partial_k \varphi_2 + W_{-1}^k \nabla_k \varphi_0 + v_0^k \partial_k \varphi_1 + v_0^k \nabla_k \varphi_{-1} + v_1^k \partial_k \varphi_0 + v_2^k \partial_k \varphi_{-1} + v_2^z = \tag{65}$$

$$= \frac{1}{L_e}\left(\partial_k^2 \varphi_2 + 2\partial_k \nabla_k \varphi_0\right) + \frac{N_A}{L_e}\left(\partial_k^2 T_2 + 2\partial_k \nabla_k T_0\right)$$

$$\partial_i v_2^i + \nabla_i v_0^i = 0 \tag{66}$$

After averaging the system of equations (63)-(66) over the fast variables, it can be seen that there are no secular terms in the order R^2. Finally, we come to the most important order R^3. In this order, the equations are following

$$\frac{1}{\Pr}\left(\partial_t v_3^i + \partial_T W_{-1}^i + W_{-1}^k \partial_k v_3^i + v_0^k \partial_k v_2^i + W_{-1}^k \nabla_k v_1^i + v_0^k \nabla_k v_0^i + v_1^k \partial_k v_1^i + v_1^k \nabla_k W_{-1}^i +\right.$$

$$\left. + v_2^k \partial_k v_0^i + v_3^k \partial_k W_{-1}^i \right) = -\partial_i P_3 - \nabla_i \left(P_1 + \overline{P}_1\right) + \partial_k^2 v_3^i + 2\partial_k \nabla_k v_1^i + \Delta W_{-1}^i -$$

$$- e_i \widetilde{R}_n \varphi_3 + e_i \widetilde{Ra} T_3 + \varepsilon_{ijk} v_3^j D_k \tag{67}$$

$$\partial_t T_3 + \partial_T T_{-1} + W_{-1}^k \partial_k T_3 + W_{-1}^k \nabla_k T_1 + v_0^k \partial_k T_2 + v_0^k \nabla_k T_0 + v_1^k \nabla_k T_1 +$$

$$+ v_1^k \nabla_k T_{-1} + v_2^k \partial_k T_0 + v_3^k \partial_k T_{-1} - v_3^z = \partial_k^2 T_3 + 2\partial_k \nabla_k T_1 + \Delta T_{-1} +$$

$$+ \frac{N_B}{L_e}(\partial_k \varphi_{-1} \partial_k T_3 + \partial_k \varphi_{-1} \nabla_k T_1 + \partial_k \varphi_0 \partial_k T_2 + \partial_k \varphi_0 \nabla_k T_0 + \partial_k \varphi_1 \partial_k T_1 + \partial_k \varphi_1 \nabla_k T_{-1} +$$

$$+ \partial_k \varphi_2 \partial_k T_0 + \partial_k \varphi_3 \partial_k T_{-1} + \nabla_k \varphi_{-1} \partial_k T_1 + \nabla_k \varphi_{-1} \nabla_k T_{-1} + \nabla_k \varphi_0 \partial_k T_0 + \nabla_k \varphi_1 \partial_k T_{-1}) +$$

$$+ \frac{N_A N_B}{L_e}(\partial_k T_{-1} \partial_k T_3 + \partial_k T_{-1} \nabla_k T_1 + \partial_k T_0 \partial_k T_2 + \partial_k T_0 \nabla_k T_0 + \partial_k T_1 \partial_k T_1 + \partial_k T_1 \nabla_k T_{-1} + \tag{68}$$

$$+ \partial_k T_2 \partial_k T_0 + \partial_k T_3 \partial_k T_{-1} + \nabla_k T_{-1} \partial_k T_1 + \nabla_k T_{-1} \nabla_k T_{-1} + \nabla_k T_0 \partial_k T_0 + \nabla_k T_1 \partial_k T_{-1}) +$$

$$+ \frac{N_B}{L_e}(\partial_z T_3 + \partial_Z T_1 - \partial_z \varphi_3 - \partial_Z \varphi_1) - \frac{2N_A N_B}{L_e}(\partial_z T_3 + \partial_Z T_1)$$

$$\partial_t \varphi_3 + \partial_T \varphi_{-1} + W_{-1}^k \partial_k \varphi_3 + W_{-1}^k \nabla_k \varphi_1 + v_0^k \partial_k \varphi_2 + v_0^k \nabla_k \varphi_0 + v_1^k \partial_k \varphi_1 + v_1^k \nabla_k \varphi_{-1} + v_2^k \partial_k \varphi_0 +$$

$$+ v_3^k \partial_k \varphi_{-1} + v_3^z = \frac{1}{L_e}\left(\partial_k^2 \varphi_3 + 2\partial_k \nabla_k \varphi_1 + \Delta\varphi_{-1}\right) + \frac{N_A}{L_e}\left(\partial_k^2 T_3 + 2\partial_k \nabla_k T_1 + \Delta T_{-1}\right) \qquad (69)$$

$$\partial_i v_3^i + \nabla_i v_1^i = 0 \qquad (70)$$

Averaging the system of equations (67)-(70) over the fast variables, we will obtain the basic secular equations that describe the evolution of large-scale perturbations:

$$\frac{1}{\mathrm{Pr}}\left(\partial_T W_{-1}^i + \nabla_k \left(\overline{v_0^k v_0^i}\right)\right) = -\nabla_i \overline{P}_1 + \Delta W_{-1}^i \qquad (71)$$

$$\partial_T T_{-1} + \nabla_k \left(\overline{v_0^k T_0}\right) = \Delta T_{-1} + \frac{N_B}{L_e}\left(\overline{\nabla_k \varphi_{-1} \nabla_k T_{-1}}\right) + \frac{N_A N_B}{L_e}\left(\overline{\nabla_k T_{-1} \nabla_k T_{-1}}\right) \qquad (72)$$

$$\partial_T \varphi_{-1} + \nabla_k \left(\overline{v_0^k \varphi_0}\right) = \frac{1}{L_e}\Delta\varphi_{-1} + \frac{N_A}{L_e}\Delta T_{-1} \qquad (73)$$

B. SMALL-SCALE FIELDS IN THE ZERO ORDER IN R

Let us consider Eqs. (52)-(55) for the zeroth order in R derived in **Appendix A**. By introducing the notation for the operators

$$\widehat{D}_W = \mathrm{Pr}^{-1}\left(\partial_t + W_{-1}^k \partial_k\right) - \partial^2, \quad \widehat{D}_T = \partial_t + W_{-1}^k \partial_k - \partial^2 - \frac{N_B}{L_e}\partial_z + \frac{2N_A N_B}{L_e}\partial_z,$$

$$\widehat{D}_\varphi = \partial_t + W_{-1}^k \partial_k - L_e^{-1}\partial^2,$$

we can write the system of equations (52)-(55) as

$$\widehat{D}_W v_0^i = -\partial_i P_0 - e_i \widetilde{R}_n \varphi_0 + e_i \widetilde{Ra} T_0 + \varepsilon_{ijk} v_0^j D_k + F_0^i \qquad (74)$$

$$\widehat{D}_T T_0 = v_0^z - \frac{N_B}{L_e}\partial_z \varphi_0 \qquad (75)$$

$$\widehat{D}_\varphi \varphi_0 = -v_0^z + \frac{N_A}{L_e}\partial^2 T_0 \qquad (76)$$

$$\partial_i v_0^i = 0 \qquad (77)$$

Small-scale oscillations of temperature and volume fraction of nanoparticles are easily found from the equations (75)-(76):

$$T_0 = \frac{\widehat{D}_\varphi + \dfrac{N_B}{L_e}\partial_z}{\widehat{L}} v_0^z, \quad \varphi_0 = -\frac{\widehat{D}_T - \dfrac{N_A}{L_e}\partial^2}{\widehat{L}} v_0^z, \quad \widehat{L} = \widehat{D}_\varphi \widehat{D}_T + \frac{N_A N_B}{L_e^2}\partial_z \partial^2 \qquad (78)$$

Let us substitute (78) in (74) and using the condition of solenoidality of the fields $\vec{v}_0$ and $\vec{F}_0$, we obtain the pressure P_0:

$$P_0 = \widehat{P}_1 u_0 + \widehat{P}_2 v_0 + \widehat{P}_3 w_0 \qquad (79)$$

Where we introduce the designations for operators

$$\widehat{P}_1 = \frac{D_2\partial_z - D_3\partial_y}{\partial^2}, \quad \widehat{P}_2 = \frac{D_3\partial_x - D_1\partial_z}{\partial^2},$$

$$\widehat{P}_3 = \frac{D_1\partial_y - D_2\partial_x}{\partial^2} + \widetilde{R}_n \cdot \frac{\partial_z\left(\widehat{D}_T - \dfrac{N_A}{L_e}\partial^2\right)}{\partial^2\,\widehat{L}} + \widetilde{Ra} \cdot \frac{\partial_z\left(\widehat{D}_\varphi + \dfrac{N_B}{L_e}\partial_z\right)}{\partial^2\,\widehat{L}}$$

and velocities: $v_0^x = u_0$, $v_0^y = v_0$, $v_0^z = w_0$. Using the formula (79), we can eliminate the pressure from the equation (74), and, as the result, we obtained a system of equations for finding the zero-order velocity field:

$$\begin{cases} \widehat{d}_{11}u_0 + \widehat{d}_{12}v_0 + \widehat{d}_{13}w_0 = \widehat{F}_0^x \\ \widehat{d}_{21}u_0 + \widehat{d}_{22}v_0 + \widehat{d}_{23}w_0 = F_0^y \\ \widehat{d}_{31}u_0 + \widehat{d}_{32}v_0 + \widehat{d}_{33}w_0 = 0 \end{cases} \qquad (80)$$

The components of the tensor $\widehat{d}_{ij}$ are

$$\widehat{d}_{11} = \widehat{D}_W + \frac{D_2\partial_x\partial_z - D_3\partial_x\partial_y}{\partial^2}, \quad \widehat{d}_{12} = \frac{D_3\partial_x^2 - D_1\partial_x\partial_z}{\partial^2} - D_3,$$

$$\widehat{d}_{13} = D_2 + \frac{D_1\partial_x\partial_y - D_2\partial_x^2}{\partial^2} + \widetilde{R}_n \cdot \frac{\partial_x\partial_z\left(\widehat{D}_T - \dfrac{N_A}{L_e}\partial^2\right)}{\partial^2\,\widehat{L}} + \widetilde{Ra} \cdot \frac{\partial_x\partial_z\left(\widehat{D}_\varphi + \dfrac{N_B}{L_e}\partial_z\right)}{\partial^2\,\widehat{L}},$$

$$\widehat{d}_{21} = D_3 + \frac{D_2\partial_y\partial_z - D_3\partial_y^2}{\partial^2}, \quad \widehat{d}_{22} = \widehat{D}_W + \frac{D_3\partial_y\partial_x - D_1\partial_y\partial_z}{\partial^2},$$

$$\widehat{d}_{23} = \widetilde{R}_n \cdot \frac{\partial_y\partial_z\left(\widehat{D}_T - \dfrac{N_A}{L_e}\partial^2\right)}{\partial^2\,\widehat{L}} + \widetilde{Ra} \cdot \frac{\partial_y\partial_z\left(\widehat{D}_\varphi + \dfrac{N_B}{L_e}\partial_z\right)}{\partial^2\,\widehat{L}} + \frac{D_1\partial_y^2 - D_2\partial_y\partial_x}{\partial^2} - D_1,$$

$$\widehat{d}_{31} = \frac{D_2\partial_z^2 - D_3\partial_z\partial_y}{\partial^2} - D_2, \quad \widehat{d}_{32} = \frac{D_3\partial_z\partial_x - D_1\partial_z^2}{\partial^2} + D_1,$$

$$\widehat{d}_{33} = \widehat{D}_W + \frac{D_1\partial_z\partial_y - D_2\partial_z\partial_x}{\partial^2} +$$

$$+\widetilde{R}_n\frac{\partial_z^2\left(\widehat{D}_T - \dfrac{N_A}{L_e}\partial^2\right)}{\partial^2\,\widehat{L}} + \widetilde{Ra} \cdot \frac{\partial_z^2\left(\widehat{D}_\varphi + \dfrac{N_B}{L_e}\partial_z\right)}{\partial^2\,\widehat{L}} - \widetilde{R}_n \cdot \frac{\left(\widehat{D}_T - \dfrac{N_A}{L_e}\partial^2\right)}{\widehat{L}} - \widetilde{Ra} \cdot \frac{\left(\widehat{D}_\varphi + \dfrac{N_B}{L_e}\partial_z\right)}{\widehat{L}}.$$

As it is known, the solution of the system of equations (80) is found by Cramer's rule:

$$u_0 = \frac{1}{\Delta}\left\{\left(\widehat{d}_{22}\widehat{d}_{33} - \widehat{d}_{32}\widehat{d}_{23}\right)F_0^x + \left(\widehat{d}_{13}\widehat{d}_{32} - \widehat{d}_{12}\widehat{d}_{33}\right)F_0^y\right\} \qquad (81)$$

$$v_0 = \frac{1}{\Delta}\left\{\left(\widehat{d}_{23}\widehat{d}_{31} - \widehat{d}_{21}\widehat{d}_{33}\right)F_0^x + \left(\widehat{d}_{11}\widehat{d}_{33} - \widehat{d}_{13}\widehat{d}_{31}\right)F_0^y\right\} \qquad (82)$$

$$w_0 = \frac{1}{\Delta}\left\{\left(\widehat{d}_{21}\widehat{d}_{32} - \widehat{d}_{22}\widehat{d}_{31}\right)F_0^x + \left(\widehat{d}_{12}\widehat{d}_{31} - \widehat{d}_{11}\widehat{d}_{32}\right)F_0^y\right\} \qquad (83)$$

Here, Δ is the determinant of the system of equations (80), which in an expanded form is

$$\Delta = \widehat{d}_{11}\widehat{d}_{22}\widehat{d}_{33} + \widehat{d}_{21}\widehat{d}_{32}\widehat{d}_{13} + \widehat{d}_{12}\widehat{d}_{23}\widehat{d}_{31} - \widehat{d}_{13}\widehat{d}_{22}\widehat{d}_{31} - \widehat{d}_{32}\widehat{d}_{23}\widehat{d}_{11} - \widehat{d}_{21}\widehat{d}_{12}\widehat{d}_{33} \qquad (84)$$

Let us write the external force $\vec{F}_0$ in the complex form

$$\vec{F}_0 = \vec{i}\,\frac{f_0}{2}\,e^{i\varphi_2} + \vec{j}\,\frac{f_0}{2}\,e^{i\varphi_1} + c.c. \tag{85}$$

Then all operators in formulae (81)-(84) act from the left on their eigenfunction:

$$\widehat{D}_{W,T,\varphi}\,e^{i\varphi_1} = e^{i\varphi_1}\,\widehat{D}_{W,T,\varphi}(\vec{k}_0,-\omega_0) = e^{i\varphi_1}\,\widehat{D}^*_{W_1,T_1,\varphi_1},\quad \widehat{D}_{W,T,\varphi}\,e^{i\varphi_2} = e^{i\varphi_2}\,\widehat{D}_{W,T,\varphi}(\vec{k}_0,-\omega_0) = e^{i\varphi_2}\,\widehat{D}^*_{W_2,T_2,\varphi_2},$$

$$\Delta e^{i\varphi_1} = e^{i\varphi_1}\Delta(\vec{k}_0,-\omega_0) = e^{i\varphi_1}\Delta^*_1,\quad \Delta e^{i\varphi_2} = e^{i\varphi_2}\Delta(\vec{k}_0,-\omega_0) = e^{i\varphi_2}\Delta^*_2, \tag{86}$$

where the new notation is introduced

$$\widehat{D}^*_{W_1} = k_0^2 - i\,\mathrm{Pr}^{-1}(\omega_0 - k_0 W_1),\quad \widehat{D}^*_{W_2} = k_0^2 - i\,\mathrm{Pr}^{-1}(\omega_0 - k_0 W_2),\quad W_1 = W^x_{-1},\quad W_2 = W^y_{-1},$$

$$\widehat{D}^*_{T_1} = k_0^2 - i(\omega_0 - k_0 W_1),\quad \widehat{D}^*_{T_2} = k_0^2 - i(\omega_0 - k_0 W_2),$$

$$\widehat{D}^*_{\varphi_1} = L_e^{-1}k_0^2 - i(\omega_0 - k_0 W_1),\quad \widehat{D}^*_{\varphi_2} = L_e^{-1}k_0^2 - i(\omega_0 - k_0 W_2).$$

$$\Delta^*_1 = \widehat{D}^*_{W_1}\left(\widehat{D}^*_{W_1}\widehat{A}^*_1 + D_1^2\right),\quad \Delta^*_2 = \widehat{D}^*_{W_2}\left(\widehat{D}^*_{W_2}\widehat{A}^*_2 + D_2^2\right),$$

$$\widehat{A}^*_{1,2} = \widehat{D}^*_{W_{1,2}} - \widetilde{R}_n \cdot \frac{\widehat{D}^*_{T_{1,2}} + \dfrac{N_A}{L_e}k_0^2}{\widehat{L}_{1,2}} - \frac{\widetilde{Ra}}{\widehat{D}^*_{T_{1,2}}}$$

Here and below, we denote the complex-conjugate quantities by an asterisk. When performing the subsequent calculations, some of the components in the tensors $\widehat{d}_{ij}$ become zero. Taking this fact into account, velocity fields of the zero approximation has the following form:

$$u_0 = \frac{f_0}{2}\,\frac{\widehat{A}^*_2}{\widehat{A}^*_2\widehat{D}^*_{W_2} + D_2^2}\,e^{i\varphi_2} + c.c. = u_{03} + u_{04} \tag{87}$$

$$v_0 = \frac{f_0}{2}\,\frac{\widehat{D}^*_1}{\widehat{A}^*_1\widehat{D}^*_{W_1} + D_1^2}\,e^{i\varphi_1} + c.c. = v_{01} + v_{02} \tag{88}$$

$$w_0 = -\frac{f_0}{2}\,\frac{D_1}{\widehat{A}^*_1\widehat{D}^*_{W_1} + D_1^2}\,e^{i\varphi_1} + \frac{f_0}{2}\,\frac{D_2}{\widehat{A}^*_2\widehat{D}^*_{W_2} + D_2^2}\,e^{i\varphi_2} + c.c. = w_{01} + w_{02} + w_{03} + w_{04} \tag{89}$$

It is easy to see that the component of the rotation parameter D_3 also drops out.

C. CALCULATION OF THE REYNOLDS STRESSES

To close the system of equations (31)-(32) that describe the evolution of the large-scale velocity fields $\vec{W}_{-1}$, it is necessary to calculate the following correlators:

$$T^{31} = \overline{w_0 u_0} = \overline{w_{01}\left(u_{01}\right)^*} + \overline{\left(w_{01}\right)^* u_{01}} + \overline{w_{03}\left(u_{03}\right)^*} + \overline{\left(w_{03}\right)^* u_{03}} \tag{90}$$

$$T^{32} = \overline{w_0 v_0} = \overline{w_{01}\left(v_{01}\right)^*} + \overline{\left(w_{01}\right)^* v_{01}} + \overline{w_{03}\left(v_{03}\right)^*} + \overline{\left(w_{03}\right)^* v_{03}} \tag{91}$$

Substituting the solutions for the small-scale velocity fields (87)-(89) obtained in **Appendix B**, into the equations (90)-(91), we can find the following expression for the correlators:

$$T^{31} = \frac{f_0^2}{4} \frac{D_2(\widehat{A}_2 + \widehat{A}_2^*)}{\left|\widehat{A}_2 \widehat{D}_{W_2} + D_2^2\right|^2} \tag{92}$$

$$T^{32} = -\frac{f_0^2}{4} \frac{D_1(\widehat{A}_1 + \widehat{A}_1^*)}{\left|\widehat{A}_1 \widehat{D}_{W_1} + D_1^2\right|^2} \tag{93}$$

Then with the definition of the operators $\widehat{D}_{W_{1,2}}$ and $\widehat{A}_{1,2}$, we can write down the series of useful relations for the calculation of T^{31} and T^{32}:

$$\left|\widehat{D}_{W_{1,2}}\right|^2 = \widehat{D}_{W_{1,2}} \widehat{D}_{W_{1,2}}^* = k_0^4 + \Pr^{-2} \widetilde{\omega}_{1,2}^2, \quad \left|\widehat{D}_{T_{1,2}}\right|^2 = \widehat{D}_{T_{1,2}} \widehat{D}_{T_{1,2}}^* = k_0^4 + \widetilde{\omega}_{1,2}^2,$$

$$\left|\widehat{D}_{\varphi_{1,2}}\right|^2 = \widehat{D}_{\varphi_{1,2}} \widehat{D}_{\varphi_{1,2}}^* = L_e^{-2} k_0^4 + \widetilde{\omega}_{1,2}^2, \quad \widetilde{\omega}_{1,2} = \omega_0 - k_0 W_{1,2}$$

$$\left|\widehat{A}_{1,2}\right|^2 = \widehat{A}_{1,2} \widehat{A}_{1,2}^* = k_0^4 + \Pr^{-2} \widetilde{\omega}_{1,2}^2 - 2\widetilde{Ra} \cdot \frac{k_0^4 - \Pr^{-1} \widetilde{\omega}_{1,2}^2}{k_0^4 + \widetilde{\omega}_{1,2}^2} + \frac{\widetilde{Ra}^2}{k_0^4 + \widetilde{\omega}_{1,2}^2} + r_{n_{1,2}},$$

$$r_{n_{1,2}} = -2\widetilde{R}_n \cdot \frac{(k_0^4 + \widetilde{\omega}_{1,2}^2)(L_e^{-1} k_0^4 - \Pr^{-1} \widetilde{\omega}_{1,2}^2) + \frac{N_A}{L_e} k_0^2 (L_e^{-1} k_0^2 - \Pr^{-1} \widetilde{\omega}_{1,2}^2 k_0^2 - \widetilde{\omega}_{1,2}^2 k_0^2 (1 + \Pr^{-1} L_e^{-1}))}{(k_0^4 + \widetilde{\omega}_{1,2}^2)(L_e^{-2} k_0^4 + \widetilde{\omega}_{1,2}^2)} +$$

$$+\widetilde{R}_n^2 \cdot \frac{k_0^4 \left(1 + \frac{2N_A}{L_e} + \frac{N_A^2}{L_e^2}\right) + \widetilde{\omega}_{1,2}^2}{(k_0^4 + \widetilde{\omega}_{1,2}^2)(L_e^{-2} k_0^4 + \widetilde{\omega}_{1,2}^2)} + 2\widetilde{R}_n \widetilde{Ra} \cdot \frac{\widetilde{\omega}_{1,2}^2 + k_0^2 L_e^{-1}\left(1 + \frac{N_A}{L_e}\right)}{(k_0^4 + \widetilde{\omega}_{1,2}^2)(L_e^{-2} k_0^4 + \widetilde{\omega}_{1,2}^2)},$$

$$\widehat{D}_{W_{1,2}} \widehat{A}_{1,2} + \widehat{D}_{W_{1,2}}^* \widehat{A}_{1,2}^* = 2(k_0^4 - \Pr^{-2} \widetilde{\omega}_{1,2}^2) - 2\widetilde{Ra} \cdot \frac{k_0^4 + \Pr^{-1} \widetilde{\omega}_{1,2}^2}{k_0^4 + \widetilde{\omega}_{1,2}^2} -$$

$$-2\widetilde{R}_n \cdot \frac{(k_0^4 + \widetilde{\omega}_{1,2}^2)(L_e^{-1} k_0^4 + \Pr^{-1} \widetilde{\omega}_{1,2}^2) + \frac{N_A}{L_e} k_0^4 (L_e^{-1} k_0^4 + \Pr^{-1} \widetilde{\omega}_{1,2}^2 + \widetilde{\omega}_{1,2}^2 (\Pr^{-1} L_e^{-1} - 1))}{(k_0^4 + \widetilde{\omega}_{1,2}^2)(L_e^{-2} k_0^4 + \widetilde{\omega}_{1,2}^2)}.$$

Using these relations, we can obtain the following expressions:

$$\widehat{A}_{1,2} + \widehat{A}_{1,2}^* = 2\left(k_0^2 - \frac{\widetilde{Ra} k_0^2}{k_0^4 + \widetilde{\omega}_{1,2}^2} - \widetilde{R}_n \cdot \frac{L_e^{-1} k_0^2 + \frac{N_A}{L_e}(L_e^{-1} k_0^4 - \widetilde{\omega}_{1,2}^2)}{L_e^{-2} k_0^4 + \widetilde{\omega}_{1,2}^2} \right),$$

$$\left|\widehat{D}_{W_{1,2}} \widehat{A}_{1,2} + D_{1,2}^2\right|^2 = \tag{94}$$

$$= \left(k_0^4 + \Pr^{-2} \widetilde{\omega}_{1,2}^2\right)\left(k_0^4 + \Pr^{-2} \widetilde{\omega}_{1,2}^2 + \frac{\widetilde{Ra}^2}{k_0^4 + \widetilde{\omega}_{1,2}^2} - 2\widetilde{Ra} \cdot \frac{k_0^4 - \Pr^{-1} \widetilde{\omega}_{1,2}^2}{k_0^4 + \widetilde{\omega}_{1,2}^2} + r_{n_{1,2}} \right) +$$

$$+2D_{1,2}^2\left(k_0^4 - \Pr^{-2} \widetilde{\omega}_{1,2}^2 - \widetilde{Ra} \cdot \frac{k_0^4 + \Pr^{-1} \widetilde{\omega}_{1,2}^2}{k_0^4 + \widetilde{\omega}_{1,2}^2} + p_{n_{1,2}} \right) + D_{1,2}^4,$$

$$p_{n_{1,2}} = -\widetilde{R}_n \cdot \frac{(k_0^4 + \widetilde{\omega}_{1,2}^2)(L_e^{-1} k_0^4 + \Pr^{-1} \widetilde{\omega}_{1,2}^2) + \frac{N_A}{L_e} k_0^4 (L_e^{-1} k_0^4 + \Pr^{-1} \widetilde{\omega}_{1,2}^2 + \widetilde{\omega}_{1,2}^2 (\Pr^{-1} L_e^{-1} - 1))}{(k_0^4 + \widetilde{\omega}_{1,2}^2)(L_e^{-2} k_0^4 + \widetilde{\omega}_{1,2}^2)}.$$

Substituting (94) in (92)-(93) we can find expressions for the Reynolds stresses in the general form:

$$T^{31} = \frac{f_0^2}{2} \frac{D_2 k_0^2 (k_0^4 + \widetilde{\omega}_2^2 - \widetilde{Ra} - l_{n_2})}{(k_0^4 + \widetilde{\omega}_2^2)\Lambda_2}, \qquad (95)$$

$$T^{32} = -\frac{f_0^2}{2} \frac{D_1 k_0^2 (k_0^4 + \widetilde{\omega}_2^2 - \widetilde{Ra} - l_{n_1})}{(k_0^4 + \widetilde{\omega}_1^2)\Lambda_1},$$

where $\Lambda_{1,2} = \left| \widehat{D}_{W_{1,2}} \widehat{A}_{1,2} + D_{1,2}^2 \right|^2$. Expressions for $l_{n_{1,2}}$ are:

$$l_{n_{1,2}} = \widetilde{R}_n \cdot \frac{L_e^{-1} + \dfrac{N_A}{L_e}\left(k_0^2 L_e^{-1} - \dfrac{\widetilde{\omega}_{1,2}^2}{k_0^2} \right)}{L_e^{-2} k_0^4 + \widetilde{\omega}_{1,2}^2} \cdot (k_0^4 + \widetilde{\omega}_{1,2}^2).$$

If the Prandtl number of the nanofluid is approximately equal to one $Pr = 1$, then the expressions for the components of the Reynolds stresses are simplified:

$$T^{31} = \frac{f_0^2 D_2 k_0^2 (k_0^4 + \widetilde{\omega}_2^2 - \widetilde{Ra} - l_{n_2})}{2(k_0^4 + \widetilde{\omega}_2^2)((k_0^4 + \widetilde{\omega}_2^2)^2 + 2(D_2^2 - \widetilde{Ra})(k_0^4 - \widetilde{\omega}_2^2) + (D_2^2 - \widetilde{Ra})^2 + r_{n_2}(k_0^4 + \widetilde{\omega}_2^2) + 2p_{n_2} D_2^2)}, \qquad (96)$$

$$T^{32} = -\frac{f_0^2 D_1 k_0^2 (k_0^4 + \widetilde{\omega}_1^2 - \widetilde{Ra} - l_{n_1})}{2(k_0^4 + \widetilde{\omega}_1^2)((k_0^4 + \widetilde{\omega}_1^2)^2 + 2(D_1^2 - \widetilde{Ra})(k_0^4 - \widetilde{\omega}_1^2) + (D_1^2 - \widetilde{Ra})^2 + r_{n_1}(k_0^4 + \widetilde{\omega}_1^2) + 2p_{n_1} D_1^2)}. \qquad (97)$$

Here the values of the coefficients $r_{n_{1,2}}$ and $p_{n_{1,2}}$ are taken with $Pr = 1$.

ORCID IDs
Michael I. Kopp, https://orcid.org/0000-0001-7457-3272; **Anatoly V. Tur**, https://orcid.org/0000-0002-3889-8130,
Volodymyr V. Yanovsky, https://orcid.org/0000-0003-0461-749X

REFERENCES
[1] S.K. Das, S. U.S Choi, W.Yu, and T. Pradeep, *Nanofluids: science and technology,* (Hoboken, New Jersey, Wiley-Interscience, 2008), pp. 397.
[2] Dhananjay Yadav, G.S. Agrawal, and R. Bhargava, International Journal of Engineering Science, 49, 1171-1184 (2011), https://doi.org/10.1016/j.ijengsci.2011.07.002
[3] Shilpi Agarwal, and B.S. Bhadauria, Continuum Mech. Thermodyn., 26, 437-445 (2014), https://doi.org/10.1007/s00161-013-0309-6
[4] R. Chand, G.C. Rana, and S. K. Kango, FME Transactions, 43, 62-69 (2015), https://scindeks.ceon.rs/article.aspx?artid=1451-20921501062C
[5] B.L. Smorodin, S.M. Ishutov, and B.I. Myznikova, Microgravity Science and Technology, 30, 95-102 (2018), https://doi.org/10.1007/s12217-017-9582-5
[6] M.I. Kopp, A.V. Tur, and V.V. Yanovsky, https://arxiv.org/abs/1706.00223v1
[7] U. Frisch, Z.S. She, and P.L. Sulem, Physica D, **28**, 382-392 (1987), https://doi.org/10.1016/0167-2789(87)90026-1
[8] M.I. Kopp, A.V. Tur, and V.V Yanovsky, Open Journal of Fluid Dynamics, **05**(04), 311-321 (2015), https://doi.org/10.4236/ojfd.2015.54032
[9] G. Rüdiger, Astron. Nachr. **299**(4), 217-222 (1978), https://doi.org/10.1002/asna.19782990408.

ВИХРОВЕ ДИНАМО В СТРАТИФІКОВАНІЙ НАНОРІДИНІ, ЩО ПОХИЛО ОБЕРТАЄТЬСЯ З ДРІБНОМАСШТАБНОЮ НЕСПІРАЛЬНОЮ СИЛОЮ
Михайло Й. Копп[a], Анатолій В. Тур[c], Володимир В. Яновський[a,b]
[a]Інститут монокристалів, Національна Академія Наук України
пр. Науки 60, 61001 Харків, Україна
[b]Харківський національний університет імені В.Н. Каразина
майдан Свободи, 4, 61022, Харків, Україна
[c]Universite Toulouse [UPS], CNRS, Institute of Research for Astrophysics and Planetology
9 avenue du Colonel Roche, BP 44346, 31028 Toulouse Cedex 4, France

В роботі отримана великомасштабна нестійкість гідродинамічного α-ефекту в стратифікованій нанорідині, що похило обертається, з урахуванням ефектів броунівської дифузії і потоку частинок під дією градієнта температури (термофорезу). Нестійкість викликається дією зовнішньої дрібномасштабної неспіральної сили, яка збуджує дрібномасштабні коливання

швидкості з нульовою спіральністю і малим числом Рейнольдса. Нелінійні рівняння для великомасштабних рухів отримані з використанням методу багатомасштабних асимптотичних розкладів за малим параметром (числом Рейнольдса). Досліджена лінійна великомасштабна нестійкість типу гідродинамічного α-ефекту в залежності від параметрів обертання D, температурної стратифікації $\widetilde{Ra}$ і концентрації наночастинок $\widetilde{R}_n$. Отриманий новий ефект генерації великомасштабних вихрових структур в нанорідині при $\widetilde{Ra} = 0$, пов'язаний зі збільшенням концентрації наночастинок. Максимальний інкремент нестійкості досягається при кутах нахилу $\theta \approx \pi / 5$ для чисел Прандтля $\mathrm{Pr} = 5$, а для чисел Прандтля $\mathrm{Pr} = 1$ при кутах нахилу $\theta \approx \pi / 2$. Встановлено, що зміна частоти параметричного впливу дозволить контролювати і відслідковувати процес генерації великомасштабних вихрових структур. Показано, що циркулярно поляризовані вихори Бельтрамі виникають в нанорідині в результаті розвитку нової великомасштабної нестійкості. В роботі досліджується режим насичення великомасштабної нестійкості в стратифікованій нанорідині, що похило обертається з зовнішньою дрібномасштабною неспіральною силою. У стаціонарному режимі була отримана динамічна система рівнянь для великомасштабних збурень поля швидкості. Отримані чисельні рішення цієї системи рівнянь, які показують існування локалізованих вихрових структур у вигляді нелінійних хвиль Бельтрамі і кінків. Профіль швидкості кінка має тенденцію бути постійним при великих значеннях Z.

КЛЮЧОВІ СЛОВА: стратифікована нанорідина, великомасштабна нестійкість, сила Коріоліса, багатомасштабні асимптотичні розкладання, α-эфект, локалізовані вихрові структури

ENERGY ACTIVATION SPECTRUM OF LOW-TEMPERATURE ACOUSTIC RELAXATION IN HIGH-PURITY IRON SINGLE CRYSTAL. SOLUTION OF THE INVERSE PROBLEM OF MECHANICAL SPECTROSCOPY BY THE TIKHONOV REGULARIZATION METHOD

ⓘ**Yuri A. Semerenko**

B. Verkin Institute for Low Temperature Physics and Engineering, National Academy of Sciences of the Ukraine
47 Nauky Ave., 61103, Kharkiv, Ukraine
E-mail: semerenko@ilt.kharkov.ua
Received February 2, 2021; revised April 20, 2021; accepted April 22, 2021

When studying the temperature dependences of the acoustic absorption and the modulus of elasticity, absorption peaks are often observed, which correspond to the characteristic step on the temperature dependence of the modulus of elasticity. Such features are called relaxation resonances. It is believed that the occurrence of such relaxation resonances is due to the presence in the structure of the material of elementary microscopic relaxors that interact with the studied vibrational mode of mechanical vibrations of the sample. In a sufficiently perfect material, such a process is characterized by a relaxation time τ, and in a real defective material by a relaxation time spectrum $P(\tau)$. Most often such relaxation processes have a thermally activated character and the relaxation time $\tau(T)$ is determined by the Arrhenius ratio $\tau(T) = \tau_0 \exp(U_0/kT)$, and the characteristics of the process will be U_0 - activation energy, τ_0 - period of attempts, Δ_0 - characteristic elementary contribution of a single relaxator to the dynamic response of the material and their spectra. In the low temperatures region the statistical distribution of parameters τ_0 and Δ_0 can be neglected with exponential accuracy, and the relaxation contribution to the temperature dependences of absorption and the dynamic elasticity modulus of the material will be determined only by the activation energy spectrum $P(U)$ of microscopic relaxors. The main task of mechanical spectroscopy in the analysis of such relaxation resonances is to determine U_0, τ_0, Δ_0 and $P(U)$. It is shown, that the problem of recovering of spectral function $P(U)$ of acoustic relaxation of a real crystal can be reduced to the solving of the Fredholm integral equation of the first kind with an approximately known right part and concerns to a class of ill-posed problems. The method based on Tikhonov regularizing algorithm for recovering $P(U)$ from experimental temperature dependences of absorption or elasticity module is offered. It is established, that acoustic relaxation in high-purity iron single crystal in the temperature range 5-100 K is characterized by two-modes spectral function $P(U)$ with maxima at 0.037 eV and 0.015 eV, which correspond to the α-peak and its α' satellite.
KEYWORDS: acoustic relaxation, Tikhonov regularization method, energy activation spectrum, acoustic absorption, modulus of elasticity

It was found [1] that the resonant frequency of forced resonant mechanical vibrations of solids is determined by both the geometric characteristics of the sample and its modulus of elasticity M. The amplitude of such resonant oscillations is proportional to the dissipation of the oscillation energy, which is characterized by the logarithmic decrement of oscillations δ. This fact underlies the method of resonant mechanical spectroscopy, which allows you to study the elastic and dissipative properties of various materials. As a rule, the temperature dependences of absorption and elastic modulus are studied. In this case, peaks are often observed on the temperature dependence of absorption, which correspond to a characteristic step on the temperature dependence of the elastic modulus. Such an absorption peak, together with the corresponding step on the temperature dependence of the elastic modulus, is commonly called relaxation resonance. In the microscopic interpretation of such relaxation resonances, it is generally accepted [1] that their appearance is associated with the presence in the bulk of the material of thermally activated elementary microscopic relaxators (for example, a pair of kinks on a dislocation line) interacting with the studied vibrational mode of mechanical vibrations of the sample. The thermal activation of an individual relaxator is characterized by the relaxation time $\tau(T)$, and its dependence on temperature T is described by the exponential Arrhenius expressiona:

$$\tau(T) = \tau_0 \exp\left(\frac{U_0}{kT}\right), \tag{1}$$

where k is the Boltzmann constant, U_0 is the activation energy, τ_0 is the period of attempts.

If the mechanical vibrations of the sample excite a system of relaxators with the same values of the parameters U_0 and τ_0, then in the resonance region in the approximation of a linear response, the temperature dependences of the

elastic and dissipative characteristics of the material have the form of a Debye peak for the vibration decrement $\delta(T,\omega)$ and a "step" for the modulus defect $\Delta M(T,\omega)/M_0$:

$$\delta(T,\omega) = 2C_r\Delta_0 \frac{\omega\tau}{1+\omega^2\tau^2}; \qquad \frac{\Delta M(T,\omega)}{M_0} = \frac{2C_r\Delta_0}{\pi}\frac{1}{1+\omega^2\tau^2} \qquad (2)$$

In a sufficiently perfect material, such a process can be associated with three parameters, the values of which are determined by the energy and geometric parameters of a defect-free crystal: U_0, τ_0 and Δ_0 (Δ_0 is the characteristic elementary contribution of an individual relaxator to the dynamic response of the crystal; C_r is the relative volume concentration of such relaxators interacting with the considered vibrational mode of the sample). And the main task of mechanical spectroscopy in the analysis of such relaxation resonances is reduced to the determination of these parameters.

In a real material, due to the presence of various defects and randomly distributed structural distortions they create, there is a statistical scatter of parameters U_0, τ_0 and Δ_0. It is known [2] that the decrement of vibrations $\bar{\delta}(T,\omega)$ and the defect of the elastic modulus $\Delta\bar{M}(T,\omega)/M_0$ of a real material with defects in the low-temperature region $kT \ll U_0$ are determined by the statistical averaging of Debye expressions (2) over the entire spectrum of activation energies U of local structural rearrangements (relaxators), characterized by a statistical distribution function $P(U)$, with a statistical spread of parameters τ_0 and Δ_0 with an exponential accuracy is negligible:

$$\bar{\delta}(T,\omega) = 2C_r\Delta_0 \int_0^\infty \frac{\omega\tau(T,U)}{1+\omega^2\tau^2(T,U)} P(U)dU ,$$

$$\frac{\Delta\bar{M}(T,\omega)}{M_0} = \frac{2C_r\Delta_0}{\pi} \int_0^\infty \frac{P(U)}{1+\omega^2\tau^2(T,U)} dU \qquad (3)$$

where $\tau(T,U) = \tau_0 \exp\left(\dfrac{U}{kT}\right)$.

In [3], it was suggested that the energy spectrum of low-temperature acoustic relaxation in iron can be described by the quasi-Gaussian distribution function

$$P^G(U) = \frac{U}{\sqrt{2\pi}DU_0} \exp\left[-\frac{(U-U_0)^2}{2D^2}\right] , \qquad (4)$$

with two parameters – the seed value of the activation energy U_0 corresponding to relaxation in an ideal defect-free crystal and its dispersion D^2. Under this assumption, it was possible to achieve a good description of the experimental temperature spectra δ and $\Delta M/M_0$ in the region of the α-peak ($U_0 = 0.037$ eV, $\tau_0 = 2.4\cdot10^{-11}$ s), observed at a temperature of ≈ 54 K (vibration frequency ≈ 88 kHz), by theoretical dependences (3) (Fig. 1).
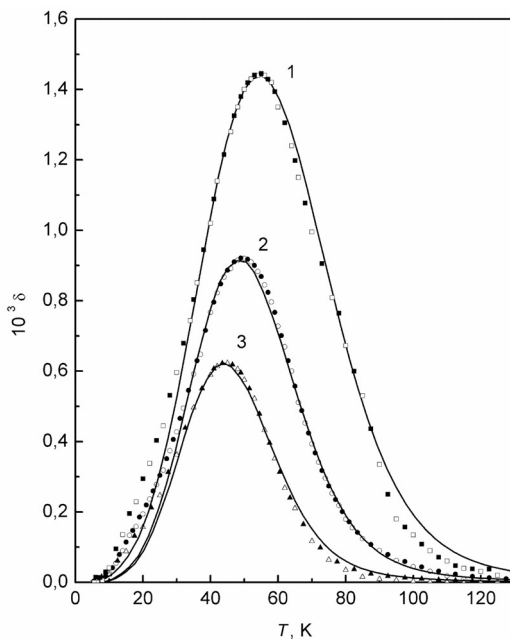
Figure 1. Temperature dependences of the vibration decrement in a single-crystal sample of high-purity iron with orientation <731> in various structural states:

1 – specimen deformed at $T = 300$ K to a residual plastic deformation of 3%, measurements were carried out immediately after deformation; 2 – the same sample, annealed at $T = 300$ K for 3 days; 3 – the same sample, annealed at $T = 300$ K for 11 years.

open symbols – experimental data [3]; ***shaded symbols*** - theoretical dependences calculated by formula (3) for the spectral function $P^T(U)$ that was found by the Tikhonov regularization method; ***solid lines*** – theoretical dependences calculated by formula (3) for the spectral function $P^G(U)$ (quasi-Gaussian distribution function of activation energy values given by expression (4) with an appropriate choice of values of distribution parameters).

However, in the temperature range $\approx 15\,\mathrm{K}$, some discrepancy between the experimental and theoretical dependences was observed. A thorough analysis of a large amount of experimental data obtained by various authors, carried out in [4], showed that this discrepancy is probably associated with the presence of a weakly expressed α'-peak, which is more clearly manifested under other experimental conditions.

It seems advisable to solve the inverse problem - to restore $P(U)$ from experimental dependences δ, $\Delta M/M_0$ and compare it with the "guessed" expression $P^G(U)$. This formulation of the problem belongs to the so-called inverse problems. The solution of inverse problems of mechanical spectroscopy has been repeatedly considered by various authors both from a theoretical and practical point of view [5], [6].

RESTORATION OF THE ACTIVATION ENERGY SPECTRUM
BY THE TIKHONOV REGULARIZATION METHOD

Following the approach proposed in [7], we consider the problem of determining the energy spectrum of acoustic relaxation in a material with defects from the known temperature spectrum of the vibration decrement $\bar{\delta}(T,\omega)$ or defect of elastic modulus $\Delta \bar{M}(T,\omega)/M_0$.

Practically without limiting the generality of further consideration, one can replace in expressions (3) the infinite upper limit of integration by some value $U_{\max}$ corresponding to the upper limit of the spectrum, then the problem of finding the spectral function $P(U)$, from a known experimental spectrum $\bar{\delta}(T,\omega)$ or $\Delta \bar{M}(T,\omega)/M_0$ at a fixed frequency $\omega = const$, is reduced to solving the Fredholm integral equation of the first kind with respect to $P(U)$:

$$\int_{U_{\min}}^{U_{\max}} K^{d,m}(T,U)P(U)dU = Z^{d,m}(T) \quad \text{or in operator form} \quad Ap = z, \tag{5}$$

where the kernel of the integral operator in the case of a decrement of vibrations and a defect of the modulus of elasticity, respectively, is

$$K^d(T,U) = 2C_r\Delta_0 \frac{\omega\tau_0 \exp\left(\dfrac{U}{kT}\right)}{1+\omega^2\tau_0^2 \exp\left(\dfrac{2U}{kT}\right)} \quad \text{and} \quad K^m(T,U) = \frac{2C_r\Delta_0}{\pi}\frac{1}{1+\omega^2\tau_0^2 \exp\left(\dfrac{2U}{kT}\right)},$$

the experimental spectrum $Z^d(T) = \bar{\delta}(T)$ and $Z^m(T) = \dfrac{\Delta \bar{M}(T)}{M_0}$.

Let, for some right-hand side $\hat{Z}^{d,m}(T)$, the function $\hat{P}(U)$ be a solution to equation (5). However, since instead of the function $\hat{Z}^{d,m}(T)$ we know only its experimental approximation $Z^{d,m}(T)$, which differs little from $\hat{Z}^{d,m}(T)$, then we can only talk about finding an approximate to the $\hat{P}(U)$ "solution" $P(U)$ of equation (5). The solution to such a problem is associated with significant difficulties caused by the lack of stability of the solution to small changes in the right-hand side. This instability is connected with the fact that if instead of the exact right-hand side $\hat{Z}^{d,m}(T)$ of Eq. (5) we know only a certain approximation $Z^{d,m}(T)$ of it and a number $\upsilon > 0$ characterizing the accuracy of the experimental data such that the deviation

$$\rho_Z(\hat{Z},Z) \le \upsilon^2, \tag{6}$$

then, as possible approximate solutions, it is natural to take functions $P(U)$ for which

$$\rho_Z(Ap,Z) \le \upsilon^2, \tag{7}$$

where

$$\rho_Z(Z_1,Z_2) = \int_{T_{\min}}^{T_{\max}} \{Z_1(T) - Z_2(T)\}^2 \, dT. \tag{8}$$

However, there are infinitely many functions $P(U)$ satisfying this condition, and among them there are functions that differ as much as you like. Consequently, under these conditions, the problem of solving the integral equation (5) is underdetermined and unstable to small changes in the right-hand side. Therefore, it is impossible to take the exact solution of this equation (with an approximate right-hand side) as an approximate solution to equation (5). To find an

approximate solution $P^\alpha(U)$ to equation (5) that satisfies the natural requirements that are embedded in the meaning of an approximate solution by the physical determinism of the phenomenon described by this equation and the possibility of physical interpretation of the solution, namely the conditions

$$P^\alpha(U) \to \hat{P}(U) \text{ at } \upsilon \to 0, \tag{9}$$

it is necessary from the entire set of formal solutions $P(U)$ that satisfy condition (7) to select a function $P^\alpha(U)$ that satisfies condition (9). This can be done if there is additional information, at least of a qualitative nature, regarding the desired solution. We will assume that the desired spectrum $P^\alpha(U)$ does not have a fine structure, i.e. we can assume that the solution to the problem under consideration is a smooth function. As a measure of smoothness, consider the quantity

$$\Omega[P] = \int_{U_{\min}}^{U_{\max}} \left\{ \xi(U) \cdot P^2(U) + \chi(U) \cdot \left(\frac{dP(U)}{dU} \right)^2 \right\} dU, \tag{10}$$

where $\xi(U)$ and $\chi(U)$ are given non-negative continuous functions satisfying the condition $\xi^2(U) + \chi^2(U) \neq 0$ for any $U \in (U_{\min}, U_{\max})$. This definition of smoothness is consistent with the visual representation of the smoothness of the graphs of functions.

Following [7], as the required spectrum $P^\alpha(U)$, we will choose from the family of approximate solutions $P(U)$ a function with the greatest smoothness (minimum fine structure). Mathematically, this problem is reduced to finding such a function $P^\alpha(U)$ that will achieve the minimum of the functional (10). The solution of such a problem for a conditional extremum is reduced to a problem for an unconditional extremum of a functional

$$M_\alpha[P,Z] = \int_{T_{\min}}^{T_{\max}} \left\{ \int_{U_{\min}}^{U_{\max}} K(T,U) P(U) dU - Z(T) \right\}^2 dT + \alpha \Omega[P], \tag{11}$$

where $\alpha > 0$ is the regularization parameter, which can be determined by a given accuracy υ and, therefore, depends on υ, i.e. $\alpha = \alpha(\upsilon)$. It can be shown [7] that $\alpha(\upsilon)$ is the function that convex downward, besides there is an estimate

$$\alpha \leq \frac{\upsilon \|A\|^2}{\|z\| - \upsilon}. \tag{12}$$

The solution to the minimum problem for functional (11) is called a regularized (approximate) solution $P^\alpha(U)$ to equation (5) and can be found from the Euler equation for the functional M_α:

$$\alpha \left\{ \xi(U) \cdot P(U) - \frac{d}{dU}\left[\chi(U) \cdot \frac{dP(U)}{dU} \right] \right\} + \int_{U_{\min}}^{U_{\max}} \bar{K}(U,t) P(t) dt = g(U), \tag{13}$$

with boundary conditions

$$\frac{dP}{dU}(U_{\min}) = 0, \qquad \frac{dP}{dU}(U_{\max}) = 0, \tag{14}$$

where $\bar{K}(U,t) = \int_{T_{\min}}^{T_{\max}} K(T,U) \cdot K(T,t) dT$, a $g(U) = \int_{T_{\min}}^{T_{\max}} K(T,U) \cdot Z(T) dT$.

Another difficulty lies in the fact that the right-hand side of (5) in our problem is the result of an experiment, i.e. known on the grid by $T : \{T_1, \cdots, T_N\}$. With this right-hand side, equation (5) has no solution at all, understood in the classical sense, i.e. determined by the formula $p = A^{-1}z$ (A^{-1} is the operator inverse to the operator A) in equation (5) since the kernel $K^{d,m}(T,U)$ has a continuous derivative with respect to T and, therefore, the right-hand side must also have a continuous derivative with respect to T. This means that in this formulation of the problem, the exact solution $\hat{P}(U)$ of this equation with an approximately known right-hand side $Z^{d,m}(T) \neq \hat{Z}^{d,m}(T)$ cannot be taken as an

approximate to $P(U)$ solution of equation (5), since such a solution may not exist. In this regard, it becomes necessary to pass from the continuous initial problem of finding regularized approximate solutions (5) to its discrete analogue. This transition is carried out by discretizing the boundary value problem for the Euler equation by solving the resulting SLAE [7]. Following the variational approach, we take a discrete analogue of stabilizer (10) and form an analogue of the smoothing functional (11). Then we turn to his Euler equation (13), which will represent the regularized SLAE. The solution to this system (with an appropriately selected regularization parameter) will be an approximate solution to the original problem.

For simplicity of further consideration, we will accept $\xi(U) \equiv \xi$ and $\chi(U) \equiv \chi$ (ξ and χ are positive numbers). Then the difference analogue of Eq. (13) on a uniform grid of N nodes by U in increments of $\Delta U = \dfrac{U_{\max} - U_{\min}}{N-1}$ will have the following form:

$$\sum_{j=2}^{N-1} \overline{K}_{ij} \cdot P_j \cdot \Delta U + \frac{\overline{K}_{i1} \cdot P_1 + \overline{K}_{iN} \cdot P_N}{2} \Delta U + \alpha\xi \cdot P_i + a\chi \frac{2P_i - P_{i-1} - P_{i+1}}{(\Delta U)^2} = g_i, \quad i = 1, \cdots, N, \tag{15}$$

where $U_i = U_{\min} + (i-1) \cdot \Delta U$, $P_i = P(U_i)$, $g_i = g(U_i)$, $\overline{K}_{ij} = \overline{K}(U_i, T_j)$. In this expression the integral is replaced by the corresponding integral sum by the trapezoidal formula, and $\dfrac{d^2 P(U)}{dU^2}$ by the corresponding difference relation.

For simplicity, we will assume that the number of grid nodes by T is also N, and the step $\Delta T = \dfrac{T_{\max} - T_{\min}}{N-1}$. Then $T_j = T_{\min} + (j-1) \cdot \Delta T$ and the values $\overline{K}_{ij}$ and g_i can also be calculated using the trapezoidal formula:

$$\overline{K}_{ij} = \sum_{m=2}^{N-1} K_{mi} \cdot K_{mj} \cdot \Delta T + \frac{K_{1i} \cdot K_{1j} + K_{Ni} \cdot K_{Nj}}{2} \Delta T \quad \text{and} \quad g_i = \sum_{j=2}^{N-1} K_{ji} \cdot Z_j \cdot \Delta T + \frac{K_{1i} \cdot Z_1 + K_{Ni} \cdot Z_N}{2},$$

where $Z_j = Z(T_j)$ and $K_{ji} = K(T_j, U_i)$.

For $i = 1$ and $i = N$, (15) contains unknown values of P_0 and P_{N+1}. To satisfy the boundary conditions (14), we put $P_0 = P_1$ and $P_{N+1} = P_N$.

System (15) can be written in matrix form with respect to the vector $P = (P_1, \cdots P_N)$:

$$B \cdot P + \alpha C \cdot P = g, \tag{16}$$

where the vector $g = (g_1, \cdots, g_N)$, the matrix B has the form:

$$B = \begin{bmatrix} \dfrac{\overline{K}_{11}}{2} \Delta U & \overline{K}_{12} \Delta U & \cdots & \overline{K}_{1N-1} \Delta U & \dfrac{\overline{K}_{1N}}{2} \Delta U \\ \vdots & \vdots & & \vdots & \vdots \\ \dfrac{\overline{K}_{N1}}{2} \Delta U & \overline{K}_{N2} \Delta U & \cdots & \overline{K}_{NN-1} \Delta U & \dfrac{\overline{K}_{NN}}{2} \Delta U \end{bmatrix},$$

and αC is a symmetric matrix of the form:

$$\begin{bmatrix} \alpha\left(\xi + \dfrac{\chi}{(\Delta U)^2}\right) & -\dfrac{\alpha\chi}{(\Delta U)^2} & 0 & 0 & \cdots & 0 \\ -\dfrac{\alpha\chi}{(\Delta U)^2} & \alpha\left(\xi + \dfrac{2\chi}{(\Delta U)^2}\right) & -\dfrac{\alpha\chi}{(\Delta U)^2} & 0 & \cdots & 0 \\ 0 & -\dfrac{\alpha\chi}{(\Delta U)^2} & \alpha\left(\xi + \dfrac{2\chi}{(\Delta U)^2}\right) & -\dfrac{\alpha\chi}{(\Delta U)^2} & \cdots & 0 \\ & \bullet & \bullet & \bullet & & \\ 0 & \cdots & 0 & 0 & -\dfrac{\alpha\chi}{(\Delta U)^2} & \alpha\left(\xi + \dfrac{\chi}{(\Delta U)^2}\right) \end{bmatrix}$$

In our case, boundary conditions (14) can be supplemented by conditions of the form: $P(U_{min}) = P(U_{max}) = 0$, in this case, the matrix αC will have the form:

$$
\begin{bmatrix}
0 & -\dfrac{\alpha\chi}{(\Delta U)^2} & 0 & 0 & \cdots & 0 \\[2ex]
0 & \alpha\left(\xi + \dfrac{2\chi}{(\Delta U)^2}\right) & -\dfrac{\alpha\chi}{(\Delta U)^2} & 0 & \cdots & 0 \\[2ex]
0 & -\dfrac{\alpha\chi}{(\Delta U)^2} & \alpha\left(\xi + \dfrac{2\chi}{(\Delta U)^2}\right) & -\dfrac{\alpha\chi}{(\Delta U)^2} & \cdots & 0 \\[1ex]
 & \bullet & & \bullet & \bullet & \\[1ex]
0 & \cdots & 0 & 0 & -\dfrac{\alpha\chi}{(\Delta U)^2} & 0
\end{bmatrix}.
$$

Thus, the problem is reduced to solving the SLAE with respect to the vector $P = (P_1, \cdots P_N)$.

DISCUSSION OF THE RESULTS

The spectral function $P^T(U)$ found by the Tikhonov regularization method has a maximum in the region of 0.04 eV corresponding to the α-peak of acoustic absorption and largely coincides with the quasi-Gaussian function $P^G(U)$ empirically selected in [3] (Fig. 2).

In this case, the position of the maximum of the $P^T(U)$ depends on the structural state of the sample. This fact numerically and qualitatively correlates with the conclusions of [3] about the change in the effective value of the activation energy $U_{eff} = \int\limits_0^\infty UP(U)dU \cong U_0 + \dfrac{D^2}{U_0}$ due to the change in the statistical scatter characterized by the dispersion parameter D (Table).
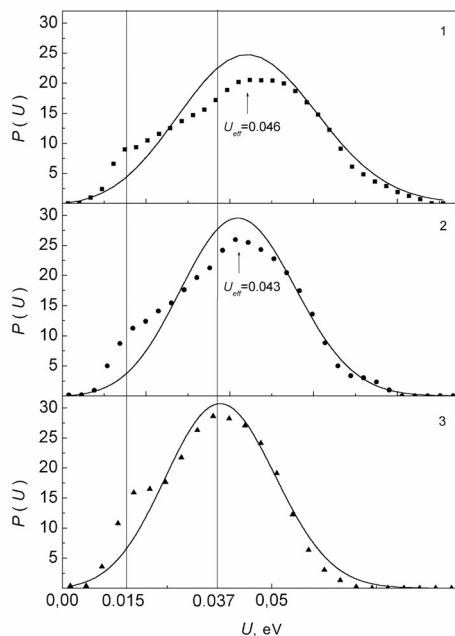
Figure 2. Spectral functions (distribution functions of activation energy values) $P^G(U)$ and $P^T(U)$ for various structural states of the sample (the numbering of structural states corresponds to that shown in Fig. 1):

■, ●, ▲ – the spectral function $P^T(U)$ which was found by the Tikhonov regularization method; *solid lines* - spectral function $P^G(U)$ calculated by formula (4) for the quasi-Gaussian distribution function with an appropriate choice of values U_0 and D

The spectral function $P^T(U)$ also has a feature in the form of a second mode in the region of 0.015 eV; the position of this feature is practically independent of the structural state of the sample. If we assume that this feature corresponds to a relaxation resonance (α'-peak) with the same value of τ_0 as the main resonance, then it should correspond to a feature in the form of a peak on temperature dependence of the δ and a step on temperature dependence of the $\Delta M/M_0$ in the region of 14-16 K (at an oscillation frequency sample 88 kHz). In [3] these features were not found experimentally, which may be associated with a significant broadening of the main relaxation resonance at a temperature of ≈ 54 K. However, in one form or another, the α'-peak was repeatedly observed by various

authors [8]-[19]. For example, in [10] a resonance in the region of 17 K was found in Fe single crystal with an orientation <100>. It was shown in [16] that annealing leads to a narrowing and a shift toward lower temperatures of the α-peak and the appearance of a α'-peak that was not observed in the initial curves. It was shown in [17], [18] that the α'-peak should be characterized by the same period of attempts as the α-peak and have a value of the order of 10^{-11} s.

Table. Acoustic relaxation parameters in a single-crystal sample of high-purity iron with orientation <731> in various structural states, according to the data of [3], [4]:

Relaxation parameters	Structural state of the sample		
	1	**2**	**3**
U_0^{α}, eV	0.037		
D^{α}, eV	0.0177	0.0143	0.0136
$C_r \Delta_0$	0.00472	0.00271	0.00180
U_{eff}^{α}, eV	0.046	0.043	0.042
$\tau_0^{\alpha} \cdot 10^{11}$, s	2.4		
$U_0^{\alpha'}$, eV	0.015		

In order to detect the α'-peak in Fe single crystals of the <731> orientation, additional experimental studies were carried out in [4]. A sample in the form of a thin plate was made from the same single crystal as in [3]. The acoustic properties of this sample were studied in the temperature range 4.5-150 K. It was found that in the undeformed sample α and α' peaks are not observed, deformation leads to the appearance of α-peak localized at 35 K and its α' satellite at a temperature of 13 K. Subsequent annealing at 320 K leads to a decrease in the height of the α peak, narrowing and shifting to lower temperatures, while the α'-peak becomes more pronounced. The analysis performed in [4] made it possible to establish the microscopic nature of the α' -peak and determine the corresponding activation energy of an elementary relaxator $U_0^{\alpha'} = 0.015$ eV; it was also shown that the activation energy values corresponding to the α'-peak have a small statistical spread, which practically does not change with a change in the structural state sample.

Thus, the values of the activation energy $U_0^{\alpha} = 0.037$ eV and $U_0^{\alpha'} = 0.015$ eV determined experimentally in [4] corresponding to the α-peak and its α' satellite are in good agreement (taking into account the statistical spread) with the positions of the peaks on the dependence $P^T(U)$ obtained by solving the inverse problem, and its substitution into expression (3) makes it possible to exhaustively describe the experimentally observed spectrum of low-temperature acoustic relaxation in iron (Fig. 1).

CONCLUSIONS

A mathematical procedure for processing experimental data is proposed that allows solving the inverse problem of low-temperature mechanical spectroscopy - to restore the energy spectrum of relaxation by analyzing the temperature dependence of acoustic absorption.

ORCID IDs

Yuri A. Semerenko, https://orcid.org/0000-0003-2268-0572

REFERENCES

[1] A.S. Nowick, and B.S. Berry, *Anelastic relaxation in crystalline solids*, (Academic Press, New York and London, 1972).
[2] V.D. Natsik, and Yu.A. Semerenko, Low Temp. Phys. **42**, 138 (2016), https://doi.org/10.1063/1.4942907.
[3] V.D. Natsik, P.P. Pal-Val, L.N. Pal-Val, and Y.A. Semerenko, Low Temperature Physics, **26**, 522 (2000); https://doi.org/10.1063/1.1306411.
[4] V.D. Natsik, and Yu.A. Semerenko, Low Temp. Phys. **45**, 551 (2019), https://doi.org/10.1063/1.5097366.
[5] H.F. Guliyev, and V.N. Nasibzadeh, Vestnik Tomskogo gosudarstvennogo universiteta. Matematica i mekhanika [Tomsk State University Journal of Mathematics and Mechanics], **54**, 5 (2018), https://doi.org/10.17223/19988621/54/1.
[6] O.V. Mozgovy, Технологические системы [Technological Systems Journal], **3**(68), 50 (2014), http://www.technological-systems.com.ua/images/journal/2014/files/ts68.pdf. (in Russian)
[7] A.N. Tikhonov, and V.Ya. Arsenin, *Solutions of Ill-Posed Problems*, (Halsted Press, 1977).
[8] M. Kakegawa, and K. Sakamoto, Jpn. J. Appl. Phys. **9**, 1057 (1970), https://doi.org/10.1143/JJAP.9.1057.
[9] K. Takita, and K. Sakamoto, Scripta Metall. **4**, 403 (1970), https://doi.org/10.1016/0036-9748(70)90110-9.
[10] P.P. Pal-Val,   V.D. Natsik,   and   S. Kadečková,   Philosophical   Magazine   A,   **56**(3),   407   (1987), https://doi.org/10.1080/01418618708214396.
[11] I.G. Ritchie, J.F. Dufresne, and P. Moser, Proc. ICIFUAS-6. ed. by R.R. Hasiguti, N. Mikoshiba, (University of Tokyo Press 1977), pp. 701.
[12] L.B. Magalas, and P. Moser, J. de Phys. Colloques, **42**, C5-97 (1981), https://doi.org/10.1051/jphyscol:1981514.
[13] P. Astie, J.P. Peyrade, and P. Groh, *Proc. ECIFUAS-3*, ed. by C.C. Smith, (Pergamon Press, 1980), pp. 49.
[14] P. Astie, J.P. Peyrade, and P. Groh, Scripta Metall. **14**, 611 (1980), https://doi.org/10.1016/0036-9748(80)90008-3.

[15] P. Astie, J.P. Peyrade, and P. Groh, J. de Phys. **42**, C5-91 (1981), http://dx.doi.org/10.1051/jphyscol:1981513.

[16] P. Astie, *Proc. of Summer School on Internal Friction in Solids*, ed. by S. Gorczyca, L.B. Magalas, (Cracow, Poland, 1984), pp. 43.

[17] L.B. Magalas, Thesis, Academy of Mining and Metallurgy, Cracov, 1982.

[18] L.B. Magalas, *Proc. of Summer School on Internal Friction in Solids*, ed. by S. Gorczyca, L.B. Magalas, (Cracow, Poland, 1984), pp. 89.

[19] Yu.A. Semerenko, *Proc. 21ᵗʰ Int. Conf. "Relaxation Phenomena in Solids"*, (Voronezh, Russia, 2004), ISBN 5-9273-0617-9, pp. 234.

СПЕКТР ЕНЕРГІЇ АКТИВАЦІЇ НИЗЬКОТЕМПЕРАТУРНОЇ АКУСТИЧНОЇ РЕЛАКСАЦІЇ В МОНОКРИСТАЛІЧНОМУ ЧИСТОМУ ЗАЛІЗІ. ВИРІШЕННЯ ЗВОРОТНОЇ ЗАДАЧІ МЕХАНІЧНОЇ СПЕКТРОСКОПІЇ МЕТОДОМ РЕГУЛЯРИЗАЦІЇ ТИХОНОВА

Ю.О. Семеренко

Інститут фізики та техніки низьких температур імені Б. Вєркіна, НАН України
пр. Науки 47, 61103, Харків, Україна

При вивченні температурних залежностей акустичного поглинання та модуля пружності часто спостерігаються релаксаційні резонанси - піки поглинання, яким на температурній залежності модуля пружності відповідає характерна сходинка. Вважається, що виникнення таких релаксаційних резонансів пов'язано з наявністю в структурі матеріалу елементарних мікроскопічних релаксаторів, що взаємодіють з досліджуваною коливальною модою механічних коливань зразка. В достатньо досконалому матеріалі такий процес характеризується часом релаксації τ, а у реальному матеріалі з дефектами - спектром часу релаксації $P(\tau)$. Найчастіше такі релаксаційні процеси мають термічно активований характер і час релаксації $\tau(T)$ визначається співвідношенням Ареніуса $\tau(T) = \tau_0 \exp(U_0/kT)$, а характеристиками процесу будуть U_0 - енергія активації, τ_0 - період спроб, Δ_0 - характерний елементарний внесок окремого релаксатора у динамічний відгук матеріалу та їх спектри. В області низьких температур $kT \ll U_0$ статистичним розподілом параметрів τ_0 та Δ_0 з експоненційною точністю можна знехтувати, а релаксаційний внесок у температурні залежності поглинання та динамічного модуля пружності матеріалу будуть визначатися тільки спектром енергій активації $P(U)$ мікроскопічних релаксаторів. Основна задача механічної спектроскопії при аналізі таких релаксаційних резонансів зводиться до визначення U_0, τ_0, Δ_0 та $P(U)$. У роботі показано, що проблема знаходження спектральної функції $P(U)$ для енергії активації акустичної релаксації в реальних кристалах з дефектами, зводиться до вирішення інтегрального рівняння Фредгольма I роду з приблизно відомою правою частиною і відноситься до класу некоректно поставлених задач. Запропоновано метод визначення $P(U)$ виходячи з експериментальних температурних залежностей акустичного поглинання чи модуля пружності, що ґрунтується на алгоритмі тихоновської регуляризації. Встановлено, що акустична релаксація у чистому монокристалічному залізі в області температур 5÷100 К характеризується двомодовою спектральною функцією $P(U)$ з максимумами в області 0.037 еВ та 0.015 еВ, що відповідають α-піку та його α' сателіту.

КЛЮЧОВІ СЛОВА: акустична релаксація, регуляризація Тихонова, спектр енергії активації, акустичне поглинання, модуль пружності

POLARIZATION EFFECTS IN THE REACTION $d + e^- \to d + e^-$

Gennadiy I. Gakh[a], [iD]Mykhailo I. Konchatnyi[a,*], [iD]Nikolay P. Merenkov[a], [iD]Andrij G. Gakh [b], [iD]Egle Tomasi-Gustafsson[c]

[a]NSC "Kharkov Institute of Physics and Technology"
Akademicheskaya, 1, 61108 Kharkov, Ukraine
[b]V.N. Karazin Kharkiv National University, 61022 Kharkov, Ukraine
[c]IRFU, CEA, Université Paris-Saclay, 91191 Gif-sur-Yvette, France
*Corresponding Author: konchatnij@kipt.kharkov.ua
Received March 28,2021; revised March 31, 2021; accepted April 20, 2021

The differential cross section and polarization observables for the elastic reaction induced by deuteron scattering off electrons at rest, $d + e^- \to d + e^-$ are calculated in the one-photon-exchange approximation. The following polarization observables were calculated: 1- the analyzing powers (asymmetries) due to the tensor polarization of the deuteron beam, 2 - the spin correlation coefficients caused by the arbitrarily polarized electron target and the vector polarized deuteron beam, 3 - the coefficients of the polarization transfer from the arbitrarily polarized target electron to the recoil electrons. The differential cross section and polarization observables have been expressed in terms of the deuteron electromagnetic form factors: G_c (charge monopole), G_M (magnetic dipole) and G_Q (charge quadrupole). Numerical estimations are given for the analyzing powers (asymmetries) due to the tensor polarization of the deuteron beam. They are calculated as functions of the deuteron beam energy for some values of the scattering angle (the angle between the deuteron beam and the recoil electron momenta). For the numerical calculation we use the existing phenomenological parametrization of the deuteron electromagnetic form factors. It turns out that the analyzing powers (asymmetries) are increasing with the growth of the deuteron beam energy and they have appreciable sensitivity to the value of the scattering angle. The specific interest of this reaction is to investigate the possibility to use this reaction for the measurement of the polarization of the high energy deuteron beams.
KEY WORDS: polarization phenomena, electron, deuteron, asymmetries, form factors.

The use of the inverse kinematics (where the projectile is much heavier than the target) in experimental investigation of some reactions allows to solve certain problems. The important feature of this kinematics in the hadron electron reactions is that the momentum transfer squared is extremely small. The inverse kinematics was previously used in a number of the experiments to measure the pion or kaon charge radius from the elastic scattering of negative pions (kaons) from electrons in a liquid-hydrogen target. The first experiment was done at Serpukhov [1] with pion beam energy of 50 GeV. Later, a few experiments were done at Fermilab with pion beam energy of 100 GeV [2] and 250 GeV [3]. At this laboratory, the electromagnetic form factors of negative kaons were measured by direct scattering of 250 GeV kaons from stationary electrons [4]. Later on, a measurement of the pion electromagnetic form factor was done at the CERN SPS [5,6] by measuring the interaction of 300 GeV pions with the electrons in a liquid hydrogen target.

The use of the inverse kinematics is proposed in a new experiment at CERN [7] to measure the running of the fine-structure constant in the space-like region by scattering high-energy muons (with energy 150 GeV) on atomic electrons, $\mu e \to \mu e$. The aim of the experiment is the extraction of the hadron vacuum polarization contribution. In the last time the inverse kinematics was used to investigate the nuclear reactions which can be hardly measured by other methods. In the paper [8] it was proposed to measure the neutron capture cross sections of unstable isotopes. To do so the authors suggested a combination of a radioactive beam facility, an ion storage ring and a high flux reactor which allow a direct measurement of neutron induced reactions over a wide energy range on isotopes with half-lives down to minutes. A direct measurement, in inverse kinematics, of the $^{17}O(\alpha,\gamma)^{21}Ne$ reaction has been performed at the DRAGON facility, at the TRIUMF laboratory, Canada [9]. At this laboratory, the $^{22}Ne(p,\gamma)^{23}Na$ reaction has, for the first time, been investigated directly in inverse kinematics [10]. A total of 7 resonances were measured. The authors of the paper [11] analyze the (p, 2p) and (p, pn) reactions data measured, in inverse kinematics, at GSI (Darmstadt, Germany) for carbon, nitrogen and oxygen isotopes in the incident energy range of 300-450 MeV/u (see [12] and references therein).

From the theoretical point of view, the inverse kinematics was considered in a number of papers. A large interest in inverse kinematics (for the case of the elastic pe scattering) was arisen due to possible applications - the possibility to build the beam polarimeters, for the high-energy polarized proton beams, in the RHIC energy range [13]. The calculation of the spin correlation parameters, for the case of polarized proton beam and electron target, are sizeable and the polarimeter using this reaction can measure the polarization of the proton beam [13]. The cross section and another polarization observables for the proton-electron elastic scattering were derived in a relativistic approach assuming the one-photon-exchange approximation [14]. The numerical estimations of the polarization observables have also been done. The authors showed that polarization effects may be sizeable in the GeV region, and that the polarization transfer coefficients for $\vec{p} + e \to \vec{p} + e$ reaction could be used to measure the polarization of the high-energy proton beams. The suggestion to use this reaction for the determination of the proton charge radius was considered in [15]. The model-

independent radiative corrections to the differential cross section for elastic proton-electron scattering have been calculated in [16] in the case of experimental setup when both the final particles are recorded in coincidence. The differential cross section for the elastic scattering of deuterons on electrons at rest is calculated taking into account the QED radiative corrections to the leptonic part of interaction [17].

In this work, we calculated, in the one-photon-exchange approximation, the differential cross section and some polarization observables for the elastic deuteron-electron scattering. Numerical estimations are given for some polarization observables. The following polarization observables were calculated: 1- the analyzing powers (asymmetries) due to the tensor polarization of the deuteron beam, 2 - the spin correlation coefficients caused by the arbitrarily polarized electron target and the vector polarized deuteron beam, 3 - the coefficients of the polarization transfer from the arbitrarily polarized target electron to the recoil electrons. Numerical estimations are given for the analyzing powers (asymmetries) due to the tensor polarization of the deuteron beam. They are calculated as functions of the deuteron beam energy for some values of the scattering angle (the angle between the deuteron beam and the recoil electron momenta). For the numerical calculation we use the existing phenomenological parametrization of the deuteron electromagnetic form factors.

UNPOLARIZED CROSS SECTION

Let us consider the reaction

$$d(p_1) + e^-(k_1) \to d(p_2) + e^-(k_2),\tag{1}$$

where the particle momenta are indicated in parentheses. The reference system is the laboratory (Lab) system, where the electron target is at rest. The maximum value of the four-momentum transfer squared, in the scattering on electrons at rest, is:

$$\left(-k^2\right)_{max} = \frac{4m^2\left(E^2 - M^2\right)}{M^2 + 2mE + m^2},\tag{2}$$

where m (M) is the electron (deuteron) mass, E is the deuteron beam energy.
In the one-photon-exchange approximation, the matrix element M of the reaction (1) can be written as:

$$M = \frac{e^2}{k^2} j_\mu J_\mu,\tag{3}$$

where $j_\mu (J_\mu)$ is the leptonic (hadronic) electromagnetic current and $k = k_1 - k_2 = p_2 - p_1$ is the four-momentum of the virtual photon. The leptonic current is

$$j_\mu = \overline{u}(k_2)\gamma_\mu u(k_1),\tag{4}$$

where $u(k_{1,2})$ is the bispinor of the incoming (outgoing) electron. The hadronic electromagnetic current can be written as

$$J_\mu = (p_1 + p_2)_\mu\left[-G_1(k^2)U_1 \cdot U_2^* + \frac{1}{M^2}G_3(k^2)\left(U_1 \cdot k U_2^* \cdot k - \frac{k^2}{2}U_1 \cdot U_2^*\right)\right] +\tag{5}$$

$$+G_2(k^2)\left(U_{1\mu}U_2^* \cdot k - U_{2\mu}^* U_1 \cdot k\right),$$

where $U_{1\mu}$ and $U_{2\mu}$ are the polarization four vectors for the initial and final deuteron states. The functions $G_i(k^2)$, i=1,2,3, are the deuteron electromagnetic form factors.

These form factors are related to the standard deuteron form factors: G_C (charge monopole), G_M (magnetic dipole) and G_Q (charge quadrupole) by the following relations:

$$G_M(k^2) = -G_2(k^2), G_Q(k^2) = G_1(k^2) + G_2(k^2) + 2G_3(k^2),\tag{6}$$

$$G_C(k^2) = \frac{2}{3}\tau\left[G_2(k^2) - G_3(k^2)\right] + \left(1 + \frac{2}{3}\tau\right)G_1(k^2), \tau = -\frac{k^2}{4M^2}.$$

The standard form factors have the following normalization:

$$G_C(0) = 1, G_M(0) = \frac{M}{m_N}\mu_d, G_Q(0) = M^2 Q_d, \tag{7}$$

where m_N is the nucleon mass, $\mu_d = 0.857 (Q_d = 0.2857 \text{ fm}^2)$ is the deuteron magnetic (quadrupole) moment.

$$|M|^2 = 16\pi^2 \frac{\alpha^2}{k^4} L_{\mu\nu} H_{\mu\nu}, L_{\mu\nu} = j_\mu j_\nu^*, H_{\mu\nu} = J_\mu J_\nu^*, \tag{8}$$

where $\alpha = e^2/4\pi = 1/137$ is the electromagnetic fine structure constant. The leptonic tensor, $L_{\mu\nu}^{(0)}(L_{\mu\nu}^{(p)})$, for unpolarized initial and final electrons (polarized electron target) averaging over the initial electron spin, has the form:

$$L_{\mu\nu}^{(0)} = k^2 g_{\mu\nu} + 2(k_{1\mu}k_{2\nu} + k_{1\nu}k_{2\mu}), L_{\mu\nu}^{(p)} = 2im\varepsilon_{\mu\nu\rho\sigma}k_\rho s_{1\sigma}, \tag{9}$$

where $s_{1\sigma}$ is the initial electron polarization four-vector which satisfies following conditions: $k_1 \cdot s_1 = 0, s_1^2 = -1$. We use the condition $\varepsilon_{1234} = 1$.
The spin density matrix of the initial deuteron has the following form:

$$\rho_{\alpha\beta}^{(i)} = -\frac{1}{3}\left(g_{\alpha\beta} - \frac{1}{M^2}p_{1\alpha}p_{1\beta}\right) + \frac{i}{2M}<\alpha\beta\eta_1 p_1> + Q_{\alpha\beta}^{(i)}, \tag{10}$$

where $<\alpha\beta ab> = \varepsilon_{\alpha\beta\rho\sigma}a_\rho b_\sigma$. Here $\eta_{1\alpha}$ and $Q_{\alpha\beta}^{(i)}$ are the four vector and tensor describing the vector and tensor polarization of the initial deuteron. The four-vector of the vector polarization satisfies the following conditions: $\eta_1^2 = -1$, $\eta_1 \cdot p_1 = 0$. The tensor $Q_{\alpha\beta}^{(i)}$ satisfies the conditions $Q_{\alpha\alpha}^{(i)} = 0$, $Q_{\alpha\beta}^{(i)} = Q_{\beta\alpha}^{(i)}$, $Q_{\alpha\beta}^{(i)}p_{1\alpha} = 0$.
The hadronic tensor $H_{\mu\nu}(0)$ which corresponds to the case of unpolarized initial and final deuterons can be written as

$$H_{\mu\nu}(0) = H_1(k^2)\tilde{g}_{\mu\nu} + \frac{1}{M^2}H_2(k^2)P_\mu P_\nu, \tag{11}$$

where $\tilde{g}_{\mu\nu} = g_{\mu\nu} - (k_\mu k_\nu)/k^2$, $P_\mu = (p_1 + p_2)_\mu$. Averaging over the spin of the initial deuteron, the structure functions $H_i(k^2)$, $i = 1, 2$, can be expressed in terms of the electromagnetic form factors as:

$$H_1(k^2) = \frac{2}{3}k^2(1+\tau)G_M^2(k^2), H_2(k^2) = M^2\left[G_C^2(k^2) + \frac{2}{3}\tau G_M^2(k^2) + \frac{8}{9}\tau^2 G_Q^2(k^2)\right]. \tag{12}$$

The expression of the differential cross section for unpolarized deuteron-electron scattering, in the coordinate system where the electron is at rest, can be written as:

$$\frac{d\sigma}{dk^2} = \frac{\pi\alpha^2}{2m^2\vec{p}^2}\frac{D}{k^4}, D = (k^2 + 2m^2)H_1(k^2) + 2\left[k^2 M^2 + 2mE(2mE + k^2)\right]\frac{H_2(k^2)}{M^2}, \tag{13}$$

where $\vec{p}$ is the momenta of the deuteron beam.

POLARIZATION OBSERVABLES

Let us choose the following orthogonal system: the z axis is directed along the direction of the deuteron beam momentum $\vec{p}$, the momentum of the recoil electron $\vec{k}_2$ lies in the xz plane (θ_e is the angle between the deuteron beam and the recoil electron momenta), and the y axis is directed along the vector $\vec{p} \times \vec{k}_2$. So, the components of the deuteron beam and recoil electron momenta are the following

$$p_x = p_y = 0, p_z = p, k_{2x} = k_2 sin\theta_e, k_{2y} = 0, k_{2z} = k_2 cos\theta_e,$$

where $p(k_2)$ is the magnitude of the deuteron beam (recoil electron) momentum.

Asymmetries A_{ij}, caused by the tensor polarized deuteron beam

Consider the scattering of the tensor polarized deuteron beam on the unpolarized electron target. The hadronic tensor which corresponds to this case can be written as

$$H_{\mu\nu}\left(Q^{(i)}\right) = H_3\left(k^2\right)\overline{Q}^{(i)}\tilde{g}_{\mu\nu} + H_4\left(k^2\right)\frac{\overline{Q}^{(i)}}{4M^2}P_\mu P_\nu + H_5\left(k^2\right)\left(P_\mu\tilde{Q}_\nu^{(i)} + P_\nu\tilde{Q}_\mu^{(i)}\right) + H_6\left(k^2\right)\tilde{Q}_{\mu\nu}^{(i)}, \tag{14}$$

where

$$\tilde{Q}_\mu^{(i)} = Q_{\mu\nu}^{(i)}k_\nu - \frac{k_\mu}{k^2}\overline{Q}^{(i)}, \tilde{Q}_\mu^{(i)}k_\mu = 0, \tilde{Q}_{\mu\nu}^{(i)} = Q_{\mu\nu}^{(i)} + \frac{k_\mu k_\nu}{k^4}\overline{Q}^{(i)} - \frac{k_\nu k_\alpha}{k^2}Q_{\mu\alpha}^{(i)} - \frac{k_\mu k_\alpha}{k^2}Q_{\nu\alpha}^{(i)}, \tag{15}$$

$$\tilde{Q}_{\mu\nu}^{(i)}k_\nu = 0, \overline{Q}^{(i)} = Q_{\alpha\beta}^{(i)}k_\alpha k_\beta.$$

The structure functions $H_i(k^2)$ are related to the deuteron electromagnetic form factors by :

$$H_3(k^2) = -G_M^2, H_4(k^2) = G_M^2 + \frac{4}{1+\tau}\left(G_C + \tau G_M + \frac{\tau}{3}G_Q\right)G_Q, \tag{16}$$

$$H_5(k^2) = -\tau(G_M + 2G_Q)G_M, H_6(k^2) = 4M^2\tau(1+\tau)G_M^2.$$

The components of the quadrupole polarization tensor $Q_{ij}^{(i)}$ which are defined in the Lab system can be related to the corresponding ones in the rest system of the deuteron beam (denote them as R_{ij}) by the following relations

$$Q_{xx}^{(i)} = R_{xx}, Q_{yy}^{(i)} = R_{yy}, Q_{xz}^{(i)} = \frac{E}{M}R_{xz}, Q_{zz}^{(i)} = \frac{E^2}{M^2}R_{zz}.$$

The dependence of the differential cross section of the reaction (1) on the polarization characteristics of the deuteron beam, in case when beam is tensor polarized, has the following form

$$\frac{d\sigma}{dk^2}\left(Q^{(i)}\right) = \left(\frac{d\sigma}{dk^2}\right)_{un}\left[1 + A_{xx}\left(R_{xx} - R_{yy}\right) + A_{xz}R_{xz} + A_{zz}R_{zz}\right], \tag{17}$$

where A_{ij}, $i,j = x,y,z$ are the asymmetries which characterize $\vec{de}$ scattering, when the deuteron beam is tensor polarized.

The expressions for the asymmetries, as a functions of the deuteron form factors, can be written as:

$$DA_{xx} = 4\tau\left(1 - \frac{k^2}{k_{max}^2}\right)\left[(m^2p^2 + \tau M^4)G_M^2 - mEk^2G_MG_Q + (1+\tau)^{-1}(M^2k^2 + 2mEk^2 + 4m^2E^2)G_Q\left(\tau G_M + G_C + \frac{\tau}{3}G_Q\right)\right],$$

$$DA_{xz} = -\frac{2\tau}{mpM}\left[-k^2\left(1 - \frac{k^2}{k_{max}^2}\right)\right]^{1/2}\left\{M^2k^2\left(M^2 + mE\right)G_M^2 + 2[m^2p^2\left(k^2 + 4mE\right) + \tag{18}\right.$$

$$\left. +2mEk^2\left(M^2 + mE\right)\right]G_MG_Q - 4(1+\tau)^{-1}\left(M^2 + mE\right)\left(M^2k^2 + 2mEk^2 + 4m^2E^2\right)G_Q\left(\tau G_M + G_C + \frac{\tau}{3}G_Q\right)\right\},$$

$$DA_{zz} = \frac{k^2}{M^2}\left\{-\left[m^2p^2 + 2\tau(\tau-1)M^4 + \tau mM^2(m+2E) + 3\tau^2\frac{M^6}{m^2p^2}\left(M^2 + 2mE + m^2\right)\right]G_M^2 + \right.$$

$$+4\tau\left[mEM^2\left(3-4\tau\right)+2\left(m^2E^2-\tau M^4\right)-3\tau E\frac{M^4}{mp^2}\left(M^2+2mE+m^2\right)\right]G_M G_Q +$$

$$+4\left(1+\tau\right)^{-1}\left(m^2E^2-2\tau mEM^2-\tau M^4\right)\left[1-2\tau-3\tau\frac{M^2}{m^2p^2}\left(M^2+2mE+m^2\right)\right]G_Q\left(\tau G_M+G_C+\frac{\tau}{3}G_Q\right)\Bigg\}.$$

Spin correlation coefficients, C_{ij}, caused by the polarized electron target and the vector polarized deuteron beam

Consider the scattering of the vector polarized deuteron beam (the polarizations of the final particles are not detected). In this case a non-zero polarization effects arise only when the electron target is also polarized. So, the part of the hadronic tensor related to the vector polarized deuteron beam and unpolarized scattered deuteron can be written as:

$$H_{\mu\nu}(\eta_1)=i(1+\tau)MG_M^2<\mu\nu\eta_1 k>+\frac{i}{2M}G_M\left(G_M-2G_C-\frac{2}{3}\tau G_Q\right)\left(P_\mu<\nu\eta_1 kp_1>-P_\nu<\mu\eta_1 kp_1>\right). \qquad (19)$$

In the considered frame, where the target electron is at rest, the polarization four-vectors of the electron target and of the deuteron beam have the following components
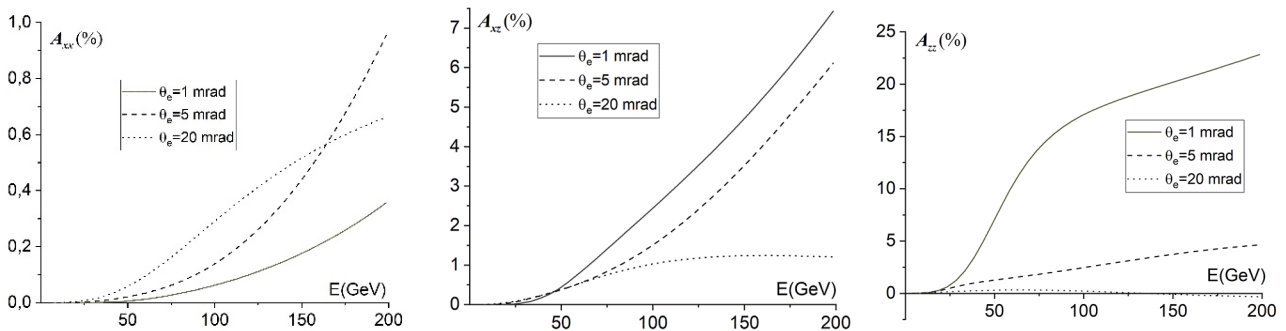
Figure 1. The asymmetries, which are caused by the tensor polarization of the deuteron beam, as a function of the deuteron beam energy E at various values of the scattering angle

$$s_1=\left(0,\vec{\xi}_1\right),\eta_1=\left(\frac{\vec{p}\cdot\vec{S}_1}{M},\vec{S}_1+\frac{\vec{p}\left(\vec{p}\cdot\vec{S}_1\right)}{M\left(E+M\right)}\right), \qquad (20)$$

where $\vec{S}_1(\vec{\xi}_1)$ is the unit vector describing the vector polarization of the deuteron beam (the electron target polarization) in its rest system.

The dependence of the differential cross section on the polarization of the initial particles has the following form:

$$\frac{d\sigma}{dk^2}\left(\vec{\xi}_1,\vec{S}_1\right)=\left(\frac{d\sigma}{dk^2}\right)_{un}\left[1+C_{xx}\xi_{1x}S_{1x}+C_{yy}\xi_{1y}S_{1y}+C_{zz}\xi_{1z}S_{1z}+C_{xz}\xi_{1x}S_{1z}+C_{zx}\xi_{1z}S_{1x}\right], \qquad (21)$$

where C_{ij}, $i,j=x,y,z$ are the spin correlation coefficients which determine the $\vec{de}$ scattering, when the deuteron beam is vector polarized and electron target is arbitrarily polarized.

The explicit expressions of the spin correlation coefficients, as a function of the deuteron form factors, can be written as:

$$DC_{yy}=-4mMk^2(1+\tau)G_M\left(G_C+\frac{\tau}{3}G_Q\right),$$

$$DC_{xx}=-2\tau mMk^2G_M\left[\left(\frac{k^2}{k_{max}^2}-1\right)G_M+2\left(1-\frac{4M^2}{k_{max}^2}\right)\left(G_C+\frac{\tau}{3}G_Q\right)\right],$$

$$DC_{xz} = \frac{k^2}{p}(mE + M^2)\left[-k^2\left(1 - \frac{k^2}{k_{max}^2}\right)\right]^{1/2} G_M[\tau G_M + 2G_C + 2\frac{\tau}{3}G_Q], \tag{22}$$

$$DC_{zx} = 4mMp\left[-k^2\left(1 - \frac{k^2}{k_{max}^2}\right)\right]^{1/2} G_M[\tau(G_M - 2G_C - \frac{2}{3}\tau G_Q) + \frac{1}{4}\frac{E+m}{m}\frac{k^2}{p^2}\left(\tau G_M + 2G_C + \frac{2}{3}\tau G_Q\right)],$$

$$DC_{zz} = -2k^2 G_M\left[2(mE - \tau M^2)\left(G_C + \frac{\tau}{3}G_Q\right) + \tau(M^2 + mE)G_M - \tau\frac{E+m}{m}\frac{M^2}{p^2}(M^2 + mE)\left(\tau G_M + 2G_C + \frac{2}{3}\tau G_Q\right)\right].$$

Coefficients of the polarization transfer from the target electron to the recoil one, t_{ij}

Consider the scattering of the unpolarized deuteron beam on the polarized electron target (the polarization of the scattered deuteron is not measured) in the case when the polarization of the recoil electron is measured.

The part of the leptonic tensor which corresponds to the case of the polarized target and recoil electron has the following form

$$L_{\mu\nu}(s_1, s_2) = -\left(k_1 \cdot s_2 k_2 \cdot s_1 + \frac{k^2}{2}s_1 \cdot s_2\right)g_{\mu\nu} + \frac{k^2}{2}\left(s_{1\mu}s_{2\nu} + s_{1\nu}s_{2\mu}\right) - \tag{23}$$

$$-s_1 \cdot s_2\left(k_{1\mu}k_{2\nu} + k_{1\nu}k_{2\mu}\right) + k_1 \cdot s_2\left(s_{1\mu}k_{2\nu} + s_{1\nu}k_{2\mu}\right) + k_2 \cdot s_1\left(s_{2\mu}k_{1\nu} + s_{2\nu}k_{1\mu}\right),$$

where $s_{2\mu}$ is the polarization four-vector of the recoil electron which satisfies the following conditions: $k_2 \cdot s_2 = 0, s_2^2 = -1$.

In the Lab system, where the target electron is at rest, the polarization four-vector of the recoil electron has the following components

$$s_2 = \left(\frac{\vec{k}_2 \cdot \vec{\xi}_2}{m}, \vec{\xi}_2 + \frac{\vec{k}_2(\vec{k}_2 \cdot \vec{\xi}_2)}{m + \varepsilon_2}\right), \tag{24}$$

where $\vec{\xi}_2$ is the unit vector describing the polarization of the recoil electron in its rest system and ε_2 is the recoil electron energy.

The dependence of the differential cross section of the reaction $d + \vec{e} \to d + \vec{e}$ on the polarizations of the initial and recoil electrons has the following form

$$\frac{d\sigma}{dk^2}(\vec{\xi}_1, \vec{\xi}_2) = \frac{1}{2}\left(\frac{d\sigma}{dk^2}\right)_{un}\left[1 + t_{xx}\xi_{1x}\xi_{2x} + t_{yy}\xi_{1y}\xi_{2y} + t_{zz}\xi_{1z}\xi_{2z} + t_{xz}\xi_{1x}\xi_{2z} + t_{zx}\xi_{1z}\xi_{2x}\right], \tag{25}$$

where t_{ij}, $i, j = x, y, z$ are the coefficients of the polarization transfer from initial electron to the recoil one.

The explicit expressions of the polarization transfer coefficients, as a function of the deuteron form factors, can be written as

$$Dt_{xx} = \left(2m^2 - k^2 sin^2\theta_e\right)\left\{H_1 + 4\frac{H_2}{M^2}\left[E^2 - \lambda\left(M^2 + 2mE\right)\right]\right\} +$$

$$+4k_2 sin\theta_e\frac{H_2}{M^2}\left\{4\lambda mpE cos\theta_e sin\theta_e + M^2 k_2\left[(1+\tau)cos\theta_e - sin\theta_e\left(\tau + 2\frac{E^2}{M^2}\right)\right]\right\}$$

$$Dt_{yy} = 2m^2\left\{H_1 + 4\frac{H_2}{M^2}\left[E^2 - \lambda\left(M^2 + 2mE\right)\right]\right\}, \tag{26}$$

$$Dt_{zz} = 4k_2 cos\theta_e\frac{H_2}{M^2}\left[\left(M^2 - 2E^2\right)k_2 cos\theta_e + 4\lambda mp\left(m + E + E cos^2\theta_e\right)\right] +$$

$$+2m^2\left(1+2\lambda cos^2\theta_e\right)\left\{H_1+4\frac{H_2}{M^2}\Big[E^2-\lambda\left(2E^2-M^2+2mE\right)\Big]\right\},$$

$$Dt_{xz}=4k_2sin\theta_e\frac{H_2}{M^2}\Big[\left(M^2-2E^2\right)k_2cos\theta_e+2mpE\Big]+$$

$$+4\lambda cos\theta_e sin\theta_e\left\{m^2H_1+\frac{H_2}{M^2}\Big[4mE\left(mE+pk_2cos\theta_e\right)+k^2\left(M^2+2mE\right)\Big]\right\},$$

$$Dt_{zx}=4k_2sin\theta_e\frac{H_2}{M^2}\Big[\left(M^2-2E^2\right)k_2cos\theta_e+2mp\left(2m\lambda+2\lambda E-E\right)\Big]+$$

$$+4\lambda cos\theta_e sin\theta_e\left\{m^2H_1+\frac{H_2}{M^2}\Big[4mE\left(mE+pk_2cos\theta_e\right)+k^2\left(E^2+p^2+2mE\right)\Big]\right\},$$

where $\lambda=-k^2/(4m^2)$.

In conclusion, the differential cross section and polarization observables for the elastic reaction induced by deuteron scattering off electrons at rest are calculated in the one-photon-exchange approximation. The following polarization observables have been calculated:

1 - the asymmetries, A_{ij}, caused by the tensor polarized deuteron beam,

2 - the spin correlation coefficients, C_{ij}, caused by the polarized electron target and the vector polarized deuteron beam,

3 - the coefficients of the polarization transfer from the target electron to the recoil one, t_{ij}.

Numerical estimations are given for the analyzing powers (asymmetries) due to the tensor polarization of the deuteron beam (see Fig.1). They are calculated using the parametrization of the electromagnetic deuteron form factors from Ref. [18].

ORCID IDs

Mykhailo I. Konchatnij, https://orcid.org/0000-0002-9972-5348; **Nikolay P. Merenkov,** https://orcid.org/0000-0002-9743-3827
Andrij G. Gakh, https://orcid.org/0000-0002-1064-1448; **Egle Tomasi-Gustafsson,** https://orcid.org/0000-0002-5263-3948

REFERENCES
[1]   G. Adylov at al., Phys. Lett. **B51,** 402(1974), https://doi.org/10.1016/0370-2693(74)90239-1.
[2]   E. B. Dally at al., Phys. Rev. Lett. **39,** 1176(1977), https://doi.org/10.1103/PhysRevLett.39.1176.
[3]   E. B. Dally at al., Phys. Rev. Lett. **48,** 375(1982), https://doi.org/10.1103/PhysRevLett.48.375.
[4]   E. B. Dally at al., Phys. Rev. Lett. **45,** 232(1980), https://doi.org/10.1103/PhysRevLett.45.232.
[5]   S. R. Amendolia et al. (NA7), Nucl. Phys. **B277**, 168 (1986), https://doi.org/10.1016/0550-3213(86)90437-2.
[6]   S. R. Amendolia et al., Phys.Lett. **B146**, 116(1984), https://doi.org/10.1016/0370-2693(84)90655-5.
[7]   G. Abbiendi(INFN, Bologna),C.M. Carloni Calame(INFN, Pavia), U. Marconi(INFN, Bologna), C. Matteuzzi(INFN, Milan Bicocca), G. Montagna(Pavia U. and INFN, Pavia) et al., Eur. Phys. J. **C77**,139 (2017), https://doi.org/10.1140/epjc/s10052-017-4633-z.
[8]   Rene Reifarth   and   Yuri   A. Litvinov,   Phys.   Rev.   ST   Accel.   Beams   17,   014701   (2014), https://doi.org/10.1103/PhysRevSTAB.17.014701.
[9]   M. P. Taggart at al., Phys. Lett. **B798,** 134894(2019), https://doi.org/10.1016/j.physletb.2019.134894.
[10] M. P. Williams at al., Phys. Rev. **C102**, 035801(2020), https://doi.org/10.1103/PhysRevC.102.035801.
[11] Nguyen Tri Toan Phuc, Kazuki Yoshida and Kazuyuki Ogata, Phys. Rev. **C100**, 064604 (2019), https://doi.org/10.1103/PhysRevC.100.064604.
[12] M. Holl at al., Phys. Lett. **B795**, 682 (2019), https://doi.org/10.1016/j.physletb.2019.06.069.
[13] I.V. Glavanakov, Yu.F. Krechetov A.P. Potylitsyn, G.M. Radutsky, A.N. Tabachenko et al., Nucl.Instrum.Meth. **A381**, 275 (1996), https://doi.org/10.1016/S0168-9002(96)00714-0.
[14] G. I. Gakh, A. Dbeyssi, D. Marchand, E. Tomasi-Gustafsson and V. V. Bytev, Phys. Rev. **C84**, 015212 (2011), https://doi.org/10.1103/PhysRevC.84.015212.
[15] G. I. Gakh, A. Dbeyssi, E. Tomasi-Gustafsson, D. Marchand and V. V. Bytev, Phys. Part.Nucl. Lett. **10**, 393 (2013), https://doi.org/10.1134/S1547477113050099.
[16] G. I. Gakh, M.I. Konchatnij, N.P. Merenkov and E. Tomasi-Gustafsson, Phys. Rev. **C95**, 055207 (2017), https://doi.org/10.1103/PhysRevC.95.055207.
[17] G. I. Gakh, M.I. Konchatnij, N.P. Merenkov and E. Tomasi-Gustafsson, Phys. Rev. **C98**, 045212 (2018), https://doi.org/10.1103/PhysRevC.98.055212.
[18] E. Tomasi-Gustafsson,   G. I. Gakh   and   C. Adamuscin,   Phys.   Rev.   **C73**,   045204   (2006), https://doi.org/10.1103/PhysRevC.73.045204.

ПОЛЯРИЗАЦІЙНІ ЕФЕКТИ В РЕАКЦІЇ $d + e^- \to d + e^-$

Геннадій І. Гах[a], Михайло І. Кончатний[a], Микола П. Меренков[a], Андрій Г. Гах[b], Егле Томасі-Густафссон[c]

[a]Національний науковий центр «Харківський фізико-технічний інститут»
61108 Україна, м. Харків, вул. Академічна, 1
[b]Харківський національний університет імені В.Н. Каразіна
61022, Україна, м. Харків, пл. Свободи, 4,
[c]IRFU, CEA, Університет Париж-Сакле, 91191, Жиф-сюр-Іветт, Франція

Диференціальний переріз та поляризаційні спостережувані для пружної реакції індукованої розсіянням дейтрона на електроні в стані спокою $d + e^- \to d + e^-$ обчислені в однофотонному наближенні. Обчислені наступні поляризаційні спостережувані: 1- аналізуючі здатності (асиметрії), 2- коефіцієнти спінових кореляцій обумовлених довільною поляризацією електрона мішені та вектора поляризації пучка дейтронів, 3- коефіцієнтів передачі поляризації від довільно поляризованого електрона мішені до електрона віддачі. Диференціальний переріз та поляризаційні спостережувані виражені в термінах електромагнітних формфакторів дейтрона: G_c (зарядовий монополь), G_M (магнітний диполь) та G_Q (зарядовий квадруполь).

Приведені числові оцінки для аналізуючих здатностей (асиметрій) обумовлених тензорною поляризацією дейтронного пучка. Вони обчислені як функції енергії пучка дейтронів для деякої величини кута розсіяння (кута між напрямом пучка дейтронів і імпульсом електрона віддачі). Для числових обчислень використано існуючу феноменологічну параметризацію електромагнітних формфакторів дейтрона. Виявляється, що аналізуючі здатності (асиметрії) збільшуються з ростом енергії пучка дейтронів і вони мають помітну чутливість до величини кута розсіювання. Особливий інтерес до цієї реакції полягає у дослідженні можливості використати таку реакцію для вимірювання поляризації пучка дейтронів високої енергії.

КЛЮЧОВІ СЛОВА: поляризаційні явища, електрон, дейтрон, асиметрії, формфактори

PACS: 84.40.-x, 84.40.Ik

MODE-CONVERTING CORRUGATIONS FOR CAVITIES OF SECOND-HARMONIC GYROTRONS WITH IMPROVED PERFORMANCE

Tetiana I. Tkachova[a,*], Vitalii I. Shcherbinin[a], Viktor I. Tkachenko[a,b]

aNational Science Center "Kharkiv Institute of Physics and Technology", 61108 Kharkiv, Ukraine
bV.N. Karazin Kharkiv National University, 61022 Kharkiv, Ukraine
*Corresponding Author: t.i.tkachova@gmail.com
Received March 23, 2021; revised April 7, 2021; accepted April 10, 2021

A new method of improving mode selection in cavities of sub-terahertz second-harmonic gyrotrons is investigated. As an example, a second-harmonic gyrotron with frequency of 0.3 THz is considered. The gyrotron is designed for collective Thomson scattering (CTS) diagnostics of fusion plasmas and has a limited output power due to competition between the operating $TE_{13,2}$ mode and first-harmonic modes. For suppression of the first-harmonic competing modes periodic longitudinal corrugations are used in the gyrotron cavity. Such corrugations can induce coupling of the normal cavity modes known as azimuthal Bloch harmonics. The corrugation depth is set close to the half- and quarter-wavelength of the operating second-harmonic mode and competing first-harmonic modes, respectively. Under this condition, longitudinal corrugations of the cavity generally have only a slight effect on the operating mode, but can initiate strong conversion of the competing modes to high-order Bloch harmonics. The full-wave method of coupled azimuthal harmonics is applied to investigate the influence of dimensions of the corrugated gyrotron cavity on eigenvalues, ohmic losses and beam-wave coupling coefficients for the operating $TE_{13,2}$ mode and the most dangerous competing modes. Using the self-consistent theory of beam interaction with the operating and competing modes, the most optimal parameters are found for a gyrotron cavity with mode-converting corrugations, which ensure the widest range of a single mode operation for the 0.3-THz second-harmonic gyrotron. It is shown that, in this range, the gyrotron output power can be increased from 100 kW to 180 kW, as required by CTS plasma diagnostics. It is found that output mode purity of the 0.3-THz second-harmonic gyrotron falls off due to mode-converting corrugations, which induce undesirable coupling of the operating $TE_{13,2}$ mode with neighboring Bloch harmonics in the output section of the gyrotron cavity.
KEYWORDS: gyrotron, cyclotron harmonic, cavity, mode-converting corrugations, starting current, output power

Gyrotron is the most powerful source of sub-terahertz waves for widespread applications, including advanced spectroscopic methods, material processing, sensing and imaging techniques, biomedical research, plasma diagnostics, etc. [1-4]. It is a vacuum electron device, which is capable of producing more than 100 kW of output power in the frequency range between 0.1 and 0.4 THz. This capability of a gyrotron makes it the only suitable radiation source for plasma diagnostics based on collective Thomson scattering (CTS) [5-7]. However, in a gyrotron, high operating frequency places a stringent requirement on applied magnetic field, which is intended to guide a helical electron beam.

This requirement is much relaxed in gyrotrons operated at the second (or higher) harmonics of the cyclotron frequency. That is why second-harmonic gyrotrons with medium-field magnets are recognized as advantageous radiation sources in the sub-terahertz-to-terahertz frequency range. However, in these gyrotrons, an additional constraint on output power emerges [5, 6]. It is imposed by competition from the first-harmonic modes, which inherently possess low oscillation thresholds (starting currents).

To discriminate against the first-harmonic competing modes advanced gyrotron cavities with improved mode selection are required. Among them are coaxial cavities [8-12]. In a coaxial cavity, the modes are discriminated by a coaxial insert. The insert dimensions are usually selected to be small enough to have only a slight effect on the operating mode. Therefore, the operation of a coaxial-cavity gyrotron benefits from little sensitivity to the fabrication imperfections and misalignment of the coaxial loading. Unlike the operating mode, competing modes, which have smaller caustic radii, are suppressed by losses induced by the coaxial insert. The first-harmonic whispering-gallery (WG) modes are usually the remaining competitors, which can hinder high-performance operation of second-harmonic gyrotrons [11, 12].

Mode-converting wall corrugations can be applied to further improve the selectivity properties of advanced cavities for second-harmonic gyrotrons [13, 14]. Contrary to impedance corrugations [15-19], such corrugations induce coupling between normal modes (azimuthal Bloch harmonics) of the cavity and thereby affect frequencies of cavity modes, their ohmic losses and coupling with an electron beam [20-22]. According to [13, 14], in a cavity of a second-harmonic gyrotron, the depth of mode-converting corrugations should be selected close to half wavelength of the operating mode. In this case, the operating mode is generally weakly affected by corrugations of the cavity wall, while characteristics of the first-harmonic competing modes undergo a material change. As a result, the corrugation width and number can be optimized in such a way as to provide the most efficient suppression of the first-harmonic competitors in a corrugated cavity of a second-harmonic gyrotron. Thus, in a second-harmonic gyrotron, the use of a cavity with optimized corrugations is expected to have a beneficial effect on stability and efficiency of single-mode operation. The aim of this paper is to provide the design of the gyrotron cavity with mode-converting corrugations, which aid in suppressing the first-harmonic WG modes and improving the performance of a second-harmonic gyrotron. As an example, we consider the 0.3-THz second-harmonic gyrotron designed for CTS diagnostics of fusion plasmas [11]. In

coaxial cavity of this gyrotron, the operating TE$_{13,2}$ mode and first-harmonic WG modes are the only modes, which are unaffected by the coaxial insert and are identical to modes supported by a hollow cylindrical cavity.

BASIC EQUATIONS

In a gyrotron, an electromagnetic radiation is produced by the interaction between a helical beam of electrons gyrating in applied magnetic field $\mathbf{B}_0 = B_0 \mathbf{e}_z$ and TE mode ($E_z = 0$) excited at the s -th harmonic of cyclotron frequency ω_{c0} in a metal cylindrical cavity. In the general form, this interaction is described by the following system of equations:

$$\begin{cases} \left(\Delta_\perp + \dfrac{\partial^2}{\partial z^2} + k^2 \right) \operatorname{Re} \mathbf{E}_\perp = -i \dfrac{4\pi k}{c} \mathbf{j}_\perp \\ \dfrac{d\mathbf{p}}{dt} = -e \left(\mathbf{E} + \dfrac{1}{c} \left[\mathbf{v} \times (\mathbf{B} + \mathbf{B_0}) \right] \right) \end{cases}, \tag{1}$$

where $\mathbf{p} = m_e \mathbf{v} \gamma$, $\mathbf{v}$, $\gamma = \left(1 - v^2/c^2\right)^{-1/2}$, e and m_e are the momentum, velocity, relativistic factor, charge and rest mass of beam electrons, respectively, $\mathbf{j}_\perp$ is the transverse component of beam current density, c is the speed of light in vacuum, $\{\mathbf{E}(\mathbf{r},t), \mathbf{B}(\mathbf{r},t)\} = \{\mathbf{E}(\mathbf{r}), \mathbf{B}(\mathbf{r})\} \exp(-i\omega t)$ are the electric and magnetic fields of TE mode, ω is the angular frequency, $k = \omega/c$.

In cylindrical coordinates $\{r, \varphi, z\}$, the field components of TE mode can be written as

$$E_r = \frac{ik}{r} V(z) \frac{\partial \Psi}{\partial \varphi}, \ E_\varphi = -ikV(z) \frac{\partial \Psi}{\partial r}, \tag{2}$$

$$B_z = k_\perp^2 V(z) \Psi, \ B_r = V'(z) \frac{\partial \Psi}{\partial r}, \ B_\varphi = \frac{1}{r} V'(z) \frac{\partial \Psi}{\partial \varphi},$$

where $V(z)$ and $k_\perp$ are the mode amplitude and transverse wavenumber, respectively, $\Psi = \Psi(r, \varphi)$ is the membrane function, which satisfies the Helmholtz equation $\Delta_\perp \Psi = -k_\perp^2 \Psi$ and describes the transverse field structure in the gyrotron cavity.

We consider an open-ended cylindrical cavity, which incorporates longitudinal wedge-shaped corrugations (Fig. 1).
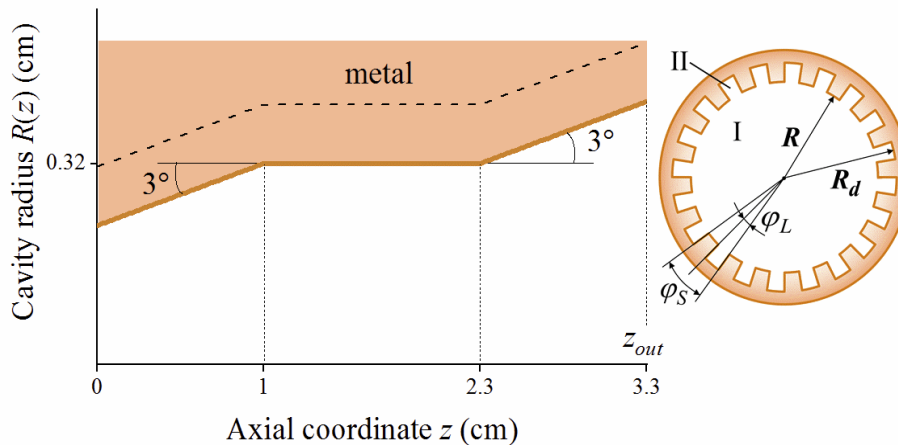
Figure 1. Longitudinal and transverse cross-sections of the corrugated cylindrical cavity

In such gyrotron cavity, the membrane function has the form [13, 20, 22]

$$\Psi = \begin{cases} \displaystyle\sum_{n=-\infty}^{\infty} A_n f_n(r) \exp(ik_n \varphi), \ 0 < r < R \\ \displaystyle\sum_{l=0}^{\infty} X_l g_l(r) \cos\left(\xi_l \left(\varphi + \frac{\varphi_L}{2} \right) \right), \ R < r < R_d \end{cases}, \tag{3}$$

where $f_n(r) = J_{k_n}(k_\perp r)/J'_{k_n}(k_\perp R)$, $k_n = m + nN$ is the azimuthal index of the n-th Bloch harmonic, N is the number

of periodic corrugations, R is the cavity radius, $g_l(r) = \dfrac{J_{\xi_l}(k_\perp r) N'_{\xi_l}(k_\perp R_d) - J'_{\xi_l}(k_\perp R_d) N_{\xi_l}(k_\perp r)}{J'_{\xi_l}(k_\perp R) N'_{\xi_l}(k_\perp R_d) - J'_{\xi_l}(k_\perp R_d) N'_{\xi_l}(k_\perp R)}$, $\xi_l = \dfrac{\pi l}{\varphi_L}$, $J_m(\cdot)$

and $N_m(\cdot)$ are the m-th order Bessel and Neumann functions, respectively, $R_d = R + d$, d and $w = \varphi_L R$ are the corrugation depth and width, respectively.

The transverse wavenumber $k_\perp = R^{-1}\chi(1 - i/(2Q_{ohm}))$ and membrane function Ψ are derived from the boundary and continuity conditions for the field (2). Here Q_{ohm} is the Q-value associated with ohmic losses of the TE mode in a metal gyrotron cavity with finite electric conductivity σ. For the TE$_{m,p}$ mode of a smooth-walled cylindrical cavity ($d = 0$ or $w = 0$), one obtains $\chi = \mu'_{m,p}$, $Q_{ohm} = Q_{ohm}^{(0)} \approx R/\delta_s(1 - m^2/\mu'^2_{m,p})$ and $\Psi = A_0 f_0(r)\exp(im\varphi)$, where δ_s is the skin-depth and $\mu'_{m,p}$ is the p-th root of the function $J'_m(\cdot)$.

The amplitude $V(z)$ of the TE mode and electron beam dynamic can be found from (1), initial conditions for beam electrons and outgoing-wave boundary conditions at both ends of the cavity (for more detail, see [14]). Hence one can determine the transverse electronic efficiency $\eta_\perp = 1 - \langle |\mathbf{p}_{\perp e}|^2/|\mathbf{p}_{\perp 0}|^2 \rangle$ as a function of beam parameters and cavity dimensions, where $\langle \cdot \rangle$ denotes averaging over the beam electrons having the initial $\mathbf{p}_{\perp 0}$ and final $\mathbf{p}_{\perp e}$ transverse momenta. The efficiency $\eta_\perp$ is greater than zero, if the beam current $I_b = \int j_z dS_\perp$ exceeds the oscillation threshold I_{st} known as a starting current.

One of the main factors affecting the interaction efficiency is the beam coupling with s-th harmonic TE mode. In a cavity with longitudinal wall corrugations, each TE mode has the form of multiple Bloch harmonics (see (3)), which have their own beam-wave coupling coefficients. For the n-th Bloch harmonic with amplitude A_n, such coefficient reads as [14]:

$$C_{n,s}^2 = A_n^2 \frac{J_{k_n - s}^2(k_\perp r_c)}{N_{mn}}, \tag{4}$$

where r_c is the beam radius,

$$N_{mn} = \sum_{n=-\infty}^{\infty} |A_n|^2 \left[\chi^2 + 2\chi f_n(\chi) + (\chi^2 - k_n^2) f_n^2(\chi) \right] + \frac{\varphi_L}{\varphi_S}\chi^2 |X_0|^2 \left[\left(\frac{R_d^2}{R^2} - \frac{1}{\chi^2} \right) g_1^2\left(\chi\frac{R_d}{R} \right) - \left(1 - \frac{1}{\chi^2} \right) g_1^2(\chi) - 1 \right] +$$

$$+ \frac{\varphi_L}{\varphi_S} \frac{\chi^2}{2} \sum_{l=1}^{\infty} |X_l|^2 \left[\left(\frac{R_d^2}{R^2} - \frac{\xi_l^2}{\chi^2} \right) g_l^2\left(\chi\frac{R_d}{R} \right) - \frac{2}{\chi} g_l(\chi) - \left(1 - \frac{\xi_l^2}{\chi^2} \right) g_l^2(\chi) - 1 \right].$$

Among Bloch harmonics, there is always a dominant harmonic with maximal beam-wave coupling strength $C_s = \max\{C_{n,s}^2\}$. Usually such harmonic has the main effect on efficiency of beam interaction with s-th harmonic TE mode supported by a corrugated gyrotron cavity.

From the knowledge of the interaction efficiency, one can determine the total power of TE mode interacting with the helical electron beam

$$P_{tot} = \eta_{el} I_b V_b, \tag{5}$$

where $\eta_{el} = \eta_\perp \alpha^2/(1 + \alpha^2)$ is the total electronic efficiency, V_b is the beam voltage, $\alpha = v_{\perp 0}/v_{z0}$ is the pitch factor, $v_{\perp 0}$ and v_{z0} are the initial transverse and longitudinal electron velocities, respectively.

Inside the interaction region, the total wave power must be balanced in accordance with the following conservation law:

$$P_{tot} = P_{out} + P_{ohm}, \tag{6}$$

where P_{out} is the output power leaked out from the output end ($z = z_{out}$) of the gyrotron cavity (Fig. 1) and P_{ohm} is the ohmic power dissipated in metal cavity walls.

For the cylindrical cavity with longitudinal wall corrugations, the power balance condition (6) can be reduced to the following dimensionless form:

$$I_0 \eta_\perp = 2 \operatorname{Re} \delta \left| f\left(\xi_{out}\right) \right|^2 + \frac{16\beta_{z0}^2}{\beta_{\perp 0}^4} \operatorname{Re}\left(Z_s G_{mn}\right), \tag{7}$$

where $I_0 = 64 \dfrac{I_b}{I_A} \dfrac{\beta_{z0}}{\gamma_0} \left[\dfrac{\beta_{\perp 0}^{s-4}}{(s-1)! 2^s} \left(\dfrac{\omega}{\omega_{c0}} \right)^{s-1} \right]^2$, $I_A = m_e c^3 / e \approx 17$ is the Alfven current, $\gamma_0 = 1 + \dfrac{eV_b}{m_e c^2}$ is the initial

relativistic factor, $\beta_{\perp 0} = \dfrac{v_{\perp 0}}{c}$, $\beta_{z0} = \dfrac{v_{z0}}{c}$, $\omega_{c0} = \dfrac{eB_0}{m_e c \gamma_0}$, $f(\xi) = -V(z) \dfrac{2\omega}{I_A \gamma_0} \dfrac{\beta_{\perp 0}^{s-4}}{(s-1)! 2^s} \left(\dfrac{\omega}{\omega_{c0}} \right)^{s-1} \sqrt{N_{mn}} \exp\left(-i\dfrac{s}{2}\pi \right)$,

$\xi = z \dfrac{k\beta_{\perp 0}^2}{2\beta_{z0}}$, $\delta = \dfrac{2\beta_{z0}}{k\beta_{\perp 0}^2} \sqrt{k^2 - k_\perp^2}$, $Z_s = (1-i)k\delta_s$ is the normalized impedance of the conducting surface,

$$G_{mn} = \int_0^{\xi_{out}} d\xi \frac{k_\perp^3 \chi}{k^3 N_{mn}} \left| f(\xi) \right|^2 \left\{ \left(1 - \frac{\varphi_L}{\varphi_S}\right) \sum_{n=-\infty}^{\infty} |A_n|^2 f_n^2(\chi) + \frac{\varphi_L R_d}{2\varphi_S R} \sum_{l=0}^{\infty} |X_l|^2 (1+\delta_{l0}) g_l^2 \left(\chi \frac{R_d}{R} \right) + \frac{N}{\pi R} \sum_{l=0}^{\infty} |X_l|^2 \int_R^{R_d} g_l^2 \left(\chi \frac{r}{R} \right) dr \right\},$$

δ_{ij} is the Kronecker delta.

The relation (7) provides useful check on numerical solutions of the self-consistent system of equations (1). As the corrugation depth or width approaches zero, it reduces to the well-known condition of power balance in a smooth-walled cylindrical gyrotron cavity [23].

EIGENVALUES AND OHMIC LOSSES OF THE CAVITY WITH LONGITUDINAL WALL CORRUGATIONS

In a gyrotron cavity, the effect of longitudinal wall corrugations is mainly determined by the ratio of corrugation depth d to mode cutoff wavelength $\lambda = 2\pi R / \chi$ and therefore is different for the first-harmonic ($s = 1$) and second-harmonic ($s = 2$) modes [13, 21]. It alters the mode eigenvalue χ, ohmic quality factor Q_{ohm} and beam-wave coupling coefficient C_s. One can take advantage from this fact with the goal to discriminate against the first-harmonic competing modes of the second-harmonic gyrotron.

As an example, the 0.3-THz second-harmonic gyrotron operated in the TE$_{13,2}$ mode [11] is considered. The beam parameters are as follows: $I_b = 10$ A, $V_b = 60$ kV, $\alpha = 1.2$ and $r_c = 0.2$ cm. The gyrotron is originally equipped with a smooth-walled coaxial cavity of the radius $R = 0.32$ cm. A coaxial insert of the cavity is used to suppress all first- and second-harmonic competing TE$_{m,p}$ modes with relatively small caustic radii $R_{m,p} = R |m| / \mu'_{m,p}$. However, it has no effect on the first-harmonic WG modes with $|m| / \mu'_{m,p} > 0.7$. These modes are close to those of a hollow cylindrical cavity and may constitute a threat to high-performance operation of the 0.3-THz second-harmonic gyrotron.

We consider longitudinal corrugations of the cavity wall as a possible means for discrimination against WG competing modes of the 0.3-THz second-harmonic gyrotron. The coaxial insert of the cavity is ignored. The corrugations are assumed to have the depth $d = 0.05$ cm and width $w = 0.02$ cm. The corrugation depth of 0.05 cm is adopted to fulfill the condition $d \approx \lambda/2$ for the operating TE$_{13,2}$ mode. Under this condition, the effect of wall corrugations on the operating mode is generally weak [13, 14].

Fig. 2a shows the cutoff frequencies $f_c = c\chi / (2\pi R)$ of the gyrotron cavity versus the number N of corrugations for $m = 13$. One can see that within the frequency spectrum, there is the mode, which has the eigenvalue close to $\mu'_{13,2}$ for a wide range of N. This mode is the operating mode, which has the form of nearly pure fundamental ($n = 0$) Bloch harmonic with $k_0 = m = 13$ and resembles the TE$_{13,2}$ mode of the conventional smooth-walled cavity. Unfortunately, in close proximity to the operating mode, there is the mode ($f_c \approx 297.34$ GHz) with dominant high-order ($n \neq 0$) Bloch component. It corresponds to the TE$_{7,4}$ mode of a smooth-walled cavity. This mode (high-order Bloch harmonic) can be coupled with the TE$_{13,2}$ mode (fundamental Bloch harmonic) for $N = 2, 3, 4, 5, 6, 10, 20$. Even though such a mode coupling is generally weak for $d \approx \lambda/2$, it may emerge in a corrugated gyrotron cavity with increase in mismatch between $d = 0.05$ cm and $\lambda/2$. Because of fairly small caustic radius of the TE$_{7,4}$ mode, this coupling must be avoided. Otherwise, one might expect suppression of the operating mode by a coaxial insert introduced in the original cavity of the 0.3-THz second-harmonic gyrotron.

For the operating and neighboring modes, the maximal beam-wave coupling coefficients C_s are shown in Fig. 2b. One can see that the operating mode exhibits the coefficient C_s, which is close to the coefficient $C_s^{(0)}$ of beam coupling

with $TE_{13,2}$ mode of the original smooth-walled cavity. The exceptions are $N = 13$ and $N = 20$. In this case, the operating $TE_{13,2}$ mode suffers from conversion to high-order Bloch harmonics, which correspond to $TE_{-13,2}$ and $TE_{-7,4}$ modes and are characterized by weak coupling with electron beam. Clearly such situation is unfavorable for the operating mode.
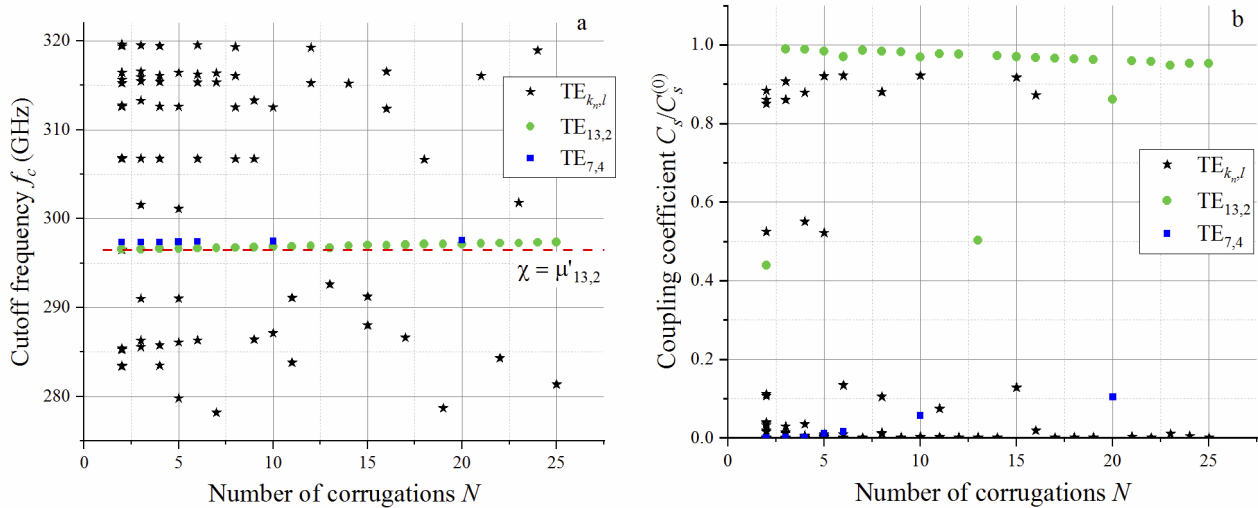
Figure 2. (a) Cutoff frequencies and (b) beam-wave coupling coefficients $C_s/C_s^{(0)}$ of modes of the corrugated gyrotron cavity versus the number N of corrugations for $m = 13$, where $C_s^{(0)}$ is the beam-wave coupling coefficient of the $TE_{13,2}$ mode of a smooth-walled cylindrical cavity

Fig. 3 shows the ohmic Q-value Q_{ohm} of the operating $TE_{13,2}$ mode versus the number of corrugations. As the conducting surface of the corrugated cavity expands with N, the ohmic Q-value decreases. For $N = 13$ and $N = 20$ one can see a distinct drop in Q_{ohm}. As discussed above, conversion of the operating mode to high-order Bloch harmonics happens in this case. Thus, in the design of the corrugated cavity for the 0.3-THz second-harmonic gyrotron, the number of corrugations must not be set to 2, 3, 4, 5, 6, 10, 13, 20 to avoid degradation of the gyrotron performance due to conversion of the operating mode to neighboring Bloch harmonics.
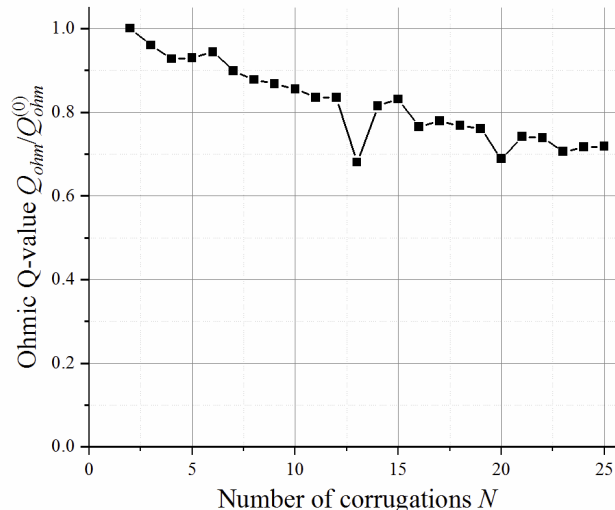
Figure 3. The ohmic Q-value of the operating mode supported by the corrugated gyrotron cavity versus the number N of corrugations, where $Q_{ohm}^{(0)}$ is the ohmic Q-value of the $TE_{13,2}$ mode of a smooth-walled cylindrical cavity

The competing WG modes of the 0.3-THz second-harmonic gyrotron are the first-harmonic modes with $m = 7, 8, 9$. For these modes, the longitudinal corrugations, which have about a quarter-wavelength depth, initiate a strong coupling of multiple Bloch harmonics [13, 14]. Fig. 4a shows the cutoff frequencies of the corrugated gyrotron cavity versus N for $m = 7, 8, 9$. It is easy to see that decrease in N magnifies the number of the first-harmonic

competing modes in the vicinity of the operating mode. These competitors have the form of complex mixture of fundamental and high-order Bloch harmonics, which correspond to whispering-gallery and volume modes, respectively. Due to presence of the volume component, the competing modes might be suppressed, once a coaxial insert is introduced into the gyrotron cavity. However, it is not the goal of the present paper to investigate such possibility. For this reason, the design consideration is restricted to the cavity with relatively large number of corrugations, which provide fairly sparse spectrum of the first-harmonic competing modes of the 0.3-THz second-harmonic gyrotron.
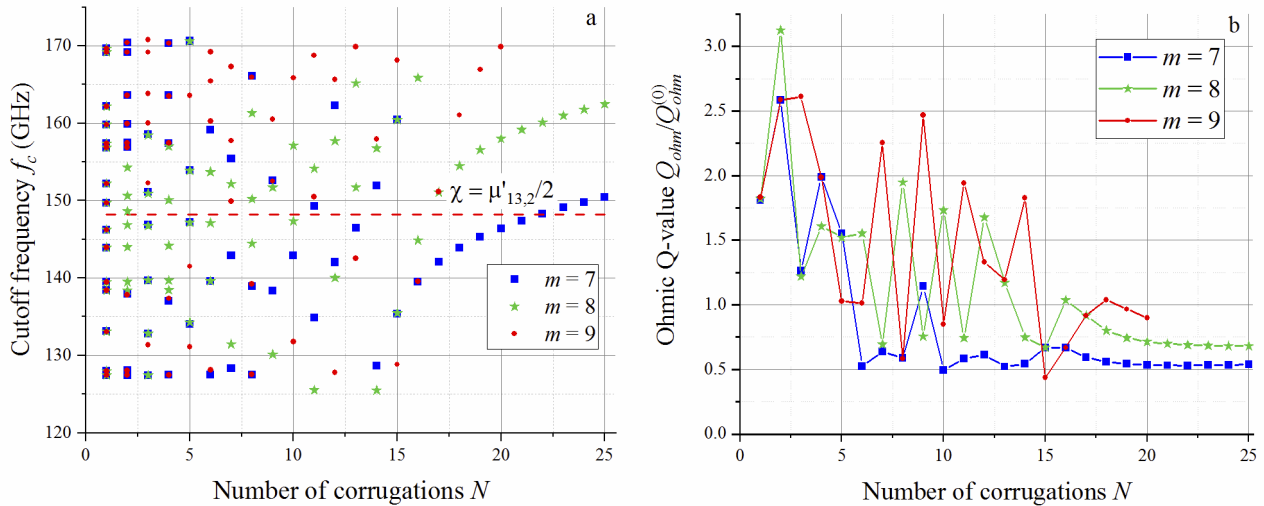
Figure 4. (a) The same as in Fig. 2a, but for $m = 7, 8, 9$, and (b) the normalized ohmic Q-values of the most dangerous competing modes with $m = 7, 8, 9$, where $Q_{ohm}^{(0)}$ is the ohmic Q-value of the TE$_{8,1}$ mode of the smooth-walled cylindrical cavity

The effect of longitudinal corrugations of the cavity wall on the ohmic losses of the first-harmonic modes with $m = 7, 8, 9$ is shown in Fig. 4b. In this figure, the ohmic Q-value is plotted as a function of N for the most dangerous competing modes having the smallest frequency separation from the operating mode. One can see that the dependence of Q_{ohm} on N is non-monotonic. This is due to the fact that the composition of Bloch harmonics for these competitors changes abruptly with number of corrugations. Because of mode conversion the competing modes can have volumetric field pattern for some N. In this case, their ohmic Q-values exceed those of the first-harmonic WG modes of the smooth-walled gyrotron cavity.

One can conclude from the above discussion that the optimal number of longitudinal corrugations for the cavity of the 0.3-THz second-harmonic gyrotron equals 15. First, for $N = 15$ the operating TE$_{13,2}$ mode is in the form of pure fundamental Bloch harmonic. Second, this mode features sufficiently high beam-wave coupling coefficient and ohmic Q-value. Third, first-harmonic competing modes are well separated from the operating mode and are somewhat suppressed by ohmic losses in the corrugated cavity. Finally, compared to the operating mode, the competing modes suffer from larger degradation of the beam-wave coupling strength in the gyrotron cavity equipped with 15 longitudinal corrugations. This can be seen from Table 1, where $C_1^{(0)}$ ($s = 1$) and $C_2^{(0)}$ ($s = 2$) are the coefficients of beam coupling with TE$_{8,1}$ and TE$_{13,2}$ modes of the smooth-walled gyrotron cavity, respectively. Thus, the optimized corrugations are expected to improve the selectivity properties of the cavity for the 0.3-THz second-harmonic gyrotron.

Table 1. Beam-wave coupling coefficients for the operating ($s = 2$, $m = 13$) and competing ($s = 1$, $m = 7, 8$) modes of the corrugated gyrotron cavity with $R = 0.32$ cm, $d = 0.05$ cm, $w = 0.02$ cm, and $N = 15$

Mode	χ	C_s	$C_s / C_s^{(0)}$
$m = 13$	19.92	0.017	0.97
$m = 7$	10.76	0.0078	0.68
$m = 8$	10.76	0.0102	0.89

BEAM-WAVE INTERACTION IN A CORRUGATED CAVITY FOR THE 0.3-THZ SECOND-HARMONIC GYROTRON

For the 0.3-THz second-harmonic gyrotron equipped with original smooth-walled cavity, the starting currents of the operating second-harmonic TE$_{13,2}$ mode and competing first-harmonic TE$_{8,1}$ mode are depicted in Fig. 5a by the dashed lines (see also [11]). One can see that the operating mode is the only oscillating mode in the wide range of magnetic fields from 5.78 T to 6.08 T, provided that the beam current equals 10 A. At the same time, at higher beam

currents the competing $TE_{8,1}$ mode presents a barrier to stable operation of the 0.3-THz second-harmonic gyrotron. Moreover, it seems likely that this mode can completely suppress the operating second-harmonic mode for $I_b \geq 15$.

Longitudinal corrugations with $d = 0.05$ cm, $w = 0.02$ cm and $N = 15$ are used in order to improve mode selection in the cavity of the 0.3-THz second-harmonic gyrotron. The effect of wall corrugations on the starting current of the operating $TE_{13,2}$ mode is shown in Fig. 5a. It is evident that this starting current is somewhat shifted due to corrugations, which have a slight effect on the eigenvalue χ, ohmic Q-value Q_{ohm} and beam-wave coupling coefficient C_s of the operating mode.
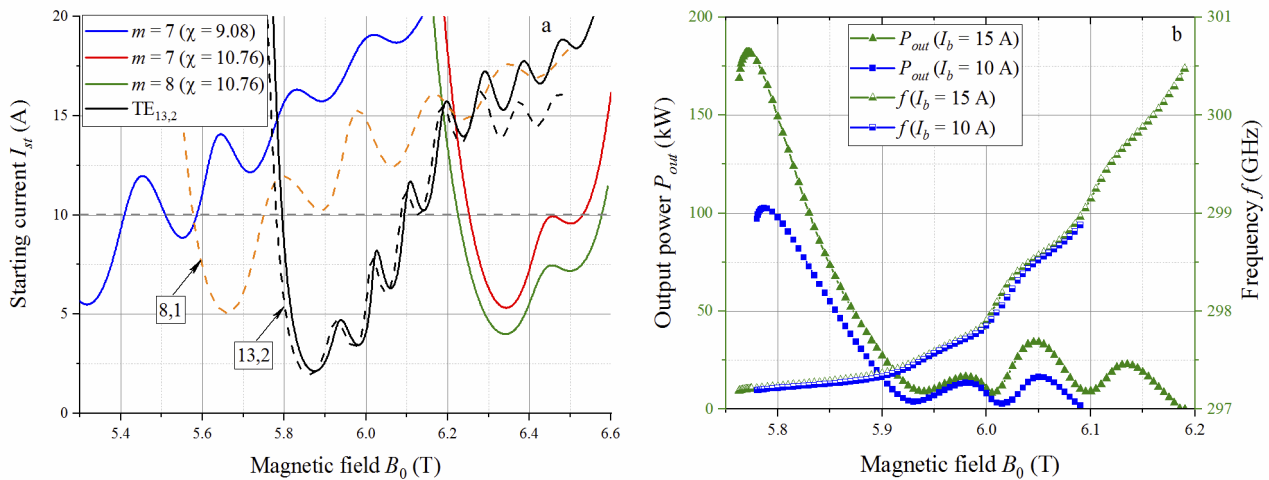
Figure 5. (a) Starting current as a function of the guided magnetic field for the operating $TE_{13,2}$ mode and first-harmonic WG modes of the 0.3-THz second-harmonic gyrotron equipped with optimized corrugated cavity and (b) the gyrotron output power versus B_0 for $I_b = 10$ A and $I_b = 15$ A

In contrast to this, the first-harmonic competing modes of the 0.3-THz second-harmonic gyrotron are radically altered by corrugations of the cavity wall. Fig. 5a shows the starting currents for the most dangerous modes, which lie close to the gyrotron operating region. Among them, there are no modes with azimuthal index $m = 9$. The remaining competing modes have the form of coupled Bloch harmonics with $|k_n| = 7$ and $|k_n| = 8$. This is because 15 corrugations of the gyrotron cavity induce coupling between co-rotating fundamental harmonics with $m = +7$ and $m = +8$ and counter-rotating negative first harmonics with $k_{-1} = -8$ and $k_{-1} = -7$, respectively. Such two pairs of coupled Bloch harmonics form two cavity modes, which have identical eigenvalues and differ in beam-wave coupling strength. Examples are two modes having the eigenvalue $\chi = 9.08$. Among them, the mode with $k_0 = m = +7$ exhibits the strongest coupling with electron beam and therefore has a fairly small starting current (Fig. 5a). By contrast, the other mode with $k_0 = m = +8$ is weakly coupled with beam and has the starting current larger than 22 A, which is far apart from the oscillation region of the operating $TE_{13,2}$ mode. As is seen from Fig. 5a, application of the cavity with optimized longitudinal corrugations extends a single-mode oscillation region of the 0.3-THz second-harmonic gyrotron. As a consequence, the operating mode becomes free from any competing modes for the beam currents up to 15 A. This situation is favorable for increasing the output power of the 0.3-THz second-harmonic gyrotron.

Fig. 5b shows the output power of the 0.3-THz second-harmonic gyrotron versus magnetic field for $I_b = 10$ A and $I_b = 15$ A. One can see that increase in beam current from 10 A to 15 A makes it possible to enhance the peak output power from 100 kW to 180 kW and widens the frequency tuning range of the operating $TE_{13,2}$ mode. It should be stressed that the operating mode is the sole oscillating mode in this range. Thus, there are no obstacles for stable single-mode operation of the 0.3-THz second-harmonic gyrotron with increased beam current and output power.

However, along with beneficial properties of the corrugated cavity for the 0.3-THz second-harmonic gyrotron, there is a drawback. The operating mode undergoes conversion to high-order Bloch harmonics in the output up-tapered section of the cavity. The reason is that, in this section, increase in cavity radius enlarges the cutoff wavelength λ of the operating mode and thus causes an increase between $\lambda/2$ and corrugation depth $d = 0.05$ cm. The operating $TE_{13,2}$ mode converts to Bloch harmonics with $k_{-1} = -2$ and $k_{-2} = -17$ in the output cavity section. As a consequence, the purity of this mode falls to about 90% in the output cross-section ($z = z_{out}$) of the cavity. Such a degradation of the output mode purity is shown in Fig. 6 and should be taken into design consideration for the RF output system of the 0.3-THz second-harmonic gyrotron.
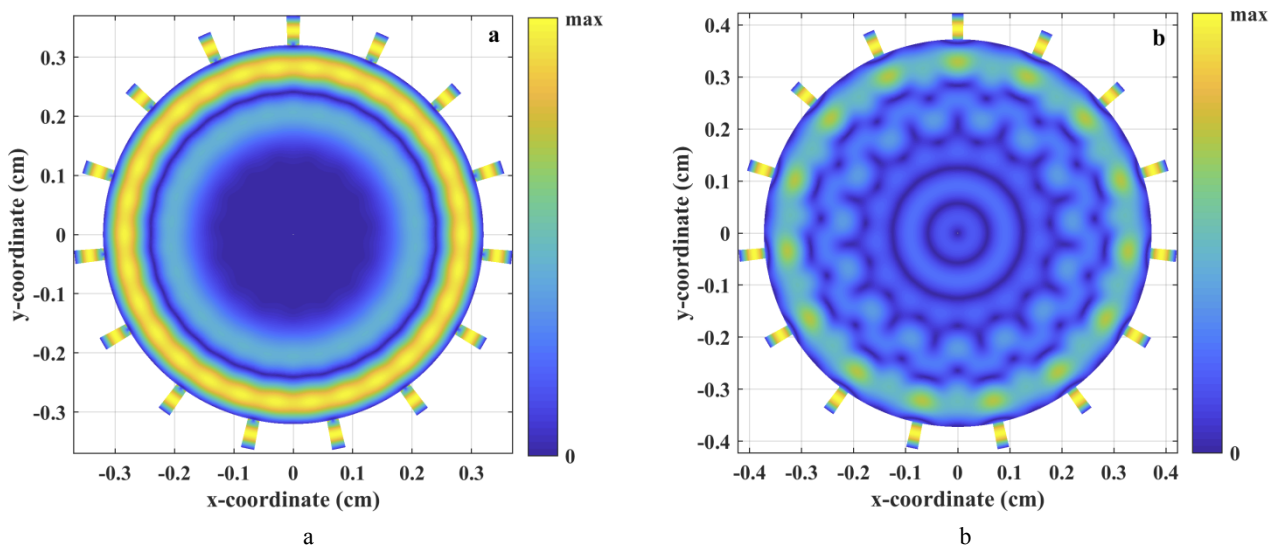
Figure 6. The transverse structure of the azimuthal electric field $\left|E_\varphi\right|$ of the operating mode in (a) the main section and (b) output end of the corrugated cavity for the 0.3-THz second-harmonic gyrotron

CONCLUSIONS

Longitudinal wedge-shaped corrugations are used to improve the selectivity properties of the cavity for second-harmonic gyrotron. As an example, a 0.3-THz second-harmonic gyrotron designed for CTS diagnostics of fusion plasmas is considered. The gyrotron operates in the $TE_{13,2}$ mode and its power-handling capability is limited by competition from the first-harmonic whispering-gallery modes. The full-wave method of coupled azimuthal harmonics is applied to investigate the eigenvalues, ohmic losses and beam-wave coupling coefficients of the second-harmonic operating and first-harmonic competing modes as functions of dimensions of a corrugated gyrotron cavity. For this cavity of the radius $R = 0.32$ cm, the optimal depth $d = 0.05$ cm, width $w = 0.02$ cm and number $N = 15$ of corrugations are determined. Such optimized corrugations are shown to have a little effect on the operating second-harmonic mode, but cause rarefaction of the spectrum of the first-harmonic competing modes. The latter fact provides the possibility to extend the single-mode oscillation range of the operating mode to higher beam currents as demonstrated by the self-consistent theory of beam-wave interaction in the corrugated gyrotron cavity. For the 0.3-THz second-harmonic gyrotron, this enables the operating beam current to be increased from 10 A to 15 A. Such increase in beam current is shown to imply the increase of the gyrotron output power from 100 kW to 180 kW and thus provides further improvement in performance of the 0.3-THz second-harmonic gyrotron. In output wave radiated from the corrugated cavity of this gyrotron, the content of the operating mode is found to be about 90%. This disadvantage calls for further investigation, but does not negate the advantages of using mode-converting wall corrugations in cavities of second-harmonic gyrotrons.

ORCID IDs

Tetiana I. Tkachova, https://orcid.org/0000-0002-4605-3429; **Vitalii I. Shcherbinin**, https://orcid.org/0000-0002-9879-208X
Viktor I. Tkachenko, https://orcid.org/0000-0002-1108-5842

REFERENCES

[1] R.J. Temkin, Int. J. Terahertz Sci. Technol. **7**(1), 1-9 (2014), https://doi.org/10.11906/TST.001-009.2014.03.01.
[2] M.Y. Glyavin, T. Idehara, and S.P. Sabchevski, IEEE Trans. Terahertz Sci. Technol. **5**(5), 788-797 (2015), https://doi.org/10.1109/TTHZ.2015.2442836.
[3] M. Blank, P. Borchard, S. Cauffman, K. Felch, M. Rosay, and L. Tometich, Int. J. Terahertz Sci. Technol. **7**(4), 177-186 (2016), https://doi.org/10.11906/TST.177-186.2016.12.17.
[4] M. Thumm, J. Infrared Millim. Terahertz Waves **41**(1), 1-140 (2020), https://doi.org/10.1007/s10762-019-00631-y.
[5] T. Notake, T. Saito, Y. Tatematsu, A. Fujii, S. Ogasawara, L. Agusu, I. Ogawa, T. Idehara, and V.N. Manuilov, Phys. Rev. Lett. **103**(22), 225002 (2009), https://doi.org/10.1103/PhysRevLett.103.225002.
[6] T. Saito, N. Yamada, S. Ikeuti, S. Ogasawara, Y. Tatematsu, R. Ikeda, I. Ogawa, T. Idehara, V.N. Manuilov, T. Shimozuma, S. Kubo, M. Nishiura, K. Tanaka, and K. Kawahata, Phys. Plasmas **19**(6), 063106 (2012), https://doi.org/10.1063/1.4729316.

[7] T. Saito, S. Tanaka, R. Shinbayashi, Y. Tatematsu, Y. Yamaguchi, M. Fukunari, S. Kubo, T. Shimozuma, K. Tanaka, and M. Nishiura, Plasma Fusion Res. **14**, 1406104 (2019), https://doi.org/10.1585/pfr.14.1406104.

[8] K.A. Avramides, C.T. Iatrou, and J.L. Vomvoridis, IEEE Trans. Plasma Sci. **32**(3), 917-928 (2004), https://doi.org/10.1109/TPS.2004.828781.

[9] K.A. Avramides, J.L. Vomvoridis, and C.T. Iatrou, in: *AIP Conference Proceedings* **807**, 264-270 (2006), https://doi.org/10.1063/1.2158787.

[10] V.I. Shcherbinin, V.I. Tkachenko, K.A. Avramides, and J. Jelonnek, IEEE Trans. Electron Devices **66**(12), 5313-5320 (2019), https://doi.org/10.1109/TED.2019.2944647.

[11] V.I. Shcherbinin, Y.K. Moskvitina, K.A. Avramides, and J. Jelonnek, IEEE Trans. Electron Devices **67**(7), 2933-2939 (2020), https://doi.org/10.1109/TED.2020.2996179.

[12] V.I. Shcherbinin, K.A. Avramides, M. Thumm, and J. Jelonnek, J. Infrared Millim. Terahertz Waves **42**(1), 93-105 (2021), https://doi.org/10.1007/s10762-020-00760-9.

[13] T.I. Tkachova, V.I. Shcherbinin, and V.I. Tkachenko, J. Infrared Millim. Terahertz Waves **40**(10), 1021-1034 (2019), https://doi.org/10.1007/s10762-019-00623-y.

[14] T.I. Tkachova, V.I. Shcherbinin, V.I. Tkachenko, Z.C. Ioannidis, M. Thumm, and J. Jelonnek, J. Infrared Millim. Terahertz Waves **42**(3), 260-274 (2021), https://doi.org/10.1007/s10762-021-00772-z.

[15] J.B. Davies, Proc. IEE-Part C **109**(15), 162-171 (1962), https://doi.org/10.1049/pi-c.1962.0022.

[16] T. Scharten, J. Nellen, and F. van den Bogaart, Proc. IEE-Part H **128**(3), 117-123 (1981), https://doi.org/10.1049/ip-h-1.1981.0019.

[17] C.T. Iatrou, S. Kern, and A.B. Pavelyev, IEEE Trans. Microw. Theory Techn. **44**(1), 56-64 (1996), https://doi.org/10.1109/22.481385.

[18] V.I. Shcherbinin, and V.I. Tkachenko, J. Infrared Millim. Terahertz Waves **38**(7), 838-852 (2017), https://doi.org/10.1007/s10762-017-0386-x.

[19] V.I. Shcherbinin, B.A. Kochetov, A.V. Hlushchenko, and V.I. Tkachenko, IEEE Trans. Microw. Theory Techn. **67**(2), 577-583 (2019), https://doi.org/10.1109/TMTT.2018.2882493.

[20] T.I. Tkachova, V.I. Shcherbinin, and V.I. Tkachenko, in: *Proc. Int. Conf. Math. Methods Electromagn. Theory (MMET'2018)* (Kyiv, Ukraine, 2018), pp. 238-241, https://doi.org/10.1109/MMET.2018.8460433.

[21] T.I. Tkachova, V.I. Shcherbinin, and V.I. Tkachenko, Problems Atomic Sci. Technol. **6**(118), 67-70 (2018), http://dspace.nbuv.gov.ua/handle/123456789/148829.

[22] T.I. Tkachova, V.I. Shcherbinin, and V.I. Tkachenko, Problems Atomic Sci. Technol. **4**(122), 31-34 (2019), https://vant.kipt.kharkov.ua/ARTICLE/VANT_2019_4/article_2019_4_31.pdf.

[23] V.I. Shcherbinin, A.V. Hlushchenko, A.V. Maksimenko, and V.I. Tkachenko, IEEE Trans. Electron Devices **64**(9), 3898-3903 (2017), https://doi.org/10.1109/TED.2017.2730252.

ГОФРИ З КОНВЕРСІЄЮ МОД ДЛЯ РЕЗОНАТОРІВ ГІРОТРОНІВ НА ДРУГІЙ ЦИКЛОТРОННІЙ ГАРМОНІЦІ ІЗ ПОЛІПШЕНИМИ РОБОЧИМИ ХАРАКТЕРИСТИКАМИ

Т.І. Ткачова[a], В.І. Щербінін[a], В.І. Ткаченко[a,b]
[a]Національний науковий центр "Харківський фізико-технічний інститут", 61108 Харків, Україна
[b]Харківський національний університет ім. В.Н. Каразіна, 61022 Харків, Україна

Досліджено новий метод поліпшення селекції мод в резонаторах суб-терагерцових гіротронів, які працюють на другій гармоніці циклотронної частоти. Як приклад розглянуто гіротрон на другій циклотронній гармоніці з частотою 0.3 ТГц. Гіротрон розробляється для застосування в системі діагностики термоядерної плазми на основі колективного Томсонівського розсіювання (CTS) та характеризується обмеженою потужністю внаслідок конкуренції робочої $TE_{13,2}$ моди з модами на першій циклотронній гармоніці. Для пригамування конкуруючих мод на першій гармоніці в резонаторі гіротрона застосовані періодичні поздовжні гофри, що викликають зв'язок нормальних базисних мод, відомих як азимутальні гармоніки Блоха. Глибина цих гофрів була обрана близькою до половини та чверті довжини хвилі для робочої моди гіротрона та конкуруючих мод на першій циклотронній гармоніці, відповідно. За такої умови поздовжні гофри на стінці резонатора мають, як правило, лише неістотний вплив на робочу моду, але разом із тим можуть призводити до сильної конверсії конкуруючих мод у гармоніки Блоха високого порядку. Строгий метод зв'язаних азимутальних гармонік застосовано для дослідження впливу розмірів гофрованого резонатора на власні значення, омічні втрати та коефіцієнти зв'язку з пучком для робочої $TE_{13,2}$ моди та найбільш небезпечних конкуруючих мод. За допомогою самоузгодженої теорії взаємодії пучка з робочою та конкуруючими модами визначені найбільш оптимальні параметри резонатора гіротрона із поздовжніми гофрами, які забезпечують найширший діапазон одномодової роботи 0.3-ТГц гіротрона на другій циклотронній гармоніці. Показано, що в даному діапазоні вихідна потужність гіротрона може бути збільшена зі 100 кВт до 180 кВт, як того потребує CTS діагностика плазми. Виявлено, що модова чистота на виході із резонатора 0.3-ТГц гіротрона на другій циклотронній гармоніці погіршується через гофрування резонатора, яке призводить до небажаного зв'язку робочої моди $TE_{13,2}$ із сусідніми гармоніками Блоха у вихідній секції резонатора гіротрона.

КЛЮЧОВІ СЛОВА: гіротрон, циклотронна гармоніка, резонатор, гофри з конверсією мод, стартовий струм, вихідна потужність.

SEMICLASSIC MODELS OF THE DISSIPATIVE REGIME OF INSTABILITY AND SUPERRADIATION OF A QUANTUM RADIATOR SYSTEM

Volodymyr M. Kuklin*, Valentin T. Lazurik, Eugen V. Poklonskiy
V.N. Karazin Kharkiv National University, Kharkiv, Ukraine
Svobody Sq. 4, Kharkiv, Ukraine, 61022
*Corresponding Author: kuklinvm1@gmail.com
Received March 2, 2021; revised April 4, 2021; accepted April 10, 2021

The paper discusses the similarity between dissipative generation and superradiance regimes for systems of excited quantum emitters placed in an open cavity. In the case of the existence of a resonator field due to reflections from the ends of the system, a dissipative generation regime is usually realized. In this case, the decrement of oscillations in the waveguide in the absence of radiators turns out to be greater than the increment of the arising instability of the system of radiators placed in the resonator. When describing this mode, the influence of the emitters on each other and the sum of their own fields is neglected. The resonator field forces the oscillators to emit or absorb quanta synchronously with it, depending on the local value of the population inversion. Lasing takes on a weakly oscillatory character due to an asynchronous change in the population inversion of the system of emitting dipoles (nutations), which have a ground and excited energy levels. To describe the process, the equations of the semiclassical theory based on the use of the density matrix are quite sufficient. In the case when there is no resonator or waveguide field, taking into account the eigenfields of the oscillators becomes essential. To simulate the superradiance process, large emitting particles are used, to describe which one should use the equations for the density matrix. It is shown that the interaction of quantum emitters in this case is due to electromagnetic fields under conditions when the overlap of their wave functions is insignificant. Equations are obtained that allow considering the process of interaction of emitters. When the emitters interact, an integral field is formed in the resonator, an increase in the intensity of which leads to synchronization of the emitters. It is shown that the characteristic times of the development of the process, as well as the attainable amplitudes of the excited fields for dissipative regimes of generation and regimes of superradiance of emitters filling an open resonator, are comparable.
KEYWORDS: dissipative regimes of generation, superradiance, open resonator.

In the well-known work [1] R. Dicke, considering the interaction of oscillators or emitters, which are actually combined into one quasiparticle, discovered the possibility of their coherent radiation. Moreover, in the quantum case, we can talk not about the phase synchronization of the oscillators, as in the classical consideration, but only about an increase in the probability of radiation, which actually leads to the same result. The overlap of their wave functions leads to an increase in the probability of spontaneous emission of this quasiparticle in comparison with the probability of emission of individual oscillators or emitters[1] [2].

If the oscillators or emitters are separated in space, the overlap of their wave functions becomes imperceptible[2]. The interaction of quantum emitters in this case is due to electromagnetic fields. In this case, the Rabi frequency determines the oscillatory nature of the change in the population inversion of the system of emitting dipoles (nutations), which have a ground and excited energy levels. The probabilities of stimulated emission and absorption of field quanta are also determined by the Rabi frequency [3].

In open systems, when the reflection of waves from the boundaries of the system is weakened, dissipative generation modes and superradiance modes can be realized [2, 4-8].

A resonator or waveguide field, the intensity of which is sufficiently high in the case of low energy losses, is formed due to reflections from the ends of the system. In this case, the influence of emitters on each other can often be neglected. The field of the resonator or waveguide forces some of the oscillators to emit and absorb quanta synchronously with it, providing a significant coherence [9]. This stimulated emission usually exceeds the sum of incoherent emitters eigenfields; therefore, taking them into account in such a regime of instability development is often insignificant.

In the superradiance mode, a resonator or waveguide field may not be present in the system of oscillators, since these modes are realized in open systems with weak reflection of the excited oscillations from the ends of the system. In a quantum system, at large values of the number of excited oscillators and their tight localization, spontaneous emission at a high density of emitters remains, as a rule, extremely insignificant in relation to the radiation induced.

Usually, in the absence of a resonator or waveguide field, the total field of such spontaneous electromagnetic emission very large number of particles of the active substance (which emit only one quantum in a rather arbitrary chaotic manner) is inversely proportional to their number and not able to synchronize them. However, with the use of an initiating external field capable of synchronizing the emitters, the superradiance regime may well be realized. If the number of emitters is small, the levels of the total spontaneous electromagnetic radiation may be sufficient to form an integral field that synchronizes the emitters, as shown below. In open systems, with a sufficiently high level of radiation from the ends

---

[1] That is, the coherence of radiation of a bunch of particles, the size of which is much smaller than the wavelength, is found both in the quantum description of this phenomenon and in the classical one.
[2] The velocity distribution of free electrons in semiconductors is indicative in this sense [9].

of the system, both a dissipative excitation mode of a waveguide or resonator field by non-interacting with each other emitters, and a superradiance mode of the system, when there is no waveguide field, and each emitter participates in creating a sufficiently intense integral field, are possible.

The aim of this work is to consider the features of dissipative generation regimes and superradiance regimes for systems of excited quantum emitters placed in an open resonator.

This is first of all comparison of the characteristic times of these processes, as well as the attainable amplitudes of the excited fields. The similarity of the superradiance regimes and dissipative regimes of generation of quantum oscillators is shown in this case.

DESCRIPTION OF GENERATION PROCESSES BY A SYSTEM OF QUANTUM EMITTERS

Thus, it is rational to consider the behavior of emitters in a quantum-mechanical way, and the field - in the classical representation. Below, we will consider the behavior of quantum emitters, the wave functions of which do not overlap and their interaction is determined only by the electromagnetic field. In this case, a semiclassical description model based on the use of a density matrix is applicable. Neglecting relaxation processes, the equations for the components of the density matrix can be written in the form

$$\frac{d}{dt}(\rho_{aa} - \rho_{bb}) = -\frac{2i}{\hbar}[d_{ba}\rho_{ab} - d_{ab}\rho_{ba}]E , \tag{1}$$

$$\frac{d}{dt}\rho_{ab} + i\omega_{ab}\rho_{ab} = -\frac{i}{\hbar}(\rho_{aa} - \rho_{bb})d_{ab}E , \tag{2}$$

where the electric field is represented in the form $E + E^* = A(t) \cdot \exp\{-i\omega t\} + A^*(t) \cdot \exp\{i\omega t\}$, and the rapidly changing polarization of one emitter has the form $d_{ba}\rho_{ab} + d_{ab}\rho_{ba}$. From $\rho_{ab} = \overline{\rho}_{ab}e^{-i\omega_{ab}t} = \overline{\rho}_{ab}e^{-i\omega t}$ let us determine slowly changing quantities for the polarization of the emitter $\overline{p} = d_{ba} \cdot \overline{\rho}_{ab}$ and $d_{ab}\overline{\rho}_{ba} = d^*_{ba} \overline{\rho}^*_{ab} = \overline{p}^*$ also write down the system of equations for the inversion of one emitter $\overline{\mu} = (\rho_{aa} - \rho_{bb})$ and $\overline{p}$:

$$\frac{d}{dt}(\rho_{aa} - \rho_{bb}) = -\frac{2i}{\hbar}[d_{ba}\overline{\rho}_{ab}A^* - d_{ab}\overline{\rho}_{ba}A] = -\frac{2i}{\hbar}[\overline{p}A^* - \overline{p}^*A] , \tag{3}$$

$$\frac{d}{dt}\overline{p} = -\frac{i}{\hbar}(\rho_{aa} - \rho_{bb})\,|\,d_{ba}\,|^2\;A . \tag{4}$$

Using these representations, one can obtain equations for the semiclassical model. In the one-dimensional case, which we restrict ourselves to, for perturbations of the electric field E, polarization P, and population inversion slowly varying with time μ, describing the excitation of electromagnetic oscillations in a two-level active medium, whose equations can be represented as (see, for example, [11, 12])

$$\frac{\partial^2 E}{\partial t^2} + \delta\frac{\partial E}{\partial t} - c^2\frac{\partial^2 E}{\partial x^2} = -4\pi\frac{\partial^2 P}{\partial t^2} , \tag{5}$$

$$\frac{\partial^2 P}{\partial t^2} + \gamma_{12}\frac{\partial P}{\partial t} + \omega^2 \cdot P = -\frac{2\omega\,|\,d_{ab}\,|^2}{\hbar}\mu E , \tag{6}$$

$$\frac{\partial \mu}{\partial t} = \frac{2}{\hbar\omega} < E\,\frac{\partial P}{\partial t} > , \tag{7}$$

where the frequency ω of the transition between the levels corresponds to the frequency of the field, we neglect the relaxation of the inversion due to external causes, δ is the decrement of absorption of the field in the medium, d_{ab} is the matrix element of the dipole moment (more precisely, its projection onto the direction of the electric field), $\mu = n \cdot (\rho_a - \rho_b)$ the difference in populations per unit volume, ρ_a and ρ_b the relative populations of levels in absence of a field, γ_{12} is the width of the spectral line, n is the density of the dipoles of the active medium.

Here, the linewidth is inversely proportional to the lifetime of the states, which is due to relaxation processes. The fields are represented as $E = [E(t) \cdot \exp\{-i\omega t\} + E^*(t) \cdot \exp\{i\omega t\}]$ and $P = [P(t) \cdot \exp\{-i\omega t\} + P^*(t) \cdot \exp\{i\omega t\}]$. Wherein $< E^2 >= 2\,|\,E(t)\,|^2$. The number of field quanta is then equal $< E^2 > /4\pi\hbar\omega = 2\,|\,E\,|^2\,/4\pi\hbar\omega = N$. For slow varying amplitudes, the equations

$$\frac{\partial E}{\partial t} + \delta_D \cdot E = 2i\pi\omega P , \tag{8}$$

$$\frac{\partial P(t)}{\partial t} + \gamma_{12} P(t) = \frac{|d_{ab}|^2}{i\hbar} \mu E,$$
(9)

$$\frac{\partial \mu}{\partial t} = \frac{2i}{\hbar} [E(t)P*(t) - E*(t)P(t)],$$
(10)

here we additionally took into account the line width γ_{12}.

From equation (6), by simple transformations, we find

$$\frac{\partial N}{\partial t} + 2\delta N = \frac{i}{\hbar} \cdot [P(t)E*(t) - P*(t)E(t)],$$
(11)

where you can get the conservation law

$$\frac{\partial N}{\partial t} + 2\delta N + \frac{\partial \mu}{2\partial t} = 0.$$
(12)

DISSIPATIVE GENERATION MODE

We are interested in the case of a large level of radiation losses ($\Theta > 1$) in a resonator filled with an active substance. We believe that the emitters do not interact with each other, but exchange energy only with the integral field of the resonator. The increment of such dissipative instability is equal $\gamma = \tilde{\gamma}_0^2 / \delta_D \gg \gamma_{12}$, that is, it significantly exceeds the natural line width, where the role of the nondissipative increment $\tilde{\gamma}_0 = \Omega_0 / \sqrt{2}$ is actually taken over by the Rabi frequency $\Omega_0 = 2|d_{ab}||E_\mu|/\hbar$, where $< E >_\mu^2 = 2|E_\mu|^2 = [4\pi\hbar\omega\mu_0]^{1/2}$. The equations that describe the radiation process of a quantum source (occupying a region b the size of the radiation wavelength) take the form

$$\frac{\partial M}{\partial \tau} = -N,$$
(13)

$$\frac{\partial N}{\partial \tau} = M \cdot N,$$
(14)

where $M = \mu / \mu_0$, $N = 4(\delta_D^2 / \tilde{\gamma}_0^2) \cdot (N / \mu_0)$, $N = < E >^2 / 4\pi\hbar\omega$ - is the number of quanta,

$\delta_D = (\int_S c < E >^2 / 4\pi) \cdot dS / \int_V (< E >^2 / 4\pi) \cdot dV \approx c / b$ is the effective decrement of the resonator field in the

absence of an active medium, b is the size of the resonator. Along the length of the system b, as in [13,14], we arrange the sectors

$$N_j(\tau = 0) = 2 \cdot N(\tau = 0) \cdot \text{Sin}^2 \{2\pi \frac{j}{S} + \alpha\},$$
(15)

moreover

$$N(\tau) = \frac{1}{S} \sum_{j=1}^{S} N_j(\tau)$$
(16)

Equations (13) - (14) for the sectors are:

$$\frac{\partial M_j}{\partial \tau} = -N_j,$$
(17)

$$\frac{\partial N_j}{\partial \tau} = M_j \cdot N_j,$$
(18)

moreover

$$M(\tau) = \frac{1}{S} \sum_{j=1}^{S} M_j(\tau),$$
(19)

Parameters: $N(\tau = 0) = 1/3600$, $M(\tau = 0) = M_j(\tau = 0) = 1$, $S = 100$.

Figures 1 and 2 show the time dependence of the average number of quanta N and inversion M.
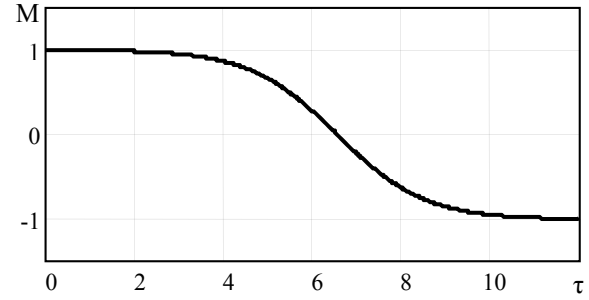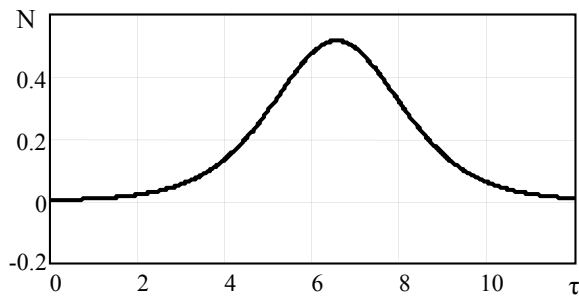
Figure 1. Time dependence of the average number of quanta N.   **Figure 2.** Time dependence of the mean inversion M.

Figure 3 shows the distribution of the inversion over the sectors Mj at different times: at the time of growth ($\tau = 4.5$), maximum ($\tau = 6.55$) and decrease ($\tau = 10$) of the number of quanta (see Fig. 1).

$\tau=4.5$ $\tau=6.55$(maximum of N) $\tau=10$
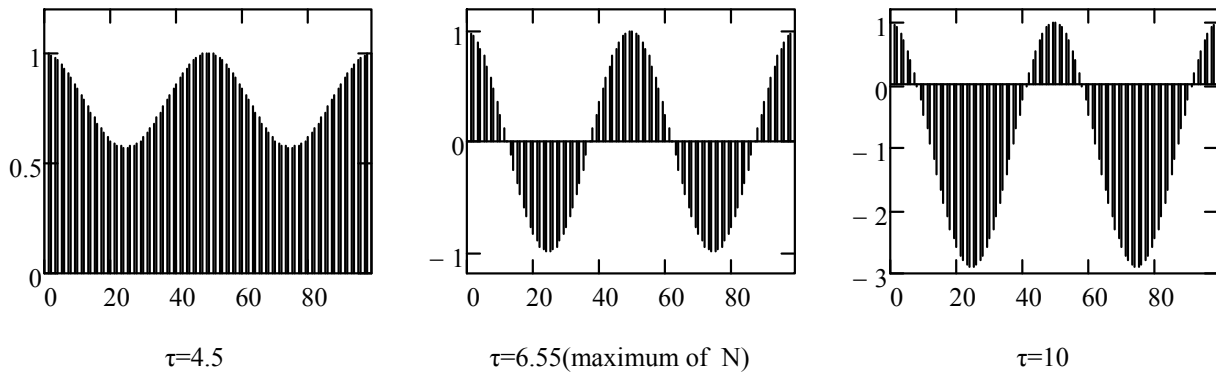
Figure 3. Distribution of inversion by sectors M_j at different points in time

SUPER RADIATION MODE

Previously, we considered the interaction of emitters with the field of a waveguide or resonator, and the emitters did not directly affect each other. In the same section, we will consider the interaction of emitters only with each other in the absence of an external resonator field. This interaction mode, with emerging self-synchronization of field generation sources, can be considered a superradiance mode. The equation for the field of an individual radiator is

$$\frac{\partial^2 E}{\partial t^2} - c^2 \frac{\partial^2 E}{\partial z^2} = 4\pi\omega^2 \cdot \overline{p} \cdot \mathrm{e}^{-i\omega t} \cdot \delta(z_0) , \tag{20}$$

where can we find the value

$$A(z,t) = \frac{i \cdot 2\pi \cdot \omega \cdot M}{c} \cdot \frac{1}{N} \sum_s \overline{p}(z_s, t) \cdot e^{ik|z-z_s|} , \tag{21}$$

where $M = n_0 \cdot b$ is the total number of emitters, and n_0 is the density of emitters per unit length.
From equations (1) - (3) we obtain a system of equations for the polarization and inversion of the j-th large particle-emitter.
where can we find the value

$$\frac{d}{dt}(\rho_{aa} - \rho_{bb}) = \frac{2i}{\hbar}[\overline{p}*A - \overline{p}A*] , \tag{22}$$

$$\frac{d}{dt}\overline{p} = -\frac{i}{\hbar}(\rho_{aa} - \rho_{bb})|d_{ba}|^2 A , \tag{23}$$

using the relations $P_j = P(z_j, \tau)$, $M_j = M(z_j, \tau)$, as well as $\mu_0 = \mu_j(\tau = 0)$,

$$z = \frac{2\pi}{k} Z, \quad \mu = \mu_0 \cdot M, \quad \bar{p} = |d_{ab}| \cdot \mu_0 \cdot P, \quad t = \tau / \gamma, \quad \Gamma_{12} = \frac{\gamma_{12}}{\gamma}, \quad n_0 \cdot b = M, \quad \text{where} \quad \gamma = \frac{2\pi \cdot \omega \cdot |d_{ba}|^2 \cdot \mu_0 \cdot n_0 \cdot b}{\hbar c} \text{ is the increment of}$$

the process, we write system (20) - (21) in the form

$$\frac{d}{dt} M_j = -2 \cdot [P_j * A_j + P_j A_j *], \tag{24}$$

$$\frac{d}{dt} P_j = M_j \cdot A_j, \tag{25}$$

where for $A_j = A(Z_j, \tau)$ the relation

$$A(Z, \tau) = \frac{1}{N} \sum_s P(Z_s, \tau) \cdot e^{i 2\pi |Z - Z_s|}. \tag{26}$$

The last expression can be represented as $A(Z, \tau) = |A(Z, \tau)| \cdot e^{i\varphi(Z, \tau)}$, $\varphi(Z, \tau)$ is the phase of the field at point Z. It should be borne in mind that for the dimensionless representation of the field we have divided by $\gamma \hbar / |d_{ba}|$. Then, for the total amplitude of the electric field in this normalization, the expression $E = 2|A(Z, \tau)|$ is valid.

It is important to note that the growth rate $\gamma = 2\pi \cdot \omega \cdot |d_{ba}|^2 \cdot \mu_{01} \cdot n_0 \cdot b / \hbar c$ in the semiclassical model of superradiance corresponds to the growth rate $\gamma = \tilde{\gamma}_0^2 / \delta_D$ of dissipative instability.

For 4000 emitters distributed at the wavelength, at $P_j(\tau = 0) = P_0 \exp(i\psi_j)$, where the polarization phases ψ_j of the emitters are random values $\psi_j \subset (0 \div 2\pi)$, $P_0 = 0.1$, $M(\tau = 0) = 1$, $\Gamma_{12} = 0$, we obtain the following results of the numerical solution. Figure 4 shows the time dependences of the field amplitude on the left and right of the system and the maximum inside the emitter and the average inversion of the system. Figure 5 shows the time dependence of the mean inversion of the system.
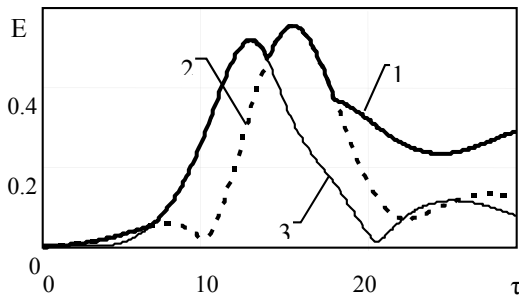
Figure 4. Dependence of the field amplitude on time, $1 - \max_Z(E(Z, \tau))$, $2 - E(Z = 0, \tau)$, $3 - E(Z = 1, \tau)$.
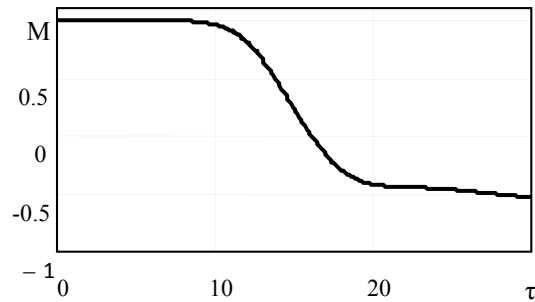
Figure 5. Dependence of the average inversion of the system $M = \frac{1}{N} \sum_j M(Z_j, \tau)$ on time

As can be seen from Figures 4 and 5, energy is pumped from the system of emitters into the electromagnetic field. The field has two approximately equal maxima at times $\tau = 13.2$ (E = 0.52) and $\tau = 15.8$ (E = 0.555). The first maximum is on the right edge of the system (Z = 1), the second is on the left (Z = 0). When setting other random initial phases of the polarization of the emitters, the field maximum of approximately the same magnitude and at approximately the same time was observed only at one of the edges of the system.

From the initial moment to reaching the maximum, the formation of a field with a minimum in the middle of the system is observed. In this case, there also occurs (mainly in the region of high fields) a decrease in the inversion and an increase in the polarization modulus. The polarization phases are also synchronized. The polarizations of neighboring emitters are rather quickly collected in a narrow band of angles. In the region of maximum fields, the polarization phases of the emitters are also synchronized with the field phase. This leads to the fact that the difference between the phase of the polarization of the emitter at a point and the phase of the field at this point is close to zero. Figure 6 shows the distributions of some characteristics at the moment $\tau = 15.8$ (the second maximum of the field on the left edge)

Figure 6a) demonstrates a field dip in the middle of the system. In fig. 6b) shows the greatest decrease in inversion at the right edge, where the first field maximum was formed; the decrease at the left edge occurs more slowly in accordance with the slower formation of the field maximum in this region.

In the region of the field maximum, the polarization modulus is larger (Fig. 6c) and the greatest synchronization of the polarization phase and the field phase (Fig. 6d). Note that at the instant $\tau = 13.2$, in the region of the field maximum

Semiclassic Models of the Dissipative Regime of Instability and Superradiation...

103
EEJP. 2 (2021)

on the right edge, there was the greatest synchronization of the polarization phase and the field phase, and the inversion decreased.
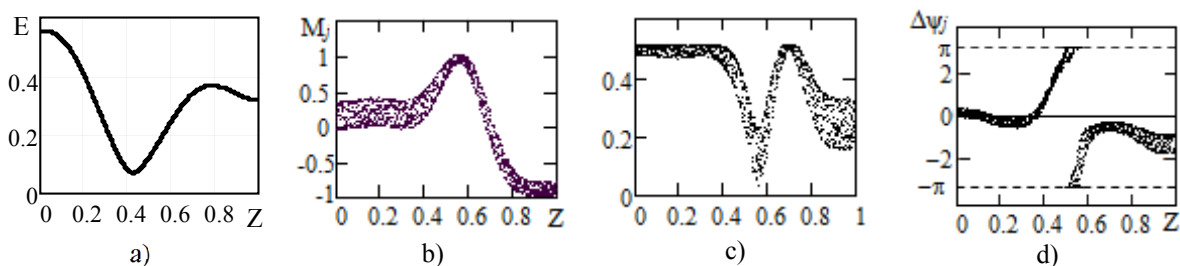
Figure 6. Distribution along the length of the system of quantities
a) field modulus, b) emitter inversion, c) emitter polarization module, d) difference between the polarization phase of the emitter and the field phase.

Further, the field falls rapidly along the edges of the system (faster on the right edge) and an area of relatively larger field in the center is formed, although it does not reach its maximum values. Figure 7-8 shows the field and inversion distribution at $\tau = 30$.
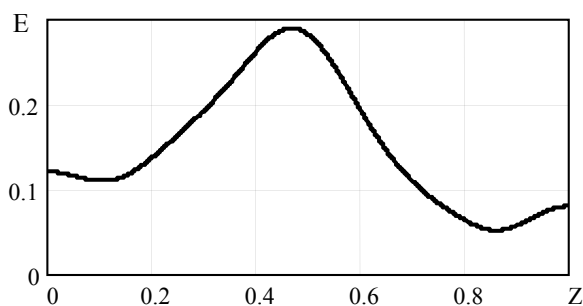
Figure 7. Distribution of the field modulus along the length of the system at $\tau = 30$.
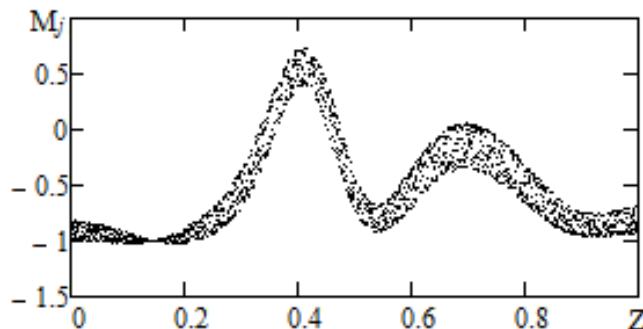
Figure 8. Distribution of the inversion of emitters along the length of the system at $\tau = 30$.

CONCLUSIONS

The similarity of dissipative generation regimes and superradiance regimes for systems of excited quantum emitters placed in an open cavity is shown.

In open systems, with a sufficiently high level of radiation from the ends of the system, both a dissipative excitation mode of a waveguide or resonator field by non-interacting with each other emitters, and a superradiance mode of the system, when there is no waveguide field, and each emitter participates in creating a sufficiently intense integral field, are possible.

The dissipative generation mode is realized in the case of the existence of only a resonator field due to reflections from the ends of the system. For this generation mode, the decrement of oscillations in the waveguide in the absence of emitters turns out to be greater than the increment of the resulting instability of the system of emitters placed in the resonator. The influence of the emitters on each other and the sum of their own fields are neglected. To describe the process, the equations of the semiclassical theory based on the use of the density matrix are quite sufficient.

The superradiance mode can manifest itself in the case when there is no resonator or waveguide field. Then taking into account the eigenfields of the oscillators becomes essential. To simulate the superradiance process, we use large emitting particles, which can be described by equations for the density matrix. It is believed that the interaction of quantum emitters in this case is due to electromagnetic fields under conditions when the overlap of their wave functions is insignificant. When the emitters interact, an integral field is formed in the resonator, an increase in the intensity of which leads to synchronization of the emitters into the cavity volume.

It is shown that the characteristic times of the development of the process, as well as the attainable amplitudes of the excited fields for dissipative regimes of generation and regimes of superradiance of emitters filling an open cavity, are practically the same. The asymmetric behavior of the field in the superradiance regime is associated with the choice of the initial conditions. You can make sure that the field strength in the superradiance mode is expressed in terms of the radiation intensity, that is, where, (see the notation in front of formula (13)).

Two values of the maxima in Fig. 4 correspond to values equal to 0.27 and 0.31, respectively. Thus, for the same resonator, the increments of superradiance and dissipative instability are practically of the same order of magnitude, and the intensities of the excited field turn out to be comparable. The saturation mechanism of instability regime is the decrease of the inversion level and also the appearance of resonator regions where induced attenuation dominates [13,14].

ORCID IDs
Volodymyr M. Kuklin, https://orcid.org/0000-0002-0310-1582; **Valentin T. Lazurik**, https://orcid.org/0000-0002-8319-0764,
Eugen V. Poklonskiy, https://orcid.org/0000-0001-5682-6694

REFERENCES
[1] R.H. Dicke, Phys. Rev. **93**, 99 (1954), https://doi.org/10.1103/PhysRev.93.99.
[2] A.V. Andreev, V.I. Emelyanov, and Yu.A. Il'inskiy, Sov. Phys. Usp. **23**(8)**,** 493–514 (1980). https://doi.org/10.1070/PU1980v023n08ABEH005024.
[3] A.S. Davydov, *Quantum Mechanics*, (Fizmatgiz, Moscow, 1963). pp. 748. (in Russian).
[4] L. Allen, and J. Eberly, *Optical resonance and two-level atoms*, (Witey-lnterscicitce Publication John Witty and Sons, New York-London-Sydney-Toronto, 1975), pp. 222.
[5] A.G. Zagorodniy, P.I. Fomin, and A.P. Fomina, Superradiance of electrons in a magnetic field and a nonrelativistic gyrotron, Dop. NAS of Ukraine, **4**, 75-80 (2004).
[6] L.I. Menshikov, Phys. Usp. **42**, 107 (1999), https://doi.org/10.1070/pu1999v042n02ABEH000521.
[7] I.P. Gabitov, V.E. Zakharov, A.V. Mikhailov, Zh. Eksp. Teor. Fiz. **86**, 1204-1216 (1984), http://www.jetp.ac.ru/cgi-bin/dn/e_059_04_0703.pdf.
[8] V.V. Zheleznyakov, V.V. Kocharovsky, and Vl.V. Kocharovsky, Sov. Phys. Usp. **159**(2) 193-260 (1989), http://dx.doi.org/10.1070/PU1989v032n10ABEH002764.
[9] Ch.H. Townes, **149**, 3686 (1965), https://doi.org/10.1126/science.149.3686.831.
[10] F.G. Bass, and Yu.G. Gurevich, *Hot electrons and strong electromagnetic waves in the plasma of semiconductors and gas discharge,* (Nauka, Mscow, 1975). pp. 400. (in Russian).
[11] Zeyger S.G., Klimontovich Yu. L., P.S. Landa, E.G. Lariontsev, and E.E. Fradkin, *Wave and fluctuation processes in lasers.* (Science, Moscow, 1974).
[12] Landa P.S. *Self-oscillations in distributed systems*. (Nauka, Moscow, 1983), pp. 320.
[13] V.M. Kuklin, and E.V. Poklonskiy, East Eur. J. Phys. **3**, 46–53 (2019), https://doi.org/10.26565/2312-4334-2019-3-06.
[14] V.V. Kostenko, V.M. Kuklin, and E.V. Poklonskiy, PAST, **3**(127), 105-109 (2020), https://vant.kipt.kharkov.ua/ARTICLE/VANT_2020_3/article_2020_3_105.pdf.

НАПІВКЛАЧИСНІ МОДЕЛІ ДИСИПАТИВНОГО РЕЖИМУ НЕСТІЙКОСТІ ТА НАДВИПРОМІНЮВАННЯ СИСТЕМИ КВАНТОВИХ ВИПРОМІНЮВАЧІВ

Куклін В.М., Лазурик В.Т., Поклонский Є.В.
Харківський національний університет імені В.Н. Каразіна, Харків, Україна
Свободи пл. 4, Харків, Україна, 61022

У роботі обговорюється подібність дисипативних режимів генерації та режимів надвипромінювання для систем збуджених квантових випромінювачів, поміщених у відкритий резонатор. У разі існування резонаторного поля за рахунок відбиття від торців системи звичайно реалізується дисипативний режим генерації. При цьому декремент коливань у хвилеводі при відсутності випромінювачів виявляється більше інкремента виникаючої нестійкості системи випромінювачів, поміщеної в резонатор. При описі цього режиму вплив випромінювачів один на одного і сума їх власних полів нехтується. Поле резонатора змушує осцилятори випромінювати або поглинати кванти синхронно з ним, в залежності від локального значення інверсії заселеності. Генерація набуває слабо осциляторний характер через несинхронну зміну інверсії заселеності системи випромінюючих диполів (нутації), що мають основний і збуджений рівні енергії. Для опису процесу цілком достатньо рівнянь напівкласичної теорії, заснованої на використанні матриці щільності. У разі, коли резонаторне або хвилеводне поле відсутнє, врахування власних полів осциляторів стає істотним. Для моделювання процесу надвипромінювання застосовуються великі частки-випромінювачі, для опису яких слід скористатися рівняннями для матриці щільності. Показано, що взаємодія квантових випромінювачів в цьому випадку обумовлена електромагнітними полями в умовах, коли перекриття їх хвильових функцій несуттєво. Отримані рівняння, що дозволяють розглянути процес взаємодії випромінювачів. При взаємодії випромінювачів в резонаторі формується інтегральне поле, зростання інтенсивності якого призводить до синхронізації випромінювачів. Показано що характерні часи розвитку процесу, а також досяжні амплітуди збуджених полів для дисипативних режимів генерації та режимів надвипромінювання випромінювачів, що заповнюють відкритий резонатор, виявляються порівнюваними.
КЛЮЧОВІ СЛОВА: дисипативні режими генерації, надвипромінювання, відкритий резонатор

MICROSTRUCTURE AND HARDENING BEHAVIOR OF ARGON-ION IRRADIATED STEELS 18Cr10NiTi AND 18Cr10NiTi-ODS

Igor Kolodiy[a],*, Oleksandr Kalchenko[a], Sergiy Karpov[a], Victor Voyevodin[a,b],
Mikhail Tikhonovsky[a], Oleksii Velikodnyi[a], Galyna Tolmachova[a],
Ruslan Vasilenko[a], Galyna Tolstolutska[a]

[a]National Science Center "Kharkov Institute of Physics and Technology", Kharkov, Ukraine
[b]V.N. Karazin Kharkiv National University, Kharkov, Ukraine
*Corresponding Author: kolodiy@kipt.kharkov.ua
Received March 29, 2021; revised April 19, 2021; accepted April 20, 2021

Microstructure and nanohardness evolution in 18Cr10NiTi and 18Cr10NiTi-ODS steels after exposure to argon ion irradiation has been studied by combination of nanoindentation tests, XRD analysis, TEM and SEM observation. ODS-modified alloy was produced on the basis of conventional 18Cr10NiTi austenitic steel by mechanical alloying of steel powder with Y(Zr)-nanooxides followed by mechanical-thermal treatment. XRD analysis has showed no significant changes in the structure of 18Cr10NiTi steel after irradiation at room and elevated temperatures (873 K) and in ODS-steel after irradiation at 873 K, whereas the evidences of domains refinement and microstrain appearance were revealed after irradiation of 18Cr10NiTi-ODS steel at room temperature (RT). Layer-by-layer TEM analysis was performed to investigate the microstructure of alloys along the damage profile. The higher displacement per atom (dpa) and Ar concentration clearly lead to increased cavities size and their number density in both steels. The swelling was estimated to be almost half for 18Cr10NiT-ODS (4.8%) compared to 18Cr10NiTi (9.4%) indicating improved swelling resistance of ODS-steel. The role of oxide/matrix interface as a sink for radiation-induced point defects and inert gas atoms is discussed. The fine dispersed oxide particles are considered as effective factor in suppressing of cavity coarsening and limiting defect clusters to small size. The hardness behavior was investigated in both non-irradiated and irradiated specimens and compared to those at RT and elevated temperature of irradiation. The hardness increase of unirradiated ODS-steel is associated mainly with grain refinement and yttrium oxides particles addition. The hardening of 18Cr10NiTi-ODS after Ar ion irradiation at RT was found to be much lower than 18Cr10NiTi. Black dots and dislocation loops are observed for both steels in the near-surface area; however, the main hardening effect is caused by the cavities. Oxide dispersion strengthened steel was found to be less susceptible to radiation hardening/embrittlement compared with a conventional austenitic steel.
KEYWORDS: austenitic steels, oxide particles, irradiation, microstructure, cavities, nanohardness, swelling, hardening, radiation resistance.

Structural materials of modern technical devices operate under extreme conditions (high temperatures, high mechanical stresses and high radiation doses). Exposure of materials under irradiation in nuclear reactors leads to changes in the crystalline structure at the atomic level due to the nucleation of various kinds of defects (such as voids, bubbles, dislocation loops and stacking faults). These defects can dramatically degrade the physical properties of reactor materials through swelling, irradiation hardening, embrittlement, irradiation creep, etc. [1].

Gen IV nuclear reactors concept imposes increased demands on structural materials. Therefore, the main challenge for reactor material science is the development of materials with high irradiation resistance that can operate at high temperature and stresses. Ni based super alloys and austenitic steels were considered to be excellent choice of material due to their close-packed structure. Austenitic stainless steels have high creep resistance but their void swelling resistance is lower compared to ferritic/martensitic steels. The void swelling resistance in austenitic stainless steel can be improved by strengthening with nano-sized stable oxide particles with high density and uniform distribution in the matrix. The interface "matrix-nanooxide" can serve as effective sink for radiation-induced point defects and increases the void swelling resistance. So, oxide dispersion-strengthened (ODS) austenitic stainless steels can be an attractive material because of their corrosion resistance, high-temperature strength and irradiation properties [2].

Apart from the void swelling neutron irradiation also degrades the mechanical performance of the austenitic stainless steels during the operation. Irradiation induced hardening due to irradiation defects and helium embrittlement are essential degradation issues encountered with nuclear structure materials. Early studies mainly focused on the macroscopic mechanical properties of steels after irradiation, but studies on crucial aspects such as microstructural evolution, the effect of inert gas implantation, and the interaction with different microstructural characteristics are rare.

Heavy ion irradiation is commonly used technique to simulate neutron damage under reactor conditions, due to the short periods of time needed to reach relatively high damage levels (several years of neutron irradiation in few hours). Moreover, the samples are not activated and therefore the study is easy to perform [3]. But, ion irradiation has a significant drawback – it produces only shallow depth of damage layer, which complicates the study of mechanical properties. The solution of the problem is possible by using of nanoindentation, TEM and SEM – methods that probe very small volumes of material which allow investigate the microstructural changes and mechanical properties after irradiation.

In the present work, we applied these methods to study the changes in the mechanical properties caused by high energy argon ions irradiation of austenitic stainless steel 18Cr10NiTi and its ODS version. Argon ion irradiation and nano-characterization were carried out to clarify the effect of nano-oxide particles on defect formation, argon precipitation and irradiation induced hardening.

MATERIAL AND METHODS

In this study 18Cr10NiTi austenitic stainless steel and it's strengthened by Y_2O_3-ZrO_2 nanooxides version were investigated. Commercial austenitic steel 18Cr10NiTi was used as initial steel. ODS steel was produced by the mechanical alloying of steel powder with 0.5wt.% of 80%Y_2O_3-20%ZrO_2 pre-synthesized nanooxides with subsequent compacting and mechanical-thermal treatment. As the result rolled types of 18Cr10NiTi-ODS steel with thickness of 200 μm were obtained. More detailed technological chain of 18Cr10NiTi-ODS steel production is described in [4].

Irradiation experiments were conducted in the accelerating-measuring system "ESU-2" [5]. The polished samples were irradiated with a 1.4 MeV Ar$^+$ ion beam at irradiation temperatures of 300 and 873 K. The error in the temperature measurement did not exceed ± 5%. The error in the beam current and, consequently of the damage dose, did not exceed ± 10%.

Calculated by SRIM 2008 [6] depth distribution profiles of damage and concentration of Ar atoms implanted in 18Cr10NiTi steel to a dose of $1 \cdot 10^{17}$ cm^{-2} are shown in Fig. 1. The damage calculations are based on the Kinchin-Pease model (KP), with a displacement energy for each alloying element was set to 40 eV, as recommended in ASTM E521-96 (2009) [7]. The average damage level of 50 dpa over the whole projective ranges of Ar$^+$ ions instead of the peak damage level was used.
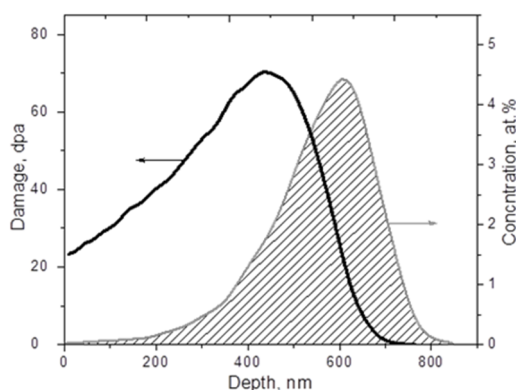
Figure 1. The depth distribution of damage and concentration of Ar atoms calculated with SRIM
for 18Cr10NiTi irradiated by 1.4 MeV Ar ions to a dose of $1 \cdot 10^{17}$ cm^{-2}

Nanohardness was measured by Nanoindenter G200 with a Berkovich type indentation tip. Each sample was applied at least 20 prints at a distance of 35 μm from each other. Nominal maximum displacement of 2000 nm was used for all measurements on unirradiated and ion-irradiated steel [8]. The methodology of Oliver and Pharr was used to find the hardness [9].

Microstructural and cavities parameter data were extracted using conventional techniques conducted on JEM-100CX and JEM-2100 transmission electron microscopes, employing standard bright-field techniques. Analysis of TEM micrographs was performed using image processing software. For transmission studies, samples of 18Cr10NiTi austenitic stainless steel and its ODS version were prepared as disks of 3 mm in diameter, which were mechanically thinned to a thickness of 0.22 mm, and then electropolished. To obtain a hole the thickness of the samples was reduced by standard jet electropolishing in a Tenupol installation in an electrolyte of 80% C_2H_5OH, 10% $HClO_4$, 10% $C_3H_8O_3$ at a voltage of 70 V at room temperature. TEM in kinematic bright-field mode was primarily used to characterize radiation-induced structures.

We divided the whole implantation range into four regions for statistical analysis of the cavity size and volume density in each region. To remove a specified depth layer of material from irradiated side of the sample the electro-pulse technique was used and then TEM studies were carried out [10]. The swelling value was calculated from the cavity size and density within each depth region. The thickness of TEM samples was determined using a convergent beam electron diffraction (CBED) pattern acquired in the two-beam approximation [11]. The thickness estimation method is based on a comparison of the measured and simulated intensity profiles across the diffraction disc. Secondary electron images produced in SEM were used for investigations of as-received and irradiated specimens in regions surrounding indents.

Structural study of samples was carried out on X-ray diffractometer DRON-2.0 in Co-Kα radiation equipped with selective absorbing β-filter and scintillation detector. All diffraction patterns were collected under the same conditions. Standard processing was carried out for diffraction patterns (background subtraction, stripping of the Kα2 doublet, approximation of the diffraction peaks by the pseudo-Voigt function) to obtain the characteristics of the peaks (diffraction angle 2θ, intensity I, integral width B, interplanar spacing d) required for further calculations.

RESULTS AND DISCUSSION

The initial pre-irradiation microstructures of 18Cr10NiTi steel and its ODS version are shown in Fig. 2. The structure of 18Cr10NiTi steel (see Fig. 2a) contains annealing twins, precipitates of second phase (carbides and titanium carbonitrides) and dislocations. Majority of perfect dislocation are extended on partial dislocation with stacking fault formation. Total dislocations density was ~ 10^8 cm^{-2}; average grain size was ~ 30 μm.

Grain structure of ODS steel (see Fig. 2b) is characterized by fine grains (average grain size was 1.2…2.0 μm) and significant concentration of precipitates with near-uniform distribution. Precipitation's size varied from several nanometers to hundreds of nanometers, but the last were a few orders less, thus, its contribution to concentration and average size was negligible.

| a | b |
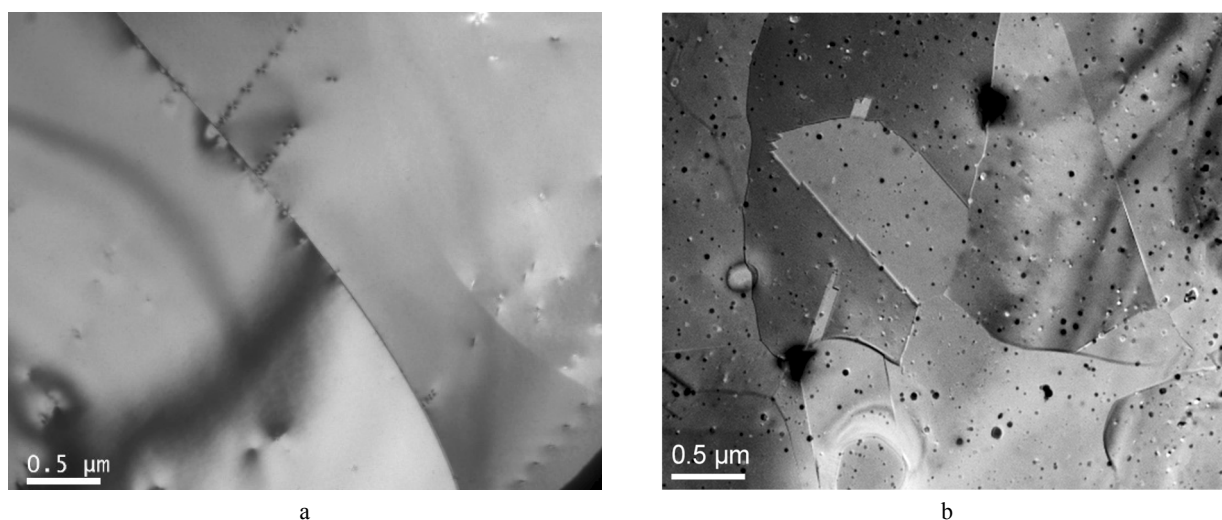
Figure 2. Initial structure of 18Cr10NiTi steel (a) and its ODS version (b)

XRD spectra of unirradiated and Ar$^+$ ion irradiated samples of 18Cr10NiTi steel and 18Cr10NiTi-ODS steel at temperatures of 300 K and 873 K are shown in Fig.3-8, results of XRD analysis are summarized in Table 1. All diffraction patterns were collected under the same conditions. The following samples were taken for analysis:

#1.   as-received sample of 18Cr10NiTi steel;
#2.   18Cr10NiTi steel after Ar$^+$ irradiation at T = 300 K;
#3.   18Cr10NiTi steel after Ar+ irradiation at T = 873 K;
#4.   initial sample of 18Cr10NiTi-ODS steel;
#5.   18Cr10NiTi-ODS steel after Ar$^+$ irradiation at T = 300 K;
#6.   18Cr10NiTi-ODS steel after Ar$^+$ irradiation at T = 873 K.

The diffraction patterns of 18Cr10NiTi steel samples in as-received state and after Ar$^+$ irradiation are virtually the same (Figs. 3-5). These samples are single-phase and consist of austenite Fe-based γ-phase with a lattice parameter a = 3.5916±5·10^{-4} Å. The intensity distribution of the austenite peaks corresponds to a weak crystallographic texture (111). The diffraction lines are rather narrow, which indicates a coarse-grained state.

In XRD spectra of unirradiated 18Cr10NiTi-ODS steel (Fig. 6) only austenite Fe-based γ-phase with a lattice parameter a = 3.5891±5·10^{-4} Å is observed. The peaks intensity distribution corresponds to the crystallographic texture (220). The diffraction peaks are rather narrow indicating a coarse-grained state. After Ar$^+$ ion irradiation at 873 K (Fig. 8) no significant change in the structure of ODS-steel is observed. The lattice parameter of austenite (a = 3.5896±5·10^{-4} Å) does not change within the measurement error.

XRD pattern of 18Cr10NiTi-ODS steel after Ar$^+$ irradiation at 300 K demonstrated some differences compared to abovementioned cases. In addition to peaks of Fe-based γ-phase which are fully correspond to those ones of the unirradiated sample a distinguishable broadened peak on the left of the (220) matrix peak was observed (Fig. 7). This peak could be attributed to the damaged matrix within the implanted layer. In this case, Ar$^+$ ion irradiation has two effects on the structure. First of all, irradiation-induced defects are pinned by nanooxide particles in the surface layer. Accumulation of dislocations (dislocation walls) in implanted layer leads to the formation of small domains separated by the dislocations induced local lattice rotations. Also, microstrain appears in this layer due to the radiation-induced formation of chaotically oriented dislocations. Both small domains size and microstrain cause peak broadening [12, 13]. Moreover, the presence of a large number of dislocation loops is confirmed by TEM micrographs (Fig. 9, a) and their number is significantly higher at 300K. Second, irradiation at 300K leads to dissolution of nanooxide precipitates [14]. Dissolution of nanooxides elements (Y, Zr and O) in implanted layer increases lattice parameter and as a consequence peak shift towards the smaller 2θ angles is observed. Also swelling causes a residual stress in the implanted layer [15], which affects the peak shift too. It should be noted, that this effect is observed only at low irradiation temperature, while at 873 K it appears to be compensated due to the high diffusion mobility of radiation-induced defects.
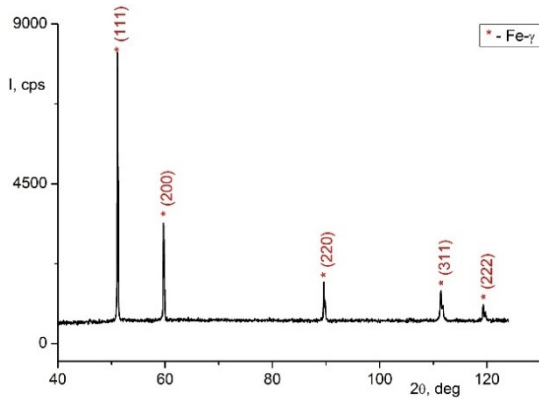
Figure 3. Diffraction pattern of sample #1.
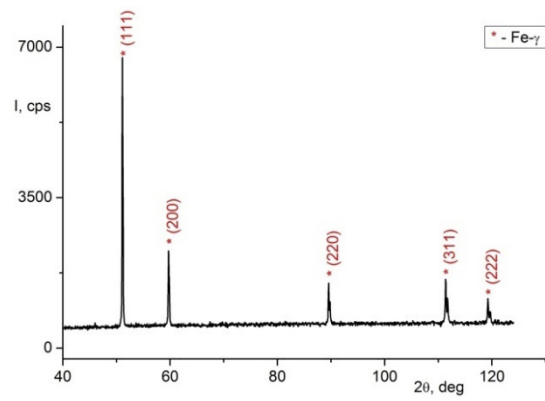
Figure 4. Diffraction pattern of sample #2.
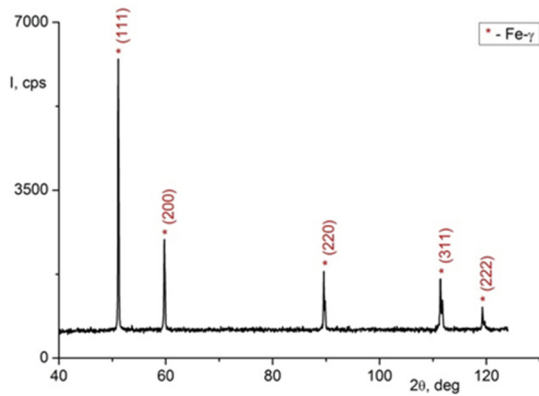
Figure 5. Diffraction pattern of sample #3.
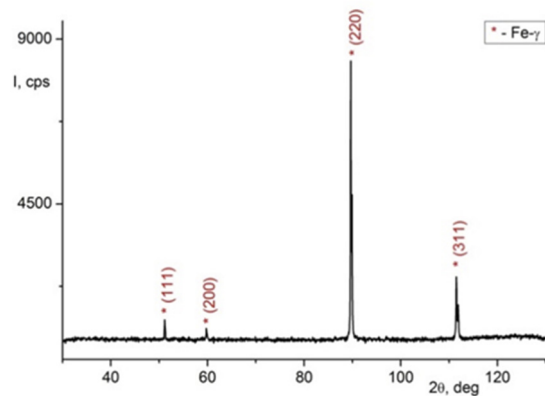
Figure 6. Diffraction pattern of sample #4.
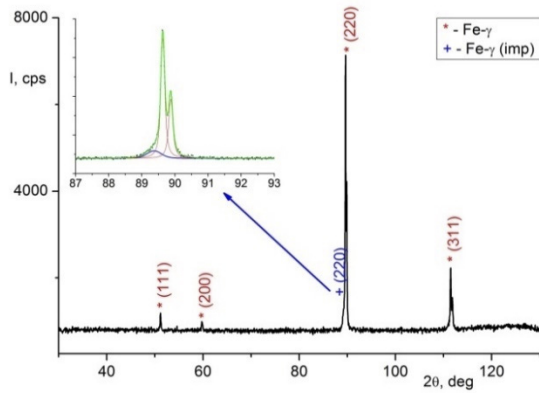
Figure 7. Diffraction pattern of sample #5.
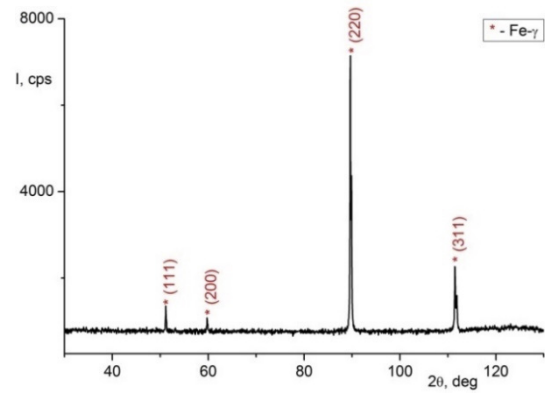
Figure 8. Diffraction pattern of sample #6.

Table 1. Phase composition and lattice parameters of investigated samples

Sample #	Phase composition	Lattice parameter, Å
1	Fe-γ	3.5915
2	Fe-γ	3.5917
3	Fe-γ	3.5916
4	Fe-γ	3.5891
5	Fe-γ	3.5896
	Fe-γ (imp)	3.595
6	Fe-γ	3.5896

Fig. 9 shows TEM micrographs of 18Cr10NiTi and 18Cr10NiTi-ODS steel samples irradiated with Ar ions to average dose of 50 dpa at room temperature (RT). In the region of the first 200 nm, irradiation-induced defects of very small-sized "black spots" and dislocation loops were observed (Fig. 9 a, c). These defects disappeared upon tilting of

sample by small degrees indicating that these are not precipitates. Fig. 9 b, d represents through-focus micrographs where some very small cavities are observed at the depth near 450 nm from surface.
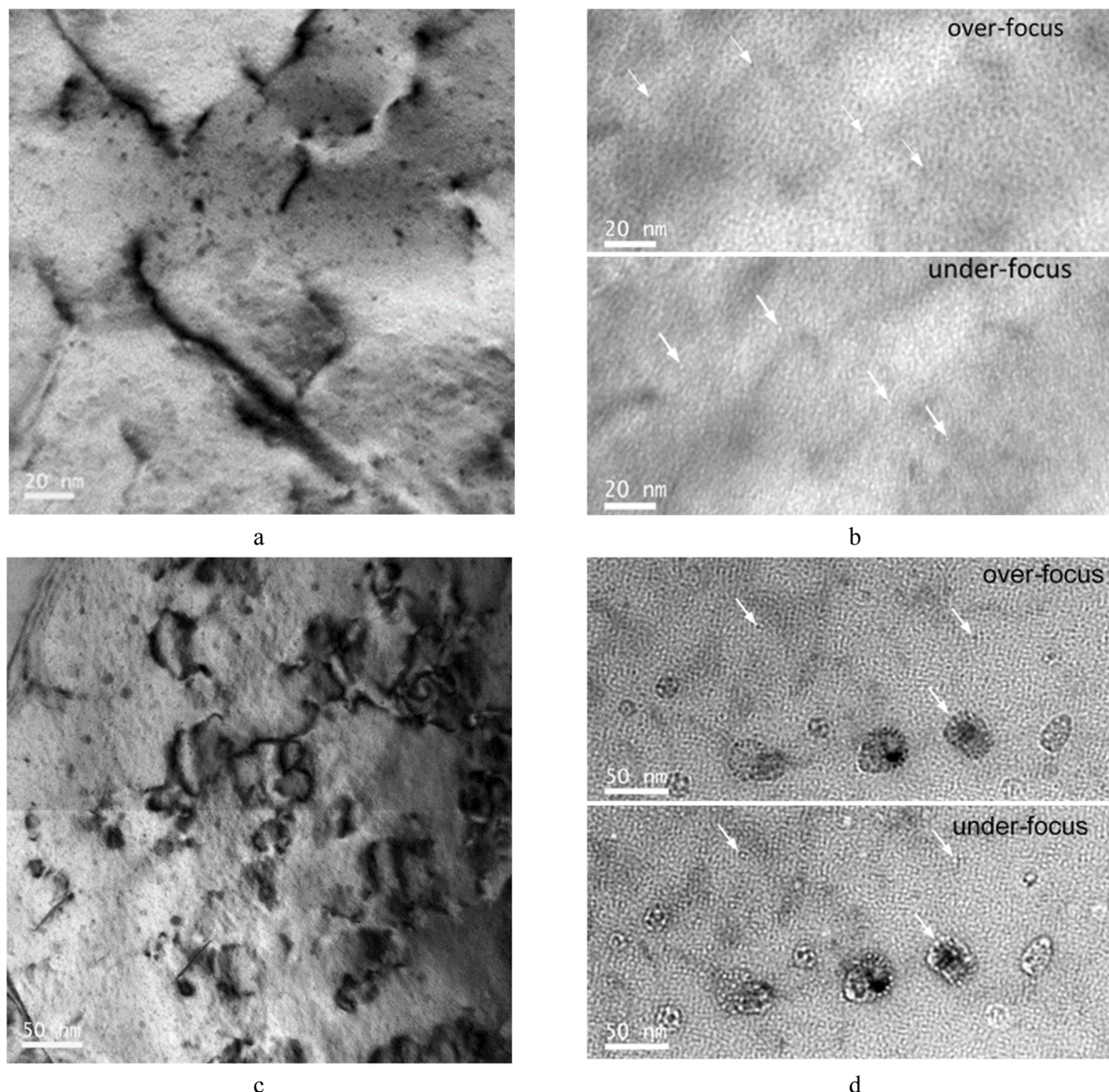
Figure 9. The microstructure of 18Cr10NiTi (a, b) and 18Cr10NiTi-ODS (c, d) at specified depth after irradiation at 300 K. (a, c) – at the depth 100 nm from surface, (b, d) – at the depth 450 nm from surface, pointing with arrows some very small cavities with a size ~ 1 nm, over-focused image +1000 nm (black cavities), under-focused image −1000 nm (white cavities).

The detection of cavities in the Ar irradiated steels at RT was complicated due to their small size. A high error must be considered for cavity sizes below 1 nm due to the amount of defocus used to detect them. Depending on the specimen thickness its value was ~1 μm in absolute values. The mean size of the cavities was 1.3 nm with the number density $1.5 \cdot 10^{24}$ m^{-3} for 18Cr10NiTi and 2-3 nm with $5 \cdot 10^{23}$ m^{-3} for 18Cr10NiTi-ODS steels. Random distribution was found, they seem not to be attached to any microstructural sinks which would indicate that the nucleation was preferential.

As the temperature of irradiation increases to 873 K, the process passes to another stage: the swelling gradually increases. Fig. 10 shows TEM micrographs of Ar implanted 18Cr10NiTi at specified depths. The higher dpa and Ar clearly lead to increased cavity size, primarily due to the presence of more numerous and larger faceted cavities (see Fig. 8, c).

Fig. 11 shows microstructure of 18Cr10NiTi-ODS steel at specified depth after argon ion irradiation at 873 K. Most cavities in ODS-steel seems to be rounded, however, there are also faceted cavities. Despite the fact that significant concentration of precipitates was distributed near-uniform over the sample, areas with reasonably inhomogeneous distribution of cavities throughout the matrix and from grain to grain and even within the same grain are observed.

Cavities observed around the precipitates have a density increased by several times and an average diameter in 2-3 times smaller than the cavities formed far from the precipitates (see some cavity clusters highlighted with ovals in

Fig. 11b,). High vacancy concentration as well as high argon atoms content contribute to the formation of porous structure both in conventional and in ODS-modified alloys. The enhanced cavities nucleation is attributed to the ability of argon to trap vacancies and stabilize them [16]. However, at the stage of cavity growth, the inflow of vacancies will be limited in the case of ODS-steel, because a significant part of the vacancies will drift towards the semicoherent matrix/precipitation interfaces to compensate for microstrains.
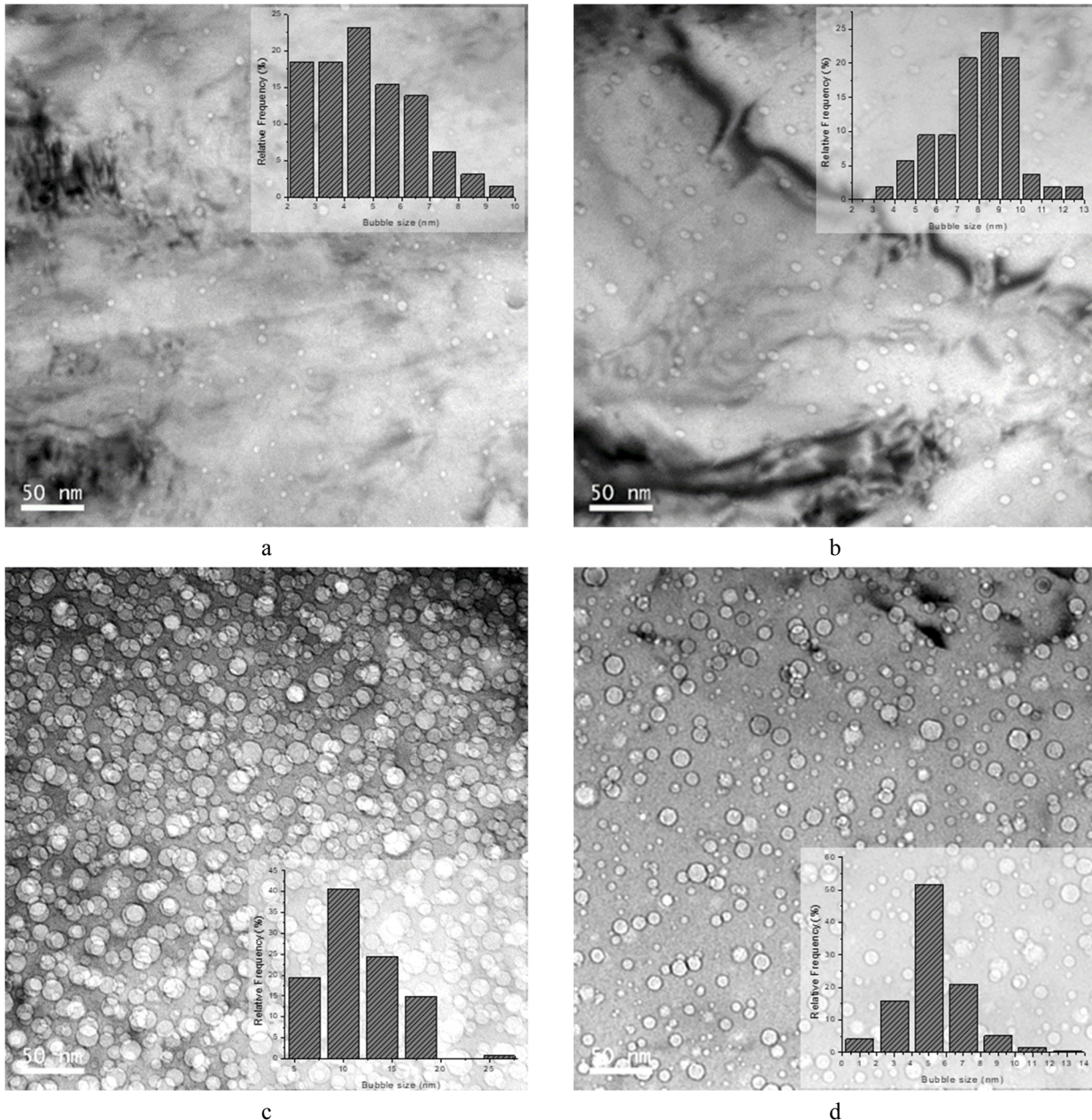
Figure 10. Microstructure of 18Cr10NiTi steel at specified depth 100 (a), 250 (b), 450 (c) and 750 nm (d) after Ar irradiation at 873 K. Cavity size distributions in steel are shown in the inserts.

The evolution of cavities diameter, density and swelling with depth for 18Cr10NiTi and 18Cr10NiTi-ODS steels irradiated with Ar ions to a dose of 50 dpa at 873 K is shown in Fig. 12. With increasing depth, the bubble sizes and densities increase up to the peak dpa region (450 nm depth) and then subsequently decrease beyond the Ar implantation peak region. The average cavity size in ODS-steel is smaller than in base 18Cr10NiTi. The depth dependences of cavity number density are virtually the same for both types of investigated steels. 18Cr10NiTi-ODS demonstrated good resistance to swelling. The swelling was estimated to be almost half for 18Cr10NiTi-ODS (4.8 %) compared to 18Cr10NiTi (9.4 %). These data suggest that the fine dispersed oxide particles are obviously effective in suppression of cavity coarsening and contributes to limiting defect clusters to small size. Part of oxide particles seems to be incoherent with respect to the matrix from TEM observations. This gives a hint that the oxide/matrix interface is the neutral sink for point defects as well as grain boundaries.
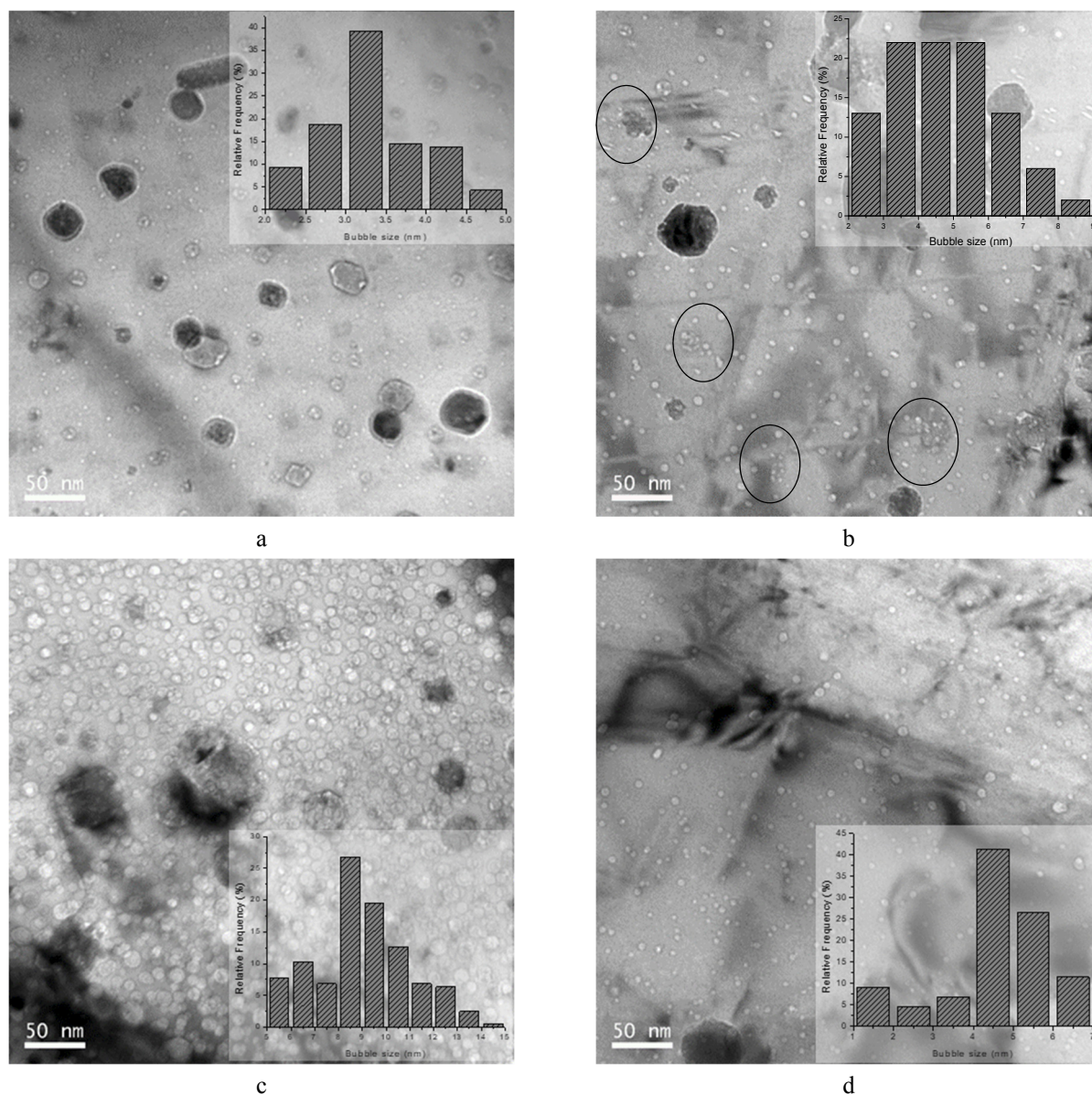
Figure 11. Microstructure of 18Cr10NiTi-ODS steel at specified depth 100 (a), 250 (b), 450 (c) and 750 nm (d) after Ar irradiation at 873 K. Cavity size distributions in steel are shown in the inserts.
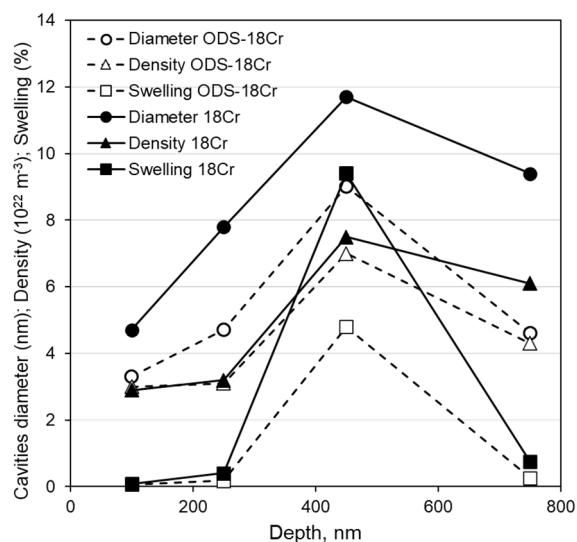
Figure 12. Depth dependences of cavities diameter, volume density and cavity swelling at different depths in 18Cr10NiTi and 18Cr10NiTi-ODS steels irradiated of Ar ions to average dose 50 dpa at 873 K

Fig. 13 shows the hardness as a function of the indenter displacement for unirradiated and irradiated 18Cr10NiTi and 18Cr10NiTi-ODS steels at RT and 873 K. For all samples in the first 150 nm, there is a significant scatter in the data through indenter tip artifacts and surface preparation effects. Therefore, data for the first 150 nm will be ignored in the rest of the analysis. There are no indications of the formation of pile-up lobes or localized slip steps indent in the unirradiated steels. The irradiated samples also showed virtual, if any, pile-up effect. For this reason, a contact area correction for the pile-up was not attempted.
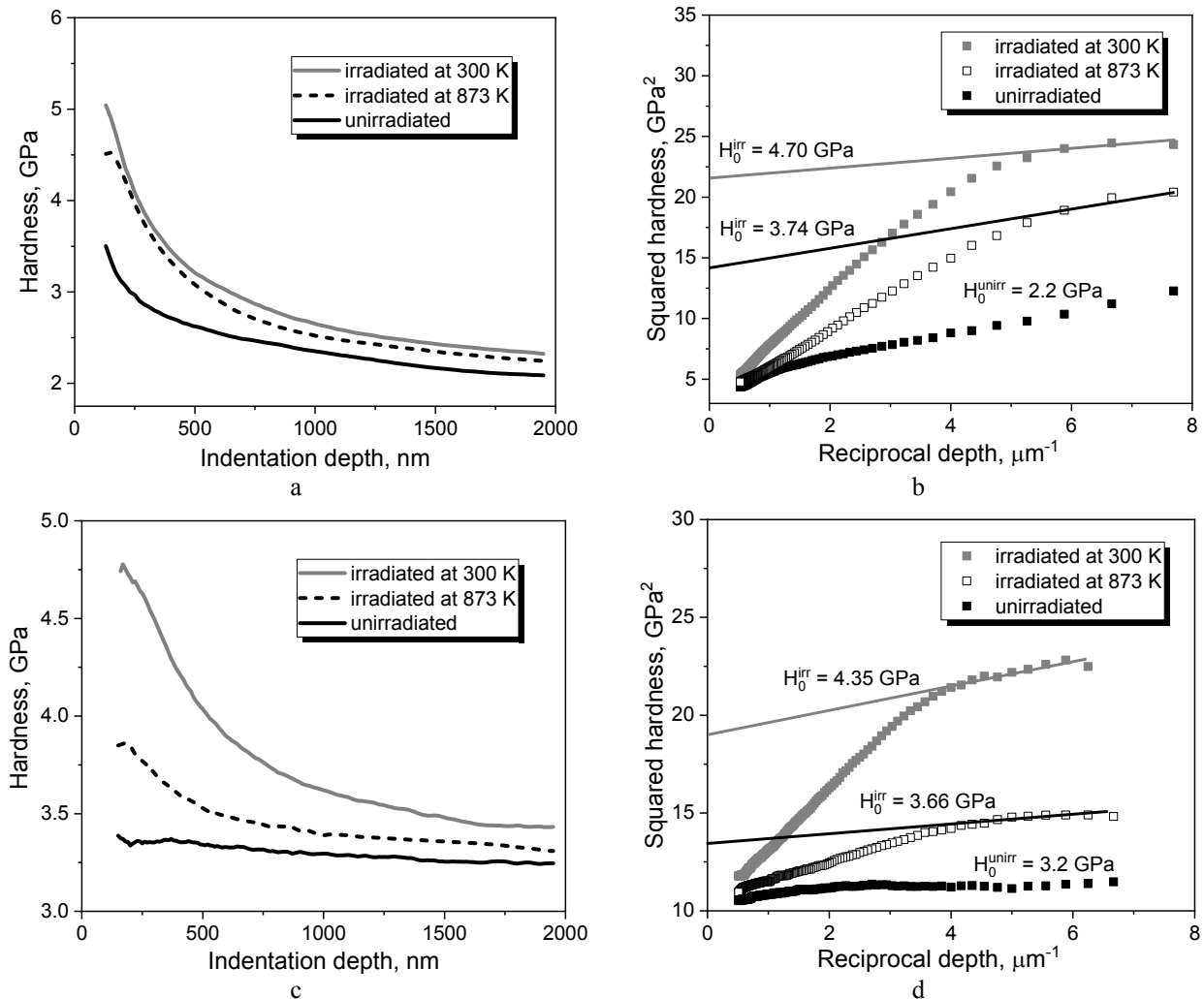
Figure 13. An averaged nanohardness vs indentation depth (a, c) and plots of the square of nanoindentation hardness against the reciprocal of indentation depth (b, d) for unirradiated and irradiated at 300 and 873 K sample of 18Cr10NiTi (a, b) and 18Cr10NiTi-ODS (c, d).

Irradiation with Ar ions up to a dose of 50 dpa at RT and 873 K leads to an increase in nanohardness of implanted layer. By redrawing the hardness profile in terms of Nix-Gao [17] plot (squared hardness vs. reciprocal depth), the bulk-equivalent hardness H_0 has been evaluated (see Fig. 13 and Table 2). Comparison of the radiation-induced hardening (ΔH, the difference of hardness values of irradiated and unirradiated materials) and the corresponding nanohardness increments described as the ratio of ΔH and H_0^{unirr} shows some differences in the data, that are likely to be associated with the difference in the irradiation temperature and microstructure.

Table 2. Experimentally determined the bulk-equivalent hardness and hardening.

Material	18Cr10NiTi			18Cr10NiTi-ODS		
	H_0, GPa	ΔH, GPa	$\Delta H/H_0^{unirr}$, %	H_0, GPa	ΔH, GPa	$\Delta H/H_0^{unirr}$, %
unirradiated	2.2			3.2		
irradiated at RT	4.70	2.5	114	4.35	1.15	36
irradiated at 873 K	3.74	1.54	70	3.66	0.46	14

In the case of unirradiated 18Cr10NiTi samples H_0^{unirr} was estimated as 2.2 GPa, while for 18Cr10NiTi-ODS samples this value was 3.2 GPa. A significant increase in hardness of unirradiated 18Cr10NiTi-ODS appears to be due to the grain refinement and precipitates as yttrium oxides.

Generally, irradiation assisted hardening in fcc metals is associated with the formation of Frank loops which, being sessile in nature, strongly impede the movement of dislocations [3, 18-20]. However, in the present study the main radiation-induced hardening effect is attributed to cavities formation. Although "black spot" defects, which are believed to be Frank loops, were also detected, their occurrence was observed mainly in a narrow near-surface region of irradiated sample (see Fig. 9). Strong dominance of cavity-type defects was revealed by TEM analysis at greater depths. Observed microstructure transformation appears to be due to the high damaging dose (50 dpa), which is forcedly associated with the accumulation of a noticeable amount of gas impurity in depth range of 200-800 nm (see Fig. 1). Due to dpa and gas concentration gradient, different types of cavities can be formed. Depending on vacancy/Ar ratio and, accordingly, internal gas pressure, the effectiveness of these cavities as obstacles to dislocation motion can vary.

According to the data of Table 2, the hardening of 18Cr10NiTi-ODS is a much lower than that of 18Cr10NiTi after Ar ion irradiation at RT. The presence of precipitates as yttrium oxides leads to the formation of nano-sized cavities with a larger size and lower number density in 18Cr10NiTi-ODS compared to conventional steel. For this reason, less hardening effect was observed in 18Cr10NiTi-DS, although the contribution of residual stress observed by XRD analysis in damaged layer of ODS-steel is also possible.

Irradiation at 873 K leads to less increase in hardness in both alloys compared to RT irradiation. Meanwhile, the difference in hardening between two steels after 873 K irradiation has become even greater. Observed tendencies appear to be associated primarily with high diffusivity of radiation-induced point defects, and gas atoms and their intensive interaction with sinks such as grain boundaries and precipitates. These processes substantially influence cavities formation and evolution. The fine dispersed oxide particles are obviously effective in suppression of cavity coarsening and contributes to limiting defect clusters to small size. At the same time, the fine-grained structure of 18Cr10NiTi-ODS has a high density of distribution boundaries, which act as absorbers of radiation defects.

Summarizing, the phenomenon known as radiation induced hardening has been experimentally demonstrated in 18Cr10NiTi austenitic stainless steel and its strengthened version. The increase in hardness values is caused by defects created during irradiation (such as cavities and dislocations), the formation of which, in turn, depends on the experimental conditions, such as radiant species nature, irradiation temperature or fluence. At evaluation of hardening behavior, it is also important to take into account other microstructural characteristics (irradiation independent) such as grain boundaries, dislocations inherent to the microstructure, precipitated or added particles as yttrium oxides (in the case of ODS). Thus, by the collection of properties, oxide dispersion strengthened 18Cr10NiTi austenitic stainless steel is less susceptible to radiation hardening/embrittlement compared to conventional austenitic steel.

CONCLUSIONS

In the present study, we applied the methods of ion irradiation, nanoindentation, XRD analysis, scanning and transmission electron microscopy to investigate the evolution of microstructure and mechanical properties of irradiated 18Cr10NiTi austenitic stainless steel and its ODS-modified version. ODS-steel was produced on the basis of conventional 18Cr10NiTi austenitic steel by mechanical alloying with nano-oxide particles. Argon ion irradiation was carried out to clarify the effect of oxide particles on defect formation, argon precipitation and irradiation induced hardening.

XRD analysis showed no significant changes in the structure of irradiated specimens, with the exception of domains refinement and microstrain appearance in ODS-steel after irradiation at room temperature.

Layer-by-layer TEM analysis revealed spatial distribution of radiation-induced defects along the damage profile. Dislocations and cavity-like defects were observed in both steels. The higher dpa and Ar concentration clearly lead to increased cavities size and their number density. The swelling was estimated to be almost half for 18Cr10NiT-ODS (4.8%) compared to 18Cr10NiTi (9.4%) indicating improved swelling resistance of ODS-steel. Fine dispersed oxide particles are shown to be effective in suppression of cavity coarsening and contributes to limiting defect clusters to small size.

The main hardening effect is caused by cavities in both steels. Due to oxide particles, the hardening of 18Cr10NiTi-ODS after Ar ion irradiation at room and elevated temperatures is lower than 18Cr10NiTi. Oxide dispersion strengthened 18Cr10NiTi austenitic stainless steel is less susceptible to radiation hardening/embrittlement compared with a conventional austenitic steel.

ORCID IDs
Igor Kolodiy, https://orcid.org/0000-0001-8598-9732; **Oleksandr Kalchenko**, https://orcid.org/0000-0003-0856-1868
Sergiy Karpov, https://orcid.org/0000-0002-6607-8455; **Victor Voyevodin**, https://orcid.org/0000-0003-2290-5313
Mikhail Tikhonovsky, https://orcid.org/0000-0001-5889-0366; **Oleksii Velikodnyi**, https://orcid.org/0000-0001-5088-6143
Galyna Tolmachova, https://orcid.org/0000-0002-0786-2979; **Ruslan Vasilenko**, https://orcid.org/0000-0002-4029-9727
Galyna Tolstolutska, https://orcid.org/0000-0003-3091-4033

REFERENCES

[1] V.N. Voyevodin, and I.M. Neklyudov, *Evolution of the Structural-Phase State and Radiation Resistance of Structural Materials,* (Kiev, Naukova Dumka, 2006). (in Russian)

[2] S.J. Zinkle, and J.T. Busby, Mat. Today, **12**, 12-19 (2009), https://doi.org/10.1016/S1369-7021(09)70294-9.

[3] G.S. Was, and R.S. Averback, Comprehensive Nuclear Materials, **1**, 195-221 (2012). https://doi.org/10.1016/B978-0-08-056033-5.00007-0.

[4] A.N. Velikodnyi, V.N. Voyevodin, M.A. Tіkhonovsky, V.V. Bryk, A.S. Kalchenko, S.V. Starostenko, I.V. Kolodiy, V.S. Okovit, A.M. Bovda, L.V. Onischenko, and G.Ye. Storogilov, PAST, **4**(92), 94-102 (2014), https://vant.kipt.kharkov.ua/ARTICLE/VANT_2014_4/article_2014_4_94.pdf. (in Russian)

[5] G.D. Tolstolutskaya, V.V. Ruzhytskiy, I.E. Kopanetz, V.N. Voyevodin, A.V. Nikitin, S.A. Karpov, A.A. Makienko, and T.M. Slusarenko, PAST, **1**, 135-140 (2010), https://vant.kipt.kharkov.ua/ARTICLE/VANT_2010_1/article_2010_1_135.pdf. (in Russian).

[6] R.E. Stoller, M.B. Toloczko, G.S. Was, A.G. Certain, S. Dwaraknath, and F.A. Garner, Nucl. Instrum. Methods Phys. Res. Sect. B: Beam Interact. Mater. Atoms, **310**, 75-80 (2013), http://dx.doi.org/10.1016/j.nimb.2013.05.008.

[7] ASTM E521-96, 2009, ASTM, https://doi.org/10.1520/E0521-96R09E01.

[8] G.N. Tolmachova, G.D. Tolstolutskaya, S.A. Karpov, B.S. Sungurov, and R.L. Vasilenko, PAST, **5**(99), 168–173 (2015), https://vant.kipt.kharkov.ua/ARTICLE/VANT_2015_5/article_2015_5_168.pdf.

[9] W.C. Oliver, and G.M. Pharr, J. Mater. Res. **7**(6), 1564-1583 (1992), https://doi.org/10.1557/JMR.1992.1564.

[10] M.B. Toloczko, F.A. Garner, V.N. Voyevodin, V.V. Bryk, O.V. Borodin, V.V. Mel'nychenko, and A.S.Kalchenko, Journal of Nuclear Materials, **453**, 323-333 (2014), https://doi.org/10.1016/j.jnucmat.2014.06.011.

[11] M. Klinger, Journal of Applied Crystallography, **50**, 1226-1234 (2017), https://doi.org/10.1107/S1600576717006793.

[12] N.N. Kumar, R. Tewari, P. Mukherjee, N. Gayathri, P.V. Durgaprasad, G.S. Taki, J.B.M. Krishna, A.K. Sinha, P. Pant, A.K. Revally, B.K. Dutta, and G.K. Dey, Radiation Effects and Defects in Solids, **1370520**, 678-694 (2017), http://dx.doi.org/10.1080/10420150.2017.1379520.

[13] P. Mukherjee, A. Sarkar, M. Bhattacharya, N. Gayathri, and P. Barat, Journal of Nuclear Materials, **395**, 37-44 (2019), https://doi.org/10.1016/j.jnucmat.2009.09.013.

[14] E. Aydogan, O. El-Atwani, M. Li, and S.A. Maloy. *Materials Characterization*., **170**, 110686 (2020). https://doi.org/10.1016/j.matchar.2020.110686.

[15] S. Ahmad, S. Bashir, D. Yousaf, and M.A. Ali, Materials Sciences and Applications, **9**, 330-344 (2018), https://doi.org/10.4236/msa.2018.93022.

[16] Y. Osetsky, and Roger E. Stoller, Journal of Nuclear Materials, **465**, 448-454 (2015), https://doi.org/10.1016/j.jnucmat.2015.05.034.

[17] W.D. Nix, H.J. Gao, J. Mech. Phys. Solid, **46**, 411–425 (1998), https://doi.org/10.1016/S0022-5096(97)00086-0.

[18] S.A. Karpov, G.D. Tolstolutskaya, B.S. Sungurov et al., Materials Science. **52**, issue 3, 377–384 (2016), https://doi.org/10.1007/s11003-016-9967-4.

[19] V.N. Voyevodin, S.A. Karpov, G.D. Tolstolutskaya, M.A. Tikhonovsky, A.N. Velikodnyi, I.E. Kopanets, G.N. Tolmachova, A.S. Kalchenko, R.L. Vasilenko, and I.V. Kolodiy, Philosophical Magazine, **100**(7), 822-836 (2020), https://doi.org/10.1080/14786435.2019.1704091.

[20] D.C. Foley, K.T. Hartwig, S.A. Maloy, P. Hosemann, X. Zhang, Journal of Nuclear Materials, **389**, 221-224 (2009), http://doi.org/10.1016/j.jnucmat.2009.02.005.

МІКРОСТРУКТУРА ТА ЗМІЦНЕННЯ СТАЛЕЙ X18H10T І X18H10T-ДЗО, ОПРОМІНЕНИХ ІОНАМИ АРГОНУ

Ігор Колодій[a], Олександр Кальченко[a], Сергій Карпов[a], Віктор Воєводін[a,b], Михайло Тихоновський[a], Олексій Великодній[a], Галина Толмачова[a], Руслан Василенко[a], Галина Толстолуцька[a]

[a]Національний науковий центр "Харківський фізико-технічний інститут", Харків, Україна
[b]Харківський національний університет імені В.Н. Каразіна, Харків, Україна

Вивчено зміну мікроструктури і нанотвердості в сталях X18H10T та X18H10T-ДЗО після опромінення іонами аргону за допомогою комбінації методів наноіндентування, рентгеноструктурного аналізу, просвічуючої та скануючої електронної мікроскопії. Модифікований ДЗО сплав був отриманий на основі звичайної аустенітної сталі X18H10T шляхом механічного легування сталевого порошку нанооксидами Y(Zr) з подальшою термо-механічною обробкою. Рентгеноструктурний аналіз не показав суттєвих змін в структурі сталі X18H10T після опромінення при кімнатній і підвищених температурах (873 K) і в ДЗО-сталі після опромінення при 873 K, тоді як ознаки подрібнення доменів і появи мікродеформації були виявлені після опромінення сталі X18H10T-ДЗО при кімнатній температурі (КТ). Пошаровий ПЕМ-аналіз проводився для дослідження мікроструктури сплавів вздовж профіля пошкоджень. Більш висока концентрація пошкоджень і Ar явно призводить до збільшення розміру порожнин і їх щільності в обох сталях. Розпухання склало майже половину для X18H10T-ДЗО (4,8%) у порівнянні з X18H10T (9,4%), що свідчить про поліпшений опір розпуханню в ОДЗ-сталі. Обговорюється роль границі розподілу оксид/матриця як стоку для радіаційних точкових дефектів і атомів інертного газу. Дрібнодисперсні частки оксиду розглядаються як ефективний фактор в пригніченні укрупнення порожнин і обмеження скупчень дефектів невеликим розміром. Поведінку твердості досліджували як на неопромінених, так і на опромінених зразках і порівнювали з такими при кімнатній температурі і підвищеній температурі опромінення. Підвищення твердості неопроміненої ДЗО-сталі в основному пов'язано з подрібненням зерна і додаванням частинок оксиду ітрію. Зміцнення сталі X18H10T-ДЗО після опромінення іонами Ar при кімнатній температурі виявилося набагато нижче, ніж X18H10T. Для обох сталей в приповерхневій області спостерігаються чорні точки і дислокаційні петлі; однак основний ефект зміцнення обумовлений порожнинами. Було встановлено, що ДЗО-сталь менш схильна до радіаційного зміцнення/окрихчення в порівнянні зі звичайною аустенітною сталлю.

КЛЮЧОВІ СЛОВА: аустенітні сталі, оксидні частинки, опромінення, мікроструктура, порожнини, нанотвердість, розпухання, зміцнення, радіаційна стійкість

EFFECT OF Ti, Al, Si ON THE STRUCTURE AND MECHANICAL PROPERTIES OF BORON-RICH Fe–B–C ALLOYS

ⓘ**Olena V. Sukhova**

Oles Honchar Dnipro National University
72, Haharin Ave., Dnipro, 49010, Ukraine
Corresponding Author: sukhovaya@ukr.net
Received February 19, 2021; revised March 31, 2021; accepted April XX, 2021

The effects of substitution of Fe in the boron-rich Fe–B–C alloys, containing 10.0–14.0 % B; 0.1–1.2 % C; Fe – the remainder, 5.0 % Ti, Al, or Si (in wt. %) have been studied with optical microscopy, X-ray diffractometry, scanning electron microscopy, energy dispersive spectroscopy. Mechanical properties, such as microhardness and fracture toughness, have been measured by Vickers indenter. The microstructure of the master Fe–B–C alloys cooled at 10 and 10^3 K/s consists of primary dendrites of Fe(B,C) solid solution and $Fe_2(B,C)$ crystals. It has been found that titanium has the lowest solubility in the constituent phases of the Fe–B–C alloys, with preferential solubility observed in the Fe(B,C) dendrites, where Ti occupies Fe positions. This element has been shown to be mainly present in secondary phases identified as TiC precipitates at the $Fe_2(B,C)$ boundaries. Titanium slightly enhances microhardness and lowers fracture toughness of the boron-rich Fe–B–C alloys due to substitutional strengthening of Fe(B,C) dendrites and precipitation of the secondary phases. The level of the content of Al or Si in the Fe(B,C) and $Fe_2(B,C)$ solid solutions and quantity of the secondary phases observed in the structure suggest that more Al or Si are left in the constituent phases as compared with Ti. These elements mainly enter the crystal lattice of $Fe_2(B,C)$ phase replacing iron atoms and form at their boundaries $AlB_{12}C$ and SiC compounds respectively. The additions of Al and Si to the boron-rich Fe–B–C alloys help to modify their fragility: while they slightly decrease microhardness values, addition of these elements improves the fracture toughness of the constituent phases. Increase in a cooling rate from 10 to 10^3 K/s does not bring about any noticeable changes in the solubility behavior of the investigated alloying elements. The rapid cooling gives rise to microhardness and fracture toughness of the phase constituents which average sizes significantly decrease. The effects of the alloying elements on the structure and mechanical properties of the investigated boron-rich Fe–B–C alloys have been explained considering differences in the atomic radii and electronic structure of the solute Ti, Al, or Si atoms.

KEYWORDS: structure, iron borides**,** alloying elements, solubility, microhardness, fracture toughness.

Materials scientists have been striving for several centuries to develop new materials that are stronger, stiffer, and more ductile than existing materials and which can be used at high temperatures [1-3]. It is very important to work out structural materials that require less processing cost and to improve their properties, such as elevated temperature strength and stiffness. Improved properties can ensure higher performance characteristics resulting in extended lifetime [4-6]. The need for these improvements is of particular importance in developing iron alloys [7,8].

The boron-rich Fe–B–C alloys containing more than 10 wt. % B have attracted lots of interest because they can give a challenging opportunity for the potential industrial usage [9,10]. Many investigations have been focused on the solidification behavior of the Fe–B–C alloys [11,12]. These alloys exhibit a broad variety of high physical, chemical, mechanical, and tribological properties [13,14]. Meanwhile, their brittleness retards the development of practical applications. Therefore, boron-rich Fe–B–C alloys have a potential for applications, such as coatings [15,16] or reinforcement particles of composite materials [17,18].

For the use of boron-rich Fe–B–C alloys in many other applications, alloying these alloys with other elements is crucial to achieve the performance specifications that are required. The elements, commonly used for alloying, include titanium, aluminum, silicon etc. [19-23]. But influence of their additions is mainly studied on the Fe–B–C alloys containing up to 3 wt. % B [24-32]. That is why, the research of the effects of alloying by titanium, aluminum, silicon of the boron-rich Fe–B–C alloys produced by the conventional solidification method as well as clarification of their solubility are particularly important for further development of these new materials. Besides, cooling rate during producing alloys also greatly contributes to the solubility of alloying elements in phase constituents thus affecting their properties [33].

Thus, better understanding of the solidification microstructure of the Fe–B–C alloys system with additional elements is essential to support the utilization of these materials. Further work is necessary to understand the solubility behavior of alloying elements in the Fe–B–C alloys and a phase change caused by their addition. Therefore, the purpose of the present work is to investigate the alloying effects of Ti, Al or Si and influence of cooling rate on the structure and mechanical properties of boron-rich Fe–B–C alloys.

MATERIALS AND METHODS

To investigate the structural and mechanical properties of the phases which are present in the cast Fe–B–C alloys cooled at 10 and 10^3 K/s, these alloys were prepared in the following compositional ranges: B (10.0–14.0 wt. %), C (0.1–1.2 wt. %), M (5 wt. %, where M – Ti, Al, or Si), Fe (the remainder). The alloys were prepared by melting of

chemically pure components (<99.99 wt. %) in alumina crucibles in a Tamman furnace. The molten alloys were cooled in the air at the rates of 10 and 10^3 K/s. The chemical analysis was carried out using SPRUT SEF-01-M fluorescent X-ray spectrometer, and each reported value corresponded to the average of three measurements.

To characterize some of structural properties, different analytical techniques were applied. Phase morphology and phase composition were characterized by light-optical microscopy (OM) using NEOPHOT-2 device and JEOL-2010 F scanning electron microscope (SEM) equipped with energy-dispersive spectrometer (EDS). The dendrite parameters of the Fe(B,C) phase, such as a diameter of secondary dendritic arms (d_0) and interdendritic distance (l_0), were measured by quantitative metallography carried out with EPIQUANT image analyzer. The X-ray diffraction (XRD) examination was performed using HZG-4A diffractometer with the Cu-K$_\alpha$ radiation to identify the existing phases of the powdered samples and measure their lattice parameters. For phase identification, measurements were taken for a wide range of diffraction angles ranging from 20° to 120° with a scanning rate of 5 deg/min.

Mechanical properties of the alloys were determined by DURASCAN 20 and PMT-3 Vickers indenters. Vickers microhardness (H_μ) measurements were done by using 0.49 N and 0.98 N loads at room temperature. The loading and unloading times were 10 s each. After the indention, radial cracks appeared from the corner of the indentation along the direction of the diagonal. The fracture toughness (K_{IC}) was evaluated from the crack length initiated at the corners of the Vickers microindentation using an empirical equation proposed in [34]. At least ten indentation tests were made, and the experimental errors were also analyzed.

RESULTS AND DISCUSSION

The major constituents of the master boron-rich Fe–B–C alloys within the investigated concentration range are Fe$_2$(B,C) and Fe(B,C) solid solutions [12]. The primary solid solution Fe(B,C) arises on the base of iron monoboride and grows in the form of three-dimensional dendrite. Solid solution Fe$_2$(B,C) is formed afterwards via peritectic reaction L+Fe(B,C)→Fe$_2$(B,C) or crystallizes directly from the liquid because its stoichiometric composition is close to the composition of the peritectic point. The carbon solubility in Fe$_2$B iron hemiboride measured by EDS is about 1.9 at%. The Fe(B,C) phase has been found to dissolve up to 1.2 at. % of carbon.

When titanium is added to Fe–B–C alloys, it dissolves in the iron borides in small amounts (Table 1) forming preferentially solid solutions with iron monoboride (Fig. 1). Only traces of the element are revealed by EDS as small but noticeable background (Fig. 1b). Consequently, at the Fe$_2$(B,C) boundaries, the numerous light crystals of TiC secondary phase are seen in the SEM micrographs. The addition of titanium that dissolves in the Fe(B,C) lattice replacing iron atoms causes some distortions due to the difference in atom size (Table 2). Besides, compared with Fe$_2$(B,C) phase, the increase in microhardness H_μ and the decrease in fracture toughness K_{IC} of Fe(B,C) crystals tend to be more marked (Table 3) while the Fe(B,C) dendrite parameters remain practically unchanged (Table 4).

Table 1. Elemental analysis (in at. %) of the doped Fe–12.1B–0.1C alloys cooled at 10 K/s

Phase	Fe	B	C	Ti	Al	Si	ΣMn,Si,Al,Fe
Fe–12.1B–0.1C–5Ti alloy							
Fe(B,C)	48.0	49.2	0.5	1.1	–	–	1.2
Fe$_2$(B,C)	65.1	31.9	0.8	0.5	–	–	1.7
TiC	–	1.20	49.2	49.3	–	–	0.3
Fe–12.1B–0.1C–5Al alloy							
Fe(B,C)	48.8	48.7	1.1	–	0.5	–	0.9
Fe$_2$(B,C)	61.4	30.8	1.8	–	4.7	–	1.3
AlB$_{12}$C	–	85.5	7.1	–	7.2	–	0.2
Fe–12.1B–0.1C–5Si alloy							
Fe(B,C)	48.6	48.9	0.4	–	–	0.8	1.3
Fe$_2$(B,C)	60.1	31.9	0.9	–	–	5.9	1.2
SiC	–	1.6	49.1	–	–	48.9	0.4

Table 2. The lattice parameters of Fe(B,C) and Fe$_2$(B,C) crystals in the doped Fe–12.1B–0.1C alloys cooled at 10 K/s

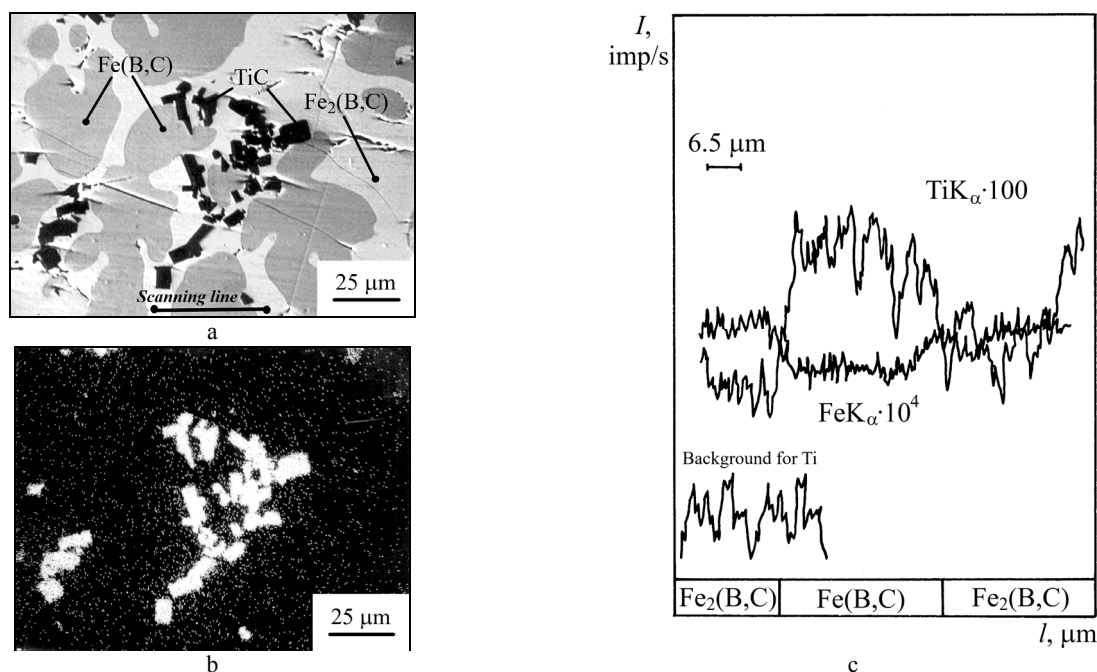| Alloying element	Fe(B,C) (rhombic lattice)			Fe$_2$(B,C) (tetragonal lattice)		
	a, Å	b, Å	c, Å	a, Å	c, Å	c/a
w/o	5.5051±0.0061	4.0628±0.0097	2.9480±0.0007	5.1130±0.0008	4.2399±0.0035	0.8292
Ti	5.5060±0.0020	4.0642±0.0003	2.9485±0.0011	5.1131±0.0012	4.2400±0.0007	0.8292
Al	5.5057±0.0031	4.0637±0.0019	2.9484±0.0009	5.1171±0.0031	4.2442±0.0015	0.8294
Si	5.5053±0.0012	4.0633±0.0030	2.9481±0.0025	5.1164±0.0007	4.2438±0.0023	0.8295

Figure 1. SEM of polished cross-sections of Fe–12.1B–0.1C alloy doped by 5 % of Ti: a – second electron image; b – elemental EDS X-ray mapping in TiKα radiation; c – elemental profile along scanning line

Table 3. Influence of alloying elements on microhardness (H_μ, GPa) and fracture toughness (K_{1C}, MPa·√м) of $Fe_2(B,C)$ and $Fe(B,C)$ solid solutions

Alloying element	V_{cool}=10 K/s				V_{cool}=10^3 K/s			
	Fe(B,C)		$Fe_2(B,C)$		Fe(B,C)		$Fe_2(B,C)$	
	H_μ	K_{1C}	H_μ	K_{1C}	H_μ	K_{1C}	H_μ	K_{1C}
w/o	17.8±0.3	2.1±0.2	15.8±0.2	2.2±0.3	20.1±0.3	5.0±0.2	17.0±0.1	4.0±0.1
Ti	18.2±0.2	1.8±0.3	16.0±0.3	2.0±0.1	20.5±0.3	4.7±0.1	17.1±0.2	3.2±0.2
Al	17.7±0.1	2.0±0.1	15.2±0.1	3.3±0.2	19.9±0.1	5.3±0.3	15.9±0.3	-
Si	17.7±0.2	2.2±0.2	15.4±0.3	3.0±0.1	20.0±0.2	5.1±0.1	16.2±0.3	-

Table 4. Influence of alloying elements on the interdendritic distance (l_0, μm) and diameter of secondary dendritic arms (d_0, μm) of Fe(B,C) dendrites

Alloying element	V_{cool}=10 K/s		V_{cool}=10^3 K/s	
	d_0	l_0	d_0	l_0
w/o	29.9±0.9	33.1±0.3	4.9±0.2	5.2±0.2
Ti	29.6±0.7	32.9±0.4	4.7±0.1	5.0±0.2
Al	28.7±0.3	32.4±0.2	4.5±0.3	4.8±0.3
Si	29.1±0.5	31.1±0.3	4.6±0.2	4.9±0.1

Unlike titanium, aluminum slightly dissolves in Fe(B,C) dendrites but preferentially – in $Fe_2(B,C)$ crystals (Fig. 2, Table 1) which is in good agreement with XRD measurements of lattice parameters of Fe(B,C) and $Fe_2(B,C)$ phases (Table 2). Besides, with boron and carbon aluminum forms $AlB_{12}C$ secondary phase that precipitates at the boundaries of $Fe_2(B,C)$ crystals (Fig. 2ab). This implies that solid solubility limit is exceeded for 5 % Al. That is why this element is continually pushed out in the melt ahead of the moving solid-liquid interface into the interdendritic regions of growing Fe(B,C) dendrites slowing their growth and causing minor refinement (Table 4). The Fe–B–C alloys with 5 % Al are softer but more ductile (Table 3). So, aluminum, as such, works in the opposite way as that described for titanium.

The additions of silicon to the boron-rich Fe–B–C alloys dissolve in negligible quantities in the dendrites of Fe(B,C) solid solution and enter mainly $Fe_2(B,C)$ phase substituting for the iron atoms (Fig. 3, Table 1, 2). In the SEM micrographs, Fe(B,C) crystals look dark (Fig. 3b). The EDS studies also indicate the formation of light crystals of SiC secondary phase at the $Fe_2(B,C)$ boundaries. This means that a portion of Si becomes incorporated into the solidified phases, but solubility limit forces the remaining solute into the residual liquid after the primary phases have formed. Therefore, alloying with this element slightly decreases dendrite parameters of Fe(B,C) crystals (Table 4). The addition of silicon to the Fe–B–C alloys does not have a substantial effect on the mechanical properties of Fe(B,C) dendrites but decreases microhardness H_μ and increases fracture toughness K_{1C} of $Fe_2(B,C)$ crystals (Table 3).
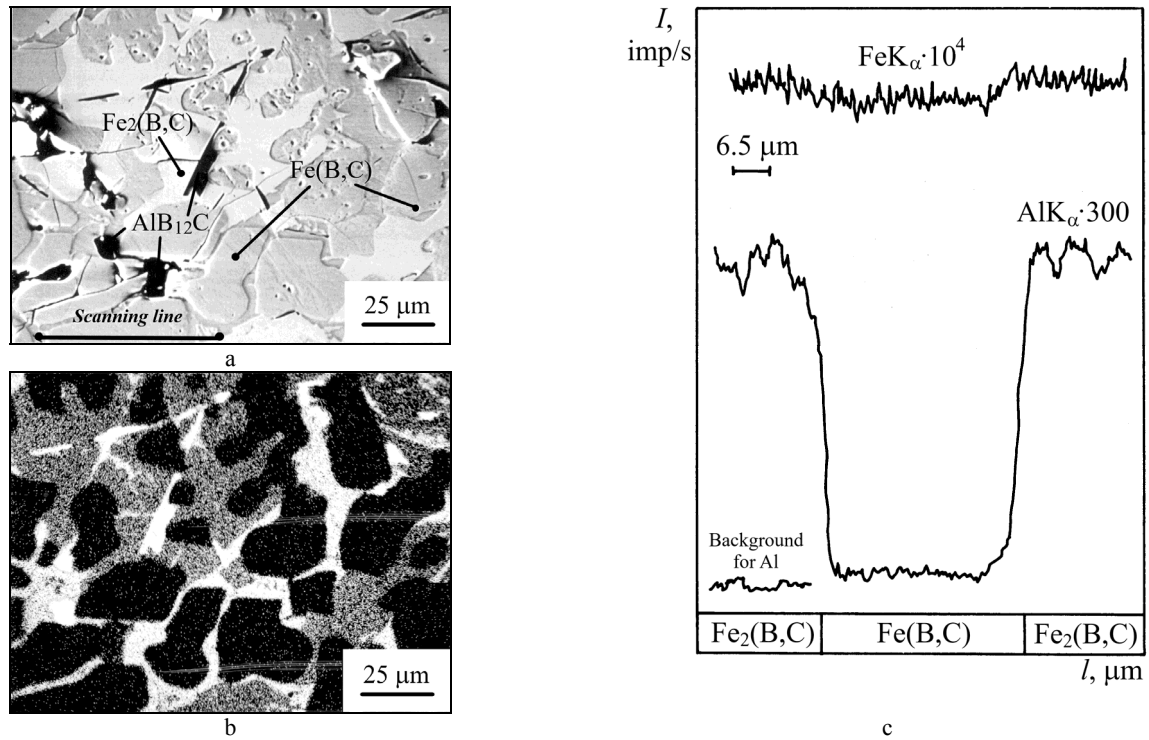
Figure 2. SEM of polished cross-sections of Fe–12.1B–0.1C alloy doped by 5 % of Al: a – second electron image; b – elemental EDS X-ray mapping in AlK_α radiation; c – elemental profile along scanning line
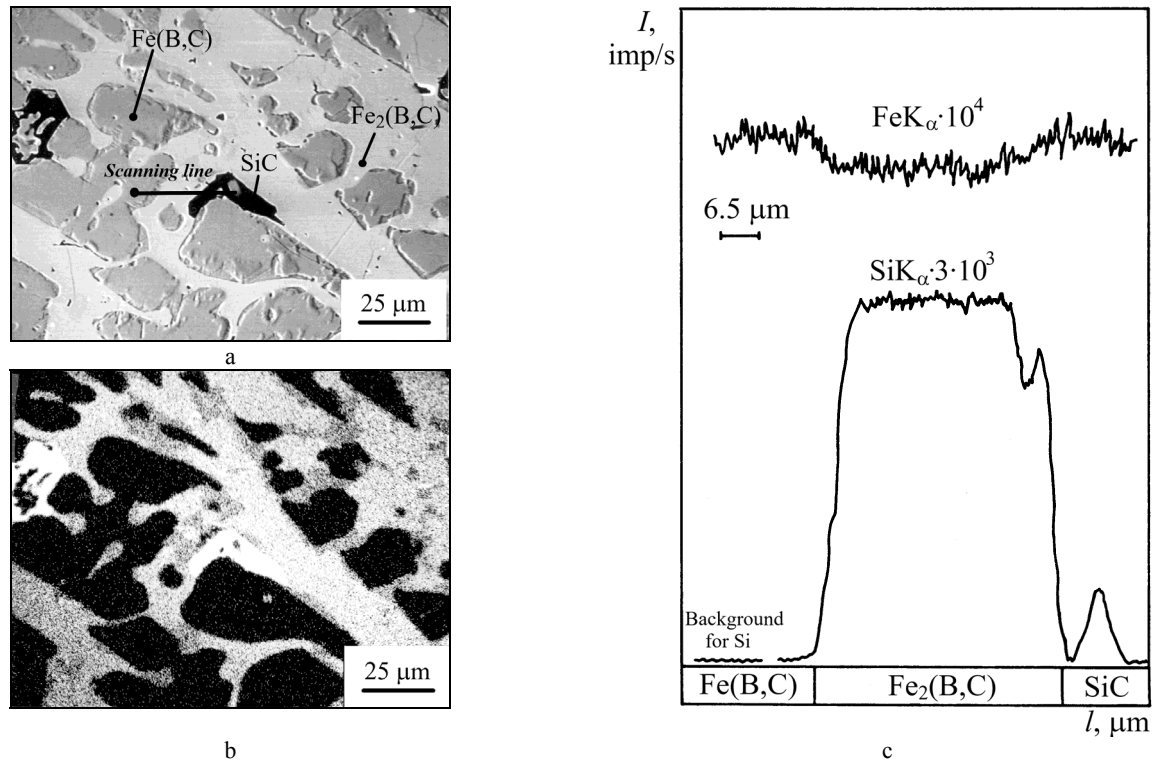
Figure 3. SEM of polished cross-sections of Fe–12.1B–0.1C alloy doped by 5 % of Si: a – second electron image; b – elemental EDS X-ray mapping in SiK_α radiation; c – elemental profile along scanning line

The increase in a cooling rate from 10 to 10^3 K/s does not bring about significant changes in the structural and phase composition of the boron-rich Fe–B–C alloys, saving Fe(B,C) and Fe$_2$(B,C) crystals become smaller (Table 4). The solubility behavior of Ti, Al, Si in the phase constituents remains unchangeable as the results of the lattice parameters measurements evidence (Table 5). The influence of alloying elements on the mechanical characteristics of the rapidly cooled alloys proves to be similar to that for the alloys cooled at the rate of 10 K/s, with higher cooling rate giving rise to higher H_μ and K_{IC} values (Table 3).

As the obtained results show, the solubility of the investigated alloying elements in the constituent phases of the boron-rich Fe–B–C alloys increases in the following sequence: Ti→Al→Si. Considering the atomic radii of the alloying elements allows to explain their solubility, as in this order the atomic radii decrease [35]. Therefore, the largest distortions are caused by alloying with Ti, and the smallest being caused by alloying with Si, followed by Al. It is also evident why titanium preferentially enters into the less close-packed rhombic lattice of Fe(B,C) dendrites than into the tetragonal lattice of $Fe_2(B,C)$ crystals. Besides, titanium gives the microhardness of Fe(B,C) crystals slight increase caused by substitutional strengthening related to the local distortions caused by the solute atom. This is because the significantly larger atom size of substituting Ti, as compared with that of Fe, interrupts the orderly arrangement of atoms in the iron monoboride lattice.

Table 5. The lattice parameters of Fe(B,C) and $Fe_2(B,C)$ crystals in the doped Fe–12.1B–0.1C alloys cooled at 10^3 K/s

Alloying element	Fe(B,C) (rhombic lattice)			$Fe_2(B,C)$ (tetragonal lattice)		
	a, Å	b, Å	c, Å	a, Å	c, Å	c/a
w/o	5.5041±0.0052	4.0596±0.0106	2.9501±0.0037	5.1120±0.0001	4.2418±0.0011	0.8298
Ti	5.5083±0.0014	4.0640±0.0029	2.9562±0.0025	5.1125±0.0020	4.2416±0.0008	0.8297
Al	5.5055±0.0033	4.0611±0.0016	2.9542±0.0041	5.1172±0.0021	4.2478±0.0040	0.8301
Si	5.5049±0.0010	4.0602±0.0008	2.9607±0.0011	5.1157±0.0004	4.2461±0.0003	0.8300

In assessing the alloying effects, it is also necessary to consider the electronic structure of the constituent phases, including the electron distribution [36]. To the properties of $Fe_2(B,C)$ and Fe(B,C) phases contribute strength and directedness of the bonds connecting atoms in their crystal lattices. The properties of Fe_2B compound are determined by the combination of the covalent Fe−B bonds and metallic Fe−Fe bonds, and those of FeB compound – by the combination of the covalent B−B bonds and metallic Fe−Fe bonds [37]. The strength of these bonds depends on the way in which the bonding electrons are localized. So, when Fe atoms are replaced by atoms of the alloying elements, the relative change in the amount of the collectivized valence electrons forming the atomic bonds is responsible for the observed changes in mechanical properties. In electronic exchange between the atoms of iron and alloying elements, energy gain may be achieved when some valence electrons of iron transfer to the outer shells of the solutes. This means that solutes should preferentially act as electron acceptors.

Considering electronic structure of titanium with incomplete *d*-shell [36], it may be concluded that any re-distribution of bonding electrons caused by replacing iron with titanium in the crystal lattices of Fe(B,C) and $Fe_2(B,C)$ phases leads to the destruction of stable configurations. That is why, titanium negligibly enters the crystal lattices of iron borides. As a result, titanium slightly contributes to the mechanical properties of Fe(B,C) and $Fe_2(B,C)$ phases and may affect the microhardness and fracture toughness of the alloys mainly via the precipitation of TiC secondary phase.

The ions of aluminum and silicon form with boron the similar atomic bonds as the atoms of iron. With their valence electrons, aluminum and silicon can form the bonds either accepting or donating shell electrons. When dissolving, these elements are most likely able to form the metal–metal bonds. This contributes to the limited solubility of these elements in the lattices of iron borides and formation of secondary phases. When Al and Si substitute Fe, the fewer electrons may take part in the electronic exchange [36], which leads to weakening atomic bonds of the $Fe_2(B,C)$ and Fe(B,C) solid solutions. Accordingly, microhardness and brittleness of these structural constituents are found to slightly decrease. Taking into account the limited dissolution of Al and Si as well as their small contribution to the bonds' energy balance, their influence on mechanical properties stands to reason.

CONCLUSIONS

The master boron-rich Fe–B–C alloys were found to consist of two major constituents, namely: Fe(B,C) and $Fe_2(B,C)$ solid solutions. When adding 5 % of Ti to Fe–B–C alloys cooled at 10 K/s, this element has low solubility in the structural constituents, preferentially dissolving in Fe(B,C) phase and forming substitutional solution. The negligible dissolution of titanium in the Fe–B–C alloys is responsible for the appearance of TiC secondary crystals at the $Fe_2(B,C)$ boundaries. The solubility behavior of titanium may be explained by its electronic structure that imposes restrictions on the exchange of valence electrons. Titanium introduces the largest lattice distortions which relates to the relatively large difference in the atomic sizes between the iron and the substituting atom. As a result, the microhardness of Fe(B,C) crystals slightly increases but the fracture toughness decreases.

Aluminum and silicon have a limited solubility in the Fe–B–C alloys dissolving preferentially in $Fe_2(B,C)$ crystals and replacing iron atoms. At that, the minor refinement of structure is observed when Al or Si are added. Al or Si are also found in the form of correspondingly $AlB_{12}C$ and SiC compounds precipitated at the $Fe_2(B,C)$ boundaries. The higher solubility of Al and Si in the boron-rich Fe–B–C alloys, as compared with Ti, may be attributed to the stronger acceptor abilities of these elements. The effects of Al and Si on the mechanical properties of the Fe–B–C alloys may be explained by a local change of the electronic structure of constituent phases which leads to weaker bonded atoms in the crystals. As a result, microhardness and brittleness of Fe(B,C) and $Fe_2(B,C)$ solid solutions slightly decrease.

With cooling rate increasing from 10 to 10^3 K/s, solubility behavior of Ti, Al, Si does not have any noticeable changes. Titanium has negligible dissolution in Fe(B,C) phase forming secondary TiC precipitates but aluminum and

silicon, on the contrary, mainly dissolve in $Fe_2(B,C)$ crystals forming $AlB_{12}C$ and SiC compounds, correspondingly, at the $Fe_2(B,C)$ boundaries due to limited solubility. Cooling rate favors the significant decrease in the dimensions of the constituent phases giving rise to their microhardness and fracture toughness.

ORCID ID

Olena V. Sukhova, https://orcid.org/0000-0001-8002-0906

REFERENCES

[1]   V.V. Shyrokov, Kh.B. Vasyliv, Z.A. Duryahina, H.V. Laz'ko, and N.B. Rats'ka, Mater. Sci. **45**(4), 473-480 (2009), https://doi.org/10.1007/s11003-010-9204-5.
[2]   S.I. Ryabtsev, V.A. Polonskyy, and O.V. Sukhova, Powder Metall. Met. Ceram. **58**(9-10), 567-575 (2020), https://doi.org/10.1007/s11106-020-00111-2.
[3]   O.V. Sukhova, V.A. Polonskyy, and K.V. Ustinova, Mater. Sci. **55**(2), 285-292 (2019), https://doi.org/10.1007/s11003-019-00302-2.
[4]   V.G. Efremenko, Yu.G. Chabak, K. Shimizu, A.G. Lekatou, V.I. Zurnadzhy, A.E. Karantzalis, H. Halfa, V.A. Mazur, and B.V. Efremenko, Mater. Des. **126**, 278–290 (2017), https://doi.org/10.1016/j.matdes.2017.04.022.
[5]   O.V. Sukhova, V.A. Polonskyy, and K.V. Ustinova, Voprosy Khimii i Khimicheskoi Tekhnologii. **6**(121), 77-83 (2018), https://doi.org/10.32434/0321-4095-2018-121-6-77-83. (in Ukrainian)
[6]   O.V. Sukhova, J. Superhard Mater. **35**(5), 277-283 (2013), https://doi.org/10.3103/S106345761305002X.
[7]   N. Pavlenko, N. Shcherbovskikh, and Z.A. Duriagina, EPJ Appl. Phys. **58**(1), 10601 (2012), https://doi.org/10.1051/epjap/2012110002.
[8]   W. Shenglin, China Weld. **27** (4), 46-51 (2018), https://doi.org/10.12073/j.cw.20180603001.
[9]   T. Van Rompaey, K. Hari Kumar, and P. Wollants, J. Alloy Compd. **334**(1-2), 173-181 (2002), https://doi.org/10.1016/s0925-8388(01)01777-7.
[10] S. Rades, A. Kornowski, H. Weller, and B. Albert, Chem. Phys. Chem. **12**(9), 1756-1760 (2011), https://doi.org/10.1002/cphc.201001072.
[11] V. Homolova, L. Ciripova, and A. Vyrostkova, J. Phase Equilibria Diff. **36**(6), 599-605 (2015), https://doi.org/10.1007/s11669-015-0424-0.
[12] O.V. Sukhova, K.V. Ustinova, and Yu.V. Syrovatko, Bull. Dnepropetrovskogo Univ. Fizika. Radioelektronika **21**(2), 76-78 (2013).
[13] J. Lentz, A. Röttger, and W. Theisen, Mater. Charact. **135**, 192-202 (2018), https://doi.org/10.1016/j.matchar.2017.11.012.
[14] J. Zhang, J. Liu, H. Liao, M. Zeng, and S. Ma, J. Mater. Res. Technol. (2019), https://doi.org/10.1016/j.jmrt.2019.09.004.
[15] O.V. Sukhova and Yu.V. Syrovatko, Metallofiz. Noveishie Technol. **33**(Special Issue), 371-378 (2011). (in Russian)
[16] Z.A. Duriagina, M.R. Romanyshyn, V.V. Kulyk, T.M. Kovbasiuk, A.M. Trostianchyn, and I.A. Lemishka, J. Achiev. Mater. Manuf. **100**(2), 49-57 (2020), https://doi.org/10.5604/01.3001.0014.3344.
[17] O.V. Sukhova, Metallofiz. Noveishie Technol. **31**(7), 1001-1012 (2009). (in Ukrainian)
[18] I.M. Spiridonova, O.V. Sukhova, and A.P. Vashchenko, Metallofiz. Noveishie Technol. **21**(2), 122-125 (1999).
[19] Z. Chen, S. Miao, L. Kong, X. Wei, F. Zhang, and H. Yu, Mater. **13**(4), 975 (2020), https://doi.org/0.3390/ma13040975.
[20] L. Rovatti, J.N. Lemke, A. Emami, O. Stejskal, and M. Vedani, J. Mater. Eng. Perform. **24**, 4755-4763 (2015), https://doi.org/10.1007/s11665-015-1798-1.
[21] J. Miettinen, V.-V. Visuri, and T. Fabritius, Arch. Metall. Mater. **66**(1), 297-304 (2021), https://doi.org/10.24425/amm.2021.134787.
[22] X. Ren, H. Fu, J. Xing, Y. Yang, and S. Tang, J. Mater. Res. **32**(16), 304-314 (2017), https://doi.org/10.1557/jmr.2017.304.
[23] O. Kon and U. Sen, Acta Phys. Pol. A **127**(4), 1214-1217 (2015), https://doi.org/10.12693/APhysPolA.127.1214.
[24] P. Sang, H. Fu, Y. Qu, C. Wang, and Y. Lei, Materwiss. Werksttech. **46**(9), 962-969 (2015) https://doi.org/10.1002/mawe.201500397.
[25] M.I. Pashechko, K. Dziedzic, and M. Barszcz, Adv. Sci. Technol. Res. **10**(31), 194-198 (2016), https://doi.org/10.12913/22998624/64020.
[26] V.V. Yemets, M.M. Dron`, and O.S. Kositsyna, J. Chem. Technol. **27**(1), 58-64 (2019), https://doi.org/10.15421/081906.
[27] S. Ma and J. Zhang, Rev. Adv. Mater. Sci. **44**, 54-62 (2016).
[28] Z.F. Huang, J.D. Xing, S.Q. Ma, Y.M. Gao, M. Zheng, and L.Q. Sun, Key Eng. Mater. **732**, 59-68 (2017), https://doi.org/https://doi.org/10.4028/www.scientific. net/kem.732.59.
[29] T.N. Baker, Ironmak. Steelmak. **46**(1), 1-55 (2019), https://doi.org/10.1080/03019233.2018.1446496.
[30] A. Sudo, T. Nishi, N. Shirasu, M. Takano, and M. Kurata, J. Nuclear Sci. Technol. **52**(10), 1308-1312 (2015), https://doi.org/10.1080/ 00223131.2015.1016465.
[31] L. Sidney, *Alloy Steel: Property and Use*, (Scitus Academics LLC, Wilmington, 2016).
[32] X. Huang, W.G. Ischak, H. Fukuyama, T. Fujisawa, and C. Yamauchi, ISIJ Int. **36**(9), 1151–1156 (1996), https://doi.org/10.2355/isijinternational.36.1151.
[33] O.V. Sukhova and K.V. Ustinova, Funct. Mater. **26**(3), 495-506 (2019), https://doi.org/10.15407/fm26.03.495.
[34] K. Niihara, R. Morena, and P.H. Hasselman, J. Mater. Sci. Lett. **1**, 13-16 (1982), https://doi.org/10.1007/BF00724706.
[35] C.J. Smithells, *Metals Reference Book*, (Butterworth and Co., London, Boston, 1976).
[36] G.V. Samsonov, I.F. Pryadko, L.F. Pryadko, *Электронная локализация в твердом теле* [*Electron Localization in Solids*], (Nauka, Moscow, 1976), pp. 339. (in Russian)
[37] G. Li and D. Wang, J. Condens. Matter. Phys. **1**, 1799-1808 (1989), https://doi.org/10.1088/0953-8984/1/10/002.

ВПЛИВ Ti, Al, Si НА СТРУКТУРУ ТА МЕХАНІЧНІ ВЛАСТИВОСТІ ВИСОКОБОРИСТИХ СПЛАВІВ Fe–B–C

Олена В. Сухова

Дніпровський національний університет імені Олеся Гончара

49010, Україна, м. Дніпро, просп. Гагаріна, 72

Досліджено вплив заміщення Fe у високобористих сплавах Fe–B–C, що містять 10,0–14,0 % B; 0,1–1,2 % C; Fe – залишок, 5,0 % Ti, Al чи Si (у ваг. %) із застосуванням методів оптичної мікроскопії, рентгеноструктурного аналізу, сканувальної електронної мікроскопії та рентгеноспектрального мікроаналізу. Механічні властивості, а саме мікротвердість та коефіцієнт тріщиностійкості, вимірювали на приладі Віккерса. Мікроструктура базових сплавів Fe–B–C, охолоджених зі швидкістю 10 та 10^3 К/с, складається з первинних дендритів твердого розчину Fe(B,C) та кристалів Fe_2(B,C). Встановлено, що титан має найнижчу розчинність у структурних складових сплавів Fe–B–C, причому Ti переважно розчиняється в решітці фази Fe(B,C), займаючи в ній позиції Fe. Показано, що цей елемент, в основному, бере участь в утворенні вторинних фаз, ідентифікованих як TiC, які спостерігаються в структурі у вигляді виділень по границям фази Fe_2(B,C). Титан незначно підвищує мікротвердість і знижує коефіцієнт тріщиностійкості високобористих сплавів Fe–B–C завдяки твердо-розчинному зміцненню дендритів Fe(B,C) та виділенню вторинних фаз. Розчинність Al та Si в фазах Fe(B,C) та Fe_2(B,C), а також кількість вторинних фаз, що утворюються в структурі, свідчать про більшу розчинність Al та Si у структурних складових порівняно з Ti. Ці елементи переважно розчиняються в кристалічній решітці фази Fe_2(B,C), заміщуючи атоми заліза, а також утворюють по її границях сполуки $AlB_{12}C$ та SiC відповідно. Додавання Al та Si до високобористих сплавів Fe–B–C незначно зменшує мікротвердість і збільшує коефіцієнт тріщиностійкості структурних складових. Підвищення швидкості охолодження з 10 до 10^3 К/с не викликає суттєвої зміни характеру розчинності досліджених легуючих елементів у високобористих сплавах Fe–B–C. Охолодження з більшою швидкістю забезпечує зростання мікротвердості та коефіцієнта тріщиностійкості структурних складових, середні розміри яких стають значно меншими. Вплив легуючих елементів на структуру та механічні властивості досліджених високобористих сплавів Fe–B–C пояснено різницею атомних радіусів та електронної структури розчинених атомів Ti, Al, Si.

КЛЮЧОВІ СЛОВА: структура, бориди заліза**,** легуючі елементи, розчинність, мікротвердість, коефіцієнт тріщиностійкості.

A VARIATIONAL TECHNIQUE FOR THERMODYNAMICS OF LIQUID $K_{1-X}Rb_X$ ALLOYS

Rajesh C. Malan[a,*], Aditya M. Vora[b]

a Applied Science and Humanities Department, Government Engineering College, Valsad-396001, Gujarat, India
b Department of Physics, University School of Sciences, Gujarat University, Ahmedabad-380009, India
*Corresponding Author: rcmgecv@gmail.com
Received February 1, 2021; revised April 9, 2021; accepted April 14, 2021

Liquid $K_{1-X}Rb_X$ binary alloys with various thermodynamical proportions of participating elements are investigated. The properties of thermodynamic interest are included in the study. The internal energy (F_{int}), Helmholtz free enrgy (F_H) and the entropy (S) have been calculated in a concentration range from $X = 0.0$ to $X = 1.0$ increasing in a step of 0.1 in the present work. Apart from the internal energy (F_{int}), various contributions to this energy are also calculated and separately depicted in the present article. A variational approach has been adopted for the present calculation. A single potential with a set of two parameters is used for the calculation of all properties of the alloys. Static Hartree local field function (H) is used to consider screening effect. Various local field correction functions are used to take into account the exchange and correlation effect. Comparison with experimental data at some concentration shows the good agreement with the presently obtained data. With the help of current results, the applied model potential found very suitable with individual parameters for thermodynamical study. As the present results provide the data even where minimum availability of the experimental findings, it can serve as a data base for the future calculation which deals with thermodynamics of the liquid alloys. Present results allow one to get proportion based tuned properties of the $K_{1-X}Rb_X$ for different requirements.
KEYWORDS: thermodynamical properties, liquid alkali alloy, pseudopotential theory, variational approach, Gibbs-Bogoliubov inequality.

The thermodynamic properties of the metals as well as alloys are of the prime importance, particularly when they are used in industry at a large scale productions or manufacturing purpose. The exact information at atomic level regarding the all aspects from thermodynamic behaviour has a great significance in this field. The thermodynamic study is possible in two alternate ways: a) experimental and b) theoretical. The former is the expensive way while the other required a dip understanding the formulation of the thermodynamic problems in terms of mathematical models. There have been lot of theoretical study carried out by various methods for thermodynamic study of liquid metals and alloys [2-7]. The pseudopotential method is the one of the successful method to demonstrate almost all type of properties in solid as well as liquid form of the matter.

The alkali group involves the metals which are having their melting points very near or just above the room temperature. This may create rapid phase change of the metals from liquid to solid or vice versa. Thus the applications of the liquid alkali metal and their binary alloys seek the information in liquid phase also. The present article involves thermodynamic study of one of the alkali-alkali binary alloy $K_{1-X}Rb_X$ using Gibbs-Bogoliubov inequality [8]. The internal energy (F_{int}) and some contributions toward it, Helmholtz free energy (F_H) and the various types of entropy of the binary system are obtained using the individual set of the parameters of the model potential suggested by Fiolhais *et al* [1]. The comparison with the others results are shown in the tabular format for each component in the next part of the manuscript.

THEORETICAL DETAIL

The present work extends the computation to the system of binary alkali alloy $Na_{1-X}K_X$. According to which for the binary system of alloy, The Helmholtz free energy (F_H) is obtained from the equation [4], [9],

$$F_H = F_{ps} + F_{iii}. \tag{1}$$

Where F_{ps} is the averaged effective potential of the system and it can be given as [4], [9][4-6],

$$F_{ps} = F_g + F_M + F_i + F_{ii}. \tag{2}$$

It includes the free energy of the electron gas F_g and first and second order perturbation parts F_i and F_{ii} respectively. Free energy of the electron gas F_g can be given as [4], [9],

$$F_g = \left[\frac{3}{10}k_f^3 - \frac{3}{10}k_f + E_c - \frac{1}{2}\gamma_g T^2\right], \tag{3}$$

where E_c is correlation energy contribution and γ_g is low temperature specific heat constant. The second term in equation (1) i.e. the free energy per particle (F_{iii}) of the binary mixture can be expressed in terms of entropy (S_{mix}) as [4], [9],

$$F_{iii} = \frac{3}{2}KT - TS_{mix}, \tag{4}$$

$$S_{mix} = S_{gas} + S_c + S_{\eta+}S_\sigma, \tag{5}$$

where S_{gas} represents the gas term, S_c is the ideal entropy of mixing, S_η corresponds to packing density (η) and S_σ arise due to the difference in hard diameters of participating elements of an alloy.

The internal energy (F_{int}) can be given as,

$$F_{int} = \frac{3}{2}k_BT + F_{eg} + F_\text{i} + F_\text{ii} + F_M. \tag{6}$$

RESULTS AND DISCUSSION

Table 1 gives the input parameters and constants used for the present calculations including potential parameters. As it is one of the key goals of the article i.e. to test parameters of Fiolhais *et al.* [1] in its original form for the study of K-Rb alloys, no change in the parameters of potential has been made.

Table 1. Potential parameters and other constants used for computation

Metal	Z	Ω (au)	η	α [1]	R [1]
K	1	535.33	0.46	3.349	0.679
Rb	1	656.17	0.43	3.228	0.755

To estimate the screening effect over the bare ion potential the Hartree local field correction function (H) [10] is used. The other local field correction functions used over the bare ion potentials are the functions suggested by Hubbard-Sham (HS) [11], [12], Vashishtha-Shingwi (VS) [13], Taylor (T) [14], Sarkar *et al.*(S) [15], Ichimaru-Utsumi (IU) [16] and Farid *et al.* (F) [17] and Nagy (N) [18].

Table 2 shows the potential independent contributions (F_i), (F_{iii}) and (F_g) to total free energy. It can be seen from the Table 2 that except F_{iii}, all are having negative contribution. The present results for F_g are compared with others results [19]. An excellent agreement of present results for F_g is obtained with compared results [19]. The present results of F_i and F_{ii} are also compared with the results of others [19].

Table 2. Various contributions to internal energy (F_{int}) $* 10^{-3}$ au

X	F_g	Others [19]	F_i	Others [19]	F_m	Others [19]	F_{iii}
0.0	-79.90	-	79.97	-	-209.48	-	-8.52
0.1	-79.77	-79.81	71.43	100.28	-205.78	-212.51	-8.69
0.2	-79.63	-79.66	74.64	98.24	-209.80	-210.26	-8.85
0.3	-79.49	-79.52	77.73	96.28	-214.99	-208.12	-9.02
0.4	-79.36	-79.37	80.70	94.41	-218.63	-206.15	-9.18
0.5	-79.22	-79.23	83.55	92.61	-219.50	-204.19	-9.34
0.6	-79.08	-79.08	86.30	90.88	-217.21	-202.31	-9.50
0.7	-78.94	-78.93	88.95	89.22	-212.17	-200.57	-9.66
0.8	-78.80	-78.78	91.50	87.62	-205.57	-199.14	-9.82
0.9	-78.66	-78.64	93.96	86.08	-199.76	-197.42	-9.98
1.0	-78.52	-	96.34	-	-200.21	-	-10.14

The reason for deviation between present results and others results [19] for F_i lies in the mathematical approach of variational method. According to variational approach, a first guess for the real function is made, which will then constrained by the boundary conditions to minimize the deviation between actual and the first guess function. The perturbation part is added to get the maximum closest result to the actual one. The deviation between the present values of F_i and that of the others is just the difference between the perturbation parts of both the results. Which has no physical significant. Hence, the deviation is not affecting on the final results of the internal energy (F_{int}). Similar logic can be applied to the calculation of F_{ii} also.

Table 3 shows F_{ii} obtained by application of various local field correction functions. The results obtained for N-function [18] are maximum whereas it is minimum due to the correction function Hartree (H) [10].

Table 3. $(F_{ii} * 10^{-3})$ *au*

X	H	HS	VS	T	S	IU	F	N	Others [19]
0.0	-14.58	-14.12	-13.68	-13.52	-13.89	-13.33	-13.31	-11.88	-
0.1	-29.36	-28.70	-28.10	-27.92	-28.40	-27.66	-27.65	-25.21	-2.68
0.2	-26.51	-25.90	-25.34	-25.16	-25.62	-24.92	-24.90	-22.68	-2.85
0.3	-18.80	-18.31	-17.85	-17.69	-18.07	-17.49	-17.48	-15.83	-3.01
0.4	-11.72	-11.37	-11.01	-10.87	-11.18	-10.71	-10.70	-9.60	-3.08
0.5	-7.84	-7.57	-7.28	-7.15	-7.41	-7.03	-7.02	-6.24	-3.22
0.6	-8.21	-7.95	-7.68	-7.57	-7.81	-7.45	-7.44	-6.66	-3.37
0.7	-12.33	-12.01	-11.70	-11.59	-11.85	-11.46	-11.45	-10.35	-3.44
0.8	-18.28	-17.86	-17.47	-17.35	-17.66	-17.18	-17.17	-15.56	-3.27
0.9	-22.07	-21.57	-21.10	-20.96	-21.33	-20.76	-20.75	-18.76	-3.46
1.0	-14.05	-13.63	-13.22	-13.08	-13.42	-12.89	-12.88	-11.41	-

Figure 1 shows the various types of entropy contributions. The ideal entropy of mixing S_c is found very low (almost zero) for each of the concentrations. The ideal gas entropy (S_g) gives the maximum contribution for entropy (S_{mix}).
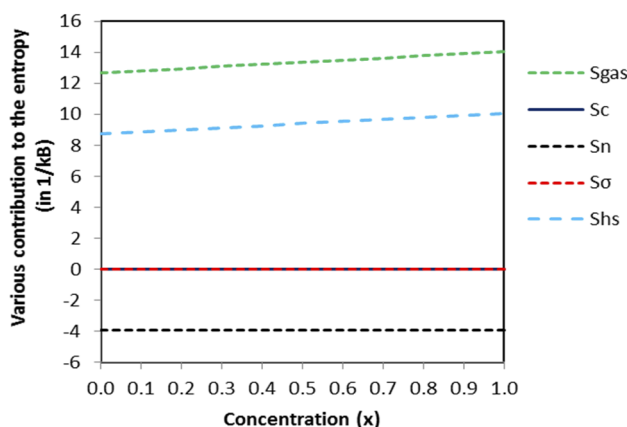
Figure 1. Entropy contributions

The internal energy (F_{int}) of the present calculation has been be compared with previously published results of Vora [2] and Thakor [19] as well as with the experimental results [5] as shown in Table 4. The internal energy (F_{int}) at higher concentration value (X) is found in a very good agreement with the experimental results [5] and the results of others [2], [19].

Table 4. Internal Energy $(-F_{int} * 10^{-3})$ *au*

X	H	HS	VS	T	S	IU	F	N	Others [2], [19]	Exp [5]
0.00	266.57	266.11	265.67	265.52	265.88	265.32	265.31	263.88	260.46	194
0.10	208.50	207.84	207.24	207.06	207.54	206.80	206.79	204.35	193.11	-
0.20	200.06	199.44	198.88	198.70	199.16	198.46	198.45	196.23	192.94	-
0.30	186.92	186.44	185.98	185.81	186.20	185.62	185.60	183.96	192.78	-
0.40	174.64	174.28	173.93	173.78	174.09	173.63	173.62	172.52	192.62	-
0.50	165.79	165.51	165.22	165.10	165.36	164.98	164.96	164.19	192.47	-
0.60	161.44	161.18	160.91	160.79	161.03	160.68	160.67	159.89	192.33	-
0.70	161.11	160.80	160.49	160.37	160.63	160.24	160.23	159.13	192.19	-
0.80	162.91	162.49	162.10	161.98	162.29	161.81	161.80	160.19	192.06	-
0.90	162.85	162.35	161.88	161.74	162.11	161.54	161.53	159.54	191.93	-
1.00	151.29	150.87	150.46	150.32	150.66	150.14	150.13	148.65	249.94	180

The agreement with the results of Thakor [19] for internal energy (F_{int}) suggests that there is no effect of deviation between the presently calculated results of F_i and the F_i calculated by Thakor [19]. Similar is the case with the presently calculated F_{ii} and the F_{ii} calculated by Thakor [19]. The Helmholtz free energy (F_H) shown in Table 5.

Table 5. Helmholtz free energy ($-F_H * 10^{-3}$) au

X	H	HS	VS	T	S	IU	F	N	Others [2], [19]	Exp [5]
0.0	311.53	311.07	310.63	310.47	310.84	310.27	310.26	308.83	270.70	199.10
0.1	252.17	251.50	250.91	250.72	251.20	250.46	250.45	248.02	212.08	198.47
0.2	250.15	249.54	248.98	248.80	249.26	248.56	248.54	246.32	212.53	197.68
0.3	244.56	244.08	243.62	243.45	243.84	243.26	243.24	241.60	212.83	196.78
0.4	238.19	237.83	237.48	237.33	237.64	237.18	237.17	236.07	213.02	195.41
0.5	232.35	232.07	231.79	231.66	231.92	231.54	231.53	230.75	213.10	193.33
0.6	227.70	227.44	227.17	227.06	227.29	226.94	226.93	226.15	213.10	192.19
0.7	224.15	223.83	223.52	223.41	223.67	223.28	223.27	222.17	213.00	192.11
0.8	220.97	220.55	220.16	220.04	220.36	219.87	219.87	218.26	212.80	192.61
0.9	216.50	216.00	215.54	215.39	215.77	215.19	215.18	213.19	212.46	191.59
1.0	206.57	206.16	205.74	205.60	205.94	205.42	205.41	203.93	262.08, 260.34	189.98

Figure 2 is given to display the trend of variation of F_H with respect to the concentration (X). It can be seen from Figure 2 that the F_H is continuously decreasing with respect to concentration (X). The similar type of trend is observed in experimental data [5]. As all correction functions are providing the almost similar results, presently only the result of H-functions are provided in order to avoid overlapping of plots of F_H.
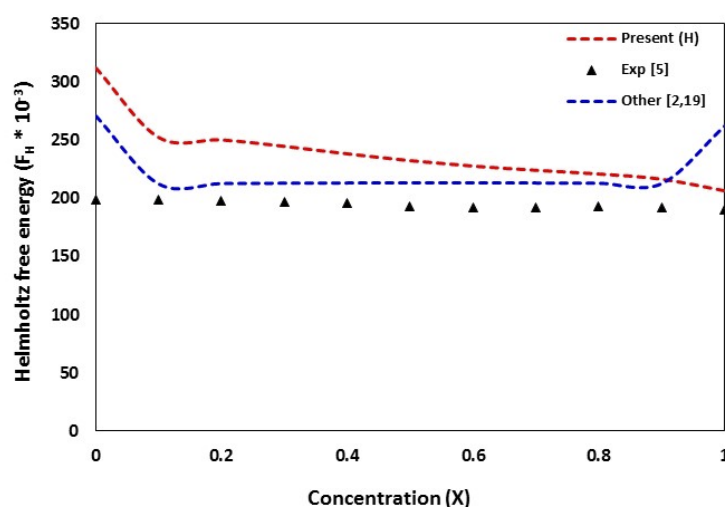
Figure 2. Helmholtz free energy ($-F_H * 10^{-3}$) au

CONCLUSION

The variational approach with Gibbs-Bogoliubov inequality [8] is applied for the calculation of thermodynamical properties of liquid K$_{1-X}$Rb$_X$ alloys. The results for the internal energy (F_{int}) and Helmholtz free energy (F_H) at various concentration (X) of participating metals are provided. Good agreement for F_H at many higher value of X is obtained between present results and other theoretical results of Vora [2] and Thakor [19] and experimental data [5]. Very less influence of correction function is found and hence the results by various local field correction function generates results very near to each other in the present study.

ORCID IDs

Rajesh C. Malan, https://orcid.org/0000-0002-6216-8007; **Aditya M. Vora,** https://orcid.org/0000-0002-2520-0266

REFERENCES

[1]   C. Fiolhais, J.P. Perdew, S.Q. Armster, J.M. MacLaren, and M. Brajczewska, Phys. Rev. B, **51**, 14001–14011 (1995), https://doi.org/10.1103/PhysRevB.51.14001.
[2]   A.M. Vora, J. Eng. Phys. Thermophys. **82**, 779–788 (2009), https://doi.org/10.1007/s10891-009-0250-5.
[3]   N. Dubinin, N.A. Vatolin, and V.V. Filippov, Russ. Chem. Rev. **83**, 987 (2014), https://doi.org/10.1070/RCR4410.

[4]   I. Umar, A. Meyer, M. Watabe, and W. Young, J. Phys. F Met. Phys. **4**, 1691 (1974), https://doi.org/10.1088/0305-4608/4/10/016.
[5]   R. Hultgren, P. D. Desai, D. T. Hawkins, M. Gleiser, and K. K. Kelley, Selected Values of the Thermodynamic Properties of Binary Alloys, Am. Soc. Metals, Metal Park, 1973.
[6]   R.C. Malan, and A.M. Vora, *AIP Conf. Proc.* **2009**, 020052, (2018), https://doi.org/10.1063/1.5052121.
[7]   R.C. Malan, and A.M. Vora, J. Nano-Electronic Phys. **10**, 03020 (2018), https://10.21272/jnep.10(1).01002.
[8]   A. Isihara, J. Phys. Gen. Phys. **1**, 539 (1968), https://doi.org/10.1088/0305-4470/1/5/305.
[9]   A.M. Vora, J. Theor. Appl. Phys. **3**, 25–32 (2010), https://www.sid.ir/FileServer/JE/134220100405.pdf.
[10] Y. Waseda, *The structure of non-crystalline materials: liquids and amorphoussolids*, (New York, McGraw-Hill, 1980).
[11] J. Hubbard, Royal Proc. London A, **243**, 336–352 (1958), https://doi.org/10.1098/rspa.1958.0003.
[12] L. Sham, Royal Proc. of London A, **283**, 33–49 (1965), https://doi.org/10.1098/rspa.1965.0005.
[13] P. Vashishta, and K. Singwi, Phys. Rev. B, **6**, 875, (1972), https://doi.org/10.1103/PhysRevB.6.875.
[14] R. Taylor, J. Phys. F Met. Phys. 8, **699** (1978), https://doi.org/10.1088/0305-4608/8/8/011.
[15] A. Sarkar, D. Sen, S. Haldar, and D. Roy, Mod. Phys. Lett. B, **12**, 639–648 (1998), https://doi.org/10.1142/S0217984998000755.
[16] S. Ichimaru, and K. Utsumi, Phys. Rev. B, **24**, 7385 (1981), https://doi.org/10.1103/PhysRevB.24.7385.
[17] B. Farid, V. Heine, G. Engel, and I. Robertson, Phys. Rev. B, **48**, 11602 (1993), https://doi.org/10.1103/PhysRevB.48.11602.
[18] I. Nagy, J. Phys. C Solid State Phys. **19**, L481 (1986), https://doi.org/10.1088/0022-3719/19/22/002.
[19] P.B. Thakor, Ph.D. Thesis, Sardar Patel University, V.V. Nagar, Gujarat, India, 2004.

ВАРІАЦІЙНИЙ МЕТОД ТЕРМОДИНАМІКИ РІДКИХ СПЛАВІВ $K_{1-X}Rb_X$

Раджеш С. Малан[a], Адітя М. Вора[b]

[a]*Факультет прикладних та гуманітарних наук, Урядовий інженерний коледж, Вальсад-396001, Гуджарат, Індія*
[b]*Фізичний факультет, Університетська школа наук, Університет Гуджарат, Ахмедабад-380009, Індія*

Досліджуються рідкі бінарні сплави $K_{1-X}Rb_X$ з різними термодинамічними пропорціями елементів, що беруть участь. У цій роботі були розраховані внутрішня енергія (F_{int}), вільна енергія Гельмгольца (F_H) і ентропія (S) в діапазоні концентрацій від $X = 0.0$ до $X = 1.0$, що збільшуються з кроком 0,1. В дослідження включені властивості термодинамічного характеру. Окрім внутрішньої енергії (F_{int}), в цій статті також розраховуються і окремо відображаються різні вклади в цю енергію. Для цього розрахунку було застосовано варіаційний підхід. Для розрахунку всіх властивостей сплавів використовується єдиний потенціал із набором двох параметрів. Статична функція локального поля Хартрі (H) використовується для урахування ефекту екранування. Для врахування ефекту обміну та кореляції використовуються різні функції локальної корекції поля. Порівняння з експериментальними даними при певній концентрації свідчить про гарний збіг з отриманими на цей час даними. Як показали поточні результати, застосований модельний потенціал виявився дуже придатним для окремих параметрів при термодинамічному дослідженні. Оскільки ці результати забезпечують дані навіть при мінімальній доступності експериментальних висновків, вони можуть служити базою даних для майбутніх розрахунків, які стосуються термодинаміки рідких сплавів. Наведені результати дозволяють отримати властивості, підібрані на основі пропорцій $K_{1-X}Rb_X$ для різних вимог.

КЛЮЧОВІ СЛОВА: термодинамічні властивості, рідкий лужний сплав, теорія псевдопотенціалу, варіаційний підхід, нерівність Гіббса-Боголюбова

INVESTIGATION ON ELECTRICAL PROPERTIES OF SOLID POLYMER SHEETS (HDPE AND LDPE) AT AUDIO FREQUENCY RANGE

Sarat K. Dash[a,*], Hari S. Mohanty[b], Biswajit Dalai[b,†]

ᵃDepartment of Physics, Regional Institute of Education (NCERT), Bhubaneswar, Odisha, 751022, India
ᵇDepartment of Physics, School of Sciences, GIET University, Gunupur 765022, Odisha, India
*Corresponding author: skdash59@yahoo.com, †biswajit@giet.edu

Two different groups of solid polymer sheets: low density polyethylene (LDPE) sample of thickness 0.006 cm and 0.007 cm along with high density polyethylene (HDPE) sample of the thickness of 0.009 cm, 0.010 cm were taken in this work. The measurement of electrical properties such as dielectric constant, ε' and dielectric loss, ε'' for LDPE and HDPE polymer sheets have been measured using a dielectric cell. The dielectric cell has been fabricated which consists of two circular parallel plates of pure stainless steel each of 5 cm diameter and 2 mm thickness. An impedance bridge (GRA 650A) was used for measurement of capacitance, C, and dissipation factor, D in the audio frequency (AF) range, 100 Hz to 10 kHz. Different samples were loaded in between the two plates of the cell and the capacitance as well as the dissipation factor were estimated from the dial readings of the bridge. Effect of frequency variation on ε', ε'', relaxation time, τ, dissipation factor, $\tan\delta$ and ac conductivity, σ were also discussed at audio frequency range. The complex permittivity, ε^*, related to free dipole oscillating in an alternating field and loss tangent, $\tan\delta$ were calculated. The frequency-dependent conductivity, dielectric behavior, and electrical modulus, both real (M') and imaginary (M'') parts of LDPE and HDPE have been studied in this work. The values of the real part of the electrical modulus (M') did not equal to zero at low frequencies and it is expected that the electrode polarization may develop in both sheets. These findings reveal an increased coupling among the local dipolar motions in a short-range order localized motion. The analysis of real (ε') and imaginary (ε'') parts of dielectric permittivity and that electrical modulus real (M') and imaginary (M'') parts signify poly dispersive nature of relaxation time as observed in Cole-Cole plots.
KEY WORDS: LDPE, HDPE, dielectric constant, dielectric loss, AC conductivity

In continuation of our earlier analysis on characterization and dielectric properties of barium zirconium titanate prepared by solid state reaction and high energy ball milling processes [1], the electrical properties of solid polymer sheet have been studied in this work which enable the industry to elicit the characteristic information as regards to its use as insulator having high dielectric breakdown strength, low dielectric loss and the ability to be easily processed and also recycled when cross linked [2, 3]. The measurement of dielectric constant is recognized as one of the important tool for understanding the molecular behavior of associating molecules [4]. Gradual evolution of dielectric theories based on such measurements has helped in this study further. The physico-chemical behavior of macromolecules could be ascertained from the study of the frequency and temperature variation of relative permittivity ε' and dielectric loss ε'' [5, 6]. Surface composition of the polymers primarily influences many industrial applications such as wetting, weathering, permeation friction, electrostatic charging and dye adsorption [7]. However, lack of precise information regarding functional groups and the surface region-a problem having no counterpart in polymer science, is an important impediment in this sphere. High density polyethylene (HDPE) and low density polyethylene (LDPE) are low cost, high tensile strength and percent elongation, has penetrated into the markets like stretching film, merchandizing bags and also non-packing application like industrial sheeting and agricultural film [8, 9]. Attempt are being made to determine the size of surface micro-cracks of irradiated polythene terthaphalate (PET) with X-Rays and nonmonotonus dependence of dissociation rate of polymer on alkali solution [10]. The physico-chemical properties of LDPE with wood fiber, induced by ion-bombardment are being extensively studied [11, 12]. The physical and chemical nature of the macromolecules and the molecular mobility of the sub-molecules can be deduced from the study of the variation of dielectric constant as well as dielectric loss with temperature and frequency and the position of the loss peak [13].

The dielectric properties of solid polyethylene have been investigated in audio frequency (AF) range because of large size of the molecules. In the present report, an attempt has been made to determine the values of dielectric constant (ε') and dielectric loss (ε'') of the solid polymers such as high density polyethylene (HDPE) and low density polyethylene (LDPE) by using an impedance bridge over a frequency range of 100 Hz to 10 kHz at 303.16 K. The cost of the design is relatively less compared to any other versatile system and can be inducted as standard experiment at an appropriate level.

THEORY

The most generally used methods for measuring dielectric constant (ε') and loss (ε'') consists of the measurement of the capacitance of an empty capacitor and the capacitance of the capacitor filled with the dielectric material. The capacitance C of a capacitor is defined as the ratio of the charge on its plates to the potential difference between them. For a parallel plate capacitor, the capacitance C can be calculated from the geometry of the system [14]

$$C = \varepsilon_0 \varepsilon' \frac{A}{d}, \tag{1}$$

where ε' is the dielectric constant of the material a dimensionless property of the material between the two plates and ε_0 is the permittivity of free space. Here A is the area of one of the plates and d is the thickness of the material. The dielectric constant is thus conveniently expressed as the ratio of the capacitance of the capacitor with the material in place to its capacitance with vacuum (or air, for which $\varepsilon' = 1.0005$ at 20°C) between the plates. If a loss-free dielectric is considered in an alternating electric field, there would be no dissipation of energy, and charging voltage and current in a capacitor would be 90° out of phase. But when subjected to an alternating field, the polar molecules of a system rotate towards an equilibrium distribution in molecular orientation with corresponding dielectric polarization. Due to either very large size of the polar molecule or high frequency of the alternating field, the rotating motion of the molecule may not be sufficiently rapid for attaining equilibrium, and then the polarization acquires a component out of phase with the electric field [15,16]. The current through a capacitor, therefore, does not lead the voltage by 90° but only by (90°-δ) where δ is often called the loss angle. Therefore, the complex permittivity (ε^*) related to free dipole oscillating in an alternating field is given by [17, 18],

$$\varepsilon^* = \varepsilon' - j\varepsilon'' = \varepsilon_\infty + \frac{\varepsilon_S - \varepsilon_\infty}{1 + j\omega\tau}, \tag{2}$$

where, ε_S and ε_∞ are the low and high frequency value of $\varepsilon'(\omega)$, $\omega = 2\pi f$, here f being the measuring frequency and τ is the relaxation time.

The real part of ε^* [19] is

$$\varepsilon' = \varepsilon_\infty + (\varepsilon_S - \varepsilon_\infty)\frac{\omega\tau}{1 + \omega^2\tau^2}. \tag{3}$$

The real part ε' is calculated as [20],

$$\varepsilon' = \frac{C}{C_a}\left(\frac{1}{1 + \tan^2\delta}\right), \tag{4}$$

where C is the measured capacitance, C_a is the empty capacitance and tanδ is the loss tangent.
The imaginary part of ε^* is given by [20]

$$\varepsilon'' = (\varepsilon_S - \varepsilon_\infty)\frac{\omega\tau}{1 + \omega^2\tau^2}. \tag{5}$$

The imaginary part ε'' is the loss factor and calculated as

$$\varepsilon'' = \varepsilon'\tan\delta. \tag{6}$$

The loss tangent is given by [21, 22]

$$\tan\delta = \frac{\varepsilon''}{\varepsilon'}. \tag{7}$$

The capacitance of a capacitor is

$$C = \varepsilon'C_a, \tag{8}$$

where C_a is the empty capacitance and ε' is the relative permittivity of the medium between the plates. The problem reduces to the measurement of capacitance of a capacitor with and without the dielectric medium for which ε' is calculated. The dielectric loss factor, ε'' is measured by an electrical bridge using the equation

$$\varepsilon'' = \varepsilon' D v, \tag{9}$$

where D is the dissipation factor and v is the operating frequency.

With measured values of ε' and ε'' at a number of frequencies above the glass transition temperature, the Cole-Cole plot ($\varepsilon' \sim \varepsilon''$) can also be drawn.

TEST METHODS
Description of the dielectric cell
The fabricated dielectric cell (Fig.1) consists of two circular parallel plates of pure stainless steel each of 5 cm diameter and 2 mm thickness. The entire system was enclosed in a wooden box of dimension 15 cm×15 cm×20 cm with removable glass plate in the front panel for loading the sample. The dielectric cell was used to measure the dielectric constant of the specimens.
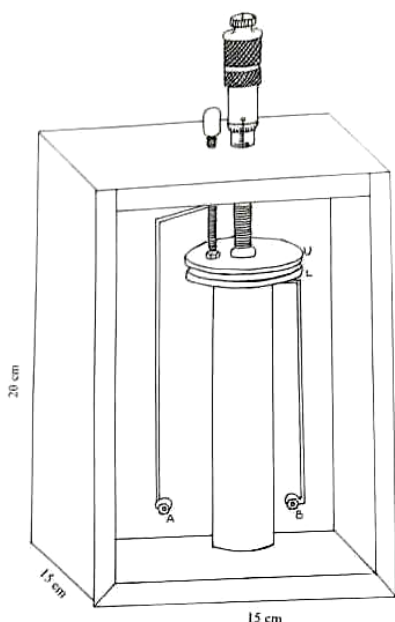
Figure 1. Dielectric cell set up

The lower plate was mounted horizontally using insulating adhesive on a plane glass plate fixed over a wooden upright. It was used as a static plate of the capacitor. The upper plate was rigidly fitted at its center to the movable head of a micrometer screw for its vertical movement while maintaining both the plates parallel to each other. The mounting of both the plates was perfectly horizontal so that both plates, when in contact, touch each other over the entire surface. The initial reading of the micrometer screw head was taken under this condition. The specimen in the form of thin plane sheets was cut into circular shape with diameter equal to that of the plates. To insert the sample between the two plates, the upper plate was moved up and the sample was placed between the plates. Therefore, the screw head was moved down till the sample sandwiched between the two plates and the final reading of the micrometer screw head was taken. These readings were used to compute the thickness of the sample. Two terminals, electrically connected to the two plates of the capacitor, were provided on the body of the box for connecting the capacitor to the bridge. The static lower plate was connected directly while the movable upper plate connected through a metal spring. The stud of the micrometer screw was held in position by fixing to the upper casing of the box.

Stray capacitance

The capacitance, C, of the capacitor used in this case is given by the relation:

$$C = \frac{\varepsilon_0 \varepsilon'}{4\pi} \frac{A}{d} + C_0 , \tag{10}$$

where ε' is dielectric constant of the sample, A is area of cross section of each of the plates which is equal to the area of cross section of the sample, d is distance between the plates which equals the thickness of the sample and C_0 is stray capacitance of the instrument.

The stray capacitance, C_0, of the instrument has been subtracted from the observed capacitance to get the corrected value to be used for measurement of ε'. The following procedure was adopted for determining the stray capacitance of the instrument. The distance between the two plates was varied and the capacitance for different capacitors with air (as dielectric material) was measured (Table 1).

Table 1. Capacitance values of the cell with various thickness of air gap to determine the stray capacitance.

Thickness of the air gap (d) in cm	0.010	0.020	0.025	0.030	0.040	0.050	0.060	0.070	0.080	0.090	0.100
1/d in cm^{-1}	100	50	40	33.33	25	20	16.67	14.3	12.5	11.11	10.0
Capacitance of the cell in $C \times 100$ pF	2.01	1.18	0.98	0.82	0.67	0.58	0.52	0.48	0.45	0.43	0.41

Figure 2. Determination of stray capacitance

A graph was plotted for C vs. 1/d (Fig. 2). The nature of the graph shows a straight line with an intercept on the Y-axis, which gives the value of stray capacitance, C_o, of the instrument, which includes the capacitance due to the connecting leads also.

Impedance bridge

The GRA impedance bridge model 650 A has been used for measurement of capacitance and dissipation factor. The bridge has an internal voltage source at 1 kHz. Alternatively, voltage source at different frequencies has also been applied externally. Different samples were loaded in between the two plates of the cell and the capacitance C as well as the dissipation factor $D (= \tan \delta)$ were estimated from the dial readings of the bridge. The frequency of the voltage source was varied from 100 Hz to 10 kHz and the above observations were repeated at number of frequencies in this range. Since the capacitance for air dielectric

already recorded for different plate separations, its value C_a was noted. This value is independent of frequency. The dielectric constant for each frequency is calculated from the relation:

$$\varepsilon' = \frac{C - C_0}{C_a - C_0},$$ (11)

where ε' is dielectric constant of the material, C_0 is stray capacitance, C_a is capacitance with air dielectric and C is capacitance of the sample as dielectric.

Since the accuracy of measurement of ε' and ε'' depends on measurement of C and $\tan\delta$ it is governed by the limit of accuracy of the impedance bridge used for measurement of C and loss tangent. The accuracy of capacitance measurement over the range 1pF to 100 µF was 1% while that of the dissipation factor measured over range of 0.002 to 1 was 5%.

Sample preparation

Commercially available low density polyethylene (LDPE) sample of thickness 0.006 cm, 0.007 cm high density polyethylene (HDPE) sample of thickness of 0.009 cm, 0.010 cm were obtained from the Central Institute of Plastic Engineering and Technology (CIPET) Extension Centre, Bhubaneswar, India. The specimens were cut to the same size as that of the capacitor plates and put inside the cell for measurement of the experimental parameters ε' and ε'' of LDPE and HDPE. The measured value of ε' of HDPE agrees with the value of static dielectric constant $\varepsilon' = 3.2$ supplied by CIPET, Bhubaneswar.

EXPERIMENTAL RESULTS AND THEIR DISCUSSION

The frequency dependent conductivity, dielectric behavior and electrical modulus of LDPE and HDPE have been studied. The dielectric constant (ε') and the dielectric loss factor (ε'') of LDPE and HDPE samples were measured at temperature 303.16K. The relevant data are displayed graphically in Figs. 3-7 and presented in Table 2. The frequency dependence of ε', ε'' and $\tan\delta$ of LDPE and HDPE samples are shown in Fig. 3 and 4.
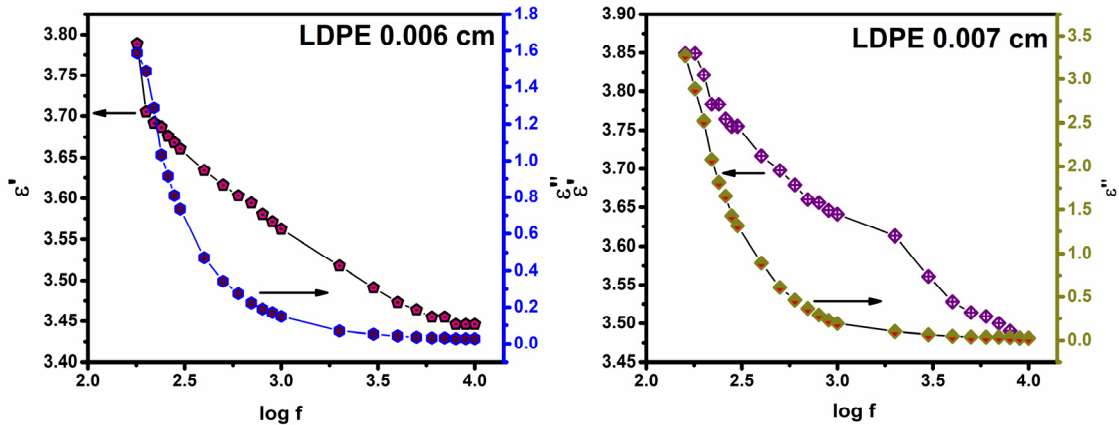
Figure 3. Variation of ε' and ε'' with frequency for LDPE sample having thickness 0.006 cm and 0.007 cm.
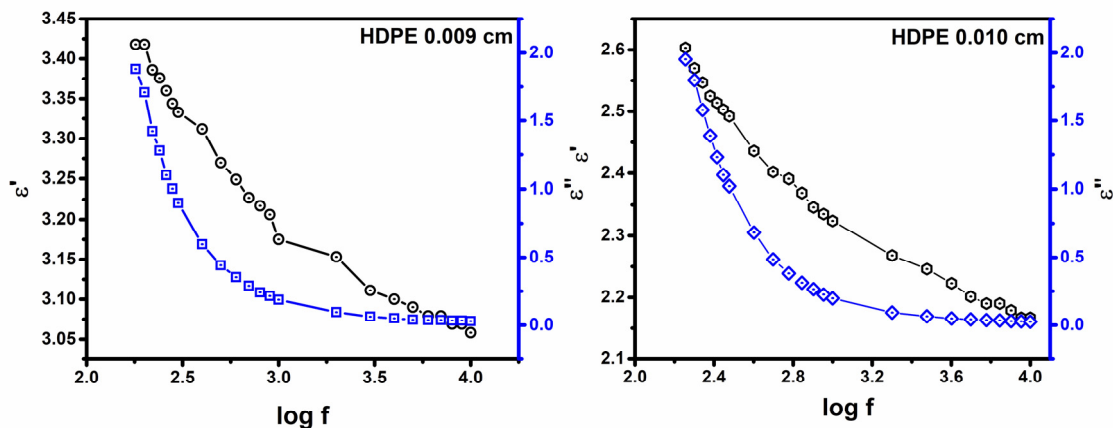
Figure 4. Variation of ε' and ε'' with frequency for HDPE sample having thickness 0.009 cm and 0.010 cm.

At very low frequencies, dipoles follow the field and the value of $\varepsilon' \sim \varepsilon_S$ at quasi-static fields. The values of ε' slightly decrease with increase in frequency as the dipoles begin to lag behind the field. Dipole then no longer follow the field at high frequencies and $\varepsilon' \sim \varepsilon_\infty$. Qualitatively such behavior is observed in the trend of ε' with frequency and in agreement with Eq. 3. Again, it is observed that there is substantial increase in dielectric constant ε' even at lower frequencies, attributes to a dipolar contribution of $\varepsilon'(\omega)$ from hopping of electrons between isolated polaron and bipolaron state. The higher values of $\varepsilon''(\omega)$ at low frequency region may be due to the frequent charged motion within the sample [19, 20] which favors electrical conductivity effects. Using the relation, $\omega_m = 1/\tau$, the relaxation time, τ for the samples is found to be 8.846×10^{-1}s.
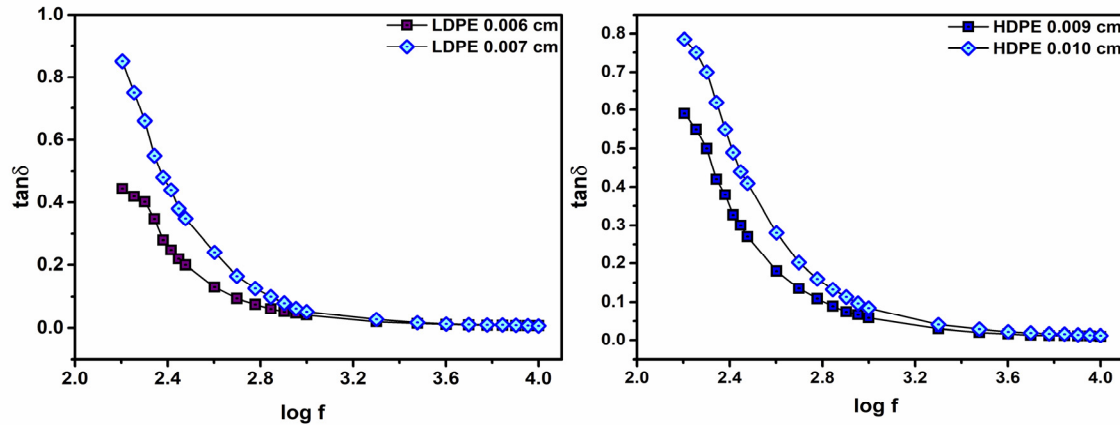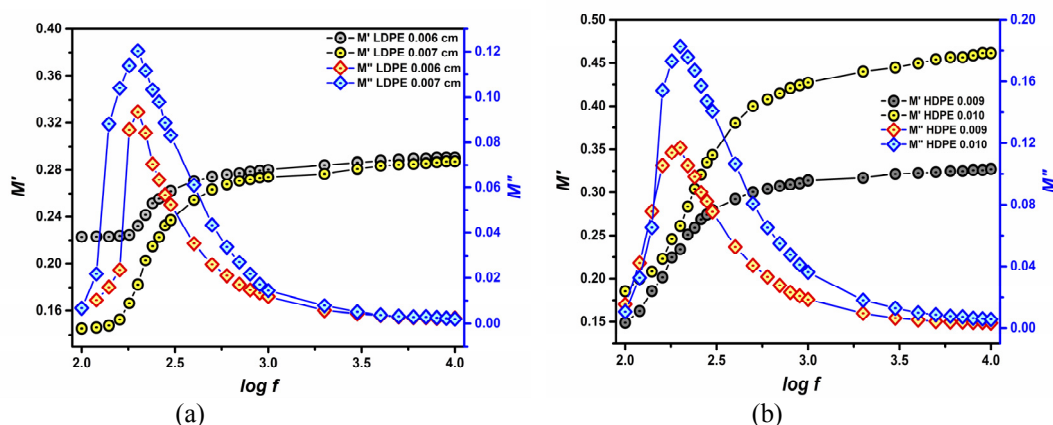

Figure 5. Variation of loss tangent with frequency for LDPE (thickness 0.006 cm and 0.007 cm) and HDPE (thickness 0.009 cm and 0.010 cm) samples.

Table 2. Dielectric constant, ε', dielectric loss, ε'' and dissipation factor, $\tan\delta$ of low density poly ethylene (LDPE) and high density poly ethylene (HDPE) samples.

Frequency f Hz	$Log f$	LDPE = 0.006 cm			LDPE = 0.007 cm			HDPE = 0.009 cm			HDPE = 0.010 cm		
		ε'	ε''	$\tan\delta$	ε'	ε''	$\tan\delta$	ε'	ε''	$\tan\delta$	ε'	ε''	$\tan\delta$
180	2.255	3.789	1.587	0.419	3.849	2.887	0.750	3.418	1.880	0.550	2.603	1.952	0.750
200	2.301	3.705	1.488	0.402	3.821	2.522	0.660	3.418	1.709	0.500	2.570	1.799	0.700
220	2.342	3.692	1.287	0.349	3.783	2.081	0.550	3.386	1.422	0.420	2.547	1.579	0.620
240	2.380	3.687	1.032	0.280	3.783	1.816	0.480	3.376	1.279	0.379	2.525	1.389	0.550
260	2.415	3.687	0.914	0.248	3.764	1.656	0.440	3.360	1.099	0.327	2.514	1.232	0.490
280	2.447	3.687	0.809	0.219	3.755	1.427	0.380	3.344	1.003	0.300	2.503	1.101	0.440
300	2.477	3.670	0.734	0.200	3.755	1.314	0.350	3.333	0.900	0.270	2.492	1.021	0.410
400	2.602	3.634	0.472	0.130	3.717	0.892	0.240	3.312	0.596	0.180	2.436	0.682	0.280
500	2.699	3.616	0.343	0.095	3.698	0.610	0.165	3.270	0.441	0.135	2.402	0.485	0.202
600	2.778	3.603	0.274	0.076	3.679	0.463	0.126	3.249	0.354	0.109	2.391	0.382	0.160
700	2.845	3.594	0.223	0.062	3.660	0.366	0.100	3.227	0.290	0.090	2.369	0.313	0.132
800	2.903	3.580	0.190	0.053	3.656	0.292	0.080	3.217	0.241	0.075	2.346	0.265	0.113
900	2.954	3.571	0.171	0.048	3.646	0.230	0.063	3.206	0.215	0.067	2.335	0.226	0.097
1000	3.000	3.562	0.150	0.042	3.641	0.193	0.053	3.175	0.187	0.059	2.324	0.197	0.085
2000	3.301	3.518	0.070	0.020	3.613	0.101	0.028	3.153	0.095	0.030	2.268	0.093	0.041
3000	3.477	3.491	0.052	0.015	3.561	0.064	0.018	3.111	0.062	0.020	2.246	0.065	0.029
4000	3.602	3.473	0.042	0.012	3.528	0.046	0.013	3.100	0.050	0.016	2.223	0.049	0.022
5000	3.699	3.464	0.035	0.010	3.514	0.039	0.011	3.090	0.040	0.013	2.201	0.042	0.019
6000	3.778	3.455	0.031	0.009	3.509	0.035	0.010	3.079	0.037	0.012	2.190	0.037	0.017
7000	3.845	3.455	0.031	0.009	3.500	0.035	0.010	3.079	0.037	0.012	2.190	0.035	0.016
8000	3.903	3.446	0.027	0.008	3.490	0.031	0.009	3.069	0.034	0.011	2.179	0.030	0.014
9000	3.954	3.446	0.027	0.008	3.481	0.028	0.008	3.069	0.034	0.011	2.167	0.028	0.013
10000	4.000	3.446	0.027	0.008	3.481	0.024	0.007	3.058	0.030	0.010	2.167	0.026	0.012

The results depict the high values of ε' and ε'' (Fig. 3-4) and $\tan\delta$ (Fig. 5) at frequencies lower than 1 kHz increase with decreasing frequency, which may be due to space-charge polarization effect [23, 24] in building up of free charge at the interface between the sample and electrode. The gradual decrease of ε', ε'' and $\tan\delta$ with frequencies,

may be due to typical characteristics of disordered polymer [24] which is in consistent with the findings of Himanshu *et al.* [25].
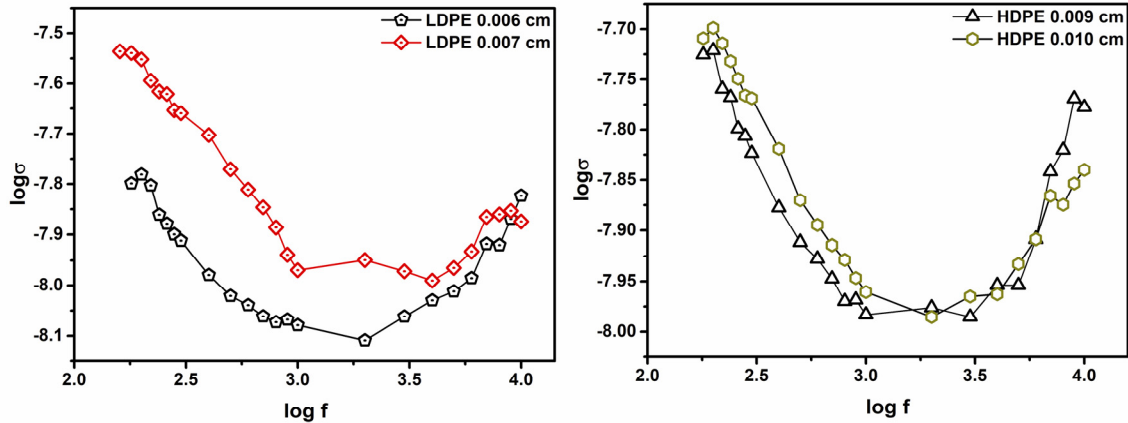
Figure 6. Variation of ac conductivity with frequency for LDPE (thickness 0.006 cm and 0.007 cm)
and HDPE (thickness 0.009 cm and 0.010 cm) samples.

The frequency variation of ac conductivity is, $\sigma_{ac} = \varepsilon_0 \omega \varepsilon''$ [26], where $\omega = 2\pi f$. The value of σ_{ac} in Fig. 6 decreases non-linearly with frequency attending minima at about 6 kHz then increases at higher frequency. The drops in σ_{ac} indicate space charge polarization and electrode polarization [18, 19]. The results of σ_{ac}, $\varepsilon'(\omega)$ for LDPE and HDPE samples show that the charge transport does not occur via the usual mechanisms attributing in favour of insulating materials and the possibility of new mechanisms along fixed polaron sites.

(a)   (b)
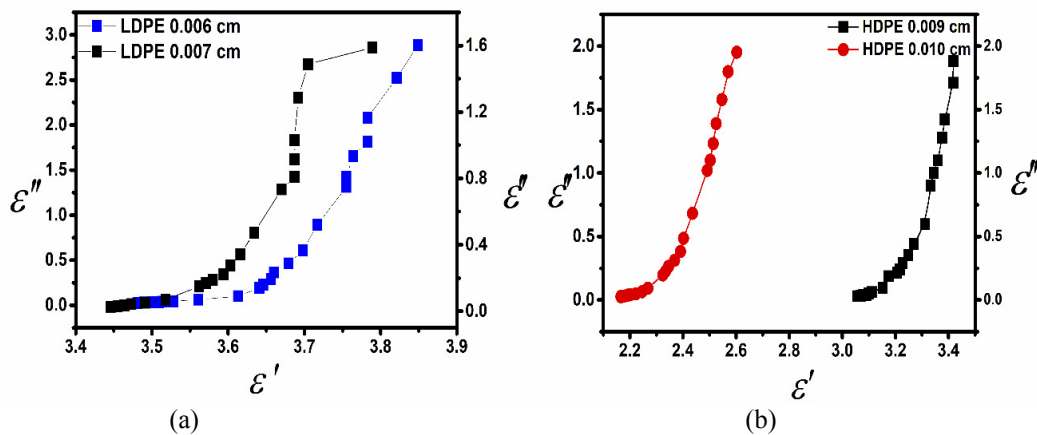
Figure 7. Cole-Cole plot of (a) LDPE (thickness 0.006 cm and 0.007 cm) and (b) HDPE (thickness 0.009 cm and 0.010 cm) samples.
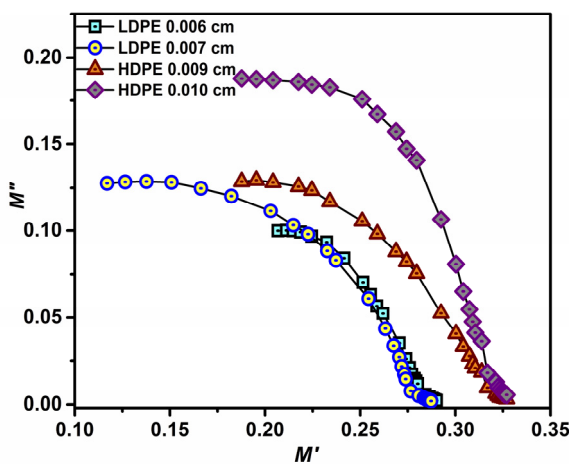
Figure 8. Cole-Cole plot of electrical modulus of LDPE (thickness 0.006 cm and 0.007 cm) and HDPE (thickness 0.009 cm and 0.010 cm) samples.

The Cole-Cole plot of the dielectric data, ε'' (loss) vs. ε' (permittivity) is shown in Fig. 7, which is not conventional semicircular type in case of an ideal single relaxation time. The plots are found to be mostly linear with a slight curvature at low-frequency region, which indicate the presence of wide range of relaxation time. The values of the real part of the electrical modulus (M') did not equal to zero at low frequencies and it is expected that the electrode polarization may develops in both the sheets. The analysis of real (ε') and imaginary (ε'') parts of dielectric permittivity and that of electrical modulus real (M') and imaginary (M'') parts (Fig. 8-9) signify poly dispersive nature of relaxation time as shown in Cole-Cole plots.

Figure 9. Variation of electrical modulus with frequency (a) LDPE (thickness 0.006 cm and 0.007 cm) and (b) HDPE (thickness 0.009 cm and 0.010 cm) samples.

The variation of electrical modulus, M' and M'' with frequency (Fig. 9) corroborates the result of ε', ε'', $\tan\delta$ and σ_{ac} of LDPE and HDPE samples.

CONCLUSIONS

The dielectric constant (ε') and dielectric loss factor (ε'') of LDPE and HDPE polymers have been measured using a dielectric cell. Conductivity (σ), dissipation factor ($\tan\delta$), relaxation time (τ), electrical modulus (M' and M'') for both LDPE and HDPE were studied. The analysis of real and imaginary parts of both dielectric permittivity and electric modulus have been performed, which show the polydispersive nature of relaxation time as confirmed by Cole-Cole plot, complex permittivity as well as the scaling behavior of the modulus spectra. It is supported by the nature of σ, $\tan\delta$ and τ data in this present study. The frequency dependence of real and imaginary parts of the electrical modulus, (M' and M'') for the samples, are depending on the filler content of LDPE and HDPE sheets.

ORCID IDs

Sarat K. Dash, https://orcid.org/0000-0001-5075-2129; **Hari S. Mohanty**, https://orcid.org/0000-0002-1230-156X
Biswajit Dalai, https://orcid.org/0000-0001-8401-7501

REFERENCES

[1]   S.K. Dash, S. Kant, B. Dalai, M.D. Swain, and B.B. Swain, Ind. J. Phy. **88**, 129-135 (2014), https://doi.org/10.1007/s12648-013-0395-0.
[2]   M.M. Solovan, H.M. Yamrozyk, V.V. Brus, P.D. Maryanchuk, East Eur. J. Phys. **4**, 154-159 (2020) https://doi.org/10.26565/2312-4334-2020-4-19.
[3]   S. Ghatge, Y. Yang, J.H. Ahn, and H.G. Hur, Appl. Biol. Chem. **63**, 27 (2020), https://doi.org/10.1186/s13765-020-00511-3.
[4]   R.K. Sarker, P. Chakraborty, P. Paul, A. Chatterjee, and P. Tribedi, Arch. Microbiol. **202**, 2117–2125 (2020) https://doi.org/10.1007/s00203-020-01926-8.
[5]   D. Manas, M. Manas, A. Mizera, P. Stoklasek, J. Navratil, S. Sehnalek, and P. Drabek, Polymers **10**, 1361 (2018), https://doi.org/10.3390/polym10121361.
[6]   M. Marin-Genesca et. al. Polymers, **12**, 1075 (2020), https://doi.org/10.3390/polym12051075.
[7]   D.Q. Tan, J. Appl. Polym. Sci. **137**, 1–32 (2020), https://doi.org/10.1002/app.49379.
[8]   A.D. Scaccabarozzi, J.I. Basham, L. Yu, P. Westacott, W. Zhang, A. Amassian, I. McCulloch, M. Caironi, D.J. Gundlach, and N. Stingelin, J. Mater. Chem. C, **8**, 15406–15415 (2020), https://doi.org/10.1039/D0TC03173A.
[9]   A. Usman, M.H. Sutanto, M. Napiah, S.E. Zoorob, S. Abdulrahman, and S.M. Saeed, Ain Shams Eng. J. (2020). https://doi.org/10.1016/j.asej.2020.06.011.
[10] K.S. Samra, R. Singh, and L. Singh, J. Macromol. Sci. Part B Phys. **59**, 65–76 (2020), https://doi.org/10.1080/00222348.2019.1687139.
[11] R. Singh, K.S. Samra, R. Kumar, and L. Singh, Radiat. Phys. Chem. **77**, 53–57 (2008). https://doi.org/10.1016/j.radphyschem.2007.03.004.
[12] L. Wang, C. Liu, S. Shen, M. Xu, and X. Liu, Adv. Ind. Eng. Polym. Res. **3**, 138-148 (2020). https://doi.org/10.1016/j.aiepr.2020.10.001.
[13] D.K. Pradhan, R.N.P. Choudhary, and B.K. Samantaray, Int. J. Electrochem. Sci. **3**, 597–608 (2008), http://electrochemsci.org/papers/vol3/3050597.pdf.
[14] C.P. Smyth, *Dielectric Behavior and Structure*, (McGraw-Hill, New York, 1955).
[15] E. A. Collins et.al, J. Chromatogr. Sci. **13**, 12A (1975), https://doi.org/10.1093/chromsci/13.7.12A-b.
[16] S.K. Dash, K.C. Mishra, S.N. Mishra, and B.B. Swain, Indian J. Pure Appl. Phys. **43**, 287–290 (2005).

[17] A.K. Jonscher, J. Mater. Sci. **24**, 372–374 (1989), https://doi.org/10.1007/BF00660983.

[18] S. Karmakar, and D. Behera, Appl. Phys. A, **124**, 745 (2018), https://doi.org/10.1007/s00339-018-2165-5.

[19] D.K. Ray, A.K. Himanshu, and T.P. Sinha, Indian J. Pure Appl. Phys. **45**, 692–699 (2007), http://nopr.niscair.res.in/bitstream/123456789/2639/1/IJPAP%2045%288%29%20692-699.pdf.

[20] G. Banhegyi, and F.E. Karasz, J. Polym. Sci. Part B Polym. Phys. **24**, 209–228 (1986), https://doi.org/10.1002/polb.1986.090240201.

[21] S. Hajra, S. Sahoo, R. Das, and R.N.P. Choudhary, J. Alloys Compd. **750**, 507–514 (2018), https://doi.org/10.1016/j.jallcom.2018.04.010.

[22] G.M. Nasr, T.A. Mohamed, and R.M. Ahmed, IOP Conf. Ser. Mater. Sci. Eng. **956**, 012002 (2020).

[23] S.A. Saafan, M.K. El-Nimr, and E.H. El-Ghazzawy, J. Appl. Polym. Sci. **99**, 3370–3379 (2006), https://doi.org/10.1002/app.23054.

[24] B.A. Shujah-Aldeen, M.Sc. Thesis, University of Sulaimani Iraq, 2007.

[25] A.K. Himanshu, D.K. Ray, and T.P. Sinha, Indian J. Phys. **79**, 1049-1052 (2005).

[26] H.S. Mohanty, A. Kumar, B. Sahoo, P.K. Kurliya, and D.K. Pradhan, J. Mater. Sci. Mater. Electron. **29**, 6966–6977 (2018), https://doi.org/10.1007/s10854-018-8683-2.

ДОСЛІДЖЕННЯ ЕЛЕКТРИЧНИХ ВЛАСТИВОСТЕЙ ТВЕРДИХ ПОЛІМЕРНИХ ЛИСТІВ (HDPE I LDPE) В АУДІОЧАСТОТНОМУ ДІАПАЗОНІ

Сарат К. Даш[a], Харі С. Моханти[b], Бісваджіт Далай[b]

[a]Фізичний факультет, Регіональний інститут освіти (NCERT), Бхубанешвар, Одіша, 751022, Індія

[b]Фізичний факультет, Школа наук, Університет GIET, Гунупур 765022, Одіша, Індія

У цій роботі були взяті тверді полімерні листи, зразок з поліетилену низької щільності (LDPE) товщиною 0,006 см, 0,007 см, і зразок поліетилену високої щільності (HDPE) товщиною 0,009 см, 0,010 см. Вимірювання електричних властивостей, таких як діелектрична константа ε' та діелектричні втрати ε'', для твердих полімерних листів LDPE та HDPE проводилось, використовуючи діелектричний елемент. Було виготовлено діелектричний елемент, який складався з двох круглих паралельних пластин із чистої нержавіючої сталі, кожна діаметром 5 см і товщиною 2 мм. Для вимірювання ємності C та коефіцієнта дисипації D в діапазоні звукової частоти (AF), від 100 Гц до 10 кГц, використовували імпедансний міст (GRA 650A). Різні зразки завантажували між двома пластинами елемента, а ємність, а також коефіцієнт дисипації оцінювали за показаннями шкали моста. Вплив зміни частоти на ε', ε'', час релаксації τ, коефіцієнт дисипації $\tan\delta$ і провідність змінного струму σ також був розглянутий для діапазону звукових частот. Розраховано комплексну діелектричну проникність ε^*, пов'язану з вільним диполем, що коливається у змінному полі, та тангенс втрат $\tan\delta$. У цій роботі було досліджено частотно-залежну провідність, діелектричний характер та електричний модуль, дійсну (M') та уявну (M'') частини LDPE та HDPE. Значення дійсної частини електричного модуля (M') не дорівнювало нулю на низьких частотах, і очікується, що поляризація електрода може розвинутися в обох листах. Ці результати виявляють зміцнення зв'язку між локальними диполярними рухами в локалізованому русі ближнього порядку. Аналіз реальної (ε') та уявної (ε'') частини діелектричної проникності, а також реальна (M') та уявна (M'') частини електричного модуля вказують на полідисперсний характер часу релаксації, як це спостерігається на графіках Коул-Коула.

КЛЮЧОВІ СЛОВА: LDPE, HDPE, діелектрична проникність, діелектричні втрати, провідність змінного струму

NUMERICAL MODELING AND ANALYSIS OF HTM-FREE HETEROJUNCTION SOLAR CELL USING SCAPS-1D

ⒾDanladi Eli[a,*], Alhassan Shuaibu[b], Muhammad Sani Ahmad[b], Jamila Tasiu[b]

[a]Department of Physical Sciences, Greenfield University, Kaduna, Nigeria
[b]Department of Physics, Kaduna State University, Kaduna, Nigeria
*Coresponding Author: danladielibako@gmail.com, +2348063307256
Received January 19, 2021; revised March 27, 2021; accepted April 10, 2021

In this research paper, a HTM-free perovskite solar cell (PSC) structure with Titanium (TiO₂), methyl ammonium lead triiodide (CH₃NH₃PbI₃) and platinum (pt) as electron transport material (ETM), photon harvester and metal back contact is proposed. Solar Cell Capacitance Simulator (SCAPS-1D) program was used to implement the model and simulation. Effect of parameters such as thickness of ETM, thickness of absorber, doping concentration of ETM & absorber and electron affinity (EA) of ETM were investigated systematically. From the obtained results, it was found that the parameters affect the performance of the solar cell. When the thickness of ETM was varied from 0.02 to 0.10 μm . The results show that photovoltaic parameters decrease with the thickness increase. When the thickness of the absorber was varied from 0.1 to 1.0 μm , the optimized value was found at thickness of 0.4 μm . When the doping concentration of absorber and EMT were varied from 10^{10}–10^{17} cm^{-3} and from 10^{15}–10^{20} cm^{-3}, the highest values of PCEs were obtained at 10^{16} cm^{-3} and 10^{20} cm^{-3} for Absorber and ETM. Also when the EA was varied in the range of 3.7 eV to 4.5 eV, the optimized value was at 3.7 eV. Upon optimization of the above mentioned parameters, power conversion efficiency (PCE) was found to be 25.75 %, short circuit current density (J$_{sc}$) 23.25 mAcm^{-2}, open circuit voltage (V$_{oc}$) 1.24 V and fill factor (FF) 89.50 %. The optimized result shows an improvement of ~1.95 times in PCE, ~1.06 times in J$_{sc}$, ~1.44 times in V$_{oc}$ and ~1.28 times in FF as compared to the initial device with the following parameters, PCE=13.22 %, J$_{sc}$=21.96 mAcm^{-2}, V$_{oc}$=0.86 V and FF=69.94 %.
KEYWORDS: perovskite solar cells, HTM free, device modeling, simulation, band gap offset

Recently, organic-inorganic metal halide perovskite solar cells have taken the renewable energy community by storm and subsequently gained attention of several world's researchers due to its high performance and low cost. Several advantages of perovskite absorber have made it a choice of candidate for application photovoltaic structures, among which include, tuned band gap, small exciton energy, excellent bipolar carrier transport, long electron-hole diffusion, and amazingly high tolerance to defects [1-7]. The properties exhibited by this material in solar cells results to enhanced power conversion efficiency from 3.9 % [8] to over 25 % [9]. However, some draw backs such as instability, electron transport resistance between TiO₂ and perovskite absorber and the use of costly hole transport material (HTM) (such as spiro-Omeotad) has prevented its outdoor usage. Therefore, the use of readily available and stable materials having high hole mobility with simple route of synthesis is desirable [10-12].

A report on perovskite solar cell without HTM was demonstrated firstly by Etgar et al. [13], where the perovskite absorber functions as a transporter of hole and harvester of photon energy simultaneously and results to a PCE of 5%. The results demonstrate simplicity and high reduction in cost of fabrication and a relatively improved stability as a result of HTM elimination. Also, in 2014, Li et al. [14] followed the same route by replacing metal back contact with laminated carbon nanotubes (CNTs) to collect holes from absorber and block electrons from ETM and results to a PCE of 6.87%. Eli et al. [9] developed a PSC without HTM with elcocarb as metal back contact to collect hole and realized a PCE of 3.80 %.

Recently a PCE of 10.95% with about 95% stability of their initial efficiency after being exposed to air (relative humidity of 25-35%) for 20 days, was demonstrated by Zhang et al [15]. In a simulation studies by Lin et al [16], a PCE of 15.02% was obtained with a structure without HTM and ZnO as ETM. Theoretical studies carried out by Wang and group [17] shows that the careful selection of thickness of the absorber and p-type doping were crucial to the PCE of the HTM-free PSCs.

The HTM-free PSC is a simple and promising way to realize good PCE but some factors deter its practical use. PSC devices mostly make use of costly gold (Au) as a back contact. The Au metal contact is not only expensive but the process of synthesis and development require the use of high-technology (such as high-vacuum evaporation technique). Platinum metal, with the work function of 5.93 [18], has been applied in perovskite solar cells with HTM and without HTM, but the PV parameters were of poor values for HTM (Jsc=7.17 mAcm⁻², Voc=0.69, FF=62.62 and PCE=3.08 %). And for the device without HTM, the PV parameters are Jsc=20.58 mAcm⁻², Voc=1.006, FF=71.07 and PCE=14.72 %.

To realize higher photovoltaic parameters and proper optimized architecture in HTM-free PSC, systematic understanding of the operational mechanism needs to be uncovered. Yet till now, numerical modeling and simulation of the HTM-free PSCs with platinum metal contact and TiO₂ ETM has seldom been reported. Platinum metal has a high work function and good chemical stability. In view of that, this research paper, attempts to present a detailed numerical modeling and simulation of HTM-free PSCs based on solar cell capacitance simulator (SCAPS) software to systematically study the influence of some material (such as thickness of ETM, thickness of absorber layer, doping concentration of

ETM, doping concentration of absorber layer, electron affinity of ETM etc), with the goal of uncovering the hidden mechanism for PCE improvement.

METHOD AND METHODOLOGY

The nature of the defect is set as Gaussian and defect density is set as 1×10^{18} cm^{-3} [19,20]. Table 1 shows the defect parameters which are used in the simulation. Basic parameters for each material used in the simulation are summarized in Table 2. Thermal velocities of hole and electron are selected as 10^7 cms^{-1} [19-22]. The optical reflectance is considered to be zero at the surface and at each interface [19]. Parameters are optimized in the study by using control variable method. The initial total defect density of the absorber layer is assumed to be 2.5×10^{13} cm^{-3}. Neutral Gaussian distribution defect is selected in the absorber layer and characteristic energy is set to be 0.1 eV [19]. One defect interface is inserted for carrier recombination. The interface defect layer (IDL) is introduced in the TiO$_2$/CH$_3$NH$_3$PbI$_3$ interface to investigate the influence of interfacial recombination on the photovoltaic performance. The work functions of the front contact and back contact are 4.40 eV and 5.93 eV respectively [18,23]. A working temperature of 300K, solar spectrum AM1.5 and a Scanning voltage of 0-1.3 V were used for all simulations.

Table 1. Defect parameters of interfaces and absorber [19,20,23]

Parameters	CH$_3$NH$_3$PbI$_3$	TiO$_2$/CH$_3$NH$_3$PbI$_3$ interface
Defect type	Neutral	Neutral
Capture cross section for electrons (cm^2)	2×10^{-14}	2×10^{-14}
Capture cross section for holes (cm^2)	2×10^{-14}	2×10^{-14}
Energetic distribution	Gaussian	Single
Energy level with respect to Ev (eV)	0.500	0.650
Characteristic energy (eV)	0.1	0.1
Total density (cm^{-3})	1×10^{15}–1×10^{19}	1×10^{17}

Table 2. Simulation parameters of PSCs devices [19, 20,23,24]

Parameters	FTO	ETM (TiO$_2$)	Absorber
Thickness (μm)	0.4	0.05	0.45
Band gap energy Eg (eV)	3.5	3.26	1.55
Electron affinity χ (eV)	4.0	4.2	3.90
Relative permittivity er	9	10	6.50
Effective conduction band density Nc (cm^{-3})	2.2×10^{18}	2.2×10^{28}	2.2×10^{18}
Effective valance band density Nv (cm^{-3})	2.2×10^{18}	2.2×10^{18}	2.2×10^{18}
Electron mobility μn (cm^2 V^{-1} s^{-1})	20	20	2
Hole mobility μp (cm^2 V^{-1} s^{-1})	10	10	2
Donor concentration N$_D$ (cm^{-3})	1×10^{19}	1×10^{17}	0
Acceptor concentration N$_A$ (cm^{-3})	0	0	1×10^{13}
Defect density N$_t$ (cm^{-3})	1×10^{15}	1×10^{15}	2.5×10^{13}

RESULTS AND DISCUSSION
Structure of PSC in the simulation and Energy level diagram of HTM free PSC device

The modeled PSC and band structure of the HTM free perovskite solar cell obtained with simulated parameters in Tables 1 and 2 are illustrated in Figure 1 (a) and (b). The interface conduction and valence band offset at the TiO$_2$/CH$_3$NH$_3$PbI$_3$ interface are ΔEc=0.31 eV and ΔEv=2.02 eV as shown in Figure 1(b).
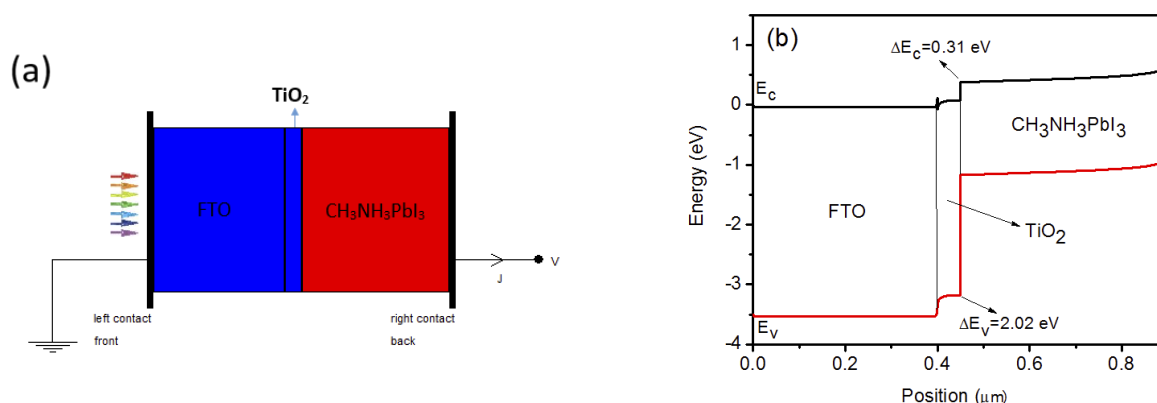
Figure 1. (a) The structure of perovskite solar cell in the simulation and (b) Energy band diagram of TiO$_2$/CH$_3$NH$_3$PbI$_3$ PSC device.

The value of ΔEc prevents the flow of electron charge carrier from the electron transport layer to perovskite layer to the pt metal contact so as to avoid quenching in the perovskite layer. While the large value of ΔEv denies the flow of holes to the platinum-back contact to prevent their recombination with the electrons in the perovskite layer. These values

can be seen important as they encouraged collection of charge carriers which results to higher photovoltaic performance in PSCs. As such, from the result of the band gap structure, TiO₂ and CH₃NH₃PbI₃ can form a p-n junction when combined together to be applied in photovoltaics.

Performance parameters from initial simulation

The J-V characteristics of the reference modeled PSC device under illumination and in the dark is shown in figure 2(a). Under illumination, a J_{sc} of 21.96 mAcm⁻², Voc of 0.86 V, FF of 69.94 %, and PCE of 13.22 % are obtained. The V_{oc} simulated in this studies agrees with V_{oc} (0.85 V) in experimental work demonstrated by a group of researchers [9]. However, the values of PCE, FF and J_{sc} are higher than ones obtained from experimental research work, this may be due to the lesser series resistance arising from pt metal contact or FTO and the optical reflectance is considered to be zero at the surface and at each interface during our simulation [25].
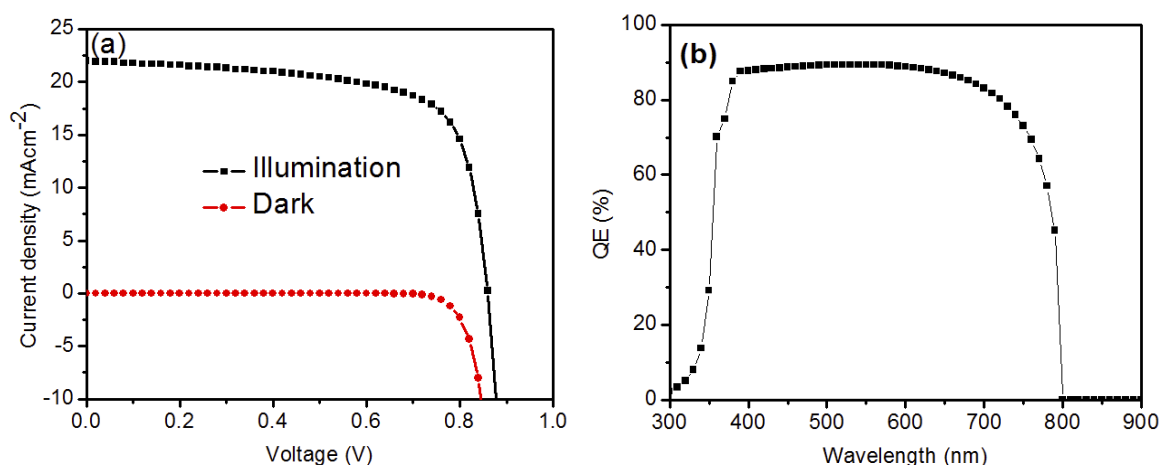
Figure 2. (a) J–V curve of PSC with initial parameters, (b) spectra of the device with initial parameters

As illustrated in Figure 2(a), Under the dark condition, there is no current flowing thereby behaving as a diode resulting to an extreme minimum value of J_{sc} when the voltage is less than the knee voltage (0.6 V) and decreases gradually when the voltage further increases [25]. This results to rectifying characteristics and this rectifying behavior is a feature of photovoltaic devices and is a consequence of the asymmetric junction needed to separate charges.

In the quantum efficiency (QE) of the device shown in figure 2 (b) which is within the wavelength of 300 nm and 900 nm has maximum attained value of 90 % at 550 nm. Optical absorption edge is red shifted to 800 nm which corresponds to a band gap of 1.55 eV in CH₃NH₃PbI₃. The QE sweeps across the whole visible spectrum which to an extent agrees with experimental work [9].

Effect of thickness of Electron transport layer

Figures 3(a), (b) and (c) show the J-V behavior, QE and the plot of solar cell parameters; V_{OC}, J_{SC}, FF and PCE versus thickness of the ETM. Thickness of ETM was varied from 0.02 to 0.10 μ m. The results show that both the PCE, Jsc, Voc and FF decrease with the thickness of ETM. The slight decrease in the photovoltaic properties is due to fractional absorption of incident light by the TiO₂ layer and the bulk/surface recombination at the interface which result to lesser electron and hole pairs extraction [26]. The decrease in FF is connected to the increase in series resistance.

Figure 3(b) displays the QE of the perovskite solar cell as a function of wavelength within the range of 300-900 nm with varied ETM layer thickness. It can be seen that the QE reaches a maximum value in the wavelength range of 380−570 nm and gradually decreases at longer wavelengths until 800 nm, which corresponds to its absorption spectrum demonstrated in figure 3(b). Table 3 shows the photovoltaic parameters obtained during the simulation.

Table 3. J-V characteristic parameters with the variation of thickness of ETM

Parameters T (μ m)	J_{sc} (mAcm⁻²)	V_{oc} (V)	FF	PCE (%)
0.02	22.05	0.88	70.17	13.63
0.03	22.01	0.87	70.11	13.40
0.04	21.98	0.86	69.96	13.28
0.05	21.96	0.86	69.94	13.22
0.06	21.94	0.86	69.91	13.18
0.07	21.93	0.86	69.91	13.17
0.08	21.92	0.86	69.91	13.15
0.09	21.90	0.86	69.91	13.15
0.10	21.89	0.86	69.92	13.14
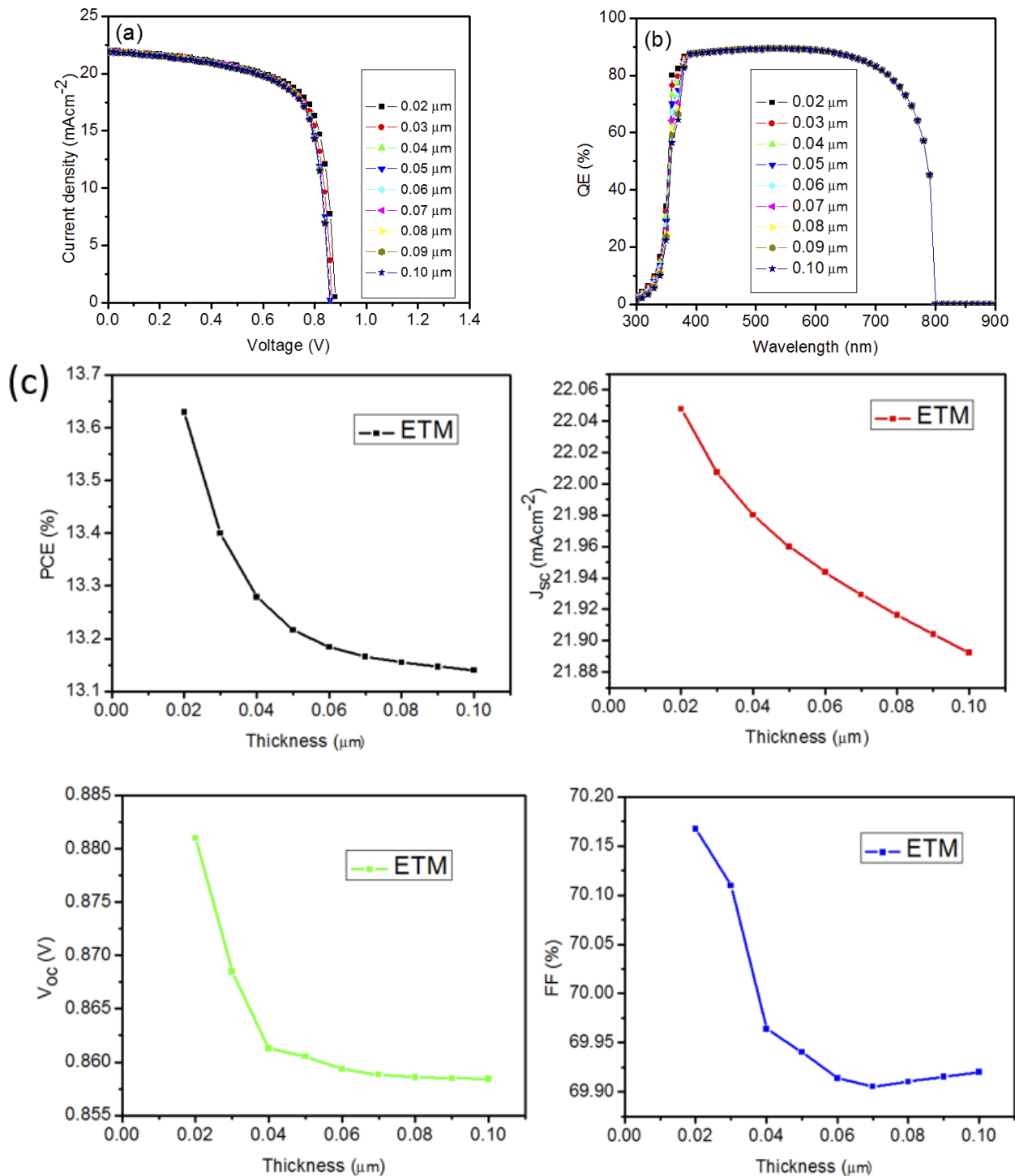
Figure 3. (a) J–V curves of PSC with different values of thickness of ETM, (b) QE with different values of thickness of ETM, (c) Variation in performance parameters of PSC with thickness of ETM.

Effect of thickness of absorber layer

The influence of thickness of absorber on the solar cell parameters; V_{OC}, J_{SC}, FF and PCE is shown in figure 4 (a). The J-V and QE of the varied absorber thickness is shown in Figure 4 (a) and (b).

As shown in Figure 4 (a), Jsc increases from 12.33 to 22.36 mAcm^{-2} with thickness increase from 0.1 to 0.6 which is due to the increase in carrier generation and dissociation, then starts decreasing from 0.7 to 1.0 μ m which is attributed to high recombination rate within the range of the thickness. FF decreases slightly with thickness increase in the perovskite layer. Table 4 shows the photovoltaic parameters obtained during the simulation. The PCE increase with increase in layer thickness from 0.1 to 0.4 μ m due to the production of new charge carriers. However, PCE decreases from thickness of 0.5 to 1.0 μ m due to lesser electron and hole pairs extraction rate that leads to recombination process [27].

Figure 4 (c) exhibits the spectral response of the PSCs as a function of wavelength with varied $CH_3NH_3PbI_3$ layer thickness within range of 300 to 900 nm. The QE first increases rapidly with the $CH_3NH_3PbI_3$ thickness increasing from 0.1 to 0.4 μ m, and the QE increase slightly after the thickness is greater than 0.4 μ m, which shows that 0.4 μ m thickness of $CH_3NH_3PbI_3$ layer can absorb most of the incident photons and the part beyond 0.4 μ m can only contribute little to the PSC performance. Therefore, the optimized perovskite absorber layer thickness is around 0.4 μ m which gives V_{OC} of 0.86 V, J_{SC} of 21.63 $mAcm^{-2}$, FF of 71.39 % and PCE of 13.21 %.
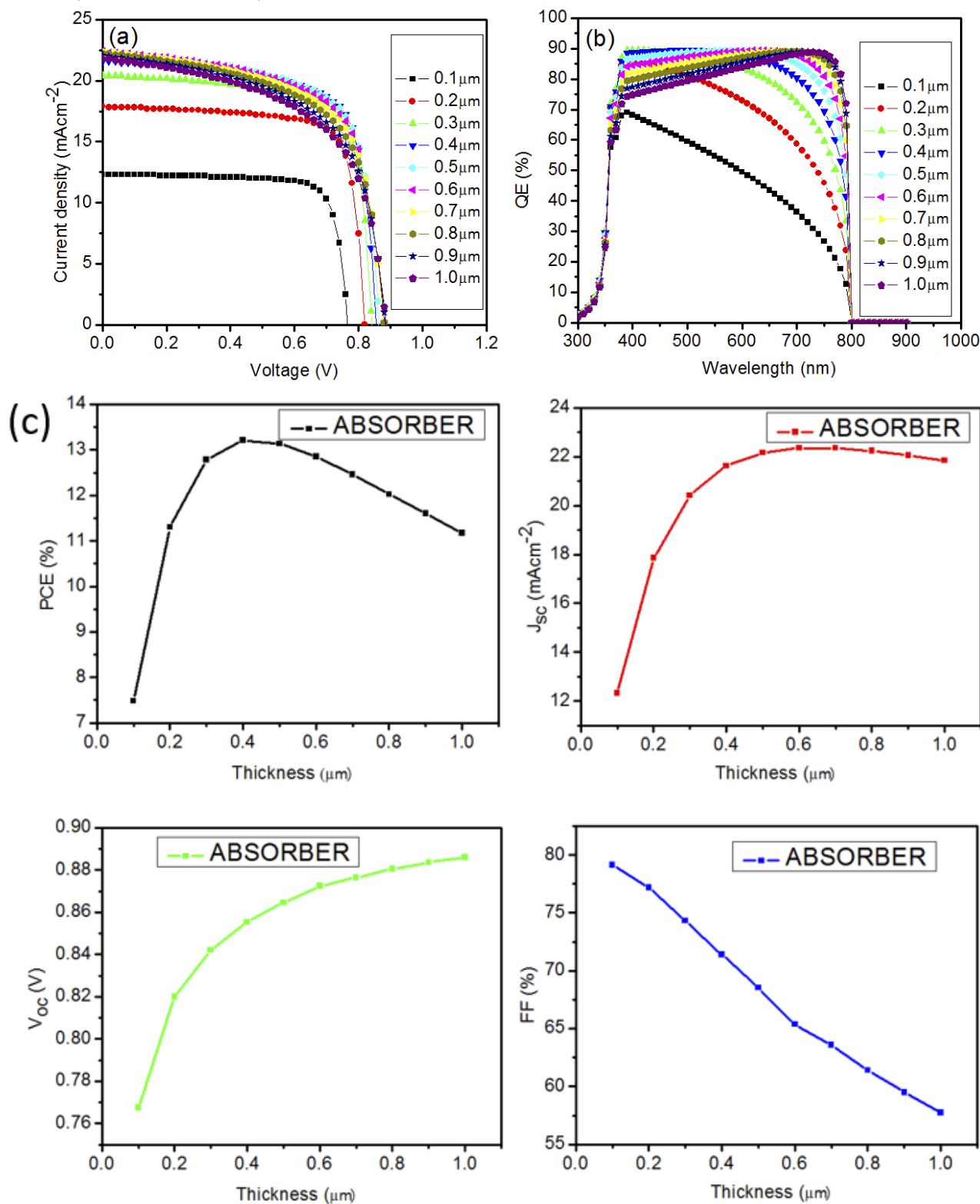
Figure 4. (a) J–V curves of PSC with different values of thickness of absorber layer, (b) QE with different values of thickness of absorber layer, (c) Variation in performance parameters of PSC with thickness of absorber layer

Table 4. J-V characteristic parameters with the variation of thickness of absorber

Parameters T (μ m)	J_{sc} (mAcm^{-2})	V_{oc} (V)	FF	PCE (%)
0.1	12.34	0.77	79.12	7.48
0.2	17.85	0.82	77.16	11.30
0.3	20.42	0.84	74.32	12.78
0.4	21.63	0.86	71.39	13.21
0.5	22.17	0.86	68.54	13.13
0.6	22.36	0.87	65.36	12.85
0.7	22.36	0.88	63.59	12.46
0.8	22.24	0.88	61.39	12.02
0.9	22.06	0.88	59.50	11.60
1.0	21.85	0.89	57.73	11.18

Effect of doping concentration (N$_A$) of absorber layer

Doping is the process of introducing impurities in absorber layer. The effect of doping concentration on the performance of perovskite solar cell is studied by choosing the values of N$_A$ in the range of 10^{10}–10^{17} cm^{-3} while keeping N$_D$ for ETM at 10^{17} cm^{-3}. Table 5 gives the performance parameters of PSCs with various values of doping concentration. The highest value of PCE was obtained with doping concentration of 10^{16} cm^{-3} which shows value of 14.89 %. The highest value of fill factor was also observed at the same N$_A$. The PCE and the FF remained constant with increase in doping concentration from 10^{10}–10^{13} cm^{-3} and increases with doping concentration from 10^{13}–10^{16} cm^{-3}. Beyond the values, a decrease in PCE and FF was noticed. The obtained results show that charge carriers are transported and collected optimally at the same irradiance when N$_A$ of the CH$_3$NH$_3$PbI$_3$ is 1×10^{16} cm^{-3}. The J$_{sc}$ and Voc remained constant with increasing N$_A$ from 10^{10}-10^{13} cm^{-3}, while beyond 10^{13} cm^{-3}, J$_{sc}$ increases with increasing N$_A$ and V$_{oc}$ decreases with increasing N$_A$. The ability of the photo-generated carriers is weak, resulting to a reduced Voc which caused a full depletion and strong electric field in the absorber layer.

The QE with respect to wavelength is as shown in Figure 5(b) with varied concentration from 10^{10}-10^{16} cm^{-3}. It can be seen that the QE rapidly increase within the wavelength range of 300 – 380 nm and thereby maintained a constant until at 630 nm before it decreases rapidly to 800 nm from 10^{10}-10^{15} cm^{-3}. From 10^{15}-10^{13} cm^{-3} a gradual decrease from the cutout of 390 nm until 800 nm was observed. The result shows that the solar cell functions effectively within the visible region.
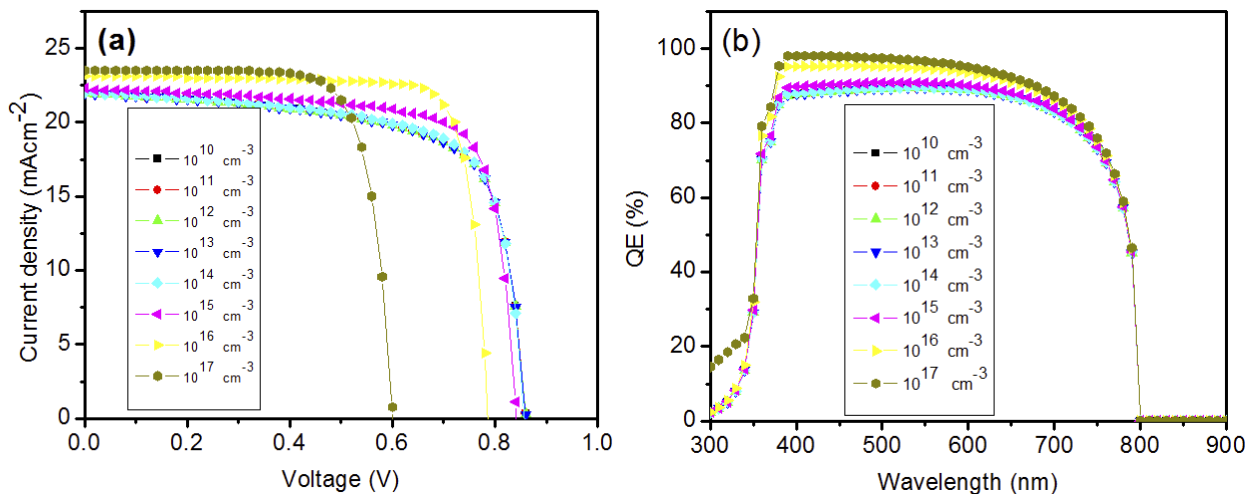
Figure 5. (a) J–V curves of PSC with different values of doping concentration in absorber layer, (b) QE with different values of doping concentration in absorber layer

Table 5. Dependence of solar cell performance on the doping concentration of Absorber layer

Parameters N$_A$(cm^{-3})	J_{sc} (mAcm^{-2})	V_{oc} (V)	FF	PCE (%)
1E+10	21.96	0.86	69.86	13.20
1E+11	21.96	0.86	69.86	13.20
1E+12	21.96	0.86	69.87	13.20
1E+13	21.96	0.86	69.94	13.22
1E+14	22.00	0.86	70.65	13.34
1E+15	22.27	0.84	75.67	14.19
1E+16	23.13	0.79	81.85	14.89
1E+17	23.54	0.61	76.12	10.77

Effect of doping concentration (N_D) of ETM

The effect of doping concentration on the performance of perovskite solar cells is examined by varying the values of N_D in the range of 10^{15}–10^{20} cm^{-3} while keeping N_A for absorber at 10^{13} cm^{-3}. Figure 6 (a) and (b) shows the J–V curves of PSC with different values of doping concentration in ETM and QE with different values of doping concentration in ETM layer. When the doping concentration is varied from 10^{15}–10^{20} cm^{-3}, it was depicted from Table 6 that, the PCE increased from 12.52 % to 16.62 %. The increase in PCE is as a result of reduction in series resistance due to increase in optical conductivity of the ETM. Hence, the doping concentration N_D is set at 10^{20} cm^{-3}. Similarly, there was increase in other photovoltaic parameters (J_{sc}, V_{oc} and FF) with increase in doping concentration values. The optimized values of the performance parameters are PCE=16.62 %, Jsc=22.24 mAcm^{-2}, Voc=1.04 V and FF=72.18%.

The increase in the photovoltaic parameters with increasing N_D could be explained as follows: Auger recombination rate decreases with doping density below 10^{20} cm^{-3}. It is seen that the quenching losses decreases when N_D is below 10^{20} cm^{-3}. We therefore speculate that, optimum doping concentration of ETM enhances the Voc and Jsc which subsequently results to higher PCE.
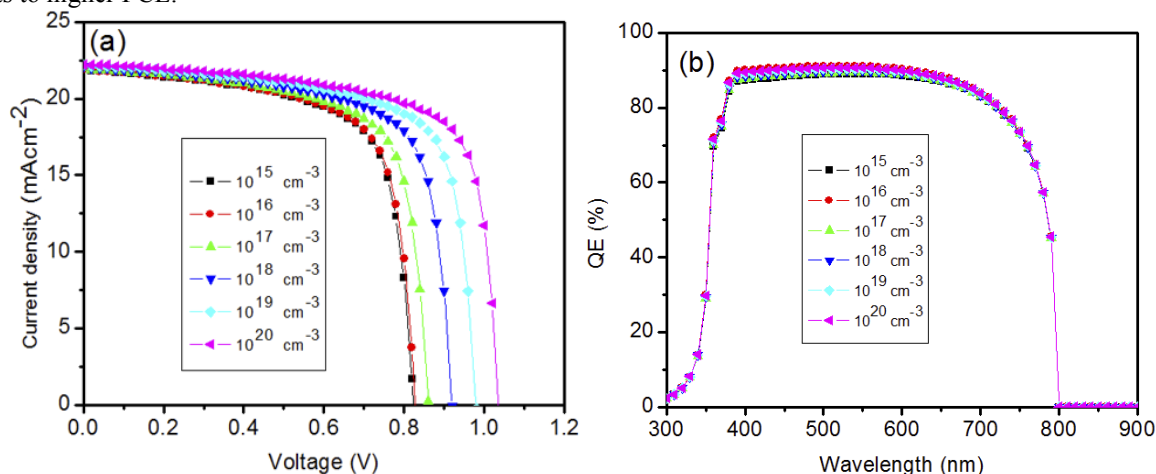
Figure 6. (a) the J–V curves of PSC with different values of doping concentration in ETM, (b) QE with different values of doping concentration in ETM layer

Table 6. Dependence of solar cell performance on the doping concentration of ETM

Parameters N_A(cm^{-3})	J_{sc} (mAcm^{-2})	V_{oc} (V)	*FF*	PCE (%)
1E+15	21.87	0.82	69.51	12.52
1E+16	21.89	0.83	69.59	12.62
1E+17	21.96	0.86	69.94	13.22
1E+18	22.07	0.92	70.59	14.33
1E+19	22.16	0.98	71.20	15.45
1E+20	22.24	1.04	72.18	16.62

Influence of electron affinity of ETM

The effect of electron affinity (EA) on the performance of perovskite solar cell is examined by varying the values of EA in the range of 3.7 eV to 4.5 eV. Figure 7 (a), (b) and (c) shows the J–V curves of PSC with different values of EA of ETM, QE with different values of EA of ETM layer and Photovoltaic parameters with respect to EA.
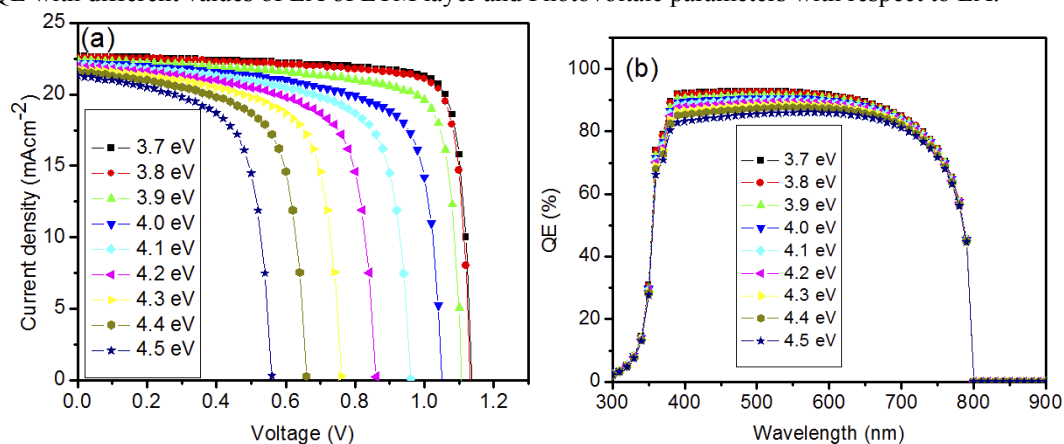
Figure 7. (a) J–V curves of PSC with different values of EA of ETM, (b) QE with different values of EA of ETM, (c) Variation in performance parameters of PSC with EA of ETM (*continued on the next page*)
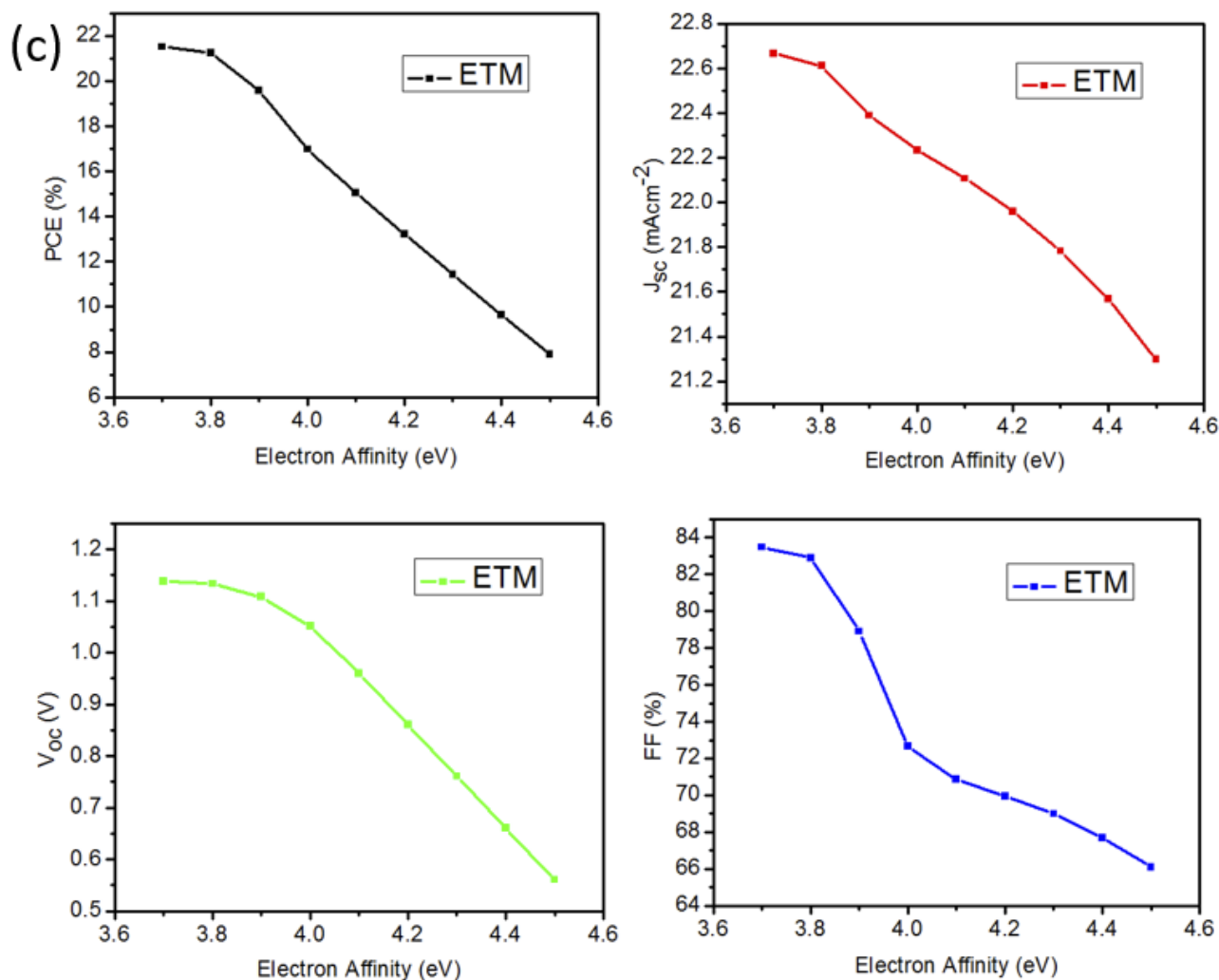
Figure 7. (a) J–V curves of PSC with different values of EA of ETM, (b) QE with different values of EA of ETM, (c) Variation in performance parameters of PSC with EA of ETM

Figures 7(c) shows variation of PCE, Voc, Jsc and FF with electron affinity of ETM and figure 7(a) show the J-V curve with different electron affinity values. The optimum photovoltaic performance was obtained at EA value of 3.7 eV, which gave PCE, Jsc, Voc and FF as shown in Table 7. It is now evident from our findings that proper selection ETM with good EA can reduce quenching losses in PSCs. Table 7 gives the performance parameters of PSCs with various values of EA.

Table 7. Dependence of solar cell performance on the electron affinity of ETM

Parameters EA (eV)	J_{sc} (mAcm^{-2})	V_{oc} (V)	*FF*	PCE (%)
3.7	22.67	1.14	83.49	21.53
3.8	22.61	1.13	82.90	21.24
3.9	22.39	1.11	78.90	19.58
4.0	22.23	1.05	72.65	16.98
4.1	22.10	0.96	70.86	15.04
4.2	21.96	0.86	69.94	13.22
4.3	21.78	0.76	69.00	11.43
4.4	21.57	0.66	67.69	9.64
4.5	21.30	0.56	66.10	7.89

Performance of PSC with Optimized parameters

After simulating the PSC, the ETM thickness, absorber thickness, doping concentration of absorber and ETM were optimized and the values are as shown in Table 8(a). The final optimized PSC gave a PCE of 25.75 %, Jsc of 23.25 mAcm^{-2}, Voc of 1.24 V and FF of 89.50 %. When the optimized result is compared with the reference initial device, an improvement of ~1.95 times in PCE, ~1.06 times in Jsc, ~1.44 times in Voc and ~1.28 times in FF is obtained over the

device that was not optimized. The behaviour of the JV curve in the dark and under illumination is as shown in figure 8(a). Experimental work of HTM free PSC published by other researchers are compared with the simulated results and summarized in Table 8(b).

In the experimental works, PCEs of 3.80 and 4.2 % were achieved for HTM free PSCs with TiO_2 as ETM. The photovoltaic parameters could be improved further to realize the high photovoltaic values achieved in the simulation. This could be realized by improving the film quality of both the absorber and ETM and also consider proper doping of the absorber and ETM in order to realize good electron density.

The energy diagram of the optimized device is as shown in figure 8(c). From the band structure, the conduction and valence band offset at the $TiO_2/CH_3NH_3PbI_3$ interface were reduced to 0.06 eV and 1.98 eV, which can be considered beneficial for the flow of photo-excited charge carriers to the front electrode and back-metal contact in order to avoid their recombination and quenching losses. The quantum efficiency also shows stronger absorber in the visible region as compared to the device without optimization as shown in figure 8(b).
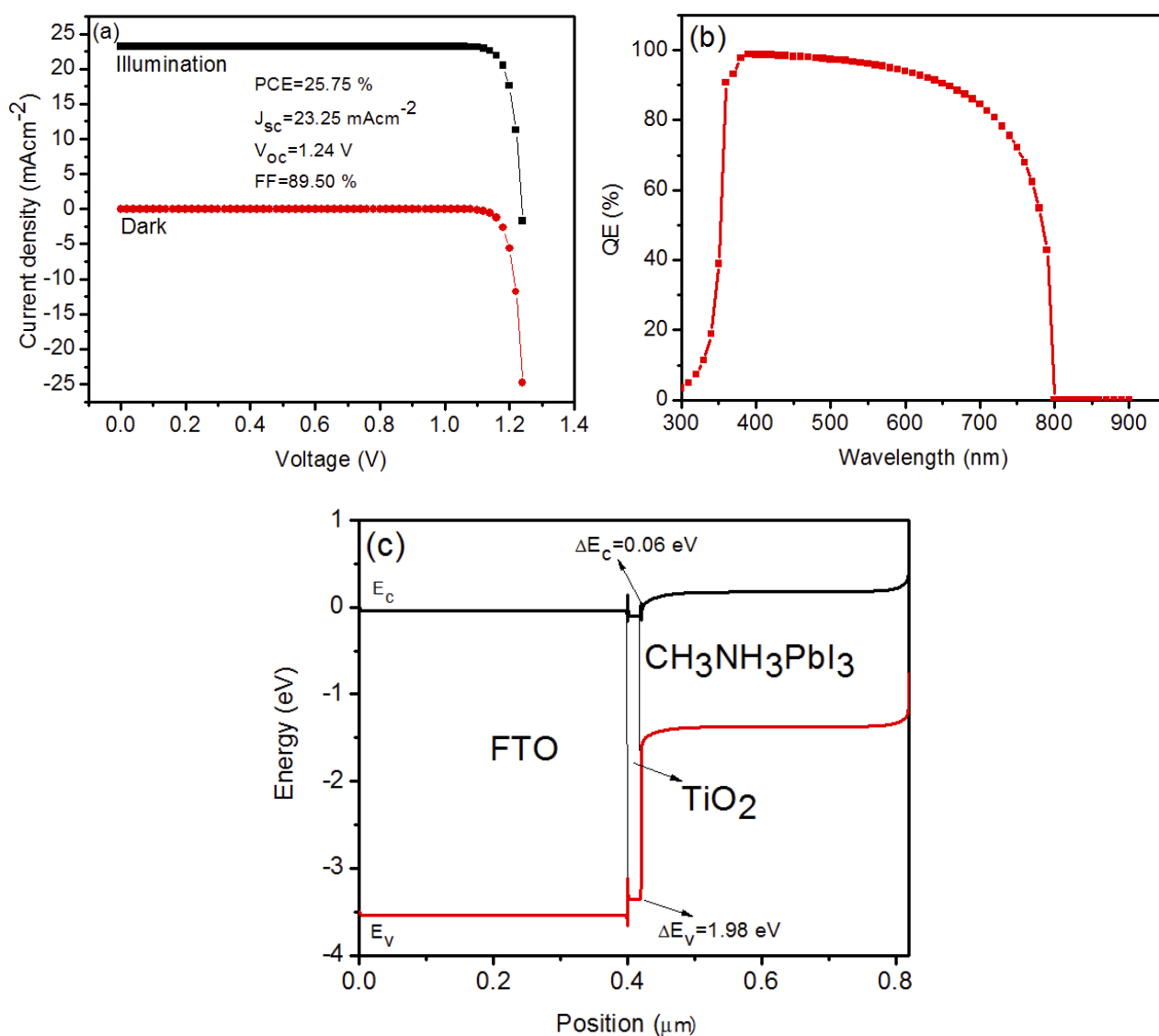
Figure 8. (a) J–V curves of PSC with Optimized parameters, (b) QE with optimized parameters and (c) Energy band diagram of $TiO_2/CH_3NH_3PbI_3$ PSC device

Table 8. (a) Optimized Parameters of the device

Optimized parameters	ETM (TiO2)	Absorber (CH3NH3PbI3)
Thickness (μm)	0.02	0.40
Doping density (N_A) (cm^{-3})	--	1E+16
Doping density (ND) (cm^{-3})	1E+20	--
Electron Affinity (EA)	3.7	--

Table 8(b). Photovoltaic parameters of HTM free perovskite solar cells reported in the experimental work in the literature and simulated results using SCAPS.

Simulation	J_{sc} (mAcm^{-2})	V_{oc} (V)	*FF*	PCE (%)
Initial	21.96	0.86	69.94	13.22
Optimized N_A of absorber	23.13	0.79	81.85	14.89
Optimized N_D of ETM	22.24	1.04	72.18	16.62
Optimized thickness of absorber	21.63	0.86	71.39	13.21
Optimized EA of ETM	22.67	1.14	83.49	21.53
Optimized thickness of ETM	22.05	0.88	70.17	13.63
Final Optimization	23.25	1.24	89.50	25.75
[9]	11.04	0.85	41.00	3.80
[28]	13.60	0.67	45.80	4.20

CONCLUSION

In this work, the HTM free PSC was investigated systematically using Solar Cell Capacitance Simulator (SCAPS-1D) program. The photovoltaic performance of the modeled device with various $CH_3NH_3PbI_3$ thicknesses, ETM thicknesses, ETM electron affinities, ETM doping concentrations and $CH_3NH_3PbI_3$ doping concentrations, has been analyzed. From the obtained results, it is found that the parameters affect the performance of the solar cell. The overall PCE, FF, Jsc, and Voc, of 25.75 %, 89.50 %, 23.25 mAcm^{-2}, and 1.24 V respectively were obtained by using all optimised parameters.

ORCID IDs

Danladi Eli, https://orcid.org/0000-0001-5109-4690

REFERENCES

[1] J.S. Manser, and P.V. Kamat, Nature Photonics, **8,** 737–747 (2014), https://doi.org/10.1038/nphoton.2014.171.
[2] H. Chen, F. Ye, W. Tang, J. He, M. Yin, Y. Wang, F. Xie, E. Bi, X. Yang, and M. Gratzel, L. Han, Nature, **550,** 92–95 (2017), https://doi.org/10.1038/nature23877.
[3] G. Xing, N. Mathews, S. Sun, S.S. Lim, Y. M. Lam, M. Gratzel, S. Mhaisalkar, and T.C. Sum, Science, **342**, 344–347 (2013), https://doi.org/10.1126/science.1243167.
[4] M. Liu, M. B. Johnston, and H. J. Snaith, Nature, **501**, 395–398 (2013), https://doi.org/10.1038/nature12509.
[5] Z. Wang, Q. Lin, F.P. Chmiel, N. Sakai, L.M. Herz, and H.J. Snaith, Nature Energy, **2,** 17135 (2017), https://doi.org/10.1038/nenergy.2017.135.
[6] Y. Liu, Z. Yang, D. Cui, X. Ren, J. Sun, X. Liu, J. Zhang, Q. Wei, H. Fan, F. Yu, X. Zhang, C. Zhao, and S. Liu, Advanced Materials, **27,** 5176–5183 (2015), https://doi.org/10.1002/adma.201502597.
[7] D. Yang, Z. Yang, W. Qin, Y. Zhang, S. Liu, and C. Li, Journal of Materials Chemistry A, **3,** 9401–9405 (2015), https://doi.org/10.1039/C5TA01824B.
[8] A. Kojima, K. Teshima, Y. Shirai, and T. Miyasaka, Journal of the American Chemical society, **131**(17), 6050-6051 (2009), https://doi.org/10.1021/ja809598r.
[9] D. Eli, M. Y. Onimisi, S. Garba, and J. Tasiu, SN Applied Sciences, **2**, 1769 (2020), https://doi.org/10.1007/s42452-020-03597-y.
[10] N. Rajamanickam, S. Kumari, V. K. Vendra, B. W. Lavery, J. Spurgeon, T. Druffel, and M.K. Sunkara, Nanotechnology, **27,** 235404 (2016), https://doi.org/10.1088/0957-4484/27/23/235404.
[11] K.G. Lim, H.B. Kim, J. Jeong, H. Kim, J.Y. Kim, and T.W. Lee, Advanced Materials, **26,** 6461–6466 (2014), https://doi.org/10.1002/adma.201401775.
[12] D. Wang, M. Wright, N.K. Elumalai, and A. Uddin, Solar Energy Materials and Solar Cells, **147,** 255–275 (2016), https://doi.org/10.1016/j.solmat.2015.12.025.
[13] L. Etgar, P. Gao, Z. Xue, Q. Peng, A.K. Chandiran, B. Liu, M.K. Nazeeruddin, and M. Gratzel, Journal of the American Chemical Society, **134**, 17396-17399 (2012), https://doi.org/10.1021/ja307789s.
[14] Z. Li, S.A. Kulkarni, P.P. Boix, E. Shi, A. Cao, K. Fu, S.K. Batabyal, J. Zhang, Q. Xiong, L.H. Wong, N. Mathews, and S.G. Mhaisalkar, ACS nano, **8,** 7, 6797-6804 (2014), https://doi.org/10.1021/nn501096h.
[15] X. Zhang, Y. Zhou, Y. Li, J. Sun, X. Lu, X. Gao, J. Gao, L. Shui, S. Wu, and J-M. Liu, Journal of materials chemistry C, **7**, 3852-3861 (2019), https://doi.org/10.1039/C9TC00374F.
[16] L. Lin, L. Jiang, Y. Qiu, and Y. Yu, Superlattices and Microstructures, **104**, 167-177 (2017), https://doi.org/10.1016/j.spmi.2017.02.028.
[17] T. Wang, J. Chen, G. Wu, and M. Li, Science China Materials, **59**(9), 703-709 (2016), https://doi.org/10.1007/s40843-016-5108-4.
[18] Haynes, W (Ed), *CRC handbook of chemistry and physics*, 97th ed. (CRC press, New York, 2017).
[19] S.Z. Haider, H. Anwar, and M. Wang, Semicond. Sci. Technol. **33**(3), 035001 (2018), https://doi.org/10.1088/1361-6641/aaa596.
[20] R Wei, M.Sc Degree Thesis, Queensland University of Technology, 2018.
[21] U. Mandadapu, S.V. Vedanayakam, and K. Thyagarajan, Indian Journal of Science Technology, **10**(11), 1-8 (2017), https://www.researchgate.net/profile/Victor-Vedanayakam-2/publication/316484058_Simulation_and_Analysis_of_Lead_based_Perovskite_Solar_Cell_using_SCAPS-1D/links/5a8afb1caca272017e639098/Simulation-and-Analysis-of-Lead-based-Perovskite-Solar-Cell-using-SCAPS-1D.pdf.

[22] M. Amalina, and M. Rusop, World Journal of Engineering, **9,** 251-256 (2012), https://doi.org/10.1260/1708-5284.9.3.251.

[23] D. Eli, M. Y. Onimisi, S. Garba, R. U. Ugbe, J. A. Owolabi, O. O. Ige, G. J. Ibeh, and A. O. Muhammed, Journal of the Nigerian Society of Physical Sciences, **1**, 72-81, (2019), https://doi.org/10.46481/jnsps.2019.13.

[24] M. I. Hossain, F. H. Alharbi, and N. Tabet, Solar Energy, **120**, 370-380 (2015), https://doi.org/10.1016/j.solener.2015.07.040.

[25] L, Lin, L, Jiang, Y, Qiu, and Y. Yu, Superlattices and Microstructures, **104**, 167-177 (2017), https://doi.org/10.1016/j.spmi.2017.02.028.

[26] P. Gao, M. Gratzel, and M. K. Nazeeruddin, Energy and Environmental Science, **7,** 2448-2463 (2014), https://doi.org/10.1039/C4EE00942H.

[27] U. Mandadapu, S.V. Vedanayakam, and K. Thyagarajan, Int. J. Eng. Sci. Invention, **2**,40-45 (2017).

[28] W. Liu, and Y. Zhang, Journal of materials chemistry A, **2**, 10244-10249 (2014), https://doi.org/10.1039/C4TA01219D.

ЧИСЛЕННЕ МОДЕЛЮВАННЯ ТА АНАЛІЗ ГЕТЕРОПЕРЕХІДНОГО СОНЯЧНОГО ЕЛЕМЕНТА БЕЗ HTM З ВИКОРИСТАННЯМ ПРОГРАМИ SCAPS-1D

Данладі Елі[a], Алхассан Шуайбу[b], Мухаммед Сані Ахмад[b], Джаміла Тасіу[b]
[a]Факультет фізичних наук, Університет Грінфілд, Кадуна, Нігерія
[b]Фізичний факультет, Державний університет Кадуни, Кадуна, Нігерія

У цій дослідницькій роботі пропонується структура перовскітного сонячного елемента (PSC), що не містить HTM (дірково-транспортувальний матеріал), з титаном (TiO$_2$), метил-амонієвим трийодидом свинцю (CH$_3$NH$_3$PbI$_3$) і платиною (Pt) в якості електронно-транспортного матеріалу (ETM), збирача фотонів та металевого зворотного контакту. Для реалізації моделі та моделювання була використана програма «Імітатор Ємності Сонячних Елементів» (SCAPS-1D). Проводилось системне дослідження впливу таких параметрів як товщина ETM, товщина поглинача, концентрація легуючих речовин ETM та поглинача, а також спорідненість до електронів (EA) електронно-транспортного матеріалу (ETM). З отриманих результатів було встановлено, що ці параметри впливають на продуктивність сонячного елемента. Коли товщина ETM змінювалась від 0,02 до 0,10 μm, результати показали, що фотоелектричні параметри зменшуються із збільшенням товщини. Коли товщина поглинача змінювалася від 0,1 до 1,0 μm, оптимізоване значення було встановлено при товщині 0,4 μm. Коли концентрація легуючих речовин поглинача та ЕМТ змінювалась від 10^{10}–10^{17} см$^{-3}$ та від 10^{15}–10^{20} см$^{-3}$, найвищі значення PCE (ефективність перетворення потужності) були отримані при 10^{16} см$^{-3}$ та 10^{20} см$^{-3}$ для поглинача та ETM. Також, коли EA (спорідненість до електронів) змінювалась в діапазоні від 3,7 до 4,5 eB, оптимізоване значення було на рівні 3,7 eB. Після оптимізації вищезазначених параметрів було встановлено, що ефективність перетворення потужності (PCE) становить: 25,75%,25,75%, щільність струму короткого замикання (J$_{sc}$) – 23,25 мАсм$^{-2}$, напруга розімкнутого контуру (V$_{oc}$) – 1,24 B, і коефіцієнт заповнення (FF) – 89,50%. Оптимізований результат показує підвищення PCE в ~ 1,95 разів, J$_{sc}$ в ~ 1,06 разів, V$_{oc}$ в ~ 1,44 рази і FF в ~ 1,28 разів порівняно з початковим пристроєм із наступними параметрами, PCE = 13,22%, J$_{sc}$ = 21,96 мАсм$^{-2}$, V$_{oc}$ = 0,86 B і FF = 69,94%.

КЛЮЧОВІ СЛОВА: перовскітний сонячний елемент, без HTM (дірково-транспортувальний матеріал), моделювання пристроїв, імітація, зміщення забороненої зони

MODELING AND SIMULATION OF LEAD-FREE PEROVSKITE SOLAR CELL USING SCAPS-1D

Omeiza Abdulmalik Muhammed[a], ⬤Danladi Eli[b,e,*], Peter Henry Boduku[c], Jamila Tasiu[c], Muhammad Sani Ahmad[c], Nuhu Usman[d]

[a]Department of Physics, Bayero University, Kano, Nigeria
[b]Department of Physics, Nigerian Defence Academy, Kaduna, Nigeria
[c]Department of Physics, Kaduna State University, Kaduna, Nigeria
[d]Department of Mathematical Sciences, Kaduna State University, Kaduna, Nigeria
[e]Department of Physical Sciences, Greenfield University, Kaduna, Nigeria
*Coresponding Author: danladielibako@gmail.com, tel. +2348063307256
Received January 28, revised March 27, 2021; accepted April 19, 2021

In this work, the effect of some parameters on tin-based perovskite ($CH_3NH_3SnI_3$) solar cell were studied through device simulation with respect to adjusting the doping concentration of the perovskite absorption layer, its thickness and the electron affinities of the electron transport medium and hole transport medium, as well as the defect density of the perovskite absorption layer and hole mobility of hole transport material (HTM). A device simulator; the one-dimensional Solar Cells Capacitance Simulator (SCAPS-1D) program was used for simulating the tin-based perovskite solar cells. The current-voltage (J-V) characteristic curve obtained by simulating the device without optimization shows output cell parameters which include; open circuit voltage (V_{oc}) = 0.64V, short circuit current density (J_{sc}) = 28.50mA/cm^2, fill factor (FF) = 61.10%, and power conversion efficiency (PCE) = 11.30% under AM1.5 simulated sunlight of 100mW/cm^2 at 300K. After optimization, values of the doping concentration, defect density, electron affinity of electron transport material and hole transport material were determined to be: 1.0×10^{16} cm^{-3}, 1.0×10^{15} cm^{-3}, 3.7 eV and 2.3 eV respectively. Appreciable values of solar cell parameters were obtained with J_{sc} of 31.38 mA/cm2, V_{oc} of 0.84 V, FF of 76.94% and PCE of 20.35%, when compared with the initial device without optimization, it shows improvement of ~1.10 times in J_{sc}, ~1.80 times in PCE, ~1.31 times in Voc and ~1.26 time in FF. The results show that the lead-free $CH_3NH_3SnI_3$ perovskite solar cell which is environmentally friendly is a potential solar cell with high theoretical efficiency of 20.35%.
KEYWORDS: electron transport layer, hole transport layer, perovskite solar cell, photovoltaic, SCAPS-1D, copper iodide.

Recently, perovskite solar cells have taken the renewable energy community by storm and subsequently gained attention of several world's researchers due to its high performance and low cost. Perovskite absorber has many advantages for its applications in photovoltaic devices, including tuned band gap, small exciton energy, excellent bipolar carrier transport, long electron-hole diffusion, and amazingly high tolerance to defects [1-3]. Owing to this astonishing properties exhibited by this material, its efficiency has increased from 3.9 % [4] to over 23 % [5,6]. However, there are some limitations in realizing its outdoor applications, such as instability, electron transport resistance between TiO₂ and perovskite absorber, the use of poisonous lead in the absorber etc. The PSCs free from poisonous lead have become the subject of interest due to its environmental friendliness. Perovskite absorber based on tin ($CH_3NH_3SnI_3$) have become an option to perovskite based on lead ($CH_3NH_3PbX_3$), because of its non-toxic nature, lower band gap of 1.3 eV and a broad visible absorption spectrum than the $CH_3NH_3PbX_3$ [7].

Researchers focus mostly on enhancing the PCE of PSCs, while overlooking the danger it poses to the environment. For PSCs technologies to compete with other photovoltaic systems, the need for a Lead free-perovskite device is worth considering so as to have devices with high PCE, low cost and carbon free systems. Most researches on PSCs is carried out using $CH_3NH_3PbX_3$ material with only few research with other perovskite materials. Most research on PSCs are on material film growth, film treatment, characterization on the various photoanodes and on the finished devices. However, the interpretation of the results acquired by experiment has often not been easy. The reason is because good theoretical models and available data on defect, band offsets, carrier density at grain boundaries, and the interfaces has not been established. Therefore, good numerical model to establish PV devices is an indispensable tool to better grasp the underlying mechanism preventing optimum performance of PSCs devices [5]. In this paper, numerical modelling and simulation of lead free PSCs with inorganic copper iodide as HTM was done with SCAPS. The results show that the lead-free $CH_3NH_3SnI_3$ perovskite solar cell which is environmentally friendly is a potential solar cell with high theoretical efficiency of 20.35% when simulated with alternate CuI as hole transport layer.

DEVICE SIMULATION PARAMETERS

The simulation of the perovskite solar cell was based on the n-p configuration which can be simulated using any thin-film simulator and therefore considered similar to the structure of thin film semiconductor based solar cell as well as a planar heterojunction.

The planar heterojunction configuration has been adopted for $CH_3NH_3SnI_3$ based solar cell with layer configuration of glass substrate/TCO (transparent conducting oxide)/ETM (TiO_2)/absorber layer ($CH_3NH_3SnI_3$)/ HTM (CuI)/back metal contact (Au) as shown in Figure 1 (a) while the energy band diagram is shown in Figure 1 (b).

Table 1 shows the values of the most useful cell parameters required for the simulation. These values were chosen on the basis of theoretical considerations, experimental data and existing literature or in some cases, reasonable estimates. Most of the parameters used for the absorber layer were extracted from the literature [8] while the parameters for interface layer in the Table 2 was also chosen based on work reported by Farhana *et al* [8]. The remaining parameters were estimated, the most important parameters (bandgap (E_g), electron mobility (μ_n), hole mobility (μ_n) etc.) for the simulation were obtained from review of literature. The work function of the cathode electrode (Au) is 5.1 eV which serves as back metal contact.
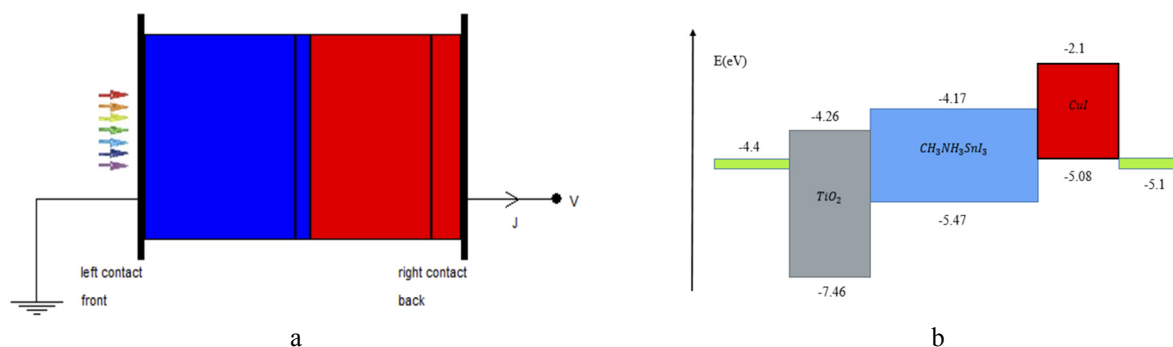
Figure 1. (a) Simulated solar cell structure (SCAPS-1D), (b) Energy band diagram

Table 1. Parameters used for simulation of perovskite solar cell structures using SCAPS-1D.

Parameters	TCO	ETM (TiO₂)	Absorber	HTM (CuI)
Thickness (μm)	0.5[8]	0.05[10]	0.40[5]	0.10
Band gap energy Eg (eV)	3.5[7]	3.20[10]	1.30[8]	2.98[9]
Electron affinity χ (eV)	4.0[5]	4.26[9]	4.20[8]	2.10[9]
Relative permittivity ϵr	9	50[8]	10[8]	6.50[9]
Effective conduction band density Nc (cm⁻³)	2.0×10^{18}	1.0×10^{21}	1.0×10^{18}	2.8×10^{19}
Effective valance band density Nv (cm⁻³)	1.8×10^{19}	2.0×10^{20}	1.0×10^{18}	1.0×10^{19}
Electron mobility μn (cm² V⁻¹ s⁻¹)	20[9]	6.0×10^{-3}	1.6	1.69×10^{-4}
Hole mobility μp (cm² V⁻¹ s⁻¹)	8	6.0×10^{-3}	1.6	1.69×10^{-4}
Donor concentration ND (cm⁻³)	2×10^{19}	5×10^{19}	0	0
Acceptor concentration NA (cm⁻³)	0	0	3.2×10^{15}	1×10^{18}
Defect density Nt (cm⁻³)	1×10^{15}	1×10^{15}	4.5×10^{16}	1×10^{15}

Table 2: Parameters of interface layer [8]

Parameters	CH₃NH₃SnI₃	TiO₂/CH₃NH₃SnI₃ interface	CH₃NH₃SnI₃/CuI interface
Defect type	Neutral	Neutral	Neutral
Capture cross section for electrons (cm²)	2×10^{-15}	2×10^{-15}	2×10^{-13}
Capture cross section for holes (cm²)	2×10^{-15}	2×10^{-15}	2×10^{-13}
Energetic distribution	Gaussian	Single	Single
Energy level with respect to Ev (eV)	0.500	0.650	0.650
Characteristic energy (eV)	0.1	0.1	0.1
Total density (cm⁻³)	1×10^{15}–1×10^{19}	1×10^{18}	1×10^{18}

The J-V characteristic curve obtained by simulating with the data in Table 1 is shown in Figure 2 with the output cell parameters V_{oc} = 0.64V, J_{sc} = 28.50mA/cm^2, FF = 61.10%, and PCE(η) = 11.30% under AM1.5 simulated sunlight of 100mW/cm^2 at 300K.
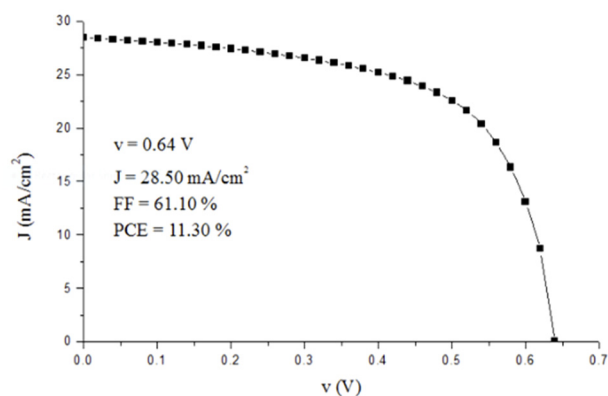
Figure 2. J–V curve of PSC with initial parameters

RESULTS AND DISCUSSION
The effect of Doping Concentration (NA) of Perovskite Absorption Layer

The perovskite $CH_3NH_3SnX_3$ (where X = Cl, Br, I) experiences instability due to atmospheric moisture content thereby making the Sn^{2+} ion to oxidize into Sn^{4+} analogue with enhanced stability within itself during doping process and hence acting as a dopant with p-type nature. In a study demonstrated earlier using $CH_3NH_3SnI_3$ as absorber, the NA was varied between 10^{14} cm^{-3} to 10^{19} cm^{-3} [10,11]. In our own work, we varied the doping concentration of the $CH_3NH_3SnI_3$ layer from 10^{13} cm^{-3} to 10^{17} cm^{-3} and compared their photovoltaic properties.

Table 3 shows photovoltaic parameters with different doping concentration.

Table 3. Dependence of solar cell performance on the doping concentration of Absorber layer

Parameters N_A(cm^{-3})	J_{sc} (mAcm^{-2})	V_{oc} (V)	*FF*	PCE (%)
1E+13	27.44	0.54	60.21	8.94
1E+14	27.49	0.54	60.37	9.01
1E+15	27.92	0.57	61.53	9.74
1E+16	27.85	0.72	65.31	13.09
1E+17	25.32	0.75	71.98	13.60
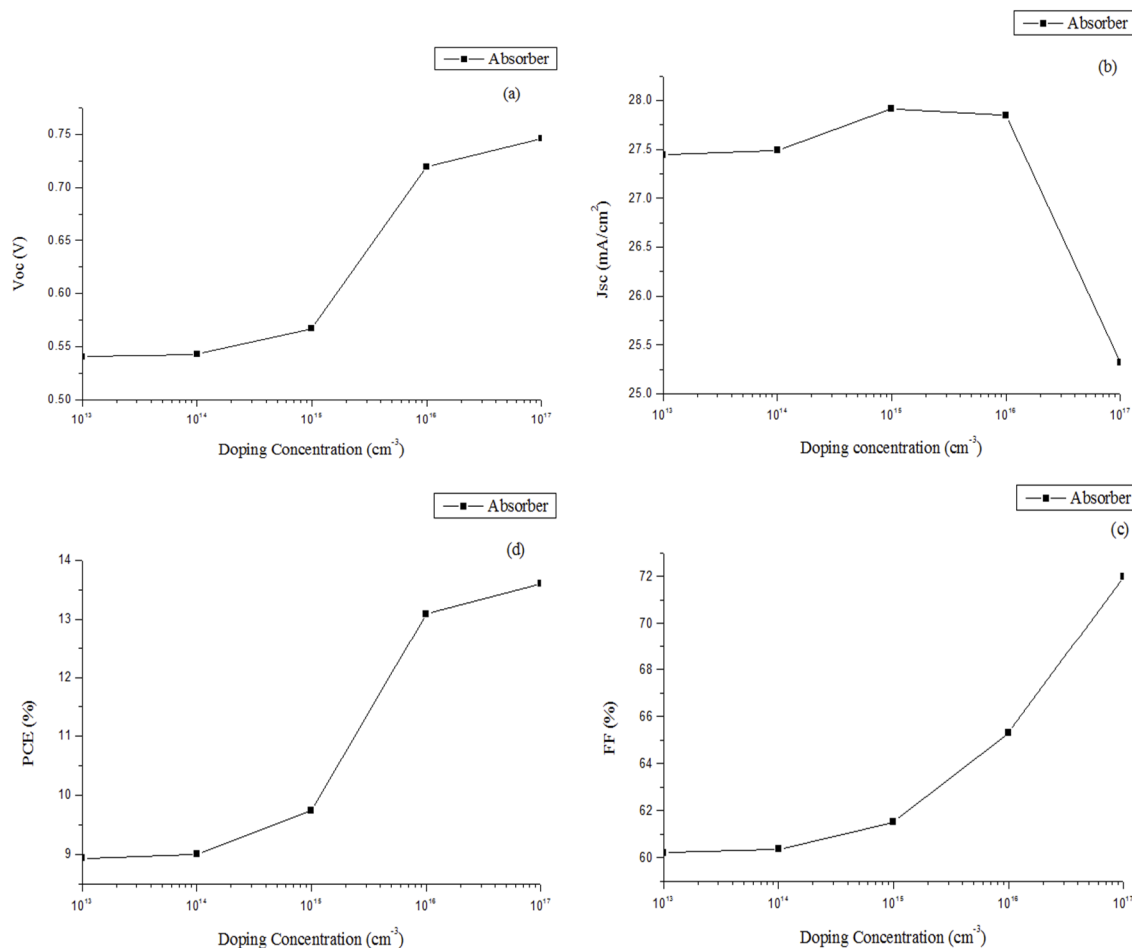
Figure 3. Variation in solar cell parameters with doping concentration of absorber.

The best performing device was obtained when N_A was set as 1.0×10^{17} cm^{-3} for the perovskite absorption layer, it gives photovoltaic parameters of 25.32 mA/cm^2 for Jsc, 0.74 V for Voc, 71.98 % for FF and 13.59% for PCE as depicted in Figure 3. The result of the champion device shows charge carriers are efficiently transported and collected at the N_A value and that suggests that, for improvement of performance of PSCs, the N_A should be 1.0×10^{17} cm^{-3}.

Our result further shows that decreasing N_A beyond 1.0×10^{17} a decrease in PCE was observed. The observed decrease in PCE with increasing N_A is due to increase in Auger recombination rate [5]. When the optimized result is compared with the reference device, we observed an enhancement that is ~17.20 % in Voc, 17.81% in FF, and ~20.35% in PCE.

Influence of Electron Affinity of HTH and ETM

The critical factor between TiO_2/perovskite/CuI is band offset which can predict the possibility of carrier recombination at the interface and is the function of V_{oc}. By changing the values of electron affinities of CuI (2.0 eV-2.8 eV) and TiO_2 (3.7 eV-4.4 eV), the band offset can be adjusted. Figure 4 shows the combined variations of V_{oc}, J_{sc}, FF and PCE with electron affinity of HTM and ETM respectively. Figure 4 explain the variation of PCE, Voc, Jsc and FF with electron affinity of ETM and HTM respectively.

The values of 2.3 eV and 3.7 eV gave the best PCEs for CuI and TiO_2 respectively. Their corresponding photovoltaic parameters are Voc of 0.63 V, Jsc of 30.79 mAcm^{-2}, FF of 68.50% and PCE of 13.32% for the CuI and Voc of 0.82 V, Jsc of 29.06 mAcm^{-2}, FF of 64.87% and PCE of 15.51% for the TiO$_2$. Increasing the EA of the ETL above 3.7 eV leads to decrease in PV performances as shown in Table 4.

When the electron affinity of ETM is higher than 3.7 eV, the Jsc and PCE decreases. When the electron affinity of HTM is lower than 2.3 eV, and above 2.3 eV, the PV parameters both decreases as shown in Table 5.

Table 4. Dependence of solar cell performance on the EA of the ETL

Parameters EA (eV)	J_{sc} (mAcm^{-2})	V_{oc} (V)	FF	PCE (%)
3.7	30.79	0.63	68.50	13.33
3.8	30.76	0.63	68.51	13.31
3.9	30.68	0.63	68.47	13.27
4.0	30.44	0.63	68.31	13.13
4.1	29.70	0.63	67.45	12.66
4.2	28.78	0.64	64.16	11.80
4.3	28.33	0.65	59.17	10.81
4.4	27.79	0.57	55.20	8.81

Table 5. Dependence of solar cell performance on the EA of HTL

Parameters EA(eV)	J_{sc} (mAcm^{-2})	V_{oc} (V)	FF	PCE (%)
2.0	28.05	0.55	59.05	9.10
2.1	28.49	0.65	61.09	11.30
2.2	28.82	0.75	62.79	13.54
2.3	29.06	0.82	64.87	15.51
2.4	29.12	0.84	62.94	15.44
2.5	29.13	0.85	56.06	13.83
2.6	29.07	0.83	47.90	11.62
2.7	29.86	0.76	41.28	9.08
2.8	25.24	0.69	18.40	3.18
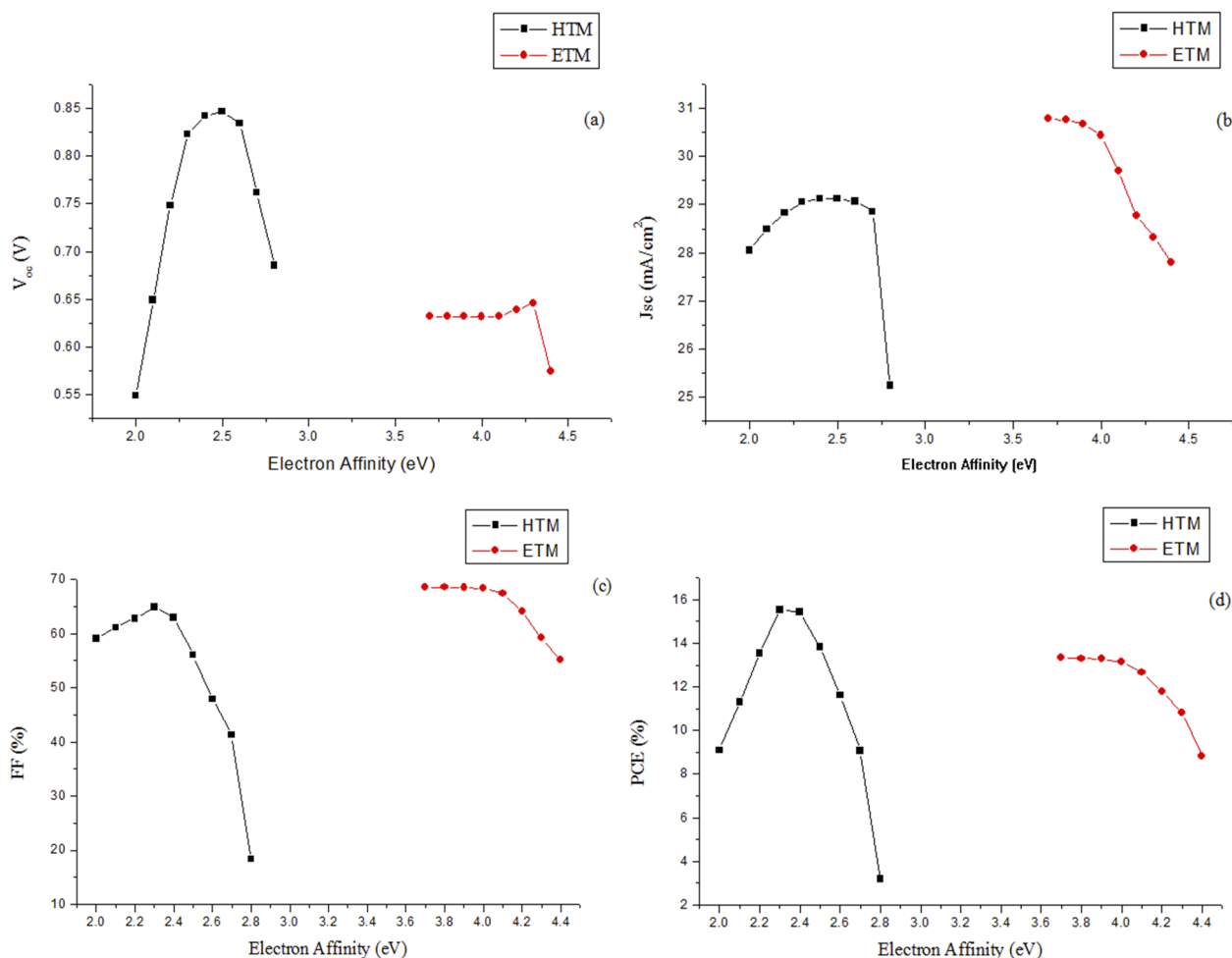
Figure 4. Variation in solar cell parameters with Electron Affinity of HTM and ETM.

It is evident that proper HTM and ETM selection with suitable electron affinity can prevent quenching of carriers and enhanced the performance of PSCs [12].

Effect of the Absorber Thickness on the Device Parameters

Thickness of absorber layer (L), affects the performance of solar cell. The influence of thickness of absorber with variation of performance parameters V_{oc}, J_{sc}, FF and PCE is shown in the Figure 5. The graphs in Figure 5 show the

variation in thickness from (0.4-1.3) μm of the absorber against the PV parameters of the PSCs. Figure 5 shows a steady increase in V_{oc}, J_{sc} and PCE from a thickness of 0.5 μm, while there is a rapid decline in values below 0.5 μm. There a steady increase in PCE with thickness also conforming with the work of Hafeez *et al.* [9]. From Figure 5, it could be deduced that the optimum thickness of the absorber is 0.7 μm, for after this thickness, a steady increment of the PCE value.

Table 6. Dependence of solar cell performance on the thickness of the Absorber layer

Parameters N_A(cm^{-3})	J_{sc} (mAcm^{-2})	V_{oc} (V)	*FF*	PCE (%)
0.2	23.40	0.53	65.24	8.14
0.3	26.78	0.58	62.79	9.83
0.4	28.49	0.65	61.09	11.30
0.5	29.41	0.69	62.59	12.69
0.6	29.91	0.71	63.61	13.46
0.7	30.28	0.72	63.93	13.90
0.8	30.59	0.73	63.73	14.16
0.9	30.82	0.73	63.33	14.33
1.0	30.98	0.74	62.84	14.43
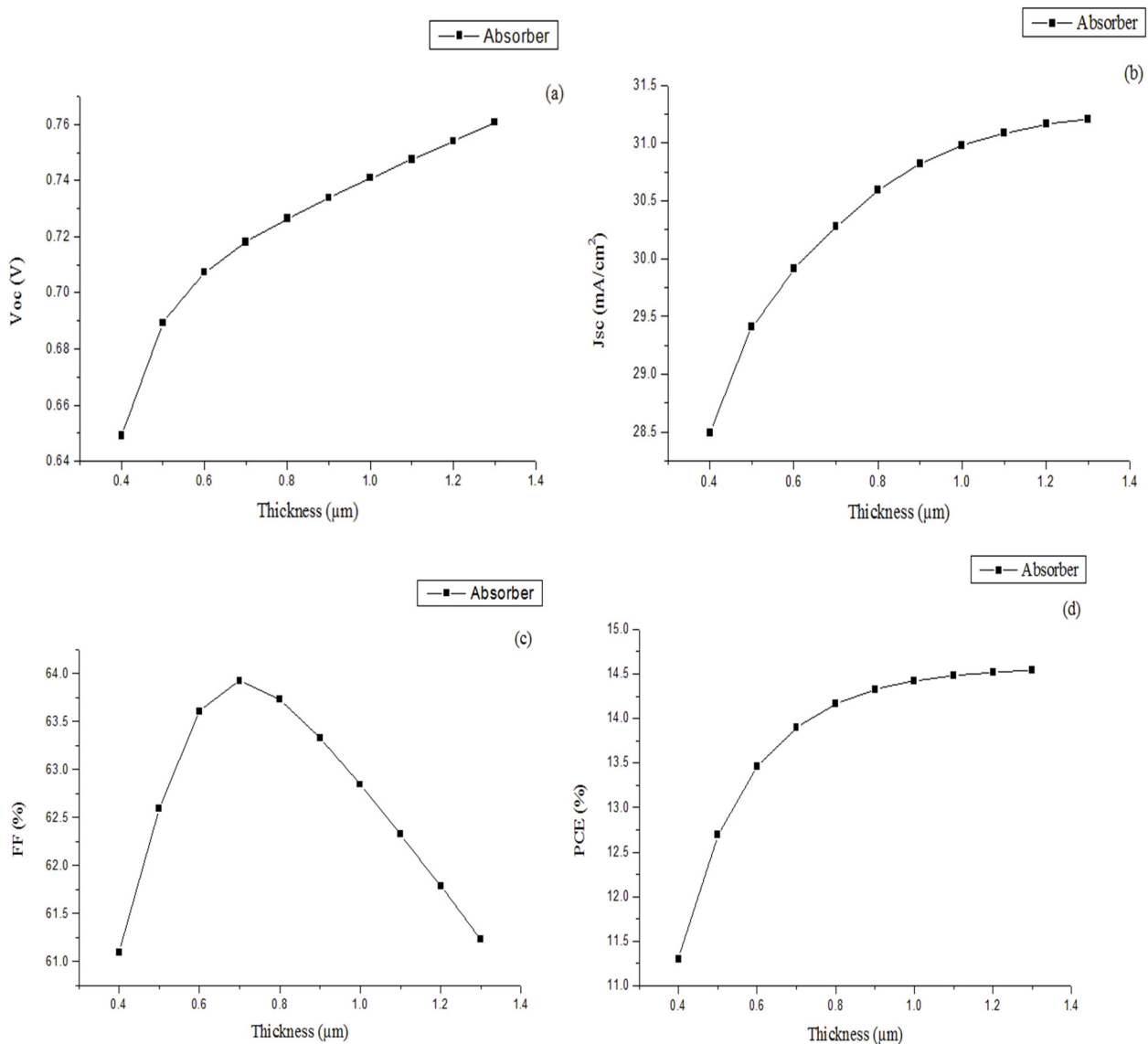
Figure 5. Variation in solar cell parameters with thickness of the absorber.

Influence of Defect Density (N_t) of Absorber Layer

For further improvement in performance of PSC, defect density is one of the crucial parameter worth investigating. The behaviour of PSC is greatly affected by the morphology and quality of absorber layer [13]. When light is irradiated upon

PSC, photoelectrons are generated in the absorber layer. If the film quality is not good enough, then defect density increases and quenching losses will become unavoidable in absorber layer which determine the Voc of the solar cell.

Table 7. Dependence of solar cell performance on the defect density of the Absorber layer

Parameters N_A(cm^{-3})	J_{sc} (mAcm^{-2})	V_{oc} (V)	FF	PCE (%)
1E+14	28.75	0.65	62.73	11.78
1E+15	28.75	0.65	62.69	11.77
1E+16	28.69	0.65	62.31	11.66
1E+17	28.18	0.64	59.47	10.80
1E+18	24.02	0.60	47.70	6.90
1E+19	9.65	0.50	29.12	1.42

The initial value of N_t in the absorber is set to be 4.5×10^{16} cm^{-3} [8]. Based on previous simulated studies the range of defect density was considered to be 10^{14} cm^{-3} to 10^{19} cm^{-3} [7].

Figure 6 depicts the variation of PV parameters with defect density (N_t) of absorber layer. The PV parameters of the PSC is enhanced greatly with decrease in the Nt in perovskite, which shows agreement with similar studies on the lead perovskite [14]. When defect density is 1.0×10^{16} cm^{-3} the cell PV property is greatly enhanced reaching a Jsc of 28.75 mA/cm^2, Voc of 0.65 V, FF of 62.73% and PCE of 11.78%. The result conforms with those of Hui-Jing *et al.,* in 2016 [7]. However, realizing such a low defect density experimentally is very difficult, so an optimized value of 1.0×10^{14} cm^{-3} was set as the defect density making all the values of the PV parameters (Jsc, Voc, FF and PCE) approximately reaching their maximum with the chosen defect density. Experimental studies, however shows that the tin-based perovskite demonstrates good charge-transport characteristics [15, 16].
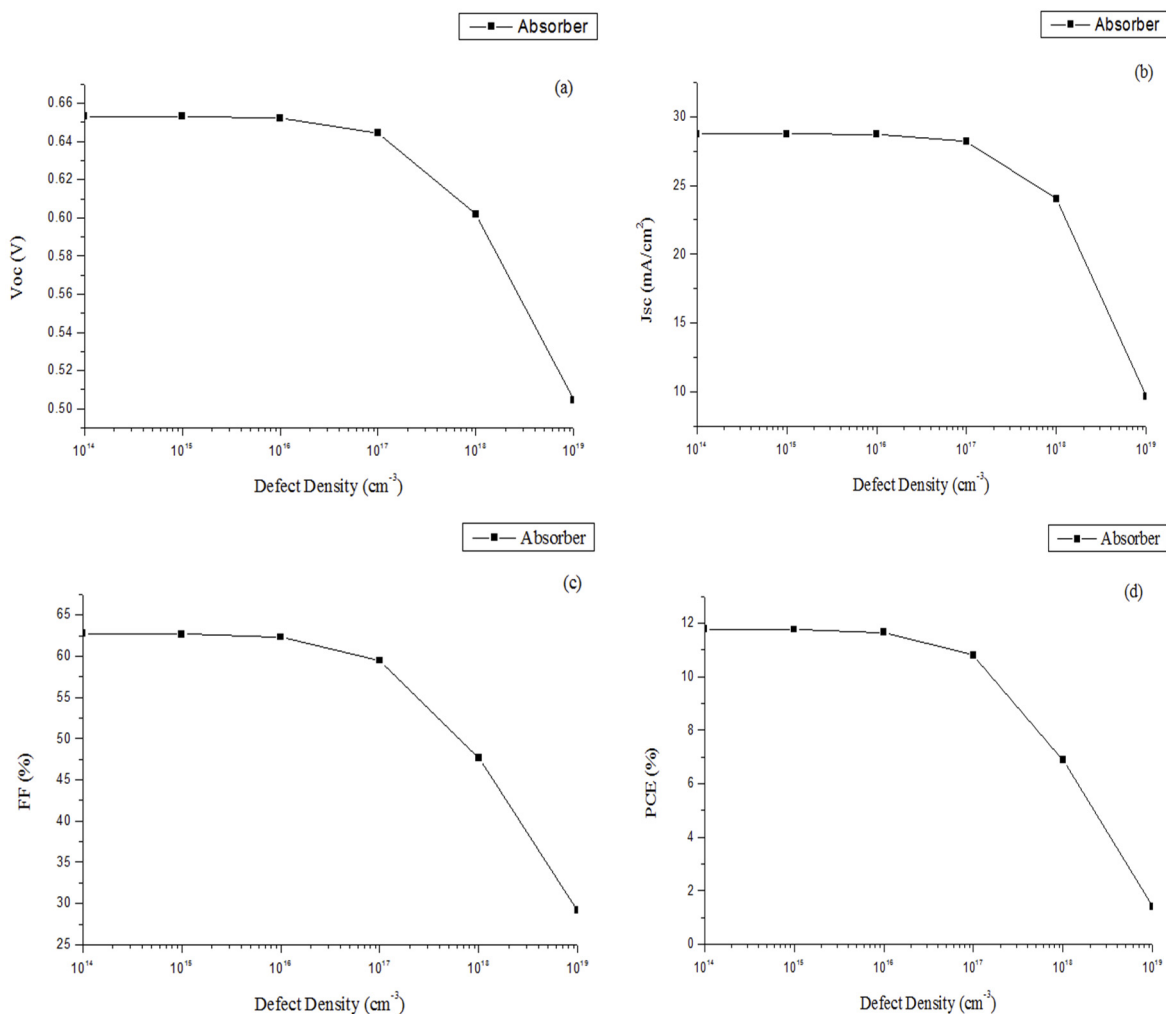
Figure 6. Variation in solar cell parameters with different values of defect density N_t

Influence of Hole Mobility of HTM

Mobility of charge Carrier in a semiconductor is among the crucial parameters in electronic devices. Actually, it measures the capacity of charge carriers to shuttle in the material as it is exposed to an external electric field. The

magnitude of the mobility directly impacts on the device performance since it determines the operation speed through the transit time across the device, the circuit operating frequency. Hole mobility is affected by doping level and doping concentration of acceptor. Lattice scattering and ionized impurity scattering limit the hole mobility in the material at low acceptor doping and high acceptor doping respectively.
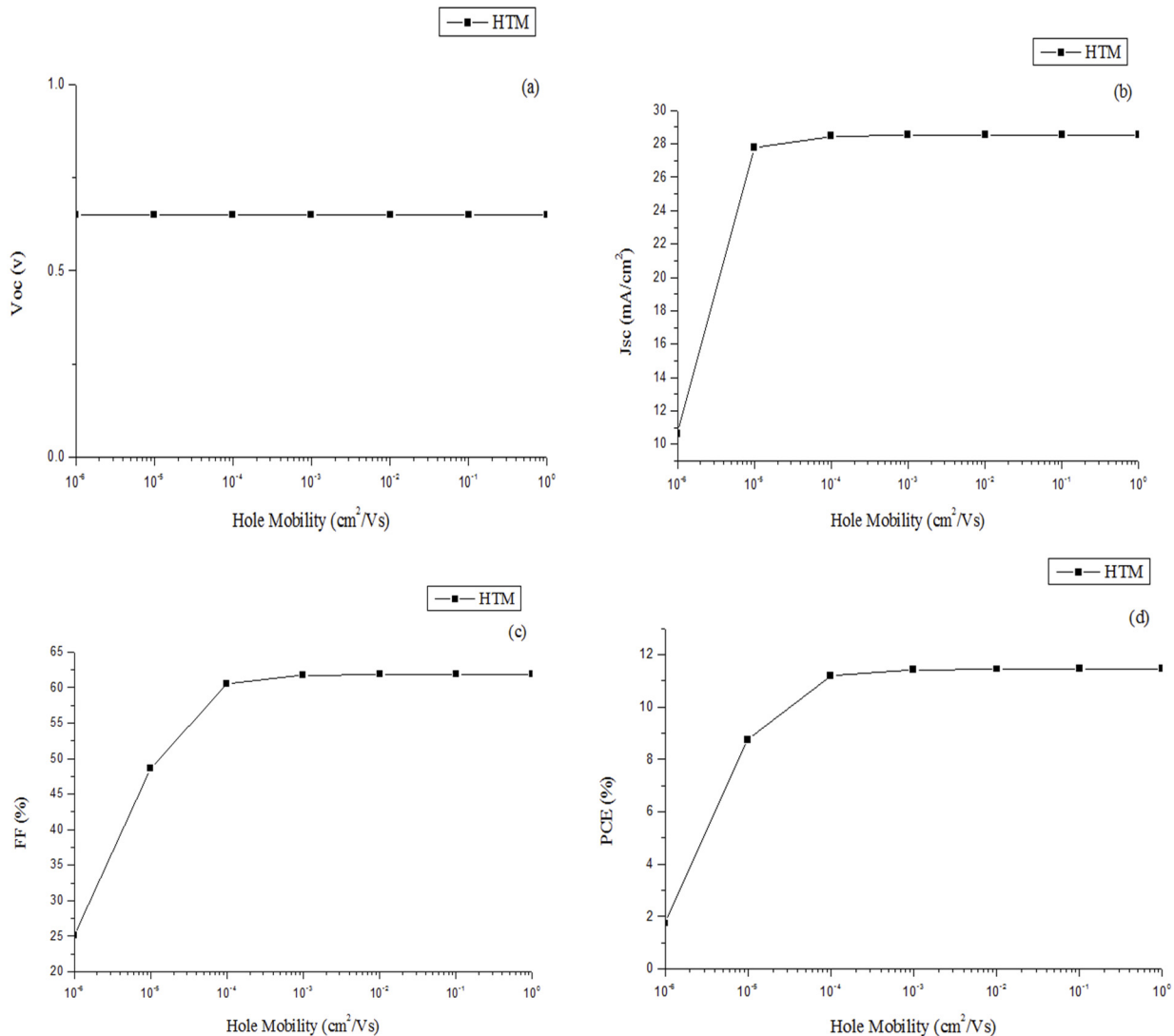
Figure 7. Variation in solar cell parameters with increasing hole mobility of HTM.

The effect of hole mobility in the hole transport material (CuI) has been computed on performance parameters. From Figure 7, (b) and (d) it shows the increase in J_{sc} and PCE with the increase in hole mobility which signifies the better charge transport and charge extraction at the HTM/absorber interface.

Table 8. Dependence of solar cell performance on the hole mobility of HTM

Parameters N_A(cm^{-3})	J_{sc} (mAcm^{-2})	V_{oc} (V)	*FF*	PCE (%)
1E-06	10.65	0.65	25.11	1.74
1E-05	27.76	0.65	48.57	8.75
1E-04	28.47	0.65	60.54	11.18
1E-03	28.52	0.65	61.73	11.43
1E-02	28.53	0.65	61.87	11.46
1E-01	25.53	0.65	61.88	11.46
1E+00	28.53	0.65	61.88	11.46

Performance of Optimized parameters

Considering all the varied parameters after simulation, such as N_A, electron affinity, Nt thickness and Hole mobility, a PCE of 20.35 % with Jsc of 31.38 mAcm^{-2}, voltage of 0.84 V, and FF of 76.94 %, which shows an improvement

of ~ 1.80 times in PCE, ~1.10 times in Jsc, 1.26 times in FF and 1.31 times in Voc over the initial cell. The final optimized parameters and optimised J–V curve are shown in Table 9(a) and Figure 8 respectively. The result was compared to other simulated and experimental work published by other researchers and the related data is summarized in Table 9(b). In Table 9(b), the best experimental PCE is 17.60 % with CuI as HTM. The Voc, FF and Jsc still need to be enhanced to achieve 20.35 % PCE.
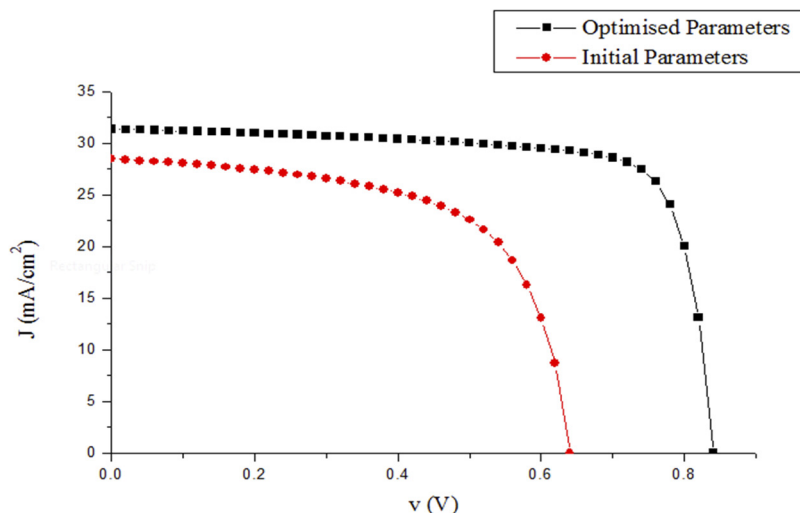
Table 9(a). Optimized parameters of the simulated device

Optimized parameters	TiO_2(ETL)	$CH_3NH_3SnI_3$(absorber)	CuI(HTL)
Doping density (cm^{-3})	---	1.0×10^{16}	---
Electron affinity (eV)	3.7	---	2.3
Defect density (cm^{-3})	---	1.0×10^{16}	---
Thickness (μm)	---	0.7	---
Hole mobility (cm²/Vs)	---	---	1.0×10^{-2}

Table 9(b). Photovoltaic parameters of CuI and Tin (Sn) based perovskite solar cells of some reported experimental and simulated works from literature using SCAPS-1D

Device	Parameters				Reference	Experiment/Simulation
	PCE (%)	FF (%)	Jsc (mA/cm²)	Voc (V)		
$CH_3NH_3SnI_3/CuI$	20.35	76.94	31.38	0.84	Current	Simulation
$CH_3NH_3PbI_3/CuI$	21.32	84.53	25.47	0.99	[9]	Simulation
$CH_3NH_3SnI_3/Cu_2O$	20.23	74.02	32.26	0.85	[8]	Simulation
$CH_3NH_3SnI_3/S$-OMETaD	6.40	42	16.80	0.88	[17]	Experiment
$CH_3NH_3PbI_3/CuI$	17.60	75	22.78	1.03	[18]	Experiment
$CH_3NH_3PbI_3/Cu_2I$	7.5	57	16.7	0.78	[19]	Experiment

CONCLUSION

Lead-free perovskite solar cells were simulated using SCAPS-1D software. An optimal thickness (0.7μm) and optimal doping concentration ($1.0 \times 10^{16} \ cm^{-3}$) of the absorber layer were identified, exceeding which will lead to degradation of solar cell performance. The simulation shows that N_t is an crucial factor to measure the PV parameters of PSCs, and the result is consistent with the researches on $CH_3NH_3PbI_3$ perovskite cell. Considering all the factors such as doping density, electron affinity, defect density and thickness, an encouraging result was obtained, Jsc of 31.38 mA/cm², Voc of 0.84 V, FF of 76.94% and PCE of 20.35%.

The final optimized parameters and optimised J-V curve were obtained. Comparison was done with other simulated results and experimental works published by the other researchers. In the literature, the best efficiency of 17.60% has been achieved for PSCs with CuI as HTM. Voc of 1.03V reported in the literature is already higher than the value through this work, while the FF and Jsc still need be increased to achieve 21.32% efficiency.

ORCID IDs

Danladi Eli, https://orcid.org/0000-0001-5109-4690

REFERENCES

[1] Z. Wang, Q. Lin, F.P. Chmiel, N. Sakai, L.M. Herz, and H.J. Snaith, Nature Energy, **2,** 17135 (2017), https://doi.org/10.1038/nenergy.2017.135.

[2] Y. Liu, Z. Yang, D. Cui, X. Ren, J. Sun, X. Liu, J. Zhang, Q. Wei, H. Fan, F. Yu, X. Zhang, C. Zhao, and S. Liu, Advanced Materials, **27**, 5176–5183 (2015), https://doi.org/10.1002/adma.201502597.

[3] D. Yang, Z. Yang, W. Qin, Y. Zhang, S. Liu, and C. Li, Journal of Materials Chemistry A, **3**, 9401–9405 (2015), https://doi.org/10.1039/C5TA01824B.

[4] A. Kojima, K. Teshima, Y. Shirai, and T. Miyasaka, Journal of the American Chemical society, 131(17), 6050-6051 (2009), https://doi.org/10.1021/ja809598r.

[5] D. Eli, M.Y. Onimisi, S. Garba, R.U. Ugbe, J.A. Owolabi, O.O. Ige, G.J. Ibeh, and A.O. Muhammed, J. Nig. Soc. Phys. Sci. **1**, 72–81 (2019), https://doi.org/10.46481/jnsps.2019.13.

[6] NREL Efficiency chart, (2019), https://www.nrel.gov/pv/assets/images/efficiencychart- 20180716.jpg.

[7] D. Hui-Jing, W. Wei-Chao, and Z. Jian-Zhuo, Chinese Phys. B, **25**, 108802 (2016), https://doi.org/10.1088/1674-1056/25/10/108802.

[8] A. Farhana, M. Rafee, S.S. Sakin, and M.U. Saeed, International Journal of Photoenergy, 9846310 (2017), https://doi.org/10.1155/2017/9846310.

[9] Syed Zulqarnain Haider, Hafeez Anwar, and Mingqing Wang, Semicond. Sci. Technol. **33**(3), 035001 (2018), https://orcid.org/0000-0002-0473-850X.

[10] F. Hao, C.C. Stoumpos, R.P.H. Chang, and M.G. Kanatzidis, J. Am. Chem. Soc. **136**(22), 8094-8099 (2014), https://doi.org/10.1021/ja5033259.

[11] F. Hao, C.C. Stoumpos, P. Guo, N. Zhou, T.J. Marks, R.P.H. Chang, and M.G. Kanatzidis, J. Am. Chem. Soc. **137**, 11445 (2015), https://doi.org/10.1021/jacs.5b06658.

[12] K.G. Lim, S. Ahn, Y.H. Kim, Y. Qi, and T.W. Lee, Energy Environ. Sci. **9**, 932–939 (2016), https://doi.org/10.1039/C5EE03560K.

[13] H. Kim, K.G. Lim, and T.W. Lee, Energy Environ. Sci. **9**, 12–30 (2016), https://doi.org/10.1039/C5EE02194D.

[14] F. Hao, K. Stoumpos, D. H. Cao, R. P. H. Chang, and M. Kanatzidis, Nature Photonics, **8**(6), 489-494 (2014) https://doi.org/10.1038/nphoton.2014.82.

[15] D.B. Mitzi, C.A. Field, Z. Schlesinger, and R.B. Laibowitz, J. Solid State Chem. **114**, 159–163 (1995), https://doi.org/10.1006/jssc.1995.1023.

[16] D.Y. Liu, M.K. Gangishetty, and T.L. Kelly, J. Mater. Chem. A, **2**, 19873-19881 (2014), https://doi.org/10.1039/C4TA02637C.

[17] N.K. Noel, D.S. Samuel, A. Antonio, W. Christian, G. Simone, H. Amir-Abbas, S. Aditya, E.E. Giles, K.P. Sandeep, B.J. Michael, P. Annamaria, M.H. Laura, and J.S. Henry, Energy Environ. Sci. **7**, 3061-3068 (2014), https://doi.org/10.1039/c4ee01076k.

[18] X. Li, J. Yang, Q. Jiang, W. Chu, D. Zhang, Z Zhou, and J. Xin, ACS Appl. Mater. Interfaces, **7b**, 14926 (2017), https://doi.org/10.1021/acsami.7b14926.

[19] G.A. Sepalage, S. Meyer, A. Pascoe, A.D. Scully, F. Huang, U. Bach, Y.B Cheng, and L. Spiccia, Adv. Funct. Mater. **25**, 5650-5661 (2015), https://doi.org/10.1002/adfm.201502541.

МОДЕЛЮВАННЯ ТА ІМІТАЦІЯ БЕЗСВИНЦЕВОГО ПЕРОВСКІТНОГО СОНЯЧНОГО ЕЛЕМЕНТА З ВИКОРИСТАННЯМ ПРОГРАМИ SCAPS-1D

Омейза Абдулмалік Мухаммед[a], Данладі Елі[b,e], Пітер Генрі Бодуку[c], Джаміля Тасю[c],
Мухаммад Сани Ахмад[c], Нуху Усман[d]
[a]Фізичний факультет, Університет Байєр, Кано, Нігерія
[b]Фізичний факультет, Нігерійська академія оборони, Кадуна, Нігерія
[c]Фізичний факультет, Університет штату Кадуни, Кадуна, Нігерія
[d]Факультет математичних наук, Університет штату Кадуна, Кадуна, Нігерія
[e]Факультет фізичних наук, Університет Грінфілд, Кадуна, Нігерія

У цій роботі було вивчено вплив деяких параметрів на перовскітний сонячний елемент (PSC) на основі олова ($CH_3NH_3SnI_3$) шляхом моделювання пристрою щодо регулювання концентрації легування перовскітного поглинаючого шару, його товщини та спорідненості транспортного середовища електронів та дірково-транспортувального середовища до електрону, а також щільності дефектів перовскітного поглинаючого шару та рухливості дірок в дірково-транспортувальному матеріалі (HTM). Моделюючий пристрій: програма одномірного імітатора ємності сонячних елементів (SCAPS-1D) була використана для моделювання перовскітних сонячних елементів на основі олова. Крива вольтамперної характеристики (J-V), отримана шляхом моделювання пристрою без оптимізації, показує вихідні параметри елемента, які включають: напругу розімкнутого контуру (V_{oc}) = 0,64 В, щільність струму короткого замикання (J_{sc}) = 28,50 мА/см², коефіцієнт заповнення (FF) = 61,10% та ефективність перетворення потужності (PCE) = 11,30% при імітованому AM1,5, сонячному світлі, = 100 мВт/см² при 300K. Після оптимізації було визначено, що значення концентрації легування, щільності дефектів, спорідненості до електронів матеріалу для транспортування електронів та дірково-транспортувального матеріалу становлять: 1.0×10^{16} cm^{-3}, 1.0×10^{15} cm^{-3}, 3.7 eВ та 2,3 eВ відповідно. Порівняно з початковим пристроєм без оптимізації, були отримані помітні значення параметрів сонячних елементів при J_{sc} = 31,38 мА/см², V_{oc} = 0,84 В, FF = 76,94% та PCE = 20,35%, що демонструє поліпшення в ~ 1,10 рази для Jsc, ~ 1,80 рази для PCE, ~ 1,31 рази для V$_{oc}$, та ~ 1,26 рази для FF. Результати показують, що безсвинцевий $CH_3NH_3SnI_3$ перовскітний сонячний елемент, який є екологічно чистим, є потенційним сонячним елементом з високою теоретичною ефективністю 20,35%.

КЛЮЧОВІ СЛОВА: шар транспортування електронів, дірково-транспортувальний шар, перовскітний сонячний елемент, фотоелектричний, SCAPS-1D, йодід міді

INFLUENCE OF ELECTRON INJECTION ON THE CHARACTERISTICS OF A HOLLOW CATHODE GLOW DISCHARGE

Stanislav V. Pogorelov[a], Volodymyr A. Timaniuk[a],*
Nikolay G. Kokodii[a,b], Ihor V. Krasovskyi[a]

[a]National University of Pharmacy, Kharkiv, Ukraine
[b]V.N. Karazin Kharkiv National University, Kharkiv, Ukraine
*Corresponding Author: vladimir.timaniuk@gmail.com, tel.: +38 095 505 39 19
Received January 18, 2021; revised March 31, 2021; accepted April 7, 2021

The article presents the results of experimental studies of a glow discharge with a hollow cathode in helium and argon gases using an auxiliary discharge as an electron emitter. The authors proposed to make the electrode common for both discharges in the form of a cylindrical metal mesh. The advantage of this design is explained as follows. The connection between the discharges is carried out through holes in the grid with a geometric transparency of 0.2, which makes it possible not only to smoothly control the glow discharge current, but also to enhance the discharge current. Plasma is known to be one of the most efficient electron emitters; however, its use as a cathode in devices with a glow discharge at low gas pressures is complicated by the fact that a grid with small holes is required to separate the electron flow from the plasma, and it is impractical to use such a system in view of low mechanical strength of the grid Since the hollow cathode works effectively at low gas pressures, the release of an electron flux from the plasma of some auxiliary discharge is possible with much larger holes in the grid separating the plasma and the hollow cathode cavity. In this case, the grid can be made such that it can withstand sufficiently high thermal loads and can operate in typical discharge modes with a hollow cathode. The injection of electrons into the cathode cavity of the glow discharge changes the radial distribution of the glow intensity, the width of the cathode dark space, and other parameters of the plasma in the cathode cavity. The influence of electrons penetrating from the auxiliary discharge into the cathode cavity of the main discharge becomes significant when the current of these electrons is comparable to or exceeds the current of electrons leaving the grid cathode surface as a result of γ-processes. In parallel with the measurement of the optical and electrical characteristics of the hollow cathode glow discharge plasma, measurements of the electron concentration were carried out by the microwave sounding method. The entire current of the auxiliary discharge penetrates into the cavity of the main discharge; however, after acceleration in the cathode dark space, the electrons penetrating from the auxiliary discharge ionize gas atoms and noticeably increase the current of the main discharge. Additional ions formed due to the ionization of the gas by the injected electrons knock out new electrons from the cathode surface, which makes it possible to increase the discharge current.
KEY WORDS: glow discharge, plasma, hollow cathode, electrons, injection.

The cathode material and conditions on its surface determine the cathode potential drop and, consequently, the discharge burning voltage [1]. The cathode potential drop is substantially determined by the efficiency of the processes of electron emission from the cathode, the totality of which is called γ-processes. The γ coefficient numerically determines the efficiency of γ-processes and depends on the cathode material and the state of its surface [2].

In many cases of using the glow discharge the aim is to reduce the cathode potential drop. This is achieved by using more efficient elements as the cathode. It is known that plasma is one of the most efficient emitters of electrons; however, its use as a cathode in devices with a glow discharge at pressures below 1 torr is hampered by the fact that a very fine grid is required to separate the electron flow from the plasma, and such system is impractical due to the low mechanical strength of the grid [3], [8]. Since, as follows from our experimental data, the hollow cathode works effectively at low (less than 5.0 Torr) gas pressures, the extraction of an electron flux from the plasma of some auxiliary discharge is possible with much larger holes in the grid separating the plasma and the cathode cavity of the hollow cathode. In this case, the grid can be made such that it can withstand sufficiently high thermal loads and can operate in typical hollow cathode discharge modes.

GOALS OF ARTICLE

The discharge tube (Fig. 1), which implements the idea of a plasma hollow cathode, includes a cylindrical hollow cathode (1) with a diameter of 30 mm and a length of 100 mm. The geometric transparency of the grid cathode is 0.2, the hole diameter is chosen so that it is less than the width of the cathode dark space in the region of optimal pressures for the cathode of a given diameter. The anodes (2) of a hollow cathode discharge, which will be called the main discharge, are two annular electrodes located coaxially with the cathode at a distance of 10 mm.

An auxiliary discharge is ignited between a cylindrical copper cathode (3) with a diameter of 90 mm and a grid cylinder (1), which plays the role of an anode in this discharge. Flat disks (4) made of insulating material shield the auxiliary discharge area from the main discharge anode in such a way that the connection between the discharges is carried out only through the holes in the grid. Even if there is no electric field in the cathode cavity of the main discharge, electrons from the anode region of the auxiliary discharge will penetrate through the holes into the grid cylinder cavity. Essentially, part of the metal surface of the hollow cathode in this design is replaced by the plasma generated in the auxiliary discharge. At a sufficiently high current of injected electrons, the main hollow cathode discharge should be considered as a non-self-sustained discharge.
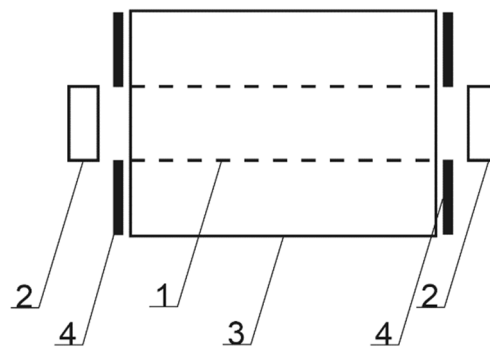
Figure 1. Construction of the discharge tube with a plasma hollow cathode: 1 - cathode of the main discharge, anode of the auxiliary discharge (grid); 2 - main discharge anodes; 3 - auxiliary discharge cathode; 4 - shielding discs.

MATERIALS AND METHODS

When the auxiliary discharge is ignited, electrons will be injected into the cathode cavity of the main discharge, which, passing through the holes in the grid cylinder, in the cathode plane of the main discharge will have thermal velocities, i.e., they are equivalent to secondary electrons knocked out of the metal by positive ions, light quanta and metastable atoms. In the cathode dark space of the hollow cathode, the injected electrons will be accelerated and create additional ionization in the cathode cavity, increasing the hollow cathode discharge current. Since the number of injected electrons depends on the auxiliary discharge current, it becomes possible to smoothly control the discharge current with a hollow cathode.

The characteristics of a discharge with a hollow cathode in the form of a grid cylinder do not qualitatively differ from the characteristics of a discharge with a solid cathode. The difference from a solid cathode is that the current-voltage characteristic of the discharge is steeper. This is apparently due to the losses through the holes of the grid of metastable atoms and photons regenerated in the negative glow.

As we can see from our experiments in helium (pressure range 0.2 - 10 Torr) and argon (pressure range 0.06 - 6 Torr) gases, the form of the dependence of the burning voltage on the pressure in the main hollow cathode discharge is determined by the motion of charged particles in the cathode cavity. A shift of the boundaries of the region of optimal pressures towards lower values is observed with an increase in the atomic mass of the gas and is due to the fact that the mean free path of electrons increases with a decrease in the atomic mass of the gas.

When the auxiliary discharge is switched on, electrons from the auxiliary discharge enter the cathode cavity through the holes in the grid. This leads to an increase in the main discharge current or, if the current is kept constant, to a decrease in the burning voltage of the main discharge. With an increase in the auxiliary discharge current, the burning voltage of the main discharge decreases, and the auxiliary discharge exerts its greatest influence in the region of optimal pressures for a hollow cathode discharge.

At high currents of the auxiliary discharge, a section where the combustion voltage of the main discharge is almost independent of the gas pressure appears on the curves. In this mode, the discharge with a hollow cathode becomes non-self-sustaining, the burning voltage of the discharge is substantially determined by the anodic potential drop.

RESULTS

The main discharge burning voltage reduction mechanism can be represented as follows (Fig. 2). Electrons injected from the auxiliary discharge into the cathode cavity enter the cathode dark space and decrease the positive ions space charge at the cathode. A decrease in the cathode potential drop and the number of ionizations performed by electrons in the cathode cavity is compensated by an increase in the effective value of the secondary emission coefficient γ.

With a decrease in the cathodic potential drop of the main discharge, the efficiency of gas ionization by additional electrons coming from the auxiliary discharge decreases. The analysis of the current–voltage characteristics of the simultaneously switched on main and auxiliary discharges shows that the degree of influence of the auxiliary discharge on the main one strongly depends on the main discharge current and increases with decreasing a hollow cathode discharge current (Fig. 3). Apparently, the influence of electrons penetrating from the auxiliary discharge into the cathode cavity of the main discharge becomes significant when the current of these electrons is comparable to or exceeds the current of electrons leaving the grid cathode surface as a result of γ-processes.

An analysis of the dependences of the main discharge current on the auxiliary discharge current for fixed voltages at the main discharge electrodes shows that the main discharge current increases, and more than the auxiliary discharge current increases (Fig. 4). Naturally, the entire current of the auxiliary discharge penetrates into the cavity of the main discharge; however, after acceleration in the cathode dark space, the electrons penetrated from the auxiliary discharge ionize the gas atoms and noticeably increase the current of the main discharge. Thus, in addition to controlling the main discharge current, current amplification is possible.
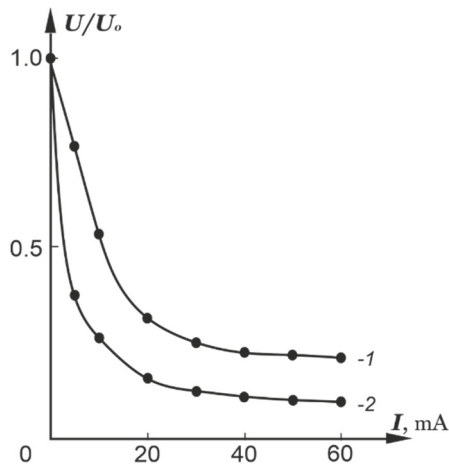
Figure 2. Dependence of the relative decrease in the main discharge burning voltage on the auxiliary discharge current at a pressure of 0.2 Torr. *I_main=10 mA, 1 – He, 2 – Ar.*
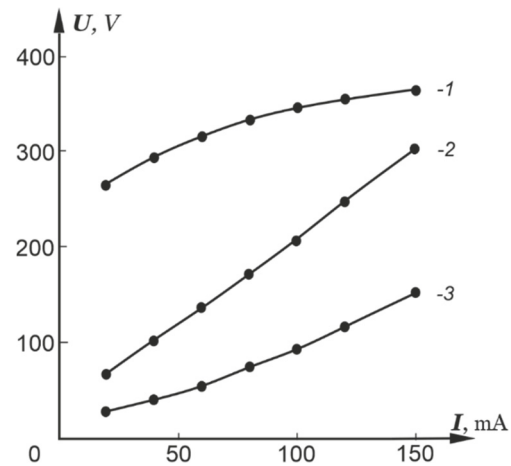
Figure 3. Current–voltage characteristics of the main discharge at various currents of the auxiliary discharge in helium at a pressure of 0.2 Torr. *1 – 0 mA, 2 – 20 mA, 3 – 50 mA.*
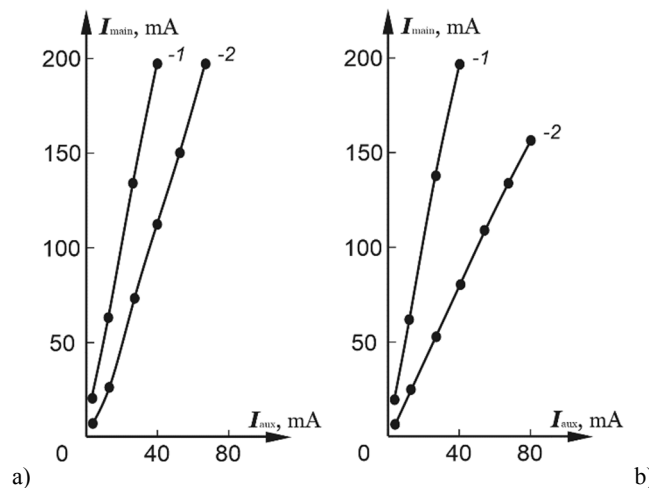
Figure 4. Dependences of the main discharge current on the auxiliary discharge current at a pressure of 0.2 Torr.
a) *He, 1 – U_main=125 V, 2 – U_main=100 V;* b) *U_main=125 V, 1 – He, 2 – Ar.*

The first ionization potential of a helium atom is approximately 1.6 times greater than the ionization potential of, for example, argon atoms, and one might assume that the gain should decrease with decreasing atomic mass of the gas. However, the number of electrons knocked out due to the bombardment of the grid cathode surface by ions will be higher in helium, since the secondary emission coefficient in this case for helium is about 2.4 times higher than for argon. Consequently, the injection of additional electrons into the cathode cavity is most effective in a helium discharge.

Due to the penetration of ions from the cathode cavity of a hollow cathode discharge into the region of the auxiliary discharge, there is also a reverse effect of the main discharge on the auxiliary one. An auxiliary discharge is fired up between a coaxially located cylindrical cathode and an anode; therefore, there are no electron oscillations in the discharge gap and the discharge characteristics are practically the same as for a linear one. When the main discharge is ignited, some of moving towards the grid cathode ions penetrate through the holes into the auxiliary discharge space. Reaching the cathode of the auxiliary discharge, these ions cause the emission of secondary electrons, as a result of which the burning voltage of the auxiliary discharge also decreases.

The probability of additional ions reaching the auxiliary discharge cathode increases with decreasing gas pressure; therefore, at low gas pressures, the effect of the main discharge on the auxiliary discharge increases. In this case, main discharge ion current can be so significant that the burning voltage of the auxiliary discharge can become equal to zero, and even reverse its sign at high currents of the main discharge. The increase in the effect of the main discharge on the auxiliary discharge at high gas pressures can apparently be explained by an increase in the probability of recombination, as a result of which ultraviolet radiation quanta penetrating through the holes in the grid appear and produce additional ionization in the auxiliary discharge region, which leads to a decrease in the burning voltage of the auxiliary discharge. Effect of the main discharge on the auxiliary one is much stronger at low currents of the auxiliary discharge.

The injection of electrons into the cathode cavity of a hollow cathode discharge changes the intensity and radial distribution of the glow, the width of the cathode dark space, and other parameters of the plasma in the cathode cavity.

Visual observations of the discharge glow in a plasma hollow cathode show that at a pressure corresponding to the upper boundary of the region of optimal pressures, the glow, which at higher pressures has a ring shape, fills the axial region of the cathode cavity. This fact once again confirms that the manifestation of the effect of the hollow cathode consists in the interaction of the opposite sections of the cathode.

Using a photomultiplier tube, which, movable along the end of the discharge tube together with a system of collimating diaphragms, integral distributions of the glow intensity over the cathode diameter were obtained (Fig. 5). With an increase in the auxiliary discharge current, the diameter of the glowing region of negative luminescence increases, and the width of the region of the cathode dark space decreases, due to an increase in the current of electrons injected from the auxiliary discharge.

One of the features of a hollow cathode discharge is the anomalously low value of the width of the cathode dark space and its weak dependence on the gas pressure [4], [9]. The width of the region of the cathode dark space in the plasma hollow cathode was measured using the curves of the radial distribution of the glow intensity. In parallel with these measurements, the discharge glow from the cathode end were photographed. It should be noted that the results obtained using both methods of measuring the width of the region of the cathode dark space are in good agreement.

With increasing pressure, the width of the region of the cathode dark space decreases, and in the region of optimal pressures it practically does not change. The width of the region of the cathode dark space depends on the value of the cathode potential drop and on the space charge density of positive ions in the cathode dark space, and these values in a hollow cathode discharge depend on the gas pressure nonmonotonically. An increase in the auxiliary discharge current leads to a noticeable decrease in the cathode space, which is caused by a decrease in the space charge density due to the entry of electrons from the auxiliary discharge into the cathode dark space (Fig. 6). With decreasing pressure, the effect of the auxiliary discharge current on the cathode space increases, which can probably be explained by the fact that an increasing fraction of electrons, penetrating from the auxiliary discharge and accelerated in the cathode dark space, begins to leave the cathode cavity without spending all their energy on ionization of gas atoms; in addition, the ionization efficiency near the ends of the cathode decreases.
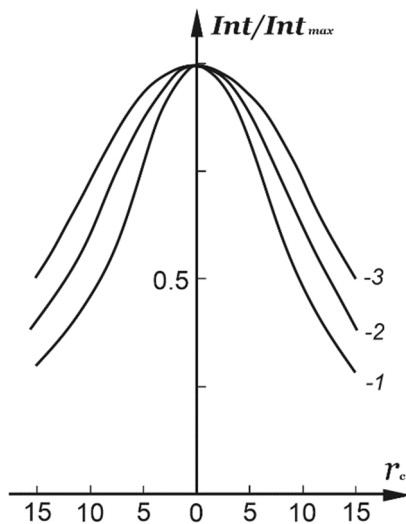
Figure 5. Normalized radial distributions of the main discharge glow intensity in helium ($P=0.2$ Torr., $I_{main}=30$ mA). $1 - I_{aux}=0$ mA, $2 - I_{aux}=10$ mA, $3 - I_{aux}=20$ mA.
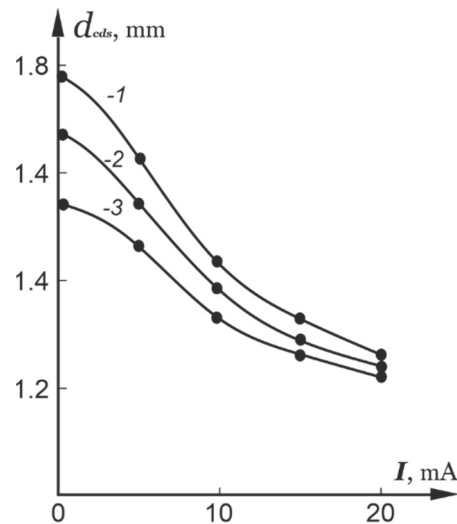
Figure 6. Dependences of the width of the region of the cathode dark space on the auxiliary discharge current in helium. $I_{main}=30$ mA, $1 - P=0.2$ Torr., $2 - P=0.3$ Torr., $3 - P=0.6$ Torr.

In parallel with the measurement of the electrical and optical characteristics of the plasma hollow cathode, the electron concentration in the cathode cavity was measured by microwave probing using wavelength of 3.1 cm. It turned out that at a constant current of the main discharge, the electron concentration in the cathode cavity is almost independent of the auxiliary discharge current. A slight increase indicates a decrease in the axial electric field in the cathode cavity.

It is of interest to estimate the magnitude of the current of electrons injected from the auxiliary discharge into the main discharge cathode cavity. For this purpose, a metal cylinder with a length equal to the cathode length was introduced coaxially into the cavity of the hollow cathode, which was used to simulate the negative glow region. The dependence of the cylinder current on the cylinder-cathode voltage was obtained for various helium pressures at a fixed auxiliary discharge current (Fig. 7). The linear logarithmic dependence of the current in the deceleration mode indicates the Maxwellian distribution of the velocities of the electrons entering the cathode cavity from the auxiliary discharge. The temperature of these electrons in the investigated range is 5-7 eV. The total current of electrons injected into the cathode cavity can be determined from the inflection point of the curves and, for example, for a pressure of 0.3 Torr, it is about 4 mA. With increasing pressure, the magnitude of this current decreases. A comparison of these results with the dependence of the main discharge current on the auxiliary current shows that the amplification of injected electrons in the cylindrical cathode cavity occurs by about an order of magnitude.
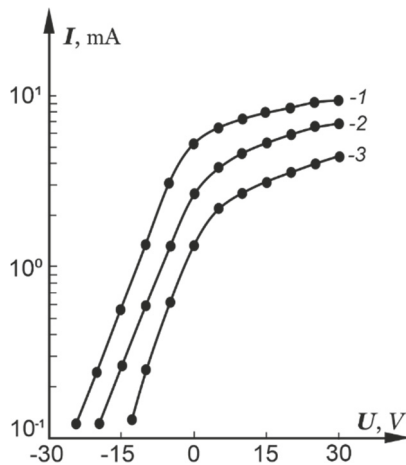
Figure 7. Dependences of the cylinder (*D=26mm*) current on the cylinder-cathode voltage in helium at $I_{aux}=10\,mA$. *1 – P=0.3* Torr., *2 – P=0.5* Torr., *3 – P=0.8* Torr.

Attempts to smoothly control the discharge current of a glow discharge using additional electrons, in particular, a grid placed in the discharge space, have been undertaken for a long time, but they were unsuccessful due to screening of the grid field after the discharge was ignited [5]. To prevent the grid from losing its control action after the discharge ignition, it is necessary to place it in the region of a unipolar space charge, as is done, for example, in electron guns with a high-voltage discharge in a cold hollow cathode [6]. In a glow discharge, the grid could continuously control the discharge current if it was placed in the region of the cathode dark space; however, the width of this region is small and changes sharply with changes in both the gas pressure and the discharge current; therefore, the operation of such devices will be unstable.

The task of controlling the discharge current when using a hollow cathode is simplified because a hollow cathode device can operate at a lower gas pressure than a flat cathode device. In this case, the width of the cathode dark space is quite large and weakly depends on the gas pressure, in the region of optimal pressures. The injection of electrons from the auxiliary discharge into the cathode cavity leads to a decrease in the cathode potential drop or, if this value is kept constant, to an increase in the current in a hollow cathode discharge.

DISCUSSIONS

In addition to controlling the main discharge current over a wide range, current amplification is also possible when electrons are injected into a hollow cathode glow discharge. After igniting the discharge, electrons from the anode region of the auxiliary discharge penetrate through the holes in the grid into the cathode cavity of a hollow cathode discharge and, having accelerated in the cathode dark space, ionize gas atoms along with electrons escaping from the cathode as a result of γ-processes [7]. Formed due to the ionization of the gas by the injected electrons additional ions knock out new electrons from the cathode, which results in amplification of current of electrons flowing into the cathode cavity.

Let us write down the boundary conditions on the inner surface of the grid cathode with the auxiliary discharge turned off:

$$j_o = j_{eo} + (1 - \alpha)j_{io}, \tag{1}$$

where j_o is the current density of the main discharge; j_{eo} and j_{io} are the densities of electron and ion currents at the cathode; α is transparency of the grid cathode. The electron and ion currents at the cathode are related by the secondary emission coefficient γ:

$$j_{eo} = \gamma j_{io}, \tag{2}$$

then one can write:

$$j_o = j_{eo}\left(1 + \frac{1-\alpha}{\gamma}\right) \tag{3}$$

When the auxiliary discharge is turned on, an additional electronic current will come out of the cathode, which we will take proportional to the current of the auxiliary discharge $\varkappa j_{aux}$, then the current of the main discharge with the auxiliary discharge turned on is:

$$j_o' = (i_{eo} + \varkappa j_{aux})\left(1 + \frac{1-\alpha}{\gamma}\right) = j_o + \varkappa j_{aux}\left(1 + \frac{1-\alpha}{\gamma}\right), \tag{4}$$

where $\varkappa$ is the factor showing what part of the auxiliary discharge current penetrates into the grid cavity.

The current gain is determined from the expression:

$$k_i = \frac{j_o}{j_{aux}} = \varkappa\left(1 + \frac{1-\alpha}{\gamma}\right). \tag{5}$$

The dependence of the current gain on the discharge mode is mainly contained in the factor $\varkappa$, the value of which is difficult to calculate, since it depends on the conditions both in the auxiliary discharge and in the main discharge cathode region. Measurement of the plasma concentration in the auxiliary discharge shows that a negative anodic potential drop should be observed in it. With an increase in the main discharge current, the field that draws electrons from the auxiliary discharge anode region increases, so the gain increases. Thus, the injection of electrons from the auxiliary discharge into

the cathode cavity makes it possible to smoothly control the current of a hollow cathode glow discharge, and it is possible to amplify the current of injected electrons. The selection of the physical conditions of the discharge (configuration and dimensions of the electrodes, the material of the cathode and the type of gas), possibly, will make it possible to optimize the parameters of the device so that it can find practical application due to the advantages inherent in gas-discharge devices with a cold cathode.

CONCLUSIONS

1.   The possibility of a significant (3-5 times) reduction in the cathode potential drop of a hollow cathode discharge due to the injection of electrons from an auxiliary discharge into the cathode cavity is shown.

2.   As a result of injection of electrons from the auxiliary discharge, the increase in the main discharge current is 5-10 times higher than one for the auxiliary discharge current.

3.   The injection of electrons into the cathode cavity at a fixed current of the main discharge leads to an increase in the plasma concentration in the cathode cavity and a decrease in the width of the cathode dark space.

4.   The injection of electrons from the auxiliary discharge into the cathode cavity makes it possible to smoothly control the current of the hollow cathode glow discharge.

ORCID IDs
Stanislav V. Pogorelov, https://orcid.org/0000-0002-0189-8655; **Volodymyr A. Timaniuk,** https://orcid.org/0000-0003-0689-6074
Nikolay G. Kokodii, https://orcid.org/0000-0003-1325-4563; **Ihor V. Krasovskyi,** https://orcid.org/0000-0003-4585-7377

REFERENCES
[1]   N.V. Gavrilov, and A.S. Kamenetskikh, ZhTF, **77**(3), 12-16 (2007), https://journals.ioffe.ru/articles/viewPDF/9070. (in Russian)
[2]   A. S. Klimov, and S.A. Ostanin, Proceedings of TUSUR University, **20**(4), 26-29 (2017), https://doi.org/10.21293/1818-0442-2017-20-4-26-29. (in Russian)
[3]   N.V. Gavrilov, D.R. Emlin, and A.S. Kamenetskikh, Tech. Phys. 53, 1308–1313 (2008), https://doi.org/10.1134/S1063784208100083.
[4]   V.V. Denisov, Y.K. Akhmadeev, N.N. Koval, I.V. Lopatin, and E.V. Ostroverkhov, Russ. Phys. J. **62**, 563-568 (2019), https://doi.org/10.1007/s11182-019-01747-3.
[5]   B.I. Moskalev, *Разряд с полым катодом [Hollow cathode discharge]*, (Energiya, Moscow, 1969), pp. 184. (in Russian)
[6]   A.S. Metel, S.N. Grigoriev, Yu.A. Melnik, and V.P. Bolbukov, Instruments and Experimental Techniques, **55**, 122–130 (2012), https://doi.org/10.1134/S0020441211060170.
[7]   V.A. Timanyuk, N.G. Kokodiy, and F.G. Diaghileva, Papers SWORLD Transport, Engineering, Physics and Mathematics, **2**(46), 95-100 (2017), https://www.sworld.com.ua/ntsw/117-2.pdf. (in Russian)
[8]   C. Yuan, A.A. Kudryavtsev, A.I. Saifutdinov, S.S. Sysoev, R. Tian, J. Yao, and Zh. Zhou. IEEE Transactions on Plasma Science, **45**, 3110-3113 (2017), https://doi.org/10.1109/TPS.2017.2758170
[9]   V.A. Lisovskiy, D.I. Khilko, R.O. Osmayev, and V.D. Yegorenkov. Eur. J. Phys. **40**, 045203 (2019), https://doi.org/10.1088/1361-6404/ab1a59.

ВПЛИВ ІНЖЕКЦІЇ ЕЛЕКТРОНІВ НА ХАРАКТЕРИСТИКИ ТЛІЮЧОГО РОЗРЯДУ ПОРОЖНИСТОГО КАТОДУ
[a]Погорелов С.В., [a]Тиманюк В.О., [a,b]Кокодій М.Г., [a]Красовський І.В.
[a]Національний фармацевтичний університет, Харків, Україна
[b]Харківський національний університет імені В.Н. Каразіна, Харків, Україна

У статті представлені результати експериментальних досліджень тліючого розряду з порожнистим катодом в атмосфері гелію та аргону з використанням допоміжного розряду в якості електронного еміттера. Автори запропонували зробити електрод у вигляді циліндричної металевої сітки загальним для обох розрядів. Переваги цієї конструкції пояснюються наступним чином. Зв'язок між розрядами здійснюється через отвори в сітці з геометричною прозорістю 0,2, що дає можливість не тільки плавно контролювати струм основного тліючого розряду, але і підсилювати струм цього розряду. Відомо, що одним з найефективніших електронних еміттерів є плазма; однак її використання в якості катода в приладах з тліючим розрядом при низькому тиску газу ускладнюється тим, що для відокремлення потоку електронів від плазми необхідна сітка з невеликими отворами, і недоцільно використовувати таку систему через малу механічну міцність сітки. Оскільки порожнистий катод ефективно працює при низькому тиску газу, виділення потоку електронів з плазми деякого допоміжного розряду можливо при значно більших отворах в сітці, що розділяє плазму і катодну порожнину. У цьому випадку сітку можна виготовити такою, щоб вона витримувала досить високі теплові навантаження і змогла працювати в типових режимах розряду з порожнистим катодом. Інжекція електронів у катодну порожнину тліючого розряду змінює радіальний розподіл інтенсивності світіння, ширину темного катодного простору та інші параметри плазми в катодній порожнині. Вплив електронів, що проникають із допоміжного розряду в катодну порожнину основного розряду, стає значним, коли струм цих електронів стає порівнянним або перевищує струм електронів, що вийшли з поверхні катода у вигляді сітки в результаті γ-процесів. Паралельно із вимірюванням оптичних та електричних характеристик плазми тліючого розряду з порожнистим катодом проводились вимірювання концентрації електронів методом мікрохвильового зондування. Весь струм допоміжного розряду проникає в порожнину основного розряду; однак, після прискорення в темному катодному просторі, електрони, що проникають із допоміжного розряду, іонізують атоми газу і помітно збільшують струм основного розряду. Додаткові іони, що утворюються внаслідок іонізації газу інжектованими електронами, вибивають нові електрони з поверхні катода, що дає можливість збільшити струм розряду.

КЛЮЧОВІ СЛОВА: тліючий розряд, плазма, порожнистий катод, електрони, інжекція.

PROPAGATION ANALYSIS OF PU RADIONUCLIDES AS A RESULT OF FIRE INCIDENTS IN THE EXCLUSION ZONE OF THE CHERNOBYL NPP IN APRIL 2020

Maryna F. Kozhevnikova*, Volodymyr V. Levenets
NSC "Kharkiv Institute of Physics & Technology" NASU
1, Academichna str., 61108, Kharkiv, Ukraine
Corresponding Author: marko@kipt.kharkov.ua
Received March 7, 2021; revised April 7, 2021; accepted April 15, 2021

In consequence of nuclear accidents that have occurred in various parts of the world, radioactive contamination of the environment is observed. The risks of spreading pollution can increase during floods, fires and some natural disasters. The lack of effective measures that aimed at eliminating possible sources of fire in the meadow zone and forest lands in the Chernobyl exclusion zone (ChEZ) leads to a high risk of fire emergence. The temporal and spatial distribution of fires shows that they occur throughout the ChEZ, including in the most contaminated areas. The risk of fires increases with climate change and measures to prevent them should be considered in emergency programs. ChEZ area is contaminated with long-lived radionuclides such as ^{137}Cs, ^{90}Sr, Pu isotopes (^{238}Pu, $^{239+240}Pu$, ^{241}Pu) and ^{241}Am. As a result of forest fires radionuclides contained in wood and underlying surface are carried out into the atmosphere along with smoke. Diseases arising under the influence of ionizing radiation from Pu and ^{241}Am isotopes pose a serious problem for human health. To assess of the spatial distribution of Pu isotopes and ^{241}Am we used data on forest fires that occurred in the Chernobyl zone in April 2020. To evaluate the dynamics of the release of radioactive substances into the atmosphere during fire incidents on the ChEZ territory, the following software products were used: NASA WorldView, HYSPLIT program. The HYSPLIT program allows to reconstruct the trajectories of radionuclide propagation in the atmosphere using meteorological data and to obtain a reliable picture of the distribution of radionuclides in the study area. The maps of the volumetric activity of Pu isotopes in the air and the fallout on the soil as a result of fires were obtained. It was found that the radioactivity due to the presence of this element in the air and during the fallout of radioactive particles on the soil is low (it reaches 1.0E-7...0.1 Bq/m^3 in the air, 1.0E-6...1 Bq/m^2 on the soil). The analysis of the propagation of Pu isotopes as a result of the movement of air masses in the places of fires in the exclusion zone of the Chernobyl nuclear power plant and the associated dangers for the population and the environment has been carried out.

KEYWORDS: Chernobyl NPP, Pu isotopes and ^{241}Am, release of radioactive substances, fire zone, distribution of radionuclides.

The spring floods of the Pripyat River and forest fires are two of the most important factors contributing to the migration of radionuclides from the ChEZ. The lack of effective measures aimed at eliminating possible sources of fire during the time after the Chernobyl accident has led to a high risk of the occurrence and spread of fires in the ChEZ zone, which includes 260,000 hectares of forests and meadows. This area is heavily contaminated with long-lived radionuclides such as ^{137}Cs, ^{90}Sr, Pu (^{238}Pu, $^{239+240}Pu$, ^{241}Pu) and ^{241}Am [1].

Since nuclear radiation slows down the rate of decomposition of inert organic materials, the amount of dead wood, ground layers of dried leaves and twigs in forest lands increases and the risk of fire increases. Forest fires that took place in the ChEZ, for example, in 1992, covered an area of 17,000 hectares, and revealed the presence of sources of ignition throughout the entire area, including in the areas most contaminated with radionuclides [2].

Fire prevention and suppression activities pose a serious health hazard to firefighters, who can reach the annual individual dose limit in a relatively small number of days.

Now the main threat to the population and the environment in the ChEZ is caused by fires in places where plants grow that have accumulated radionuclides as a result of the migration of radioactive particles from the soil cover. The degree of public exposure associated with the burning of radioactive wood and grass depends on the distribution of contamination in the combustion material, the amount of contaminated combustible material and the type of fire.

The accumulation of each radioactive element is special for different plant species. Currently from 70 to 85% of radionuclides are concentrated in the upper soil layers of forests and meadows, as well as in the layer of organic residues on the soil surface in forests and mosses, and from 15 to 30 % are deposited on trees (bark, needles, wood and branches) or grass. The mass of dead wood in the ChEZ, contaminated with radioactivity, is estimated at $1.4 \cdot 10^6$ m^3, which may lead to further growth of forest fires. According to forecasts [2], the amount of contaminated dead wood in the ChEZ will be $2.4 \cdot 10^6$ m^3 in 2020.

Forests most at risk of fire are concentrated in the central and northern parts of the ChEZ and include the most contaminated areas in the west and northeast of the ChNPP.

The temporal and spatial distribution of fires shows that they occur throughout the ChEZ, including in the most contaminated areas, within a radius of 10 km from the Chernobyl nuclear power plant, where there is the highest activity level for the isotopes ^{137}Cs, ^{90}Sr, Pu and ^{241}Am. It is also obvious that in the north and north-east of this zone, fires regularly cross the border between Ukraine and Belarus. Fires become more frequent in the spring. The highest risk of fires is observed in July and August.

As a result of forest fires in ChEZ, radionuclides contained in wood and underlying surface are carried out into the atmosphere along with smoke. The transport of ^{90}Sr, ^{137}Cs and Pu isotopes during fires occurs in the form of smoke

particles and mineral dust. Dust particles, from 2 to 100 microns in diameter, are deposited again near the source. Small particles of two types, ranging in size from 0.04 to 0.07 microns and from 0.1 to 0.3 microns, are carried over considerable distances and may have a negative effect on humans if inhaled.

The data of the automatic radiation monitoring system under the control of the State Ecological Center show a pronounced increase in the volumetric activity of radionuclides in the air of the ChEZ during large fires. Individual radionuclides can migrate more than 100 km from the fire zone, thereby exposing the population to a dose of radiation above the permissible limit.

The aim of this work is to assess the risks of the spread of Pu and ^{241}Am radionuclides in the ChEZ and beyond, as a result of fires in places where plants grow and accumulate dead wood with a high level of radioactive contamination by these isotopes. It is supposed to assess the risk of radioactive impact on the population and the environment associated with this process and to determine possible ways to reduce the negative consequences.

SUBJECT OF STUDY AND INPUT DATA

The explosion of the Chernobyl nuclear power plant reactor in 1986 caused the release of about 12,000 PBq of radioactive material into the atmosphere. At present, the radioactive contamination of the soil is determined by the presence of isotopes ^{137}Cs, ^{90}Sr, ^{238,239,240,241}Pu, ^{241}Am. The bulk of these radionuclides during the release was part of the particles of irradiated nuclear fuel (the fuel component of the Chernobyl radioactive fallout) [3].

In this regard, the maps of the density of contamination with these radionuclides for the territory of the near zone of the Chernobyl NPP are similar (Fig.1 and Fig.2).
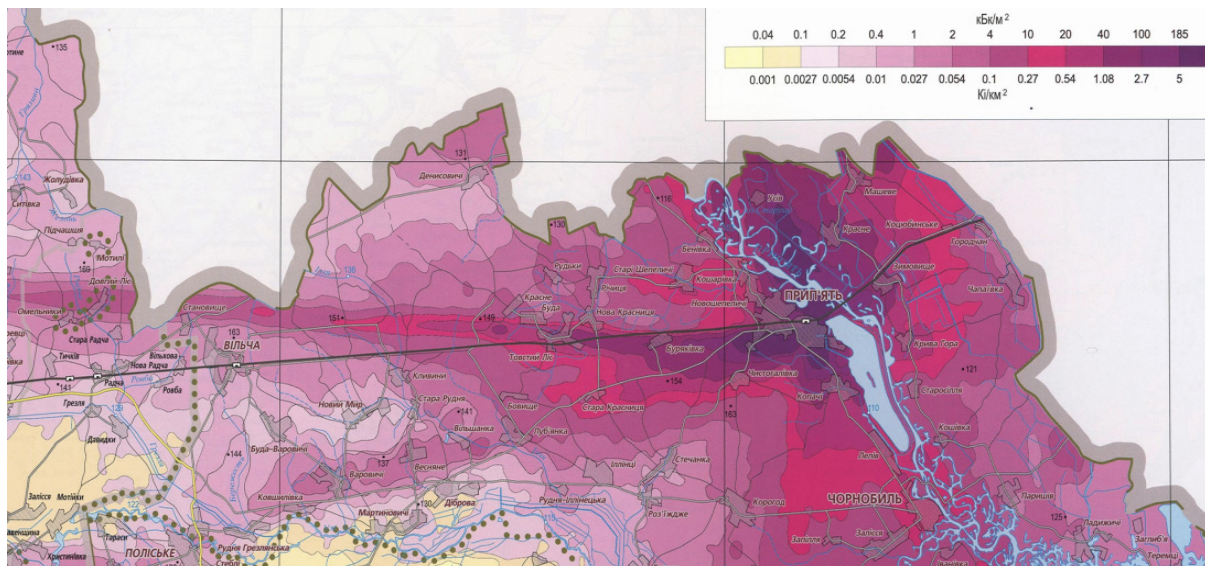
Figure 1. Total contamination of the ChEZ surface with Pu isotopes [4]
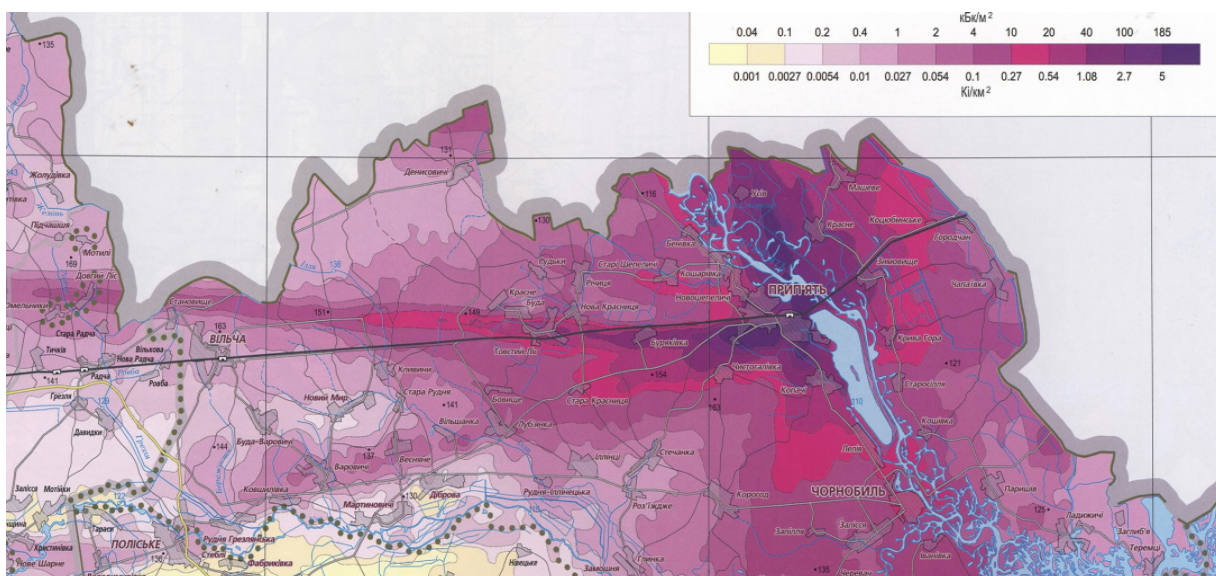
Figure 2. Total surface contamination ChZO ^{241}Am [4]

The zone within a radius of 10 km directly around the Chernobyl nuclear power plant is heavily contaminated with Pu and [241]Am isotopes. Figures 1 and 2 show the total contamination of the ChEZ surface with Pu and [241]Am isotopes, respectively [4].

The decay of β-emitting [241]Pu ($T_{1/2}$=14.4 years) gives rise to long-lived α-radionuclides [241]Am ($T_{1/2}$= $4.32 \cdot 10^2$ years) and [237]Np ($T_{1/2}$= $2.14 \cdot 10^6$ years), which have a high radio toxicity. Calculations have shown that by now about 90% of the [241]Pu isotope has already decayed and turned into [241]Am. Unlike [241]Pu, [241]Am compounds have a higher solubility and, therefore, a higher migration capacity [5].

Diseases arising under the influence of ionizing radiation from Pu and [241]Am isotopes pose a serious problem for human health.

Possible routes of Pu and [241]Am entering the human body: as a result of inhalation, during food intake, through the skin. Lifetime carcinogenic risk factors were calculated for almost all radionuclides, including isotopes of Pu and [241]Am (Table 1). Food intake is usually the most common type of exposure. However, the risk coefficient for this route of intake is much lower than for inhalation [6].

To assess the spatial distribution of Pu isotopes and [241]Am, we used data on forest fires that occurred in the Chernobyl zone in April 2020 [7]. In this work, the electronic Atlas of Ukraine was used to assess the density of radioactive contamination in the areas of combustion. Radioactive contamination with recalculation of activity of Pu isotopes in soil for 2020 [4].

Table 1. Radiological risk factors

Isotope	Lifetime carcinogenic risk	
	Inhalation (pCi^{-1})	Ingestion (pCi^{-1})
[241]Am	2.4×10^{-8}	9.5×10^{-11}
[241]Pu	2.8×10^{-10}	1.9×10^{-12}
[238]Pu	3.0×10^{-8}	1.3×10^{-10}
[239]Pu	2.9×10^{-8}	1.3×10^{-10}
[240]Pu	2.9×10^{-8}	1.3×10^{-10}

The areas of fire burnout were taken into account for two main categories of landscapes: forest and meadows. The forest category included all areas covered with woody vegetation (coniferous and deciduous), and the category of meadows also included drained areas covered with reeds, which, as a rule, became the primary source of fire development. The areas of water bodies, roads and other man-made unnatural objects were not taken into account for calculating the areas of fire.

SPATIAL ANALYSIS METHODS

To assess the dynamics of the release of radioactive substances into the atmosphere during fire incidents on the ChEZ territory, the following software products were used: NASA WorldView, HYSPLIT program [8], data on radioactive contamination of territories [4,9]. To identify fire incidents and estimate their parameters in the Worldview tool the MODIS Fire and Thermal Anomalies product was used, which operates with data from the Terra (MOD14) and Aqua (MYD14) satellites, as well as the combined Terra and Aqua satellite product (MCD14).

The HYSPLIT program allows to reconstruct the trajectories of radionuclide propagation in the atmosphere using meteorological data and to obtain a reliable picture of the distribution of radionuclides in the study area. The basic model simulation input parameters are: starting time (year, month, day, hour); location (starting locations, as latitude, longitude, and height); start time and duration of the dispersion (i.e., run-time); pollutant characteristics (number of pollutant species, emission rates, emission duration).

The input meteorological data necessary for HYSPLIT-4 were taken from the meteorological model calculations based on in-situ measurement results.

RESULTS OF THE RESEARCH

Forest fires broke out in an area heavily contaminated in 1986 during the Chernobyl accident. These fires reached the ChEZ and the area around the NPP on April 8, 2020 (Fig. 3). According to some estimates, the area of fire reached 20,000 hectares [10].

The total area of fires on the territory of the ChEZ around the Chernobyl NPP and in the adjacent territories of the Polessky district of the Kiev region, as well as in the Ovruch district of the Zhytomyr region for the period from 2 to 20 April was determined at 870 km^2. Of these, about 445 km^2 are combustion zones in a fire in the Ovruch district of the Zhytomyr region; 340 km^2 is the area of the territories burned out during the period of the fire in the Polessky district (the main part on the territory of the ChEZ). In the exclusion zone around the Chernobyl nuclear power plant, about 65 km^2 burned out, as well as about 20 km^2 on the left bank of the Pripyat river [7].

The total takeaway of Pu isotopes in the smoke fraction, which could be transferred to a long distance outside the burnout zones during fires, is 59 MBq (of which from fires in the Polessky district of ChEZ and adjacent territories about 25 MBq and from fires in the area of Chistogalovka village and cooling pond of the ChNPP (CP ChNPP) in ChZO about 19 MBq) [7].

Figure 3 shows a summary map of the fires detected from the satellite in the period from 2 to 20 April, 2020. On April 8, the fire incidents began in several points of the Ovruch district of the Zhytomyr region. They are not related to the primary source of fires in the exclusion zone, but the north-western wind caused dispersion of the combustion products contaminated with ^{137}Cs in the direction of Kiev, therefore the radiological situation in Kiev for April 8 was formed under the influence of sources of fire formation mainly outside the ChEZ.

In the period from April 8 to April 10 in Kiev the highest levels of ^{137}Cs activity in aerosols were observed for the period of fire formation (according to the UkrGMI and CGO (Central Geophysical Observatory)). The data in the range from 0.2 to 0.6 mBq/m^3. Background volumetric activities were observed in almost 100 times lower [7]. During the period of fire formation, according to observations in Kiev, the averaged volumetric activity of ^{137}Cs in the air did not exceed 1 mBq /m^3.

On April 8 hotbeds of fire also developed directly in the exclusion zone (Fig. 4).
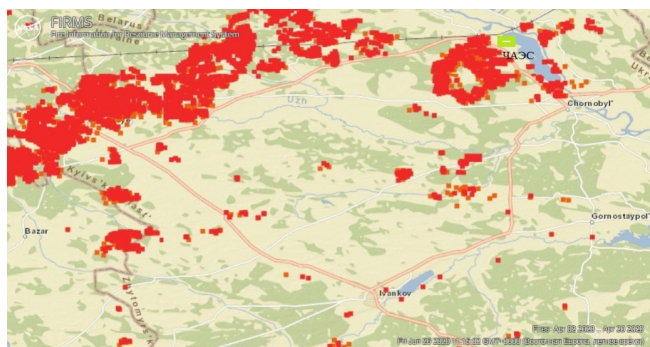
Figure 3. A summary map of the fires detected from the satellite in the period from 2 to 20 April 2020. The fire zone is highlighted in red
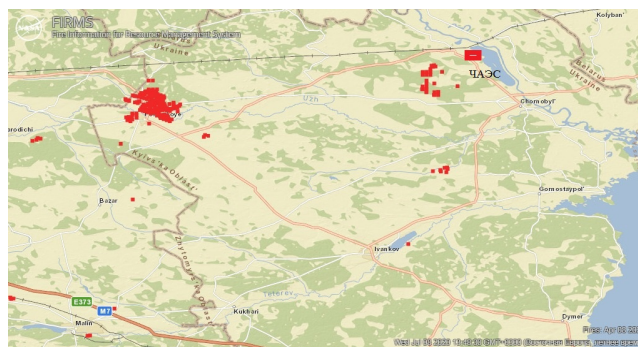
Figure 4. Map of fire sites on April 8, 2020. The fire zone is highlighted in red

To study the spatial distribution of Pu isotopes, the period from 8 to 13 April 2020 was chosen. At this time, the largest removal of radionuclides from the ChEZ territory was observed. For calculations, a source height of 20 m was chosen, and the removal duration was 24 hours.

Figure 5 shows the dynamics of the activity removal of radionuclides in radioactive aerosols from a fire during this period in the area of Kopachi village - Chistogalovka village - CP ChNPP [7]. The largest removal of Pu isotopes from fires occurred on April 9 and April 13, 2020.
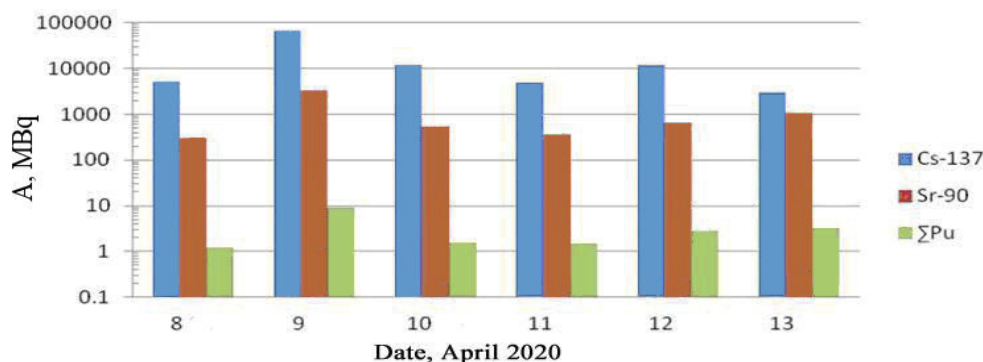
Figure 5. Dynamics of the activity removal of radionuclides in radioactive aerosols from a fire in period from April 8 to April 13, 2020 in the area Kopachi village - Chistogalovka village - CP ChNPP

To analyze the propagation of Pu isotopes as a result of fires on the territory of the ChEZ the maps of the volumetric activity of radionuclides in the air and during fallout on the soil in the period from April 8 to April 13, 2020 were constructed.

Figure 6 shows a map of the volumetric activity of Pu radionuclides in the air on April 9, 2020 from a fire in the area of Kopachi village – Chistogalovka village. The wind changes direction from the northwest, which led to the transfer of combustion products towards Kiev - to the west. Accordingly, the main centers of fires expanded eastward, and the zones of ignition in the near 10 km zone around the Chernobyl NPP also expanded. In particular, a fire in the area of the source of the initial ignition (in the Polessky district) begins to spread eastward (the area of combustion was about 21 km^2) [7].
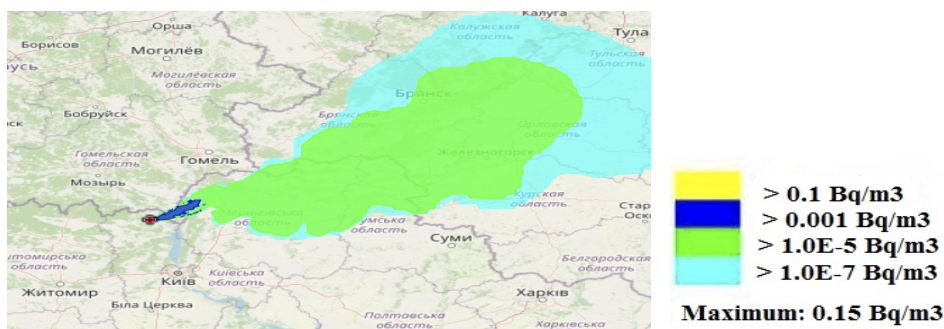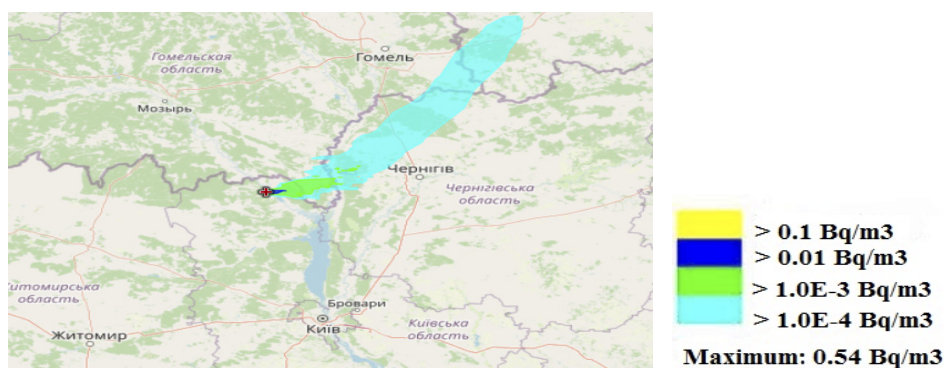
Figure 6. The volumetric activity of Pu isotopes in the air on April 9, 2020
from a fire in the area with Kopachi village - Chistogalovka village (for 24 hours), the source height is 20 m

Figure 7 shows a map of the surface activity of Pu isotopes during the fallout on the soil on April 9, 2020.
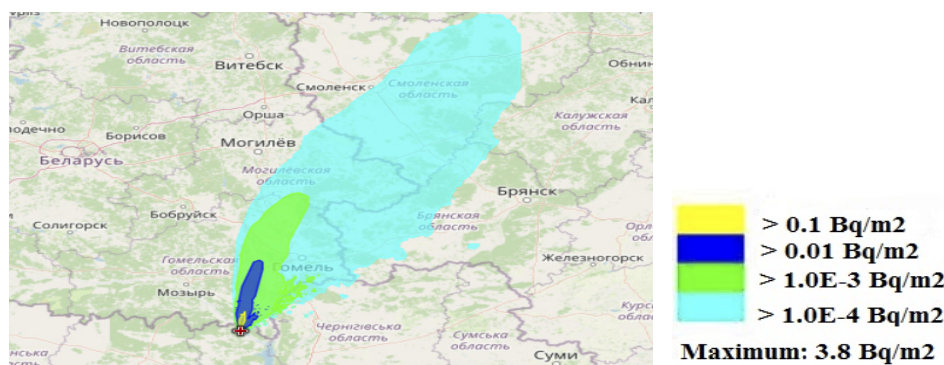

Figure 7. The surface activity of Pu isotopes during deposition on the soil on April 9, 2020 from a fire in the area with Kopachi village - Chistogalovka village (for 24 hours), the source height is 20 m

Figure 8 shows a map of the volumetric activity of Pu isotopes in the air on April 13, 2020 from a fire in the area with Kopachi village - Chistogalovka village.

Figure 8. The volumetric activity of Pu isotopes in the air on April 13, 2020
from a fire in the area with Kopachi village - Chistogalovka village (for 24 hours), the source height is 20 m

The combustion centers in the Polessky district spread in the northeastern direction and crossed the zone of the location of the so-called fuel trace of radioactive fallouts of 1986 year. The area of combustion was about 18 km^2. The combustion on the territory of the Red Forest covered 3.5 km^2. The wind had a northeasterly direction, so the territory of Ukraine, Belarus and Russia was subjected to Pu pollution. Figure 9 shows a map of the surface activity of Pu isotopes during the fallout on the soil on April 13, 2020.

On the fuel traces of the Chernobyl radioactive fallout due to the radioactive decay of ^{241}Pu, the accumulation and increase in the activity of ^{241}Am occurs over time. The maximum activity of ^{241}Am will be reached approximately 70 years after the Chernobyl accident, by 2056, while the activity of ^{241}Am will be no more than 20% higher than the level as of 2017-2018 (Table 2). During the increase in the activity of ^{241}Am (about 50 years), the activity of long-lived ^{239}Pu ($T_{1/2} = 24100$ years) and ^{240}Pu ($T_{1/2} = 6563$ years) will practically not change, while the activity of ^{238}Pu ($T_{1/2} = 87.74$ years) due to its radioactive decay, it will decrease by 40%. As a result, the total activity of α-emitting radionuclides will slightly increase over the next 50 years, and then monotonously decrease.

At the same time, the maximum of the total activity of α-emitting radionuclides will exceed the level as of 2017-18 by only 6%. With equal dose coefficients per unit of inhalation intake activity for alpha emitting radioisotopes

Pu and ^{241}Am (Table 2), such a slight change in their activity over the next 50 years will not have a significant effect on the value of conservative estimates of inhalation doses for personnel and for the population [11].

Figure 9. The surface activity of Pu isotopes during the fallout on the soil on April 13, 2020
from a fire in the area with Kopachi village - Chistogalovka village (for 24 hours), the source height is 20 m

Since an increase in the activity of ^{241}Am by 20% in the next 50 years (Table 2) will not have a significant effect on the change in the formation of inhalation doses of internal and external irradiation of personnel and the environment in the ChEZ, no significant changes in approaches to control the spread of ^{241}Am are required. However, since there is evidence of a significantly higher assimilability of ^{241}Am by meadow vegetation compared to $^{239, 240}$Pu [12], over time the problem of the spread of this nuclide along with combustion products or through the food chain can create additional risks for the environment and humans. Therefore, permanent tracking of ^{241}Am migration is an important link in the creation of a comprehensive system for monitoring radiation contamination of territories and predicting negative consequences for the population.

Table 2. [10] Dynamics of changes in the specific activity of α-emitting radionuclides in the fuel component of Chernobyl radioactive fallout, Bq/g

Radionuclides	Year								
	2017	2021	2026	2031	2036	2046	2056	2076	2186
^{238}Pu	6.3E+6	6.1E+6	5.8E+6	5.6E+6	5.4E+6	5.0E+6	4.6E+6	3.9E+6	3.6E+6
^{239}Pu	5.1E+6	5.1E+6	5.1E+6	5.1E+6	5.1E+6	5.1E+6	5.1E+6	5.1E+6	5.1E+6
^{240}Pu	7.8E+6	7.8E+6	7.8E+6	7.8E+6	7.8E+6	7.8E+6	7.7E+6	7.7E+6	7.7E+6
^{241}Am	2.5E+7	2.6E+7	2.8E+7	2.8E+7	2.9E+7	3.0E+7	3.0E+7	3.0E+7	2.9E+7
Σ	4.4E+7	4.5E+7	4.6E+7	4.7E+7	4.7E+7	4.7E+7	4.7E+7	4.6E+7	4.6E+7

The long-lived Pu radionuclides fell out in the composition of fuel particles with a high specific mass. Therefore, they did not spread over long distances, and the density of soil surface contamination, according to preliminary data, exceeded the limits established for them practically only within the boundaries of the 30-km exclusion zone. Pu is characterized by a very low ability to penetrate biological membranes. Therefore, the coefficients of its accumulation by plants from the soil and entering the human body are several orders of magnitude lower than for Sr and Cs [1]. Pu isotopes are present in forest organic matter in insignificant amounts and remain fixed in the mineral fraction of soil contaminated in 1986. Thus, its re-transport during fires in the ChEZ is low.

CONCLUSIONS

The maps of the volumetric activity of Pu isotopes in the air and the fallout on the soil as a result of fires in April 2020 were obtained. As a result of the distribution analysis of Pu radionuclides in the territory under consideration, it was found that the radioactivity due to the presence of this element in the air and during the fallout of radioactive particles on the soil is low (it reaches 1.0E-7...0.1 Bq/m^3 in the air, 1.0E-6...1 Bq/m^2 on the soil). Despite the high radiotoxicity of Pu isotopes, the contribution from the resulting radioactivity to the radiation exposure of the population through inhalation or consumption of food will be insignificant.

The risk of fires in the ChEZ increases with climate change and measures to prevent them should be considered in emergency programs.

This information will provide important insight into the dynamics of accumulation, transformation, and migration of Pu and ^{241}Am isotopes. And also to study the impact of ionizing radiation from fires in the ChEZ on the environment.

ORCID IDs

Maryna F. Kozhevnikova, https://orcid.org/0000-0003-2464-3847
Volodymyr V. Levenets, https://orcid.org/0000-0002-6439-0576

REFERENCES

[1] B.S. Prister, A.A. Klyuchnikov, V.G. Baryakhtar, V.M. Shestopalov, and V.P. Kukhar, *Проблемы безопасности атомной энергетики. Уроки Чернобыля* [*Nuclear power safety problems. Lessons from Chernobyl*], (NAS of Ukraine, Institute of NPP safety problems, Kyiv, 2016), pp. 356. (in Russian)

[2] S.V. Zibtsev, J.G. Goldammer, S. Robinson, and O.A. Borsuk, Unasylva, **243/244**(66), 40-51 (2015), http://www.fao.org/3/I4447E/i4447e.pdf.

[3] V. Kashparov, S. Levchuk, M. Zhurba, V. Protsak, Yu. Khomutinin, N.A. Beresford, and J.S. Chaplow, ESSD, **10**, 339-353 (2018), https://doi.org/10.5194/essd-10-339-2018.

[4] L.Ya. Tabachny, and etc, *Атлас Україна. Радіоактивне забруднення* [*Atlas Ukraine. Radioactive interference*], (TOV "Intellectual Systems GEO", 2008), pp. 52. (in Ukrainian)

[5] M.F. Kozhevnikova, V.V. Levenets, I.L. Rolik, and A.A. Shchur, PAST, **3**(109), 26-30 (2017), https://vant.kipt.kharkov.ua/ARTICLE/VANT_2017_3/article_2017_3_26.pdf. (in Russian)

[6] J. Peterson, M. MacDonell, L. Haroun, and F. Monette, *Radiological and Chemical Fact Sheets to Support Health Risk Analyzes for Contaminated Areas*, (Argonne National Laboratory Environmental Science Division, 2007), pp. 133, https://www.philrutherford.com/Radiation_Links/ANL_ContaminantFactSheets_All_070418.pdf.

[7] V. Protsak, O. Voitsekhovych, and G. Laptev. *Estimation of radioactive source term dynamics for atmospheric transport during wildfires in Chernobyl zone in spring 2020.* (Ukrainian Hydrometeorological Institute, Kiev, 2020). https://uhmi.org.ua/msg /fire2020/analytical.pdf. (in Ukrainian)

[8] R.R. Draxler, and G.D. Hess, *Description of the HYSPLIT-4 Modeling System.* Silver Spring: Air resources Laboratory, NOAA Technical Memorandum ERL ARL-224. pp. 22. (1997), https://www.arl.noaa.gov/documents/reports/arl-224.pdf

[9] M. De Cort, Y.S. Tsaturov, Directorate-General for Research and Innovation (European Commission), European Commission, *Atlas of cesium deposition on Europe after the Chernobyl accident,* (Office for Official Publications of the European Communities, Luxembourg, 1998), pp. 63, https://op.europa.eu/s/oXu8

[10] Information note n°5, (IRSN, 2019), pp. 11, https://www.irsn.fr/EN/newsroom/News/Documents/IRSN_Information-Report_Fires-in-Ukraine-in-the-Exclusion-Zone-around-chernobyl-NPP_05052020.pdf

[11] Assessment of the distribution of radionuclides and the impact of industrial facilities in the Chernobyl exclusion zone (Final Report). INRIR, 2018, 217 p. http://chornobyl-gef.com/wp-content/uploads/2018/05/Assesment-of-Distr.-Radioact.pdf

[12] O.A. Shurankova, and V.P. Kudryashov, Problems of health and ecology, **1**(7), 67-71 (2006), https://elib.gsmu.by/handle/GomSMU/1075. (in Russian)

АНАЛІЗ ПОШИРЕННЯ РАДІОНУКЛІДІВ PU В РЕЗУЛЬТАТІ ПОЖЕЖ У КВІТНІ 2020 р В ЗОНІ ВІДЧУЖЕННЯ ЧОРНОБИЛЬСЬКОЇ АЕС

М.Ф. Кожевнікова, В.В. Левенець

Національний науковий центр «Харківський фізико-технічний інститут», НАНУ
вул. Академічна, 1, 61108, Харків, Україна

Внаслідок ядерних аварій, що сталися в різних частинах світу, спостерігається радіоактивне забруднення навколишнього середовища. Ризики поширення забруднення можуть зростати під час повені, пожеж та деяких стихійних лих. Відсутність ефективних заходів, спрямованих на ліквідацію можливих джерел пожежі в луговій зоні та лісових угіддях у зоні відчуження Чорнобиля (ЧЗВ), призводить до високого ризику виникнення пожежі. Часовий та просторовий розподіл пожеж свідчить про те, що вони трапляються на всій території ЧЗВ, у тому числі в найбільш забруднених районах. Ризик пожеж зростає зі зміною клімату, і заходи щодо їх запобігання слід враховувати в надзвичайних програмах. Територія ЧЗВ забруднена довгоживучими радіонуклідами, такими як ^{137}Cs, ^{90}Sr, ізотопи Pu (^{238}Pu, $^{239 + 240}Pu$, ^{241}Pu) та ^{241}Am. В результаті лісових пожеж радіонукліди, що містяться в деревині та підстильній поверхні, потрапляють в атмосферу разом з димом. Хвороби, що виникають під впливом іонізуючого випромінювання ізотопів Pu та ^{241}Am, становлять серйозну проблему для здоров'я людини. Для оцінки просторового розподілу ізотопів Pu та ^{241}Am було використано дані про лісові пожежі, які сталися в Чорнобильській зоні в квітні 2020 р. Для оцінки динаміки викидів радіоактивних речовин в атмосферу під час пожеж на території ЧЗВ, використовувались програмні продукти: NASA WorldView, програма HYSPLIT. Програма HYSPLIT дозволяє за допомогою метеорологічних даних реконструювати траєкторії поширення радіонуклідів в атмосфері та отримати достовірну картину розподілу радіонуклідів на досліджуваній території. Отримано карти об'ємної активності ізотопів Pu в повітрі та випадінь на ґрунті в результаті пожеж. Встановлено, що обумовлена присутністю цього елемента радіоактивність в повітрі та при випаданні радіоактивних частинок на ґрунт невисока (досягає в повітрі 1.0E-7...0.1 Бк/м³, на ґрунті 1.0E-6...1 Бк/м²). Проведено аналіз поширення ізотопів Pu в результаті переміщення повітряних мас у місцях пожеж в зоні відчуження Чорнобильської АЕС та пов'язаних з цим небезпек для населення та навколишнього середовища.

КЛЮЧОВІ СЛОВА: Чорнобильська АЕС, ізотопи Pu та ^{241}Am, викид радіоактивних речовин, зона пожежі, розподіл радіонуклідів.

MOLECULAR DYNAMICS STUDY OF INSULIN MUTANTS

Olga Zhytniakivska*, Uliana Tarabara, Valeriya Trusova,
Kateryna Vus, Galyna Gorbenko

Department of Medical Physics and Biomedical Nanotechnologies, V.N. Karazin Kharkiv National University
4 Svobody Sq., Kharkiv, 61022, Ukraine
Corresponding Author: olya_zhitniakivska@yahoo.com
Received April 1, 2021; revised April 22, 2021; accepted April 23, 2021

Human insulin, a small protein hormone consisting of A-chain (21 residues) and B-chain (30 residues) linked by three disulfide bonds, is crucial for controlling the hyperglycemia in type I diabetes. In the present work molecular dynamics simulation (MD) with human insulin and its mutants was used to assess the influence of 10 point mutations (His^{A8}, Val^{A10}, Asp^{B10}, Gln^{B17}, Ala^{B17}, Gln^{B18}, Asp^{B25}, Thr^{B26}, Glu^{B27}, Asp^{B28}), 6 double mutations (Glu^{A13}+Glu^{B10}, Ser^{A13}+Glu^{B27}, Glu^{B1}+Glu^{B27}, Ser^{B2}+Asp^{B10}, Asp^{B9}+Glu^{B27}, Glu^{B16}+Glu^{B27}) and one triple mutation (Glu^{A15}+Asp^{A18}+Asp^{B3}) in the protein sequence on the structure and dynamics of human insulin. A series of thermal unfolding MD simulations with wild type (WT) human insulin and its mutants was performed at 400 K with GROMACS software (version 5.1) using the CHARMM36m force field. The MD results have been analyzed in terms of the parameters characterizing both the global and local protein structure, such as the backbone root mean-square deviation, gyration radius, solvent accessible surface area, the root mean-square fluctuations and the secondary structure content. The MD simulation data showed that depending on time evolution of integral characteristics, the examined mutants can be tentatively divided into three groups: 1) the mutants His^{A8}, Val^{A10}, Ala^{B17}, Asp^{B25}, Thr^{B26}, Glu^{B27}, Glu^{A13}+Glu^{B10}, Glu^{B1}+Glu^{B27} and Glu^{B16}+Glu^{B27}, which exert stabilizing effect on the protein structure in comparison with wild type insulin; 2) the mutants Gln^{B17}, Asp^{B10}, Ser^{B2}+Asp^{B10} and Glu^{A15}+Asp^{A18}+Asp^{B3} that did not significantly affect the dynamical properties of human insulin with a minimal stabilizing impact; 3) the mutants Asp^{B28}, Asp^{B9}+Glu^{B27} and Ser^{A13}+Glu^{B27}, Gln^{B18}, destabilizing the protein structure. Analysis of the secondary structure content provided evidence for the influence of Asp^{B28}, Asp^{B9}+Glu^{B27} and Ser^{A13}+Glu^{B27}, Gln^{B18} on the insulin unfolding. Our MD results indicate that the replacement of superficial nonpolar residues in the insulin structure by hydrophilic ones gives rise to the increase in protein stability in comparison with the wild type protein.
KEYWORDS: human insulin, mutants, molecular dynamics simulation, amyloid.

Human insulin, a small protein hormone consisting of an acidic A-chain (21 residues) and a basic B-chain (30 residues) linked by three disulfide bonds, is crucial for controlling the hyperglycemia in type I diabetes [1-3]. However, medical and pharmaceutical applications of this hormone are complicated by its predisposition for aggregation and formation of amyloid fibrils [4-8]. Specifically, it was shown that insulin is capable of forming the amyloid fibrils at the sites of the repeated insulin injection during the therapy of patients with diabetes, thereby inducing the localized insulin-derived amyloidosis (insulin amyloidoma) [4,5]. Moreover, the tendency of insulin to form amyloid fibrils under stressful conditions (elevated temperature, agitation, pH, etc.) represents a serious obstacle during industrial purification, storage and drug delivery of protein-based pharmaceuticals [6,7]. Despite extensive research efforts, the exact molecular details of the insulin amyloid transformation are still under debate. The insulin fibril formation *in vitro* is usually described by the classical nucleation-dependent polymerization model [1,8,9]. However, many other mechanisms for insulin fibrillization have been proposed including the heterogeneous nucleation [10], colloidal coagulation model [9,11] and downhill polymerization [9,11,12].

The *in vitro* oligomerization and aggregation of insulin is essentially controlled by environmental conditions such as pH [13,14], ionic strength [15,16], temperature [14,17,18], the presence of ions [19,20], and protein concentration [14,21]. Previous studies suggested that the early stages of insulin fibrillation are governed mainly by hydrophobic interactions [22,23]. However, several lines of evidence pointed out the importance of the electrostatic interactions in the insulin fibrillization at the initial stage of nucleation [9,23,24]. It is believed that the flexible B-chain of insulin is more important for the protein transition into amyloid state than the rest of molecule [14,23, 25-27]. However, using screening of the amyloid-forming insulin sequence Eisenberg's team suggested at least two protein segments responsible for the insulin amyloid conversion: the L^{B11}VEALYL^{B17} segment of the B-chain accounting for the formation of fibril spine and the S^{A12}LYQLENY^{A19} segment from the A-chain stabilizing the fibril structure [27]. Furthermore, it was showed that the disordered N-terminal segments of both A-and B–chains along with the residues Leu^{B15}, Phe^{B24} and Tyr^{A19} may also contribute to fibril formation [28]. In addition, the surfaces consisting of His^{B10}, Leu^{B17}, Tyr^{B16}, Phe^{B25} and Thr^{A8} were assumed as the potential sites that trigger insulin fibrillization [14,28]. Notably, both A- and B-chains of insulin by their own are capable of forming the amyloid fibrils under denaturing conditions [24]. Intriguingly, the mutations in the C-terminus of human insulin B-chain were reported to affect the amyloidogenic propensity of the protein [14,29-31]. Specifically, the removal of five residues from the B-chain led to the enhancement of insulin fibrillization [14], while the mutants T30R and K29R/T30R showed different resistance against stress-induced fibril growth on the initial stage of nucleation [23]. Furthermore, the delay in the lag phase of insulin fibrillization was observed for the point mutations H10D and L17Q [31], whereas the substitution of Pro^{B28} with (4S)-hydroxyproline (Hzp) resulted in the higher resistance to fibril formation [32].

The aim of the present study was to assess the influence 10 point mutations (His^{A8}, Val^{A10}, Asp^{B10}, Gln^{B17}, Ala^{B17}, Gln^{B18}, Asp^{B25}, Thr^{B26}, Glu^{B27}, Asp^{B28}), 6 double mutations (Glu^{A13}+Glu^{B10}, Ser^{A13}+Glu^{B27}, Glu^{B1}+Glu^{B27}, Ser^{B2}+Asp^{B10}, Asp^{B9}+Glu^{B27}, Glu^{B16}+Glu^{B27}) and one triple mutation (Glu^{A15}+Asp^{A18}+Asp^{B3}) in the human insulin sequence on the protein structure and dynamics. To this end, a series of thermal unfolding MD simulations with wild type (WT) protein and its mutants was performed.

MOLECULAR DYNAMICS SIMULATIONS

The molecular dynamics simulations were conducted with GROMACS software (version 5.1) using the CHARMM36m force field with TIP3P water model [33]. The starting structure for simulations was taken from the Protein Data Bank (PDB entry for human insulin 3I3Z). The mutations His^{A8}, Val^{A10}, Asp^{B10}, Gln^{B17}, Ala^{B17}, Gln^{B18}, Asp^{B25}, Thr^{B26}, Glu^{B27}, Asp^{B28}, Glu^{A13}+Glu^{B10}, Ser^{A13}+Glu^{B27}, Glu^{B1}+Glu^{B27}, Ser^{B2}+Asp^{B10}, Asp^{B9}+Glu^{B27}, Glu^{B16}+Glu^{B27}, Glu^{A15}+Asp^{A18}+Asp^{B3} were introduced to the protein sequence using the web-based graphical interface CHARMM-GUI. The input files for MD calculations were prepared using the CHARMM-GUI Quick MD simulator [34].

The human insulin and its mutants were solvated in the rectangular box fitted to protein size. The minimal distance from the protein molecule to the box edges was 10 Å. To obtain a neutral total charge of the system the required amount of positive ions was added. The number of atoms in the solvated protein systems varied from 14670 to 17573. The Particle Mesh Ewald algorithm was used to treat the long-range electrostatic interactions [35]. The minimization and equilibration of the system were performed during 100 ps and 500 ps, respectively. The time step for MD simulations was 2 fs. The trajectories and coordinates were saved every 2 ps for further analysis. The whole time interval for MD calculations was 100 ns. The MD simulations of the human insulin and its mutants were performed at 400 K and a pressure 1 bar. The analysis tools provided by GROMACS were used to calculate the root mean-square deviations (RMSD), root mean-square fluctuations of the C-alpha atoms (RMSF), radius of gyration (Rg) and solvent-accessible surface area (SASA) per residue. The evolution of the secondary structure was followed using the VMD Timeline tool [36] and Tcl scripts.

RESULTS AND DISCUSSION

To examine the changes in the conformational behaviour of the mutated human insulin as compared to its wild type counterpart we analysed the thermal unfolding trajectories by calculating the parameters reflecting the changes in both the global and local protein structure (RMSD, Rg, SASA, RMSF) and the secondary structure content. Fig. 1 shows the changes of the backbone root mean square deviations with time.
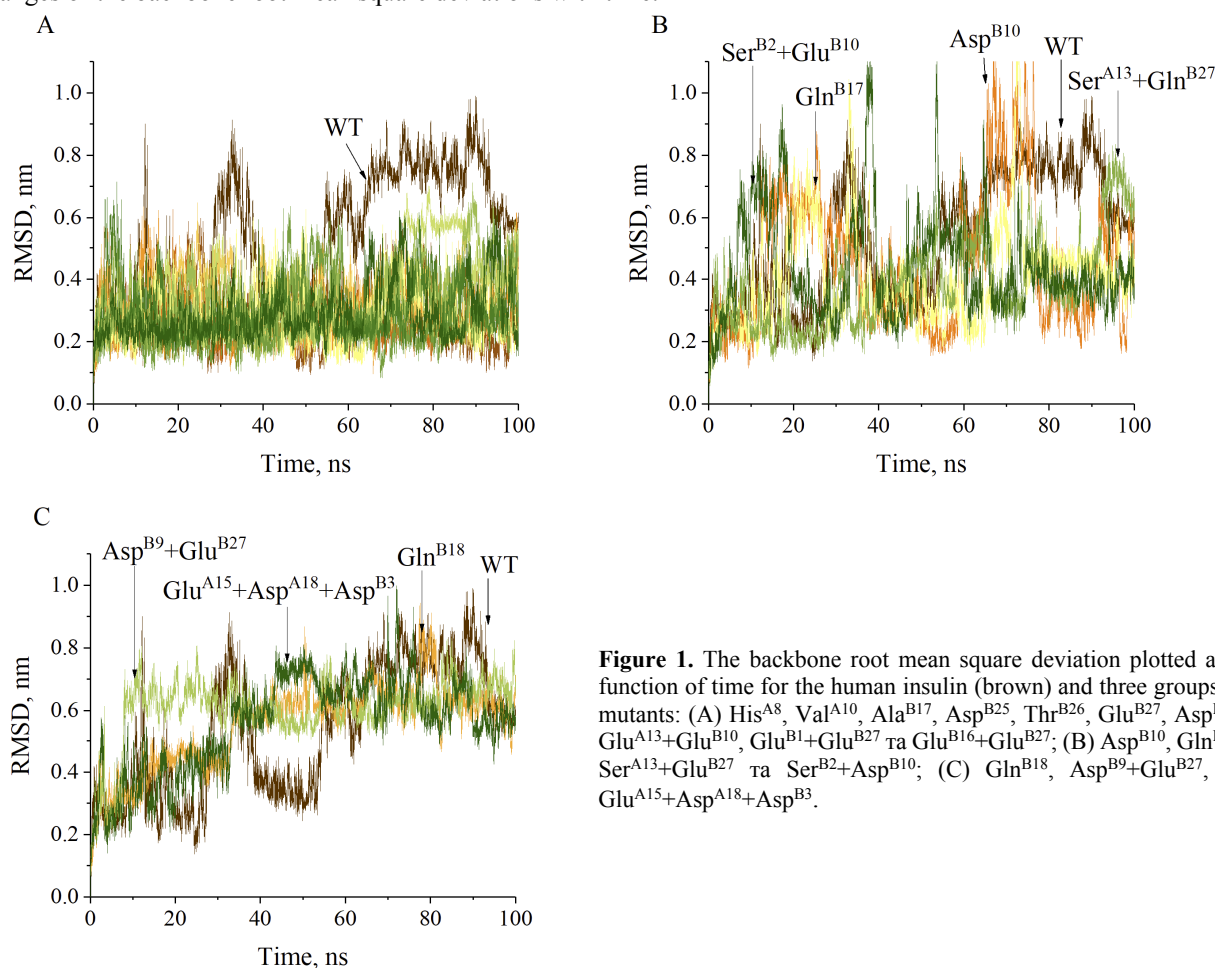
Figure 1. The backbone root mean square deviation plotted as a function of time for the human insulin (brown) and three groups of mutants: (A) His^{A8}, Val^{A10}, Ala^{B17}, Asp^{B25}, Thr^{B26}, Glu^{B27}, Asp^{B28}, Glu^{A13}+Glu^{B10}, Glu^{B1}+Glu^{B27} та Glu^{B16}+Glu^{B27}; (B) Asp^{B10}, Gln^{B17}, Ser^{A13}+Glu^{B27} та Ser^{B2}+Asp^{B10}; (C) Gln^{B18}, Asp^{B9}+Glu^{B27}, та Glu^{A15}+Asp^{A18}+Asp^{B3}.

As seen in Fig. 2, the calculated RMSD values for human insulin and its mutants do not exceed 1 nm, except short-time fluctuations of Asp^{B10}, Gln^{B17} and $Ser^{B2}+Asp^{B10}$ Notably, for the WT insulin the time dependence of RMSD is characterized by four periods: 1) strong fluctuations ~ 0.3 nm with deviations up to 0.9 nm during the first 25 ns of simulation; 2) a slight increase of RMSD values to 0.66-0.78 nm during the next 3ns followed by the fluctuations at this level during ~ 8 ns; 3) substantial decrease of RMSD values to 0.33-0.38 nm starting from ~36 ns; 4) gradual RMSD increase to 0.6-0.8 nm remaining almost stable during the last 50 ns of the simulation. The RMSDs of mutants His^{A8}, Val^{A10}, Ala^{B17}, Asp^{B25}, Thr^{B26}, Glu^{B27}, Asp^{B28}, $Glu^{A13}+Glu^{B10,}$ $Glu^{B1}+Glu^{B27}$ and $Glu^{B16}+Glu^{B27}$ were significantly lower during the simulation time compared with the WT insulin. As seen in Fig. 2, the mutants Gln^{B18}, $Asp^{B9}+Glu^{B27}$and $Glu^{A15}+Asp^{A18}+Asp^{B3}$ showed higher RMSDs during the first 60 ns of the simulation relative to WT protein and similar type of deviations throughout the following 40 ns of RMSD trajectories. In turn, the simulation of mutants Asp^{B10}, Gln^{B17}, $Ser^{A13}+Glu^{B27}$ and $Ser^{B2}+Asp^{B10}$ produced less stable trajectories in comparison with WT insulin.
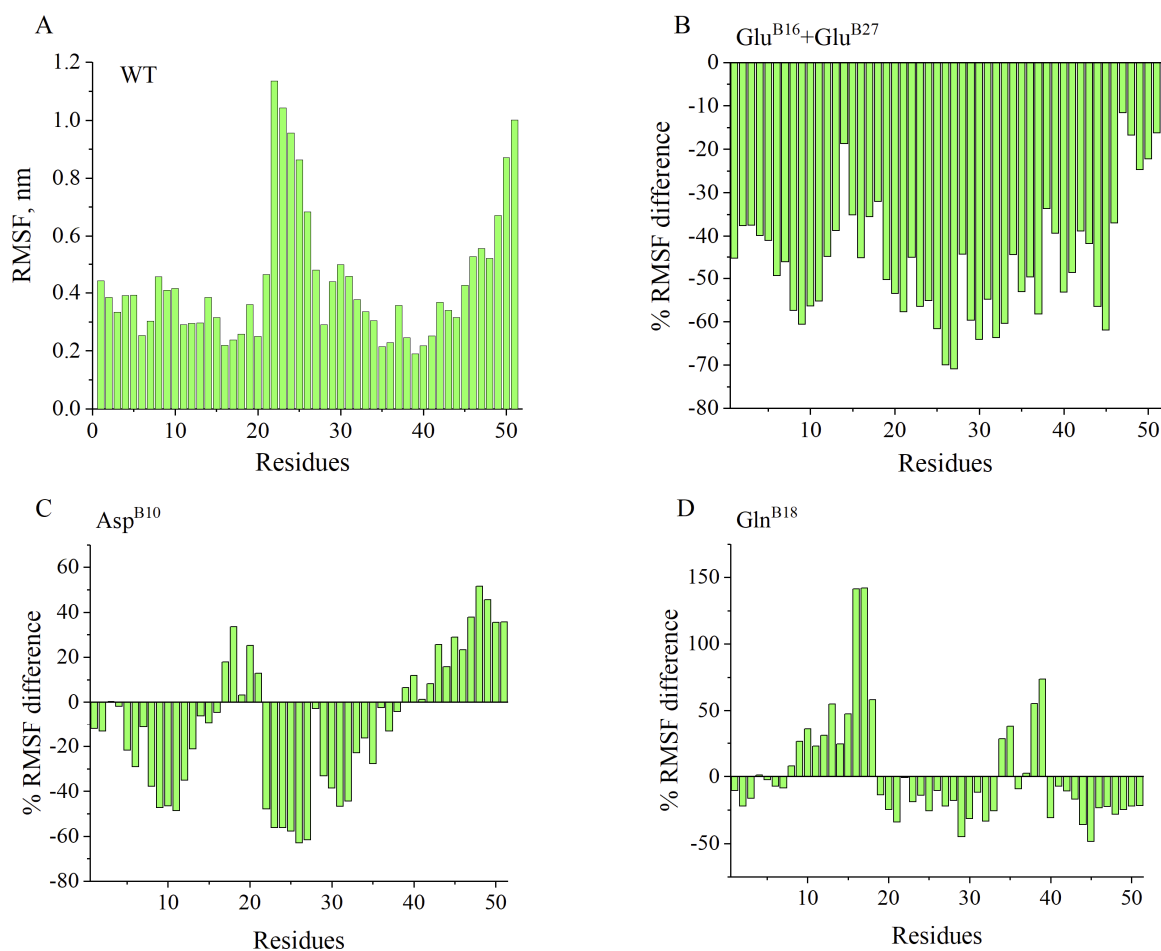
Figure 2. The root mean square fluctuations of the C-alpha atoms of WT insulin(A) and the relative changes in root-mean-square fluctuations for $Glu^{B16}+Glu^{B27}$ (B), Asp^{B10} (C), Gln^{B18} (D) insulin mutants, calculated as $\left(\dfrac{RMSF_{mut}}{RMSF_{WT}}-1\right)\cdot 100\%$.

To determine how the mutations affect the dynamic behavior of amino acid residues, the RMSF values of the C-alpha atoms of WT insulin and mutants were calculated (Fig. 2). The RMSF values for the majority of the WT protein residues ranged from 0.2 to 0.5 nm during the simulation (Fig. 2.A). The only exception were the residues 22-26 (RMSFs vary from 0.68 to 1.14 nm) representing the first five residues of the N-terminal region of B-chain, and the residues 46-51 (RMSFs vary from 0.52 to 1.0 nm), belonging to the end of the C-terminal of this chain. The analysis of the relative changes in RMSF revealed that both N- and C-terminal regions of B-chain in all mutants fluctuate stronger that in the WT insulin with the magnitude of this effect being dependent on the type of mutation (data not shown). More specifically, there are three main tendencies in the relative changes of RMSF, according to which all examined mutants can be divided into three groups. The representatives of the first group (Val^{A10}, Ala^{B17}, Asp^{B28}, $Ser^{A13}+Glu^{B27}$, $Glu^{B1}+Glu^{B27}$ and $Asp^{B9}+Glu^{B27}$) are characterized by strong fluctuations of similar amplitudes on both N- and C-terminal regions of B-chain. The second group contains Gln^{B18}, Glu^{B27} and $Glu^{A15}+Asp^{A18}+Asp^{B3}$ mutants which, like WT insulin, display significantly higher fluctuations in the N-terminal region in comparison with C-terminal part of B-chain. For all other mutants under study (the third group) the relative changes of RMSF values were opposite to those observed for the second

group. The obtained results are in good agreement with the experimental evidence for the higher conformational flexibility of B-chain with respect to the rest of the protein [29,31].

Notably, some mutants have significantly larger fluctuations in A-chain residues compared to the 7-22 sequence of the core of B-chain. Specifically, higher RMSFs were observed for Val^{A10} (1-5, 13-15 and 18-19 A-chain residues), Gln^{B18} (8-10 and 13-18 A-chain residues), Asp^{B25} (1-5, 10 and 12-15 A-chain residues), Asp^{B28} (1-5 and 12-15 A-chain residues), $Ser^{A13}+Glu^{B27}$ (1-5 and 11-14 A-chain residues), $Ser^{B2}+Asp^{B10}$ (1-4 and 14 A-chain residues), $Glu^{A15}+ Asp^{A18}+Asp^{B3}$ (8-10 A-chain residues). Remarkably, although the above results demonstrate the increase in RMSFs (in comparison with B-chain) for the polypeptide fragment consisting of 8-19 residues responsible for the stabilization of insulin fibrils [28,30], the mutations didn't significantly modify the conformation of this region, since the mutated and WT insulin showed nearly similar RMSFs for this sequence of residues.

It has been suggested previously that local unfolding of the B11-B17 fragment of insulin causes the increase in fibrillization rate [37]. However, as seen in Fig. 2 (panels B-D) the fluctuations of these residues were even smaller than those for WT protein. Nevertheless, the comparison of the relative changes in root-mean-square fluctuations of WT insulin and its mutants indicates the stabilizing effect of mutations His^{A8}, Val^{A10}, Ala^{B17}, Asp^{B25}, Thr^{B26}, Glu^{B27}, $Glu^{A13}+Glu^{B10}$, $Glu^{B1}+Glu^{B27}$ and $Glu^{B16}+Glu^{B27}$ on virtually all protein residues (the relative changes in root-mean-square fluctuations $\leq$ 74%). Notably, the highest fluctuations were observed for the variant Gln^{B18} which is characterized by the increase of A16 and A17 RSMFs to ~ 141% compared to WT insulin. The analysis of the relative changes in the RMSF revealed that the region B20-B30 fluctuates stronger in the mutants $Glu^{A15}+Asp^{A18}+Asp^{B3}$ (~39%), Gln^{B17} (~67%), Asp^{B10} (~52%), $Ser^{A13}+Glu^{B27}$ (~ 65%), $Ser^{B2}+Asp^{B10}$ (~66%) and Gln^{B18} (~73%) than in the WT protein. The mutants Asp^{B28}, $Ser^{A13}+Glu^{B27}$, Gln^{B18} have significantly larger fluctuations in the A8-A18 region, with RMSF difference ranging from ~35% to ~72%. By considering the amount of residues fluctuating stronger than in the WT protein, along with the maximal positive and negative relative RMSF changes, we observed that the destabilizing impact of mutants on the protein dynamics increases in the following row: Asp^{B25} < $Asp^{B9}+Glu^{B27}$ < $Glu^{A15}+Asp^{A18}+Asp^{B3}$ < Gln^{B17} < Asp^{B28} < Asp^{B10} < $Ser^{A13}+Glu^{B27}$ < $Ser^{B2}+Asp^{B10}$ < Gln^{B18}.

Fig. 3 represents the time-course evolution of the radius of gyration.
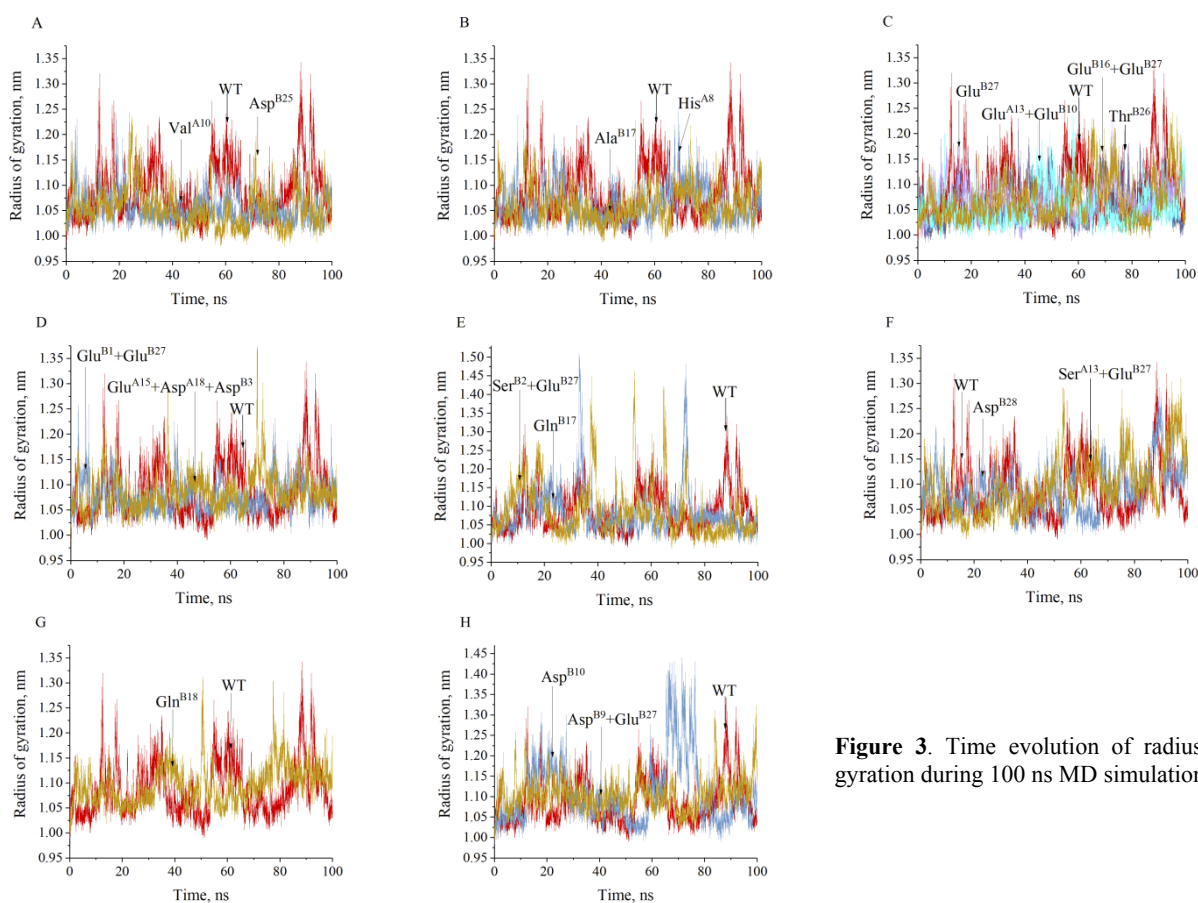
Figure 3. Time evolution of radius of gyration during 100 ns MD simulations.

The Rg value of the WT insulin rises from ~1 to ~1.34 nm. The approximation of the time dependence of the radius of gyration by the linear function showed that the slop of graph increases with time from ~ 1.07 nm at the beginning of simulation to ~ 1.1 nm at 100 ns. Since the gyration radius correlates with the extent of protein unfolding, the approximation of the time evolution of the radius of gyration by the linear function allowed us to identify the three groups of mutants. The first group contains $Glu^{A13}+Glu^{B10}$, $Glu^{B16}+Glu^{B27}$, Thr^{B26}, Glu^{B27}, His^{A8}, Ala^{B17}, $Val^{A10}$and Asp^{B25} whose

approximation lines are positioned below the approximation line of WT protein (Fig. 2.A-C). The second group includes $Glu^{B1}+Glu^{B27}$, $Glu^{A15}+ Asp^{A18}+Asp^{B3}$, $Ser^{B2}+Asp^{B10}$, Gln^{B17}, Asp^{B28}, $Ser^{A13}+Glu^{B27}$ and Gln^{B18}, whose approximation lines are comparable with that for WT protein (Fig. 2.E-F), while Gln^{B1}, Asp^{B10} and $Asp^{B9}+Glu^{B27}$ with approximation lines located significantly higher than that for WT insulin constitute the third group.

To assess the alterations in the environment of hydrophobic residues during the simulation, we concentrated on the relative changes in the solvent accessible surface area per residue SASA (Fig. 4). For WT insulin the SASA values do not exceed 1.8 nm. We found that polar A5, A8, A21, B4, positively charged (B5, B10, B22, B29), negatively charged (A4, B13, B21), aromatic (A14, B1, B16, B25, B26) and three nonpolar residues (A10, B17 та B30) are highly accessible to the solvent during the simulation time (Fig. 4). Notably, the profiles of SASA per residue were similar for mutated and WT insulin, indicating that A14, B1, B21 and B29 residues are more accessible to water than the other residues in the protein sequence. Considering the number of residues whose SASA values are higher relative to WT protein, the examined mutants were found to follow the order: $Ala^{B17} = Glu^{B27} < Glu^{B16}+Glu^{B27} < Val^{A10}$, $Glu^{A13}+Glu^{B10} = Thr^{B26} = His^{A8}$, $Gln^{B18} < Glu^{B1}+Glu^{B27} = Asp^{B25} < Gln^{B17} < Ser^{A13}+Glu^{B27} < Asp^{B28}$, $Ser^{B2}+Asp^{B10} = Glu^{A15}+Asp^{A18}+Asp^{B3} < Asp^{B9}+Glu^{B27} = Asp^{B10}$.
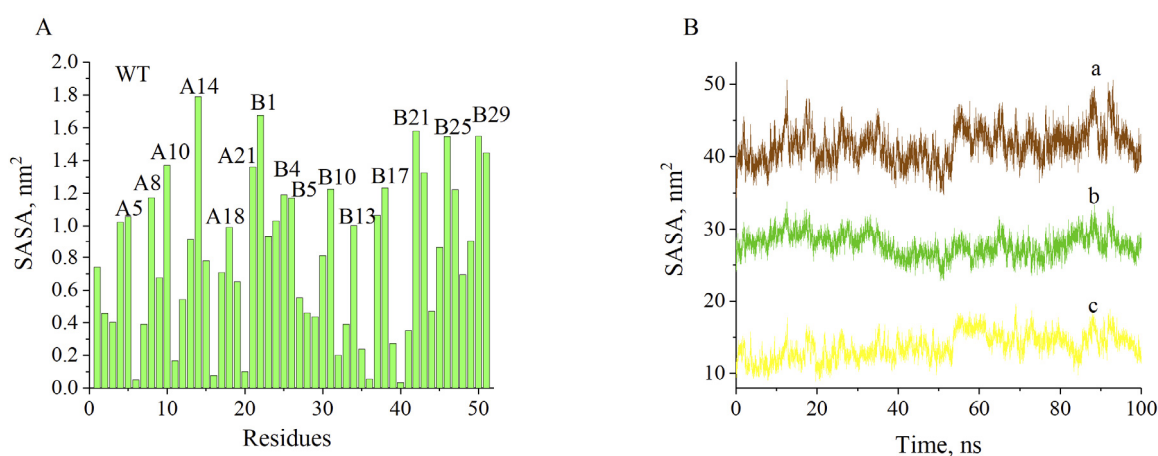
Figure 4. The solvent accessible surface area per residue (A) and time evolution of SASA (B) for whole protein (a), its hydrophobic (b) and hydrophilic (c) residues calculated for wild type insulin.

Notably, depending on the decrease or increase of SASA relative to WT protein, all residues can be divided into two groups. The first group includes the residues A4, A7, A17, A20, B1, B7, B9, B12, B13, B16-B22, B47 and B29, whose SASA is greater than that of WT insulin. In turn, the residues of the second group (A1-A3, A5, A6, A8-A14, A16, A19, A21, B2-B6, B8, B10, B11, B14, B15, B23-B25, B28, B30) are characterized by lower SASA values. Remarkably, the hydrophobic residues represent ~ 32% and ~ 63% of all residues in the first and second groups, respectively, being indicative of the decreased solvent accessibility of nonpolar and aromatic residues of mutants in comparison with WT protein.

To take a closer look on the impact of hydrophobic and hydrophilic residues on the solvent accessible surface area, the time evolution of SASA values was analyzed for: 1) all protein residues; 2) hydrophobic residues; and 3) hydrophilic residues (Fig. 4.B). The approximation of the time-course SASA evolution by the linear function for all protein residues and independently for hydrophobic and hydrophilic residues showed that:

1) The growth of the total SASA value with time is caused by the increase of both the hydrophobic and hydrophilic SASAs for Asp^{B10}, Ala^{B17}, Gln^{B18}, Thr^{B26}, Asp^{B28}, $Glu^{A13}+Glu^{B10}$, $Ser^{A13}+Glu^{B27}$ та $Glu^{B16}+Glu^{B27}$;

2) The increase of the total SASA value with time for the wild type protein and the mutants Glu^{B27}, $Glu^{A15}+Asp^{A18}+Asp^{B3}$, $Asp^{B9}+Glu^{B27}$ results from the increase of the solvent accessibility of hydrophobic residues;

3) A slight increase of the total SASA for His^{A8} and $Glu^{B1}+Glu^{B27}$ reflects the increase of the solvent accessibility of hydrophilic residues;

4) The decrease of the total SASA with time observed for Gln^{B17}, originates from the reduction of SASAs for hydrophilic residues;

5) The solvent accessibility of both hydrophobic and hydrophilic residues reduces for Val^{A10}, Asp^{B25} and $Ser^{B2}+Asp^{B10}$

The above results indicate that the replacement of superficial nonpolar residues by hydrophilic ones increases the insulin stability in comparison with the wild type protein.

Next, to clarify the effect of mutations on the insulin unfolding pathway, we analyzed the time course of the changes in protein secondary structure through determining the percentage of residues adopting the α-helix, β-sheet or 3_{10}-helix conformations during the simulation (Table 1). It appeared that the content of α-helices rises from 35% to 50% in the following raw: $Asp^{B9}+Glu^{B27} < Gln^{B18} < Ser^{A13}+Glu^{B27} < Asp^{B28} < Asp^{B25} < Glu^{B16}+Glu^{B27} < Glu^{B1}+Glu^{B27} < Val^{A10} < Thr^{B26} < Ala^{B17} < His^{A8} < Glu^{B27} < Glu^{A13}+Glu^{B10} < WT < Glu^{A15}+ Asp^{A18}+Asp^{B3} < Ser^{B2}+Asp^{B10} <$

$Asp^{B10} < Gln^{B17}$. Given that the native insulin contains 3 α-helices (47%), the above results can be explained either by the destruction of α-helices during the simulation or the appearance of the additional α-helix conformations. In turn, we observed only small percentage of β-sheets (absent in the native conformation) increasing in the order: $Asp^{B9}+Glu^{B27} < Glu^{A15} < Asp^{A18}+Asp^{B3} < Val^{A10} < WT < Gln^{B18} < Ser^{B2}+Asp^{B10} < Thr^{B26} < Ala^{B17} < Asp^{B25} < Asp^{B10} < His^{A8} < Glu^{B27} < Glu^{B16}+Glu^{B27} < Ser^{A13}+Glu^{B27} < Asp^{B28} < Glu^{A13}+Glu^{B10} < Gln^{B17} < Glu^{B1}+Glu^{B2}$.

Table 1. The percentage of residues adopting α-helix, β-sheet or 3_{10}-helix conformations during the simulation

Protein	β-sheet	α-helix	3_{10} –helix
WT	0.04	46.0	3.1
His^{A8}	0.18	45.0	1.7
Val^{A10}	0.02	44.5	2.7
Asp^{B10}	0.16	47.0	1.7
Gln^{B17}	1.73	50.0	1.2
Ala^{B17}	0.08	44.9	2.4
Gln^{B18}	0.04	36.1	4.6
Asp^{B25}	0.15	43.7	2.1
Thr^{B26}	0.08	44.7	3.1
Glu^{B27}	0.24	45.7	2.5
Asp^{B28}	0.72	38.6	3.7
$Glu^{A13}+Glu^{B10}$	0.87	45.8	1.5
$Ser^{A13}+Glu^{B27}$	0.30	37.0	3.7
$Glu^{B1}+Glu^{B27}$	2.08	44.5	2.9
$Ser^{B2}+Asp^{B10}$	0.08	47.5	1.3
$Asp^{B9}+Glu^{B27}$	0	34.7	5.0
$Glu^{B16}+Glu^{B27}$	0.30	44.3	2.6
$Glu^{A15}+ Asp^{A18}+Asp^{B3}$	0	46.7	4.3

To characterize the changes in the secondary structure of mutants during the simulation, we analyzed the time evolution of α-helices (Fig. 6). The wild type insulin was characterized by the fluctuations of the α-helices content at the level ~ 42 % (first 25 ns of simulation), followed by the substantial increase of the percentage of α-helices till ~60 % during the next 15 ns period, after which a slight helicity decrease was observed until achievement of the initial level of fluctuations to the end of the simulation. The curve of the time evolution of α-helices for $Glu^{A15}+ Asp^{A18}+Asp^{B3}$ was almost identical to that for WT protein. Moreover, the fluctuations of the α-helices content from ~ 33 % till ~ 51 % was observed for $Glu^{B1}+Glu^{B27}$, $Glu^{B16}+Glu^{B27}$, His^{A8}, Val^{A10}, Ala^{B17}, Thr^{B26}, Glu^{B27}, $Glu^{A13}+Glu^{B10}$, reflecting the stability of their secondary structure during the simulation.
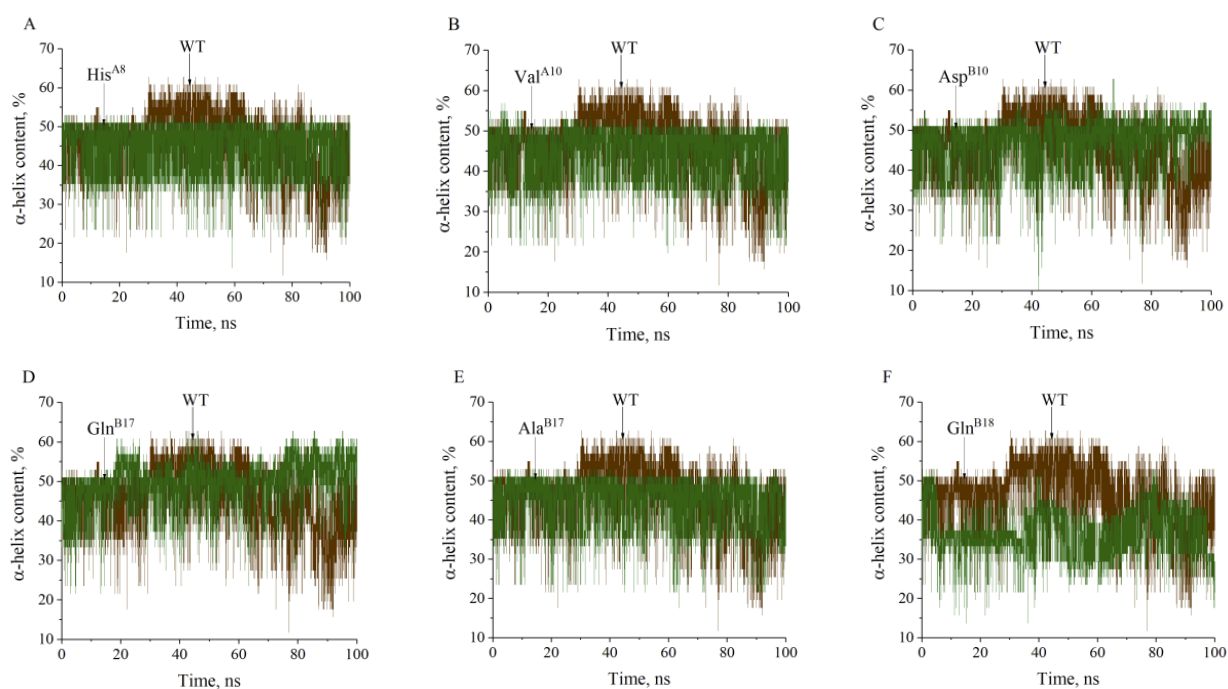
Figure 6. Time evolution of the α-helices of wild type protein (brown) and mutants (green)
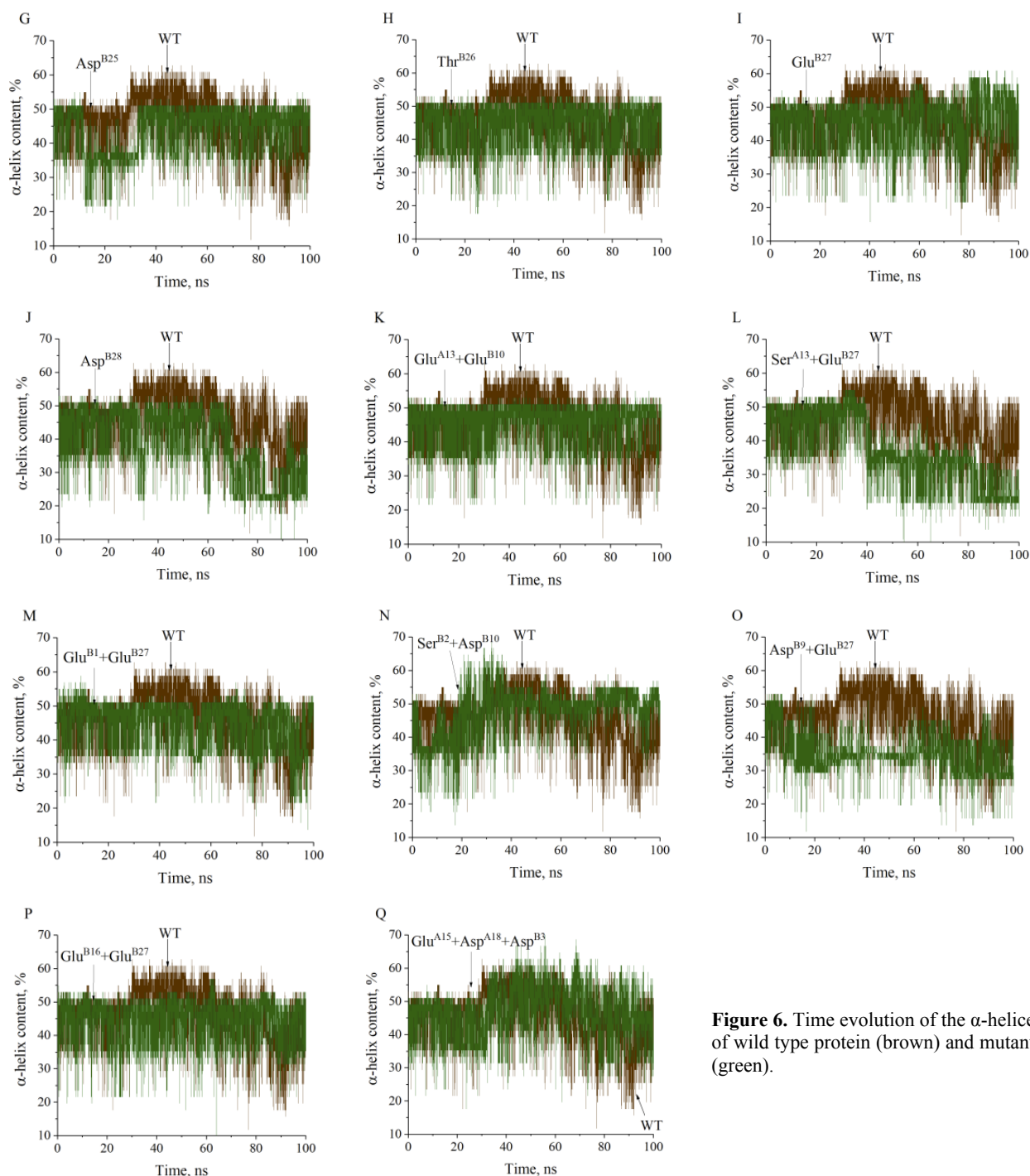(*continued on next page*)

Figure 6. Time evolution of the α-helices of wild type protein (brown) and mutants (green).

In turn, a slight increase of the percentage of α-helices was observed for Asp^{B10} (till ~ 47-54 %) and Gln^{B17} (till ~ 46-61 %) during the simulation. Notably, the decrease of the α-helices content with time was inherent to Asp^{B25} (~ 25-38% during the period 11-33 ns), Asp^{B28} (~ 22-36% from the 70 ns), $Ser^{A13}+Glu^{B27}$ (~ 22-36 starting after 38 ns), Gln^{B18} (~ 29-46 % beginning from 5 ns) and $Asp^{B9}+Glu^{B27}$ (~ 28-44% 36 starting after 7 ns). The analysis of the secondary structure content evidenced a higher unfolding extent of AspB28, AspB9+GluB27, SerA13+GluB27, GlnB18 in comparison with the WT protein.

CONCLUSIONS

To summarize, the present study indicates that introduction of 10 point mutations (His^{A8}, Val^{A10}, Asp^{B10}, Gln^{B17}, Ala^{B17}, Gln^{B18}, Asp^{B25}, Thr^{B26}, Glu^{B27}, Asp^{B28}), 6 double mutations ($Glu^{A13}+Glu^{B10}$, $Ser^{A13}+Glu^{B27}$, $Glu^{B1}+Glu^{B27}$, $Ser^{B2}+Asp^{B10}$, $Asp^{B9}+Glu^{B27}$, $Glu^{B16}+Glu^{B27}$) and one triple mutation ($Glu^{A15}+Asp^{A18}+Asp^{B3}$) in the protein sequence has different impact on the structural and dynamical properties of the human insulin. The MD simulation results showed that depending on time evolution of integral characteristics such as the backbone root mean-square deviation, gyration radius, solvent accessible surface area, the root mean-square fluctuations and the secondary structure content, the examined

mutants can be tentatively divided into three groups: 1) the mutants His^{A8}, Val^{A10}, Ala^{B17}, Asp^{B25}, Thr^{B26}, Glu^{B27}, $Glu^{A13}+Glu^{B10}$, $Glu^{B1}+Glu^{B27}$ and $Glu^{B16}+Glu^{B27}$, exerting a stabilizing effect on the protein structure in comparison with wild type insulin; 2) the mutants Gln^{B17}, Asp^{B10}, $Ser^{B2}+Asp^{B10}$ and $Glu^{A15}+Asp^{A18}+Asp^{B3}$ that did not significantly affect the dynamical properties of human insulin having a minimal stabilizing impact; 3) the mutants Asp^{B28}, $Asp^{B9}+Glu^{B27}$, $Ser^{A13}+Glu^{B27}$ and Gln^{B18} destabilizing protein structure. The analysis of the time dependencies of the secondary structure content highlights the influence of Asp^{B28}, $Asp^{B9}+Glu^{B27}$, $Ser^{A13}+Glu^{B27}$ and Gln^{B18} on the insulin unfolding. Moreover, our MD results indicate that substitution of the nonpolar residues in the insulin structure by hydrophilic ones caused the increase in protein stability in comparison with wild type protein.

ORCID IDs
Olga Zhytniakivska, https://orcid.org/0000-0002-2068-5823; **Uliana Tarabara,** https://orcid.org/0000-0002-7677-0779
Valeriya Trusova, https://orcid.org/0000-0002-7087-071X; **Kateryna Vus,** https://orcid.org/0000-0003-4738-4016
Galyna Gorbenko, https://orcid.org/0000-0002-0954-5053

REFERENCES
[1] Q. Hua, Protein Cell. **1**, 537-551 (2010), https://doi.org/10.1007/s13238-010-0069-z.
[2] F. Hu, Diabetes Care. **34**, 1249-1257 (2011), https://doi.org/10.2337/dc11-0442.
[3] M. Atkinson, G. Eisenbarth, and A. Michels, The. Lancet. **383**, 69-82 (2014), https://doi.org/10.1016/S0140-6736(13)60591-7.
[4] M. Nakamura, Y. Misumi, T. Nomura, W. Oka, A. Isoguchi, K. Kanenawa, T. Masuda, T. Yamashita, Y. Inoue, Y. Ando, and M. Ueda, Diabetes. **68**, 609-616 (2019), https://doi.org/10.2337/db18-0846.
[5] T Nagase, K. Iwaya, K. Kogure, T. Zako, Y. Misumi, M. Kikuchi, K. Matsumoto, M. Noritake, Y. Kawachi, M. Kobayashi, Y. Ando, and Y. Katsura, J. Diabetes Investig. **11**, 1002-1005 (2020), https://doi.org/10.1111/jdi.13199.
[6] Z.B. Taraghdari, R. Imani, and F. Mohabatpour, Macromol. Biosci. **19**, 1800458 (2019), https://doi.org/10.1002/mabi.201800458.
[7] M. Akbarian, Y. Ghasemi, V. Uversky, and R. Yousefi. Int. J. Pharm. **547**, 450-468 (2018), https://doi.org/10.1016/j.ijpharm.2018.06.023.
[8] L. Nielsen, R. Khurana, A. Coats, S. Frokjaer, J. Brange, S. Vyas, V.N. Uversky, and A.L. Fink, Biochemistry. **40**, 6036-6046 (2001), https://doi.org/10.1021/bi002555c.
[9] M. Groenning, S. Frokjaer, and B. Vestergaard, Curr. Protein. Pept. Sci. **10**, 509-528 (2009), https://doi.org/10.2174/138920309789352038.
[10] F. Librizzi, and C. Rischel, Protein Sci. **14**, 3129-3134 (2005), https://doi.org/10.1110/ps.051692305.
[11] A. Podesta, G. Tiana, P. Milani, and M. Manno. Biophys J. **90**, 589-597 (2006), https://doi.org/10.1529/biophysj.105.068833.
[12] S. Grudzielanek, R. Jansen, and R. Winter, J. Mol. Biol. **351**,879-894 (2005), https://doi.org/10.1016/j.jmb.2005.06.046.
[13] A. Noormägi, K. Valmsen, V Tõugu, and P. Palumaa, Protein J. **34,** 398–403 (2015), https://doi.org/10.1007/s10930-015-9634-x.
[14] J. Brange, L. Andersen, E. Laursen, G. Meyn, and E. Rasmussen, J. Pharm. Sci. **86**, 517-525 (1997), https://doi.org/10.1021/js960297s.
[15] M. Ziaunys, T. Sneideris, and V. Smirnovas, Phys. Chem. Chem. Phys. **20**, 27638-276455 (2018), https://doi.org/10.1039/C8CP04838J.
[16] M. Muzaffar, and A. Ahmad, Plos ONE. **20**, e27906 (2011), https://doi.org/10.1371/journal.pone.0027906.
[17] I. Bekard, and D. Dunstan, Biophys J. **97**, 2521-2531 (2009), https://doi.org/10.1016/j.bpj.2009.07.064.
[18] M. Sorci, R. Grassucci, I. Hahn, J. Frank, and G. Belfort, Proteins. **77,** 62–73 (2009), https://doi.org/10.1002/prot.22417.
[19] C.G. Frankær, P. Sønderby, M.B. Bang, R.V. Mateiu, M. Groenning, J. Bukrinski, and P. Harris, J. Struct. Biol. **199,** 27–38 (2017), https://doi.org/10.1016/j.jsb.2017.05.006.
[20] A. Noormagi, J. Gavrilova, J. Smirnova, V. Tõugu, and P. Palumaa, Biochem. J. **430,** 511–518 (2010), https://doi.org/10.1042/BJ20100627.
[21] J. Hansen, Biophys. Chem. **39,** 107–110 (1991), https://doi.org/10.1016/0301-4622(91)85011-E.
[22] A. Ahmad, V. Uversky, D. Hong, and A. Fink, J. Biol. Chem. **280** 42669–42675 (2005), https://doi.org/10.1074/jbc.M504298200.
[23] M. Akbarian, R. Yousefi, A.A. Moosavi-Movahedi, A. Ahmad, and V.N. Uversky, Biophys. J. **117,** 1626–1641 (2019), https://doi.org/10.1016/j.bpj.2019.09.022.
[24] D.P. Hong, A. Ahmad, and A.L. Fink, Biochemistry. **45**, 9342-9353 (2006), https://doi.org/10.1021/bi0604936.
[25] D.P. Hong, and A.L. Fink, Biochemistry, **44**, 16701-16709 (2005), https://doi.org/10.1021/bi051658y.
[26] R. Huang, N. Maiti, N. Philips, P.R. Carey, and M.A. Weiss, Biochemistry. **45**, 10278-10293 (2006), https://doi.org/10.1021/bi060879g.
[27] M.I. Ivanova, S.A. Sievers, M.R. Sawaya, J.S. Wall, and D. Eisenberg, PNAS, **106**, 18990-18995 (2009), https://doi.org/10.1073/pnas.0910080106.
[28] X.Q. Hua, and M.A. Weiss, J. Biol. Chem. **279**, 21449-21460 (2004), https://doi.org/10.1074/jbc.M314141200.
[29] M. Bouchard, J. Zurdo, E.J. Nettleton, C.M. Dobson, and C.V. Robinson, Protein. Sci. **9**, 1960–1967 (2008), https://doi.org/10.1110/ps.9.10.1960.
[30] V. Babenko, and W. Dzwolak, FEBS Lett. **587,** 625–630 (2013), https://doi.org/10.1016/j.febslet.2013.02.010.
[31] L. Nielsen, S. Frokjaer, J. Brange, V.N. Uversky, and A.L. Fink, Biochemistry, **40,** 8397–8409 (2001), https://doi.org/10.1021/bi0105983.
[32] S.A. Lieblich, K.Y. Fang, J.K.B. Cahn, J. Rawson, J. LeBon, H.T. Ku, and D.A. Tirrell, J. Am. Chem. Soc. **139,** 8384–8387 (2017), https://doi.org/10.1021/jacs.7b00794.
[33] J. Huang, and A. MacKerell, J. Comput. Chem. **34**, 2135–2145 (2013), https://doi.org/10.1002/jcc.23354.
[34] S. Jo, J. Lim, J. Klauda, and W. Im, Biophys. J. **97**, 50-58 (2009), https://doi.org/10.1016/j.bpj.2009.04.013.
[35] T. Darden, D. York, and L. Pedersen, J. Chem. Phys. **98**, 10089–10092 (1993), https://doi.org/10.1063/1.464397.
[36] W. Humphrey, A. Dalke, and K. Schulten, J. Mol. Graph. **14**, 33–38 (1996), https://doi.org/10.1016/0263-7855(96)00018-5.
[37] T.S. Choi, J.W. Lee, K.S. Jin, and H.I. Kim, Biophys. J. **107**, 1939-1949 (2014), https://doi.org/10.1016/j.bpj.2009.04.013.

МОЛЕКУЛЯРНО-ДИНАМІЧНЕ ДОСЛІДЖЕННЯ МУТАНТІВ ІНСУЛІНУ
О. Житняківська, У. Тарабара, В. Трусова, К. Вус, Г. Горбенко
Кафедра медичної фізики та біомедичних нанотехнологій, Харківський національний університет імені В.Н. Каразіна
м. Свободи 4, Харків, 61022, Україна

Інсулін людини, невеликий гормон пептидної природи, що складається з А-ланцюга (21 залишок) та Б- ланцюга, які зв'язані між собою трьома дисульфідними містками, має важливе значення для контролю глікемії при діабеті I типу. У даній роботі методом молекулярно-динамічного моделювання досліджено вплив 10 точкових мутацій (His^{A8}, Val^{A10}, Asp^{B10}, Gln^{B17}, Ala^{B17}, Gln^{B18}, Asp^{B25}, Thr^{B26}, Glu^{B27}, Asp^{B28}), 6 подвійних мутацій ($Glu^{A13}+Glu^{B10}$, $Ser^{A13}+Glu^{B27}$, $Glu^{B1}+Glu^{B27}$, $Ser^{B2}+Asp^{B10}$, $Asp^{B9}+Glu^{B27}$, $Glu^{B16}+Glu^{B27}$) та однієї потрійної мутації ($Glu^{A15}+Asp^{A18}+Asp^{B3}$) на структуру та динаміку інсуліну людини. З використанням програмного пакету GROMACS (версія 5.1) і силового поля CHARMM36m, було проведено серію 100 нс молекулярно-динамічних (МД) симуляцій дикого типа інсуліну людини (WT) та його мутантів при температурі 500 К. Результати МД моделювання були проаналізовані в термінах параметрів, що характеризують як глобальну так і локальну структуру білка, таких як середньоквадратичне відхилення остову ланцюга, радіус інерції, площа поверхні, доступна для розчинника, середньоквадратичні флуктуації та вміст вторинної структури. Результати молекулярно-динамічного моделювання продемонстрували, що в залежності від еволюції інтегральних характеристик, усі досліджені мутанти можна умовно розділити на три групи: 1) мутанти His^{A8}, Val^{A10}, Ala^{B17}, Asp^{B25}, Thr^{B26}, Glu^{B27}, $Glu^{A13}+Glu^{B10}$, $Glu^{B1}+Glu^{B27}$ та $Glu^{B16}+Glu^{B27}$, що мають стабілізуючий вплив на структуру білка у порівнянні з диким типом інсуліну; 2) мутанти Gln^{B17}, Asp^{B28}, Asp^{B10}, $Ser^{B2} + Asp^{B10}$ та $Glu^{A15} + Asp^{A18} + Asp^{B3}$, які істотно не впливали на динаміку білка або мали незначний стабілізуючий вплив; 3) мутанти $Asp^{B9} + Glu^{B27}$, $Ser^{A13} + Glu^{B27}$ та Gln^{B18}, що дестабілізували структуру білка. При аналізі еволюції вторинної структури отримані докази впливу мутацій Asp^{B28}, $Asp^{B9}+Glu^{B27}$, $Ser^{A13}+Glu^{B27}$ та Gln^{B18} на ступінь розгортання інсуліну. Результати МД демонструють, що заміна неполярних залишків в структурі інсуліну на гідрофільні, підвищує стабільність білка порівняно з інсуліном дикого типу.
КЛЮЧОВІ СЛОВА: людський інсулін, мутанти, молекулярно-динамічне моделювання, аміолоїд.

MODELING OF MOLECULAR MECHANISMS OF RADIATION ADAPTIVE RESPONSE FORMATION

Maryna A. Bondarenko[a,*], **Olga V. Zaytseva**[a,†], **Valerija M. Trusova**[b,††]

ᵃKharkiv National Medical University, 4 Nauki Ave., Kharkiv, 61022, Ukraine
ᵇV.N. Karazin Kharkiv National University, 4 Svobody Sq., Kharkiv, 61022, Ukraine
*Corresponding Author: ma.bondarenko@knmu.edu.ua
†E-mail: ov.zaitseva@knmu.edu.ua, ††E-mail: valerija.trusova@karazin.ua
Received April 26, 2021; revised April 30, 2021; accepted May 6, 2021

The phenomenon of adaptive response is expressed in the increase of resistance of a biological object to high doses of mutagens under the conditions of previous exposure to these (or other) mutagens in low doses. Low doses of mutagen activate a number of protective mechanisms in a living object, which are called hormetic. Thus, the adaptive response and hormesis are links in the same chain. Radiation hormesis refers to the generally positive effect of low doses of low LET radiation on biological objects. The phenomenology of radiation-induced adaptive response and radiation hormesis for biological objects of different levels of organization is considered; the review of existing theories describing the dose-effect relationship has been reviewed. The hypothesis proposing one of the mechanisms of formation of radiation adaptive response of cells taking into account the conformational structure of chromatin has been submitted. The analysis of modern concepts of the phenomenon of hormesis on the basis of modeling of molecular mechanisms of formation of hormetic reactions to low-dose low LET radiation has been carried out. The parameters that can be used for quantitative and graphical evaluation of the phenomenon of hormesis was considered, and a formula for calculating the coefficient of radiation-induced adaptive response has been proposed. A review of mathematical models describing the radiation relative risk of gene mutations and neoplastic transformations at low-dose irradiation of cohorts has been performed. The following conclusions have been made: radiation hormesis and adaptive response are generally recognized as real and reproducible biological phenomena, which should be considered as very important phenomena of evolutionarily formed biological protection of living organisms from ionizing radiation. The hormesis model of dose-response relationship makes much more accurate predictions of a living object's response to radiation (or other stressors) in the low-dose range than the linear threshold (LNT) model does. The LNT model can adequately describe reactions only in the region of high doses of radiation, and, therefore, extrapolation modeling of biological object's reactions from the zone of high doses to low doses is not correct.
KEY WORDS: adaptive response, radiation hormesis, dose-effect relationship, low radiation doses, cancer risk.

Сучасні дослідження [1-3] свідчать, що адаптивна відповідь є одним з механізмів захисту біологічних об'єктів від дії радіації та інших агентів хімічної та фізичної природи в високих дозах. Адаптивна відповідь виражається в підвищенні стійкості біологічного об'єкту до високих доз мутагенів при попередньому впливі на нього цими мутагенами в малих дозах і розвивається через кілька годин або діб після першого (адаптуючого) впливу.

Незважаючи на те, що феномен адаптивної відповіді відомий понад п'ятдесят років, механізм його залишається остаточно нез'ясованим і математично не описаним.

Дослідження механізмів формування адаптивної відповіді тісно пов'язане із з'ясуванням механізмів явища гормезису – стимулюючої дії невеликих доз стресорів різної природи. Іншими словами, якщо вплив високих рівнів стресорів є пригнічуючим, то низькі (легкі, сублетальні і субтоксичні) дози є стимулюючими. Помічено, що гормезисні прояви на кривих залежності "доза-ефект" зустрічаються у різних представників біоти, починаючи від вірусів і бактерій і закінчуючи приматами і людиною.

Під радіаційним гормезисом (від лат. hormaein – збуджувати, англ. hormesis) розуміють загально позитивну дію рідкоіонізуючого випромінювання у діапазонах низьких доз і потужностей доз на біологічні об'єкти різних рівнів інтеграції. Радіаційний гормезис може виявлятися, наприклад, у вигляді прискорення проліферації клітин, росту опромінених біологічних об'єктів, стимулюванні рівня імунітету організму (рослинного та тваринного), вірулентності патогенів тощо.

МЕХАНІЗМИ ФОРМУВАННЯ АДАПТИВНОЇ ВІДПОВІДІ

Багато дослідників [4-10] вважають, що для формування адаптивної відповіді необхідна активація системи репарації ДНК. Це припущення ґрунтується на ряді фактів. Так, спостерігався підвищений УФ-індукований позаплановий синтез ДНК в адаптованих клітинах. Було показано також, що інгібітори білкового синтезу пригнічують формування адаптивної відповіді. Крім того, необхідність приблизно 4-х годинної експозиції після адаптуючої дози для розвитку радіорезистентності клітин є також доказом індукції певних ферментних систем. Причому після адаптуючої дози в клітинах були виявлені нові білки [11]. З цих результатів випливає, що цитогенетична адаптивна реакція пов'язана не тільки з активацією репараційних ферментів, але й з індукцією захисних білків. Лімфоцити були першим типом клітин людини, на яких була продемонстрована адаптивна реакція на низькі дози опромінювання. Після низької дози (1 – 10 сГр) впливу Х-променями на лімфоцити

периферичної крові людини була відзначена індукція двох нових білків 14 кДа і 35 кДа. Ці білки не утворюються ні при більш низьких, ні при більш високих дозах радіації і, можливо, забезпечують розвиток подальшої стійкості клітин. Більше того, в адаптивній реакції приймають участь білки, які в неопромінених клітинах виявлені не були [12, 13]. В клітинах мишей, які хронічно опромінювались низькими дозами Х-променів, відзначалася підвищена активність ДНК-полімерази [14].

В роботі [15] відзначається, що при опроміненні біологічних об'єктів у макромолекулах, зокрема ДНК, виникають додаткові до спонтанних радіаційно-індуковані ушкодження, число однониткових та двониткових розривів зростає із ростом дози опромінення. В роботі [16] показано, що низькі дози радіації стимулюють утворення специфічних білків, які беруть участь у процесах репарації ДНК. При цьому відбувається тимчасове інгібування синтезу ДНК, внаслідок чого у клітини з'являється додатковий час для репарації ушкоджень ДНК. Інгібування синтезу, як припускають автори, може також стимулювати утворення перехоплювачів вільних радикалів, в результаті чого опромінені клітини стають більш радіорезистентними до подальших впливів більш високих доз радіації [16]. Припускається існування зв'язку між розвитком гормезису та утворенням активних форм кисню (АФК) та активних форм азоту (АФА) [17].

Автори [6, 18-22] також вважають, що механізм формування адаптивної відповіді пов'язаний з активацією системи репарації ДНК. Доказом цього положення служить відсутність радіаційної адаптивної відповіді в клітинах, дефектних по репарації пошкоджень ДНК. У зв'язку з цим слід зазначити, що клітини деяких організмів не здатні до формування адаптивної відповіді, що демонструє генетичну варіабельність людей.

Цілком зрозумілою є думка про те, що в механізмі адаптивної відповіді велику роль відіграє подовження клітинного циклу (якщо адаптуюча доза дається в G_0 фазі). У цьому випадку збільшується період часу, необхідний для здійснення всіх репаративних процесів після опромінення [9, 18, 23, 24].

Відомі дані [21], що показують зміну експресії низки генів і регуляторних РНК після дії малих доз радіації. Ці епігенетичні показники дозволяють пояснити індивідуальні відмінності у величині радіоадаптивної відповіді.

Відомо, що в ролі стресора може виступати не тільки іонізуюче випромінювання, а і, наприклад, хімічні речовини, температурний фактор, тощо. Так встановлено, що адаптуючими факторами можуть виступати малі дози іонізуючої радіації (рентгенівського, гамма випромінювання), H^3-тімідину, перекису водню, тепловий шок, ряд хімічних мутагенів [6-9]. При цьому в попередньо обробленій мутагеном клітині формується стійкість не тільки до відповідного агенту, але і до інших стрес-агентів. Це явище відомо як перехресна адаптивна відповідь. Проводячи аналогію з вірусним інфікуванням, можна згадати приклади появи неспецифічних факторів імунітету, наприклад, утворення інтерферону, індукованого одним вірусом і активного по відношенню до великого числа інших вірусів.

Феномен адаптивної відповіді в якійсь мірі можна порівнювати з ефектом вакцинації, коли контакт з малими дозами збудника (бактерій, вірусів) не викликає патологічного процесу, а індукує стимуляцію імунітету і стійкість до високих доз відповідного збудника [25-27].

Існує гіпотеза про те, що низькі дози іонізуючого випромінювання стимулюють активацію механізмів відновлення, які захищають від хвороб і які взагалі не активуються за відсутності іонізуючого випромінювання. Результат дії малих доз радіації відрізняється від відповіді на вплив високих доз і пов'язаний з активацією захисних систем клітини. У нормальних клітинах після впливу малих доз виявлено стимуляцію ендогенної антиоксидантної системи репарації, а на рівні організму відповідь на дію малих доз радіації супроводжується і активацією імунної системи. Показано, що низькі дози радіації можуть стимулювати імунологічні реакції шляхом полегшення процесу передачі сигналу [23, 28-34].

Однією з гіпотез, що пояснює формування радіоадаптивної відповіді, є припущення про гетерогенність популяції клітин по радіочутливості [20]. За цієї умови при першому адаптуючому опроміненні малими дозами іонізуючої радіації радіочутливі клітини гинуть, а ті клітини, що залишилися, створюють картину підвищеної радіостійкості при повторному опроміненні. Однак в такому випадку важко пояснити перехресну адаптивну відповідь, коли в якості адаптуючого до радіації фактора використовують не радіацію, а інші мутагени. Чутливість до різних факторів детермінується різними генами, і відбір, наприклад, не міг би супроводжуватися відбором радіочутливих клітин. В такому випадку радіоадаптивна відповідь мала б бути відсутньою, але перехресна адаптивна відповідь відома, і її важко пояснити з цих позицій [35, 36].

Сучасні дослідження радіоадаптивної реакції [37-39] вказують на те, що активація цього захисного ефекту досягала максимуму при адаптуючій дозі 1 мГр, а потім залишалася на рівні максимуму в діапазоні адаптуючих доз між 1 мГр і 500 мГр за умови опромінювання з низькою потужністю дози (рис. 1).

Оскільки γ-випромінювання ^{60}Со 1 мГр дає в середньому один електронний трек на ядро клітини ссавців [40], це найнижча експозиція, яку може отримати клітина. Таким чином, результати вказують на те, що максимальний захисний ефект відбувся у відповідь на першу дозу випромінювання, і що при більших дозах, коли кожна клітина, безперечно, отримувала кілька треків, адаптивна реакція не була більшою (або меншою). Однак через випадкову природу випромінювання доза, яка в середньому дає один трек на клітину, насправді не забезпечує трек у кожній клітині. Велика фракція клітин, що зазнали впливу 1 мГр, не отримує жодного треку, тоді як менша фракція отримує 2 і більше треки. Більш високі дози (10–500 мГр), де клітини, безперечно, отримували кілька треків, не призвели до більшої реакції, ніж доза 1 мГр. Таку ситуацію можна пояснити

існуванням ефекту «сторонніх спостерігачів»: біологічною реакцією клітин, які не були експоновані, на події у сусідніх експонованих клітинах. Це означає, що експоновані клітини виробляють біологічний сигнал, який передається через оточуюче середовище неекспонованим клітинам. Такий сигнал може виділятися протягом приблизно 24 годин.
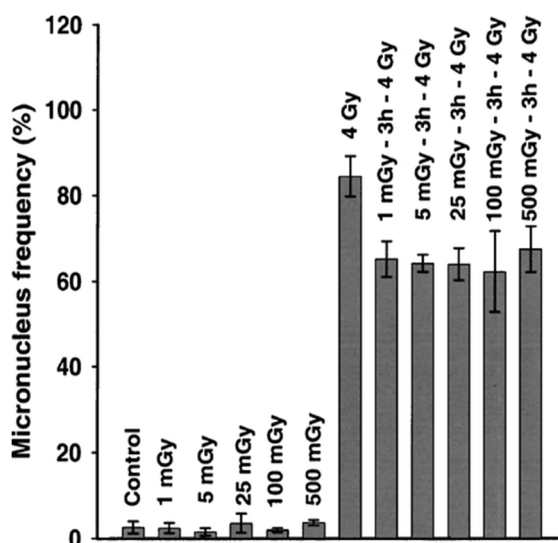

Рисунок 1. Адаптація нормальних клітин фібробластів людини, спричинена впливом різних доз γ-опромінення ^{60}Со при 37°С, виміряна частотою утворення мікроядер у двоядерних клітинах (по осі ординат). Всі клітини інкубували протягом 3 годин при 37°С після впливу адаптуючої дози (1 мГр, 5 мГр, 25 мГр, 100 мГр або 500 мГр) та перед опроміненням контрольною дозою 4 Гр. Контрольні неадаптовані клітини піддавались опроміненню дозою 4 Гр. Клітини, що зазнали впливу будь-якої адаптуючої експозиції до застосування дози 4 Гр, суттєво відрізнялись від клітин, що зазнавали впливу лише дози 4 Гр; $p < 0,05$. m ± SD, $n = 3$ (з [39]).

ГІПОТЕЗИ І МОДЕЛІ РАДІАЦІЙНОЇ АДАПТИВНОЇ ВІДПОВІДІ

Процес формування адаптивної відповіді умовно проходить в два етапи: спочатку біологічний об'єкт піддається впливу невеликої дози мутагену, а через певний час переходять до другого етапу – об'єкт вдруге піддається впливу мутагену, але вже у значно вищій дозі. Завдяки певним реакціям на першому низькодозовому етапі реалізується явище адаптивної відповіді.

Дослідження [15, 41-45] адаптивних реакцій живих об'єктів показують, що перший етап формування адаптивної відповіді є проявом гормезису. На цьому етапі включається низка реакцій на пошкодження, що підвищують стресостійкість біологічного об'єкту, і ушкодження на другому етапі вже не такі значні, як вони могли би бути без попередньої адаптуючої дози.

При оцінці явища радіаційного гормезису слід враховувати, що реакція біологічного об'єкта на дію фактора стресу, зокрема радіаційного, залежить як від характеристик радіаційного фактора (доза, потужність дози, лінійна передача енергії (ЛПЕ)), так і від властивостей об'єкта опромінення, від характеристик його вихідного стану, зокрема поточної стійкості/чутливості до дії стресора. Якщо об'єкт на момент повторної дії стрес-агента ще знаходиться у перехідному стані активації захисних реакцій, він менш уразливий, тобто адаптований для нового удару завдяки поточній підвищеній стресостійкості. Часто гормезис асоціюють виключно зі стимуляцією, але це, на наш погляд, занадто спрощений підхід. Стимуляцію слід розглядати, скоріше, як захисну відповідь біологічного об'єкта на пошкоджуючу дію стрес-фактора і один з етапів розвитку реакції на його вплив. При цьому радіостимуляція має транзитивний, тимчасовий характер; наприклад, на рівні клітини вона триває протягом приблизно трьох клітинних циклів. Аналіз механізмів формування радіаційної адаптивної відповіді свідчить про те, що радіаційна адаптивна відповідь - це один з доказів існування радіаційного гормезису.

Визнання гормезису як життєздатної теорії «доза-реакція» було обмеженим до недавнього часу частково через погане концептуальне розуміння, неналежне спеціальне використання цього поняття, а також відсутність розуміння певних механізму гормезису [46-52]. Вивчаючи історію цієї теорії, стає ясно, що як фармакологічні, токсикологічні, так і радіологічні дослідження надають докази герметичної реакції на низьку дозу стресора, але ретроспективне вивчення досліджень може бути проблематичним.

Лінійна безпорогова модель залежності «доза-ефект»

Автори [53] досліджують основні чинники, які сприяли маргіналізації радіаційного гормезису на початку і середині 20-го століття. Найбільш важливим фактором, що вплинув на «зникнення» поняття радіаційного гормезису, була відсутність згоди з приводу того, як визначити це поняття і кількісно описати його характеристики при розгляді залежності «доза-реакція». Якби радіаційний гормезис був визначений як помірна зверхкомпенсація порушення гомеостазу, що узгоджувалося б з переважаючими уявленнями в області хімічного

гормезису, це послужило б теоретичною і практичною основою відповіді на критику цієї гіпотези. Другим критичним фактором, не на користь гіпотези радіаційного гормезису, стала відсутність визнання радіологами концепції хімічного гормезису, яка була більш обгрунтованою і узагальненою, ніж концепція радіогормезису. Третій фактор полягав в тому, що серйозна наукова критика наявності стимулюючого впливу низьких доз радіації була підтримана Міжнародним комітетом з радіаційного захисту (МКРЗ), внаслідок чого радіаційна гормезична гіпотеза була виключена із запланованих широкомасштабних досліджень.

Ще в 1956 році МКРЗ запропонував прийняти «лінійну безпорогову модель» (англ., LNT model - linear non-threshold model). Постулатом, на якому неявно базується LNT концепція, є припущення про те, що канцерогенний ефект внаслідок дії радіації лінійно залежить від дози опромінення, тобто є постійним на одиницю дози, незалежно від дози та потужності дози. МКРЗ пояснив свій вибір моделі наступним чином.

Оскільки про існування порогової дози невідомо, передбачається, що навіть найменші дози дають пропорційно малий ризик індукції малігнізації. Подібним чином, внаслідок нестачі відомостей про характер залежності «доза-ефект» при індукції малігнізації у людини, особливо при тих рівнях доз, які важливі для радіологічного захисту, Комітет не бачить ніякої практичної альтернативи для цілей радіологічного захисту прийняттю припущення про лінійну залежність між дозою та ефектом, а також того, що доза діє кумулятивно. Комітет знає, що припущення про безпороговість і про повну адитивність всіх доз можуть бути некоректними, але навряд чи вони будуть вести до недооцінки ризику [54].

Наукова коректність LNT моделі протягом останніх десятиліть була приводом для численних дискусій [55-59] і останнім часом набула нового інтересу. Частина дослідників пояснює існування LNT моделі концепцією про те, що низькі рівні радіації збільшують мутації, і, наче б то, збільшення кількості мутацій веде до пропорційного збільшення числа ракових захворювань.

З іншого боку, існує безліч свідчень на користь існування радіаційного гормезису, тобто проти LNT моделі, включаючи дослідження когорт, що вижили після атомних бомбардувань, фонової радіації, радіації навколишнього середовища, хворих на рак, медичного опромінення та професійного опромінення. Отже існують достатньо вагомі докази наявності радіаційного гормезису і його захисної дії при впливі низьких доз [60-62].

Порогова доза ушкоджуючого впливу іонізуючого випромінювання

За останні роки науковцями підсумовані дані про молекулярні і клітинні наслідки опромінення іонізуючим випромінюванням в малих дозах. Розглянуто ефекти на рівні геному - пошкодження ДНК і їх репарація, модифікація структури хроматину, апоптоз і цитогенетичні пошкодження, експресія генів і синтез нових білків, а також віддалені наслідки променевого впливу (мутагенез, неопластична трансформація та інше). Вивчено зміни структури і складу клітинних мембран, стимуляція проліферації, модифікація систем антиоксидантного захисту тощо.

При цьому зроблено висновок [15, 57-62], що порогова доза шкідливого впливу іонізуючого випромінювання таки існує, але величина її залежить від рівня біологічної інтеграції, на якому знаходиться об'єкт. При гострому опроміненні найбільш низький дозовий поріг відзначається на молекулярному і клітинному рівнях (цитогенетичні ефекти та репродуктивна загибель клітин відбувається при дозах в діапазоні 1 – 2 сГр). На рівні тканин, органів та цілого організму порогова ушкоджуюча доза підвищується і становить приблизно 10 – 20 сГр. В діапазоні доз нижче 1-2 сГр включно ушкоджуючих ефектів опромінювання не виявляються, а, навпаки, саме в цій області відзначаються прояви явища гормезису. Деякий ризик появляється при дозі від 2 до 5 сГр, де зареєстровано нижню межу тестованих цитогенетичних пошкоджень. Оскільки доза 2 – 5 сГр найбільшою мірою сприяє прояву радіоадаптивної відповіді, цей діапазон може бути названий зоною виразних «умовно сприятливих» і невиразних ушкоджуючих ефектів випромінювання. При пролонгованому та хронічному опроміненні зберігаються закономірності зростання дозового шкідливого порогу від молекулярного та клітинного рівня до рівня організму (для молекулярно-клітинного рівня цей поріг перевищує рівень природного радіаційного фону на 2 – 3 порядки, для рівня організму - до 5 порядків). При більшій дозі (особливо, починаючи з 10 сГр) вираженість несприятливих ефектів випромінювання зростає і з'являється значний ризик прояву віддалених наслідків. Рівень цитогенетичних пошкоджень підвищується і починає лінійно залежати від дози випромінювання, а ефекти гормезису та радіаційної адаптації виражені слабо або зовсім відсутні [63].

Специфікою прояву гормезису є різноманітність проявів ефектів і механізмів радіостимуляції на різних рівнях структурно-функціональної організації біологічних об'єктів - від молекулярного до рівня організму. Слід враховувати, що дози, які є стимулюючими на більш високому рівні, знаходяться на межі з пошкоджуючими дозами для нижчого рівня. Тобто якщо при певній дозі на рівні спостережуваного рівня розвиваються субпошкодження, то на нижчому рівні організації можуть відбуватися значні пошкодження об'єкту та його складових. Радіаційну стимуляцію на даному рівні можна розглядати як вторинну реакцію (наслідок) пошкоджень і наступних відновлюваних реакцій на попередньому, нижчому рівні. Отже треба розрізнювати інтервали стимулюючих/ушкоджуючих порогових доз для різних рівнів біологічної організації, причому чим вищий рівень інтеграції живого об'єкта, тим вищою є для нього стимулююча доза. Таким чином, реакція на вплив низьких доз може еволюціонувати від пошкодження на молекулярному рівні до корисної адаптаційної реакції на рівні всього організму. Якщо подивитись з іншого боку, при оцінці дії низьких доз іонізуючого випромінювання

неможна забувати, що стимуляція на рівні організму не завжди може вважатися синонімом корисності – кожна стимуляція взагалі і, зокрема, радіаційна, має свою "ціну", оскільки при стимуляції на рівні фізіологічних реакцій одночасно може відбуватися і накопичення генетичних порушень на клітинному рівні.

Зрозуміло, що механізми стимуляції на різних рівнях організації також відрізняються, отже більш високий рівень організації живого володіє більш широким спектром механізмів захисту і стимуляції, а отже і стимулюючі дози для нього будуть більш високими.

В опублікованому дослідженні зарубіжних радіобіологів було виявлено, що опромінення фібробластів рентгенівськими променями в дозі 1 мГр призводить до двократного підвищення рівня двониткових розривів ДНК [64]. Однак вказане збільшення рівня нерепарованих розривів було відзначено для тієї клітинної популяції, яка знаходиться у спокої. Як тільки клітини починали ділитися, показник повертався до норми. Автори зазначеної роботи вважають, що при цьому включався захисний механізм апоптозу, який елімінував клітини, що мали ушкодження, (як відомо, без проліферації клітин немає мутагенезу і канцерогенезу). З цієї точки зору виявлений феномен настільки малої дози, як 1 мГр, може розглядатися як стимуляція захисного механізму, який видаляє найбільш «слабкі клітини» (тобто клітини з найбільш слабкими механізмами репарації – такими, що індукція пошкоджень в них стає можливою навіть після «флюорографічної» дози). Як вважають авторитетні фахівці в галузі радіобіології [6, 15, 46-47], більшість ефектів, виявлених для найменших доз опромінення, можуть бути впевнено віднесені до стимулюючих (як це має місце, наприклад, у разі радіоадаптивної відповіді після впливу доз в діапазоні 0,2 – 20 мГр).

Результати вивчення опромінених когорт в результаті атомних бомбардувань, а також людей, що проживають в областях з підвищеним природним радіаційним фоном і в регіонах з високими рівнями радонової експозиції та ін. [54], демонструють в більшій кількості сприятливі, гормезисні ефекти радіації в малих дозах. Зокрема, автори [65] представили безліч фактів гормезису і наявності порогів не тільки для рідко-, але і для щільноіонізуючого випромінювання.

РЕЗУЛЬТАТИ ДОСЛІДЖЕНЬ
Гіпотеза одного з можливих механізмів адаптивної відповіді

Нами пропонується нова гіпотеза існування одного з молекулярних механізмів явища радіоадаптивної відповіді, спостережуваної при дії на клітини рідкоіонізуючих випромінювань в малих дозах. Вона полягає в наступному.

Головною причиною загибелі клітини є, як відомо, ушкодження ниток ДНК цієї клітини, які не репаруються, тобто, ушкодження її хроматину. Але хроматин клітини неоднорідний. Він може існувати в клітині і у вигляді гетерохроматину з максимальною мірою компактизації ниток ДНК, і у вигляді еухроматину зі значною мірою "розплітання" цих ниток, що необхідно для зчитування генетичної інформації. Ця думка знаходить підтвердження у авторів [5, 7, 9, 11]. Генетичний апарат активно функціонуючої клітини знаходиться в стані еухроматину і, отже, є більш уразливим для ушкоджуючих дій, чим, такий у неактивної клітини, що знаходиться в стані гетерохроматину, тобто в стані з максимальною мірою компактизації ниток ДНК. Тому при дії на клітину ушкоджуючих чинників включаються захисні механізми, і на начальному етапі клітина прагне перейти в найбільш компактний і менш уразливий стан хроматину, тобто в стан гетерохроматину.

Можливо, один із механізмів такого переходу клітин у новий режим функціонування пов'язаний з індукцією змін у конформаційній структурі хроматину, що, у свою чергу, приводить до змін у експресії генів [67, 68]. Вважається також [68, 69], що зміна конформації певних ділянок ДНК, в значній мірі, залежить від зміни концентрації низькомолекулярних іонів.

Таким чином, при дії на клітину ушкоджуючими чинниками в малих дозах і в певному інтервалі часу, необхідному для максимально повної компактизації хроматину, клітина мало ушкоджується або не ушкоджується взагалі, але сигнал про наявність ушкоджуючої дії виробляється. Це і обумовлює максимально можливий перехід хроматину клітини в гетерохроматин в якості реакції у відповідь з метою мінімізації можливого подальшого ушкодження клітини при великих дозах. Іншими словами, коли клітина опиняється під впливом малих доз ушкоджуючих чинників, вона має можливість оперативно, без значних для себе витрат перейти в стан гетерохроматину і, тим самим, істотно ослабити міру ушкодження ДНК при подальших значних рівнях ушкоджуючих чинників. Таким механізмом адаптивної відповіді клітини можна, зокрема, пояснити і неспецифічність реакції клітин на ушкоджуючі дії. На користь цього трактування механізму формування адаптивної відповіді говорять також дані про активацію полімерази АДФ рибози, що необхідно для реалізації обговорюваного ефекту як "палива" цього процесу.

Кількісна оцінка адаптивної відповіді

Застосування методу комп'ютерного мікроскопічного сканування для визначення клоногенної здатності клітин зробило можливим прецизійне визначення виживаності клітин ссавців при дозах, нижчих за 1 Гр. Ще одним, не менш важливим аспектом для розуміння поняття гормезису і адаптивної відповіді є моделювання та математичне описання вказаних процесів. Наразі актуальною проблемою є визначення параметрів, за допомогою яких можна було б кількісно описати і чисельно оцінити гормезисні та адаптивні ефекти в усіх діапазонах доз.

На сьогодні не існує загальноприйнятих кількісних характеристик, якими можна було б користуватися при визначенні наявності або ступеню вираженості проявів гормезису і адаптивної відповіді при розгляданні залежності «доза-ефект». Зазвичай в якості критерію для оцінки радіаційного ефекту при побудові і аналізі цієї залежності використовують генетичні пошкодження – хромосомні аберації, сестринські хроматидні обміни, мікроядерний тест, генні мутації, кількість ушкоджень або розривів ниток ДНК, виживаність клітин, тощо.

Нами пропонується нова розрахункова формула для оцінки адаптивного відгуку за допомогою індексу адаптивної відповіді (K) як функції ймовірності утворення генетичних пошкоджень при опроміненні біологічних об'єктів низькими дозами низької потужності рідкоіонізуючого випромінювання:

$$K = \frac{(P_a - P_c) + (P_t - P_c)}{P_{at} - P_c},$$

де P_c - ймовірність генетичних пошкоджень в контрольній групі клітин – клітин, які не опромінювалися, (стохастичні аберації); P_a - ймовірність генетичних пошкоджень після опромінення адаптуючою дозою; P_t - ймовірність генетичних пошкоджень після опромінення дозою, що тестувалася; P_{at} - ймовірність генетичних пошкоджень після опромінення спочатку адаптуючою дозою, потім дозою, що тестувалася.

За відсутності будь-якої адаптуючої дози $P_a - P_c = 0$, а ймовірність утворення генетичних пошкоджень $P_{at} = P_t$, тобто коефіцієнт адаптивної відповіді $K = 1$ (адаптивна відповідь відсутня); якщо значення коефіцієнта $K > 1$, це означає, що адаптивна відповідь має місце, і чим активніше працюють захисні механізми, тим більше значення K перевищує одиницю. Значення індексу адаптивної відповіді $K < 1$ відповідатимуть стану підвищення радіочутливості клітин.

Для перевірки розрахунків за допомогою запропонованої формули були використані літературні експериментальні дані, в яких в якості генетичних пошкоджень застосовувався анафазний метод аберації хромосом. Дослідження [70] проводили на асинхронній популяції клітин китайського хом'ячка лінії V-79, які знаходились в логарифмічній фазі росту. Тривалість мітотичного циклу клітин китайського хом'ячка складала 12 годин. Для опромінення використовували гама-випромінювання ^{60}Co з потужністю дози 18 сГр/хв. При вивченні адаптуючої відповіді інтервал між адаптуючою дозою і дозою, що тестувалася, складав 5 годин; фіксація проводилась через 5 годин.

При застосуванні вказаної формули припускалося, що ймовірність утворення хромосомних аберацій пропорційна відсотку клітин з хромосомними абераціями.

В таблиці 1 наведені результати експерименту на клітинах китайського хом'ячка по виявленню за допомогою цитогенетичного критерію залежності індукції адаптивної відповіді від дози попереднього опромінення при часі фіксації 5 годин. За наведеною вище формулою обчислено індекс (K) адаптивної відповіді.

Таблиця 1. Цитогенетичні пошкодження та індекс адаптивної відповідь при опроміненні клітин китайського хом'ячка в адаптуючій дозі 1 сГр, 5 сГр або 20 сГр і в дозі, що тестувалася, 100 сГр (час фіксації 5 годин).

Адаптуюча доза D_a, сГр	$P_c, \times 10^{-2}$	$P_a, \times 10^{-2}$	$P_t, \times 10^{-2}$	$P_{at}, \times 10^{-2}$	K
0	8,4± 0,7	-	21,0 ± 0,9	-	1
1	8,4± 0,7	9,3 ± 0,8	21,0 ± 0,9	21,3 ± 1,1	1,1
5	8,4± 0,7	10,3 ± 1,0	21,0 ± 0,9	21,0 ± 1,0	1,2
20	8,4± 0,7	14,4 ± 1,0	21,0 ± 0,9	17,0± 0,9	2,2

За результатами обчислення коефіцієнта адаптивної відповіді видно, що в інтервалі адаптуючих доз від 1 сГр до 20 сГр та при подальшому застосуванні дози, що тестувалася, 100 сГр найбільший індекс K для клітин китайського хом'ячка відповідав адаптуючій дозі 20 сГр. В експерименті було зазначено, що збільшення величини адаптуючої дози D_a не давало зменшення кількості хромосомних аберацій, а, навпаки, підвищувало радіочутливість клітин, тобто ймовірність утворення аберацій зростала, а, отже, і індекс адаптивної відповіді знижувався до 1. В разі, коли адаптуюча доза не застосовувалась ($D_a = 0$), індекс також дорівнював одиниці.

ПРО НЕПРАВОМІРНІСТЬ ЛІНІЙНОЇ ЕКСТРАПОЛЯЦІЇ ЕФЕКТІВ ВИСОКИХ ДОЗ НА НИЗЬКІ

Питання біологічної дії низьких доз іонізуючих випромінювань має багато аспектів, серед яких одним з найважливіших є проблема, пов'язана з екстраполяцією ефектів, які викликають великі дози, на біологічні реакції після опромінення в області низьких доз. В теперішній час накопичується все більше експериментальних даних, які свідчать про неправомірність лінійної екстраполяції ефектів високих доз на низькі.

Вважається, що найбільш негативним наслідком опромінення біологічних об'єктів є розвиток неопластичних трансформацій. Ряд дослідників [71-73] на основі численних експериментальних даних показали, що завдяки гормезису низькі дози опромінення, навпаки, захищають від раку, що приводить до «негативного

нахилу» в області низьких доз для кривої «доза-реакція». Високі ж дози гальмують захист, викликаючи у подальшому збільшення ризику виникнення раку із збільшенням дози. Таку залежність часто називають U- або J-подібною кривою реакції на дозу.

Аналізуючи цю криву в області низьких доз, автор [74] пропонує математичну модель оцінки відносного ризику (англ., RR – relative risk) розвитку негативних наслідків (зокрема, розвитку радіаційної неотрансформації) в горметичній зоні опромінення - HRR модель (англ., HRR – hormesis relative risk). Горметична дозова зона знаходиться трохи вище природного фонового опромінювання. Для цієї зони відзначається нелінійна залежність відносного ризику виникнення раку від дози. Підвищення дози більше за фонову активує захисні горметичні процеси, що запобігає збільшенню відносного ризику виникнення раку із зростанням дози вище одиниці. Горметичні процеси регулюються захисною міжклітинною та внутрішньоклітинною сигналізацією.

Захисна сигналізація, як передбачається, активується низькими дозами випромінювання з низьким рівнем ЛПЕ і забезпечує видалення аберрантних клітин з організму за допомогою p53-залежних та p53-незалежних сигнальних шляхів апоптозу та стимульованого імунітету [75-77]. Захисна сигналізація може також включати систему репарації ДНК, якщо перевищено поріг пошкоджень [78]. Можливими винятками з повного горметичного захисту є дуже маленькі та діти, які можуть не мати значного навантаження генетично нестабільних клітин, які беруть участь у передачі сигналів, пов'язаних із захисним p53-незалежним апоптозом.
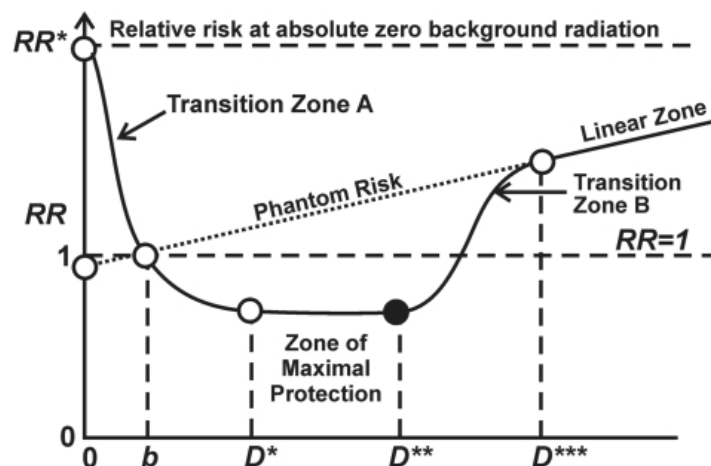

Рисунок 2. Схематичне зображення моделі HRR. По осі абсцис – загальна поглинута доза випромінювання (*D*), по осі ординат – відносний ризик (RR – relative risk) опромінювання. RR^* - відносний ризик при абсолютному нулі випромінювання. Шкала доз коливається від гіпотетичної абсолютної нульової дози опромінення (*D=0*) до доз, що перевищують дозу *b* (англ., background) природного радіаційного фону. Дози *D**, *D*** - граничні дози зони максимального горметичного захисту (zone of maximal protection), *D**** - права границя перехідної (транзитної) зони B – перехідної від зони максимального захисту до зони лінійної залежності відносного ризику від дози (linear zone).

Для активації захисної сигналізації в моделі HRR потрібні дози, вищі за природні фонові, причому вони варіюються у різних людей. Однак ще вищі дози (вищі за дозу D^{**}) інгібують захист, спричиняючи збільшення відносного ризику, оскільки променеве навантаження зростає до значення, при якому горметичний захист пригнічується, причому у всіх людей. З цього моменту передбачається, що починає працювати лінійна залежність «доза-ефект», яка екстраполюється до RR =1 при фоновому випромінюванні *b*. Саме так працює модель LNT для екстраполяції від високих доз до низьких.

Експоненціальне зростання RR до значення RR^{**} (перехідна зона A) із зменшенням дози нижче дози b підтверджується епідеміологічними даними про показники смертності від раку легень людини [79], що пов'язувалось зі зниженням здатністю клітин до репарації ДНК [78], втратою захисного апоптозу [77], та втратою стимуляції імунних функцій [80] при опроміненні в дозах, нижчих за природні фонові.

Горметична функція $RR(D)$ (середня для населення) може бути оцінена як результат ймовірнісного зважування між її двома компонентами: компонентом LNT (RR_{LNT}), який застосовується до незахищених гормезисом осіб, та горметичним компонент (RR_{HORM}), який застосовується до захищених осіб.

$$RR(D) = PROTEC(D) \cdot RR_{HORM}(D) + (1 - PROTEC(D)) \cdot RR_{LNT}(D)$$

Вагова функція *PROTEC(D)* є функцією ймовірності активації захисту (радіаційного гормезису) як функція дози D, яка перевищує природний фон. *PROTEC(D)* представляє частку опроміненої популяції, яка захищена через p53-незалежний апоптоз та індукований імунітет і, як очікується, залежить від генетичних та інших характеристик популяції. У перехідній зоні A коефіцієнт захисту *PROTEC*(D) збільшується від нуля до 1 і залишається на рівні 1 над зоною максимального захисту. У зоні переходу B цей коефіцієнт зменшується з 1 до 0. Для лінійної зони *PROTEC(D)=0*, і отже $RR(D)=RR_{LNT}(D)$.

Наведене рівняння використовується для характеристики середнього показника *RR* для населення та застосовується до доз опромінення, що перевищують природний фон. У горметичній зоні функція *RR*$_{HORM}$*(D)* дорівнює

$$RR_{HORM}(D) = 1 - PROFAC,$$

в інших зонах вона дорівнює 1. Для природного фонового опромінення *RR(D) =1.*

Коефіцієнт захисту (*PROFAC*) - це очікувана частка випадків раку, яких можна уникнути завдяки радіаційному гормезису. *PROFAC* стосується як захисного p53-незалежного апоптозу, так і активації імунного функціонування, але не стосується репарації ДНК [75].

Функція *RR*$_{LNT}$*(D)* переважно залежить від здатності клітин до репарації ДНК [75]. При дозах, що перевищують порогову дозу *D***, всі захисні реакції (p53-незалежний апоптоз та стимуляція імунної системи) пригнічуються, крім p53-залежної ДНК-репарації, і тоді відбувається перехід у так звану «лінійну зону». Лінійна зона відповідає тій дозовій області, в якій в основному проводилась більшість епідеміологічних досліджень, коли дослідники заявляли про залежність «доза-реакція» як про лінійну безпорогову (LNT) залежність.

Наявність перехідної зони A, коли відносний ризик різко зростає до значення *RR** при дозі опромінення, нижчій за фонове значення (*b*), свідчить про те, що пригнічення фонового випромінювання може згубно вплинути на життєздатність багатьох організмів.

Життя на нашій планеті еволюціонувало в умовах постійного впливу фонового іонізуючого випромінювання. Первинні радіонукліди, пов'язані з радіоактивним поділом, такі як ^{238}U, ^{232}Th, ^{235}U та ^{40}K, існували з часу створення Землі, тобто ще $4,6 \cdot 10^9$ років тому. За період еволюції Землі вплив фонового випромінювання знизився приблизно з 7,0 мГр/рік до 1,35 мГр/рік [81]. Живі організми еволюціонували протягом 3,8 мільярда років (одноклітинні) і 600 мільйонів років (багатоклітинні) під впливом постійної і доволі жорсткої радіації. Логічно припустити, що ті види, що вижили і продовжуюсь своє існування сьогодні, за час еволюції набули оптимальних механізмів захисту від іонізуючого випромінювання і виробили ефективні системи протистояння в межах діапазонів доз, які впливали протягом еволюції (2-20 мЗв/рік [82]).

Основною складовою нашого організму є вода. Основним ефектом дії енергії рідкоіонізуючого випромінювання є іонізація води з утворенням вільних радикалів - активних форм кисню (АФК), активних форм азоту (АФА), які є основними джерелами пошкодження ДНК. З іншого боку, саме вільні радикали, є важливими «другими месенджерами» в різних шляхах трансдукції сигналів, важливих для стимуляції імунітету, ініціації росту та проліферації клітин; тому вони відіграють важливу роль у багатьох життєво важливих процесах. Вільні радикали, що утворюються після впливу фонового випромінювання, можуть діяти як праймери для певних захисних метаболічних процесів, впливаючи тим самим на життєздатність усіх живих організмів. Таким чином, іонізуюче випромінювання в дозах, близьких до фонових, відіграє дуже важливу роль у визначенні адаптаційного потенціалу організму.

Цікавим і новим є той факт, що сучасна світова наукова спільнота виокремлює три види радіаційного гормезису [75] і на сьогодні класифікує їх таким чином.

1. Радіаційний гормезис (англ., Radiation hormesis): мала доза опромінення (легкий стрес) або помірна доза, що дається періодично з низькою швидкістю (періодичні легкі стреси), активізує захисні процеси та знижує рівень біологічної шкоди до спонтанного рівня і нижче.

2. Радіаційно обумовлений гормезис (англ., Radiation conditioning hormesis): ця форма гормезису стосується ситуації, коли мала доза опромінення (легкий стрес) або помірна доза, що вводиться з низькою швидкістю (тривалий легкий стрес), активує захисні процеси, які, в свою чергу, пригнічують шкоду від подальшої великої пошкоджуючої дози опромінення.

3. Пост-радіаційно обумовлений гормезис (англ., Radiation post-exposure conditioning hormesis): пошкодження, які зазвичай спричинені великою дозою опромінення або великою дозою якогось іншого стресора, зменшуються в результаті подальшого впливу невеликої дози опромінення (легкий стрес) або помірної дози, наданої з низькою швидкістю (неодноразові м'які стреси).

Вітчизняна література називає перший вид гормезису «радіаційним гормезисом», другий - «адаптивною відповіддю», обговорення третього виду нам не відомо, хоча, на наш погляд, запропонована класифікація має сенс і відповідає існуючим наразі експериментальним даним.

Сучасні дослідження [83-91] доводять, що модель радіаційного гормезису, на відміну від моделі LNT, передбачає, що низькі дози радіації спричиняють множинні адаптивні реакції, і такі реакції можуть запобігти певним негативним наслідкам для здоров'я. Що стосується здатності до репарації ДНК, результуючий ефект може залежати від балансу між швидкістю пошкодження ДНК (лінійної дози) та конкретними механізмами, що відповідають за клітинний захист. Отже, реакція на вплив низьких доз радіації може змінюватись - від пошкодження на молекулярному рівні до корисної адаптаційної реакції на рівні всього організму. Коли доза не перевищує 0,1 Гр, корисні результати, як правило, переважають шкідливі.

Горметичні ефекти низьких доз радіації, а також згубні ефекти великих доз та їх вплив на тривалість життя схематично продемонстровані автором [84] на рисунку 3.
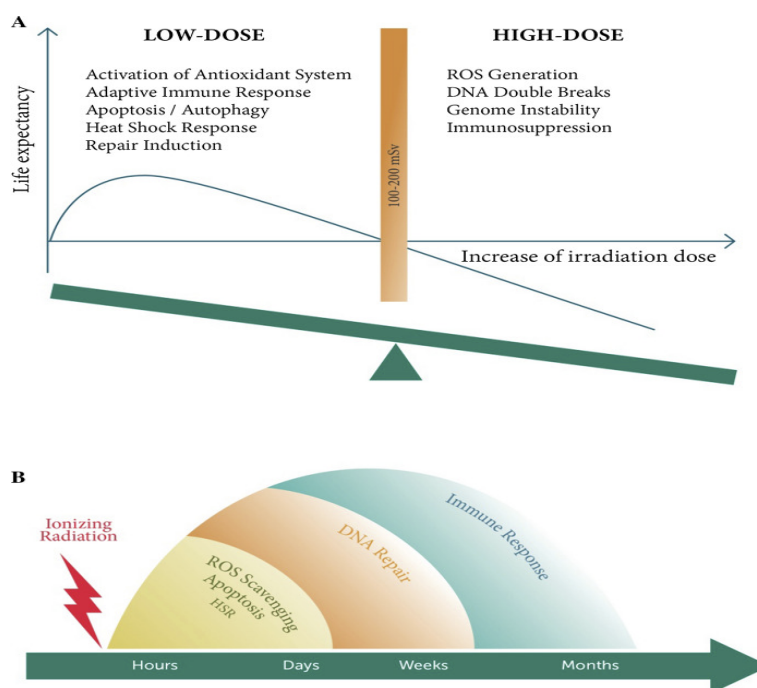
Рисунок 3. А – Залежність тривалості життя (life expectancy) від дози іонізуючого випромінювання (irradiation dose). В - Молекулярні механізми горметичної реакції організму на вплив низьких доз іонізуючого випромінювання (ionizing radiation).

Низькі дози, швидше за все, можуть стимулювати механізми відновлення, здатні нейтралізувати первинну шкоду (на клітинному рівні) та захистити весь організм від подальшого стресового впливу – радіаційного або іншого. Крім того, завдяки цим процесам, переднеопластичні та інші пошкоджені клітини можуть бути еліміновані за допомогою апоптозу, імунного нагляду та клітинної конкуренції. Ключові механізми цієї радіаційно-індукованої горметичної реакції включають: викид активних форм кисню (АФК), синтез білків тепловий шок, секрецію специфічних факторів росту та цитокінів, активацію рецепторів клітинної мембрани, а також компенсаторну проліферацію клітин. Ці процеси, ймовірно, опосередковані скоординованими адаптивними змінами в специфічних епігенетичних шляхах.

Таким чином, можна відзначити, що в протилежність теорії про те, що навіть низькі дози радіації є канцерогенними, широко опубліковані горметичні ефекти та дослідження молекулярних механізмів формування цих ефектів у сукупності демонструють, що низькі дози/потужності доз випромінювання з низьким рівнем ЛПЕ 1) активують захисні сигнальні шляхи апоптозу та стимулюють імунітет; 2) захищають від спонтанних хромосомних пошкоджень, мутацій, новоутворень та раку; 3) захищають від раку, спричиненого хімічним або радіаційним впливом у великих дозах.

Інтерес до горметичних ефектів низькодозової радіації не є лише теоретичним, він має також хорошу перспективу клінічного застосування. Одним із напрямків потенційного використання горметичних реакцій і адаптивної відповіді в терапії онкохворих є запобігання росту пухлини, інвазії та метастазування за допомогою загального опромінення тіла в низьких дозах за певний до застосування хіміо- або радіотерапії. Так, дослідники [92] продемонстрували, що якщо загальне опромінення тіла мишей дозою 75 мГр відбувалося перед щепленням клітин раку легенів Льюіса, обсяг трансплантованих пухлин був значно меншим, ніж у мишей, що одержали пухлину без попереднього впливу дозою 75 мГр. Крім того, 40-денна смертність була значно знижена, середня тривалість життя значно збільшена, а метастази пухлинних клітин значно зменшені у мишей, які отримували адаптивну дозу радіації перед лікуванням.

Ці дослідження припускають, по-перше, що стимульована низькими дозами імунна функція здатна запобігати раку, спричиненому радіацією великих доз, а також інгібувати ріст та інвазію імплантованих пухлинних клітин. По-друге, низькі дози радіації також можуть підвищити ефективність радіо- або хіміотерапії онкохворого не тільки за рахунок стимуляції імунітету для інгібування та елімінації залишкових після радіо- чи хіміотерапії ракових клітин, а і завдяки адаптивній відповіді нормальних тканини на побічну токсичність, індуковану терапевтичною дозою. Отже, явище радіоадаптивної відповіді може бути ефективно використано при променевій терапії і хіміотерапії, а саме, для захисту нормальних тканин, що оточують пухлину, від дії високих доз радіації, оскільки веде до підвищення як радіо-, так і хіміорезистентності нормальних клітин до дії генотоксичних чинників. Резистентність більшості злоякісних клітин після впливу малих доз радіації не змінюється. Фракційний вплив малих доз радіації на пухлину може індукувати збільшення радіочутливості злоякісних клітин.

ВИСНОВКИ

Радіаційний гормезис і адаптивну відповідь слід віднести до дуже важливих феноменів еволюційно сформованого біологічного захисту живих організмів від дії іонізуючого випромінювання.

В даний час гормезис і адаптивна відповідь загальновизнані як реальні та відтворювані біологічні явища.

Особливістю феномену радіаційного гормезису є багаторівневість та ієрархічність біологічних реакцій - від молекулярного до рівня організму. Отже, слід враховувати співвідношення шкідливих і корисних ефектів на кожному конкретному рівні організації живого, а також те, що одна і та ж доза може бути шкідливою на низькому рівні, але позитивною на більш високому.

Для подальшого з'ясування суті поняття «гормезис» необхідне застосування всіх існуючих науково-природничих методів з різних областей знань. На даному етапі досліджень існують експериментальні дані, описані біологічні і біохімічні механізми феномену, але практично відсутнє кількісне описання характеристик горметичних реакцій, фізико-математичне моделювання та інтерпретування їх молекулярних механізмів, що є дуже важливою основою для підтвердження або відкидання теорії гормезису як явища.

За останні два десятиліття вивчення гормезису накопичена велика кількість доказів існування горметичних реакцій, узагальнено численні концептуальні та експериментальні досягнення, молекулярні механізми утворення, але питання про визначення співвідношення гормезисних і ушкоджуючих ефектів при опроміненні біологічних об'єктів в малих дозах все ще залишається відкритим.

Численними експериментами продемонстровано, що горметична модель залежності «доза-реакція» робить набагато точніші прогнози відповіді живого об'єкту на опромінення (або на інші стресори) у зоні низьких доз, ніж лінійна безпорогова модель. Лінійна модель може адекватно описувати реакції лише в області високих доз, а, отже, екстраполяційне моделювання біологічних реакцій із зони високих доз на низькі не є коректним. На сьогоднішній день, ймовірніше всього, інтеграція лінійної моделі в зоні високих доз і гормезисної моделі в області низьких доз могла б найбільш вірно відтворити залежність «доза-ефект» для біологічних об'єктів різних рівнів організації.

Дослідження молекулярних механізмів гормезису та адаптивної відповіді може дати значний клінічний та соціальний ефекти. Один з напрямків потенційного використання цих феноменів є підвищення ефективності хіміо- та радіотерапії шляхом застосування низької адаптуючої дози за певний час до терапевтичної дози. При цьому завжди слід враховувати, що механізми радіаційно індукованої адаптивної відповіді відрізняються своєю складністю, множинністю і мінливістю: навіть для одного біологічного об'єкту існує багато шляхів розвитку горметичних реакцій та формування адаптивної відповіді, причому не завжди можливо передбачити, який з них буде реалізовано в умовах конкретного експерименту або клінічного випадку.

ORCID IDs

Maryna A. Bondarenko, https://orcid.org/0000-0002-0203-0161, **Olga V. Zaytseva,** https://orcid.org/0000-0002-0330-1568
Valeriya M. Trusova, https://orcid.org/0000-0002-7087-071X

REFERENCES

[1] M. Doss, M.P. Little, and C.G. Orton, Med. Phys. **41(7)**, 070601 (2014), https://doi.org/10.1118/1.4881095.
[2] L.E. Feinendegen, M. Pollycove, and R.D. Neumann, Dose-Response, **8,** 227–252 (2010), https://doi.org/10.2203/dose-response.09-035.
[3] J.A. Siegel, C.W. Pennington, and B. Sacks, J. Nucl. Med. **58**, 1–6 (2017), https://doi.org/10.2967/jnumed.116.180182.
[4] M. Pollycove, and L.E. Feinendegen, Hum. Exp. Toxicol. **22**, 290–306 (2003), https://doi.org/10.1191/0960327103ht365oa.
[5] Q. Cheng, N. Barboule, P. Frit, D. Gomez, O. Bombarde, B. Couderc, Guo-Sheng Ren, B. Salles, and P. Calsou, Nucl. Acids Res. **39**(22), 9605-9619 (2011), https://doi.org/10.1093/nar/gkr656.
[6] G.D. Zasukhina, Радиационная биология. Радиоэкология [Radiation biology. Radioecology], **1**, 58-63 (1999). (in Russian)
[7] C.Y. Kaminski, M. Dattoli, J.M. Kaminski, Dose Response **18**(2), 1559325820913788 (2020). https://doi.org/10.1177/1559325820913788
[8] I.A. Bodnarchuk, Радиационная биология. Радиоэкология [Radiation biology. Radioecology], **42**(1), 36-42 (2002). (in Russian)
[9] I.A. Bodnarchuk, Радиационная биология. Радиоэкология [Radiation biology. Radioecology], **43**(1), 19-28 (2003). (in Russian)
[10] M. Eidemuller, E. Holmberg, P. Jacob, M. Lundell, and P. Karlsson, Mutat Res. **775**, 1–9 (2015), https://doi.org/10.1016/j.mrfmmm.2015.03.002.
[11] A.N. Osipov, G. Buleeva, E. Arkhangelskaya, and D. Klokov, Mutat Res. **756**, 141–145 (2013), https://doi.org/10.1016/j.mrgentox.2013.04.016.
[12] M.S. Pearce, J.A. Salotti, M.P. Little, K. McHugh, C. Lee, K.P. Kim, N.L. Howe, C.M. Ronckers, P. Rajaraman, A.W. Craft, L. Parker, A. Berrington de González, Lancet. **380**, 499–505 (2012), https://doi.org/10.1016/S0140-6736(12)60815-0.
[13] W.H. Hsieh, I.F. Lin, J.C. Ho, and P.W. Chang, Br. J. Cancer, **117**, 1883–1887 (2017), https://doi.org/10.1038/bjc.2017.350.
[14] V.R. Bruce, S.A. Belinsky, K. Gott, and Y. Liu, Dose Response, **10**, 516–526 (2012), https://scholarworks.umass.edu/dose_response/vol10/iss4/9.
[15] D.M. Grodzinskiy, Yu.V. Shilina, O.M. Miheyev, and M.I. Gushcha, Проблеми безпеки атомних електростанцій і Чорнобиля [Problems of safety of nuclear power stations and Chornobyl], **3**(2), 17-28 (2005). (in Ukrainian)
[16] T. Ikushima, H. Aritomi H., and J. Morista, Mut. Res., **358**(2), 193-198 (1996), https://doi.org/10.1016/s0027-5107(96)00120-0.
[17] D.M. Grodzinskiy, Радіобіологія [Radiobiology], (Lybid, Kyiv, 2000), pp. 448. (in Ukrainian)

[18] L.H. Eydus, Биофизика [Biophysics], **50**(4), 693-703 (2005). (in Russian)
[19] M.A. Kadhim, S.R. Moore, and E.H. Goodwin, Mutation Research, **568**(1), 21-32 (2004), https://doi.org/10.1016/j.mrfmmm.2004.06.043.
[20] D.M. Spitkovskiy, Радиобиология [Radiobiology], **32**(3), 382-400 (1992). (in Russian)
[21] V.F. Mikhaylov, and G.D. Zasukhina, Успехи современной биологии [Advances in modern biology], **3**, 244-252 (2002). (in Russian)
[22] S.B. Chernikov, V.Ya. Gotlib, and I.I. Pelevina, Радиационная биология. Радиоэкология [Radiation biology. Radioecology], **33**(1(4)), 537-541 (1993). (in Russian)
[23] I.I. Pelevina, A.V. Aleshchenko, M.M. Antoshchina, V.A. Biryukov, O.B. Karyakin, O.V. Ktitorova, N.G. Minayev, A.M. Serebryanyi, Радиационная биология. Радиоэкология [Radiation biology. Radioecology], **57**(6), 565–572 (2017). (in Russian)
[24] C. Tomasetti, L. Li, and B. Vogelstein, Science, **355**, 1330–1334 (2017), https://doi.org/10.1126/science.aaf9011.
[25] J.R. Moffett, Hum. Exp. Toxicol., **29**(7), 539-43 (2010), https://doi.org/10.1177/0960327110369855.
[26] L. Pruimboom, and F.A.J. Muskiet, Medical Hypotheses, **120**: 28-42 (2018), https://doi.org/10.1016/j.mehy.2018.08.002.
[27] E.J. Calabrese, D.G. Gaurav, and K. Rachna, Dose-Response, **15**(2) (2017), https://journals.sagepub.com/doi/abs/10.1177/1559325817704760.
[28] I.I. Pelevina, V.V. Petushkova, V.A. Biryukov, A.V. Akleyev, Ye.A. Neyfah, N.G. Minayeva, O.V. Ktitorov, A.V. Aleshchenko, and R.I. Pleshakova, Радиационная биология. Радиоэкология [Radiation biology. Radioecology], **59**(3), 261-273 (2019).
[29] J.A. Horas, O.R. Olguin, and M.G. Rizzotto, Phys. Med. Biol. **50**, 1689-1701 (2005), https://doi.org/10.1088/0031-9155/50/8/005.
[30] A. Joubert, K. Gamo, Z. Bencokova, J. Gastaldo, W. Rénier, N. Chavaudra, V. Favaudon, C. Arlett, and N. Foray, Int. J. Radiat. Biol., **84**, 1–19 (2008), https://doi.org/10.1080/09553000701797039.
[31] O. Garzón, M.C. Plazas, and E.J. Salazar, Tecciencia, **9**(17), 15-22 (2014), http://www.scielo.org.co/pdf/tecci/v9n17/v9n17a03.pdf.
[32] V.G. Knigavko, M.A. Bondarenko, and O.V. Zaytseva, J. of Clinical and Diagnostic Research, **12**(11), XE01–XE04 (2018), https://doi.org/10.7860/JCDR/2018/36371.12236.
[33] L.E. Feinendegen, and R.D. Neumann, Hum Exp Toxicol., **25**(1), 11-7 (2006), https://doi.org/10.1191/0960327106ht579oa.
[34] V.F. Mikhailov, and G.D. Zasukhina, Успехи современной биологии [Advances in modern biology], **3**, 244-252 (2020), https://doi.org/10.31857/S0042132420030060. (in Russian)
[35] A.V. Brenner, M.D. Tronko, M. Hatch, et al., Environ. Health Perspect., **119,** 933–939 (2011), https://doi.org/10.1289/ehp.1002674.
[36] A. Farooque, R. Mathur, A. Verma, et al. Expert Rev. Anticancer Ther. **11**, 791–802 (2011), https://doi.org/10.1586/era.10.217.
[37] R.E.J. Mitchel, Nonlinearity in Biology, Toxicology, and Medicine, **2**(3), 173–183 (2004), https://doi.org/10.1080/15401420490507512.
[38] E.J. Broome, D.L. Brown, and R.E.J. Mitchel, Radiat. Res. **158**(2), 181–186 (2002), https://doi.org/10.1667/0033-7587(2002)158[0181:drfatl]2.0.co;2.
[39] E.J. Broome, D.L. Brown, and R.E.J. Mitchel, Int. J. Radiat. Biol. **75**, 681–690 (1999), https://doi.org/10.1080/095530099140014.
[40] V.P. Bond, L.E. Feinendegen, and J. Booz, Int. J. Radiat. Biol. **53**(1), 1–12 (1988), https://doi.org/10.1080/09553008814550361.
[41] D. Bhattarcharjee, Mut. Res. **358**, 231-235 (1996), https://doi.org/10.1016/s0027-5107(96)00125-x.
[42] A.N. Mikheyev, N.I. Gushcha, Yu.Yu. Malinovskiy, and D.M. Grodzinskiy, Докл. НАН Украины [Reports of the NAS of Ukraine], **10**, 177 – 174 (1998). (in Russian)
[43] O.M. Mikheyev, M.I. Gushcha, and Yu.V. Shilina, Фізіологія рослин в Україні на межі тисячоліть [Plant physiology in Ukraine at the boundary of the millenniums], **2**, 82-88 (2001). (in Ukrainian)
[44] A.N. Mikheyev, N.I. Gushcha, and Yu.V. Shilina, Радиационная биология. Радиоэкология [Radiation biology. Radioecology], **44**(3), 324-327 (2004). (in Russian)
[45] S. Tang, J. Liang, C. Xiang, Y. Xiao, X. Wang, J. Wu, G. Li, and R.A. Cheke., J. R. Soc. Interface. **16**(157) (2019), https://doi.org/10.1098/rsif.2019.0468.
[46] E.J. Calabrese, and L.A. Baldwin, Human Experiment. Toxicol., **19**, 2-31 (2000), https://doi.org/10.1191/096032700678815585.
[47] E.J. Calabrese, and L.A. Baldwin, Hum. Exp. Toxicol., **19**(1), 41-75 (2000), https://doi.org/10.1191/096032700678815602.
[48] V.G. Petin, I.I. Morozov, N.M. Kabakova, and T.A. Gorshkova, Радиационная биология. Радиоэкология [Radiation biology. Radioecology], **43**(2), 176-178 (2003). (in Russian)
[49] A. M. Kuzin, Идеи радиационного гормезиса в атомном веке [Radiation hormesis ideas in the atomic age], (Nauka, Moscow, 1995), pp. 158. (in Russian)
[50] R.M. Macklis, and B. Bresford, J. Nucl. Med. **32**, 350-359 (1991).
[51] C. Mothersill, and C. Seymour, Int J Radiat Biol. **95**(7), 851-860 (2019), https://doi.org/10.1080/09553002.2019.1589016.
[52] L.H. Eydus, and V.L. Eydus, Радиационная биология. Радиоэкология [Radiation biology. Radioecology], **41**(5), 627-630 (2001). (in Russian)
[53] E.L. Kendig, H.H. Le, and M.B. Scott., Int. J. Toxicol. **29**(3), 235-246 (2010), https://doi.org/10.1177/1091581810363012.
[54] C.Y. Kaminski, M. Dattoli, and J.M. Kaminski, Dose Response, **18**(2), 1559325820913788 (2020), 10.1177/1559325820913788.
[55] A.M. Vayserman, L.V. Mekhova, N.M. Koshel, and V.P. Voytenko, Радиационная биология. Радиоэкология [Radiation biology. Radioecology], **50**(6), 691-702 (2010). (in Russian)
[56] B. Sacks, and G. Meyerson, Health Phys. **116**(6), 807-816 (2019), https://doi.org/10.1097/HP.0000000000001033.
[57] E.J. Calabrese., and L.A. Baldwin, Hum. Exp. Toxicol. **19**(1), 76-84 (2000), https://doi.org/10.1191/096032700678815611.
[58] J.A. Siegel, C.W. Pennington, and B. Sacks, J. Nucl. Med. **58**(1), 1–6 (2017), https://doi.org/10.2967/jnumed.116.180182.
[59] A.M. Kellerer, Radiat Environ Biophys. **39**(1), 17-24 (2000), https://doi.org/10.1007/pl00007679.
[60] E.J. Calabrese, Mutat. Res. **511**(3), 181-9 (2002), https://doi.org/10.1016/s1383-5742(02)00013-3.
[61] E.J. Calabrese, Arch. Toxicol. **83**(3), 227-47 (2009), https://doi.org/10.1007/s00204-009-0411-5.
[62] M. Doss, Journal of Nuclear Medicine, **59**(12), 1786-1793 (2018), https://doi.org/10.2967/jnumed.118.217182.

[63] K. Rothkamm, and M. Lubrich, Proc. Natl. Acad. Sci. USA, **100**(9), 5057-5062 (2003), https://doi.org/10.1073/pnas.0830918100.

[64] T.P. Golivets, B.S. Kovalenko, and D.V. Volkov, Научные ведомости, Серия: Медицина. Фармация [Scientific statements, Series: Medicine. Pharmacy], **16**(135(19)), 5-13 (2012). (in Russian)

[65] L.A. Buldakova, and V.S. Kalistratova, Радиационное воздействие на организм – положительные эффекты [Radiation effects on the body - positive effects], (Inform-Atom, Moscow, 2005), pp. 246. (in Russian)

[66] P. Maguire, C. Mothersill, B. McClean, et al., Radiat. Res. **167**(4), 485-492 (2007), https://doi.org/10.1667/RR0159.1.

[67] S.A. Geraskin, Радиационная биология. Радиоэкология [Radiation biology. Radioecology], **35**(5), 563-571 (1995). (in Russian)

[68] D.M. Spitkovskiy, Радиационная биология. Радиобиология [Radiation biology. Radioecology], **32**(3), 382-400 (1992). (in Russian)

[69] V.K. Mazurik, and V.F. Mikhaylov, Радиационная биология. Радиоэкология [Radiation biology. Radioecology], **41**(3), 272-289 (2001). (in Russian)

[70] L.N. Shmakova, O.A. Zeid, T.A. Fadeyeva, Ye.A. Krasavin, and P.V. Kutsalo, Радиационная биология. Радиоэкология [Radiation biology. Radioecology], **40**(4), 405-409 (2000). (in Russian)

[71] E.J. Calabrese, and L.A. Baldwin, Trends. Pharmacol. Sci. **22**(6), 285-291 (2001), https://doi.org/1016/s0165-6147(00)01719-3.

[72] E.J. Calabrese, Toxicol Appl. Pharmacol. **197**(2), 125-136 (2004), https://doi.org/10.1016/j.taap.2004.02.007.

[73] E.J. Calabrese, Environ. Pollut. **138**(3), 379-412 (2005), https://doi.org/10.1016/j.envpol.2004.10.001.

[74] B.R. Scott, Dose-Response **6**(4), 333–351 (2007), https://doi.org/10.2203/dose-response.07-005.Scott.

[75] B.R. Scott, Dose-Response **5**(2), 131-141 (2007), https://doi.org/10.2203/dose-response.05-037.Scott.

[76] Y. Yao, and W. Dai, J. Carcinog. Mutagen. **5**, 1000165 (2014), https://doi.org/10.4172/2157-2518.1000165.

[77] B.R. Scott BR, and J. Di Palma, Dose-Response **5**(3), 230–255 (2007), https://doi.org/10.2203/dose-response.06-002.Scott.

[78] K. Rothkamm, and M. Löbrich, Proc. Nat. Acad. Sci. USA **100**(9), 5057-5062 (2003), https://doi.org/10.1073/pnas.0830918100.

[79] B.L. Cohen, Health Phys. **68**(2), 157-174 (1995), https://doi.org/10.1097/00004032-199502000-00002.

[80] L. Shu-Zheng, Dose Response **5**(1), 39-47 (2007), https://doi.org/10.2203/dose-response.06-108.Liu.

[81] A.M. Vaiserman, Dose Response **8**(2), 172–191 (2010), https://doi.org/10.2203/dose-response.09-037.Vaiserman.

[82] M. Tubiana, A. Aurengo, D. Averbeck, and R. Masse, Radiat. Environ. Biophys. **44**(4), 245-251 (2006). http://refhub.elsevier.com/S0009-2797(18)31101-3/sref2

[83] A. Vaiserman, A. Koliada, O. Zabuga, and Y. Socol, Dose Response **16**(3), 1559325818796331 (2018), https://doi.org/10.1177/1559325818796331.

[84] A. Vaiserman, J.M. Cuttler, and Y. Socol, Biogerontology, **22**, 145–164 (2021), https://doi.org/10.1007/s10522-020-09908-5.

[85] V. Calabrese, C. Cornelius, A.T. Dinkova–Kostova, E.J. Calabrese, and M.P. Mattson, Antioxid Redox Signal. **13**(11), 1763–1811 (2010), https://doi.org/10.1089/ars.2009.3074.

[86] Y. Shibamoto, and H. Nakamura, Int. J. Mol. Sci. **19**(8), 2387 (2018), https://doi.org/10.3390/ijms19082387.

[87] L.E. Feinendegen, Br. J. Radiol. **78**(925), 3-7 (2005), https://doi.org/10.1259/bjr/63353075.

[88] L.E. Feinendegen, M. Pollycove, and R.D. Neumann, Exp. Hematol. **35**(4S1), 37–46 (2007), https://doi.org/10.1016/j.exphem.2007.01.011.

[89] B.R. Scott BR, and S. Tharmalingam, Chem. Biol. Interact. **301**, 34–53 (2019), https://doi.org/10.1016/j.cbi.2019.01.013.

[90] B.M. Kim, Y. Hong, and S. Lee, Int. J. Mol. Sci. **16**(11), 6880–26913 (2015), https://doi.org/10.3390/ijms161125991.

[91] A.M. Vaiserman, Rejuvenation Res. **11**(1), 9–42 (2008), https://doi.org/10.1089/rej.2007.0579.

[92] S. Jin, H. Jiang, and L. Cai, Radiation Medicine and Protection **1**(1), 2-6 (2020). https://doi.org/10.1016/j.radmp.2020.01.004.

МОДЕЛЮВАННЯ МОЛЕКУЛЯРНИХ МЕХАНІЗМІВ ФОРМУВАННЯ РАДІАЦІЙНОЇ АДАПТИВНОЇ ВІДПОВІДІ

Марина А. Бондаренко[a], Ольга В. Зайцева[a], Валерія М. Трусова[b]

[a]Харківський національний медичний університет, пр. Науки, 4, Харків, 61022, Україна
[b]Харківський національний університет імені В.Н. Каразіна, пл. Свободи, 4, Харків, 61022, Україна

Явище адаптивної відповіді виражається у підвищенні стійкості біологічного об'єкта до високих доз мутагенів за умов попереднього впливу на нього цими (або іншими) мутагенами в малих дозах. Малі дози мутагена вмикають у живому об'єкті низку захисних механізмів, які одержали назву горметичних. Отже адаптивна відповідь і гормезис – це ланки одного ланцюга. Під радіаційним гормезисом розуміють загально позитивну дію рідкоіонізуючого випромінювання у діапазонах низьких доз та низьких потужностей доз на біологічні об'єкти. В роботі розглянуто феноменологію радіаційно індукованої адаптивної відповіді та радіаційного гормезису для біологічних об'єктів різних рівній організації, здійснено огляд існуючих теорій, які описують залежність «доза-ефект». Представлено гіпотезу, що пропонує один з механізмів формування радіаційної адаптивної відповіді клітин з урахуванням конформаційної структури хроматину. Проведено аналіз існуючих концепцій явища гормезису на основі моделювання молекулярних механізмів формування горметичних реакцій на низькодозові рідкоіонізуючі випромінювання. Розглянуто параметри, які можливо застосовувати для кількісного та графічного оцінювання феномену гормезису, а також запропоновано формулу для розрахунку коефіцієнту радіаційно індукованої адаптивної відповіді. Здійснено огляд математичних моделей, що описують радіаційний ризик виникнення генних мутацій та неопластичних трансформацій при низькодозовому опромінюванні когорт. Зроблено такі висновки: радіаційний гормезис і адаптивна відповідь загальновизнані як реальні та відтворювані біологічні явища, які слід віднести до дуже важливих феноменів еволюційно сформованого біологічного захисту живих організмів від дії іонізуючого випромінювання. «Горметична модель» залежності «доза-реакція» робить набагато точніші прогнози відповіді живого об'єкту на опромінення (або на інші стресори) у зоні низьких доз, ніж «лінійна безпорогова модель». Остання може адекватно описувати реакції лише в області високих доз, а, отже, екстраполяційне моделювання біологічних реакцій із зони високих доз на низькі не є коректним.

КЛЮЧОВІ СЛОВА: адаптивна відповідь, радіаційний гормезис, залежність доза-ефект, низькі дози радіації, ризик розвитку раку.

INSTRUCTIONS FOR PREPARING MANUSCRIPT IN EAST EUROPEAN JOURNAL OF PHYSICS

Nikita F. Author[a],*, Peter V. Co-author(s)[b],†

[a]Affiliation of first author
[b]Affiliation of second author (if different from first Authors)
*Corresponding Author: corresponding_authors@mail.com, [a]ORCID ID
†E-mail: co_authors@mail.com, [b]ORCID ID
Received October 25, 2020; revised November 25, 2020 accepted December 5, 2020

Each paper must begin with an abstract. The abstract should be typed in the same manner as the body text (see below). Please note that these Instructions are typed just like the manuscripts should be. The abstract must have at least **1800 phonetic symbols**, supplying general information about the achievements, and objectives of the paper, experimental technique, methods applied, significant results and conclusions. Page layout: the text should be printed on the paper **A4** format, at least **5 pages**, with margins of: **Top - 3, Bottom, Left and Right - 2 cm**. The abstract, keywords should be presented **in English** (only for foreign authors), **and Ukrainian**.
KEYWORDS: there, must, be, 5-10 keywords

This is introduction section. This paper contains instructions for preparing the manuscripts. The text should be prepared in "**doc" or "docx"** format.

INSTRUCTIONS

The text should be typed as follows:
• **title**: Times New Roman, 12 pt, ALL CAPS, bold, 1 spacing, centred;
• **authors**: name, initials and family names; Times New Roman, 12 pt, bold, 1 spacing, centred;
• **affiliation(s)**: Times New Roman, 9 pt, italic, 1 spacing, centred;
• **abstract**: Times New Roman, 9 pt, 1 spacing, justified;
• **body text**: Times New Roman, 10 pt, 1 spacing, justified; paragraphs in sections should be indented right (tabulated) for 0.75 cm;
• **section titles**: Times New Roman, 10 pt, bold, 1 spacing, centred, without numbering, one line should be left, blank above section title;
• **subsection titles**: Times New Roman, 10 pt, bold, 1 spacing, centred, without numbering in accordance to the section (see below), one line should be left blank above subsection title;
• **figure captions**: width of the figure should be 85 or 170 mm, Figures should be numbered (**Figure 1.**) and titled below Figures using sentence format, Times New Roman, 9 pt, 1 spacing, centred (if one line) or justified (if more than one line); one line should be left blank below figure captions;
• **table captions**: width of the table should be 85 or 170 mm, tables should be numbered (**Table 1.**) and titled above tables using sentence format, Times New Roman, 10 pt, 1 spacing, justified, Tables should be formatted with a single-line box around the outside border and single ruling lines between rows and columns; one line should be left blank below tables;
• **equations**: place equations centred, numbered in Arabic (1), flush right, equations should be specially prepared in **MathType** or "**Microsoft Equation"** one line should be left blank below and above equation.

Additional instructions

Numerated figures and tables should be embedded in your text and placed after they are cited. Only sharp photographs and drawings are acceptable. Letters in the figures should be 3 mm high. The figures should be presented in one of the following graphic formats: jpg, gif, pcx, bmp, tif.

REFERENCES

Cite references in AIP style (https://guides.lib.monash.edu/citing-referencing/aip). Numbering in the order of referring in the text, e.g. [1], [2-5], etc. References should be listed in numerical order of citation in the text at the end of the paper (justified), Times New Roman, 9 pt, 1 spacing.

Journal Articles
[1]   T. Mikolajick, C. Dehm, W. Hartner, I. Kasko, M.J. Kastner, N. Nagel, M. Moert, and C. Mazure, Microelectron. Reliab. **41**, 947-950 (2001), https://doi.org/10.1016/S0026-2714(01)00049-X.
[2]   S. Bushkova, B.K. Ostafiychuk, and O.V. Copaiev, Physics and Chemistry of Solid State. **15**(1), 182-185 (2014), http://page.if.ua/uploads/pcss/vol15/!1501-27.pdf. (in Ukrainian)
[3]   M. Yoshimura, E. Nakai, K. Tomioka, and T. Fukui, Appl. Phys. Lett. **103**, 243111 (2013), http://dx.doi.org/10.7567/APEX.6.052301.

E-print Resourses with Collaboration Research or Preprint
[4]   M. Aaboud et al. (ATLAS Collaboration), Eur. Phys. J. C, **77**, 531 (2017), http://dx.doi.org/10.1140/epjc/s10052-017-5061-9
[5]   Sjöstrand et al., *Comput. Phys. Commun.* **191,** 159-177 (2015), https://doi.org/10.1016/j.cpc.2015.01.024.
[6]   Boudreau, C. Escobar, J. Mueller, K. Sapp, and J. Su, (2013), http://arxiv.org/abs/1304.5639.

Books
[7]   S. Inoue, and K.R. Spring, *Video Microscopy*: *The fundamentals*, 2nd ed. (Plenum, New York, 1997), pp. 19-24.
[8]   I. Gonsky, T.P. Maksymchuk, and M.I. Kalinsky, *Біохімія Людини [Biochemistry of Man],* (Ukrmedknyga, Ternopil, 2002), pp. 16. (in Ukrainian)

Edited Books
[9]   Z.C. Feng, editor, *Handbook of Zinc Oxide and Related Materials: Devices and Nano Engineering, vol. 2*, (CRC Press/Taylor & Francis, Boca Raton, FL, 2012)

Book Chapters
[10] P. Blaha, K. Schwarz, G.K.H. Madsen, D. Kvasnicka, and J. Luitz, in: *WIEN2K, An Augmented Plane Wave Plus Local Orbitals Program for Calculating Crystal Properties,* edited by K. Schwarz (Techn. Universität Wien, Austria, 2001).
[11] M. Gonzalez-Leal, P. Krecmer, J. Prokop, and S.R. Elliot, in: *Photo-Induced Metastability in Amorphous Semiconductors*, edited by A.V. Kolobov (Wiley-VCH, Weinheim, 2003), pp. 338-340.
[12] A. Kochelap, and S.I. Pekar, in: *Теория Спонтанной и Стимулированной Хемилюминесценции Газов [Theory of Spontaneous and Stimulated Gas Chemiluminescence]* (Naukova dumka, Kyiv, 1986), pp. 16-29. (in Russian)

Conference or Symposium Proceedings
[13] C. Yaakov, and R. Huque, in: *Second International Telecommunications Energy Symposium Proceedings*, edited by E. Yow (IEEE, New York, 1996), pp. 17-27.
[14] V. Nikolsky, A.K. Sandler, and M.S. Stetsenko, in: *Автоматика-2004: Матеріали 11 Міжнародної Конференції по Автоматичному Управлінню [Automation-2004: Materials of the 11th International Conference on Automated Management]* (NUHT, Kyiv, 2004), pp. 46-48. (in Ukrainian)

Patent
[15] I.M. Vikulin, V.I. Irha, and M.I. Panfilov, Patent Ukraine No. 26020 (27 August 2007). (in Ukrainian)

Thesis / Dissertation
[16] R.E. Teodorescu, Ph.D. dissertation, The George Washington University, 2009.

Special Notes
1. Use International System of Units (SI system). 2. It is undesirable to use acronyms in the titles. Please define the acronym on its first use in the paper. 3. Refer to isotopes as ^{14}C, ^{3}H, ^{60}Co, etc.

Наукове видання

СХІДНО-ЄВРОПЕЙСЬКИЙ ФІЗИЧНИЙ ЖУРНАЛ
Номер 2, 2021

EAST EUROPEAN JOURNAL OF PHYSICS
No 2, 2021

Збірник наукових праць
англійською та українською мовами